23. Lecture 23: 3D vision

23.1 Introduction to 3D Perception from 2D Images

In this part of the course we explore how deep neural networks can process and predict 3D information from various inputs, particularly focusing on inferring three-dimensional structures from two-dimensional images. Unlike classical computer vision tasks that operate strictly in 2D, 3D vision tasks aim to reconstruct or understand the three-dimensional structure of the world. These tasks are essential in applications ranging from autonomous navigation to augmented reality.

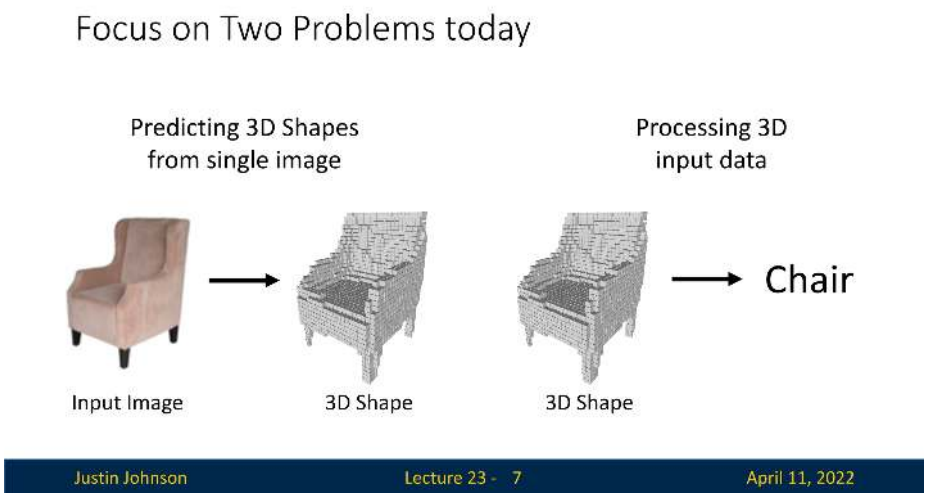

Figure 23.1: Left: Inferring 3D shape (voxel grid) from a single 2D image. Right: Classifying an object from its 3D representation.

23.1.1 Core Tasks in 3D Vision

In this chapter, our main focus will be on two core 3D vision tasks:

1. **3D Shape Prediction:** Given a single 2D image (e.g., of an armchair), the model predicts a corresponding 3D structure, such as a voxel grid that represents the shape of the object. This task is inherently ill-posed due to the loss of depth information in the 2D projection.
2. **3D-Based Classification:** Given a 3D representation (e.g., a voxel grid), the model predicts the semantic class of the object (e.g., "armchair"), showing understanding from structural geometry.

Beyond these core problems, 3D vision encompasses a broad range of challenges such as motion estimation from depth, simultaneous localization and mapping (SLAM), multi-view reconstruction, and more. Importantly, due to the strong geometric structure of the 3D world, many classical vision algorithms (e.g., stereo triangulation) remain highly relevant and are often integrated with or benchmarked against learning-based methods.

23.1.2 3D Representations

A variety of representations can capture the geometry of 3D objects. While differing in format, all serve the common goal of describing shape and structure in three dimensions:

- **Depth Map:** A 2D grid where each pixel stores the distance (in meters) from the camera to the nearest surface point along the ray passing through that pixel. Captured by RGB-D sensors (e.g., Microsoft Kinect), these are often called *2.5D* images since they only encode visible surfaces, not occluded regions.
- **Voxel Grid:** A 3D array of binary or real-valued occupancies representing whether a volume element (voxel) is occupied.
- **Point Cloud:** A sparse set of 3D points capturing surface geometry.
- **Mesh:** A polygonal surface composed of vertices, edges, and faces—typically used in graphics.
- **Implicit Surface:** A continuous function (e.g., signed distance function) where the zero-level set defines the surface of the object.

Despite differing computational properties and storage formats, all these representations aim to capture the same underlying 3D structure.

23.2 Predicting Depth Maps from RGB Images

One of the most accessible and widely studied 3D vision tasks is estimating a dense depth map from a single RGB image. This process, known as *monocular depth estimation*, aims to assign a depth value to each pixel, producing a 2.5D representation of scene geometry from a monocular input. The task is fundamentally *ill-posed*, as multiple 3D scenes can correspond to the same 2D projection, making monocular depth estimation a challenging problem that requires strong visual priors.

A common and effective architectural design for this task is the **fully convolutional encoder-decoder network**, which is well-suited to dense prediction tasks. These models process an input image through an encoder to extract semantically rich features and subsequently reconstruct a dense depth map via a decoder that upsamples these features to the input resolution. The fully convolutional nature of this pipeline ensures that the spatial correspondence between input pixels and output predictions is preserved, enabling pixel-aligned depth estimation.

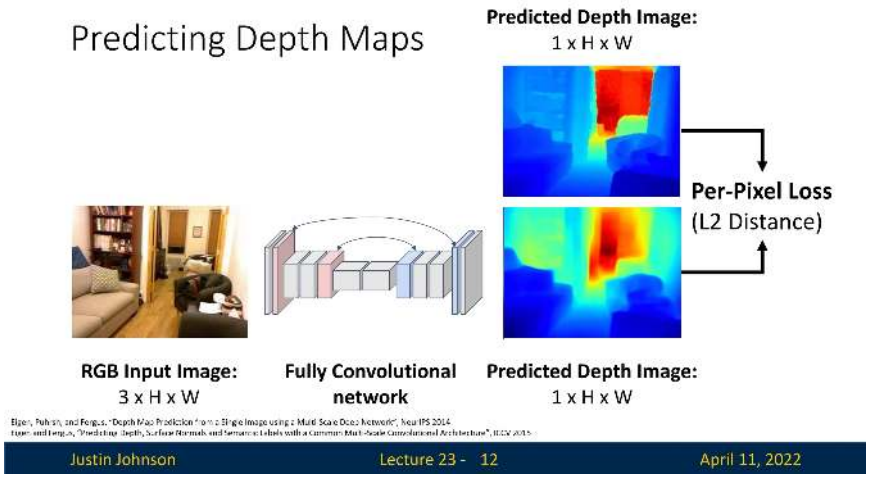

Figure 23.2: Naive approach to monocular depth prediction using a fully convolutional encoder-decoder network with pixelwise ℓ_2 loss.

The **encoder** typically consists of a convolutional backbone (e.g., ResNet) pretrained on large-scale classification datasets like ImageNet. Through successive layers of strided convolutions, the encoder compresses the spatial resolution of the input while increasing the semantic abstraction and receptive field. This enables the network to aggregate both local texture and global scene layout, capturing information necessary for reasoning about object scale, occlusion, and perspective.

The **decoder** reverses this spatial compression, gradually upsampling the feature maps to predict a dense depth map. In U-Net-style architectures, *skip connections* are employed to concatenate feature maps from early encoder layers with corresponding decoder stages, facilitating the recovery of fine-grained details such as object boundaries and thin structures. This *coarse-to-fine* decoding strategy is particularly effective in reconciling global context with local spatial accuracy.

Several influential models build upon this framework:

- **MiDaS** [511] emphasizes generalization across diverse datasets. Later versions of MiDaS replace convolutional encoders with *Vision Transformers (ViTs)*, leveraging global self-attention to capture long-range dependencies and scene-level structure. This shift enables more coherent depth maps, particularly in unfamiliar environments.
- **BTS (From Big to Small)** [320] enhances the decoder with *local planar guidance (LPG)* modules. These modules predict local plane parameters at multiple resolutions, guiding the reconstruction of depth maps by assuming piecewise planar geometry—a useful trait we can use for scenes with man-made structures or flat surfaces.
- **DPT (Dense Prediction Transformer)** [510] combines a ViT encoder with a convolutional decoder, explicitly designed for dense prediction tasks. DPT treats the image as a sequence of patches from the outset, enabling early global context aggregation. The decoder then reconstructs high-resolution outputs while retaining global consistency, resulting in state-of-the-art depth estimation performance on several benchmarks (at the time of publication).

While the architectural choices vary across models, the core principles remain consistent: extract semantically meaningful, globally aware features with the encoder; restore spatial detail and pixelwise correspondence with the decoder. These systems have made monocular depth estimation viable for real-time applications such as AR, robotics, and autonomous navigation, where dense 3D understanding from a single image is both efficient and essential.

Loss Function and the Limitations of Absolute Depth Regression

A foundational approach to monocular depth estimation is to directly regress the ground truth depth using a pixel-wise ℓ_2 loss:

$$\mathscr{L}_{\text{depth}} = \frac{1}{N}\sum_{i=1}^{N}\left(d_i - \hat{d}_i\right)^2,$$

where d_i denotes the ground truth depth and $\hat{d}_i$ is the predicted depth at pixel i, for a total of N pixels. This objective treats depth estimation as a supervised regression task, optimizing the per-pixel distance between prediction and annotation.

Scale-Depth Ambiguity and the Need for Invariant Losses

Despite its simplicity, the ℓ_2 loss fails to account for a fundamental limitation in monocular depth estimation: *scale-depth ambiguity*. Given only a single RGB image, there exist infinitely many 3D scenes that could yield the same 2D projection. For example, a small object placed close to the camera may appear identical in the image to a larger object situated farther away. This ambiguity makes the estimation of absolute scale from monocular input fundamentally ill-posed.

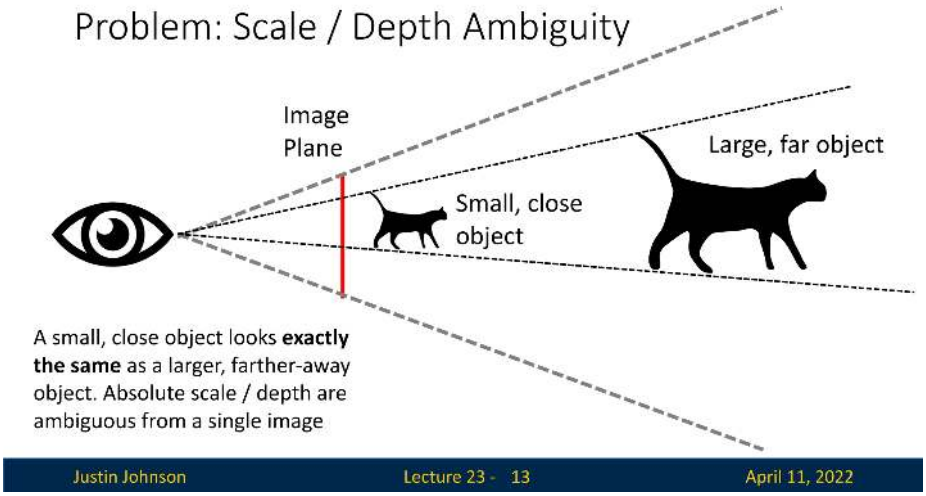

Figure 23.3: Scale-depth ambiguity in monocular images: a nearby small toy cat and a distant real cat can produce indistinguishable 2D projections.

While cues such as object size priors, vanishing points, or scene layout may offer some information, the absolute scale remains ambiguous without auxiliary data. Consequently, modern methods replace or augment the naïve ℓ_2 objective with loss functions that are *invariant to scale and shift* and that emphasize *relative structure*.

Scale-Invariant Log-Depth Loss

Monocular depth estimation suffers from *scale-depth ambiguity*: an image alone does not reveal whether a small object is nearby or a large object is far away. This ambiguity renders absolute depth supervision fundamentally ill-posed without geometric cues. To address this, [141] proposed a *scale-invariant loss* that focuses on preserving *relative scene structure* while remaining agnostic to global depth scale.

Let $\hat{d}_i$ and d_i denote the predicted and ground truth depth at pixel i, respectively. Define the log-space residual at each pixel as

$$\delta_i = \log \hat{d}_i - \log d_i = \log \left(\frac{\hat{d}_i}{d_i} \right).$$

This transforms multiplicative depth errors—such as those caused by an overall scaling mistake—into additive biases in log space. For example, if all predictions are off by a constant factor s, then $\delta_i = \log s$ for all i.

The scale-invariant loss is given by:

$$\mathscr{L}_{\text{SI}} = \frac{1}{n} \sum_{i=1}^{n} \delta_i^2 - \frac{1}{n^2} \left(\sum_{i=1}^{n} \delta_i \right)^2.$$

The first term penalizes pixelwise errors in log-depth, while the second term subtracts the squared mean residual. This centering step ensures that uniform log-space errors—i.e., global scaling shifts—do not contribute to the loss. In the case where $\hat{d}_i = s \cdot d_i$ for all i, we have $\delta_i = \log s$ and the two terms cancel exactly, yielding zero loss.

Pairwise Interpretation

An equivalent expression of the same loss emphasizes its structural nature:

$$\mathscr{L}_{\text{SI}} = \frac{1}{n^2} \sum_{i,j} \left[\left(\log \hat{d}_i - \log \hat{d}_j \right) - \left(\log d_i - \log d_j \right) \right]^2.$$

Here, the loss is computed over all pixel pairs, enforcing that the *difference in predicted log-depth* between any two pixels matches the difference in ground truth log-depth. This pairwise comparison naturally preserves the *relative depth ordering and ratios* across the image, which define the 3D scene structure up to scale.

Weighted Loss for Training

In practice, [141] used a weighted variant of the loss to trade off scale sensitivity and structure preservation. The training objective is:

$$\mathscr{L}_{\text{train}} = \frac{1}{n} \sum_{i} \delta_i^2 - \lambda \cdot \frac{1}{n^2} \left(\sum_{i} \delta_i \right)^2,$$

where $\lambda \in [0,1]$ determines how strongly the loss penalizes global scale errors. Setting $\lambda = 0$ recovers the standard log-MSE, while $\lambda = 1$ gives the fully scale-invariant loss. The authors found $\lambda = 0.5$ to offer a good balance—preserving global scale roughly while improving structural coherence and visual quality of the depth maps.

Why a Single Global Scale Correction Suffices

Monocular images lack metric information, so networks often make consistent *global* depth errors—predicting all depths as uniformly too large or too small. This happens because, without geometric supervision, the model can recover scene structure (e.g., which objects are closer) but not absolute scale.

Importantly, such scale errors are not local: the network does not typically stretch some parts of the scene while shrinking others. Instead, the entire scene is scaled by a single factor s, yielding predictions $\hat{d}_i = s \cdot d_i$ for all pixels i. For instance, if a model interprets a real cat as a small nearby toy, it will likely interpret a real car as a small toy car—misestimating scale consistently across objects and spatial regions.

This uniformity arises because the only available supervision—the ground truth depth—reveals the correct scale globally. Thus, if the network makes a pure scaling mistake, it will affect all depths equally, and a single correction factor suffices to align prediction with ground truth:

$$\frac{\hat{d}_i}{\hat{d}_j} = \frac{s \cdot d_i}{s \cdot d_j} = \frac{d_i}{d_j}.$$

The *scale-invariant loss* captures this by canceling out any constant log-depth offset across the image. It ensures the network is trained to preserve relative structure, while ignoring inevitable global scale ambiguity in monocular input.

Scale and Shift-Invariant Losses in MiDaS and DPT

Training monocular depth models on diverse datasets poses a core challenge: different datasets often encode depth with varying units, unknown camera baselines, or arbitrary scale and shift. For example, structure-from-motion yields depths up to scale, while stereo systems may produce disparities with dataset-specific offsets. Comparing predictions directly to such ground truth is ill-defined.

To address this, MiDaS [511] and DPT [510] adopt a *scale and shift invariant objective* that aligns predictions to ground truth before measuring error. Specifically, they operate in *inverse depth* (disparity) space—numerically stable and compatible with diverse sources—and fit an affine transformation to the predicted disparity $\hat{d} \in \mathbb{R}^N$ to match the ground truth $d \in \mathbb{R}^N$. The aligned prediction is given by:

$$\hat{d}_{\text{aligned}} = a\hat{d} + b,$$

where $a \in \mathbb{R}$ (scale) and $b \in \mathbb{R}$ (shift) are computed via closed-form least-squares.

Robust Trimmed MAE and Multi-Scale Gradient Losses

Once aligned, the model minimizes two complementary objectives that address distinct challenges in real-world training data:

1. Trimmed Mean Absolute Error (tMAE). Rather than computing loss over all pixels, MiDaS and DPT discard the highest residuals—typically the top 20%—and compute the L1 error over the remaining high-confidence set $\mathscr{I} \subset \{1,\ldots,N\}$:

$$\mathscr{L}_{\text{tMAE}}(d,\hat{d}) = \frac{1}{|\mathscr{I}|} \sum_{i \in \mathscr{I}} \left| a\hat{d}_i + b - d_i \right|.$$

This trimmed loss improves robustness in two ways. First, the use of L1 error prevents extreme residuals from dominating the loss—unlike L2, which excessively penalizes large errors. Second, trimming ensures that corrupted or misaligned pixels (e.g., due to missing depth, motion blur, or sensor artifacts) do not influence training. In effect, it converts noisy datasets into reliable training signals by emphasizing clean, consistent regions first, and gradually incorporating harder cases as the model improves.

2. Multi-Scale Gradient Matching. While the trimmed MAE loss ensures accuracy on reliable pixels, it does not capture how depth *changes* across space—that is, it ignores the local geometry of surfaces. To remedy this, MiDaS and DPT incorporate a *multi-scale gradient loss* that encourages the predicted depth map to exhibit the same structural transitions and surface boundaries as the ground truth.

The *depth gradient* at a pixel refers to the rate of change in depth with respect to its horizontal and vertical neighbors. In flat, smooth regions (e.g., walls, floors), depth changes slowly and the gradient is small. At object boundaries or depth discontinuities (e.g., the edge of a chair or the silhouette of a person), depth shifts abruptly and the gradient is large. Thus, gradients serve as a proxy for *geometry*: they capture where and how the scene bends, steps, or ends.

Mathematically, the spatial gradient ∇d_i is computed using finite differences in the x and y directions—typically as:

$$\nabla d_i = (d_{i+\hat{x}} - d_i,\ \ d_{i+\hat{y}} - d_i)\,,$$

where $\hat{x}$ and $\hat{y}$ denote offsets to right and bottom neighbors. This simple local operation reveals the slope of the depth surface around each pixel.

The multi-scale gradient loss compares these gradients between prediction and ground truth at various spatial resolutions:

$$\mathscr{L}_{\text{grad}} = \sum_{s} \frac{1}{N_s} \sum_{i=1}^{N_s} \left\| \nabla \hat{d}_i^{(s)} - \nabla d_i^{(s)} \right\|_1 .$$

The use of an L1 norm ensures robustness to local mismatches. The summation over scales s (e.g., full, half, quarter resolution) allows the model to reason about both coarse structure (e.g., floor-to-wall transitions) and fine details (e.g., edges of thin objects).

Why it works: Traditional pixel-wise losses tend to average out sharp transitions, producing overly smooth or blurry depth maps. Gradient supervision counteracts this by explicitly penalizing structural mismatches. It teaches the model not only to match depth values, but to replicate the *contours and discontinuities* that define the geometry of the scene.

In effect, this loss forces the network to answer: *Where do depth changes occur? How sharply? Do they match real-world object boundaries?* The result is depth predictions with sharper edges, more accurate occlusions, and higher geometric fidelity—particularly important in zero-shot transfer settings where structure is more reliable than absolute scale.

Summary

While pixel-wise ℓ_2 loss offers a straightforward entry point to monocular depth estimation, it fails to resolve the ill-posed nature of global scale recovery. Modern approaches instead adopt *scale- and shift-invariant losses* in log-depth or inverse-depth space, often augmented with *gradient structure terms*. These advances—combined with diverse training data and stronger architectures—have led to state-of-the-art results in monocular depth estimation across benchmarks such as KITTI, NYUv2, and ETH3D.

23.3 Surface Normals as a 3D Representation

In addition to depth maps, another powerful per-pixel 3D representation is that of *surface normals*. For each pixel in the input image, the goal is to estimate a 3D unit vector that represents the orientation of the local surface at that point in the scene. Surface normals are tightly linked to the underlying geometry of the object and provide a complementary view to depth.

Unlike depth, which encodes the distance between the camera and scene points, surface normals capture *orientation*, offering critical cues for understanding shape, curvature, and object boundaries.

Visualizing Normals

Since each surface normal is a unit vector in $\mathbb{R}^3$, they can be visualized as RGB images by mapping the x, y, and z components of each normal vector to the red, green, and blue color channels, respectively. This visualization provides intuitive insight into the orientation of different surfaces.

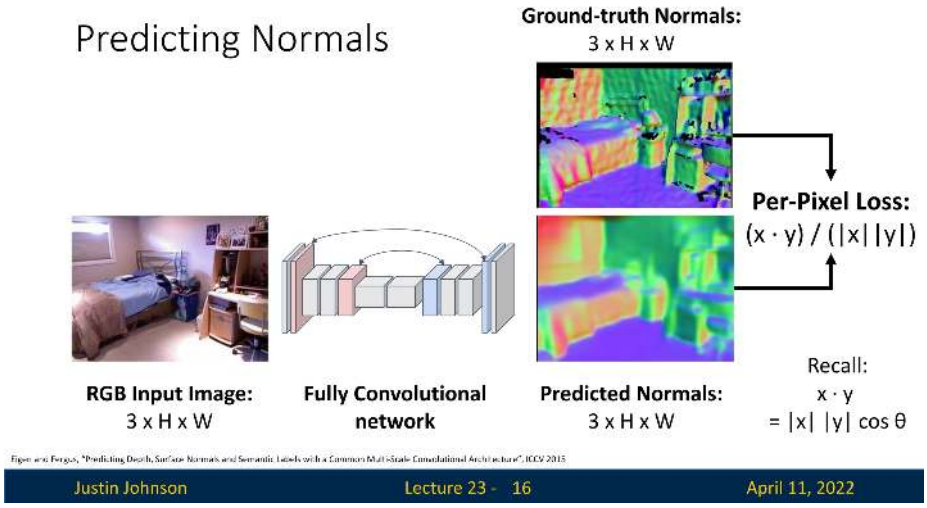

Figure 23.4: Visualizing surface normals: blue indicates upward-facing normals (e.g., floor, bed top), red and green indicate horizontal orientations. Mixed colors reflect diagonal or mixed-direction normals.

Learning Surface Normals

Similar to depth prediction, surface normal estimation can be framed as a dense regression task using a fully convolutional network. The network predicts a unit vector $\hat{\mathbf{n}}_i \in \mathbb{R}^3$ for each pixel i, and the objective is to align it with the corresponding ground truth normal $\mathbf{n}_i \in \mathbb{R}^3$. Since the predicted and ground truth vectors should have the same direction regardless of scale, a natural loss function is the cosine similarity loss:

$$\mathscr{L}_{\text{normal}} = \frac{1}{N}\sum_{i=1}^{N}\left(1 - \frac{\hat{\mathbf{n}}_i \cdot \mathbf{n}_i}{\|\hat{\mathbf{n}}_i\|_2 \cdot \|\mathbf{n}_i\|_2}\right),$$

where $\cdot$ denotes the dot product and $\|\cdot\|_2$ is the Euclidean norm. Note that since ground truth normals are unit vectors, predicted vectors are often explicitly normalized before loss computation.

Multi-Task Learning

In practice, tasks like dense segmentation and surface normal prediction are often trained jointly in a multi-task setup, sharing the same encoder but having separate decoders. This setup encourages the model to learn a richer and more consistent geometric understanding of the scene.

Limitations

While both depth and surface normals provide dense and informative representations of the visible geometry in an image, they share a critical limitation: they are inherently restricted to *visible surfaces*. Occluded regions, hidden backsides, and self-occlusions are not represented, leading to incomplete scene understanding. To address this, more global 3D representations such as voxels, point clouds, or meshes are necessary, as they model complete volumetric structure beyond the image plane.

23.4 Voxel Grids

To model 3D geometry beyond visible surfaces, one of the most intuitive volumetric representations is the *voxel grid*. A voxel grid discretizes 3D space into a cubic lattice of resolution $V \times V \times V$, where each voxel encodes occupancy information—typically as a binary value: 1 if the voxel is occupied by an object, and 0 otherwise. This can be viewed as the 3D analog of a 2D binary segmentation mask, but extended to volumetric space.

Voxel grids offer a conceptually simple and regular structure, making them attractive for early 3D learning pipelines. The representation is reminiscent of how objects are composed in voxel-based environments such as Minecraft, where entire scenes are built from discrete blocks.

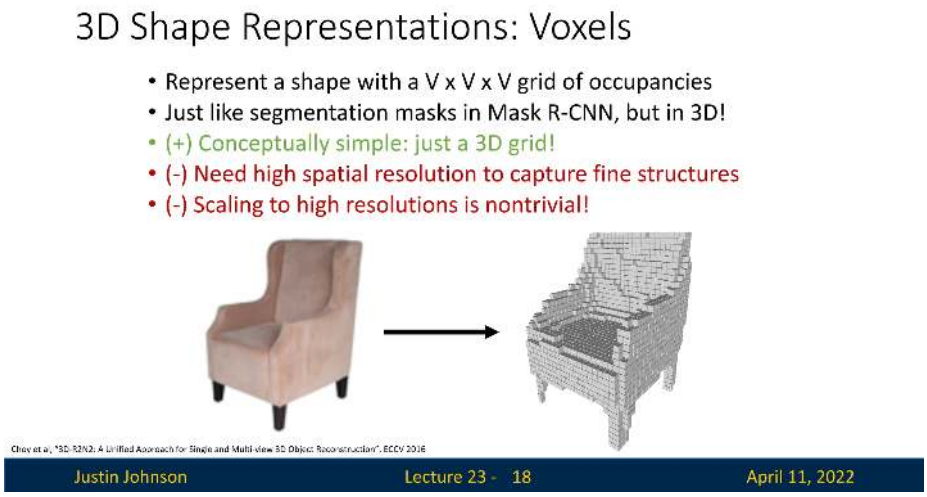

Figure 23.5: Voxel grids: Pros and cons. Left: regular grid and simplicity of representation. Right: loss of detail in high-frequency regions such as armrests of the sofa, due to limited resolution.

Advantages

The voxel grid format enables straightforward adaptation of classical CNN-based architectures to 3D data by replacing 2D convolutions with 3D convolutions. Since the voxel grid is regular and aligned to a grid structure, operations like pooling, upsampling, and convolution generalize naturally from 2D to 3D.

Limitations

A critical downside of voxel-based representations is their *poor scalability with resolution*. The memory and computational cost of processing a voxel grid scales cubically with resolution: storing a grid of resolution V requires $O(V^3)$ space. This rapidly becomes intractable for high-resolution scenes or objects, and fine details are lost at coarse voxel resolutions.

3D Convolutional Processing

Similar to 2D convolution, a 3D convolution applies a local filter over spatial neighborhoods in the voxel grid. The kernel is a 3D volume of shape $k \times k \times k$ (typically $k = 3$ or 5), and it slides across the grid to compute local features:

$$y(i,j,k) = \sum_{u,v,w} x(i+u, j+v, k+w) \cdot w(u,v,w),$$

where x is the input voxel grid or feature map, w is the learned 3D kernel, and y is the resulting activation map. These operations can be stacked in deep 3D convolutional networks to perform classification, segmentation, or shape completion.

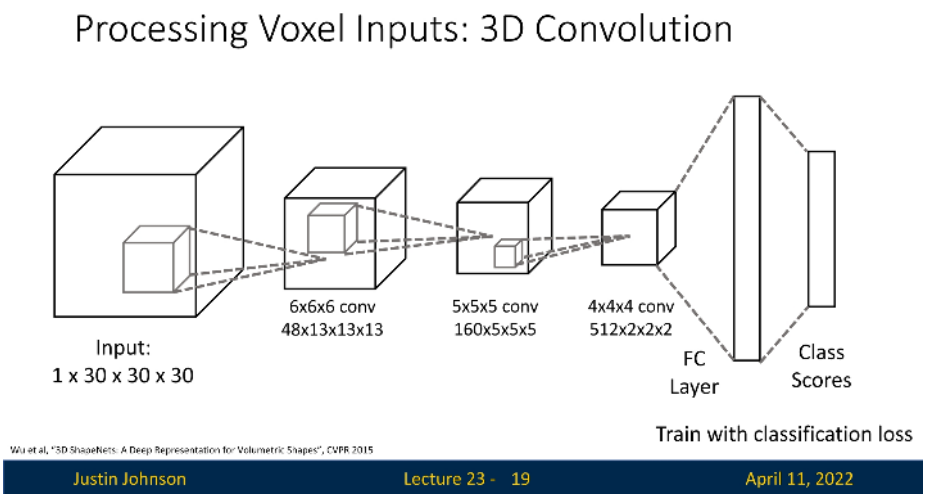

Figure 23.6: Processing voxel inputs using 3D convolutions for shape classification. The input is a $30 \times 30 \times 30$ occupancy grid representing the 3D shape. The network applies successive 3D convolutions: a $6 \times 6 \times 6$ kernel producing a $48 \times 13 \times 13 \times 13$ feature volume, followed by a $5 \times 5 \times 5$ kernel yielding $160 \times 5 \times 5 \times 5$, and a $4 \times 4 \times 4$ kernel producing $512 \times 2 \times 2 \times 2$. A fully connected layer maps the final volume to class scores. Adapted from Wu et al. [705].

Application Example: Image-to-Voxel Prediction

A representative application of voxel-based shape representation is 3D reconstruction from a single RGB image. In this example, an image of an *armchair* is processed by a 2D convolutional neural network to extract high-level visual features. These features are then projected into a latent 3D space and refined through a sequence of 3D convolutional layers, ultimately producing a predicted voxel occupancy grid.

The pipeline begins with a $3 \times 112 \times 112$ input image, which is passed through a 2D CNN backbone to generate a compressed feature representation. This feature tensor is reshaped or lifted into a 3D voxel grid of shape $1 \times V \times V \times V$ (e.g., 32^3). The lifted volume is then processed by 3D convolutional filters that reason about the spatial structure of the object in three dimensions.

The final output is a binary or probabilistic voxel grid indicating which regions of 3D space are likely to be occupied by the object. In our example, the network successfully reconstructs the volumetric shape of an armchair directly from a single view.

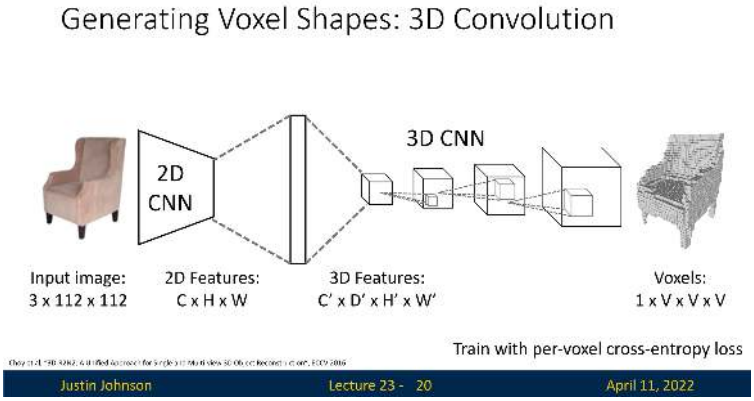

Figure 23.7: Image-to-voxel inference pipeline. A $3 \times 112 \times 112$ RGB image is processed by a 2D CNN to extract features, which are lifted into a latent 3D voxel grid and refined by 3D convolutions. The output is an occupancy grid representing the shape of the object—in this case, an armchair.

This architecture exemplifies how convolutional models can bridge 2D visual perception and 3D spatial reasoning. The voxel grid serves as an interpretable intermediate representation, enabling volumetric reasoning for tasks such as shape completion, reconstruction, etc.

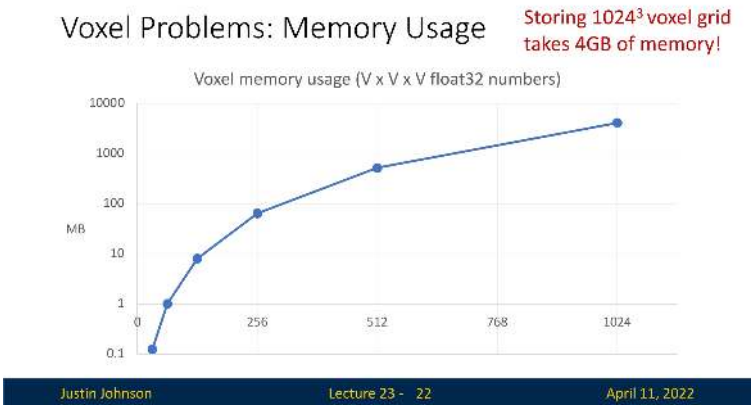

Figure 23.8: Voxel representation memory usage scales cubically with resolution. A $V \times V \times V$ grid storing 32-bit floats grows rapidly: a 256^3 grid requires roughly 64 MB, while a 1024^3 grid exceeds 4 GB. This cubic growth severely limits the feasibility of high-resolution volumetric models, motivating the exploration of more memory-efficient 3D representations.

As can be seen in figure 23.8, due to the cubic growth of memory and compute with resolution, voxel-based methods are constrained in practice, motivating alternative representations such as point clouds, triangle meshes, and neural implicit fields for higher-fidelity modeling. One thing we can do though, is try to scale voxels based on Oct-Trees.

23.4.1 Scaling Voxel Grids with Octrees

Standard voxel grids suffer from a key limitation: memory and computation grow cubically with resolution. For instance, going from a 32^3 to 128^3 grid multiplies storage cost by a factor of $4^3 = 64$. At high resolutions, this becomes intractable—even though most of the grid is typically empty or homogeneous. This makes dense voxelization wasteful and limits its ability to capture fine geometric detail.

To overcome this inefficiency, Tatarchenko et al. introduced the *Octree Generating Network (OGN)* [609], which replaces dense grids with a sparse hierarchical structure called an *octree*.

Octrees: Intuition and Structure

An octree is a tree-based representation that adaptively subdivides 3D space. Starting from a single cube that covers the full scene (the root), each cube is recursively split into eight subcubes (octants)—but only when that region contains surface detail. Empty or homogeneous regions remain unrefined.

- **Uniform regions** (e.g., open air or flat walls) are stored as large, coarse octree nodes.
- **Detailed regions** (e.g., object boundaries or thin parts) are recursively subdivided to finer scales.

This *adaptive spatial resolution* means memory is focused where it matters: on the surface.

From Dense to Adaptive

To illustrate the impact, consider representing a car at different voxel resolutions:

- A dense 128^3 grid would allocate over two million voxels, even for empty space.
- In contrast, an octree might use only thousands of voxels—concentrated near the car's surface.

This reduces overall memory complexity from $O(n^3)$ to approximately $O(n^2)$, since the object's surface is a 2D manifold embedded in 3D space.

Octree Generating Networks (OGNs)

OGN is a convolutional architecture that generates high-resolution 3D shapes in octree format. It starts with a coarse prediction of shape (e.g., 8^3 or 16^3) and recursively refines it. The model learns to predict:

- which voxels should be subdivided (occupancy probabilities),
- and what features to pass to each child octant (learned latent codes).

At each refinement level, the network only expands voxels flagged as informative. This enables high-fidelity 3D shape generation—without wasting memory on empty regions.

Surface-Driven Efficiency

The advantage of octrees becomes clearest at high resolutions. Rather than processing millions of voxels uniformly, OGNs focus computation where object geometry is complex. For example, flat car doors are left coarse, while wheels or window edges are subdivided further.

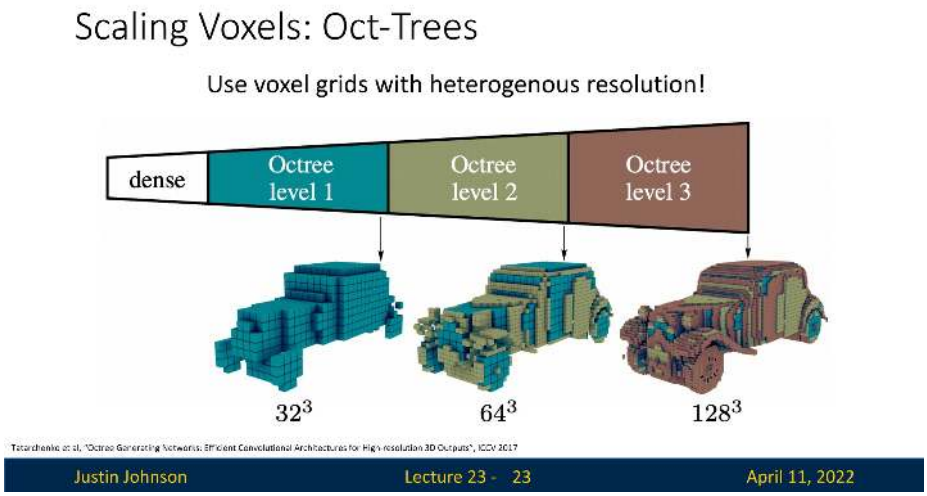

Figure 23.9: Octree-based shape reconstruction from OGN [609]. Left: initial coarse level (32^3, blue) captures the basic structure of the car. Middle: refinement to level 2 (64^3, green) improves resolution near surfaces such as wheels and front grill. Right: full octree refinement to level 3 (128^3, brown) adds fine details and completes the car's geometry while avoiding redundant subdivisions in empty space.

Why and How Octrees Work

Octrees address storage inefficiency by adaptively refining the voxel grid *only where necessary*, enabling surface-focused representations with far less memory.

How it works: The octree starts with a coarse resolution (e.g., 32^3) and maintains a tree where each node represents a voxel. Each node can be classified as:

- `empty`: the voxel contains no surface and is not refined further;
- `filled`: the voxel lies entirely inside the object and needs no further subdivision;
- `mixed`: the voxel intersects a surface and is therefore recursively subdivided into 8 children.

The key challenge is determining which voxels to refine.

Predicting Subdivision with Neural Networks

At each level of refinement, the octree maintains a sparse set of *active leaf voxels*. For each such voxel, the network predicts:

1. A feature vector for the current voxel (using sparse 3D convolutions on the octree structure).
2. An *occupancy classification score* for the voxel itself.
3. A set of 8 binary flags, one for each potential child voxel. indicating whether that subregion should be refined.

The voxel is only subdivided if at least one child is predicted as `filled` or `mixed`—that is, likely to be part of the object's interior or intersect the surface. These predictions are made using a `split prediction head` that branches off the decoder.

Training with Supervised Supervision

OGNs are trained end-to-end using ground truth voxel occupancy grids, from datasets like ShapeNet. The training process proceeds in a coarse-to-fine manner:

- **At level** l (e.g., 32^3): The network processes the current octree level and predicts occupancy and subdivision flags for each voxel.
- **Ground truth comparison:** The predicted occupancy labels and subdivision decisions are supervised using binary cross-entropy losses against a precomputed ground truth octree. These labels are derived by voxelizing the 3D CAD mesh and marking voxels as `filled`, `empty`, or `mixed`.
- **Subsequent levels:** Only voxels marked for refinement are subdivided. Their children become the active set for the next finer resolution level (e.g., 64^3, then 128^3, etc.).

This recursive supervision continues until the desired maximum resolution is reached. The result is a hierarchical, sparsely populated voxel grid that concentrates resolution along object surfaces, drastically reducing memory and computation.

Why It Works

- **Focuses computation:** By refining only ambiguous voxels, the model avoids spending resources on empty space or flat interiors.
- **Learns detail adaptively:** The network learns *where* detail is needed from data, rather than relying on hand-crafted refinement rules.
- **Enables higher resolutions:** Because only a subset of voxels are represented at each level, OGNs can generate outputs at resolutions like 256^3 or 512^3 with the memory footprint of a much smaller dense grid.

This learned coarse-to-fine generation strategy allows octree-based models to efficiently capture complex geometry while remaining scalable, making them highly effective for high-resolution 3D shape prediction tasks.

Limitations and Motivation for Point-Based Methods

Despite their efficiency, octrees still discretize space into axis-aligned cubes, which limits their ability to model very fine surface curvature or sharp boundaries without deep subdivisions. Moreover, generating and traversing octree hierarchies can introduce implementation complexity and latency in practice.

These limitations motivate an alternative family of 3D representations: *point clouds*. Unlike voxel grids or octrees, point clouds represent surfaces directly via sampled points in $\mathbb{R}^3$, bypassing the need to discretize space altogether. Although voxel representation is pretty common in practice, and point-based methods do not benefit from the grid structure useful in convolutional networks, they are intriguing as they offer greater flexibility and memory efficiency, especially for capturing fine-grained surface geometry.

In the following part, we explore point cloud representations and the neural architectures designed to process them effectively.

23.5 Point Clouds

A *point cloud* is a flexible, sparse, and surface-centric representation of 3D geometry. It models an object as a set of P points in $\mathbb{R}^3$, each corresponding to a sampled position on the visible surface:

$$\mathscr{P} = \{\mathbf{p}_i \in \mathbb{R}^3 \mid i = 1, \ldots, P\}$$

Unlike voxel grids, which discretize the 3D space uniformly and incur cubic memory costs, point clouds only represent surface points, yielding a compact and efficient encoding. This representation aligns naturally with real-world sensor data, such as LiDAR in autonomous vehicles.

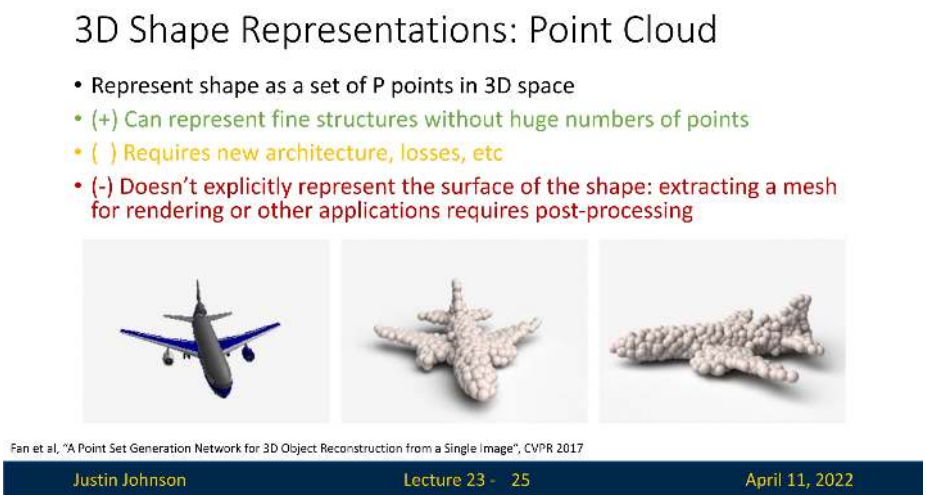

Figure 23.10: Airplane represented as a point cloud, from [152]. Fine structures such as wings and tail are densely sampled, while coarse regions like the fuselage use fewer points.

Advantages

Point clouds allow for high-resolution geometric modeling without the cubic scaling of voxel-based methods. They efficiently capture fine details such as airplane wings or chair slats using a relatively small number of points (as shown in figure 23.10), while coarser regions like planar surfaces can be represented sparsely.

Limitations

Point clouds do not encode surface connectivity or topology. This limits their utility for downstream applications such as mesh rendering or physics simulation, which rely on explicit surface structure. Additionally, point clouds are unordered and irregularly sampled, requiring specialized neural architectures for effective processing.

Rendering

Since mathematical points are infinitesimal, visualizations inflate each point into a finite-radius sphere. This creates the illusion of a continuous surface but does not resolve the lack of connectivity. To use point clouds for graphics or simulation, surface reconstruction via meshing algorithms is often necessary.

Applications

Point clouds are a core representation in 3D perception and are widely used in robotics, AR/VR, and autonomous driving. In particular, LiDAR sensors deployed on self-driving vehicles emit laser pulses to scan the environment and return a dense set of 3D points corresponding to surfaces in the scene. This raw point cloud data forms the foundation for several high-level tasks:

- **Obstacle detection and tracking:** Dynamic objects such as vehicles, pedestrians, and cyclists are localized and tracked in 3D space, enabling collision avoidance and motion planning.
- **Semantic scene understanding:** Each point in the cloud can be semantically labeled as `road`, `building`, `vegetation`, etc., supporting downstream reasoning about the environment.
- **Mapping and localization:** Aggregated LiDAR scans are used to construct high-definition (HD) maps for accurate self-localization and route planning. These maps include fine-grained structures such as lane boundaries, curbs, and traffic signs.
- **Multi-sensor fusion:** Point clouds are often fused with camera and radar inputs to improve robustness under challenging conditions, such as poor lighting or weather, where single modalities may fail.

By capturing precise geometric structure independent of appearance, point clouds enable spatial reasoning and metric-scale perception, making them indispensable for autonomous systems operating in complex, dynamic environments.

23.5.1 Point Cloud Generation from a Single Image

Fan et al. [152] introduce a landmark framework for reconstructing 3D shapes as point sets directly from a single RGB image. Unlike voxel grids or multi-view representations, point clouds are efficient, resolution-independent, and naturally suited to surface-level geometry. The model predicts an unordered set of 3D points

$$\hat{S} = \{\hat{y}_i\}_{i=1}^{P_1+H'W'P_2} \subset \mathbb{R}^3,$$

which approximates the visible object surface.

Architecture Overview

The model follows an encoder–decoder structure with a *dual-branch* output head designed to capture both global object structure and fine surface detail.

- The **encoder** is a convolutional neural network that maps the input image $I \in \mathbb{R}^{3\times H\times W}$ to a latent feature tensor $F \in \mathbb{R}^{C\times H'\times W'}$. This feature map encodes rich spatial information about the input's underlying 3D geometry.
- The **decoder** splits into two complementary branches:
  - **Fully-Connected (Global) Branch:** The feature map F is flattened and passed through a multi-layer perceptron (MLP) to produce a fixed set of P_1 3D points:

    $$\hat{S}^{\mathrm{g}} = \{\hat{y}_i^{\mathrm{g}}\}_{i=1}^{P_1} \subset \mathbb{R}^3.$$

    The output dimensionality is predetermined—e.g., a final layer with $3 \cdot P_1$ units reshaped into a $P_1 \times 3$ matrix. This branch captures the global structure, pose, and coarse silhouette of the object. The hyperparameter P_1 is typically chosen to balance expressiveness and efficiency, and remains fixed during training and inference.

– **Convolutional (Local) Branch:** Rather than collapsing spatial dimensions, this branch operates directly over the $H' \times W'$ grid of the encoded feature map. At each spatial location (i, j), a shared MLP (implemented as 1×1 convolution) predicts P_2 3D points:

$$\hat{S}^{\mathrm{l}} = \{\, \hat{y}^{\mathrm{l}}_{i,j,k} \,\}_{i=1}^{H'} {}_{j=1}^{W'} {}_{k=1}^{P_2} \subset \mathbb{R}^3.$$

Each point is generated relative to a canonical 2D grid anchor, allowing the network to model high-frequency surface detail. The weight-sharing mechanism enforces translation-equivariant behavior across the image, which is particularly effective for capturing fine geometry such as edges, contours, and thin structures. Because it preserves spatial layout, this branch provides dense, localized surface coverage.

The final output is the union of both branches:

$$\hat{S} = \hat{S}^{\mathrm{g}} \cup \hat{S}^{\mathrm{l}}, \quad \text{with} \quad |\hat{S}| = P_1 + H'W'P_2.$$

This architecture enables the model to combine a globally consistent shape prior (via the FC branch) with spatially grounded local refinement (via the convolutional branch), yielding geometrically faithful point cloud reconstructions with efficient capacity allocation.

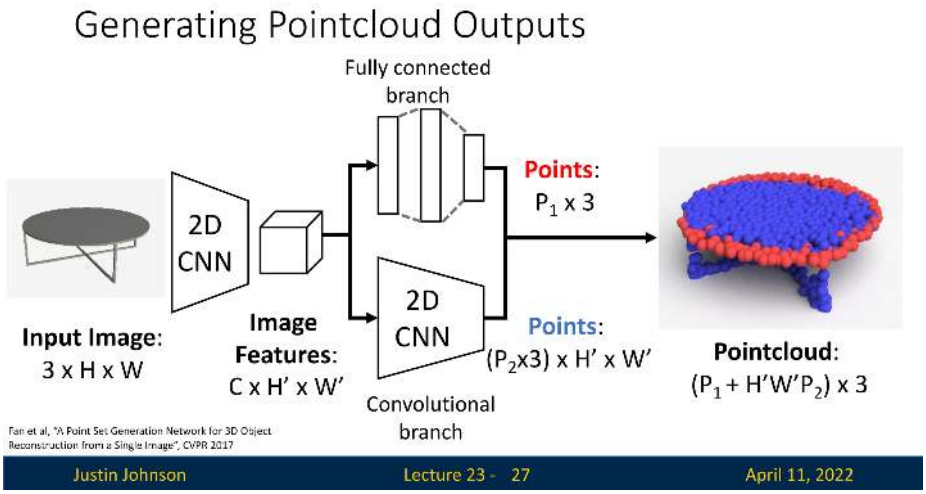

Figure 23.11: Dual-branch point cloud generation network of Fan et al. [152]. A 2D CNN encodes the input image into spatial features. The fully-connected branch (red) predicts P_1 global points, while the convolutional branch (blue) predicts P_2 points per spatial location, yielding $H'W'P_2$ local points. Their union forms the final output $\hat{S}$.

Architectural Motivation

This dual-path architecture reflects a coarse-to-fine design philosophy:

- The **global branch** supplies a stable structural prior, capturing the object's pose, orientation, and rough geometry.
- The **local branch** attends to spatially localized visual cues, enriching the surface detail with high-frequency geometric structure—particularly beneficial for recovering thin parts and sharp edges.

Together, they allow the network to generate accurate and detailed 3D reconstructions while keeping output size and model complexity manageable.

Loss Function: Chamfer Distance

When predicting 3D point clouds, we aim to generate a set of points that matches a ground-truth shape surface. Crucially, both the predicted and target sets are *unordered*—permuting point indices does not change the represented shape. This calls for a *set-based* loss function that is invariant to point ordering and flexible to varying cardinality.

Fan et al. address this with the *Chamfer Distance* (CD), a symmetric, differentiable measure of dissimilarity between two point sets:

- $S_1 \subset \mathbb{R}^3$: predicted point cloud (previously $\hat{S}$)
- $S_2 \subset \mathbb{R}^3$: ground-truth point cloud (previously S)

The Chamfer Distance is defined as:

$$d_{\text{CD}}(S_1, S_2) = \sum_{x \in S_1} \min_{y \in S_2} \|x - y\|_2^2 + \sum_{y \in S_2} \min_{x \in S_1} \|x - y\|_2^2.$$

Each term plays a complementary role:

- The *forward term* ensures that every predicted point $x \in S_1$ has a close match in the target set S_2. This promotes accurate surface fitting and penalizes extraneous predictions.
- The *backward term* guarantees that every target point $y \in S_2$ is approximated by at least one predicted point $x \in S_1$. This ensures full coverage of the ground-truth surface, even when the model predicts fewer points than the reference.

The bidirectional structure is key: even if $|S_1| \neq |S_2|$, the loss still compares them fairly by asking how well each set "explains" the other through nearest-neighbor matching. The use of minimum distances makes the loss permutation-invariant, and its differentiability (almost everywhere) enables end-to-end gradient-based optimization. Efficient computation is facilitated via KD-trees or approximate nearest neighbor search. The only situation in which the loss will be 0 is when the two sets are the same (each point in one is exactly on a point in the other), which is what we wanted to achieve.

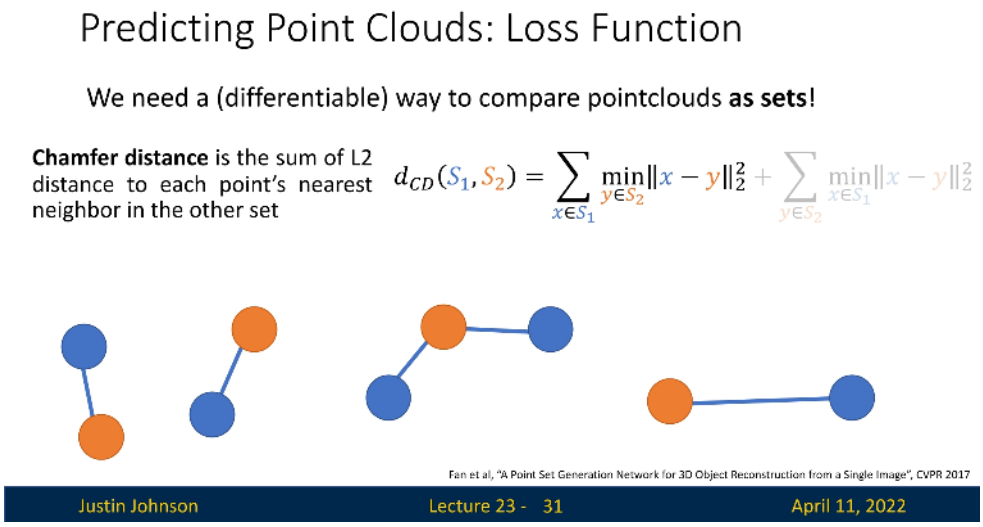

Figure 23.12: Chamfer distance (forward term): for each predicted point $x \in S_1$, find its nearest ground-truth match $y \in S_2$.

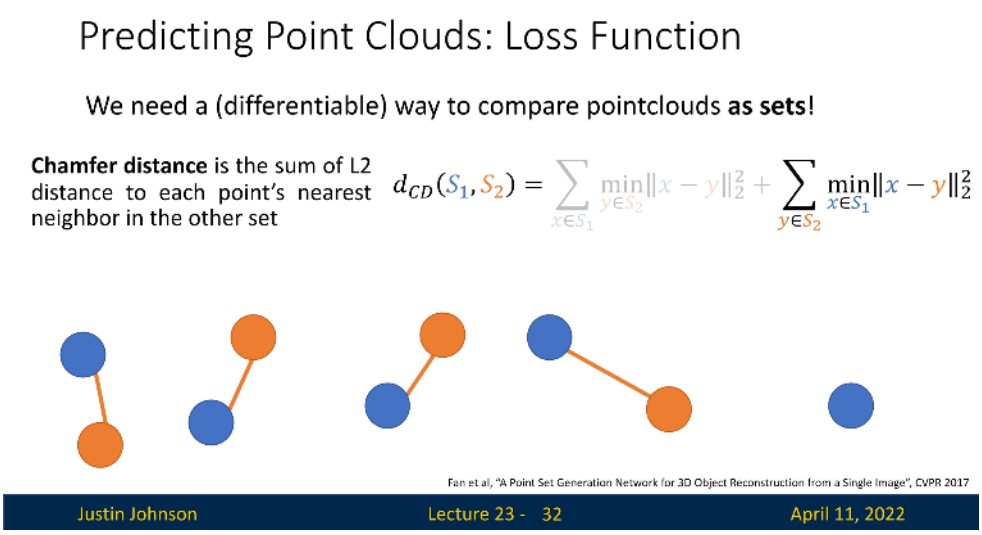

Figure 23.13: Chamfer distance (backward term): for each ground-truth point $y \in S_2$, find the nearest predicted point $x \in S_1$ to ensure coverage.

Intuition and Impact

The Chamfer Distance aligns naturally with the set-based nature of point clouds. By evaluating how well two sets approximate each other through nearest neighbors, it handles variable point counts and spatial distributions with ease. This makes it ideal for training neural networks to generate dense 3D surfaces from sparse supervision. Fan et al.'s use of Chamfer loss, coupled with a dual-branch decoder and CNN encoder, marked the first end-to-end framework to lift 2D images into 3D point sets with high geometric fidelity—laying the groundwork for many subsequent advances in point-based and implicit shape reconstruction.

23.5.2 Learning on Point Clouds: PointNet and Variants

Unlike images or voxels, point clouds are unordered and lack an inherent grid structure. This makes standard convolutional architectures unsuitable for directly processing them. *PointNet* [489] introduces a neural network architecture specifically designed to handle raw point sets while respecting their permutation invariance.

Core Design: Set-Invariance via Shared MLP and Symmetric Pooling

Let the input be a point cloud $\mathscr{P} = \{p_i\}_{i=1}^{P} \subset \mathbb{R}^3$, represented as a tensor $\mathbb{R}^{P\times 3}$. PointNet processes this set in a permutation-invariant fashion using the following components:

1. **Shared MLP:** Apply the same MLP to each point independently:

$$\text{MLP}(p_i) \in \mathbb{R}^D, \quad i = 1, \ldots, P$$

yielding a per-point feature matrix in $\mathbb{R}^{P\times D}$. Shared weights ensure permutation invariance across the set.

2. **Symmetric Aggregation:** Collapse the point cloud into a global descriptor using a permutation-invariant operator (e.g., max-pooling):

$$h_{\text{global}} = \max_{i=1}^{P} \text{MLP}(p_i) \in \mathbb{R}^D.$$

   The result is independent of input order and size.
3. **Prediction Head:**
   - *Classification*: Pass h_{global} through fully-connected layers to produce output scores in $\mathbb{R}^C$.
   - *Segmentation*: Concatenate h_{global} back to each per-point feature, then apply another shared MLP to predict per-point labels.

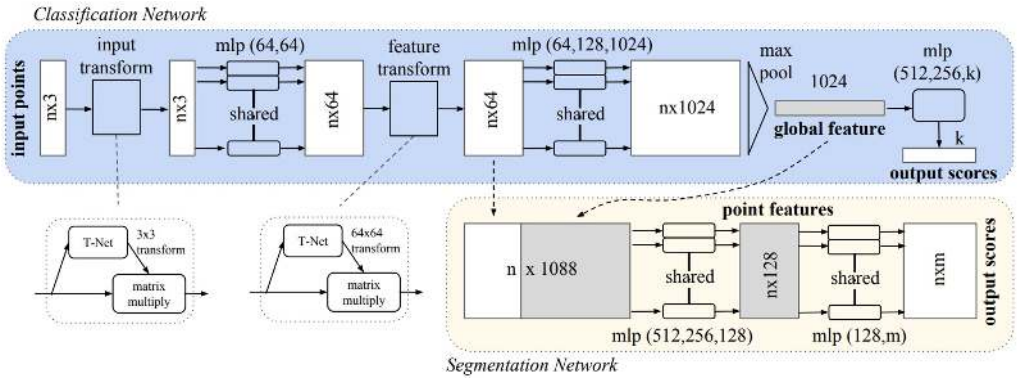

Figure 23.14: PointNet architecture (Qi et al., 2017). The classification network (left) takes n points, applies input and feature transformations, aggregates via max-pooling, and outputs class scores for k categories. The segmentation network (right) extends this by concatenating per-point and global features to predict labels at each point. MLP layer sizes are shown in brackets; BatchNorm+ReLU is used at each layer, and Dropout appears in the final FC layer for classification.

Pose Normalization via T-Net Modules

To improve invariance to arbitrary spatial transformations, PointNet incorporates two optional *Transformation Networks* (T-Nets) that learn to align both the input point cloud and its intermediate feature representations to canonical frames.

- **Input T-Net:** This module predicts a spatial alignment for the raw coordinates $\mathscr{P} \in \mathbb{R}^{P\times 3}$. It follows the PointNet architecture—shared MLPs, max-pooling, and fully connected layers—to regress a 3×3 transformation matrix, which is then applied directly to the input points. This normalization step removes global rotation and translation ambiguity, ensuring that the downstream network processes consistently oriented data.
- **Feature T-Net:** A second T-Net operates on the intermediate per-point feature vectors (e.g., after the first shared MLP), predicting a $D \times D$ transformation matrix to align feature embeddings in the latent space. This matrix is applied before aggregation, improving the stability and semantic consistency of learned features across different object poses and variations.

- **Regularization:** To ensure that the predicted feature transformation is approximately orthogonal (i.e., preserves information), a regularization loss of the form

$$L_{\text{reg}} = \left\| I - AA^\top \right\|_F^2$$

is added to the training objective, where $A \in \mathbb{R}^{D\times D}$ is the predicted transformation matrix and $\|\cdot\|_F$ denotes the Frobenius norm.

By learning to normalize both geometric and feature-level representations, these T-Net modules enhance the model's robustness to pose variation and improve the reliability of downstream classification or segmentation predictions.

Hierarchical Reasoning via Iterative Refinement

Beyond the basic structure, subsequent variants of PointNet can perform multi-stage feature fusion:

- After the first max-pooling yields $h_{\text{global}} \in \mathbb{R}^D$, it is concatenated with each point feature to form $\mathbb{R}^{P\times 2D}$.
- A shared MLP processes these enriched per-point vectors.
- A second max-pooling generates a refined global descriptor.
- This sequence—concat, MLP, pooling—can be repeated multiple times, allowing the network to capture hierarchical, higher-order shape attributes.

This iterative deep set reasoning retains permutation invariance while progressively enhancing the model's expressive power.

Legacy and Evolution

PointNet demonstrated that symmetry-aware, set-based architectures can rival or surpass volumetric CNNs in classification and segmentation—while using significantly less memory and supporting higher-resolution geometry. Its simple yet powerful design has led to a series of influential extensions that form the backbone of modern 3D deep learning pipelines.

23.5.3 PointNet++: Hierarchical Feature Learning on Point Clouds

While PointNet [489] introduced a powerful set-based paradigm for point cloud processing, it suffers from a key limitation: the inability to explicitly model local geometric structures. Because PointNet aggregates all point features globally in a single pooling operation, it lacks sensitivity to fine-grained local patterns—much like trying to classify a shape without noticing its edges or corners.

PointNet++ [490] addresses this limitation by introducing a **hierarchical architecture** that recursively applies PointNet within spatially localized regions. This structure enables the model to learn point-wise features at progressively larger contextual scales, akin to how CNNs build up representations from local patches to full-image semantics.

The core architectural unit in PointNet++ is the **Set Abstraction (SA) module**, which consists of three main stages:

1. **Sampling:** From the full point set, a representative subset is selected as *centroids* of local regions. This is typically performed using *Farthest Point Sampling (FPS)*, which ensures even spatial coverage of the point cloud by selecting points that are maximally distant from one another. This avoids clustering in high-density areas and helps capture the object's full spatial extent.

2. **Grouping:** For each sampled centroid, a local neighborhood is defined. The standard method is a *ball query*, which includes all points within a fixed radius. This spatially bounded grouping ensures that the local features extracted are consistent and scale-aware. (Alternatively, k-nearest neighbors can be used, though ball queries preserve fixed spatial context).
3. **PointNet Encoding:** Within each local neighborhood, a mini-PointNet is applied—mapping the points into a local reference frame (relative to the centroid) and computing a feature vector via shared MLPs and symmetric max-pooling. This step captures local geometric properties such as curvature, edges, or flatness.

By stacking multiple SA modules, PointNet++ constructs a deep hierarchy of features—from local patches to global shape descriptors—allowing robust recognition of both coarse and detailed structure.

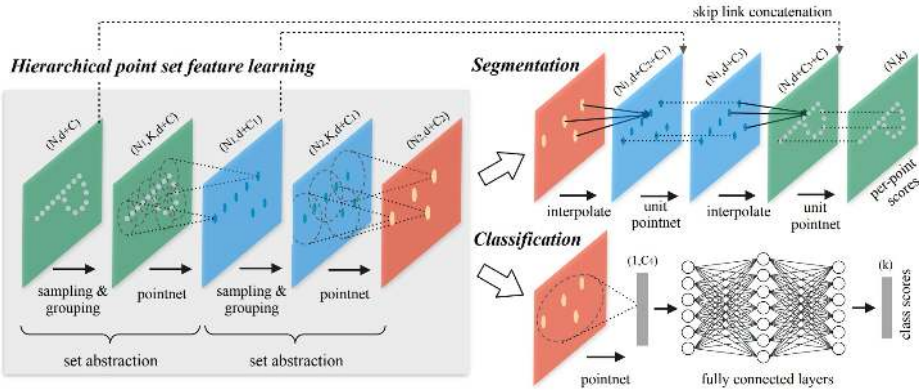

Figure 23.15: Hierarchical feature abstraction in PointNet++ [490]. Local regions are formed via sampling and grouping, then encoded by mini-PointNets. Higher abstraction levels operate on increasingly larger receptive fields.

Density-Adaptive Grouping and Robustness

A major challenge in real-world point clouds—such as those acquired via LiDAR or RGB-D sensors—is the presence of *non-uniform sampling density*. Nearby surfaces often result in dense clusters of points, while distant or occluded areas may be sparsely sampled. If a network uses a fixed-radius neighborhood (as in single-scale grouping), it may gather too few points in sparse regions (leading to unstable features), or be unnecessarily redundant in dense regions (wasting computation).

To address this, *PointNet++* [490] introduces two **density-adaptive grouping strategies** that allow feature learning to adapt across varying sampling densities:

- **Multi-Scale Grouping (MSG):** For each centroid in the set abstraction layer, MSG performs multiple ball queries of increasing radii (e.g., small, medium, large), forming concentric local neighborhoods of different scales. Each group is processed by a separate mini-PointNet, and the resulting feature vectors are concatenated into a unified multi-scale representation.
  Intuition: In dense regions, small-radius neighborhoods suffice to capture fine detail; in sparse regions, larger-radius neighborhoods ensure geometric coverage. MSG makes the model robust to such density variations at the cost of increased computation due to multiple parallel branches.

- **Multi-Resolution Grouping (MRG):** As a more efficient alternative, MRG leverages the hierarchical nature of PointNet++. At each level L_i, the feature for a local region is computed by *concatenating*:
  - a low-resolution feature from the previous level L_{i-1}, summarizing a large, sparse context;
  - a high-resolution feature from a mini-PointNet applied to the raw points in the local region at level L_i.

  This dual-path design allows the network to dynamically emphasize coarse or fine structure depending on local point density.
  Intuition: When a region is well-sampled, detailed features from the current level dominate; when sparse, the network falls back on coarse summaries inherited from deeper layers.

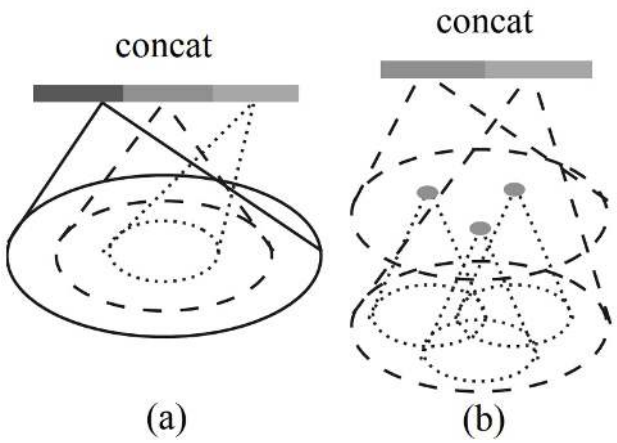

Figure 23.16: Multi-scale and multi-resolution grouping strategies from PointNet++ [490]. (a) **Multi-Scale Grouping (MSG)**: for each centroid, multiple neighborhoods at different radii are constructed and processed by parallel mini-PointNets; their features are concatenated to form a scale-robust representation. (b) **Multi-Resolution Grouping (MRG)**: combines coarse features propagated from previous abstraction levels with fine features extracted from raw points at the current level, allowing efficient adaptation to non-uniform sampling densities.

Random Input Dropout: During training, PointNet++ further improves robustness by randomly dropping input points. This encourages the model to generalize across incomplete or sparsely sampled inputs—a common scenario in real-world 3D capture.

Feature Propagation for Dense Prediction

For tasks like semantic segmentation—where per-point predictions are required—PointNet++ uses a **feature propagation** module to interpolate and upsample coarse features back to the original resolution. This is achieved via:

- *Distance-weighted interpolation* from nearby subsampled points.
- *Skip connections* from earlier levels in the hierarchy.

This ensures that each point benefits from both its raw input and the abstracted global features accumulated through the hierarchy.

Summary and Impact

PointNet++ marks a major evolution in point cloud learning. By extending PointNet with hierarchical spatial reasoning, local neighborhood modeling, and density-aware design, it achieved state-of-the-art performance across classification, segmentation, and 3D object detection benchmarks at its time of publication. The hierarchical Set Abstraction modules provide a powerful and general-purpose building block for modern geometric deep learning pipelines.

Extensions and Improvements

Numerous architectures have extended the PointNet++ paradigm to enhance expressiveness, efficiency, and scalability:

- **PointNeXt** [491] revisits PointNet++ with modern training techniques, simplified blocks, and residual connections for improved accuracy.
- **DGCNN** [684] introduces dynamic edge convolutions over local graphs, capturing fine-grained geometric relations across neighboring points.
- **Point Transformers** [702, 789] apply attention mechanisms to model long-range interactions in the point set, enabling context-aware reasoning.

These models now underpin many 3D perception systems, spanning applications in classification, segmentation, shape generation, and scene understanding.

Toward Structured Representations

While point clouds offer an efficient and flexible surface representation, they lack explicit connectivity. This motivates the transition toward structured outputs such as triangle meshes and implicit surfaces, which support physically grounded operations like rendering, simulation, and editing.

23.6 Triangle Meshes for 3D Shape Modeling

Triangle meshes are among the most widely used representations for 3D shapes in computer graphics, simulation, and geometric learning. A triangle mesh explicitly defines the surface of a 3D object using a finite set of *vertices* and *faces*. Let $\mathscr{V} = \{\mathbf{v}_i \in \mathbb{R}^3 \mid i = 1, \ldots, V\}$ denote the set of 3D vertex coordinates, and let $\mathscr{F} = \{(i, j, k) \mid i, j, k \in [1, V]\}$ denote the set of triangular faces, each indexed by three vertices.

This representation defines a piecewise-linear manifold embedded in 3D, enabling efficient rendering and geometric reasoning. Each face defines a planar triangle bounded by edges, and the entire mesh approximates a continuous surface.

Advantages of Triangle Meshes

Triangle meshes are the standard in real-time and offline 3D applications due to several key properties:

- **Surface explicitness:** Meshes represent the actual 2D surface geometry embedded in 3D, facilitating accurate surface-based computations such as rendering, shading, and physical simulation.
- **Adaptive resolution:** Large triangles can be used in smooth regions, while dense subdivisions can capture high-curvature or detailed regions, yielding compact yet expressive representations.
- **Rich annotations:** Meshes can carry per-vertex attributes such as surface normals, color, and texture coordinates, which are interpolated over the mesh faces for shading and alignment.

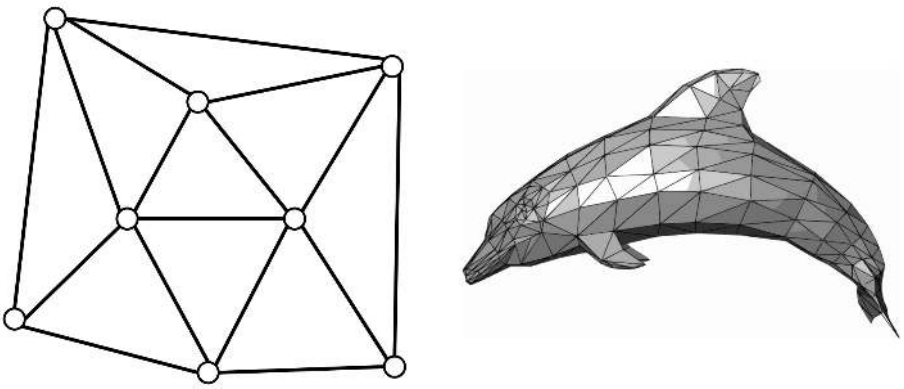

Figure 23.17: Left: A schematic triangle mesh with explicit vertices and faces. Right: A dolphin mesh reconstructed from real-world geometry. Adapted from lecture slides.

Despite their efficiency, predicting triangle meshes from raw data (e.g., RGB images or point clouds) presents significant challenges: the output structure is non-Euclidean, connectivity must be preserved, and operations such as upsampling or interpolation are nontrivial. The next subsection introduces a model that addresses these challenges through learned graph-based mesh deformation.

23.6.1 Pixel2Mesh: Predicting Triangle Meshes

Pixel2Mesh [665] is a landmark method for generating 3D triangle meshes directly from a single RGB image. Unlike voxel-based approaches—which scale cubically in memory—or point cloud methods—which lack surface connectivity and require post-processing to extract usable geometry—Pixel2Mesh predicts structured mesh outputs: surfaces defined by vertices, edges, and faces. This makes it particularly suitable for applications that require explicit topology, such as simulation, CAD, or rendering.

Pre-Pixel2Mesh Landscape

Prior to mesh-based methods, 3D learning architectures primarily explored two output formats:

- **Voxel grids:** Compatible with 3D convolutions and spatial reasoning, but constrained by high memory usage. Even modest resolutions (e.g., 64^3) require hundreds of thousands of cells, limiting detail.
- **Point clouds:** More efficient and flexible, but inherently unstructured. Without connectivity, they cannot express surface geometry directly, making downstream tasks such as meshing or simulation error-prone.

Core Proposition

Pixel2Mesh offers a structurally informed alternative by modeling 3D shape as a *deformable mesh graph*. Starting from a fixed-topology, genus-0 template (typically an ellipsoid), the network learns to *iteratively deform* vertex positions to match the object depicted in the image. This progressive refinement approach reframes the task: instead of generating structure from scratch, the model predicts *residual displacements*—small, local adjustments to an existing shape. This both simplifies learning and naturally preserves manifold topology, as the mesh's connectivity remains unchanged across deformations.

Key Innovations

Pixel2Mesh introduced a number of interlinked architectural ideas that made this formulation tractable:

- **Coarse-to-Fine Refinement:** The model deforms the mesh over multiple stages. After each deformation step, the mesh is *upsampled*—that is, each face is subdivided to increase resolution—enabling the network to model fine-grained surface detail while maintaining stability early on.
- **Graph Convolution on Meshes:** Deformations are computed using *graph convolutional networks (GCNs)*, which aggregate information across neighboring vertices based on mesh connectivity. This allows localized, topology-aware reasoning.
- **Vertex-Aligned Features:** To connect 2D image content with the 3D mesh, the model projects each vertex onto the image plane and samples CNN features at the corresponding location. These features are passed to the GCN to guide deformation, grounding mesh updates in visual evidence.
- **Chamfer Distance for Mesh Supervision:** Pixel2Mesh supervises mesh prediction by comparing the predicted vertex set $\mathscr{V} \subset \mathbb{R}^3$ to a ground-truth point cloud $\mathscr{S}_{\text{gt}}$ using the symmetric Chamfer Distance:

$$\mathscr{L}_{\text{Chamfer}} = \sum_{x \in \mathscr{V}} \min_{y \in \mathscr{S}_{\text{gt}}} \|x - y\|_2^2 + \sum_{y \in \mathscr{S}_{\text{gt}}} \min_{x \in \mathscr{V}} \|x - y\|_2^2.$$

Although simple and differentiable, this loss only supervises vertex positions and ignores the interiors of mesh faces—potentially allowing distortions like sagging or warping between correctly placed vertices.
Later work, such as *GEOMetrics* [574], improves on this by comparing point clouds sampled from the entire predicted surface, offering finer surface-level supervision.

High-Level Pipeline

Pixel2Mesh transforms a single RGB image into a 3D triangle mesh through a progressive mesh deformation pipeline that unifies convolutional image features and geometric mesh reasoning. The method begins with two inputs: a 2D image and a coarse, genus-0 mesh template (typically an ellipsoid centered in front of the camera). This template serves as the canonical starting point for all reconstructions and encodes strong priors on manifoldness and mesh topology.

The network refines this initial mesh in three stages, each consisting of deformation, unpooling, and feature update modules. The process is structured as follows:

1. **Image Feature Extraction:** A 2D convolutional backbone (e.g., VGG-16) processes the input RGB image to extract multi-scale feature maps from intermediate layers (e.g., `conv3_3`, `conv4_3`, `conv5_3`). These maps encode both low-level textures and high-level semantic patterns, offering a rich perceptual signal that guides the 3D reconstruction process.
2. **Vertex-to-Image Feature Pooling:** Each mesh vertex is projected onto the image plane using known camera intrinsics. At the projected 2D coordinates, features are bilinearly sampled from the image's multi-level CNN maps and concatenated to the vertex's current geometric descriptor. This projection-based pooling serves as the only available cue during inference, anchoring the 3D reconstruction to image evidence. It provides the graph network with localized appearance information, helping it decide where and how to displace each vertex and add detail.
3. **Graph Convolution for Deformation:** The mesh is represented as a graph, with vertices as nodes and edges defined by mesh connectivity. A *Graph Convolutional Network (GCN)* processes this structure, updating each vertex's feature vector by aggregating information from its neighbors. The GCN is composed of multiple layers, expanding each vertex's receptive field and enabling contextual reasoning across the surface. Crucially, the image-aligned features from the pooling step guide the GCN's residual predictions—telling the network *how to deform the shape* in 3D to better match the visual evidence.
4. **Graph Unpooling for Resolution Increase:** To increase geometric detail, the mesh is upsampled after each deformation stage using *edge-based unpooling*. New vertices are inserted at the midpoints of edges, and connectivity is updated to preserve the mesh's manifold structure. The positions and features of new vertices are initialized by averaging their endpoints, allowing the network to seamlessly enrich surface detail without altering global shape or topology.
5. **Iterative Refinement:** The refined mesh is passed through multiple deformation stages, each repeating the cycle of vertex-to-image feature pooling (Step 2), GCN-based displacement prediction (Step 3), and graph unpooling (Step 4). This iterative coarse-to-fine strategy begins with a low-resolution mesh that captures global structure—benefiting from short graph diameters and large effective receptive fields—and progressively increases resolution to recover fine surface details. As the mesh converges toward the target shape, vertex projections align more accurately with relevant regions in the image, enhancing the quality of sampled features and enabling increasingly precise geometric corrections at each stage.

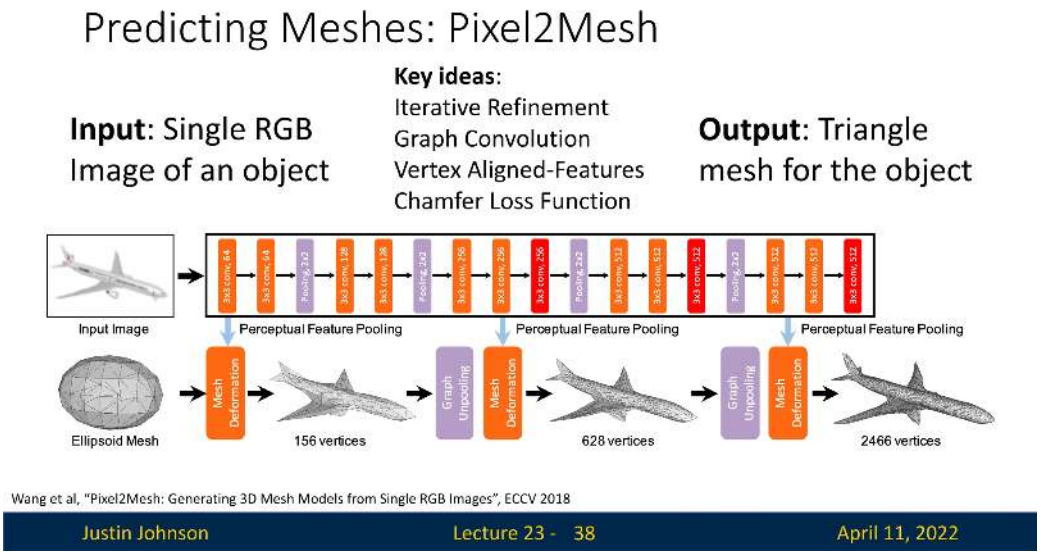

Figure 23.18: Pixel2Mesh architecture overview. Starting from a coarse ellipsoid mesh, the model applies a sequence of mesh deformation blocks, each guided by per vertex extracted 2D image-aligned features and processed via graph convolutions. Between deformation blocks, *graph unpooling* operations increase mesh resolution by inserting new vertices at edge midpoints, preserving surface shape while enabling finer geometric detail in subsequent refinements. As the mesh evolves, vertex projections better align with informative regions in the image, improving both feature sampling and deformation accuracy.

This multi-stage architecture offers a powerful compromise between efficiency and fidelity. The low-resolution mesh allows efficient global shape reasoning in early layers, while unpooling introduces degrees of freedom necessary for high-resolution surface detail. By integrating 2D image cues at every stage and learning deformation through graph-based reasoning, Pixel2Mesh generates detailed, topologically consistent 3D meshes from a single image.

Graph-Based Feature Learning

A core challenge in learning from 3D meshes is that they are *non-Euclidean* structures. Unlike images or voxels, which lie on regular grids with fixed-size neighborhoods and translation-invariant kernels, triangle meshes consist of irregularly connected vertices with no global coordinate frame. To apply learning methods to this setting, Pixel2Mesh treats the mesh as a graph $\mathcal{G} = (\mathcal{V}, \mathcal{E})$, where:

- **Nodes ($\mathcal{V}$)** are mesh vertices. Each vertex $i \in \mathcal{V}$ is assigned a feature vector $\mathbf{f}_i \in \mathbb{R}^d$, initialized using its 3D coordinates $\mathbf{v}_i \in \mathbb{R}^3$, and later enriched through graph-based message passing.
- **Edges ($\mathcal{E}$)** encode mesh connectivity. Two nodes i and j share an edge if their corresponding vertices are adjacent on a triangle face. This forms the local neighborhood $\mathcal{N}(i)$ around each vertex.

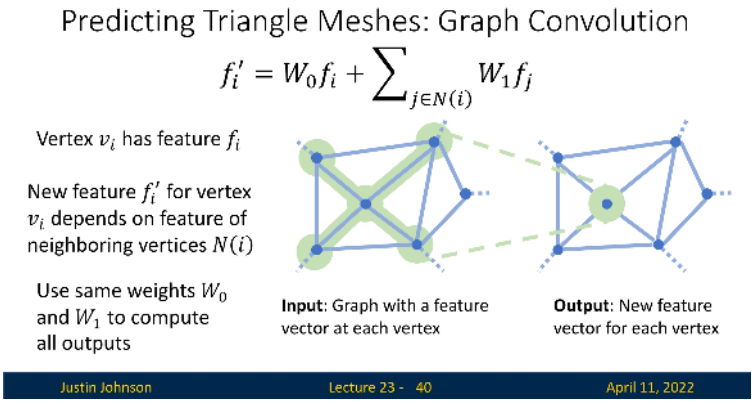

Figure 23.19: Graph convolution on meshes: each vertex aggregates features from its 1-ring neighbors using shared learnable weights.

To extend the receptive field across the mesh and support complex shape reasoning, Pixel2Mesh stacks multiple such layers into a 14-layer *Graph Convolutional ResNet (G-ResNet)*. The inclusion of residual (skip) connections helps stabilize optimization, facilitates deeper architectures, and allows low-level geometry to be preserved and reused throughout the network. As features propagate through the GCN, each vertex gains access to increasingly broader geometric context—essential for learning coherent deformations informed by both local surface cues and global object structure.

This graph-based feature hierarchy ultimately enables each vertex to predict a residual 3D displacement vector $\Delta \mathbf{v}_i$, which updates its position without altering mesh connectivity. Subsequent parts detail how these features are fused with 2D image evidence and used to deform the mesh toward the target shape.

To increase the expressive capacity of the network, Pixel2Mesh stacks 14 such layers into a deep *Graph Convolutional ResNet (G-ResNet)*. This depth enables each vertex to aggregate information from increasingly distant nodes, expanding its *receptive field* over the graph. Unlike grids, graphs can have highly irregular connectivity, and so reaching distant vertices may require many layers of message passing. Skip connections—added between GCN layers—help mitigate this by stabilizing gradient flow during training and facilitating feature reuse. In the context of mesh deformation, these residual paths are particularly useful: they allow the network to retain low-level spatial signals (e.g., coarse geometry or symmetric structures) while progressively layering on fine-grained, high-level shape refinements.

Predicting Vertex Positions via Graph Projection

At the end of each mesh deformation block, the G-ResNet outputs a refined feature vector $\mathbf{f}_i \in \mathbb{R}^d$ for each vertex i. These features encode both geometric structure (through message passing over the mesh) and semantic cues (through vertex-aligned image features). To convert these features into updated vertex coordinates, Pixel2Mesh applies a simple yet crucial operation: a final linear layer referred to as the *graph projection layer*.

Formally, the new 3D position of each vertex is predicted as:

$$\mathbf{v}_i^{\text{new}} = W_{\text{proj}} \mathbf{f}_i,$$

where $W_{\text{proj}} \in \mathbb{R}^{d \times 3}$ is a learnable weight matrix shared across all vertices. This transformation maps the high-dimensional vertex features directly into absolute 3D space.

Importantly, this step does *not* compute or apply a residual displacement. The network predicts the final 3D position outright. Although this may seem counterintuitive—many deformation-based models favor residual updates for stability—the Pixel2Mesh architecture learns this coordinate regression implicitly, leveraging the structured feature learning of the G-ResNet. The underlying mesh structure and feature propagation already encode strong geometric priors, making direct position regression viable and effective.

Throughout this process, the mesh's topology remains fixed: only vertex positions are updated, not their connectivity. This allows each deformation block to operate over a stable graph structure while progressively refining the mesh surface. After this coarse shape is aligned with the image, *graph unpooling* increases mesh resolution by inserting new vertices at edge midpoints. Subsequent deformation blocks then focus on finer-scale geometry, aided by a denser mesh and more localized 2D image alignment.

Edge-Based Graph Unpooling for Mesh Resolution Refinement

After each stage of coarse deformation, Pixel2Mesh increases the mesh resolution to allow more fine-grained geometric refinement. This is achieved via a carefully designed *graph unpooling* operation that avoids the artifacts common in naive subdivision schemes. Instead of inserting new vertices at triangle centroids (which creates low-degree, poorly connected nodes), Pixel2Mesh uses an *edge-based unpooling* strategy inspired by classical mesh subdivision methods.

The unpooling procedure is as follows:

- A new vertex is inserted at the midpoint of each edge in the mesh.
- This new vertex is connected to the two endpoints of the edge.
- For every triangle in the original mesh, the three mid-edge vertices are connected to form a new inner triangle.

This process subdivides each original triangle into four smaller triangles and preserves regularity in vertex degree and local topology. To initialize the features of the new mid-edge vertices, the network simply averages the features of the parent vertices:

$$\mathbf{f}_{\text{new}} = \frac{1}{2}(\mathbf{f}_i + \mathbf{f}_j),$$

where i and j are the endpoints of the edge. This yields smooth and stable feature transitions for subsequent GCN layers.

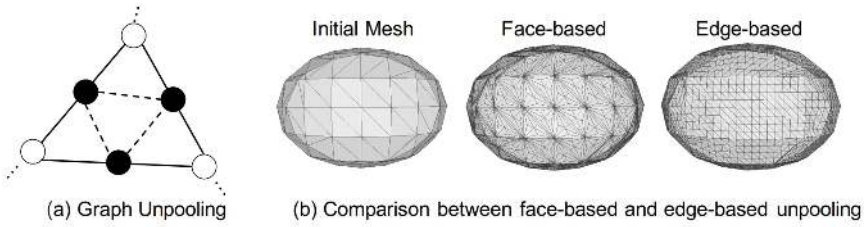

Figure 23.20: Graph unpooling in Pixel2Mesh (adapted from [665]): (a) New vertices (black) are inserted at edge midpoints and connected via dashed edges. (b) Face-based unpooling leads to irregular vertex degrees and topological imbalance, while edge-based unpooling preserves mesh regularity and uniform structure.

This coarse-to-fine unpooling scheme allows Pixel2Mesh to expand its receptive field and prediction granularity in tandem. The three-stage pipeline uses meshes with 156, 628, and finally 2466 vertices—an architecture that mirrors the increasing complexity of the shape being reconstructed. Early blocks handle the "big picture," while later blocks focus on refining sharp contours, smooth curvatures, and small geometric details.

Image-to-Mesh Feature Alignment

A key innovation in *Pixel2Mesh* is its ability to guide 3D mesh deformation using 2D visual cues extracted from the input image. This involves bridging two fundamentally different data domains: the regular, grid-aligned structure of 2D images and the irregular, graph-based structure of 3D meshes. Pixel2Mesh realizes this connection through a *Perceptual Feature Pooling* module, which aligns each mesh vertex with semantically relevant image features and dynamically refines that alignment at each deformation stage.

The process begins with a pretrained VGG-16 network (frozen during training), used to extract multi-scale image features from the input RGB image. Features are taken from three intermediate layers—`conv3_3`, `conv4_3`, and `conv5_3`—which together capture both fine textures and abstract semantics. These layers yield feature maps at decreasing spatial resolutions and increasing channel dimensionality.

For each vertex i in the current mesh, the following steps are performed:

1. **Projection to the Image Plane:** The 3D vertex position $\mathbf{v}_i = (x_i, y_i, z_i) \in \mathbb{R}^3$ is projected to 2D image coordinates using known perspective camera intrinsics:

$$(u_i, v_i) = \left(\frac{f_x x_i}{z_i} + c_x, \frac{f_y y_i}{z_i} + c_y \right).$$

   This maps the 3D point to the location on the image where it is expected to appear.
2. **Bilinear Feature Sampling:** At each projected coordinate (u_i, v_i), bilinear interpolation is applied to the VGG feature maps to retrieve image-aligned descriptors. This interpolation ensures that features can be sampled at subpixel resolution and maintains differentiability throughout the pipeline.

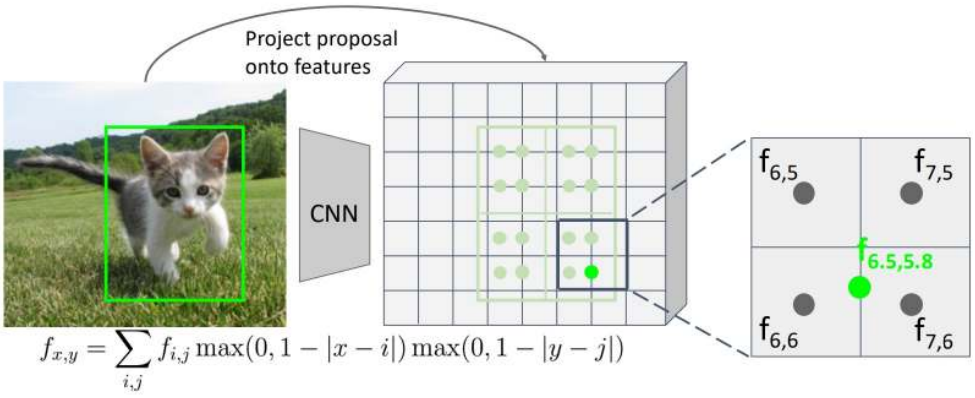

Figure 23.21: Bilinear interpolation retrieves CNN features at non-integer projected positions. This mechanism resembles RoIAlign and allows smooth vertex-to-image alignment.

3. **Multi-Scale Feature Fusion:** The sampled feature vectors from `conv3_3`, `conv4_3`, and `conv5_3` are concatenated to form a unified descriptor $\mathbf{f}_i^{\text{img}} \in \mathbb{R}^{1280}$ (e.g., 256 + 512 + 512 channels). This vector encodes both local appearance and high-level semantics around the vertex projection.
4. **Fusion with Graph Features:** The perceptual feature $\mathbf{f}_i^{\text{img}}$ is concatenated with the vertex's geometric feature $\mathbf{f}_i \in \mathbb{R}^d$, as computed by previous graph convolution layers. The resulting fused descriptor is then passed to the next G-ResNet deformation block to guide shape refinement.

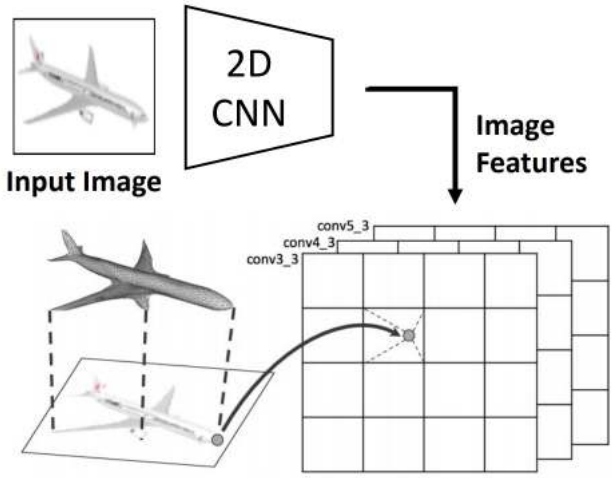

Figure 23.22: Image feature alignment: each mesh vertex is projected onto the input image and associated with interpolated CNN features. These features are fused with graph features and passed to the GCN.

Importantly, this perceptual pooling process is not static—it is repeated *at the beginning of every mesh deformation block* using the current mesh geometry. This creates a dynamic feedback loop:

- In the first stage, vertex projections from the initial ellipsoid are poorly aligned with the object, so pooled features are coarse and ambiguous.
- After the first deformation block updates vertex positions, the mesh becomes better aligned with the image.
- When pooling is reapplied in the next stage, projections land on more semantically meaningful image regions, yielding more informative features.
- This cycle continues, with improved mesh geometry enabling better feature alignment, which in turn enables more precise deformations.

This iterative loop—*deform* $\rightarrow$ *reproject* $\rightarrow$ *repool*—is central to Pixel2Mesh's effectiveness. Rather than relying on static image features, the model continuously refines its 2D–3D correspondence, allowing later stages to make sharper, semantically aware deformations based on increasingly accurate visual cues. The tight coupling of image perception and geometric reasoning enables the network to generate high-fidelity 3D surfaces even from a single image input.

Loss Function for Mesh Prediction in Pixel2Mesh

To guide the deformation of a coarse mesh into a high-quality 3D reconstruction, Pixel2Mesh employs a composite loss function that balances geometric accuracy, surface regularity, and structural plausibility. The loss is applied not only to the final output but also at each intermediate stage in the coarse-to-fine refinement pipeline.

Primary Objective: Chamfer Distance (Vertex-to-Vertex)

The central supervision signal is the symmetric *Chamfer Distance* between the predicted mesh vertices V_{pred} and a set of ground-truth vertices V_{gt}, both sampled from respective meshes:

$$\mathscr{L}_{\text{Chamfer}} = \sum_{v \in V_{\text{pred}}} \min_{u \in V_{\text{gt}}} \|v - u\|_2^2 + \sum_{u \in V_{\text{gt}}} \min_{v \in V_{\text{pred}}} \|u - v\|_2^2$$

This term ensures that each predicted vertex lies close to some part of the ground-truth surface, and vice versa. While originally designed for unordered point sets, this metric is used here as a surrogate for surface similarity. It is efficient and differentiable, but has limitations—it evaluates only the positions of vertices and not the geometry of faces.

Laplacian Smoothness Loss

To enforce local geometric coherence and prevent unrealistic surface artifacts, Pixel2Mesh introduces a *Laplacian regularization term* that encourages smooth vertex deformations. This loss penalizes deviations in the *Laplacian coordinates* of each vertex before and after deformation. The Laplacian coordinate of vertex i is defined as the offset between its position and the average of its immediate neighbors:

$$\delta_i = \mathbf{v}_i - \frac{1}{|\mathscr{N}(i)|} \sum_{j \in \mathscr{N}(i)} \mathbf{v}_j$$

After a deformation block updates the mesh to new vertex positions $\mathbf{v}_i'$, the updated Laplacian coordinate is denoted δ_i'. The Laplacian loss penalizes the change in these coordinates:

$$\mathscr{L}_{\text{Lap}} = \sum_i \left\| \delta_i' - \delta_i \right\|_2^2$$

This loss serves a dual purpose depending on the stage of mesh refinement. In early stages, when the mesh is still close to the initial ellipsoid, the Laplacian coordinates are small and uniform; the loss encourages smooth, globally consistent deformations, helping prevent tangled or self-intersecting geometry. In later stages, once the mesh has learned a plausible coarse shape, the Laplacian coordinates reflect learned local structure. Penalizing changes to these coordinates helps *preserve previously learned surface details*, ensuring that finer deformations do not overwrite or distort earlier predictions.

Intuitively, this loss encourages vertices to move *together with their neighbors*, discouraging isolated spikes, noisy fluctuations, or jagged artifacts—especially in high-curvature or thin regions. As such, it acts as a learned shape stabilizer throughout the deformation pipeline.

Edge Length Regularization

As the mesh undergoes progressive refinement through unpooling, Pixel2Mesh introduces additional vertices and edges to increase spatial resolution. While this enables finer geometric detail, it also introduces new degrees of freedom that can destabilize the mesh—especially during early training or coarse-to-fine transitions. Without proper constraints, vertices may drift far from their neighbors, forming "flying vertices" connected by abnormally long edges. To suppress such artifacts, Pixel2Mesh applies an *edge length regularization* term, defined as:

$$\mathscr{L}_{\text{edge}} = \sum_{(i,j)\in\mathscr{E}} \|\mathbf{v}_i - \mathbf{v}_j\|_2^2,$$

where $\mathscr{E}$ is the set of all mesh edges at the current refinement stage. This loss penalizes the absolute squared length of each edge, thereby encouraging spatial coherence among neighboring vertices.

While this formulation is unnormalized in the original paper, its contribution to the overall loss is controlled via a fixed hyperparameter λ, ensuring stability across deformation stages despite increasing edge count. Importantly, this term does *not* compare edge lengths to their prior values or enforce a canonical length. Instead, it acts as a dynamic local tether, discouraging over-extension without constraining the mesh to a rigid template.

This regularizer is especially critical immediately after graph unpooling. Newly added vertices—typically initialized at edge midpoints—are still trainable and unconstrained by prior geometry. The edge length loss ensures that their deformations remain consistent with the surrounding structure, preventing unstable stretching and promoting uniform vertex spacing.

Together with the Laplacian and normal consistency terms, this loss helps maintain the integrity of the mesh during deformation, guiding the network toward smooth, coherent, and physically plausible reconstructions.

Normal Consistency Loss

To enhance visual quality and ensure correct surface orientation, a normal loss penalizes misalignment between predicted edges and ground-truth normals:

$$\mathscr{L}_{\text{normal}} = \sum_i \sum_{j\in\mathscr{N}(i)} \left\langle v_i - v_j, n_q \right\rangle^2$$

Here, n_q is the normal at the closest point q on the ground-truth mesh to vertex v_i. This loss encourages edges to lie tangent to the surface, improving shading behavior and geometric realism. It captures higher-order consistency beyond just vertex positions.

Total Loss

The final loss combines all components with fixed scalar weights:

$$\mathscr{L}_{\text{total}} = \mathscr{L}_{\text{Chamfer}} + \lambda_1 \mathscr{L}_{\text{normal}} + \lambda_2 \mathscr{L}_{\text{Lap}} + \lambda_3 \mathscr{L}_{\text{edge}}$$

Pixel2Mesh uses $\lambda_1 = 1.6 \times 10^{-4}$, $\lambda_2 = 0.3$, and $\lambda_3 = 0.1$. These weights were selected empirically to ensure that geometric fidelity is prioritized while still promoting mesh regularity and perceptual realism.

Limitations and Future Directions

While this loss formulation is effective, it has several shortcomings:

- **Vertex-Only Supervision:** The Chamfer loss evaluates only discrete vertex positions, not the full surface defined by mesh faces.
- **Sagging Faces:** Large triangles may sag or bulge between correctly placed corner vertices without incurring loss, as interior deviations are unobserved.
- **Oversmoothing Risk:** The combination of Laplacian and edge constraints may suppress sharp features or fine details if not balanced carefully.
- **Triangulation Bias:** Matching based on vertex positions can penalize geometrically similar surfaces with differing connectivity.

Later methods such as GEOMetrics address these issues by introducing *surface-based sampling* and differentiable point sampling from triangle interiors, allowing more accurate and complete loss computation over the full mesh surface.

Enrichment 23.6.1.1: Differentiable Surface Sampling in GEOMetrics

Surface-to-Surface Comparison with Differentiable Sampling

A central innovation in GEOMetrics is its replacement of vertex-based supervision with full *surface-level* comparison. Pixel2Mesh constrains only mesh vertex positions using a Chamfer loss against a fixed ground-truth point cloud, ignoring the geometry of the mesh faces that connect them. As a result, large triangles can sag or bulge without penalty as long as their corner vertices remain close to the sampled ground truth—leading to visible artifacts.

To resolve this, GEOMetrics computes a symmetric distance between dense point clouds sampled from the *entire surface* of both meshes. The primary loss during early training is the **Point-to-Point Chamfer Distance**:

$$\mathscr{L}_{\text{PtP}} = \sum_{p \in S_{\text{pred}}} \min_{q \in S_{\text{gt}}} \|p - q\|_2^2 + \sum_{q \in S_{\text{gt}}} \min_{p \in S_{\text{pred}}} \|q - p\|_2^2$$

Here, S_{pred} and S_{gt} are point clouds sampled online from the predicted and ground-truth meshes, respectively. This loss encourages every sampled point on one surface to be close to *some* point on the other, and vice versa—ensuring both coverage and correspondence. The symmetric form (sum of minimum distances in both directions) avoids degenerate solutions like mode collapse, where one shape covers the other but not vice versa.

Because sampling is performed over triangle interiors rather than vertex sets, $\mathscr{L}_{\text{PtP}}$ is invariant to vertex count, mesh tessellation, or triangulation pattern—making it a true *surface-level* supervision signal.

Point-to-Surface Loss and Fine-Tuning

While $\mathscr{L}_{\text{PtP}}$ is efficient and effective early in training, it remains an approximation: it compares discrete samples rather than true surfaces. During *fine-tuning*—the later stage of training when coarse structure has converged—GEOMetrics switches to the more precise **Point-to-Surface loss**:

$$\mathscr{L}_{\text{PtS}} = \sum_{p \in S_{\text{pred}}} \min_{f \in \mathscr{F}_{\text{gt}}} \text{Dist}(p, f)^2 + \sum_{q \in S_{\text{gt}}} \min_{f' \in \mathscr{F}_{\text{pred}}} \text{Dist}(q, f')^2$$

This loss computes the squared distance from each sampled point to the nearest triangle *face* on the opposing mesh, rather than to another sampled point.

This leads to a more geometrically faithful signal, especially in regions where faces are large or sparsely sampled—e.g., flat areas or sharp edges. By comparing to the continuous mesh surface (via face planes), $\mathscr{L}_{\text{PtS}}$ avoids underestimating distances due to poor sampling density, making it better suited for high-precision surface alignment during final optimization.

Differentiable Surface Sampling via Reparameterization

To ensure end-to-end differentiability, GEOMetrics samples surface points from the predicted mesh using a two-stage stochastic procedure:

- **Area-weighted face selection:** Each triangle is selected with probability proportional to its area, ensuring uniform sampling over the surface.
- **Barycentric sampling:** For a triangle with vertices v_1, v_2, v_3, a sample point r is drawn using:

$$r = (1-\sqrt{u})v_1 + \sqrt{u}(1-w)v_2 + \sqrt{u}wv_3, \quad u, w \sim \mathscr{U}(0,1)$$

This formula produces points uniformly distributed over triangle interiors. Crucially, r is a smooth function of the triangle vertices and the sampled random variables u, w. Through the **reparameterization trick**—where u, w are held fixed during backpropagation—gradients from the loss propagate cleanly to the vertex positions. This makes it possible for the model to learn mesh geometry from supervision applied directly to its surface.

In practice, thousands of points (typically 3k–10k) are sampled per mesh per iteration, enabling fine-grained geometric feedback across the full predicted surface. This helps eliminate artifacts such as sagging triangles or curvature mismatches that would go unnoticed under vertex-only supervision.

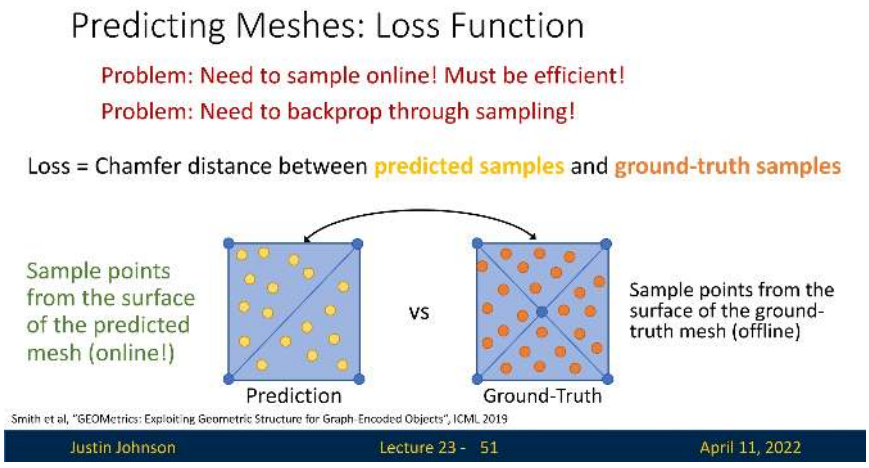

Figure 23.23: Differentiable surface-aware Chamfer loss in GEOMetrics. Thousands of points are sampled online from predicted and ground-truth mesh surfaces using area-weighted triangle selection and barycentric coordinates. The resulting loss provides uniform supervision across the entire surface and allows gradients to flow through the reparameterized sampling process.

Complete Loss Formulation in GEOMetrics

Beyond surface alignment, GEOMetrics incorporates two additional regularizers for mesh quality:

- **Edge Length Regularization** $\mathscr{L}_{\text{edge}}$: discourages stretched edges and flying vertices.
- **Laplacian Regularization** $\mathscr{L}_{\text{lap}}$: promotes local smoothness by minimizing differences between a vertex and the average of its neighbors.

The complete training objective is:

$$\mathscr{L}_{\text{total}} = w_1\mathscr{L}_{\text{PtS}} + w_2\mathscr{L}_{\text{edge}} + w_3\mathscr{L}_{\text{lap}} + w_4\mathscr{L}_{\text{latent}}$$

where $\mathscr{L}_{\text{latent}}$ is a perceptual loss that encourages global structural consistency using an auxiliary mesh-to-voxel autoencoder. Weights w_i are fixed scalars tuned for empirical balance.

Adaptive Mesh Refinement via Face Splitting

Perhaps even more impactful than its loss function is GEOMetrics' ability to *adaptively modify mesh topology*. Unlike Pixel2Mesh, which deforms a mesh with fixed vertex count and connectivity, GEOMetrics dynamically adds new vertices and faces during training. It identifies high-curvature or high-error regions and splits faces accordingly—concentrating resolution where it is needed most. This allows GEOMetrics to capture sharp details and fine contours without overloading flat regions with unnecessary vertices, leading to more efficient and expressive meshes.

This synergy between:

- *accurate surface-level supervision*.
- *adaptive geometric capacity*.

is what enables GEOMetrics to surpass previous models like Pixel2Mesh++ in reconstruction fidelity.

Advantages Over Vertex-Based Supervision

Unlike Pixel2Mesh's vertex-to-point Chamfer loss, GEOMetrics' point-to-point surface loss:

- **Supervises the entire surface**, including triangle interiors.
- **Handles varying mesh resolutions**, as supervision is decoupled from vertex count.
- **Respects valid geometric variation**, allowing alternative triangulations of the same surface to be treated equally.
- **Provides dense feedback**, improving training stability and reconstruction fidelity.

Combined with adaptive face splitting, this loss enables GEOMetrics to produce smoother, more accurate, and topologically robust 3D shapes—closely matching the true surface geometry and not just sparse surface samples.

Limitations of Pixel2Mesh and the Motivation for Successor Models

While *Pixel2Mesh* introduced a landmark approach to deforming 3D meshes from a single RGB image using graph-based convolutions, several fundamental limitations restrict its generality and reconstruction quality. These include limited supervision, fixed-topology constraints, and reliance on single-view input. Each of these weaknesses directly motivated the development of successor models such as *Pixel2Mesh++* [689] and *Mesh R-CNN* [177].

Single-View Ambiguity and 2.5D Reconstruction

Pixel2Mesh is designed for single-view reconstruction. As a result, it struggles to infer geometry for regions not visible in the input image—such as the back of a chair or the underside of a car—because no direct pixel-level evidence is available. The model must hallucinate plausible completions from learned priors, often leading to reconstructions that appear reasonable from the input view but become implausible from novel viewpoints. This limitation manifests as a *2.5D facade*, where only the visible surfaces are accurate.

Pixel2Mesh++ [689] addresses this challenge by introducing a *multi-view deformation network*, which jointly optimizes mesh refinements over multiple input images with known camera poses. This enforces cross-view consistency, improves alignment across viewpoints, and reduces ambiguity from occluded regions—ultimately producing shapes that are globally correct, not just front-facing.

Topological Rigidity and the Genus-0 Constraint

Because Pixel2Mesh deforms a fixed ellipsoid mesh, it inherits a genus-0 topology by design. The graph unpooling operations add vertices and increase resolution, but never alter the global connectivity. As such, the model cannot represent structures with holes, handles, or disconnected components (e.g., mugs, chairs, or lamps).

This motivated the development of *Mesh R-CNN* [177], which replaces template deformation with a two-stage voxel-to-mesh pipeline. A coarse voxel occupancy grid is first predicted and then converted into a mesh using a differentiable surface extraction method. This allows the resulting mesh to assume arbitrary topology—including high-genus structures—removing the restrictive genus-0 bottleneck entirely.

Surface-Level Supervision and Over-Smoothing Limitations

Pixel2Mesh originally supervised mesh deformation by applying the symmetric Chamfer Distance between predicted vertex positions and a pre-sampled ground-truth point cloud. While effective for guiding coarse shape, this *vertex-only supervision* ignores the faces connecting the vertices. As a result, the model can produce meshes where the corners of triangles are well-aligned, yet the interiors may sag or bulge—creating visibly inaccurate geometry that incurs no loss penalty.

This deficiency is exacerbated by the use of strong regularizers—such as Laplacian and edge length losses—which encourage smooth deformations. Combined with the inherently diffusive nature of graph convolutions, these constraints often lead to *over-smoothed* reconstructions that lack sharp creases, high-frequency detail, or geometric precision in sparsely sampled regions.

Pixel2Mesh++ [689] directly addresses this issue by incorporating a *resampled surface-level Chamfer loss*. Instead of comparing vertex coordinates, it samples dense point clouds from the predicted mesh surface using area-weighted barycentric sampling and computes the Chamfer loss against the ground-truth surface. This resampling improves gradient coverage over the full mesh and provides more reliable supervision in regions with irregular tessellation or thin structures.

GEOMetrics [574] builds further on this idea by introducing fully differentiable sampling operations and designing losses that explicitly evaluate *surface-to-surface geometry*. Its Point-to-Point (PtP) loss compares dense sampled point clouds, while the more refined Point-to-Surface (PtS) loss measures exact distances from predicted points to ground-truth triangle faces—yielding higher fidelity and stronger surface alignment. These losses not only address sagging artifacts, but also resolve ambiguities due to vertex layout or triangulation mismatches.

While both Pixel2Mesh++ and GEOMetrics move beyond vertex-based loss functions, the key distinction lies in formulation. Pixel2Mesh++ retains the Chamfer framework but improves its application via surface sampling; GEOMetrics reformulates the loss to reflect the mesh's implicit surface, enabling direct point-to-face supervision.

Domain Shift and Real-World Generalization

Trained primarily on synthetic datasets like ShapeNet, Pixel2Mesh suffers from a domain gap when tested on real-world imagery. Lighting variation, clutter, occlusion, and camera calibration errors can all destabilize the vertex-to-image feature alignment step. This leads to inconsistent updates and poor reconstruction quality in natural scenes.

Mesh R-CNN [177] takes a different route: by grounding its pipeline in instance detection via Mask R-CNN, it gains robustness to diverse, real-world input. Mesh generation is conditioned on high-confidence 2D detections, improving generalization to cluttered, multi-object scenes.

Summary and Takeaways

Pixel2Mesh introduced a foundational framework for 3D mesh reconstruction from single RGB images, combining graph-based deformation, vertex–image alignment, and progressive refinement. However, key limitations—including its reliance on single-view input, fixed genus-0 template topology, and vertex-only supervision—highlighted the need for more flexible and accurate approaches.

The first evolution in this direction was *Pixel2Mesh++* [689], which enriched the original framework without discarding its template-based foundations. By incorporating multi-view image input and surface-aware losses via differentiable mesh sampling, it improved geometric fidelity and alleviated ambiguity from occlusion and limited field-of-view—yet still operated under a fixed-topology deformation regime.

More structurally transformative approaches soon followed:

- **GEOMetrics** [574] enhanced surface-level supervision through dense differentiable sampling and adaptive face splitting. This resolved vertex sparsity and sagging-face artifacts while enabling targeted geometric refinement—but remained limited to low-genus templates.
- **Mesh R-CNN** [177] broke free from the fixed-topology constraint altogether. By predicting voxel-based occupancy maps followed by mesh extraction and refinement, it enabled the generation of arbitrary topology—including holes, handles, and disconnected parts—marking a major departure from template-based reconstruction.

Together, these successor models reflect a progression: from enriching Pixel2Mesh with multi-view cues and improved losses, to redefining the reconstruction pipeline entirely. As we now transition to *Mesh R-CNN*, we will see how voxel-driven, detection-aware pipelines offer a powerful alternative for general-purpose, topology-flexible 3D mesh reconstruction.

23.6.2 Mesh R-CNN: Topology-Aware Mesh Reconstruction from Real-World Images

Motivation and Key Ideas

Traditional mesh reconstruction pipelines, such as Pixel2Mesh (Section 23.6.1), deform a fixed-topology template mesh (typically genus-0), which fundamentally limits their capacity to represent real-world objects with topological complexity—such as holes, multiple parts, or disconnected components.

Mesh R-CNN [177] introduces a hybrid reconstruction paradigm that overcomes this limitation by integrating two complementary representations:

- A **voxel-based prediction branch** first estimates a coarse 3D shape from the input image. Since voxel grids are regular and topology-agnostic, this stage can represent arbitrary structures, including objects with holes or non-manifold parts.
- A **mesh refinement branch** then converts the voxel output into a triangular mesh and applies graph-based neural operations to improve surface fidelity and geometric detail.

While voxel grids offer topological flexibility, they suffer from low resolution and quantization artifacts due to memory constraints. Mesh R-CNN resolves this by converting the voxel output into a surface mesh using the `cubify` operation, and then refining the mesh using a graph convolutional network (GCN). This two-stage process combines the strengths of volumetric and surface-based approaches: arbitrary topology from voxels, and high-resolution detail from meshes.

The entire system is trained end-to-end using paired RGB images and watertight 3D meshes, enabling amodal 3D shape prediction even in the presence of occlusion.

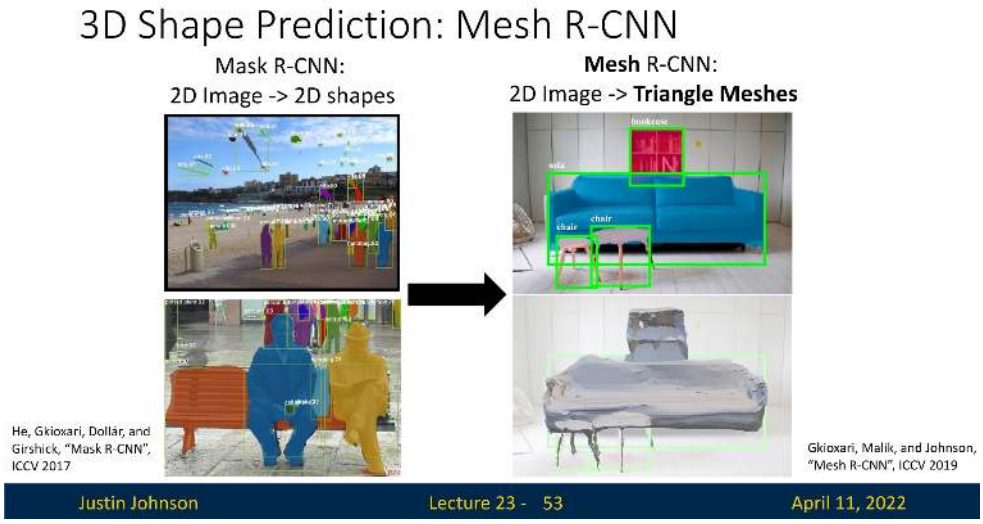

Figure 23.24: Mesh R-CNN augments Mask R-CNN [209] to move from 2D instance segmentation to 3D shape prediction. The pipeline proceeds from 2D object detection to voxel prediction and finally to mesh refinement.

Mask R-CNN as Backbone for 2D Instance Segmentation

Mesh R-CNN builds on the Mask R-CNN architecture introduced in Section 15.5.1, which performs 2D object detection and instance segmentation by augmenting Faster R-CNN with a pixel-level segmentation head. Given an input image, Mask R-CNN produces:

- Bounding box proposals for object instances.
- RoI-aligned feature maps for each proposal.
- Binary segmentation masks and class labels for each instance.

Mesh R-CNN inherits these components and reuses RoI-aligned features to bootstrap 3D shape prediction in the following stages.

The Mesh Prediction Head: A Hybrid Voxel-to-Mesh Strategy

With Mask R-CNN as its 2D perception backbone (Section 15.5.1), *Mesh R-CNN* augments this architecture with a dedicated 3D shape prediction branch, called the *mesh head*. This component reconstructs a full 3D mesh for each detected object instance and is designed to balance **topological flexibility** with **geometric precision**.

The key architectural insight is to decompose the reconstruction task into two complementary and end-to-end trainable stages:

1. **Voxel Prediction:** For each object detected by Mask R-CNN, a coarse 3D occupancy grid is predicted from RoI-aligned image features. This voxel grid serves as a topology-agnostic representation that can naturally encode complex structures—including holes, thin parts, and disconnected components—without being constrained by mesh connectivity or genus. Because voxel occupancy is defined per grid cell, this stage supports per-instance reconstructions with arbitrary and varying topology.
2. **Mesh Refinement:** The predicted voxel grid is converted into a watertight triangle mesh using a dedicated `cubify` operation, which replaces each occupied voxel with a triangulated cuboid, merges shared vertices and edges, and removes interior faces. This produces an initial mesh whose topology directly mirrors the voxelized shape. To improve geometric fidelity, the mesh is then refined by a sequence of *graph convolutional layers* that deform vertex positions while preserving the established connectivity.

This voxel-to-mesh pipeline addresses a major limitation of prior methods like Pixel2Mesh, which were constrained to deforming a single genus-0 template mesh and thus unable to represent objects with complex topologies. By deferring mesh construction until after a coarse shape has been predicted, Mesh R-CNN avoids prematurely committing to a fixed topology and instead enables the reconstruction of multiple, topologically diverse meshes—one per detected instance—even from a single input image.

Crucially, the voxel and mesh branches are trained jointly within a fully differentiable framework. The voxel grid is supervised via a binary occupancy loss, while the mesh is optimized using surface-level objectives such as Chamfer distance, normal consistency, and edge regularization (all seen previously with Pixel2Mesh). This tight integration enables the system to learn both *what* to reconstruct (via voxels) and *how* to reconstruct it accurately (via mesh refinement), resulting in high-quality 3D predictions that generalize across diverse object categories and scene configurations.

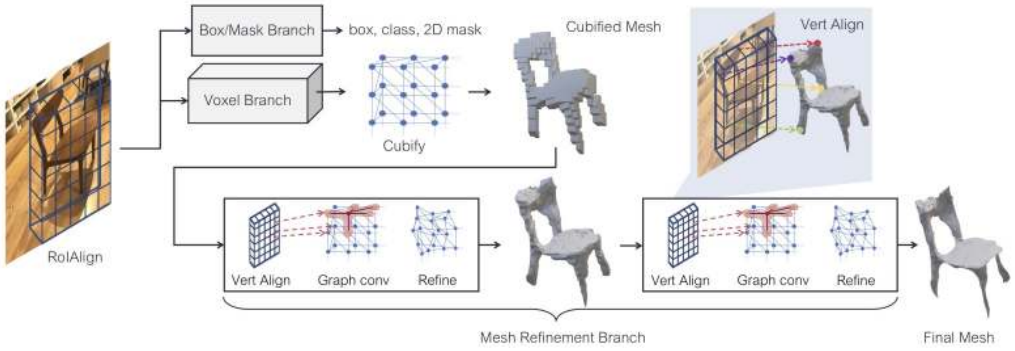

Figure 23.25: **System overview of Mesh R-CNN.** The architecture extends Mask R-CNN by adding a 3D shape prediction head. For each detected object, the voxel branch first predicts a coarse 3D occupancy grid aligned with the camera frustum. This voxel scaffold is then converted into a watertight mesh via the `cubify` operation and refined through a cascade of graph-based mesh deformation stages (similarly to 23.6.1). Each refinement step incorporates both 3D geometry and 2D image features. *Figure reproduced from Gkioxari et al. [177].*

The Voxel Branch for Topological Flexibility

The first stage of the mesh head in Mesh R-CNN is the **voxel prediction branch**, which estimates a coarse 3D shape for each detected object as a voxel occupancy grid. Voxel representations are topology-agnostic by construction: they impose no constraints on surface connectivity and can naturally represent complex geometric structures—including holes, disconnected components, and non-manifold parts—without requiring a mesh template. This stands in contrast to methods like *Pixel2Mesh* (Section 23.6.1), which deform a fixed-topology genus-0 sphere and thus cannot model diverse shape topologies.

In Mesh R-CNN, the voxel branch uses RoI-aligned features from the Mask R-CNN backbone to predict occupancy probabilities over a grid of shape $G \times G \times G$, where $G = 24$ or 48 depending on the dataset. Specifically, $G = 48$ is used for synthetic datasets like ShapeNet, while $G = 24$ is used for real-image datasets like Pix3D to manage memory constraints. Each voxel (i, j, k) receives a scalar logit, which is transformed via a sigmoid activation into an occupancy probability $p_{ijk}^{\text{pred}} \in [0, 1]$. This probabilistic grid forms a coarse but flexible volumetric scaffold that directly determines the topology of the output mesh in the next stage.

Perspective-Aware Voxel Grid via Camera Frustum Alignment

To ensure metric grounding and spatial consistency, Mesh R-CNN defines its voxel grid within a **camera-aligned 3D frustum**. This volume is constructed using the predicted 2D bounding box and known camera intrinsics K, anchoring the 3D grid in true physical coordinates rather than in an arbitrary canonical frame. The process consists of two phases: constructing the 3D voxel volume, and populating it with 2D-aligned features.

Phase 1: Constructing the Frustum-Aligned Voxel Grid

Step 1: Defining the Frustum Volume. Given a Region of Interest (RoI) bounding box

$$\mathscr{B} = (u_{\min},\ v_{\min},\ u_{\max},\ v_{\max}),$$

and a known camera intrinsics matrix K, Mesh R-CNN constructs a perspective frustum in 3D by back-projecting the four image-plane corners of $\mathscr{B}$ using K^{-1}. Each back-projected ray originates at the camera center and passes through a bounding box corner, defining the edges of the viewing frustum.

To bound the depth extent of the object, these rays are truncated between near and far depth planes, z_{near} and z_{far}, which define the front and back clipping planes of the frustum. These values are not fixed in the paper but are dataset-dependent; for example, values like 0.5m to 2.5m may be used for indoor objects, while normalized scales are often applied for datasets like ShapeNet. The key point is that the frustum adapts to the RoI and camera parameters, ensuring that the predicted voxel grid aligns with the object's visible volume in camera coordinates.

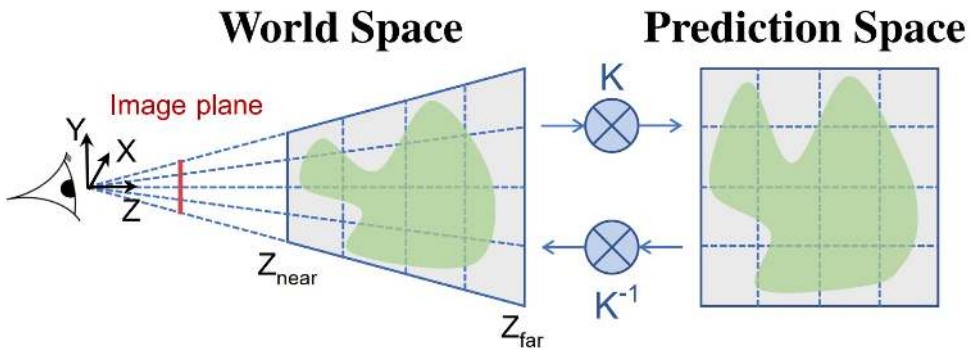

Figure 23.26: **Frustum-aligned prediction space in Mesh R-CNN.** Rather than predicting occupancy in a uniform world-aligned cube, Mesh R-CNN defines voxel predictions in a space aligned with the image plane. This is achieved by applying the camera intrinsics matrix K during voxel warping; applying K^{-1} transforms the voxel coordinates back into 3D world space. The result is a truncated frustum bounded by near and far depth planes $(z_{\text{near}}, z_{\text{far}})$, centered on the detected object. This frustum-aware grid mirrors the actual viewing volume of the camera, ensuring that voxel resolution is higher for nearby regions and coarser at greater depths—naturally encoding perspective and spatial priors. For background on camera intrinsics and perspective projection, see [568]. *Figure adapted from Gkioxari et al. [177].*

Step 2: Canonical Grid Initialization. A logical voxel grid $\mathscr{G} \in [-1,1]^3$ is instantiated with shape $G \times G \times G$. This canonical cube serves as a resolution-independent coordinate frame for voxel predictions. Each voxel index (i,j,k) is mapped to a normalized position $(x,y,z) \in [-1,1]^3$, where:

- $x = -1$ denotes the leftmost extent and $x = 1$ the rightmost.
- $y = -1$ denotes the bottom and $y = 1$ the top.
- $z = -1$ corresponds to the front of the volume (near plane), and $z = 1$ to the back (far plane).

Step 3: Perspective-Aware Warping. To map $\mathscr{G}$ into the physical frustum, each normalized coordinate (x, y, z) is transformed into a 3D point (X, Y, Z) using a homography induced by the camera intrinsics and frustum geometry. This transformation ensures:

- Voxels near the camera are tightly packed and represent small metric volumes.
- Voxels deeper in the frustum span larger volumes, mimicking perspective scaling.

This warping is applied before voxel prediction begins, allowing the 3D CNN to operate over a regular grid while producing perspective-consistent outputs.

Phase 2: Lifting 2D Features into 3D

Intuition. Rather than explicitly constructing a 3D feature volume, Mesh R-CNN leverages a fully-convolutional 2D network to infer 3D shape by predicting vertical voxel columns directly from RoI-aligned image features.

Step 4: RoI Feature Extraction. The Mask R-CNN backbone provides RoI-aligned feature maps $F \in \mathbb{R}^{C \times G \times G}$ for each object proposal, where G denotes the spatial resolution of the voxel grid along the horizontal and vertical image axes.

Step 5: 2D Fully-Convolutional Prediction. A small 2D fully-convolutional network—analogous in structure to the Mask R-CNN mask head—is applied to F to produce an output tensor of shape $G \times G \times G$. Here, each pixel location in the $G \times G$ grid corresponds to a column of G occupancy logits along the depth axis of the voxel grid.

Step 6: Voxel Probability Estimation. A sigmoid activation is applied to the output logits to obtain voxel-wise probabilities:

$$p_{ijk}^{\text{pred}} = \sigma(\ell_{ijk}) \quad \text{for all } (i, j, k) \in [0, G)^3,$$

where ℓ_{ijk} is the logit corresponding to voxel (i, j, k). The result is a perspective-aware, topology-flexible volumetric prediction aligned with the camera frustum.

Phase 3: Voxel Supervision and Mesh Conversion

Intuition. Starting from a voxel-aligned feature volume, we now convert the predicted occupancy grid into a coarse surface mesh. The `cubify` step transforms this discrete structure into a watertight mesh suitable for graph-based refinement.

Step 7: Voxel-Wise Binary Cross-Entropy. The voxel prediction head outputs a probability grid $p^{\text{pred}} \in [0, 1]^{G \times G \times G}$ representing the likelihood of occupancy at each voxel location.
This is trained against a binary ground-truth volume $p^{\text{gt}} \in \{0, 1\}^{G \times G \times G}$ using voxel-wise binary cross-entropy:

$$\mathscr{L}_{\text{voxel}} = \frac{1}{G^3} \sum_{i,j,k} \text{BCE}(p_{ijk}^{\text{pred}},\ p_{ijk}^{\text{gt}}).$$

This encourages the network to produce a volumetric shape estimate that captures object structure and supports topological variation.

Step 8: Thresholding the Occupancy Grid. At inference time, the predicted voxel probabilities are binarized using a fixed threshold $\tau = 0.2$, as used in the original Mesh R-CNN experiments on ShapeNet and Pix3D:

$$V_{ijk} = \mathbb{1}[p_{ijk}^{\text{pred}} > \tau].$$

This produces a binary voxel occupancy grid $V \in \{0,1\}^{G \times G \times G}$ that defines the object's coarse 3D shape. *Note:* The threshold τ can be adjusted per dataset to balance recall and precision, though 0.2 was found to work well empirically in the original evaluations [177].

Step 9: Cubify: Voxel Grid to Watertight Mesh. The `cubify` operator [177] transforms the binary voxel volume V into a triangle mesh $\mathscr{M} = (\mathscr{V}, \mathscr{F})$ using the following procedure:

Step 9:a. *Cube Placement.* For each occupied voxel $V_{ijk} = 1$, a unit cube is placed at grid location (i, j, k), consisting of 8 vertices and 12 triangle faces.

Step 9:b. *Face Culling.* If a neighboring voxel in any of the six axial directions is also occupied, the shared face between cubes is removed. This avoids redundant geometry and ensures watertightness.

Step 9:c. *Vertex Merging.* Once all cube faces are placed and pruned, duplicate vertices and edges are merged, yielding a coherent mesh with consistent connectivity and arbitrary topology.

Vectorized Cubify for Efficient Execution. A naive implementation of `cubify` would loop over all G^3 voxel cells, checking and processing each one. To make this practical for end-to-end training, Mesh R-CNN implements a fully vectorized version:

- The binary occupancy grid is convolved with small 3D kernels that detect voxel boundaries and interior faces.
- Face presence masks are computed in parallel across the grid.
- A custom CUDA kernel emits all vertices and triangles in a batched, GPU-accelerated fashion.

This reduces cubification time from over 300 ms to roughly 30 ms per batch ($N = 32$, $G = 32$), making it feasible to include mesh conversion directly within the training loop.

Summary and Advantages

The perspective-aware voxel branch enables Mesh R-CNN to predict topologically diverse 3D shapes directly from image features while preserving metric accuracy and view consistency. By warping a canonical voxel grid into the camera frustum and anchoring each voxel to a pixel-aligned image location, this design provides:

- **Topological flexibility:** Arbitrary shapes with holes, disconnected parts, etc.
- **Metric grounding:** Voxel predictions are made in camera space, aligned with the object's true scale and depth.
- **Learning efficiency:** The network operates over a regular cube, while projection and warping handle geometry and alignment.

This voxel branch forms the foundation for Mesh R-CNN's full 3D mesh reconstruction pipeline.

Mesh Refinement Branch: Image-Guided Graph Deformation

The voxel branch provides a coarse, topology-flexible mesh extracted via `cubify`, but the resulting geometry is blocky and lacks high-fidelity surface detail. The **mesh refinement branch** addresses this by iteratively displacing the vertices of the cubified mesh using image-guided graph convolutions, producing a final shape aligned with both 2D appearance and 3D structure.

Fixed-Topology Refinement Pipeline

Let $\mathscr{M}^{(0)} = (\mathscr{V}, \mathscr{E}, \mathscr{F})$ denote the triangle mesh output by cubification. This mesh has fixed topology and vertex count determined entirely by the voxel resolution (e.g., 24^3). Unlike Pixel2Mesh (Section 23.6.1), Mesh R-CNN performs *no graph unpooling or vertex subdivision*. Instead, the refinement branch updates vertex positions across three deformation stages $s = 1, 2, 3$, each comprising several stages.

(a) **VertAlign** [177]: Each vertex $\mathbf{v}_i^{(s-1)} \in \mathbb{R}^3$ is projected onto the image plane via the camera intrinsics K. A RoI-aligned CNN feature map is bilinearly sampled at this projected location, yielding an image feature vector. This feature is concatenated with the vertex's current latent feature vector $\mathbf{f}_i^{(s-1)}$, enriching it with 2D appearance context.

(b) **Graph Convolutional Layers**: Several residual GCN layers propagate and transform vertex features based on the mesh's fixed edge structure $\mathscr{E}$. These operations aggregate information from neighboring vertices while preserving geometric and topological coherence.

(c) **Vertex Displacement Prediction**: A linear MLP head predicts a 3D displacement $\Delta\mathbf{v}_i^{(s)} \in \mathbb{R}^3$ for each vertex. The updated position is computed via residual addition:

$$\mathbf{v}_i^{(s)} = \mathbf{v}_i^{(s-1)} + \tanh(\Delta\mathbf{v}_i^{(s)}),$$

where the `tanh` activation stabilizes training by bounding displacement magnitude.

This pipeline produces progressively refined meshes $\mathscr{M}^{(1)}, \mathscr{M}^{(2)}, \mathscr{M}^{(3)}$, each with the same vertex connectivity as $\mathscr{M}^{(0)}$, but improved geometric fidelity.

Loss Functions

Voxel Supervision Loss. The voxel branch predicts a coarse 3D occupancy grid $p^{\text{pred}} \in [0,1]^{G\times G\times G}$, supervised by binary cross-entropy against a ground-truth volume $p^{\text{gt}} \in \{0,1\}^{G\times G\times G}$:

$$\mathscr{L}_{\text{voxel}} = \lambda_{\text{voxel}} \cdot \frac{1}{G^3} \sum_{i,j,k} \text{BCE}\left(p_{ijk}^{\text{pred}},\, p_{ijk}^{\text{gt}}\right), \qquad \lambda_{\text{voxel}} = \begin{cases} 1 & \text{ShapeNet} \\ 3 & \text{Pix3D} \end{cases}$$

This term encourages the model to predict a coarse but topologically valid structure that serves as the scaffold for mesh generation.

Mesh Refinement Loss. At each refinement stage $s = 1, 2, 3$, the model samples **5,000 points** from the predicted mesh $P^{(s)}$ and the ground-truth mesh Q and evaluates three differentiable geometric losses:

- *Chamfer Distance*:

$$\mathscr{L}_{\text{cham}}^{(s)} = \frac{1}{|P^{(s)}|} \sum_{p\in P^{(s)}} \min_{q\in Q} \|p-q\|_2^2 + \frac{1}{|Q|} \sum_{q\in Q} \min_{p\in P^{(s)}} \|q-p\|_2^2.$$

- *Normal Consistency*:

$$\mathscr{L}_{\text{norm}}^{(s)} = \frac{1}{|F|} \sum_{f \in F} \left(1 - \frac{\mathbf{n}_f \cdot \mathbf{n}_f^{\text{gt}}}{\|\mathbf{n}_f\| \cdot \|\mathbf{n}_f^{\text{gt}}\|} \right).$$

- *Edge Length Regularization*:

$$\mathscr{L}_{\text{edge}}^{(s)} = \frac{1}{|E|} \sum_{(i,j) \in E} \|\mathbf{v}_i - \mathbf{v}_j\|_2^2.$$

This term plays a crucial role in maintaining mesh integrity by discouraging *very short edges* that can lead to self-intersections and degenerate faces. While its formulation mathematically penalizes longer edges more heavily due to its squared length structure, its *functional effect during training*—especially in conjunction with shape- and normal-alignment terms—is to prevent vertex collapse. Extremely short edges often arise when adjacent vertices are pulled too close together, causing local triangle degeneracy and overlapping surfaces. By imposing a soft constraint on edge length, this loss nudges the mesh toward a more regular, uniformly tessellated structure, helping eliminate artifacts like face folding, wrinkling, and self-intersections.

Empirical ablations in the paper confirm that removing this term leads to "degenerate predicted meshes with many overlapping faces" [177], while including it significantly improves mesh quality by preserving geometric plausibility.

Each stage's refinement loss is:

$$\mathscr{L}^{(s)} = \lambda_{\text{cham}} \mathscr{L}_{\text{cham}}^{(s)} + \lambda_{\text{norm}} \mathscr{L}_{\text{norm}}^{(s)} + \lambda_{\text{edge}} \mathscr{L}_{\text{edge}}^{(s)}, \qquad \mathscr{L}_{\text{mesh}} = \frac{1}{3} \sum_{s=1}^{3} \mathscr{L}^{(s)}.$$

Training Variants. To balance quantitative accuracy and visual quality, Mesh R-CNN defines the following loss weight settings:

Variant	λ_{cham}	λ_{norm}	λ_{edge}
Best (ShapeNet, Pix3D)	1.0	0	0
Pretty (ShapeNet)	1.0	0	0.2
Pretty (Pix3D)	1.0	0.1	1.0

The "Best" variant optimizes Chamfer distance exclusively for quantitative benchmarks. The "Pretty" variant adds smoothness terms: on **ShapeNet**, a moderate edge weight promotes mesh regularity; on **Pix3D**, both edge and normal terms are boosted to improve robustness on real images.

Summary. The voxel loss captures coarse topological structure, while the mesh losses refine geometry by aligning surfaces (Chamfer), smoothing normals, and avoiding degenerate edges. This multi-stage supervision enables Mesh R-CNN to produce meshes that are both structurally sound and visually plausible from single RGB images.

Summary

Mesh R-CNN's refinement branch combines fixed-topology triangle meshes from voxel predictions with per-vertex 2D image features to produce detailed, amodal 3D shapes. Unlike Pixel2Mesh, which deforms and subdivides a template mesh, Mesh R-CNN freezes mesh connectivity after voxelization and performs all refinement through graph-based vertex displacements. This avoids topological restrictions, maintains geometric consistency, and enables scalable, instance-specific mesh generation in real-world scenes.

Experiments and Ablations

Mesh R-CNN undergoes comprehensive empirical evaluation on both synthetic and real-world data, focusing on its ability to predict accurate and topologically diverse 3D meshes from single images. The experiments evaluate detection, reconstruction, robustness to occlusion, and the effects of various architectural choices.

Datasets

Two benchmark datasets are used:

- **ShapeNet** [76]: Used for validating the mesh prediction module. It contains clean renderings of CAD objects with known camera parameters.
- **Pix3D** [593]: A real-world dataset pairing 2D images with aligned 3D shapes, including cluttered scenes and occlusions. Mesh R-CNN is the first system to tackle *joint detection and shape inference* on this dataset.

Evaluation Metrics

The system is evaluated using:

- **Chamfer Distance (CD)**: Measures point-wise distance between predicted and ground-truth surfaces.
- **Normal Consistency (NC)**: Penalizes misaligned surface normals.
- **F1$_\tau$ Score**: Harmonic mean of precision and recall over distance threshold τ.
- **AP$_{\text{mesh}}$**: For Pix3D, combines 2D detection and 3D reconstruction quality. A prediction is correct if its class is correct, it is not a duplicate, and its F1$_{0.3}$ score exceeds 0.5.
- **AP$_{\text{box}}$, AP$_{\text{mask}}$**: Standard COCO-style detection and segmentation metrics, also reported on Pix3D.

Key Results on ShapeNet

Mesh R-CNN significantly outperforms prior work including Pixel2Mesh+, 3D-R2N2, and PSG. Its "Best" variant achieves a Chamfer distance of 0.306 and F1$_\tau$ of 74.84 on the standard test set. On the "Holes Test Set"—a curated subset of 534 objects with visible holes—Mesh R-CNN far exceeds template-based methods like Pixel2Mesh+, which are limited by their fixed-topology assumptions.

Figure 23.27: Qualitative ShapeNet comparisons. While Pixel2Mesh+ fails to represent holes due to spherical initialization, Mesh R-CNN produces topologically faithful reconstructions for chairs, tables, and other perforated objects (Adapted from ICCV 2019 talk).

Key Results on Pix3D

On real-world scenes, Mesh R-CNN outperforms all baselines (Voxel-Only, Sphere-Init, Pixel2Mesh+) in AP_{mesh} across nearly all object categories. Performance gains are especially notable for topologically complex classes like bookcases (+21.6%), tables (+16.7%), and chairs (+7.3%).

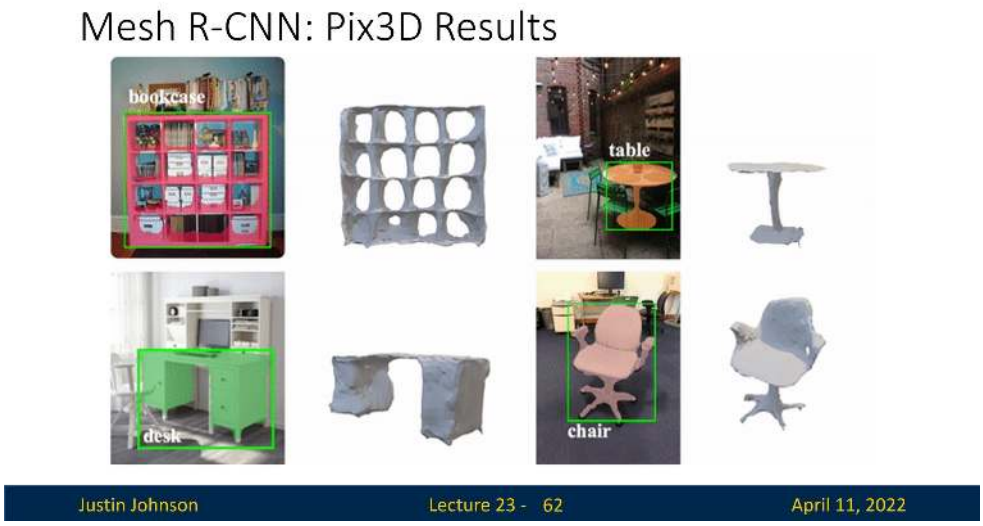

Figure 23.28: Qualitative Pix3D reconstructions. Mesh R-CNN successfully captures complex scene structures including desks, tables, and bookshelves.

Amodal Completion

Mesh R-CNN is capable of completing occluded object geometry. As shown in the following figure, it reconstructs sofas occluded by dogs and chairs, enabled by volumetric reasoning and perceptual feature alignment.

Figure 23.29: Amodal shape completion: Mesh R-CNN reconstructs full geometry despite occlusion (e.g., sofa behind dog and chair).

Failure Modes

Errors in the 2D segmentation stage can propagate to 3D mesh prediction. The following figure shows a bookshelf with missing compartments due to segmentation holes in the input mask.

Figure 23.30: Failure case: segmentation noise in 2D leads to missing geometry in the 3D mesh.

Ablation Studies

The performance of Mesh R-CNN is validated through ablation studies that isolate the impact of each architectural and supervisory component. These experiments, conducted on ShapeNet and Pix3D, quantitatively and qualitatively demonstrate why voxel-based initialization, iterative refinement, and geometric regularization are all essential for high-fidelity mesh prediction.

- **Voxel-Only:** In this setting, the mesh refinement branch is removed and the final mesh is directly obtained via `cubify` on the voxel occupancy grid. While this preserves coarse topology, the resulting meshes are blocky and lack fine detail. On ShapeNet, the voxel-only model yields a Chamfer distance of **0**.**916** and an F1@0.3 score of **33**.**1**%, significantly worse than the full model's **0**.**133** Chamfer and **86**.**6**% F1@0.3 [177, Table 2]. Similarly, on Pix3D, voxel-only achieves an AP_{mesh} of only **5**.**3**% vs. **51**.**1**% for the full system (Stage 1, COCO pretraining). These results confirm that the voxel branch alone is insufficient for detailed surface recovery; mesh refinement is indispensable.
- **Pixel2Mesh+ and Sphere-Init:** These baselines deform a fixed-topology template mesh (typically a genus-0 sphere) using GCN layers. While adequate for simple shapes, they cannot represent objects with holes or disconnected parts. On ShapeNet's "Holes Test Set," Pixel2Mesh+ achieves a Chamfer distance of **0**.**137** and F1@0.3 of **85**.**5**%, underperforming Mesh R-CNN's **0**.**130** and **86**.**7**% respectively [177, Table 2]. The performance gap is especially pronounced on Pix3D, where Mesh R-CNN achieves an AP_{mesh} of 48.2% on chairs and 70.2% on bookcases in Stage 1, compared to 26.7% and 34.1% respectively for Pixel2Mesh+, yielding substantial improvements of $+21.5\%$ and $+36.1\%$. These results underscore the limitations of fixed-topology deformation approaches and demonstrate the superiority of Mesh R-CNN's voxel-initialized pipeline, which enables prediction of meshes with arbitrary topology, better aligned to the structural diversity present in real-world images.

- **Refinement Stages:** Mesh R-CNN performs mesh refinement in three sequential stages, each consisting of vertex-image alignment, graph convolution, and vertex updates. This coarse-to-fine process allows the model to progressively capture global structure and fine surface detail. While the ShapeNet Chamfer distance for the full model with three stages is **0**.**133** [177, Table 2], the paper does not report direct Chamfer values for single- or two-stage variants on ShapeNet. However, a related ablation on Pix3D reveals that reducing from three to one refinement step degrades AP_{mesh} from **51**.**1**% to **48**.**6**% [177, Table 4]. This validates the benefit of iterative refinement. Although Mesh R-CNN does not visualize per-stage refinement qualitatively, earlier works like Pixel2Mesh show clear improvements in surface smoothness and structure across multiple GCN blocks [665, Figure 6], supporting the intuition that repeated refinement is essential for accurate and detailed reconstructions.
- **Loss Term Importance:** The edge length regularization loss $\mathscr{L}_{\text{edge}}$ plays a crucial role in ensuring mesh plausibility and geometric stability. While minimizing Chamfer distance alone may improve quantitative alignment, it can produce structurally degenerate results. Mesh R-CNN explicitly demonstrates this tradeoff: removing edge regularization (i.e., setting $\lambda_{\text{edge}} = 0$) yields a lower Chamfer distance of **0**.**133** for the "Best" model on ShapeNet, whereas including it with $\lambda_{\text{edge}} = 0.2$ in the "Pretty" model increases Chamfer distance to **0**.**171** [177, Table 2]. However, this quantitative gain comes at the cost of mesh quality. As visually shown in Figure 5, the absence of edge regularization leads to self-intersecting, overlapping faces and triangle clumping [177, Figure 5]. On Pix3D, the "Pretty" model uses a stronger regularization weight $\lambda_{\text{edge}} = 1.0$, which helps preserve surface coherence and avoid mesh collapse in cluttered scenes. These results, along with similar findings in prior work such as Wang et al. [665, Figure 5], confirm that while edge regularization may reduce agreement with point-based metrics, it is essential for producing visually plausible and topologically stable meshes.

Conclusion

These experiments demonstrate that Mesh R-CNN overcomes the limitations of fixed-topology methods by enabling variable-topology meshes, robust 3D inference from cluttered scenes, and end-to-end optimization of 2D and 3D objectives.

23.7 Implicit Surface Representations

From Discrete to Continuous Geometry

Traditional 3D shape representations—such as voxel grids, point clouds, or triangle meshes—explicitly enumerate spatial elements. In contrast, *implicit surface representations* define a shape as the level set of a continuous function $f : \mathbb{R}^3 \to 0, 1$. Given any spatial coordinate $\mathbf{x} \in \mathbb{R}^3$, the function $f(\mathbf{x})$ determines whether the point lies inside, outside, or on the object's surface. The surface is then implicitly defined as the set $\{\mathbf{x} \mid f(\mathbf{x}) = \tau\}$, where τ is a fixed threshold—typically $\tau = 0$ for signed distance fields or $\tau = 0.5$ for occupancy fields.

Occupancy Fields vs. Signed Distance Functions

Two widely used formulations of f are:

- **Occupancy Function:** Models the probability that a point is *inside* the object. The function $f(\mathbf{x}) \in [0, 1]$ outputs a probability, and the surface is implicitly defined by the decision boundary $\{\mathbf{x} \mid f(\mathbf{x}) = 0.5\}$.
- **Signed Distance Function (SDF):** Outputs the signed Euclidean distance from point $\mathbf{x}$ to the nearest surface. The sign indicates whether the point is inside (negative) or outside (positive), and the surface is given by the zero-level set $\{\mathbf{x} \mid f(\mathbf{x}) = 0\}$.

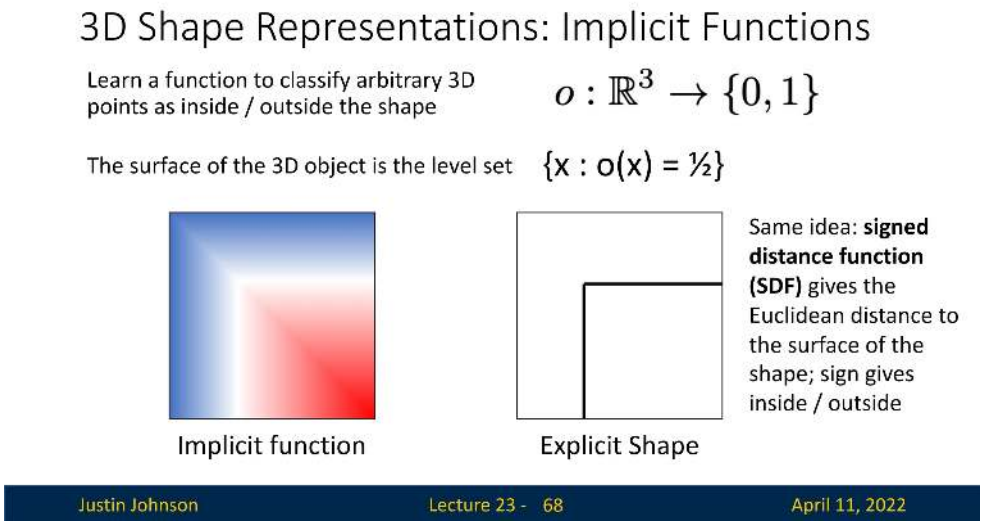

Figure 23.31: Left: explicit triangle mesh. Right: corresponding implicit field where the decision boundary $f(\mathbf{x}) = 0.5$ defines the surface.

Neural Implicit Models

Modern methods represent the function f using a small multi-layer perceptron (MLP), which maps 3D coordinates $\mathbf{x} \in \mathbb{R}^3$ to scalar values indicating occupancy or distance. This neural network can be evaluated at arbitrary resolutions and enables high-fidelity shape representation with a compact memory footprint. Notable examples include *Occupancy Networks* [425] and *DeepSDF* [467], both of which learn shape fields by regressing values pointwise.

Why Surface Extraction Is Required

Although neural implicit models are continuous and memory-efficient, they do not produce an explicit mesh directly. Most downstream tasks—such as rendering, simulation, or surface loss computation—require a triangulated mesh as output. This motivates dedicated extraction procedures that convert the learned function f into an explicit surface. The next subsection introduces one such method: *Multi-Scale Iso-surface Extraction (MISE)*, which constructs a mesh by progressively refining a voxel grid where the level set $f(\mathbf{x}) = \tau$ intersects.

23.7.1 Multi-Scale IsoSurface Extraction (MISE)

Occupancy Networks represent 3D geometry not as explicit meshes or voxels, but as the decision boundary of a learned *implicit function* $f_\theta(\mathbf{p}, \mathbf{x})$. Here, $\mathbf{p} \in \mathbb{R}^3$ is a spatial query point, and $\mathbf{x}$ is a conditioning input (e.g., an image or latent vector). The function predicts whether $\mathbf{p}$ lies inside the object depicted by $\mathbf{x}$, typically using a threshold $\tau = 0.5$ to define the surface. To extract an explicit mesh from this continuous field, Occupancy Networks use the *Multiresolution IsoSurface Extraction* (MISE) algorithm [425], which adaptively refines a voxel grid around the surface and outputs a high-resolution mesh.

Step 1 **Coarse Grid Initialization:** To locate the surface approximately, MISE first defines a coarse 3D voxel grid (e.g., 32^3) that spans the object's bounding box. The occupancy network $f_\theta(\mathbf{p}, \mathbf{x})$ is evaluated at each corner of the grid. Voxels whose corners straddle the threshold τ—i.e., some values are above and some below—are marked *active*, since the surface likely intersects them. This step efficiently identifies the region of interest without exhaustively evaluating the entire volume.

Step 2 **Octree Subdivision:** Instead of densely refining the whole grid, MISE recursively subdivides only the active voxels into eight subvoxels (octree refinement). New corner points introduced by the subdivision are evaluated by f_θ, and voxels are again checked for surface crossings. This process is repeated for N levels. The result is a spatial hierarchy that is fine near the implicit surface and coarse elsewhere, reducing computation and memory without sacrificing detail.

Step 3 **Marching Cubes Extraction:** Once the highest refinement level is reached, the Marching Cubes algorithm [391] is applied to the final voxel grid. Each voxel's eight occupancy values define a binary pattern (inside vs. outside), used to index a precomputed triangulation lookup table. Triangles are placed within the voxel by interpolating along edges where occupancy transitions across τ. Assembled over the full grid, this produces a watertight, manifold mesh approximating the surface.

Step 4 **Mesh Refinement via Gradient Descent:** The initial mesh may lie slightly off the true surface due to grid discretization. To correct this, each vertex $\mathbf{v} \in \mathscr{V}$ is optimized using gradient descent to minimize the loss

$$\mathscr{L}_{\text{align}} = \sum_{\mathbf{v} \in \mathscr{V}} \left(f_\theta(\mathbf{v}, \mathbf{x}) - \tau \right)^2 .$$

The gradient $\nabla_{\mathbf{v}} f_\theta(\mathbf{v}, \mathbf{x})$ guides each vertex toward the level set $f_\theta = \tau$, effectively "snapping" the mesh onto the continuous surface. This removes stair-step artifacts and enhances surface fidelity.

Each step in MISE builds upon the last: the coarse grid identifies candidate surface regions; octree subdivision focuses resolution near the surface; Marching Cubes generates an explicit triangle mesh; and gradient refinement polishes the mesh using the implicit signal. The result is a high-resolution, watertight mesh faithful to the learned 3D shape.

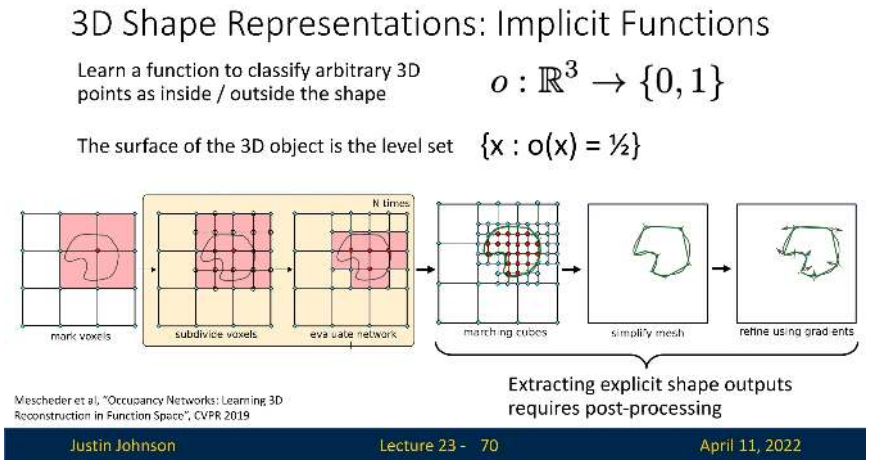

Figure 23.32: Multi-resolution surface extraction in Occupancy Networks [425]. The function is queried across a hierarchical voxel grid, refined at boundaries, and meshed via Marching Cubes.

23.7.2 Implicit Surface Advantages & Limitations

Advantages

Implicit surface representations offer several key benefits:

- **Resolution Independence:** Surfaces can be reconstructed at arbitrary resolution with no cubic memory growth.
- **Topological Flexibility:** No constraints on the number of components, holes, or genus of the reconstructed surface.
- **Differentiability:** Enables accurate normals, gradient-based surface optimization, and differentiable rendering.

Limitations

Despite their flexibility, implicit methods have drawbacks:

- **Post-Processing Required:** Explicit mesh output demands surface extraction, often involving non-differentiable Marching Cubes or costly optimization.
- **Slow Evaluation:** Each point query requires a forward pass through the network; querying millions of points is expensive.
- **Supervision Demands:** High-quality training requires accurate surface-level supervision, often obtained from watertight CAD models.

Relation to Octrees and Voxel Refinement

As in Octree Generating Networks (OGNs), implicit representations benefit from adaptive subdivision. Unlike OGNs, however, implicit models do not need to explicitly store voxel contents—pointwise evaluation suffices. This makes them ideal for continuous or parametric 3D learning pipelines.

23.8 General 3D Topics

This section outlines three foundational aspects relevant across most 3D reconstruction pipelines: metrics for shape comparison, the choice of coordinate systems, and the major datasets used for training and evaluation. Understanding these design decisions is critical for interpreting model performance and selecting the right tools for the task at hand.

23.8.1 Shape Comparison Metrics

Voxel IoU: Intuitive but Limited

In 2D image tasks, metrics like Intersection-over-Union (IoU) for bounding boxes and segmentation masks are widely used. A natural idea is to extend IoU to 3D by voxelizing the shape and comparing binary occupancy grids. However, this introduces several issues, as discussed by Tatarchenko et al. [611]:

- **Loss of fine structures:** Thin parts (e.g., table legs or airplane wings) may disappear when voxelized at coarse resolutions.
- **Representation mismatch:** Point clouds and meshes must be rasterized to voxels, introducing approximation error.
- **Metric collapse:** At low overlap, IoU scores saturate near zero and fail to distinguish plausible from implausible reconstructions.

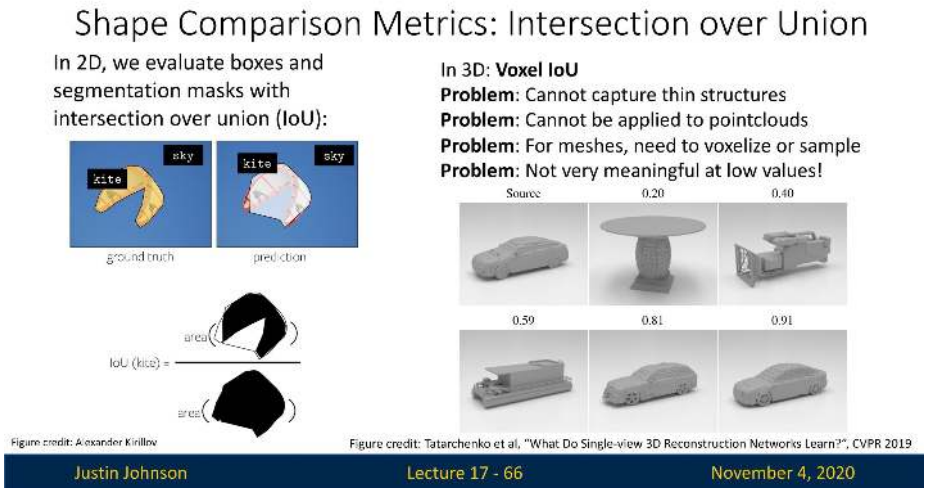

Figure 23.33: Limitations of 3D IoU: (Left) Summary of common pitfalls. (Right) Visualization of the metric failing to capture geometry differences in a kite example.

Chamfer Distance: Simple and Effective

A widely adopted alternative is the *Chamfer distance (CD)*, which compares two point clouds by computing nearest-neighbor distances in both directions:

$$\mathrm{CD}(P,Q) = \frac{1}{|P|}\sum_{p\in P}\min_{q\in Q}\|p-q\|_2^2 + \frac{1}{|Q|}\sum_{q\in Q}\min_{p\in P}\|q-p\|_2^2.$$

CD works well for arbitrary 3D representations and is differentiable, making it a common loss function. However, it is highly sensitive to outliers due to its reliance on squared ℓ_2 distances.

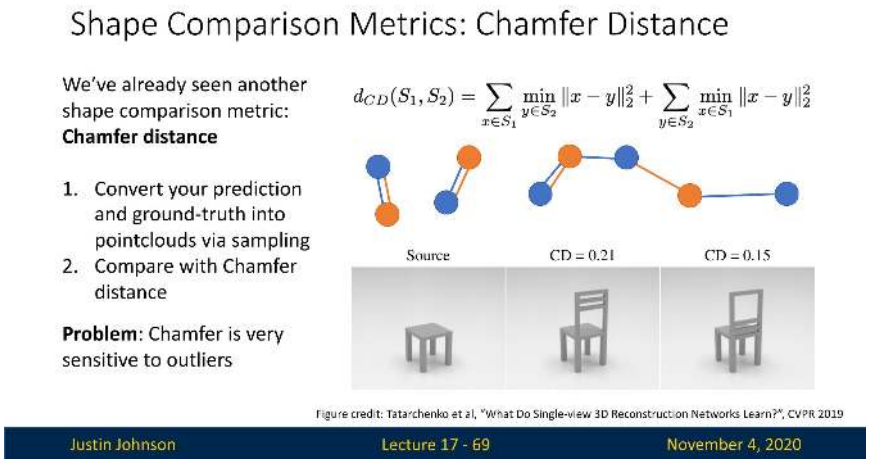

Figure 23.34: Comparison of Chamfer Distance (CD) against a ground-truth table. Both predicted shapes are structurally similar chairs that share the same flat seat base as the table, differing primarily in their back support. The chair with shorter back support (right) receives a lower CD of 0.15, as its geometry more closely matches the table. The chair with taller back support (left) receives a higher CD of 0.21, despite the backrest being the only mismatch. This illustrates CD's sensitivity to peripheral outliers: small localized differences—far from the main shape—can disproportionately inflate the score.

F1 Score: Thresholded Surface Accuracy

To address CD's sensitivity, we can compute *precision* and *recall* over thresholded nearest-neighbor distances:

- **Precision@t:** Fraction of predicted points within distance t of the ground-truth surface.
- **Recall@t:** Fraction of ground-truth points within distance t of the prediction.
- **F1@t:** Harmonic mean: $\dfrac{2 \cdot \text{Precision@}t \cdot \text{Recall@}t}{\text{Precision@}t + \text{Recall@}t}$

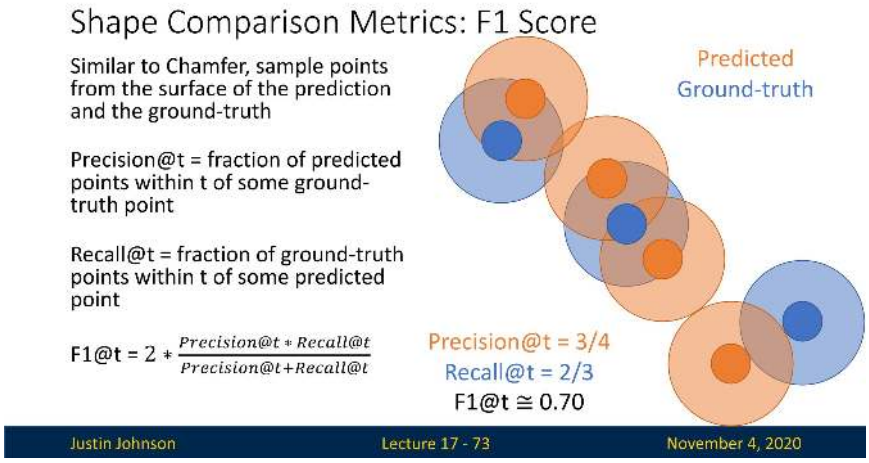

Figure 23.35: F1 score-based shape evaluation: More robust to outliers and informative across different geometric scales.

Threshold Sensitivity

F1@t is only meaningful at the right spatial scale. Too small a t penalizes fine misalignments; too large a t washes out detail. Therefore, it is standard practice to report F1@t for multiple values of t.

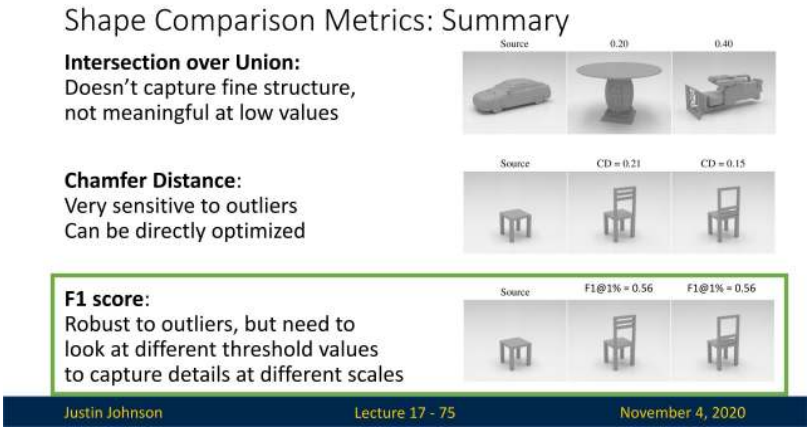

Figure 23.36: Comparative behavior of shape metrics across thresholds. F1 curves often reveal performance differences that CD and IoU miss.

23.8.2 Camera Coordinates: Canonical vs. View-Aligned

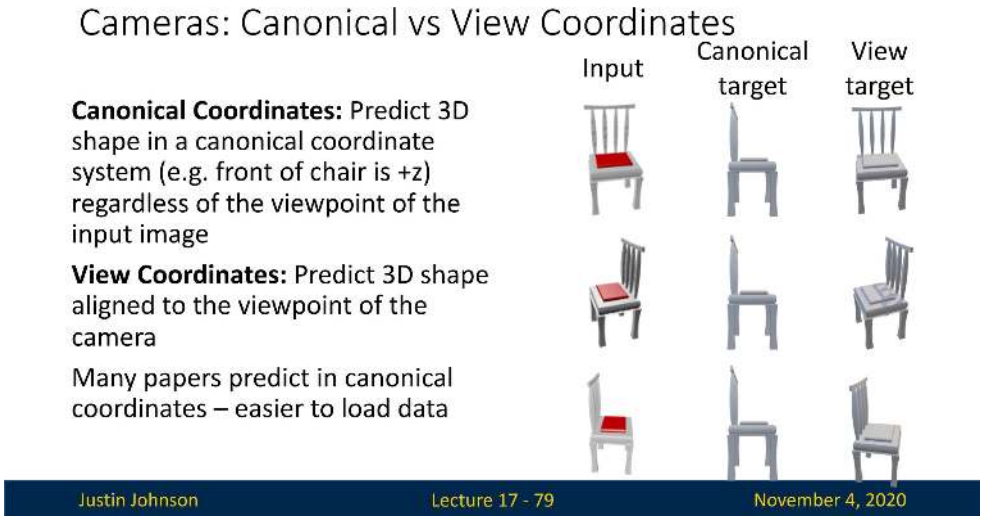

Figure 23.37: Canonical (mid column) vs view-aligned (last column) coordinate systems for chair reconstruction. The latter preserves direct alignment with the input image (first column).

Canonical Coordinates

Many 3D pipelines predict objects in a canonical orientation (e.g., front of chair = $+z$), which simplifies training and dataset organization. However, this introduces a disconnect between the input viewpoint and the output geometry, forcing the model to learn pose estimation as a side task.

View Coordinates

Alternatively, we can predict shapes aligned with the input camera pose. This simplifies feature alignment and improves generalization. The 2018 CVPR study by Shin et al. [565] demonstrates that view-coordinates lead to better results on novel objects and unseen categories.

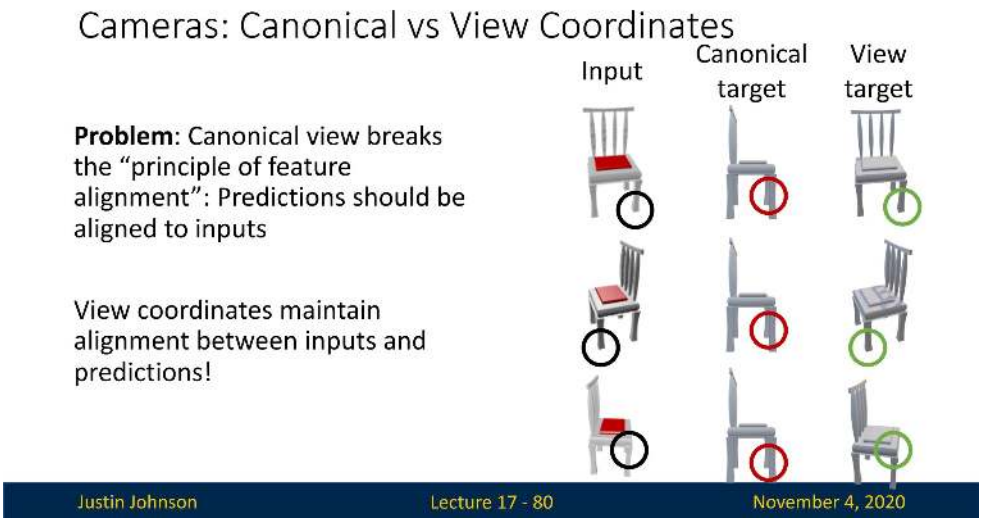

Figure 23.38: Feature alignment: View coordinates maintain spatial consistency between input features and predicted geometry.

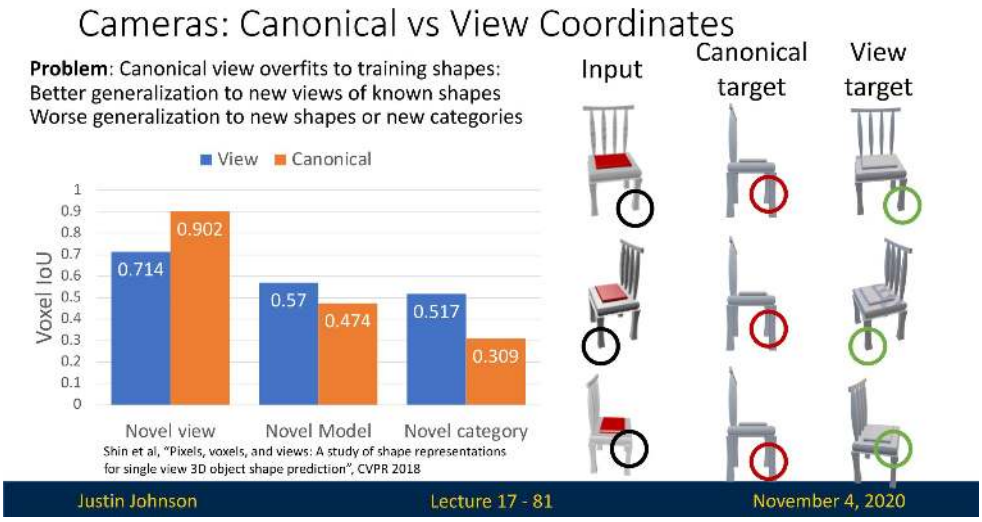

Figure 23.39: Generalization gap: Canonical prediction overfits to training shapes. View-aligned models perform better on novel objects and categories.

Conclusion

Unless a downstream task requires a fixed coordinate frame (e.g., assembly simulation), predicting in view coordinates is preferred due to its alignment benefits and superior generalization.

23.8.3 3D Datasets

Core Benchmarks for Single-View Reconstruction

3D reconstruction methods typically train and evaluate on a handful of publicly available datasets. The two most influential are *ShapeNet* and *Pix3D*, which together define the synthetic-to-real spectrum of object-level benchmarks.

ShapeNet

ShapeNet [76] is the dominant synthetic dataset for learning object geometry from images. It provides clean, manifold CAD meshes with consistent alignment and dense annotations.

- **Scale:** Over 50,000 3D models across 55 categories. The *Core v2* split uses 13 categories for benchmarking.
- **Images:** Each object is rendered from 20–25 uniformly sampled viewpoints on a hemisphere.
- **Advantages:** Large scale, watertight geometry, and complete surface supervision.
- **Limitations:** Synthetic only; lacks real lighting, texture variation, or background context. Category distribution is skewed (e.g., chairs dominate).

Pix3D

Pix3D [593] bridges synthetic geometry with real-world scenes. It aligns 3D furniture CAD models with natural RGB images of the same object instances, captured in real environments.

- **Scale:** 219 unique 3D models and 17,000 real images across 9 furniture categories.
- **Advantages:** Contains lighting variation, clutter, and occlusion; includes ground-truth pose, segmentation, and mesh alignment.
- **Limitations:** Small object coverage; only one labeled object per image; annotations are sometimes incomplete or noisy.

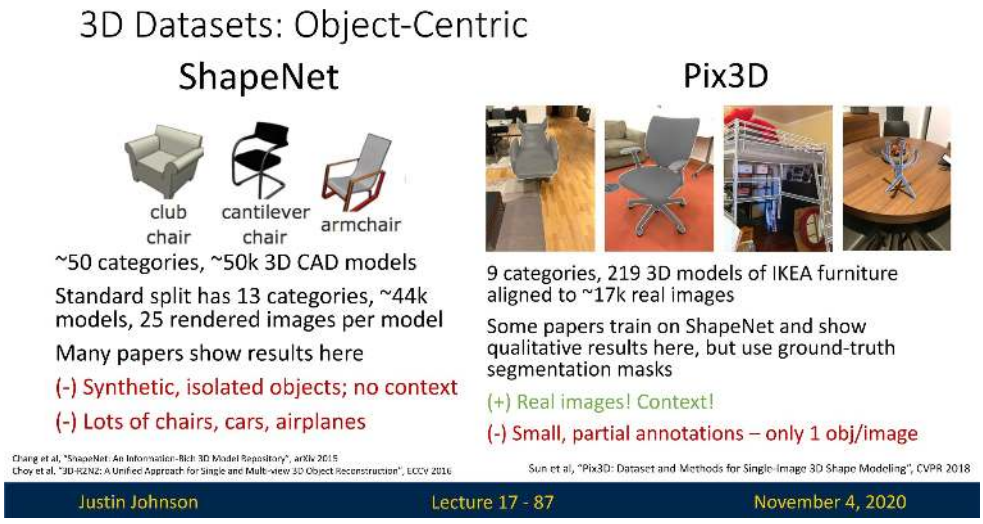

Figure 23.40: Comparison of ShapeNet (left) and Pix3D (right). ShapeNet offers synthetic scale and geometric cleanliness; Pix3D provides real-world variation and appearance realism.

Training Strategy
A common pipeline is to pretrain on ShapeNet for geometry learning and fine-tune or evaluate qualitatively on Pix3D to test robustness to clutter, occlusion, and real-world image statistics.

However, as 3D learning expands, modern benchmarks increasingly push beyond these datasets in scale, realism, and diversity.

CO3D: Common Objects in 3D
CO3D [521] comprises internet-scale videos of common objects (e.g., bottles, toys, shoes) captured using handheld phones. It includes camera poses and multi-view image sequences.

- **Scale:** Over 1.5 million frames from 50 categories; hundreds of object instances per class.
- **Use Case:** Training category-specific NeRFs and multi-view consistent models.
- **Strengths:** Real-world occlusion and lighting; dense image-based supervision.

Objaverse and Objaverse-XL
Objaverse [117] is a web-scale dataset of Creative Commons–licensed 3D assets, released to support foundational 3D vision models and text–3D learning.

- **Scale:** 10M+ meshes across a wide spectrum of categories; many include textures and captions.
- **Use Case:** Pretraining CLIP-style vision–language–geometry models.
- **Strengths:** Unprecedented diversity and licensing openness; extensible for 3D GenAI.
- **Challenges:** Inconsistent mesh quality and scaling; preprocessing required.

ScanNet
ScanNet [113] provides RGB-D video scans of real-world indoor scenes with semantic and instance segmentation labels.

- **Scale:** 1,500 scans and over 2.5 million RGB-D frames.
- **Use Case:** Scene-level 3D understanding, SLAM, and real-world domain generalization.
- **Strengths:** Photorealism, full-scene context, dense camera trajectories.
- **Limitations:** No watertight ground-truth meshes; reconstructed via noisy TSDF fusion.

Supplementary Datasets
While most reconstruction benchmarks focus on visual realism, other datasets support tasks like analytic surface modeling or object detection.

- **ABC Dataset** [300]: 1M parametric CAD models in STEP format, designed for curvature estimation and surface fitting. Rich in metadata but lacks textures and everyday context.
- **ModelNet** [705]: 12k CAD meshes across 10 or 40 categories. Still common in point cloud classification; now largely superseded by ShapeNet.
- **PartNet** [439]: Over 26k 3D models with fine-grained, hierarchical part annotations—useful for segmentation and affordance tasks.
- **Objectron** [3]: Short AR videos with annotated 3D bounding boxes for 15 object categories. Captures real-world scale and motion but only provides sparse 3D annotations.

Summary
ShapeNet and Pix3D remain the standard benchmarks for mesh-level shape prediction. Newer datasets like CO3D and Objaverse expand the task to multi-view learning and massive-scale generalization. Scene-level datasets like ScanNet and industrial corpora like ABC enable new frontiers in physical realism, structure, and simulation fidelity. A robust training curriculum typically begins with synthetic pretraining and proceeds to real-world fine-tuning.

23.9 Neural Radiance Fields (NeRF)

23.9.1 Problem Setup: Novel View Synthesis with Known Cameras

What Is Novel View Synthesis?

Imagine taking several photos of a scene—say, a Lego bulldozer—from different known positions. Now imagine rendering a new image of that same scene from a viewpoint *you never captured*. This task is called **novel view synthesis**: the goal is to generate realistic images of a scene as it would appear from arbitrary camera positions, given only a sparse set of observed images and their corresponding camera poses. This problem sits at the intersection of geometry, appearance modeling, and rendering—and is central to applications in virtual reality, 3D reconstruction, and photorealistic simulation.

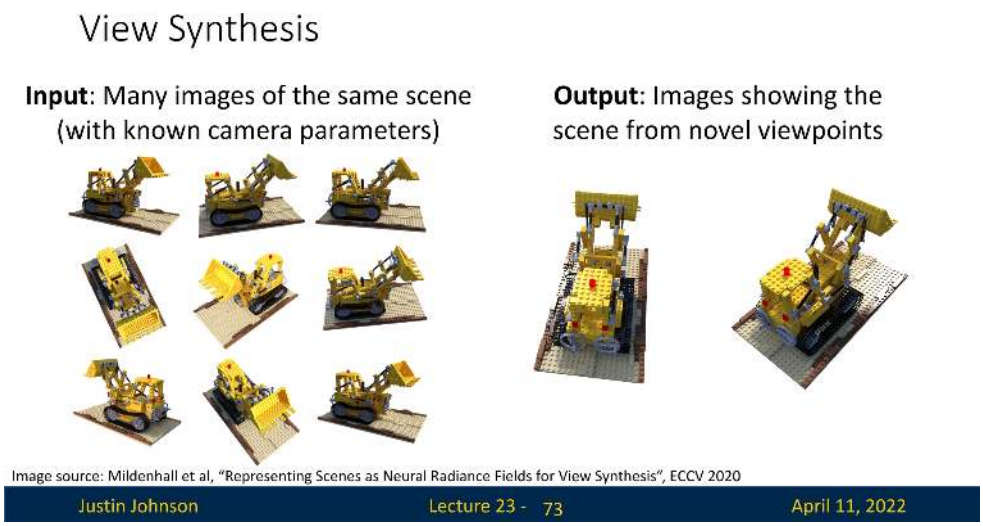

Figure 23.41: NeRF performs novel view synthesis: given images from known viewpoints, it renders unseen views (example: Lego bulldozer).

Limitations of Traditional Novel View Synthesis Pipelines

Classical novel view synthesis systems follow a brittle, multi-stage pipeline rooted in explicit 3D reconstruction [553, 558, 785]:

- **Structure-from-Motion (SfM).** Estimates camera intrinsics and extrinsics by matching 2D features across views and triangulating sparse 3D keypoints.
- **Multi-View Stereo (MVS).** Densifies the sparse point cloud using stereo correspondence and depth estimation across calibrated views.
- **Surface reconstruction and texturing.** Generates a mesh or voxel grid and back-projects color information from input images to produce a renderable surface.

This pipeline is highly sensitive to noise. The explicit geometry produced in early stages must support all downstream tasks; any errors in pose estimation, depth prediction, or surface reconstruction propagate without correction.

In practice, these systems frequently fail due to several structural limitations:

- **Limited view coverage.** Geometry is only recovered where multiple views overlap. Occluded or unobserved regions remain incomplete or hallucinated [558].
- **Photometric assumptions.** Most SfM–MVS methods assume Lambertian surfaces and brightness constancy. Real-world effects such as specularities, translucency, and variable illumination violate these assumptions, corrupting correspondence and depth estimates [779].
- **Sparse inputs and wide baselines.** With few input images or large viewpoint shifts, feature correspondences become unreliable, degrading both pose and geometry [2].
- **Textureless or repetitive regions.** Surfaces lacking distinctive features—e.g., white walls—or containing repeated patterns confuse matching algorithms, leading to holes or incorrect geometry [785].
- **Error accumulation and memory cost.** Small mismatches, pose drift, and meshing artifacts accumulate through the pipeline. High-resolution volumetric grids also incur steep memory and computational costs [558].

Moreover, traditional methods commit to a *single explicit surface*. Modeling view-dependent phenomena (e.g., reflections, specular highlights) requires hand-designed reflectance functions (e.g., BRDFs) that are difficult to estimate and rarely generalize across real-world conditions.

Neural Radiance Fields (NeRF) [369, 429] were introduced to overcome these fragilities. Rather than reconstructing a discrete surface, NeRF learns a *continuous*, view-conditioned radiance field from posed images. Novel views are rendered directly by integrating this field along camera rays via differentiable volume rendering—yielding sharper, more consistent results even under challenging visibility, appearance, and lighting conditions.

23.9.2 A New Paradigm: Neural Fields

Neural Radiance Fields (NeRF) [429] exemplify a transformative shift in view synthesis: from pipelines that reconstruct explicit 3D geometry to models that learn *neural fields*, also known as *implicit neural representations*. Rather than discretizing scenes into meshes or voxel grids, neural fields represent continuous volumetric functions using the parameters of a multilayer perceptron (MLP). These functions take spatial coordinates—optionally conditioned on direction—and output physical scene properties such as radiance, density, or occupancy.

Scene Representation

In NeRF, the scene is defined by a function

$$F_\Theta : (x, y, z, \theta, \phi) \mapsto (\sigma, \mathbf{c}) \in \mathbb{R}_{\geq 0} \times [0,1]^3,$$

where $(x, y, z) \in \mathbb{R}^3$ denotes a location in world coordinates and (θ, ϕ) specify the viewing direction using spherical coordinates. The output consists of:

- **Volume density σ**: a scalar indicating the probability of light terminating (i.e., hitting material) at the queried point.
- **Radiance $\mathbf{c}$**: an RGB value specifying the color emitted from that point in direction (θ, ϕ).

This directional dependence enables the model to capture view-dependent phenomena like specular highlights or reflections.

Why Only Direction Matters

Notably, NeRF conditions on the viewing direction rather than the full camera pose. This is because the color emitted at a given location depends only on the *relative angle* between the viewing ray and the local surface normal—not on the absolute camera orientation. The roll angle (in-plane camera rotation) does not affect light interaction and is therefore omitted from the input.

Training Supervision: From Images to Rays

NeRF is trained on a set of images with known camera intrinsics and extrinsics. For each pixel, a corresponding 3D ray is defined using the camera model, and the radiance field is queried along that ray. The goal is to learn Θ such that the predicted color along each ray matches the observed pixel value. This requires accurate knowledge of the camera parameters associated with each image in the dataset.

23.9.3 Camera Parameters as a Prerequisite

For NeRF to model and render a scene accurately, it must first understand the relationship between each 2D input image and the shared 3D world coordinate system. This requires, for every image, a complete specification of the camera's parameters—both internal and external. These parameters form the geometric scaffolding that enables NeRF to associate each pixel with a corresponding 3D ray.

- **Intrinsics** define the internal projection geometry of the camera and are typically encoded by a 3×3 calibration matrix K_k for image k. This matrix specifies the focal lengths (f_x, f_y) and the principal point (c_x, c_y), which together determine how 3D points in camera coordinates are projected onto the 2D image plane:

$$K_k = \begin{bmatrix} f_x & 0 & c_x \\ 0 & f_y & c_y \\ 0 & 0 & 1 \end{bmatrix}$$

  Optional intrinsics may also include lens distortion parameters, though these are typically omitted or corrected in NeRF datasets.
- **Extrinsics** define the pose of the camera with respect to a global world coordinate frame. They consist of a rotation matrix $\mathbf{R}_k$ and a translation vector $\mathbf{t}_k$ for image k, which together specify a camera-to-world transformation $[\mathbf{R}_k \mid \mathbf{t}_k] \in \mathrm{SE}(3)$. This mapping is essential for expressing 3D locations consistently across all views.

These parameters are crucial because NeRF learns a function over 3D world coordinates. To supervise this function using 2D image pixels, the model must be able to trace each pixel's ray through the scene—originating from the camera's position and passing in the direction that pixel subtends in space. Without accurate intrinsics and extrinsics, this mapping from pixel to 3D ray cannot be defined, and the network cannot learn a consistent radiance field.

In practice, these camera parameters are not usually provided with the dataset and must be estimated from the images themselves. Their accuracy is critical: small errors in estimated poses result in misaligned rays, which in turn degrade the consistency of supervision across views. This often leads to blurred reconstructions or ghosting artifacts in rendered images, especially in regions of fine structure or high frequency detail.

Accordingly, before training NeRF, a robust geometric calibration step must be performed to recover per-image intrinsics and extrinsics. The standard approach is to estimate these parameters from the image set itself using classical techniques based on multi-view geometry.

Recovering Camera Parameters via SfM

As previously mentioned, in most real-world datasets, explicit camera parameters are not available. To bridge this gap, NeRF typically relies on classical *Structure-from-Motion (SfM)* [553] pipelines to estimate both intrinsic and extrinsic parameters directly from the image collection. This process aligns the entire dataset into a unified 3D coordinate frame and enables ray construction for NeRF training.

SfM recovers this calibration through the following multi-stage optimization:

1. **Feature correspondence:** Local image features (e.g., SIFT) are detected and matched across image pairs to establish 2D correspondences—keypoints that observe the same 3D point across views.
2. **Triangulation:** Using matched keypoints and camera projection geometry, 3D point locations are triangulated, resulting in a sparse point cloud that defines the underlying scene structure.
3. **Bundle adjustment:** A global nonlinear optimization jointly refines all estimated camera parameters and 3D points by minimizing reprojection error. This adjusts the intrinsics, extrinsics, and 3D structure to best explain the observed 2D matches across the dataset.

The result is a calibrated camera model for each image, typically consisting of a pose $\mathscr{P}_k = (\mathbf{R}_k, \mathbf{t}_k) \in \mathrm{SE}(3)$ and an intrinsics matrix K_k. Together, these determine the origin and direction of every ray traced from pixel to world, anchoring the supervision of NeRF's radiance field.

However, SfM is not infallible. Challenging image regions—such as occlusions, textureless surfaces, or large baselines—can lead to pose drift and imperfect alignments. These miscalibrations cause ray inconsistencies across views and may lead to visual artifacts such as ghosting or blur. To address this, many NeRF variants treat the poses as learnable parameters and jointly optimize them alongside the radiance field, refining camera geometry in tandem with appearance modeling.

With camera calibration complete, each pixel in each training image defines a 3D ray in world space. The next stage is to evaluate the neural radiance field along these rays using differentiable volume rendering.

23.9.4 Volume Rendering: From Rays to Pixels

Once calibrated rays are constructed from the camera intrinsics and extrinsics, the NeRF pipeline proceeds to synthesize pixel colors by simulating how light accumulates along each ray. This is achieved through a process known as *volume rendering*, a classical technique from graphics that models a ray traversing a semi-transparent scene.

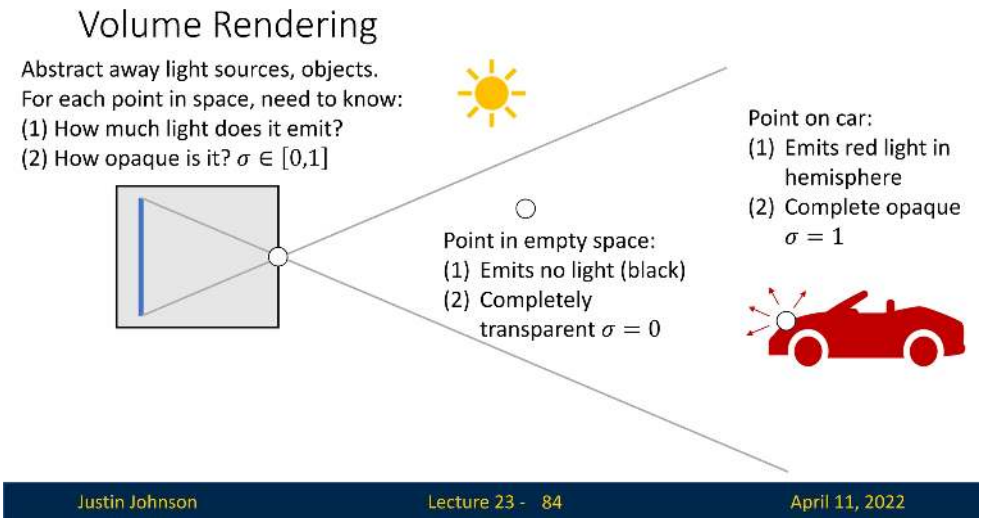

Figure 23.42: Volume rendering setup from the pinhole camera model. Light reflects off surfaces in the scene and enters the camera through a pinhole, projecting onto a virtual image plane. The key questions at each sampled 3D point are: (1) how much light does it emit? and (2) how opaque is it? Points on the object (e.g., car) emit colored light and are opaque ($\sigma = 1$), while empty space emits no light and is fully transparent ($\sigma = 0$).

To determine the color of a single pixel, NeRF casts a ray from the camera's optical center into the 3D scene, simulating how light accumulates along that path. Under the pinhole camera model, every ray originates from a single 3D point—the *camera center*—and passes through a specific location on the image plane. This ray is parameterized as:

$$\mathbf{r}(t) = \mathbf{o} + t\mathbf{d}, \quad t \in [t_n, t_f],$$

where:

- $\mathbf{o} \in \mathbb{R}^3$ is the ray origin in world coordinates. It corresponds to the physical center of projection—the point through which all rays pass—and is computed for image k from its extrinsics:

  $$\mathbf{o}_k = -\mathbf{R}_k^\top \mathbf{t}_k.$$

  This expression inverts the camera pose transformation $[\mathbf{R}_k \mid \mathbf{t}_k]$, yielding the camera's location in the global coordinate frame.
- $\mathbf{d} \in \mathbb{S}^2$ is the unit direction vector that points from the camera center $\mathbf{o}$ through the *center* of pixel (u, v) on the image plane. It is carefully constructed so that the ray intersects the sub-pixel center of the target pixel, ensuring accurate alignment and avoiding aliasing artifacts.

To compute $\mathbf{d}$, NeRF inverts the pinhole projection model in three steps:

1. **Target the pixel center:** Pixels are indexed by integer raster coordinates $(u, v) \in \mathbb{Z}^2$, which reference their top-left corners. To model light paths more precisely, NeRF offsets these coordinates by $+\frac{1}{2}$, aiming the ray through the center of the square pixel:

$$\mathbf{p}_{\text{pix}} = \begin{bmatrix} u + \frac{1}{2} \\ v + \frac{1}{2} \\ 1 \end{bmatrix}.$$

   This homogeneous 2D point lies on the image plane and acts as the projected target for the ray.
2. **Unproject to camera space:** The camera intrinsics matrix $K \in \mathbb{R}^{3\times 3}$,

$$K = \begin{bmatrix} f_x & 0 & c_x \\ 0 & f_y & c_y \\ 0 & 0 & 1 \end{bmatrix},$$

   encodes the focal lengths and principal point. Applying the inverse intrinsics yields a direction vector in the camera's local 3D frame:

$$\mathbf{d}_{\text{cam}} = K^{-1}\mathbf{p}_{\text{pix}}.$$

   This vector points from the camera origin through the pixel center, intersecting the virtual image plane at depth $z = 1$.
3. **Transform to world space and normalize:** To express the ray direction in global coordinates, we rotate the camera-frame direction using the inverse rotation:

$$\mathbf{d}_{\text{world}} = \mathbf{R}^{\top}\mathbf{d}_{\text{cam}}, \quad \mathbf{d} = \frac{\mathbf{d}_{\text{world}}}{\|\mathbf{d}_{\text{world}}\|_2}.$$

The resulting ray $\mathbf{r}(t) = \mathbf{o} + t\mathbf{d}$ travels through two key points: the camera center $\mathbf{o}$ and the 3D location that maps—via projection—to the center of pixel (u, v). This construction ensures that each pixel defines a unique 3D ray that is both photometrically accurate and geometrically aligned.

- $t \in [t_n, t_f]$ is the *depth parameter* along the ray. Each value of t specifies a point $\mathbf{r}(t)$ in 3D space. The interval bounds the segment of the ray used for rendering: t_n avoids camera-adjacent voids, and t_f limits traversal to a relevant portion of the scene.

This setup defines the geometric foundation for NeRF's differentiable volume rendering pipeline: each pixel gives rise to a calibrated 3D ray that queries the scene via learned color and density functions, enabling accurate supervision from multiview imagery.

The color of a pixel is modeled as a continuous accumulation of radiance along its viewing ray:

$$\mathscr{C}(\mathbf{r}) = \int_{t_n}^{t_f} \underbrace{T(t)}_{\text{transmittance}} \cdot \underbrace{\sigma(\mathbf{r}(t))}_{\text{density}} \cdot \underbrace{\mathbf{c}(\mathbf{r}(t), \mathbf{d})}_{\text{radiance}} \, dt.$$

This integral aggregates light contributions from all points $\mathbf{r}(t)$ along the ray segment between a near bound t_n and far bound t_f. At each infinitesimal location, the integrand quantifies how much light is emitted, how much material is present, and how likely that light is to reach the camera unoccluded.

- The *volume density* $\sigma(\mathbf{r}(t)) \in [0,1]$ acts as a soft occupancy field—higher values indicate denser or more opaque regions, while $\sigma = 0$ corresponds to empty space.
- The *radiance* $\mathbf{c}(\mathbf{r}(t), \mathbf{d}) \in [0,1]^3$ gives the RGB color emitted from point $\mathbf{r}(t)$ in viewing direction $\mathbf{d}$.
- The *transmittance* $T(t) \in [0,1]$ denotes the survival probability of light traveling from the camera to depth t, without being blocked by foreground matter.

Why an integral? Because the scene is modeled as a continuous volumetric field, there is no single surface to sample. Instead, light can originate from anywhere along the ray. Each point emits some color, attenuated by the surrounding medium, and contributes only a tiny amount. The integral sums up these infinitesimal contributions from all depths $t \in [t_n, t_f]$, forming a composite pixel color. This approach mirrors how light propagates through translucent media in physics and allows smooth transitions, semi-transparent edges, and view-dependent blending.

More precisely, $\sigma \cdot \mathbf{c}\, dt$ represents the amount of light emitted by a small segment dt around $\mathbf{r}(t)$, and $T(t)$ scales this emission based on how much of it survives traversal through the density field in front of it. The closer the point is to the camera, the less likely it is to be occluded, making early segments contribute more strongly. Distant points can only affect the pixel color if transmittance remains high—i.e., if the path before them is transparent.

The transmittance term is computed as an exponential of the accumulated density:

$$T(t) = \exp\left(-\int_{t_n}^{t} \sigma(\mathbf{r}(s))\, ds\right).$$

This expression is a solution to the radiative transfer equation under absorption-only conditions and follows the Beer–Lambert law. It encodes the idea that every unit of density along the path slightly diminishes light transmission. The more material encountered before t, the smaller $T(t)$ becomes. Thus, occlusion emerges naturally from integration—no hard surfaces or visibility heuristics are needed.

This continuous, differentiable formulation enables NeRF to produce photorealistic renderings with accurate soft shadows, translucency, and gradual occlusion. It replaces discrete surface modeling with an elegant volumetric framework in which geometry and appearance emerge implicitly from learned density and radiance fields.

Discretizing the Rendering Equation: Stratified Sampling and Alpha Compositing

Evaluating the continuous integral is analytically intractable for neural fields. NeRF approximates it by sampling N depths $t_1, \ldots, t_N$ uniformly or via hierarchical importance sampling along the ray. At each sampled point $\mathbf{r}(t_i)$, the MLP predicts:

$$\sigma_i := \sigma(\mathbf{r}(t_i)), \qquad \mathbf{c}_i := \mathbf{c}(\mathbf{r}(t_i), \mathbf{d}).$$

Assuming that density is constant over the small interval $[t_i, t_{i+1}]$, we define:

$$\delta_i := t_{i+1} - t_i, \qquad \alpha_i := 1 - \exp(-\sigma_i \delta_i),$$

where α_i approximates the *opacity*—the probability that the ray terminates inside segment i.

The discrete transmittance T_i up to segment i is thus:

$$T_i := \prod_{j=1}^{i-1} (1 - \alpha_j) = \exp\left(-\sum_{j=1}^{i-1} \sigma_j \delta_j\right),$$

the probability that light successfully traverses all prior segments without being absorbed.

With these components, the rendered pixel color is approximated as:

$$\hat{\mathscr{C}}(\mathbf{r}) = \sum_{i=1}^{N} T_i \cdot \alpha_i \cdot \mathbf{c}_i.$$

This rule is mathematically equivalent to front-to-back *alpha compositing*, where each semi-transparent segment contributes its color, modulated by its own opacity and the transparency of everything in front.

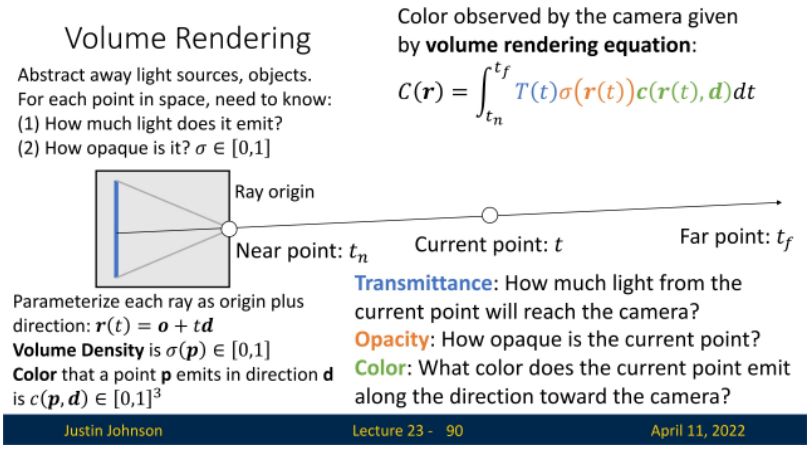

Figure 23.43: Discrete volume rendering along ray $\mathbf{r}(t) = \mathbf{o} + t\mathbf{d}$. The network predicts density σ_i and color $\mathbf{c}_i$ at N points sampled along the ray. Each segment's contribution is attenuated by accumulated transmittance T_i and its own opacity α_i.

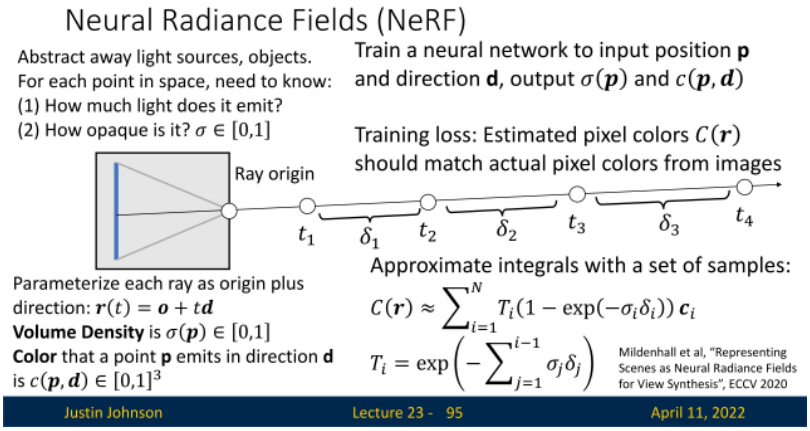

Figure 23.44: Discrete approximation of volume rendering along a ray $\mathbf{r}(t) = \mathbf{o} + t\mathbf{d}$. The network samples $N = 4$ points at depths t_1, t_2, t_3, t_4 within the interval $[t_n, t_f]$, spaced by intervals $\delta_i = t_{i+1} - t_i$. For each point $\mathbf{r}(t_i)$, the MLP predicts a density σ_i and view-dependent color $\mathbf{c}_i$. These are combined via alpha compositing to produce an estimated pixel color $\hat{\mathscr{C}}(\mathbf{r})$, which is supervised (i.e., compared to $\mathscr{C}(\mathbf{r})$) to match the ground truth image color via ℓ_2 loss.

From Pixel Color to Supervised 3D Sampling

Once a ray $\mathbf{r}(t) = \mathbf{o} + t\mathbf{d}$ is constructed for pixel (u, v), NeRF must supervise the unknown 3D scene based solely on the pixel's ground-truth color $\mathscr{C}(\mathbf{r}) \in [0,1]^3$. There is no direct annotation for which points along the ray contain surfaces or emit light; supervision is available only at the endpoint of the entire rendering process. The core insight of NeRF is that even this sparse signal is sufficient: if a radiance field is to match all observed views, it must explain how light accumulates along each ray to produce the correct color.

To turn this sparse supervision into dense learning signal, NeRF samples N 3D points along the ray. Although these points differ in location $\mathbf{r}(t_i)$, they all share the same viewing direction $\mathbf{d}$, which defines how color should vary based on perspective. Each point is passed to a neural network f_θ, yielding:

$$\sigma_i := \sigma(\mathbf{r}(t_i)), \qquad \mathbf{c}_i := \mathbf{c}(\mathbf{r}(t_i), \mathbf{d}),$$

where $\sigma_i \in \mathbb{R}_{\geq 0}$ is the predicted volume density and $\mathbf{c}_i \in [0,1]^3$ is the view-dependent color. These are combined via front-to-back alpha compositing to produce an estimated pixel color:

$$\hat{\mathscr{C}}(\mathbf{r}) = \sum_{i=1}^{N} T_i \cdot \alpha_i \cdot \mathbf{c}_i, \qquad \alpha_i = 1 - \exp(-\sigma_i \delta_i), \qquad T_i = \prod_{j=1}^{i-1} (1 - \alpha_j),$$

where $\delta_i = t_{i+1} - t_i$ is the spacing between samples.

This entire pipeline is fully differentiable. NeRF defines an ℓ_2 reconstruction loss between the rendered color and ground truth:

$$\mathscr{L}_{\text{recon}} = \left\| \hat{\mathscr{C}}(\mathbf{r}) - \mathscr{C}(\mathbf{r}) \right\|_2^2,$$

and uses backpropagation to update the MLP weights θ. Each pixel thus supervises not just a point sample, but an entire ray of 3D locations, encouraging the network to learn a coherent global representation.

Hierarchical Sampling: Coarse-to-Fine Supervision and Loss

To allocate computation effectively along each ray, NeRF employs a *coarse-to-fine* sampling strategy using two separate but jointly trained MLPs. The first stage explores the ray with uniform coverage, while the second concentrates on promising regions—typically those with higher predicted opacity. Both networks are optimized with ground-truth pixel color supervision, allowing the model to learn geometry and appearance jointly.

- **Coarse stage (exploration):** NeRF begins by drawing N_c samples along the ray $\mathbf{r}(t) = \mathbf{o} + t\mathbf{d}$ using stratified sampling. The interval $[t_n, t_f]$ is divided into equal-width bins, and one depth value is jittered uniformly within each:

  $$t_i \sim \mathscr{U}\left[\frac{i-1}{N_c}(t_f - t_n) + t_n,\ \frac{i}{N_c}(t_f - t_n) + t_n \right].$$

  Each corresponding 3D location $\mathbf{r}(t_i)$ is passed through the *coarse MLP*, which predicts density σ_i and radiance $\mathbf{c}_i$. These are composited into an initial pixel color estimate $\hat{\mathscr{C}}_{\text{coarse}}(\mathbf{r})$, supervised by the known ground-truth color $\mathscr{C}(\mathbf{r})$ from the training image:

  $$\mathscr{L}_{\text{coarse}} = \left\| \hat{\mathscr{C}}_{\text{coarse}}(\mathbf{r}) - \mathscr{C}(\mathbf{r}) \right\|_2^2.$$

- **Fine stage (refinement):** The coarse compositing weights

  $$w_i := T_i \cdot \alpha_i$$

  define a piecewise PDF over the ray that emphasizes surface-adjacent regions. From this distribution, N_f additional samples $\{t'_j\}$ are drawn. These fine samples are merged with the coarse ones, and the union is passed to a second *fine MLP*, which outputs improved density and color estimates. These are composited into a higher-resolution prediction $\hat{\mathscr{C}}_{\text{fine}}(\mathbf{r})$, also supervised via a reconstruction loss:

  $$\mathscr{L}_{\text{fine}} = \left\| \hat{\mathscr{C}}_{\text{fine}}(\mathbf{r}) - \mathscr{C}(\mathbf{r}) \right\|_2^2.$$

The final training objective combines both stages:

$$\mathscr{L}_{\text{total}} = \mathscr{L}_{\text{coarse}} + \mathscr{L}_{\text{fine}}.$$

This coarse-to-fine architecture allows the coarse MLP to guide sampling adaptively—allocating more effort where surfaces are likely to be.

Why This Works: Learning Geometry from Pixel Colors

At a glance, NeRF's approach seems almost paradoxical: the model has no knowledge of surfaces, yet learns to infer geometry purely from pixel-level color supervision. This works because each pixel's color constrains the entire ray beneath it. By rendering sampled 3D points into a single prediction $\hat{\mathscr{C}}(\mathbf{r})$, NeRF creates a differentiable bridge between thousands of possible 3D explanations and a single observed RGB triplet.

- **Supervision Distribution:** Although we supervise only one color per ray, gradients flow through all points that contributed to the composited prediction—distributing signal to every sample $\mathbf{r}(t_i)$.
- **Emergent Surfaces:** The only way to consistently satisfy these ray-level constraints across all views is to assign high density σ to points where many rays agree on a visual transition—i.e., surfaces.
- **Efficient Focus:** Hierarchical sampling ensures that fine-level computation is concentrated around informative regions, reducing noise and improving convergence.

Together, this architecture allows NeRF to transform sparse RGB supervision into a globally consistent volumetric reconstruction. It replaces dense 3D supervision with a powerful ray-based training signal that not only enables photorealism, but also implicitly discovers geometry.

A Differentiable Rendering Engine for View Synthesis

The NeRF rendering pipeline is fully differentiable: all operations—depth sampling, MLP querying, and the computation of per-sample density σ_i, color $\mathbf{c}_i$, opacity α_i, transmittance T_i, and accumulated pixel color—are smooth and continuous. This enables the system to be trained end-to-end via gradient descent, minimizing a reconstruction loss between predicted colors $\hat{\mathscr{C}}(\mathbf{r})$ and ground-truth image values $\mathscr{C}(\mathbf{r})$.

At inference time, this same mechanism enables photorealistic *novel view synthesis*: given an unseen camera pose, rays are cast through each pixel and evaluated against the learned radiance field to render new, realistic images of the scene.

To support such high-fidelity synthesis, the underlying model must capture detailed scene geometry and appearance, including fine spatial structure and subtle view-dependent effects. NeRF achieves this by modeling the radiance field as a continuous function parameterized by a compact Multi-Layer Perceptron (MLP), which maps each sampled 5D coordinate $(\mathbf{x}, \mathbf{d})$ to a scalar volume density σ and a direction-conditioned color $\mathbf{c}$.

In practice, this modeling approach must be paired with careful input parameterization and architectural choices to ensure stable optimization and accurate reconstruction. The next subsection introduces the key components—starting with how raw input coordinates are encoded and how the radiance field network is structured to support expressive, high-quality view synthesis.

23.9.5 Practical Implementation Details

To realize photorealistic view synthesis in practice, Neural Radiance Fields (NeRF) rely on careful architectural design choices and encoding strategies that address the limitations of standard neural networks in representing fine spatial and angular detail. We begin by discussing the core technique that enables high-frequency reconstruction—*positional encoding*—and then present the structure of the neural network used to model the radiance field.

Positional Encoding for High-Frequency Detail

A key challenge in training Multi-Layer Perceptrons (MLPs) to represent complex 3D scenes is their inherent *spectral bias*—a tendency to learn and prioritize low-frequency (smooth) functions during optimization [502]. This empirically common phenomenon limits an MLP's ability to accurately reconstruct fine geometric detail or rapidly varying texture when operating directly on raw spatial or angular coordinates.

In the context of NeRF, this bias manifests as *blurry surfaces, oversmoothed edges*, and a general failure to capture high-frequency content such as thin structures, sharp contours, or specular highlights. Though MLPs are universal function approximators, their convergence rate for high-frequency components is significantly slower [506]. This results in poor early representations and long training times for high-resolution detail, with the network often getting stuck in smooth approximations of the scene.

This limitation stems from the inductive properties of MLPs: small changes in the input—such as a slight shift in spatial location or viewing angle—tend to produce small changes in the output, especially when the input space is unstructured and low-dimensional. As shown in Fourier-domain analyses of coordinate-based MLPs, deeper or wider networks alone do not resolve this issue [502, 506]. High-frequency functions require precise, localized output variations, which are difficult to express using standard activation dynamics and gradient descent unless the input is carefully encoded.

To address this, NeRF introduces a simple yet powerful solution: *positional encoding*. Instead of feeding raw 3D coordinates $\mathbf{x} \in \mathbb{R}^3$ and 2D viewing directions $\mathbf{d} \in \mathbb{S}^2$ directly into the MLP, each scalar input value p is transformed by a fixed encoding function $\gamma(p)$, which projects it into a high-dimensional space of sinusoids at exponentially increasing frequencies:

$$\gamma(p) = \left(\sin(2^0\pi p), \cos(2^0\pi p), \ldots, \sin(2^{L-1}\pi p), \cos(2^{L-1}\pi p)\right).$$

This transformation is applied independently to each component of $\mathbf{x}$ and $\mathbf{d}$, resulting in a total input dimensionality of $3(2L+1)+3(2L'+1)$ when using L frequency bands for position and L' for direction.

The motivation behind this transformation is grounded in Fourier analysis. Positional encoding effectively "injects" a spectrum of basis functions into the input space, allowing the network to represent high-frequency signals through linear combinations of these sinusoids in the first layer. Rather than forcing the MLP to learn such frequency structure through deep nonlinear compositions—which is inefficient and prone to convergence issues—this encoding enables the model to access high-frequency expressivity from the start.

Empirical results confirm the importance of this technique: models trained without positional encoding exhibit significantly reduced visual fidelity, slower convergence, and inability to recover fine detail. In contrast, networks using positional encoding successfully reconstruct sharp surfaces, reflective materials, and detailed textures [429]. Subsequent theoretical analysis shows that positional encoding modifies the neural tangent kernel (NTK) of the MLP to increase its bandwidth and flatten its spectrum, improving gradient flow and allowing more balanced learning of low- and high-frequency components [604].

Intuition Behind Positional Encoding

To grasp the role of positional encoding in NeRF, it helps to consider how an MLP "sees" space. When fed raw spatial or angular coordinates, the network operates in a smooth, low-frequency regime: small changes in input tend to produce only small changes in output. While this behavior is appropriate for modeling gradual variations, it becomes a liability when the scene contains sharp edges, fine textures, or high-frequency lighting effects. In such cases, the desired output—radiance or density—may change rapidly over very small spatial intervals. Standard MLPs struggle to express such localized variation due to their *spectral bias* toward smooth functions.

This limitation arises because MLPs must synthesize high-frequency behavior through deep compositions of nonlinearities, which is both inefficient and slow to converge. As a result, renderings trained on raw coordinates tend to exhibit blurred contours and oversmoothed detail—especially near thin structures or specular surfaces.

Positional encoding addresses this problem by enriching each scalar input with a fixed set of sinusoidal functions at multiple frequencies:

$$\gamma(p) = \left(\sin(2^0\pi p), \cos(2^0\pi p), \ldots, \sin(2^{L-1}\pi p), \cos(2^{L-1}\pi p)\right).$$

This mapping transforms the input space such that small changes in position or direction can produce large, expressive shifts in the encoded representation—especially in the higher-frequency components. Crucially, this does not destabilize the network; rather, it gives the MLP access to a spectrum of variation that it can combine linearly in the first layer, allowing it to model both smooth regions and sharp transitions with ease.

An intuitive analogy is that of a painter. Feeding raw coordinates into an MLP is like giving an artist only broad brushes: suitable for outlining large shapes, but incapable of capturing intricate structure. Positional encoding equips the model with a complete set of tools—from coarse rollers to ultra-fine brushes—so it can render both global layout and detailed texture. The high-frequency "ink" is already embedded in the input; the MLP need only learn how to blend it.

Importantly, positional encoding does not increase the model's depth or parameter count. Instead, it reformulates the input representation to align with the underlying complexity of the radiance field. By embedding frequency structure directly into the input space, it enables the network to express high-detail content from the very beginning of training—accelerating convergence and dramatically improving reconstruction fidelity.

Network Architecture and Functional Mapping

The NeRF network is a fully-connected MLP with ReLU activations. Its design reflects a structural separation between geometric and appearance representations, achieved via a two-stage processing pipeline.

The input 3D location $\mathbf{x}$, encoded via $\gamma(\mathbf{x})$, is passed through a series of 8 layers, each with 256 units and ReLU activations. A skip connection concatenates the original positional encoding $\gamma(\mathbf{x})$ to the output of the 4th layer. This first stage outputs two quantities:

- A scalar volume density σ, representing how likely the ray is to terminate at that location.
- A learned feature vector $\mathbf{h} \in \mathbb{R}^{256}$ representing local geometry and appearance context.

To model view-dependent effects, the encoded viewing direction $\gamma(\mathbf{d})$ is concatenated with $\mathbf{h}$, and passed through an additional 1-hidden-layer MLP (with 128 units) to predict RGB color $\mathbf{c} \in [0,1]^3$.

This separation allows the network to maintain consistent density across all directions while permitting directional variation in emitted color, enabling the modeling of non-Lambertian surfaces such as specular highlights and reflections.

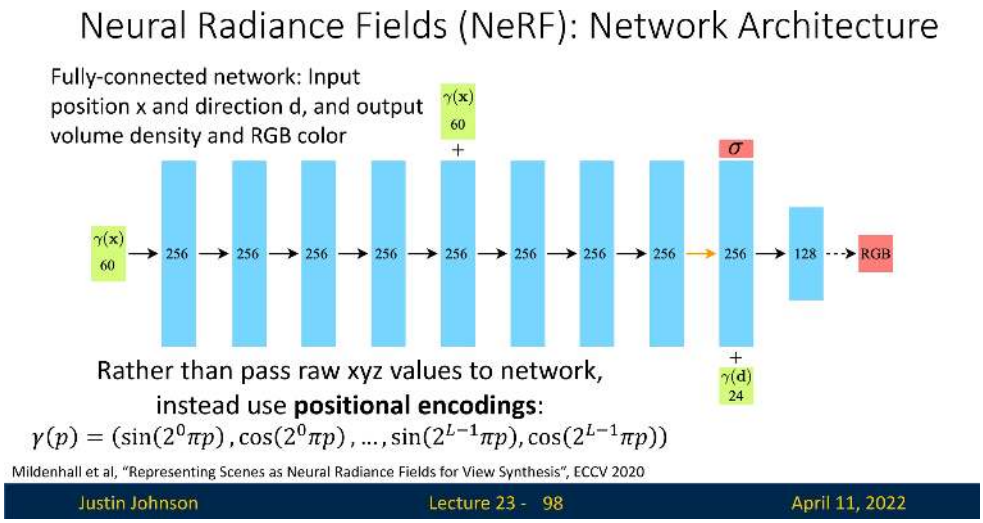

Figure 23.45: NeRF network architecture. Positional encodings are applied to both position and viewing direction inputs. The MLP first predicts volume density and intermediate features from position, then conditions RGB color on the viewing direction.

Together, the positional encoding and network design allow NeRF to map input rays to realistic colors with high accuracy.

Training vs. Inference: Pixel-Level Supervision and Scene Reconstruction

Although NeRF is trained using a loss defined at the level of individual image pixels, its learned representation is fundamentally volumetric: a continuous 5D field that maps 3D spatial locations and 2D viewing directions to color and density. A natural question arises—how can independent pixelwise comparisons to ground-truth RGB values yield a globally consistent 3D scene representation?

The key insight is that each pixel, while evaluated in isolation during training, arises from a unique ray that passes through the shared 3D environment. As the model is optimized to match the color seen along each ray, it must learn a radiance field whose volumetric structure explains not just isolated pixels but the appearance of entire scenes across multiple views. If the model were to hallucinate geometry or color in one ray that contradicts observations in another, the accumulated error across views would remain high. Thus, consistency across views serves as a powerful regularizer: even though supervision is pixel-local, the shared volumetric MLP must reconcile all views into a coherent underlying scene.

Training Procedure

NeRF is trained on a dataset of posed RGB images $\{I_k\}_{k=1}^{K}$, where each image I_k is accompanied by known camera intrinsics and extrinsics. For each *scene*, a dedicated neural radiance field is trained from scratch using all available views—unlike models trained across multiple scenes, NeRF does not require train/validation/test image splits for learning. Instead, novel view synthesis is evaluated on held-out camera poses after scene reconstruction is complete.

At each iteration, a batch of camera rays $\mathbf{r} = \mathbf{o} + t\mathbf{d}$ is randomly sampled from the set of all training pixels across all images. Each ray is then evaluated using a two-stage *hierarchical sampling* scheme. In the first pass, N_c coarse depth samples $\{t_i\}$ are drawn along the ray via stratified sampling, and the corresponding 3D points $\mathbf{r}(t_i)$ are passed through the MLP to predict volume densities σ_i and view-dependent colors $\mathbf{c}_i$. The coarse rendering $\hat{\mathscr{C}}_c(\mathbf{r})$ is computed using discrete volume rendering.

These weights are then used to inform a second round of importance sampling, focusing on regions of high density. An additional N_f fine samples are drawn along each ray and passed through a separate MLP (or the same MLP reused) to produce the final rendering $\hat{\mathscr{C}}_f(\mathbf{r})$. Both renderings are supervised against the ground-truth pixel color $\mathscr{C}(\mathbf{r})$ using an ℓ_2 loss:

$$\mathscr{L}_{\text{train}} = \sum_{\mathbf{r}\in\mathscr{B}} \left[\left\| \hat{\mathscr{C}}_c(\mathbf{r}) - \mathscr{C}(\mathbf{r}) \right\|_2^2 + \left\| \hat{\mathscr{C}}_f(\mathbf{r}) - \mathscr{C}(\mathbf{r}) \right\|_2^2 \right],$$

where $\mathscr{B}$ is the minibatch of rays. This loss is minimized via gradient descent, with gradients backpropagated through the entire rendering pipeline—including MLP evaluations, opacity computation, and alpha compositing. Over time, this process encourages the network to discover a coherent 3D radiance field that explains all views simultaneously.

Although the training signal is defined at the pixel level, the MLP must synthesize a global function that satisfies all camera rays across the scene.

Inference Procedure

At inference time, NeRF renders novel views from previously unseen camera poses. Given new camera intrinsics and extrinsics—either provided as ground truth or estimated via structure-from-motion tools like COLMAP—a ray is cast through the center of each pixel in the desired output image resolution. For each ray $\mathbf{r}(t) = \mathbf{o} + t\mathbf{d}$, NeRF applies the same stratified and hierarchical sampling strategy used during training.

Sampled 3D points along the ray are passed through the trained MLP to predict volume densities σ_i and view-dependent colors $\mathbf{c}_i$. These are combined via discrete volume rendering:

$$\hat{\mathscr{C}}(\mathbf{r}) = \sum_{i=1}^{N} T_i \cdot \alpha_i \cdot \mathbf{c}_i,$$

where α_i and T_i represent the segment opacity and transmittance, respectively. This process is repeated independently for every ray—effectively synthesizing the image pixel by pixel using only forward passes through the network.

Inference is parallelizable across rays and pixels, making it well-suited for GPU execution. However, it remains computationally intensive: each output frame requires evaluating hundreds of MLP queries per pixel. This results in high-fidelity but slow rendering, with original NeRF models taking tens of seconds per image on modern GPUs for small scenes up to days for more complex and high-resolution one on weaker GPUs.

Why Pixel-Level Supervision Works

Although NeRF is trained with per-pixel supervision, it does not learn isolated 2D mappings for each image. Instead, the volumetric rendering process couples every pixel to a ray that traverses the 3D scene, and these rays intersect and overlap across views. As a result, the color of each pixel depends on the shared radiance field that defines density and appearance throughout space.

This coupling turns local pixel errors into global constraints: an incorrect prediction at any point along a ray affects not just one pixel, but all others whose rays pass through the same region. Minimizing the total photometric loss across all training images therefore requires the model to discover a single, consistent radiance field that simultaneously explains all views. In this sense, NeRF performs multi-view 3D reconstruction not through explicit geometry, but through radiance field alignment guided by view-dependent color integration.

The shared MLP must assign densities and colors that are jointly plausible across viewpoints—encoding accurate 3D structure, coherent surface geometry, and realistic appearance effects such as specularities or occlusions. Crucially, this global consistency acts as an implicit regularizer: if a sharp edge or fine surface detail is modeled inconsistently across views, the resulting rendering error remains high and drives the network to correct it. This prevents the network from overfitting to individual images and enforces smooth, physically plausible reconstructions.

Outlook

The training and inference procedures outlined above empower NeRF to produce photorealistic images from novel viewpoints, relying on learned volumetric representations encoded within a neural network. However, this expressivity comes at a significant computational cost: each frame requires casting thousands of rays and performing hundreds of MLP evaluations per pixel, both during optimization and at test time. In the parts that follow, we examine NeRF's empirical performance through experiments and ablations, before turning to its limitations and the growing body of work aimed at improving efficiency, scalability, and generalization.

23.9.6 Experiments and Ablation Studies

To validate the NeRF architecture, Mildenhall et al. [429] conducted extensive experiments on both synthetic and real-world datasets. These included comparisons with prior methods and ablation studies to isolate the contributions of key design components.

Quantitative and Qualitative Evaluation

To assess the effectiveness of NeRF, Mildenhall et al. [429] evaluated their model on two distinct datasets:

- **Realistic Synthetic 360°**: A custom Blender-rendered dataset of eight scenes, each containing complex geometry and non-Lambertian materials. Each scene provides 100 training views and 200 held-out test views at a resolution of 800×800 pixels.
- **Real Forward-Facing**: A real-world dataset derived from handheld captures of eight indoor/outdoor scenes. These images were processed with COLMAP to extract camera poses, and 1/8 of the views were held out for evaluation.

Evaluation used the following standard image quality metrics:

- **PSNR** (Peak Signal-to-Noise Ratio): A log-domain pixel-wise fidelity metric, expressed in decibels. Higher values indicate better reconstruction accuracy.
- **SSIM** (Structural Similarity Index Measure): A perceptual metric capturing local luminance, contrast, and structure similarity. Ranges from 0 to 1; higher is better.
- **LPIPS** (Learned Perceptual Image Patch Similarity): Measures perceptual similarity using deep features. Lower values indicate better perceptual fidelity.

Method	**PSNR** ↑	**SSIM** ↑	**LPIPS** ↓
SRN [573]	22.26	0.846	0.170
Neural Volumes (NV) [389]	26.05	0.893	0.160
LLFF [428]	24.88	0.911	0.114
NeRF [429]	**31.01**	**0.947**	**0.081**

Table 23.1: Quantitative comparison on the *Realistic Synthetic 360°* dataset [429]. NeRF achieves the highest performance across all metrics, demonstrating superior geometric reconstruction, perceptual realism, and high-frequency detail.

These results highlight NeRF's significant improvement over prior methods. Compared to SRN and LLFF, NeRF improves PSNR by more than 6 dB, increases structural similarity, and cuts LPIPS perceptual error nearly in half.

Figure 23.46: Qualitative comparisons on held-out views from the Realistic Synthetic 360° dataset [429]. NeRF recovers intricate structures and materials (e.g., Lego gears, Microphone grille) and captures non-Lambertian effects. In contrast, LLFF exhibits ghosting and aliasing, while SRN and NV yield blurred or distorted geometry.

Ablation Studies

To understand which components most influence NeRF's performance, the authors conducted a series of ablations on the Realistic Synthetic 360° dataset. The study evaluated the effects of disabling positional encoding (PE), view-dependence (VD), and hierarchical sampling (H), as well as reducing the number of input views and adjusting frequency hyperparameters.

Row	Configuration	L	#Img	(N_c, N_f)	PSNR
1	No PE, VD, H	–	100	(256, –)	26.67
2	No Positional Encoding	-	100	(64, 128)	28.77
3	No View Dependence	10	100	(64, 128)	27.66
4	No Hierarchical Sampling	10	100	(256, –)	30.06
5	Far fewer images	10	25	(64, 128)	27.78
6	Fewer images	10	50	(64, 128)	29.79
7	Lower frequency ($L = 5$)	5	100	(64, 128)	30.59
8	Higher frequency ($L = 15$)	15	100	(64, 128)	30.81
9	**Full Model (baseline)**	10	100	(64, 128)	**31.01**

Table 23.2: Ablation study from [429]. Each row disables or modifies one component of the full model. PE = Positional Encoding, VD = View Dependence, H = Hierarchical Sampling. All metrics averaged across 8 scenes.

Key observations:

- **Positional Encoding (PE)** is indispensable for capturing high-frequency details such as edges, textures, and specular boundaries. Disabling PE (Row 2) reduces PSNR from 31.01 to 28.77, a 2.24 dB drop. This confirms that raw 3D inputs (xyz) are insufficient due to the spectral bias of MLPs, which favor learning smooth, low-frequency functions. PE provides the network with high-frequency sine and cosine basis functions, significantly improving representation capacity.
- **View Dependence (VD)** enables NeRF to model view-dependent effects like specular highlights and non-Lambertian reflectance. Removing view direction inputs (Row 3) yields a PSNR of 27.66, a 3.35 dB drop from the full model. Visually, surfaces appear matte and unrealistically static across viewpoints. This component is essential for photorealism and dynamic lighting effects.
- **Hierarchical Sampling (H)** improves both accuracy and training efficiency by allocating more samples to high-opacity regions. Disabling it (Row 4) leads to a moderate drop of 0.95 dB (PSNR 30.06 vs. 31.01) and increases training cost. While the rendering quality remains competitive, the uniform sampling strategy is computationally inefficient, often allocating samples to empty space, causing more noisy predictions.
- **Number of Input Views** directly affects reconstruction quality. Reducing the number of input images from 100 (Row 9) to 50 (Row 6) or 25 (Row 5) lowers PSNR to 29.79 and 27.78, respectively. Notably, even with only 25 views, NeRF still outperforms all prior baselines evaluated on 100 views, demonstrating robustness. However, performance declines in occluded or textureless regions, especially under extreme sparsity.
- **Frequency Parameter** L controls the number of sine/cosine frequency bands in PE. Lowering L to 5 (Row 7) leads to underfitting, decreasing PSNR to 30.59. Increasing L to 15 (Row 8) slightly reduces performance (30.81), likely due to overfitting or gradient instability. Thus, $L = 10$ (Row 9) offers a well-balanced tradeoff between expressivity and stability.

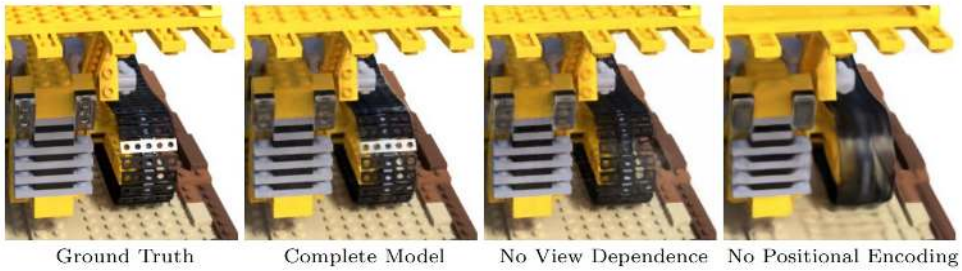

Figure 23.47: Ablation visualization from [429]. Without view dependence, specular highlights disappear, e.g., on the bulldozer tread. Without positional encoding, the model fails to recover high-frequency geometry and textures, leading to blurred reconstructions.

These experiments validate the necessity of all three architectural innovations—Fourier-based input encoding, view-dependent radiance modeling, and hierarchical sampling—for achieving NeRF's high-fidelity results. Removing any one of these leads to degraded reconstructions and/or reduced realism, and sometimes even to slower convergence.

23.9.7 Limitations of the Original NeRF Architecture

Despite the seminal impact of NeRF on 3D view synthesis, the original architecture introduced by [429] exhibits several foundational limitations that have since motivated a wave of follow-up research. These limitations are not isolated flaws but rather systemic consequences of NeRF's core design—a monolithic, scene-specific MLP that implicitly encodes geometry and radiance in millions of uninterpretable parameters. This subsection outlines six key bottlenecks, each of which inspired entire subfields of NeRF variants and accelerations.

1. Computational Inefficiency: Prohibitive Training and Inference Time

The most immediate drawback of NeRF is its extreme computational cost. Training a single scene typically requires tens to hundreds of GPU-hours, rendering it impractical for real-time or interactive use. Even inference is slow: to render a single image, NeRF must trace thousands of rays and query the MLP hundreds of times per ray, leading to total long runtimes per frame. This high latency renders applications such as virtual walkthroughs, VR/AR environments, or online editing infeasible without significant acceleration strategies. As we will see in subsequent parts, this limitation motivated a wave of speed-focused methods including Plenoxels [160], Instant-NGP [443], and TensoRF [80].

2. Data Hungriness and Pose Sensitivity

NeRF requires dense and accurate supervision: typically 100 or more posed input images for each scene. With sparse views, the model tends to overfit, memorizing training pixels and producing incorrect geometry with "floaters"—hallucinated density blobs in empty space. Moreover, NeRF assumes externally provided camera poses, often estimated via SfM pipelines such as COLMAP. Pose errors—especially in large or low-texture scenes—can severely degrade reconstruction quality, introducing ghosting and multi-exposure artifacts. These dependencies make NeRF fragile in real-world settings, where pose estimation and dense capture are often unavailable or noisy.

3. Static Scene Assumption

The original NeRF architecture assumes the scene is completely static during capture. Even minor motion—e.g., waving trees, moving pedestrians, changing shadows—violates this assumption. Since the MLP must learn a consistent radiance field, it fails to reconcile inconsistencies in dynamic scenes, leading to ghosting, blur, or averaged-out artifacts. Consequently, NeRF cannot model temporal phenomena or non-rigid deformation without significant modification. This limitation gave rise to dynamic variants such as D-NeRF [488] and subsequent temporally aware architectures.

4. Poor Scalability to Large or Unbounded Scenes

The architectural choice to encode an entire scene in a single MLP imposes a severe scalability bottleneck. As the physical extent of the scene increases—e.g., modeling a building, city block, or 360° landscape—the network's finite capacity becomes insufficient. The result is coarse geometry and low-frequency, blurry reconstructions. Additionally, the fixed near and far depth bounds used in NeRF's ray sampling mechanism are ill-suited for outdoor, forward-facing, or horizon-spanning scenes. These challenges spurred modular representations such as Block-NeRF [602], which decompose large scenes into a grid of smaller NeRFs with overlapping coverage and shared appearance embeddings.

5. Inadequate Robustness to Real-World Imaging Conditions

Most NeRF experiments are performed on sanitized datasets of clean, low dynamic range (LDR), well-lit images. In contrast, real-world imagery often suffers from HDR saturation, sensor noise, motion blur, lens artifacts, and non-uniform exposure. The original NeRF, trained on LDR values, fails to reconstruct true radiance under such conditions. Moreover, it lacks mechanisms for denoising or compensating for exposure variation. Recent works like RawNeRF [430] address this by operating on raw sensor data directly, enabling robust HDR synthesis and improved fidelity under challenging lighting.

6. Non-Editable and Opaque Representation

Finally, NeRF's learned radiance field is entirely implicit—stored in millions of weights of an MLP. This makes downstream operations such as object editing, segmentation, relighting, or geometry manipulation extremely difficult. In traditional 3D representations (e.g., meshes or voxels), editing corresponds to direct manipulation of structures with semantic meaning. In NeRF, by contrast, even deleting an object or changing its appearance would require retraining the model or resorting to finetuning tricks. This "black-box" nature remains a key challenge and an active area of research. Later approaches like Control-NeRF [315] and NeRFShop [260] aim to bridge this gap by decoupling editable features from rendering logic.

Summary

The limitations of the original NeRF—its slowness, data hungriness, fragility, and lack of editability—are all downstream consequences of its monolithic, implicit MLP-based design. Recognizing this, researchers have shifted towards more modular, explicit, and hybrid representations. As we will see in upcoming parts, these improvements not only alleviate NeRF's bottlenecks but also expand its capabilities to dynamic scenes, outdoor environments, real-time applications, and creative workflows.

Enrichment 23.10: NeRF: Acceleration and Representation Revisions

While the original NeRF architecture achieved groundbreaking results in novel view synthesis, it suffered from severe computational bottlenecks and restrictive design choices. This limitation gave rise to two key research directions:

- **Making NeRFs faster**: by improving both scene representation and the rendering pipeline;
- **Rethinking representation itself**: by exploring whether implicit MLPs are the optimal abstraction for radiance fields.

This subsection surveys the most prominent families of acceleration techniques and scene representation variants—each representing a distinct research trajectory in the evolving landscape of neural rendering.

Explicit Voxel and Point Grid Representations

A fundamental insight that motivated the first wave of NeRF accelerations is that the full power of an MLP may not be necessary to represent a static radiance field. In the original NeRF, each query along a ray—at a specific 3D point and viewing direction—requires a forward pass through a deep, overparameterized network. This becomes prohibitively slow when hundreds of queries must be processed per pixel in the image. If instead one could *cache* the radiance field explicitly in space, the model could avoid MLP evaluation altogether and retrieve color and density via simple, differentiable lookups.

This leads to a powerful tradeoff: **speed versus memory**. By storing radiance and density in spatial grids—either dense or sparsely populated—methods can dramatically reduce inference time and enable real-time rendering. The price is cubic memory growth with resolution, requiring careful grid design or pruning to scale. The following two methods exemplify this family of approaches.

Enrichment 23.10.1: Plenoxels: Sparse Voxel Grids with Spherical Harmonics

Plenoxels [160] introduce a fully explicit scene representation that removes neural networks from the NeRF rendering pipeline. Instead of approximating the radiance field using a continuous MLP $f_\theta(\mathbf{x}, \mathbf{d})$, Plenoxels define a sparse 3D voxel grid in which each *voxel corner*—corresponding to a 3D coordinate in space—stores:

- A scalar **volume density** $\sigma \in \mathbb{R}_+$, analogous to NeRF, encoding how much matter is present at that spatial location.
- **Spherical harmonics (SH)** coefficients for view-dependent RGB color. For SH degree l, each corner stores $(l+1)^2$ coefficients per color channel (e.g., 9 per channel for $l = 2$):

$$\mathbf{c}(\mathbf{x}, \mathbf{d}) = \sum_{\ell=0}^{l} \sum_{m=-\ell}^{\ell} \mathbf{a}_{\ell m} \cdot Y_{\ell m}(\mathbf{d}),$$

where $Y_{\ell m}(\mathbf{d})$ is the SH basis evaluated at viewing direction $\mathbf{d}$, and $\mathbf{a}_{\ell m} \in \mathbb{R}^3$ are the learnable RGB coefficients.

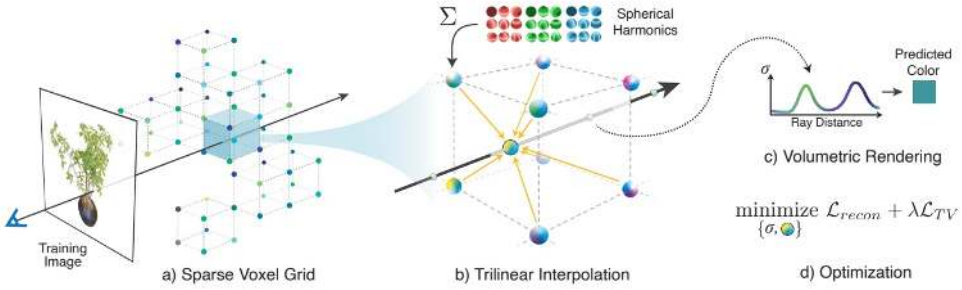

Figure 23.48: Overview of the Plenoxel model, adapted from [160]. (a) A sparse voxel grid stores SH coefficients and densities at each corner. (b) Sampled points along rays interpolate these values. (c) Volume rendering integrates color and opacity. (d) Grid parameters are optimized via a reconstruction loss and regularization.

Inference and Volume Rendering.

For each ray $\mathbf{r}(t) = \mathbf{o} + t\mathbf{d}$, Plenoxels sample a set of points $\mathbf{r}(t_i)$ within the interval $[t_n, t_f]$, as in NeRF. For each point:

- The *trilinear interpolation* of densities and SH coefficients is computed from the eight corners of the voxel enclosing $\mathbf{r}(t_i)$.
- The interpolated SH coefficients are combined with the viewing direction $\mathbf{d}$ via SH basis functions to compute the radiance $\mathbf{c}_i \in [0,1]^3$.
- These values $(\sigma_i, \mathbf{c}_i)$ are integrated along the ray using the same differentiable alpha compositing rule as NeRF:

$$\hat{\mathscr{C}}(\mathbf{r}) = \sum_{i=1}^{N} T_i \cdot \alpha_i \cdot \mathbf{c}_i, \quad \alpha_i = 1 - \exp(-\sigma_i \delta_i), \quad T_i = \prod_{j=1}^{i-1} (1 - \alpha_j).$$

This process is far more efficient than evaluating an MLP for each query point.

Training via Reconstruction Loss.

Plenoxels are trained using the same loss as NeRF. For a ray with known ground-truth color $\mathscr{C}(\mathbf{r})$, the predicted color $\hat{\mathscr{C}}(\mathbf{r})$ is supervised by:

$$\mathscr{L}_{\text{recon}} = \left\| \hat{\mathscr{C}}(\mathbf{r}) - \mathscr{C}(\mathbf{r}) \right\|_2^2.$$

To ensure smoothness and avoid artifacts, the authors also apply a total variation regularization term to both the SH coefficients and densities.

Why Spherical Harmonics?

Spherical harmonics are a compact, differentiable basis for modeling smooth directional variation. At each spatial point, SHs allow the color to change with viewpoint (e.g., capturing specularities), while still being efficient to store and evaluate. Importantly, their basis functions $Y_{\ell m}(\mathbf{d})$ are fixed and directional—so the only learnable parameters are the SH coefficients per corner.

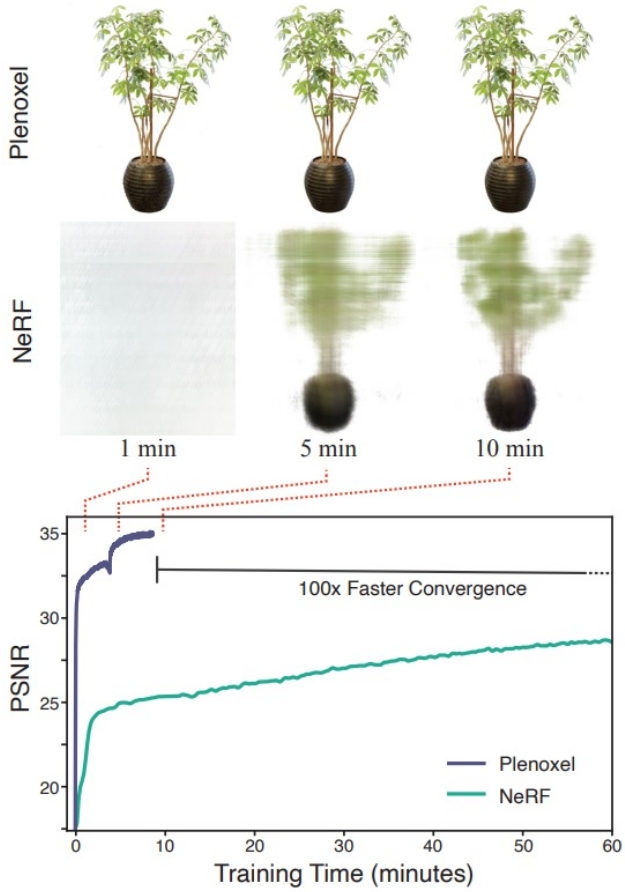

Figure 23.49: Training comparison between NeRF and Plenoxels [160]. Plenoxels reconstruct meaningful geometry within a minute, while NeRF requires tens of minutes for similar fidelity.

Fast Convergence via Coarse-to-Fine Refinement.
The voxel grid is initialized at a low resolution (e.g., 128^3), with voxels that have low opacity pruned early. As training progresses, high-opacity regions (likely to contain object surfaces) are adaptively subdivided into finer voxels. This hierarchical approach allows Plenoxels to focus memory and resolution only where detail is required.

Core Insight and Tradeoffs.
Plenoxels' design replaces learned neural scene functions with a sparse, explicit grid of radiance information. The grid is fully differentiable, fast to query, and optimized directly—avoiding the need for costly MLP forward passes. However, this performance comes at the cost of memory: voxel-based representations scale cubically with resolution, and require pruning and sparsity to remain tractable.

Key insight: By combining spherical harmonics with sparse voxel grids, Plenoxels offer a radiance field representation that is fast to optimize and evaluate, enabling high-quality novel view synthesis in minutes rather than hours.

Enrichment 23.10.2: DVGO: Direct Optimization on Dense Voxel Grids

Direct Voxel Grid Optimization (DVGO) [591] accelerates novel view synthesis by replacing NeRF's implicit MLP with a fully explicit scene representation: a dense voxel grid storing volume densities and appearance features. This design allows DVGO to train up to two orders of magnitude faster than NeRF while retaining differentiable volumetric rendering.

A *dense grid* refers to a regular axis-aligned 3D array covering a bounded scene volume, where every voxel is allocated and updated during training—unlike sparse grids, which store only occupied regions. This simplifies memory layout and interpolation, but requires careful bounding and coarse-to-fine scheduling to manage memory usage.

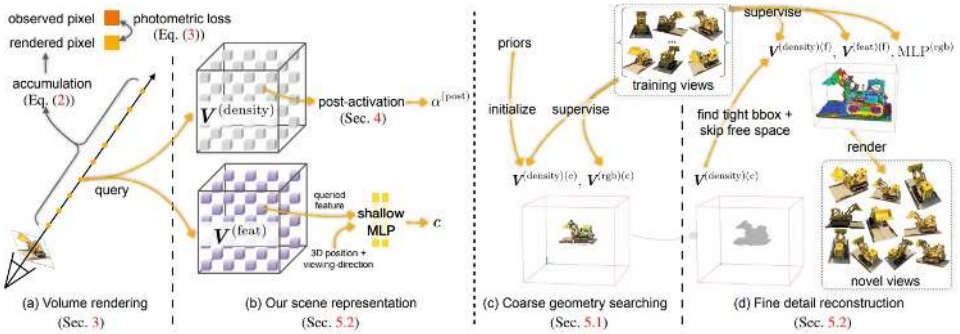

Figure 23.50: DVGO framework overview, adapted from [591]. A ray is cast and sampled at 3D points. Trilinear interpolation retrieves density and appearance features from a dense voxel grid. A lightweight MLP decodes RGB values. Differentiable volume rendering is used for supervision.

Rendering Pipeline

DVGO preserves the volumetric rendering framework of NeRF but replaces the implicit MLP with an explicit, grid-based representation. The rendering process is composed of the following steps:

- **1. Ray Sampling:** For each pixel, a ray is cast as $\mathbf{r}(t) = \mathbf{o} + t\mathbf{d}$, where $\mathbf{o}$ is the camera origin and $\mathbf{d}$ is the viewing direction. The ray is sampled at depths $\{t_i\}_{i=1}^{N}$, yielding 3D sample points $\mathbf{x}_i = \mathbf{r}(t_i)$.
- **2. Grid Query via Trilinear Interpolation:** Each point $\mathbf{x}_i$ is mapped into the dense voxel grid. DVGO retrieves the interpolated density $\sigma(\mathbf{x}_i) \in \mathbb{R}$ and a learned appearance feature $\mathbf{f}(\mathbf{x}_i) \in \mathbb{R}^C$ using trilinear interpolation from the eight surrounding voxels.
- **3. Color Decoding:** To produce RGB color, DVGO offers two options:
  - **Direct RGB:** The feature $\mathbf{f}$ is directly interpreted as an RGB vector—this is the fastest and view-independent mode.
  - **Tiny MLP:** A shallow two-layer MLP with the viewing direction $\mathbf{d}$ as input decodes the color as $\mathbf{c}_i = \text{MLP}(\mathbf{f}, \mathbf{d})$. This captures simple view-dependent effects at minimal cost.
- **4. Volume Rendering:** Colors $\mathbf{c}_i$ and opacities $\alpha_i = 1 - \exp(-\sigma_i \delta_i)$ are combined using alpha compositing:

$$T_i = \prod_{j=1}^{i-1}(1-\alpha_j), \quad \hat{\mathbf{C}}(\mathbf{r}) = \sum_{i=1}^{N} T_i \cdot \alpha_i \cdot \mathbf{c}_i.$$

The model is trained to minimize the reconstruction loss:

$$\mathscr{L} = \left\| \hat{\mathscr{C}}(\mathbf{r}) - \mathscr{C}(\mathbf{r}) \right\|_2^2.$$

Coarse-to-Fine Upsampling and Fine Detail Reconstruction

DVGO's training proceeds in a progressive manner: it begins with a coarse voxel grid (e.g., 128^3) and upsamples it at fixed iteration checkpoints (e.g., after 2k and 4k steps) to finer resolutions (e.g., 256^3, 512^3). Each upsampling operation uses trilinear interpolation to initialize the finer grid from the coarser one. Crucially, nonlinear activations (e.g., ReLU or softplus) are applied *after* interpolation—this **post-activation strategy** enhances sharp surface modeling and reduces high-resolution artifacts.

This multi-resolution training schedule enables the model to:

- Quickly capture global geometry with minimal compute at low resolution,
- Preserve continuity and prior learning when upsampling,
- Refine high-frequency details and textures in later training phases without restarting optimization.

During inference, only the final high-resolution grid is used.

Foreground–Background Decomposition

To support both bounded and unbounded scenes, DVGO introduces a two-grid decomposition. The foreground region is represented with a dense voxel grid aligned to a tight bounding box. For unbounded backgrounds (e.g., skies or distant terrain), DVGO uses a secondary cylindrical grid in log-depth space. Rays first accumulate color and opacity from the foreground; if the transmittance remains nonzero, they continue into the background grid.

DVGOv2 Improvements

DVGOv2 [591] builds on DVGO with several technical enhancements that improve both training efficiency and rendering fidelity:

- **Distortion-Aware Loss:** A fast implementation of the distortion regularization from mip-NeRF 360 [29], reducing complexity from $\mathscr{O}(N^2)$ to $\mathscr{O}(N)$.
- **Adaptive Learning Rate:** Voxels observed from fewer views are assigned lower learning rates to reduce overfitting to sparse observations.
- **Low-Opacity Initialization:** The density grid is initialized to near-zero opacity to avoid redundant clouds in empty regions.
- **Cuboid Grid Parameterization:** Supports unbounded scenes via a contracted cuboid grid inspired by mip-NeRF 360.

These changes lead to faster convergence, better generalization, and improved visual quality, especially in complex or forward-facing scenes.

Comparison to Plenoxels and NeRF

- **NeRF:** Relies on a deep MLP to model density and color, requiring multiple hours of training per scene. DVGO eliminates the MLP for geometry and uses only a shallow decoder for color, yielding up to $100\times$ faster training.
- **Plenoxels:** Employs sparse voxel grids with spherical harmonics (SH) for view-dependent color. While more memory-efficient, SH can introduce ringing artifacts and requires custom CUDA kernels. DVGO, in contrast, uses dense grids and is implemented in pure PyTorch, making it easier to adopt and extend.

Efficiency and Tradeoffs

Quantitative benchmarks on the LLFF dataset highlight the tradeoffs:

- **Training Time:** DVGOv2 converges in ~10.9 minutes vs. 24.2 minutes for Plenoxels.
- **Quality:** DVGOv2 achieves slightly better PSNR (26.34 vs. 26.29) and lower LPIPS (0.197 vs. 0.210).
- **Inference Time:** DVGOv2 is slightly slower (0.07–0.36 s per image) than Plenoxels (~0.0667 s), due to its dense grid.

DVGO is ideal for rapid prototyping, differentiable pipelines, and simpler research codebases. Plenoxels remains competitive in memory-constrained or real-time settings. The choice depends on application constraints: DVGO favors training speed and modularity; Plenoxels favors compactness and high-speed inference.

Performance Across Scene Types

DVGO and its improved variant DVGOv2 [592] deliver strong rendering quality across diverse benchmarks while significantly accelerating training. DVGOv2 incorporates distortion-aware loss, low-opacity initialization, and adaptive learning rates for enhanced convergence, especially in real-world or unbounded settings.

Method	Train Time	PSNR↑	SSIM↑	LPIPS↓
Synthetic-NeRF (8 scenes)				
DVGO	14.2m	31.95	0.957	0.053
Plenoxels	11.1m	31.71	0.958	0.049
Instant-NGP	**5.0m**	**33.18**	–	–
TensoRF (L)	17.6m	33.14	0.963	0.047
DVGOv2 (L)	6.8m	32.76	0.962	0.046

Table 23.3: Results on Synthetic-NeRF [429].

Method	Train Time	PSNR↑	SSIM↑	LPIPS↓
LLFF (forward-facing)				
NeRF [429]	~1440m	26.50	0.811	0.250
Plenoxels	24.2m	26.29	**0.839**	0.210
TensoRF (S)	19.7m	26.51	0.832	0.217
TensoRF (L)	25.7m	**26.73**	**0.839**	0.204
DVGOv2 w/o $\mathscr{L}_{\text{dist}}$	13.9m	26.24	0.833	0.204
DVGOv2	**10.9m**	26.34	0.838	**0.197**

Table 23.4: LLFF benchmark results. DVGOv2 achieves strong accuracy with fast training and compact grids.

Method	Train Time	PSNR↑	SSIM↑	LPIPS↓
Tanks&Temples (unbounded)				
NeRF++	hours	**20.49**	0.648	0.478
Plenoxels	27.3m	20.40	**0.696**	**0.420**
DVGOv2 w/o $\mathscr{L}_{\text{dist}}$	22.1m	20.08	0.649	0.495
DVGOv2	**16.0m**	20.10	0.653	0.477

Table 23.5: Results on unbounded inward-facing Tanks&Temples dataset.

Method	Train Time	PSNR↑	SSIM↑	LPIPS↓
mip-NeRF 360 (unbounded)				
NeRF	hours	24.85	0.659	0.426
NeRF++	hours	26.21	0.729	0.348
mip-NeRF 360	hours	**28.94**	**0.837**	**0.208**
DVGOv2 w/o $\mathscr{L}_{\text{dist}}$	16.4m	24.73	0.663	0.465
DVGOv2 ($p = 2$)	13.2m	24.80	0.659	0.468
DVGOv2 ($p = \infty$)	14.0m	25.24	0.680	0.446
DVGOv2 ($p = \infty$)*	15.6m	25.42	0.695	0.429

Table 23.6: Results on mip-NeRF 360 dataset. (*) denotes longer schedule with cuboid contraction.

Final Remarks

DVGO and DVGOv2 establish voxel-based grids as powerful alternatives to neural radiance fields. By combining dense 3D grids, post-activation interpolation, and shallow decoders, they offer rapid convergence with minimal architectural complexity. DVGOv2 further enhances training stability and scalability for real-world and unbounded scenes—making it a highly competitive baseline for fast and differentiable view synthesis.

Hash-Based Feature Grid Representations

While voxel-based methods accelerate NeRF by caching scene representations in spatial grids, they suffer from cubic memory growth as resolution increases. To overcome this bottleneck, a new family of approaches—starting with Instant-NGP—replaces dense voxel grids with compact *multiresolution hash encodings*. These techniques map 3D points to feature vectors via hash tables that sparsely index multiscale grids. The result is a flexible and memory-efficient representation that supports fast training, real-time rendering, and high fidelity.

Core Tradeoff. Hash-based grids strike a balance between speed and quality, avoiding the memory overhead of dense voxel fields while adapting to scene complexity. However, they introduce stochasticity due to hash collisions—multiple spatial locations may share a feature if they fall into the same hash bucket—potentially adding noise to reconstructions. Despite this, hash encodings have proven remarkably robust and scalable across datasets.

Enrichment 23.10.3: Instant-NGP: Multiscale Hash Encoding for Real-Time NeRF

Instant-NGP [443] revolutionized radiance field rendering by achieving real-time training and inference through a novel **multi-resolution hash encoding** and a fully optimized GPU pipeline. The method decouples scene resolution from memory usage by mapping 3D positions to compact, trainable feature vectors via hash tables. These features, concatenated across multiple spatial scales, are passed to a small neural decoder to predict density and color.

Multiscale Hash Encoding

Instant-NGP replaces dense voxel grids with a compact, adaptive alternative: a **multiresolution hash grid** encoding. The key idea is to approximate the benefits of a high-resolution voxel grid without paying its cubic memory cost. Instead of explicitly allocating every voxel, the method uses a hierarchy of virtual grids combined with spatial hashing and trilinear interpolation to extract meaningful features at arbitrary 3D positions.

At each level $\ell \in \{1,\dots,L\}$, the scene is conceptually divided into a $2^\ell \times 2^\ell \times 2^\ell$ regular grid. For a given point $\mathbf{x} \in \mathbb{R}^3$, Instant-NGP performs the following steps at level ℓ:

1. **Voxel identification:** Scale $\mathbf{x}$ to the grid resolution and identify the indices of the 8 surrounding voxel corners.
2. **Hash lookup:** Each corner index is passed through a fixed spatial hash function:
$$h(x,y,z) = ((x \cdot p_1) \oplus (y \cdot p_2) \oplus (z \cdot p_3)) \bmod T,$$
where p_1, p_2, p_3 are large primes, $\oplus$ denotes bitwise XOR, and T is the fixed hash table size.
3. **Feature interpolation:** Each hash index retrieves a trainable feature vector from a table specific to level ℓ. These 8 vectors are then interpolated using *trilinear interpolation*, weighted by the relative position of $\mathbf{x}$ within the voxel, to obtain a level-specific embedding $\mathbf{f}_\ell(\mathbf{x}) \in \mathbb{R}^F$.

This process is repeated independently at all L levels. The resulting embeddings are concatenated:

$$\mathbf{f}(\mathbf{x}) = \bigoplus_{\ell=1}^{L} \mathbf{f}_\ell(\mathbf{x}) \in \mathbb{R}^{L \cdot F}.$$

Motivation and Benefits

This design achieves fine-grained spatial adaptivity using constant memory per level. At coarse levels, the grid size is typically smaller than T, so the hash function provides a near one-to-one mapping. At fine levels, where the number of grid points exceeds T, multiple spatial positions map to the same slot—creating *collisions*. These collisions are tolerated and implicitly resolved through training: the feature vectors stored in each hash slot are optimized via backpropagation, and the network learns to disambiguate overlapping mappings by adjusting gradients according to relevance.

This approach yields several key benefits:

- **Compactness:** Each hash table is small and fixed-size, yet the total system covers extremely high spatial resolution.
- **Continuity:** Trilinear interpolation smooths transitions between nearby points.
- **Adaptivity:** Regions with high-frequency detail attract stronger gradients, naturally concentrating representational capacity.
- **Efficiency:** All hash lookups and interpolations are lightweight and fully parallelizable on modern GPUs.

Hash Function and Learning Dynamics

Instant-NGP encodes 3D positions using a multiresolution hierarchy of spatial hash tables. Each level $\ell \in \{1,\dots,L\}$ maintains a separate hash table: an array of T learnable feature vectors in $\mathbb{R}^F$. The table does not store voxels explicitly. Instead, a fixed spatial hash function maps integer voxel indices to table slots:

$$h(x,y,z) = ((x \cdot p_1) \oplus (y \cdot p_2) \oplus (z \cdot p_3)) \bmod T,$$

where p_1, p_2, p_3 are large primes, and $\oplus$ denotes bitwise XOR. The table size T is fixed (typically $T \in [2^{14}, 2^{19}]$).

Given a query point $\mathbf{x} \in \mathbb{R}^3$, the encoding proceeds as follows:

1. **Multiscale voxelization:** For each level ℓ, $\mathbf{x}$ is scaled to the level's virtual grid and enclosed voxel cell. The 8 surrounding integer voxel corners $\{\mathbf{c}_i\} \subset \mathbb{Z}^3$ are identified.
2. **Hash-based lookup:** Each corner $\mathbf{c}_i = (x_i, y_i, z_i)$ is hashed to index $h(x_i, y_i, z_i)$, retrieving a feature vector $\mathbf{v}_i \in \mathbb{R}^F$ from the level's table.
3. **Interpolation:** The 8 vectors $\{\mathbf{v}_i\}$ are trilinearly interpolated using $\mathbf{x}$'s relative position in the voxel to obtain $\mathbf{f}_\ell(\mathbf{x}) \in \mathbb{R}^F$.

The results from all L levels are concatenated to form the full encoding:

$$\mathbf{f}(\mathbf{x}) = \bigoplus_{\ell=1}^{L} \mathbf{f}_\ell(\mathbf{x}) \in \mathbb{R}^{L \cdot F},$$

which is passed to a lightweight MLP to predict volume density σ and emitted color $\mathbf{c}$.

The only trainable parameters in this encoding stage are the feature vectors $\{\mathbf{v}_i\}$ in the hash tables. These are initialized randomly and updated during training. Although the hash function and voxel coordinates are fixed and non-differentiable, the downstream operations—interpolation, concatenation, and the MLP—are differentiable. This allows gradients from the output loss to backpropagate to the retrieved vectors:

$$\text{loss} \to \text{MLP} \to \mathbf{f}(\mathbf{x}) \to \mathbf{f}_\ell(\mathbf{x}) \to \text{weights} \to \{\mathbf{v}_i\}.$$

Since trilinear interpolation is a linear operation, gradients are distributed proportionally to the interpolation weights. Each feature vector $\mathbf{v}_i$ receives a meaningful update via gradient descent, despite being accessed through a non-differentiable hash index.

This design decouples the spatial access mechanism from learning. The hash function defines a fast, fixed indexing scheme; the MLP never sees raw coordinates $\mathbf{x}$, only the feature-based encoding $\mathbf{f}(\mathbf{x})$. Learning proceeds entirely by adjusting the content of the hash tables to minimize prediction error.

To decorrelate nearby spatial positions, the hash function applies two transformations: each coordinate is multiplied by a large prime to stretch the input space, then the results are combined using bitwise XOR to mix their bits. This ensures that adjacent voxel indices—such as (x,y,z) and $(x,y,z+1)$—produce distant hash indices, scattering neighboring points across the table and reducing local redundancy.

Since the hash table size T is fixed and shared across all levels, collisions are resolution-dependent. At coarse levels, the number of possible voxel corners is small relative to T, so collisions are rare. At fine levels, however, the voxel grid grows cubically, quickly exceeding T and making collisions inevitable—i.e., distinct locations mapping to the same feature vector.

Instant-NGP does not resolve these collisions structurally. Instead, it relies on implicit resolution through gradient-based optimization. During training, multiple points may share a feature vector, but their contributions differ: voxels near high-frequency structures (e.g., edges or textured surfaces) produce stronger gradients, which dominate the updates. Voxels in smooth or empty regions contribute weak gradients and have little effect. This causes the optimizer to adaptively reallocate memory: important areas receive sharper, more expressive encodings, while uninformative regions are compressed.

The multiresolution hierarchy further mitigates the effects of collisions. Even if two points collide at one level, they are unlikely to do so across all L levels. Since the final encoding $\mathbf{f}(\mathbf{x}) = \bigoplus_{\ell=1}^{L} \mathbf{f}_\ell(\mathbf{x})$ aggregates interpolated features across resolutions, most spatial positions retain a nearly unique representation. This enables the MLP to distinguish between distinct locations reliably, despite heavy parameter sharing.

This collision-tolerant design enables Instant-NGP to maintain high fidelity with a compact memory budget: a fixed-size hash table per level suffices to encode large scenes efficiently, while multiscale encoding and gradient-driven adaptivity ensure representational capacity is focused where it matters most.

Fast MLP Decoder and View Conditioning

The final concatenated multiscale embedding $\mathbf{f}(\mathbf{x})$, along with an encoding of the viewing direction $\mathbf{d}$, is passed to a lightweight MLP decoder:

$$(\sigma, \mathbf{c}) = f_\theta(\mathbf{f}(\mathbf{x}), \mathbf{d}).$$

This MLP typically has 2–3 layers and is implemented with the `tiny-cuda-nn` library, which fuses matrix multiplication and activation layers into a single CUDA kernel. This reduces memory traffic and enables the entire forward/backward computation to execute in microseconds.

The network outputs:

- A scalar **density** $\sigma \in \mathbb{R}_+$, controlling opacity along the ray.
- An RGB **color** vector $\mathbf{c} \in [0,1]^3$, which can depend on the view direction via $\mathbf{d}$.

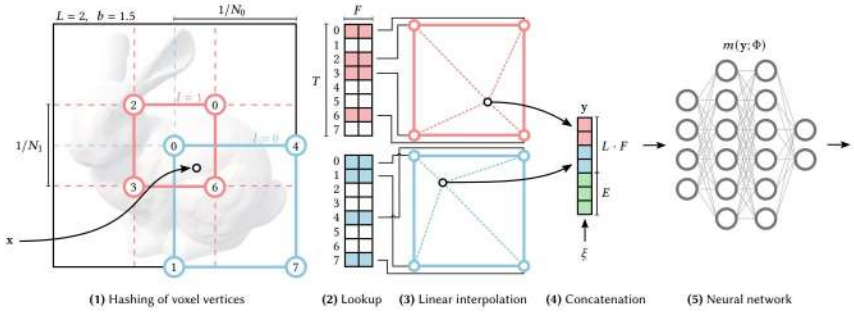

Figure 23.51: Instant-NGP architecture. Input points are encoded with multi-resolution hash grids, passed to a fused MLP along with viewing direction, and output density and color are used for volume rendering.

This architecture supports real-time training and rendering by combining a compact, hash-based spatial encoding with an extremely efficient neural decoder.

Occupancy Grid Acceleration

To reduce the number of MLP evaluations in empty space, Instant-NGP employs a coarse *occupancy grid* that accelerates volume rendering by identifying which regions of the scene are likely to contain nonzero density. This grid is dynamically updated during training and acts as a binary mask that allows rays to skip regions deemed empty, leading to speedups of $10\times$ to $100\times$ in large scenes.

The grid is a 3D bitfield over a coarse voxelization of the scene's bounding volume. For any sample point along a camera ray, the renderer first checks the occupancy bit of the voxel containing the point. If the bit is unset (i.e., the region is marked as empty), the sample is skipped and the MLP is not queried. This drastically reduces redundant computation in free space and occluded volumes.

The occupancy grid is not static; it is updated periodically based on the current predictions of the model. Specifically, Instant-NGP maintains a separate floating-point density grid (not visible to the renderer) to accumulate raw density values over time. Every N training steps (e.g., $N = 16$), the system performs the following update:

1. A set of candidate grid cells is selected for update, using a combination of uniform sampling and rejection sampling near occupied regions.
2. For each selected cell, a random 3D point $\mathbf{x}$ within the cell is chosen.
3. The MLP is queried at $\mathbf{x}$ to obtain its predicted volume density $\sigma(\mathbf{x})$.
4. The cell's accumulated density value is updated by taking the maximum of the existing value and $\sigma(\mathbf{x})$.
5. The final occupancy bit is set if this value exceeds a threshold ε; otherwise, the cell remains marked as empty.

Importantly, the MLP is *not* evaluated at the eight corners of each voxel for this purpose. Instead, it is evaluated at a single random point within the cell, which is sufficient to detect occupied space due to the smoothness of the learned density field. This process ensures that the occupancy grid reflects the evolving geometry of the scene, pruning away empty regions while preserving regions with fine detail.

At rendering time, this grid enables efficient ray marching: rays are advanced in larger steps through empty regions and subdivided only when approaching occupied space. Combined with Instant-NGP's compact encoding, this mechanism enables high-fidelity novel view synthesis at interactive frame rates.

Training and Inference

Training follows the same NeRF paradigm: rays are sampled, feature vectors are encoded from hash tables, densities and colors are predicted, and volume rendering integrates them into pixel colors. The MSE loss is backpropagated through the entire system, including the hash table entries (which are learnable) and the MLP. During inference, the process is purely feed-forward and supports 100+ FPS rendering on modern GPUs.

Advantages and Limitations

- **Speed and Efficiency:** Instant-NGP achieves dramatic acceleration over prior NeRF methods. With hash-based encoding and optimized CUDA kernels, it reaches high-quality reconstructions in just seconds. For example, on the LEGO scene, Instant-NGP matches or surpasses NeRF's performance (32.54 PSNR) in under 15 seconds of training (see the below table). Real-time rendering is also enabled at over 60 FPS.
- **Quality and Convergence:** Despite its speed, Instant-NGP does not sacrifice fidelity. After just 1 minute of training, it consistently outperforms NeRF [429] and NSVF [370], and achieves results competitive with or exceeding mip-NeRF [30]. Notably, the hash-encoded model reaches 33.18 average PSNR in 5 minutes—higher than all baselines.
- **Compactness:** The hash encoding decouples memory consumption from scene resolution. Each level uses a fixed-size table of T feature vectors, yielding predictable memory use (e.g., $2-8$ MB), regardless of spatial complexity.
- **Adaptivity:** Collisions in the hash tables are not explicitly resolved. Instead, gradient-based optimization allocates representational capacity where needed: voxels near surfaces or textures produce stronger gradients and dominate updates to shared entries. This enables the model to prioritize detail-rich regions while ignoring redundant space.
- **Limitations:**
  - Requires custom CUDA kernels and optimized memory layouts, limiting ease of deployment across platforms.
  - Primarily suited for dense photometric supervision; extensions to sparse-view or semantic tasks are nontrivial.
  - Hash collisions may introduce subtle artifacts in high-frequency regions.

Table 23.7: PSNR comparison on the eight synthetic scenes from the NeRF dataset. Instant-NGP (Hash) achieves top quality within seconds to minutes, outperforming NeRF [429] and NSVF [370], and approaching or exceeding mip-NeRF [30]. Data from [443].

Method	Mic	Ficus	Chair	Hotdog	Materials	Drums	Ship	Lego	Avg.
Instant-NGP (Hash, 1s)	26.09	21.30	21.55	21.63	22.07	17.76	20.38	18.83	21.20
Instant-NGP (Hash, 5s)	32.60	30.35	30.77	33.42	26.60	23.84	26.38	30.13	29.26
Instant-NGP (Hash, 15s)	34.76	32.26	32.95	35.56	28.25	25.23	28.56	33.68	31.41
Instant-NGP (Hash, 1m)	35.92	33.05	34.34	36.78	29.33	25.82	30.20	35.63	32.64
Instant-NGP (Hash, 5m)	36.22	33.51	35.00	37.40	29.78	26.02	31.10	36.39	**33.18**
mip-NeRF (hours)	36.51	33.29	35.14	37.48	30.71	25.48	30.41	35.70	33.09
NSVF (hours)	34.27	31.23	33.19	37.14	32.68	25.18	27.93	32.29	31.74
NeRF (hours)	32.91	30.13	33.00	36.18	29.62	25.01	28.65	32.54	31.01
Instant-NGP (Freq., 1m)	26.62	24.72	28.51	32.61	26.36	21.33	24.32	28.88	26.67
Instant-NGP (Freq., 5m)	31.89	28.74	31.02	34.86	28.93	24.18	28.06	32.77	30.06

Key insight: By replacing dense voxel grids with multiresolution hash encodings and using a fully fused MLP, Instant-NGP transforms NeRF into a memory-efficient and GPU-optimal rendering system capable of real-time operation.

Enrichment 23.10.4: Nerfacto: Merging Instant-NGP & NR Pipelines

Nerfacto [605] generalizes the Instant-NGP architecture into a more robust and modular neural rendering pipeline. It retains the core speed advantages of multiresolution hash encodings, but integrates a range of techniques from more expressive NeRF variants—including Mip-NeRF 360, NeRF-W, and Ref-NeRF—to support complex, real-world data. Developed within the `Nerfstudio` framework, Nerfacto prioritizes flexibility, semantic extensibility, and practical usability over raw speed alone.

At the core, Nerfacto still uses a hash-encoded MLP to map each sampled 3D point $\mathbf{x} \in \mathbb{R}^3$ and view direction $\mathbf{d} \in \mathbb{S}^2$ to a predicted color and density. Like Instant-NGP, it queries a multiresolution hash grid to produce a high-frequency encoding $\mathbf{f}(\mathbf{x})$, which is fed to a compact decoder network.

However, Nerfacto departs from Instant-NGP in three major ways:

- **Proposal Network Sampling:** Nerfacto improves ray efficiency by using a hierarchy of lightweight proposal networks—small hash-encoded MLPs—that predict coarse density distributions. These guide sample placement toward regions of likely scene content, reducing wasted queries and enhancing edge sharpness. This replaces the occupancy grid with a more learned, view-adaptive sampling strategy, similar to mip-NeRF 360.
- **Hybrid Feature Fusion:** In addition to 3D hash features, Nerfacto optionally fuses image-space features from 2D convolutional encoders. These image features can inject view-specific cues, aiding the model in tasks like relighting, semantic rendering, or pose correction. The final input to the MLP decoder is a concatenation of 3D features, view direction encodings, and (optionally) per-image appearance embeddings or 2D descriptors.
- **Extended Output and Losses:** Unlike Instant-NGP—which focuses solely on color and density prediction—Nerfacto supports multi-head outputs and diverse losses, including surface normals, depth supervision, semantic labels, or photometric consistency across views. This makes it suitable for real-world, unbounded scenes captured with noisy camera poses and lighting variation.

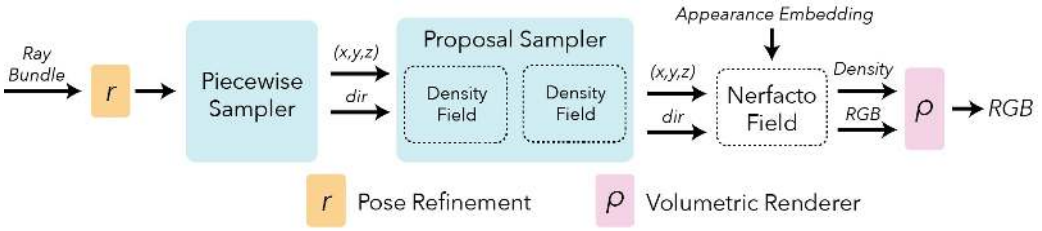

Figure 23.52: Nerfacto pipeline [605]. Hash-encoded 3D features and auxiliary 2D features are fused before MLP decoding. The network is trained using RGB, geometric, and semantic losses.

By combining fast hash-based encoding with modular losses, proposal sampling, and auxiliary inputs, Nerfacto enables real-time training and visualization even in messy, in-the-wild datasets. While Instant-NGP is best suited for clean, object-centric scenes with pre-registered cameras, Nerfacto handles general scenes with pose noise, dynamic lighting, and semantic supervision. It offers a practical middle ground between research flexibility and production deployment.

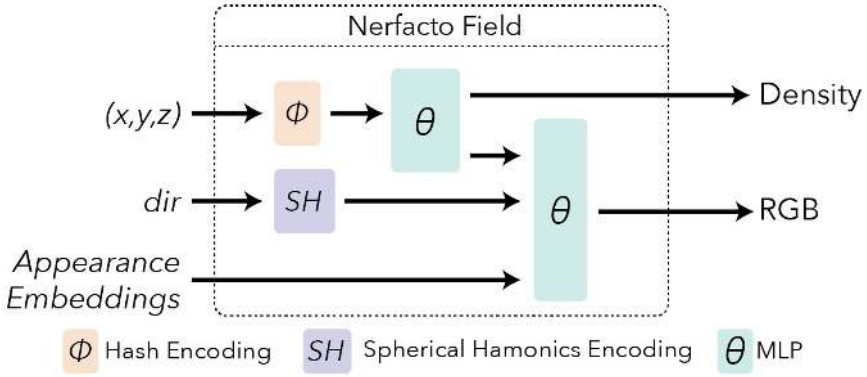

Figure 23.53: Volume rendering output of Nerfacto [605]. Despite real-time training, the model recovers sharp surfaces and textures.

Applications and Design Goals

Nerfacto is engineered not only for high-quality novel view synthesis, but also as a general-purpose backbone for a wide range of NeRF-style applications. Its modular design, efficient encoding, and support for auxiliary supervision make it suitable for both academic experimentation and real-world deployment. Key goals include:

- **Reusability:** Nerfacto supports downstream tasks such as relighting, surface extraction, and semantic segmentation. Fine-tuning is straightforward, enabling rapid adaptation to new scenes or objectives.
- **Speed:** By retaining Instant-NGP's hash-based encoding and efficient volumetric rendering, Nerfacto preserves real-time training and inference speeds—despite additional model components and loss terms.
- **Robustness:** Nerfacto is designed to operate under imperfect capture conditions, including sparse viewpoints, noisy poses, and variable lighting. It generalizes well with minimal hyperparameter tuning and works effectively across both bounded and unbounded scenes.

Compared to Instant-NGP—which focuses on maximal efficiency for object-centric datasets with known poses—Nerfacto emphasizes extensibility and supervision-rich learning. Its architecture accommodates semantic objectives, auxiliary features, and dynamic inputs without sacrificing rendering quality or speed.

Core Insight and Tradeoffs

Nerfacto's core insight is that fast hash-based scene encoding can be extended into a flexible, semantically-aware rendering framework. The multiresolution hash grid compresses spatial variation across scales, while learned decoders map fused 3D and 2D features to rich volumetric outputs. This allows the model to achieve high fidelity with a compact parameter budget.

Although hash collisions are unavoidable at fine resolutions, their impact is mitigated by the multilevel encoding: even if two spatial positions collide at one resolution, they are unlikely to collide across all levels. This ensures that the final encoding $\mathbf{f}(\mathbf{x})$ remains discriminative and expressive, preserving sharp detail and accurate color prediction, just like in Instant-NGP.

Key insight: Nerfacto demonstrates that real-time neural rendering does not require sacrificing flexibility or supervision. By combining Instant-NGP's memory efficiency with neural field modularity, it bridges efficient graphics pipelines and modern learning-based scene understanding.

Enrichment 23.10.5: TensoRF: Tensor-Factorized Fields

TensoRF [80] proposes a compact and interpretable alternative to MLP-based NeRF-style radiance field models. The scene is still represented as a continuous 5D function

$$\mathscr{F}(\mathbf{x},\mathbf{d}) = (\sigma,\mathbf{c}),$$

mapping a 3D location $\mathbf{x} \in \mathbb{R}^3$ and a viewing direction $\mathbf{d} \in \mathbb{S}^2$ to a scalar volume density $\sigma \in \mathbb{R}$ and a view-dependent RGB color $\mathbf{c} \in \mathbb{R}^3$.

Overview

Vanilla NeRF computes features by feeding spatial coordinates into a coordinate-based MLP, which is queried at every sampled point along a ray. TensoRF replaces this with an explicit, low-rank tensor representation that stores features in a structured form and can be queried directly via interpolation. This change shifts most computation from deep networks to simple lookups and lightweight decoding, reducing both memory and runtime while preserving compatibility with NeRF's differentiable volume rendering framework. Conceptually, the model consists of:

- A **4D spatial feature tensor** $\mathscr{T} \in \mathbb{R}^{X\times Y\times Z\times C}$, storing a feature vector of dimension C at each spatial location $\mathbf{x} = (x,y,z)$;
- A lightweight **decoder** S that maps features and a view direction $\mathbf{d}$ to the density σ and RGB color $\mathbf{c}$.

Radiance Field Decomposition via Tensor Approximation

The latent feature field $\mathscr{T}$ is decomposed into:

- **Geometry tensor** $\mathscr{T}_\sigma \in \mathbb{R}^{X\times Y\times Z\times C_\sigma}$ — features used for density estimation.
- **Appearance tensor** $\mathscr{T}_c \in \mathbb{R}^{X\times Y\times Z\times C_c}$ — features used for predicting view-dependent color.

These combine as $\mathscr{T} = [\mathscr{T}_\sigma \mid \mathscr{T}_c]$ with $C = C_\sigma + C_c$.

Rather than store $\mathscr{T}$ densely, TensoRF learns a small number $R = R_\sigma + R_c$ of axis-aligned **vector–matrix (VM) factors**, acting as compressed tensor components. For any point $\mathbf{x} \in [0,1]^3$:

- Geometry features are reconstructed by summing R_σ geometry VM components.
- Appearance features are reconstructed by summing R_c appearance VM components.
- These are passed to density and color heads to compute $\sigma(\mathbf{x})$ and $\mathbf{c}(\mathbf{x},\mathbf{d})$, respectively.

This factorization reduces storage complexity from $\mathscr{O}(N^3C)$ for a dense voxel grid to $\mathscr{O}(N^2RC)$, enabling high-resolution reconstructions without prohibitive memory costs.

Vector–Matrix (VM) Decomposition

Each tensor field in TensoRF—whether the geometry tensor $\mathscr{T}_\sigma$ or the appearance tensor $\mathscr{T}_c$—is not stored as a dense 4D grid. Instead, it is approximated using a sum of R low-rank **vector–matrix (VM)** components. For any continuous 3D query point $\mathbf{x} = (x,y,z) \in [0,1]^3$, each rank-$r$ component evaluates as:

$$\hat{A}_r(\mathbf{x}) = v_r^{(x)}(x)\cdot M_r^{(y,z)}(y,z) + v_r^{(y)}(y)\cdot M_r^{(x,z)}(x,z) + v_r^{(z)}(z)\cdot M_r^{(x,y)}(x,y),$$

where:

- $v_r^{(i)}(\cdot) \in \mathbb{R}^{N_i}$ is a learnable 1D vector defined along axis $i \in \{x,y,z\}$, evaluated via **linear interpolation**.
- $M_r^{(j,k)}(\cdot,\cdot) \in \mathbb{R}^{N_j\times N_k}$ is a learnable 2D matrix over the orthogonal plane (j,k), evaluated via **bilinear interpolation**.

Each term behaves like a 3D slab: a vector modulates variation along one axis while the matrix textures the perpendicular plane. This makes VM components far more expressive than CP decomposition's fully separable outer products, enabling detailed structures such as diagonal surfaces or 2D textures with fewer components.

Interpolation: From Discrete Grids to Continuous Coordinates

TensoRF learns vector and matrix values at discrete grid locations (e.g., $N_x = 128$ entries along the x-axis), but rendering requires evaluating them at continuous 3D coordinates. This is achieved by differentiable interpolation:

1. Normalization. All 3D sample points are first mapped from world coordinates into the normalized unit cube $[0,1]^3$ that encloses the scene. If a ray exits this cube, integration stops and no further queries are made.

2. Linear interpolation (1D vectors). For a coordinate $x \in [0,1]$ and vector $v_r^{(x)} \in \mathbb{R}^{N_x}$, we:

$$u = x \cdot (N_x - 1), \quad i = \lfloor u \rfloor, \quad \alpha = u - i,$$

$$v_r^{(x)}(x) = (1-\alpha) \cdot v_r^{(x)}[i] + \alpha \cdot v_r^{(x)}[i+1].$$

This blends the two neighboring entries based on the fractional offset α. If x aligns with a grid cell center (e.g., $\alpha = 0$), it degenerates to a direct lookup.

3. Bilinear interpolation (2D matrices). For a matrix $M_r^{(y,z)} \in \mathbb{R}^{N_y \times N_z}$ and normalized coordinates $(y,z) \in [0,1]^2$:

$$u = y \cdot (N_y - 1), \quad v = z \cdot (N_z - 1),$$

$$i = \lfloor u \rfloor, \quad j = \lfloor v \rfloor, \quad \alpha = u - i, \quad \beta = v - j,$$

$$\begin{aligned} M_r^{(y,z)}(y,z) = {} & (1-\alpha)(1-\beta) \cdot M[i,j] + \alpha(1-\beta) \cdot M[i+1,j] \\ & + (1-\alpha)\beta \cdot M[i,j+1] + \alpha\beta \cdot M[i+1,j+1]. \end{aligned}$$

Example. Suppose $x = 0.5$, and $N_x = 128$. Then $u = 63.5$, so we interpolate between $v_r^{(x)}[63]$ and $v_r^{(x)}[64]$ with equal weights. If $y = 0.7$, $z = 0.2$, and $N_y = N_z = 128$, we blend the four matrix entries around cell $(89, 25)$ according to the local offsets α, β.

Differentiability and Training Efficiency

Since linear and bilinear interpolation are piecewise-linear functions of $\mathbf{x}$, gradients propagate through them during backpropagation. This enables end-to-end training of all vector and matrix values using volume rendering loss, just like weights in a neural network.

VM decomposition thus achieves a balance between expressiveness and efficiency. Each axis-aligned component requires only a small number of memory lookups (2 for vectors, 4 for matrices), and scales quadratically in spatial resolution rather than cubically like voxel grids. This makes TensoRF compact, fast, and differentiable, with no need for deep MLPs at inference time.

Geometry: View-Independent Density Estimation

To compute the scalar volume density at a query point $\mathbf{x} \in [0,1]^3$, TensoRF evaluates all geometry VM components and linearly combines them using learned scalar weights $w_r^{(\sigma)}$. This sum is then passed through a shifted `Softplus` activation:

$$\sigma(\mathbf{x}) = \log\left(1 + \exp\left(\sum_{r=1}^{R_\sigma} w_r^{(\sigma)} \cdot \hat{A}_{\sigma,r}(\mathbf{x}) + \beta\right)\right),$$

where $\beta \in \mathbb{R}$ is a learned bias.

This *decoder-free* formulation directly outputs a non-negative scalar density without using a neural network. The `Softplus` function, defined as

$$\texttt{Softplus}(z) = \log(1 + \exp(z)),$$

smoothly approximates the ReLU function and ensures that the predicted density is always positive. The shifted variant $\texttt{Softplus}(z+\beta)$ improves training stability and expressiveness.

Appearance: View-Dependent Color Prediction

To model view-dependent color, TensoRF uses a separate set of VM components. Each component $r \in \{1, \ldots, R_c\}$ contributes a 3D appearance feature vector at point $\mathbf{x}$, constructed by concatenating the outputs from its three axis–plane interactions:

$$\mathbf{f}_c^{(r)}(\mathbf{x}) = \left[v_r^{(x)}(x) M_r^{(y,z)}(y,z), \quad v_r^{(y)}(y) M_r^{(x,z)}(x,z), \quad v_r^{(z)}(z) M_r^{(x,y)}(x,y)\right].$$

The full appearance descriptor is then computed by summing over all such components:

$$\mathbf{f}_c(\mathbf{x}) = \sum_{r=1}^{R_c} \mathbf{f}_c^{(r)}(\mathbf{x}) \in \mathbb{R}^{C_c}.$$

This feature vector is projected using a learned matrix $B \in \mathbb{R}^{P \times C_c}$, where P is the number of latent appearance channels used by the color decoder. The projected feature is combined with a frequency-encoded view direction $\mathbf{s}(\mathbf{d})$, and passed to a lightweight decoder S:

$$\mathbf{c}(\mathbf{x}, \mathbf{d}) = S\left(B \cdot \mathbf{f}_c(\mathbf{x}),\, \mathbf{s}(\mathbf{d})\right).$$

The decoder S is typically a two-layer MLP or a small set of spherical harmonic (SH) basis functions. This architecture enables efficient modeling of view-dependent lighting and appearance while maintaining fast inference.

Comparison to CP Decomposition

TensoRF also explores a CP (CANDECOMP/PARAFAC) decomposition of the form:

$$\mathscr{T}(x,y,z) = \sum_{r=1}^{R} v_r^{(x)}(x) \cdot v_r^{(y)}(y) \cdot v_r^{(z)}(z),$$

where each rank-r term is the outer product of three 1D vectors defined along the spatial axes. This formulation is highly compact, requiring only $\mathscr{O}(NR)$ memory for resolution N, but suffers from a strong separability constraint: each component captures only rank-1 correlations across

the three dimensions. As a result, it lacks the capacity to model complex structures such as depth discontinuities, slanted edges, or fine textures, unless the rank R is increased substantially.

In contrast, the vector–matrix (VM) decomposition adopted in TensoRF breaks this constraint by coupling two spatial axes per term. Each component $\hat{A}_r(\mathbf{x})$ includes bilinear interaction over a 2D matrix (e.g., y-z) modulated by variation along the third axis (e.g., x). This allows a single VM component to encode high-frequency planar details or axis-aligned surface patterns that would require many CP terms to approximate.

Mathematically, the VM decomposition relaxes the strict separability constraint of CP by modeling 2D spatial interactions explicitly through matrix components. This increases the expressive power of each rank-r term while preserving a tractable memory footprint of $\mathcal{O}(N^2R)$, significantly more scalable than dense voxel grids yet more flexible than rank-1 CP.

Empirically, this design enables TensoRF-VM to achieve superior tradeoffs between accuracy, efficiency, and compactness. The model converges rapidly—typically within a few to tens of minutes—while attaining higher PSNR than both CP-based variants and dense-grid baselines. Furthermore, its compact factorized representation yields scene models as small as 30–75MB that match or exceed the visual fidelity of MLP-based NeRFs, with real-time rendering performance and substantially reduced parameter count.

Summary

TensoRF's VM decomposition reframes 3D scene representation as a problem in efficient multilinear algebra. It enables fast, continuous queries, low memory usage, and real-time rendering without relying on deep MLPs. The combination of geometry and appearance factorization into interpretable, axis-aligned vector–matrix components provides both practical acceleration and theoretical insight into compact neural field design.

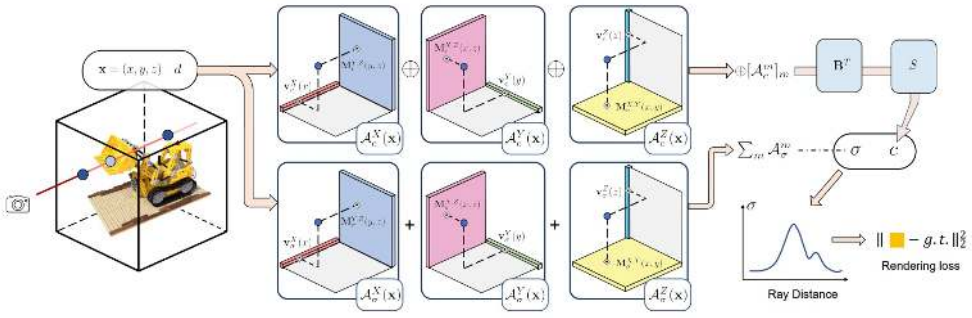

Figure 23.54: TensoRF VM architecture [80]. Each 3D point $\mathbf{x}$ is reconstructed from axis-aligned vector–matrix components. Density is predicted additively; color is produced from appearance features and view direction using a shallow decoder.

Quantitative Comparison

TensoRF achieves excellent reconstruction quality while offering faster training and reduced memory. The following table compares TensoRF against major baselines on standard NeRF benchmarks, including Synthetic-NeRF, NSVF, and Tanks & Temples:

Table 23.8: Quantitative results from [80]. TensoRF (VM-192) achieves strong PSNR and SSIM with orders-of-magnitude faster training and smaller model size than most voxel-based methods.

Method	Time	Size (MB)	Synthetic-NeRF		NSVF		Tanks & Temples	
			PSNR↑	SSIM↑	PSNR↑	SSIM↑	PSNR↑	SSIM↑
NeRF [429]	35h	5.0	31.01	0.947	30.81	0.952	25.78	0.864
NSVF [370]	>48h	-	31.75	0.953	35.18	0.979	28.48	0.901
Plenoxels [160]	11.4m	778.1	31.71	0.958	-	-	27.43	0.906
DVGO [591]	15.0m	612.1	31.95	0.957	35.08	0.975	28.41	0.911
TensoRF (VM-192)	**17.4m**	**71.8**	**33.14**	**0.963**	**36.52**	**0.982**	**28.56**	**0.920**

Qualitative Results

As shown in the below figure, TensoRF produces sharp, photorealistic reconstructions with accurate geometry and appearance. Notably, it recovers fine details such as the floor and shadows in synthetic scenes more faithfully than NeRF or Plenoxels, and exhibits fewer aliasing artifacts.

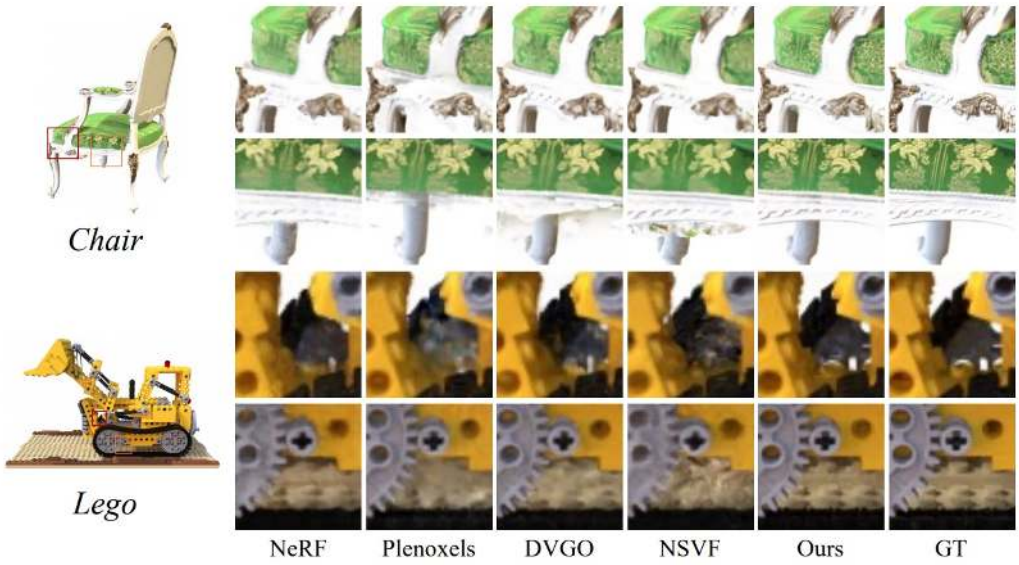

Figure 23.55: Qualitative results from [80]. TensoRF (VM-192) recovers finer geometric and appearance details compared to NeRF [429], Plenoxels [160], DVGO [591], and NSVF [370].

Key insight: TensoRF shows that tensor decomposition offers a memory-efficient and accurate alternative to MLP-heavy or voxel-based radiance field models. By factorizing spatial variation into 1D and 2D components, it achieves state-of-the-art results with significantly reduced overhead.

Enrichment 23.10.6: Mip-NeRF: Anti-Aliased Radiance Fields

Motivation: scale ambiguity and aliasing

In standard NeRF [429], each pixel is modeled as a single, infinitesimally thin ray, even though in reality a pixel sees a finite footprint in the scene. This footprint corresponds to a cone-shaped region

of space whose size grows with depth. When training with mixed-scale imagery (both close-up and distant views), NeRF's point-sampled positional encoding ignores the footprint size entirely, forcing the network to reconcile incompatible signals.

Without scale awareness, two characteristic artifacts appear:

- **Aliasing in distant views:** A faraway pixel's footprint may intersect fine geometry that is smaller than the pixel can resolve. Sampling only at its center captures spurious high-frequency detail, producing jagged edges or temporal shimmer.
- **Over-smoothing in close-up views:** To remain consistent with coarse, distant observations, the model suppresses fine detail in close-ups, leading to blurriness and loss of texture.

While supersampling (casting multiple rays per pixel) can reduce both problems by averaging over the footprint, it does not guarantee perfect removal of aliasing and is prohibitively expensive — each extra ray multiplies the number of MLP evaluations.

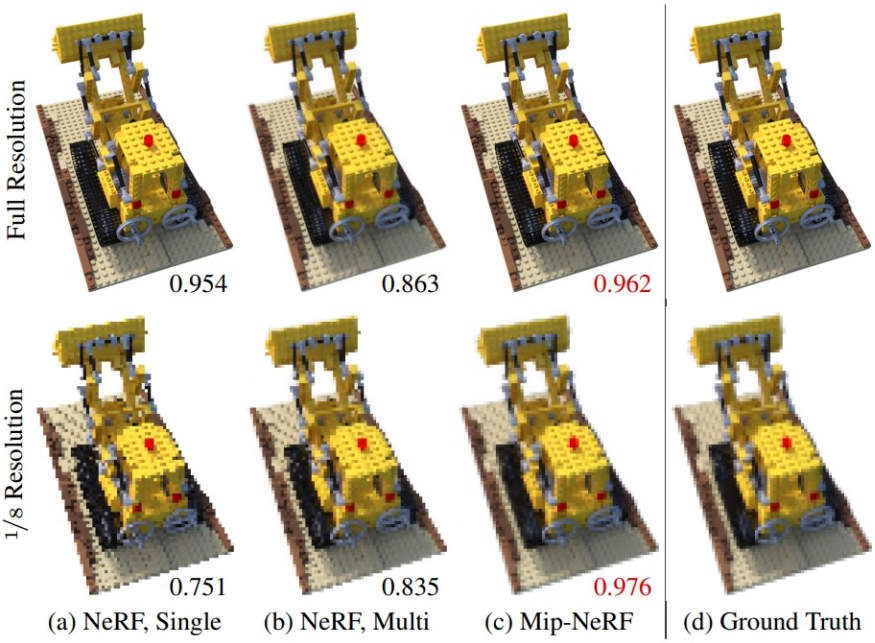

Figure 23.56: Aliasing in NeRF [30]. (a) NeRF trained on high-res images suffers aliasing at lower resolutions or when zooming. (b) Multi-scale training with NeRF only partially fixes this. (c) Mip-NeRF yields less aliasing in its renderings across all scales. (d) Ground truth.

From pixels to cones

In a real pinhole camera, a pixel does not capture light from a single infinitesimal ray, but from a continuous bundle of rays passing through its finite footprint on the image plane. These rays form a cone whose apex is at the camera center and whose axis points through the pixel center. The further we travel along this cone into the scene, the larger its cross-section becomes — so the same pixel may correspond to a tiny region on a nearby surface but a much larger region on a distant one. To model a pixel's contribution faithfully, we therefore need to account for how both the *position* and the *spatial extent* of the region it covers change with depth, setting the stage for a depth-wise decomposition of the cone.

Why cones are divided into frustums

In volumetric rendering, the color of a pixel is obtained by integrating scene density and radiance along the corresponding camera ray. For a cone-shaped pixel footprint, doing this integration over the *entire* cone in one step is both impractical and physically inaccurate:

- **Depth variation:** The scene's density and emitted color change continuously with depth.
- **Occlusion:** Objects at different distances can block each other, so visibility changes along the viewing direction.
- **Light transport:** The transmittance — the fraction of light that reaches the camera — must be updated incrementally as we progress through space.

If we treated the entire cone as a single unit, these effects would be averaged together indiscriminately, erasing important depth-dependent structure.

The remedy is to discretize the cone into a sequence of depth intervals

$$[t_0, t_1],\ [t_1, t_2],\ \ldots,$$

each forming a *frustum* — the portion of the cone between two depth planes. This is conceptually similar to NeRF's point sampling along a ray, but instead of single points, each sample now represents a finite 3D region with a nonzero cross-section. By working with frustums, we can:

- Associate each segment with its own spatial footprint size, enabling scale-aware encoding.
- Capture how density, color, and visibility change between consecutive depth ranges.
- Incrementally update transmittance and accumulate contributions in a physically consistent manner.

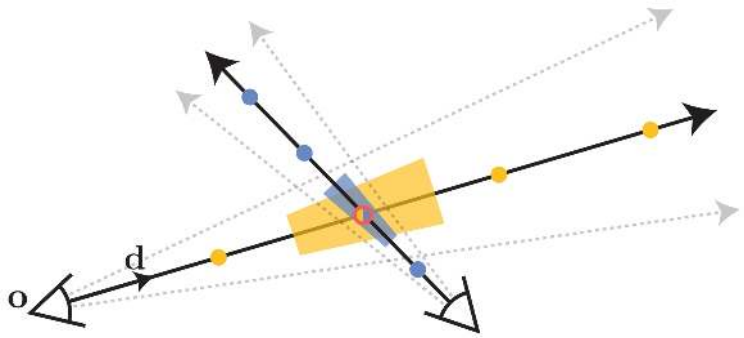

Figure 23.57: Volume coverage ambiguity [30]. NeRF samples points along rays (dots), which can alias across resolutions. Mip-NeRF casts cones and integrates over the entire volume seen by a pixel (trapezoids), resolving ambiguity and encoding scale.

From frustums to a pixel's color

Once the cone is split into frustums, the rendering process accumulates their contributions to produce the final pixel value. For the k-th frustum, the network predicts a *mean density* σ_k and a *mean color* $\mathbf{c}_k$ that represent the frustum's aggregated appearance. These are then combined using the standard volume rendering equation:

$$C_{\text{pixel}} = \sum_{k=1}^{N} T_k \, \alpha_k \, \mathbf{c}_k,$$

where:

- $\alpha_k = 1 - \exp(-\sigma_k \Delta t_k)$ is the frustum's opacity given its depth thickness Δt_k,
- $T_k = \prod_{j=1}^{k-1}(1 - \alpha_j)$ is the transmittance — the fraction of light that reaches frustum k without being blocked by earlier segments.

This discrete summation mirrors NeRF's point-based accumulation but replaces points with scale-aware volumetric regions.

Crucially, unlike the original NeRF [429], which applies positional encoding to a single 3D point along each ray sample, Mip-NeRF instead asks:

> *What is the **average** positional encoding of all points within this frustum?*

Here, "positional encoding" refers to the same Fourier feature mapping used in NeRF to represent high-frequency variation in color and density. Averaging these features over the frustum volume acts as a principled low-pass filter: sub-frustum spatial variation is integrated out, while coarser structure is preserved. This transforms each sample into a scale-aware volumetric descriptor rather than a potentially aliased point measurement.

From pixels to cones

In the pinhole camera model, a pixel corresponds not to a single infinitesimal ray, but to the set of rays passing through its finite footprint on the image plane. These rays form a *cone* with apex at the camera center $\mathbf{o} \in \mathbb{R}^3$ and central axis along the unit ray direction $\mathbf{d} \in \mathbb{R}^3$ through the pixel center.

At a depth t along $\mathbf{d}$, the cone's cross-section is the back-projection of the pixel's footprint into 3D space. If the pixel is square with width w (in world-space units at the image plane) and the camera has focal length f (same units), similar triangles show that this cross-section is a square whose *side length*—the physical distance between two opposite edges—is:

$$S(t) = \frac{w}{f} t.$$

At unit depth ($t = 1$), this reduces to $S = \frac{w}{f}$, the side length of the footprint in world units when projected to 1 meter from the camera.

Approximating the footprint as a disk

To simplify later analytic derivations, Mip-NeRF replaces the square cross-section at each depth with a rotationally symmetric disk of radius $r(t)$, producing a right circular cone. If we simply took $r(t) = S(t)/2$ so the disk matched the square's width, the two shapes would differ in their *second moments* (spatial variances), meaning they would have different frequency responses and thus different effective blur sizes.

To ensure the disk has the same spatial spread as the square, Mip-NeRF uses *variance matching*. For a shape centered at the origin, the marginal variance along one axis is:

$$\mathrm{Var}_{\mathrm{square}} = \frac{S^2}{12}, \qquad \mathrm{Var}_{\mathrm{disk}} = \frac{R^2}{4},$$

where S is the square's side length and R is the disk's radius. Equating these variances:

$$\frac{S^2}{12} = \frac{R^2}{4} \quad \Rightarrow \quad R = \frac{S}{\sqrt{3}}.$$

Thus the matched disk radius at depth t is:

$$r(t) = \frac{S(t)}{\sqrt{3}} = \frac{w}{f\sqrt{3}}\,t,$$

so the radius grows linearly with depth with slope

$$\dot{r} = \frac{w}{f\sqrt{3}},$$

representing the disk radius per unit depth.

Why variance matching? Variance measures the average squared distance of footprint points from its center, directly controlling the degree of spatial smoothing. Matching variances ensures that the simplified disk and the true square blur high-frequency detail in the same way, while the disk's rotational symmetry allows later analytic treatment of frustums. This makes it possible for Mip-NeRF to replace costly Monte Carlo integration with closed-form Gaussian-based anti-aliasing in subsequent steps.

Frustum geometry and indicator function

To formalize this region of space, Mip-NeRF defines an indicator function

$$\mathrm{F}(\mathbf{x}, \mathbf{o}, \mathbf{d}, \dot{r}, t_0, t_1),$$

which returns 1 if a 3D point $\mathbf{x} \in \mathbb{R}^3$ lies inside the conical frustum defined by origin $\mathbf{o}$, axis $\mathbf{d}$, slope $\dot{r}$, and depth bounds t_0, t_1, and 0 otherwise:

$$\mathrm{F}(\mathbf{x}, \mathbf{o}, \mathbf{d}, \dot{r}, t_0, t_1) = \mathbb{1}\left\{ \left(t_0 < \frac{\mathbf{d}^\top(\mathbf{x}-\mathbf{o})}{\|\mathbf{d}\|_2^2} < t_1 \right) \wedge \left(\frac{\mathbf{d}^\top(\mathbf{x}-\mathbf{o})}{\|\mathbf{d}\|_2 \, \|\mathbf{x}-\mathbf{o}\|_2} > \frac{1}{\sqrt{1+(\dot{r}/\|\mathbf{d}\|_2)^2}} \right) \right\}. \quad (23.1)$$

This condition performs two geometric checks:

- **Depth check:** The term

$$\frac{\mathbf{d}^\top(\mathbf{x}-\mathbf{o})}{\|\mathbf{d}\|^2} \in (t_0, t_1)$$

measures how far along the ray axis the projection of $\mathbf{x}$ lies. Here:
  - $\mathbf{x}-\mathbf{o}$ is the displacement from the ray origin.
  - The dot product $\mathbf{d}^\top(\mathbf{x}-\mathbf{o})$ gives the scalar projection of this displacement onto $\mathbf{d}$.
  - Division by $\|\mathbf{d}\|^2$ converts this projection into a true depth value even if $\mathbf{d}$ is not unit length.

The inequality enforces that the point lies between the near and far depth planes of the frustum.

- **Angular check:** This condition tests whether the point $\mathbf{x}$ lies inside the angular aperture of the cone defined by the pixel footprint.
  First, recall that the vector $\mathbf{d}$ is the central ray direction of the cone, and $\mathbf{x}-\mathbf{o}$ is the vector from the camera origin to the point $\mathbf{x}$. The angle between these two vectors is:

  $$\theta = \angle(\mathbf{d}, \mathbf{x}-\mathbf{o}),$$

  whose cosine can be computed via the dot product:

  $$\cos(\theta) = \frac{\mathbf{d}^\top(\mathbf{x}-\mathbf{o})}{\|\mathbf{d}\|\,\|\mathbf{x}-\mathbf{o}\|}.$$

  The cone's *half-angle* α is the angular radius of its cross-section as seen from the apex. From the slope definition $\dot{r}$ (radius per unit depth), we have:

  $$\tan(\alpha) = \frac{\dot{r}}{\|\mathbf{d}\|},$$

  and therefore:

  $$\cos(\alpha) = \frac{1}{\sqrt{1+(\dot{r}/\|\mathbf{d}\|)^2}}.$$

  The check:

  $$\frac{\mathbf{d}^\top(\mathbf{x}-\mathbf{o})}{\|\mathbf{d}\|\,\|\mathbf{x}-\mathbf{o}\|} > \frac{1}{\sqrt{1+(\dot{r}/\|\mathbf{d}\|)^2}}$$

  is equivalent to testing:

  $$\cos(\theta) > \cos(\alpha).$$

  Since $\cos(\theta)$ decreases monotonically with θ over the range $[0,\pi]$, the inequality $\cos(\theta) > \cos(\alpha)$ means:

  $$\theta < \alpha.$$

  In words: the angular deviation of $\mathbf{x}$ from the cone axis is smaller than the cone's half-angle, so $\mathbf{x}$ lies *within* the cone's aperture rather than outside it.
  Why this matters: The frustum is defined not only by near and far depth limits along the axis, but also by the cone's angular extent. Even if a point lies between t_0 and t_1 in depth, it must also pass this angular check to ensure it projects back to the same pixel footprint on the image plane. Without this test, the frustum definition would include points that are too far off-axis to be observed through the pixel.

Together, these checks precisely describe the 3D frustum volume subtended by a pixel over a given depth range. With this exact region defined, Mip-NeRF can next express the *expected positional encoding* over the frustum as a normalized volume integral—providing the starting point for the derivation that follows.

Expected positional encoding over a frustum

Given the frustum region described by the indicator function F from (23.1), Mip-NeRF defines the *expected positional encoding* as the mean of the NeRF positional encoding $\gamma(\mathbf{x})$ over all 3D points $\mathbf{x}$ lying within the frustum.

Formally, let $\mathbf{X}$ be a random point drawn *uniformly* from the frustum volume

$$R = \{\mathbf{x} \in \mathbb{R}^3 \mid \mathrm{F}(\mathbf{x}, \mathbf{o}, \mathbf{d}, \dot{r}, t_0, t_1) = 1\}.$$

The uniform density on R is

$$p(\mathbf{x}) \;=\; \frac{1}{\mathrm{Vol}(R)} \mathbb{1}_R(\mathbf{x}), \quad \mathrm{Vol}(R) = \int_{\mathbb{R}^3} \mathbb{1}_R(\mathbf{x})\, d\mathbf{x}.$$

The expectation of $\gamma(\mathbf{X})$ under p is therefore

$$\mathbb{E}[\gamma(\mathbf{X})] = \int_{\mathbb{R}^3} \gamma(\mathbf{x})\, p(\mathbf{x})\, d\mathbf{x} = \frac{1}{\mathrm{Vol}(R)} \int_R \gamma(\mathbf{x})\, d\mathbf{x}.$$

Substituting the frustum indicator F for $\mathbb{1}_R$ gives

$$\gamma^*(\mathbf{o}, \mathbf{d}, \dot{r}, t_0, t_1) = \frac{\int_{\mathbb{R}^3} \gamma(\mathbf{x})\, \mathrm{F}(\mathbf{x}, \mathbf{o}, \mathbf{d}, \dot{r}, t_0, t_1)\, d\mathbf{x}}{\int_{\mathbb{R}^3} \mathrm{F}(\mathbf{x}, \mathbf{o}, \mathbf{d}, \dot{r}, t_0, t_1)\, d\mathbf{x}}. \tag{23.2}$$

Here:

- The **denominator** is the frustum's volume — the total measure of all 3D points that project to the given pixel between depths t_0 and t_1.
- The **numerator** integrates the encoded feature vector $\gamma(\mathbf{x})$ over exactly the same set of points.

Their ratio is thus the *uniform average* of $\gamma(\mathbf{x})$ over the frustum.

Intuition

The expected positional encoding in (23.2) is the *uniform average* of $\gamma(\mathbf{x})$ over the frustum R. Formally, if $\mathbf{x} \sim \mathrm{Uniform}(R)$, then

$$\mathbb{E}[\gamma(\mathbf{x})] = \frac{1}{\mathrm{Vol}(R)} \int_R \gamma(\mathbf{x})\, d\mathbf{x}.$$

In the discrete case, this would be approximated as

$$\frac{1}{N} \sum_{i=1}^{N} \gamma(\mathbf{x}_i), \quad \mathbf{x}_i \overset{\text{i.i.d.}}{\sim} \mathrm{Uniform}(R),$$

and taking $N \to \infty$ recovers the continuous form above. The denominator in (23.2) normalizes the numerator, converting it from a *total sum over space* into a *mean per unit volume*.

In the original NeRF formulation, each pixel is represented by a single infinitesimally narrow ray, so $\gamma(\mathbf{x})$ is evaluated only along that 1D path. This ignores the fact that a real pixel integrates light over a finite footprint on the image plane, corresponding to a continuum of rays forming a conical frustum in 3D space. Mip-NeRF instead averages $\gamma(\mathbf{x})$ over this entire frustum, embedding the pixel's *full visual support* directly into its feature vector.

This volumetric averaging acts as a built-in *low-pass filter*. If the wavelength of a sinusoidal component in $\gamma(\mathbf{x})$ is smaller than the frustum's cross-section, its oscillations average out, attenuating high-frequency terms that would otherwise cause aliasing when rendering at resolutions or viewing distances different from training. Frequencies with wavelengths larger than the frustum remain unaffected, preserving resolvable detail. The result is *scale consistency*: textures that are smooth at a distance will not develop spurious high-frequency artifacts up close, and fine details will naturally fade with distance rather than alias into incorrect patterns.

A straightforward way to compute the average in (23.2) is to approximate it via Monte Carlo sampling: draw points uniformly inside the frustum and average their encodings. While conceptually simple, this approach is inefficient in practice:

- **High variance:** Monte Carlo estimates fluctuate due to sampling noise, especially for the high-frequency sinusoidal terms in $\gamma(\mathbf{x})$.
- **Computational cost:** Achieving stable, low-variance estimates requires many samples per pixel, inflating training and rendering time.
- **Missed structure:** The positional encoding $\gamma(\mathbf{x})$ is composed of sinusoidal basis functions, whose integrals over certain geometric shapes can be computed exactly.

To avoid stochastic approximation entirely, Mip-NeRF replaces each frustum segment with a *moment-matched Gaussian* distribution $\mathcal{N}(\mu,\Sigma)$ that has the same first and second moments as the true frustum. This substitution retains the key spatial statistics while making the expected positional encoding $\mathbb{E}[\gamma(\mathbf{X})]$ analytically tractable. With this Gaussian model in place, the integral in (23.2) reduces to closed-form expressions for the mean and covariance of $\mathbf{X}$.

Moment-matched Gaussian approximation

To enable closed-form evaluation of (23.2), Mip-NeRF replaces the uniform distribution over a frustum segment with a *Gaussian* $\mathcal{N}(\mu,\Sigma)$ having the same first and second moments. The idea is that the frustum is a truncated cone whose geometry is simple enough that we can compute these moments analytically, and then replace the frustum with a Gaussian of matching mean and covariance.

Frustum-centric coordinates We first align our coordinate system so that the ray direction is the t-axis:

$$\hat{\mathbf{d}} = \frac{\mathbf{d}}{\|\mathbf{d}\|}, \qquad \mathbf{x}(t,\mathbf{u}) = \mathbf{o} + t\,\hat{\mathbf{d}} + \mathbf{u},$$

where:

- $t \in [t_0, t_1]$ is the depth along the ray,
- $\mathbf{o} \in \mathbb{R}^3$ is the ray origin,
- $\mathbf{u} \in \mathbb{R}^3$ is a vector perpendicular to $\hat{\mathbf{d}}$.

The frustum's circular cross-section at depth t has radius

$$r(t) = \dot{r}\,t,$$

where $\dot{r}$ is the cone's angular radius in world units (essentially the pixel footprint's half-width projected into 3D space).

Marginal depth distribution $p(t)$

A key step in Mip-NeRF's Gaussian frustum approximation is to characterize the *depth distribution* of points within a pixel's 3D footprint. For a given pixel, this footprint is modeled as a right circular cone originating at the camera center $\mathbf{o}$ and extending along the viewing ray. The cone has slope $\dot{r}$ (radius per unit depth), chosen to match the pixel's footprint on the image plane.

At a distance t from $\mathbf{o}$ along the ray, the cone's cross–section is a disk of radius

$$r(t) = \dot{r}\,t,$$

and therefore exact area

$$A(t) = \pi\,[r(t)]^2 = \pi\,(\dot{r}\,t)^2.$$

A thin slab between depths t and $t + dt$ has volume element

$$dV(t) = A(t)\,dt = \pi\,(\dot{r})^2\,t^2\,dt.$$

The *uniform-in-volume* assumption means that the probability of sampling a point in a slab is proportional to its volume. Deeper slabs have larger cross–sections and therefore more 3D volume per unit depth. Taking the unnormalized marginal depth density to be the *actual* slice area gives

$$p_{\text{unnorm}}(t) = \pi\,(\dot{r})^2\,t^2, \qquad t \in [t_0, t_1],$$

where t_0 and t_1 are the near and far bounds of the frustum segment.

To convert $p_{\text{unnorm}}(t)$ into a probability density, we divide by its total mass over $[t_0, t_1]$:

$$p(t) = \frac{p_{\text{unnorm}}(t)}{\displaystyle\int_{t_0}^{t_1} p_{\text{unnorm}}(\tau)\,d\tau} = \frac{\pi(\dot{r})^2\,t^2}{\displaystyle\int_{t_0}^{t_1} \pi(\dot{r})^2\,\tau^2\,d\tau} = \frac{t^2}{\displaystyle\int_{t_0}^{t_1} \tau^2\,d\tau}.$$

The geometric constants π and $(\dot{r})^2$ cancel exactly, so no arbitrary constant C must be introduced.

Evaluating the remaining denominator:

$$\int_{t_0}^{t_1} \tau^2\,d\tau = \left[\frac{\tau^3}{3}\right]_{t_0}^{t_1} = \frac{t_1^3 - t_0^3}{3},$$

yields the closed form

$$p(t) = \frac{3t^2}{t_1^3 - t_0^3}, \qquad t \in [t_0, t_1].$$

This density is the correct marginal for uniform-in-volume sampling, and is later used to compute the *mean depth* μ_t and *depth variance* σ_t^2 of the Gaussian frustum. By contrast, weighting by $1/A(t)$ would correspond to sampling uniformly *along the axis*, giving each depth slice equal probability regardless of its volume—an assumption inconsistent with volumetric pixel modeling.

Mean depth μ_t

In probability theory, the mean (expected) value of a continuous random variable t with probability density function (PDF) $p(t)$ is

$$\mu_t \;=\; \mathbb{E}[t] \;=\; \int_{t_0}^{t_1} t\, p(t)\, dt. \tag{23.3}$$

In our frustum setting, the marginal depth density $p(t)$ is proportional to the cross-sectional area at depth t, which grows as t^2 for a cone. Normalizing over $[t_0, t_1]$ yields

$$p(t) = \frac{3t^2}{t_1^3 - t_0^3}, \qquad t \in [t_0, t_1].$$

Substituting into Eq. 23.3:

$$\mu_t = \frac{3}{t_1^3 - t_0^3} \int_{t_0}^{t_1} t^3\, dt = \frac{3}{t_1^3 - t_0^3} \left[\frac{t^4}{4}\right]_{t_0}^{t_1} \tag{23.4}$$

$$= \frac{3\,(t_1^4 - t_0^4)}{4\,(t_1^3 - t_0^3)}. \tag{23.5}$$

Why not the midpoint? If $p(t)$ were uniform, the mean would be $(t_0 + t_1)/2$. Here, $p(t) \propto t^2$ upweights deeper slices because they occupy more volume, shifting μ_t toward t_1.

Stable reparameterization of μ_t

When $t_1 \approx t_0$, Eq. 23.5 can suffer from catastrophic cancellation. To avoid this, define

$$t_\mu = \frac{t_0 + t_1}{2}, \qquad t_\delta = \frac{t_1 - t_0}{2},$$

so that $t_0 = t_\mu - t_\delta$ and $t_1 = t_\mu + t_\delta$. Using the binomial expansions

$$(t_\mu + t_\delta)^3 - (t_\mu - t_\delta)^3 = 6\, t_\mu^2\, t_\delta + 2 t_\delta^3,$$

$$(t_\mu + t_\delta)^4 - (t_\mu - t_\delta)^4 = 8\, t_\mu^3\, t_\delta + 8\, t_\mu\, t_\delta^3,$$

Eq. 23.5 simplifies to

$$\mu_t = t_\mu \;+\; \frac{2\, t_\mu\, t_\delta^2}{3 t_\mu^2 + t_\delta^2}, \tag{23.6}$$

which is exactly the mean formula in the Mip-NeRF paper.

Axial variance σ_t^2

The variance along the ray is

$$\sigma_t^2 \;=\; \mathbb{E}[t^2] - \mu_t^2, \tag{23.7}$$

where the second moment is

$$\mathbb{E}[t^2] = \frac{3}{t_1^3 - t_0^3} \int_{t_0}^{t_1} t^4\, dt = \frac{3}{t_1^3 - t_0^3} \left[\frac{t^5}{5}\right]_{t_0}^{t_1} \tag{23.8}$$

$$= \frac{3\,(t_1^5 - t_0^5)}{5\,(t_1^3 - t_0^3)}. \tag{23.9}$$

Stable reparameterization of σ_t^2
Substitute t_μ, t_δ and use

$$(t_\mu + t_\delta)^5 - (t_\mu - t_\delta)^5 = 10t_\mu^4 t_\delta + 20t_\mu^2 t_\delta^3 + 2t_\delta^5,$$

along with the cubic difference above, to obtain

$$\mathbb{E}[t^2] = \frac{3\,(t_\mu^4 + 2t_\mu^2 t_\delta^2 + \frac{1}{5}t_\delta^4)}{3t_\mu^2 + t_\delta^2}.$$

Similarly, squaring Eq. 23.6 gives

$$\mu_t^2 = \frac{(3t_\mu^3 + 3t_\mu t_\delta^2)^2}{(3t_\mu^2 + t_\delta^2)^2}.$$

Substituting into Eq. 23.7 yields the closed form

$$\sigma_t^2 = \frac{t_\delta^2}{3} - \frac{4t_\delta^4\left(12t_\mu^2 - t_\delta^2\right)}{15\left(3t_\mu^2 + t_\delta^2\right)^2}, \tag{23.10}$$

which matches the formulation in the Mip-NeRF paper and remains numerically stable for small t_δ.

Radial (perpendicular) variance σ_r^2
Alongside the axial statistics (μ_t, σ_t^2), the Gaussian frustum approximation also needs to capture the spread of points *perpendicular* to the ray axis. If the axial variance σ_t^2 describes how far points are distributed *along* the beam (depth uncertainty), then σ_r^2 quantifies how far they spread *sideways* at a given depth.
Flashlight analogy. Imagine shining a flashlight in a dark room. The light beam widens as it travels away from the source, creating a circular spot that grows with distance. The axial variance tells us how *long* the illuminated region is along the beam; the radial variance tells us how *wide* it is at each depth. Both are needed to fully describe the shape of the illuminated volume.
Role in completion. Together, σ_t^2 and σ_r^2 form the two orthogonal variance components of the frustum:

- σ_t^2: spread *parallel* to the ray — measures the frustum's *thickness* in depth.
- σ_r^2: spread *perpendicular* to the ray — measures the frustum's *width* in either orthogonal direction.

Combining them into a covariance matrix yields a full 3D Gaussian that moment-matches the frustum, enabling Integrated Positional Encoding to adjust high-frequency features according to both depth uncertainty and footprint size.

Step 1: Conditional second moment at fixed depth At a given depth t, the cross-section of the frustum is a disk of radius

$$R_t \;=\; r(t) \;=\; \dot{r}t,$$

where $\dot{r}$ is the cone slope (radius per unit depth). We want the *per-axis radial variance* at this depth — i.e., the variance of the x-coordinate (or y-coordinate) of points uniformly distributed inside this disk.

Why an area integral? The definition of the conditional second moment of the radial distance is:

$$\mathbb{E}[\rho^2 \mid t] \;=\; \frac{\displaystyle\int_{\text{disk}} \rho^2 \, dA}{\displaystyle\int_{\text{disk}} dA},$$

where:

- $\rho = \sqrt{x^2 + y^2}$ is the Euclidean distance from the axis in the perpendicular plane.
- dA is an infinitesimal area element.
- The denominator normalizes by the total cross-sectional area, ensuring the result is the *mean* of ρ^2 over the disk.

Switching to polar coordinates. In polar coordinates (ρ, θ), the area element is $dA = \rho \, d\rho \, d\theta$ and the disk is parameterized by:

$$0 \le \rho \le R_t, \qquad 0 \le \theta < 2\pi.$$

Substituting into the definition gives:

$$\mathbb{E}[\rho^2 \mid t] = \frac{\displaystyle\int_0^{2\pi}\int_0^{R_t} \rho^2 \cdot \rho \, d\rho \, d\theta}{\displaystyle\int_0^{2\pi}\int_0^{R_t} \rho \, d\rho \, d\theta} \qquad \text{(definition of mean over the disk)} \tag{23.11}$$

$$= \frac{\displaystyle\int_0^{2\pi}\int_0^{R_t} \rho^3 \, d\rho \, d\theta}{\pi R_t^2}. \tag{23.12}$$

Evaluating the integrals. The angular integration yields 2π, so:

$$\mathbb{E}[\rho^2 \mid t] = \frac{2\pi}{\pi R_t^2} \int_0^{R_t} \rho^3 \, d\rho = \frac{2}{R_t^2} \left[\frac{\rho^4}{4} \right]_0^{R_t} = \frac{R_t^2}{2}.$$

From radial to per-axis variance. Because the distribution is rotationally symmetric, the variance splits evenly between the x and y axes:

$$\mathbb{E}[x^2 \mid t] \;=\; \mathbb{E}[y^2 \mid t] \;=\; \frac{\mathbb{E}[\rho^2 \mid t]}{2} = \frac{R_t^2}{4}. \tag{23.13}$$

This per-axis quantity is what will later be averaged over t to obtain the unconditional radial variance σ_r^2.

Step 2: Averaging over depth The unconditional per-axis radial variance is the expectation of Eq. 23.13 over the marginal depth density $p(t)$ from the frustum geometry:

$$\sigma_r^2 = \mathbb{E}[x^2] = \int_{t_0}^{t_1} \frac{R_t^2}{4} \, p(t) \, dt \tag{23.14}$$

$$= \int_{t_0}^{t_1} \frac{\dot{r}^2 t^2}{4} \cdot \frac{3t^2}{t_1^3 - t_0^3} \, dt = \frac{3\dot{r}^2}{4\,(t_1^3 - t_0^3)} \int_{t_0}^{t_1} t^4 \, dt. \tag{23.15}$$

Evaluating the remaining polynomial integral:

$$\int_{t_0}^{t_1} t^4\,dt = \left[\frac{t^5}{5}\right]_{t_0}^{t_1} = \frac{t_1^5 - t_0^5}{5}.$$

Thus:

$$\sigma_r^2 = \dot{r}^2\,\frac{3\,(t_1^5 - t_0^5)}{20\,(t_1^3 - t_0^3)}, \qquad t \in [t_0, t_1]. \tag{23.16}$$

Numerical stability via midpoint–half-width parameterization. As in the axial variance case, direct evaluation of Eq. 23.16 can suffer from catastrophic cancellation when $t_1 \approx t_0$. To mitigate this, Mip-NeRF reparameterizes:

$$t_\mu = \frac{t_0 + t_1}{2}, \qquad t_\delta = \frac{t_1 - t_0}{2},$$

so that

$$t_0 = t_\mu - t_\delta, \qquad t_1 = t_\mu + t_\delta.$$

The difference-of-powers terms in Eq. 23.16 then become:

$$t_1^3 - t_0^3 = (t_\mu + t_\delta)^3 - (t_\mu - t_\delta)^3 = 6t_\mu^2 t_\delta + 2t_\delta^3 = 2t_\delta\left(3t_\mu^2 + t_\delta^2\right),$$

$$t_1^5 - t_0^5 = (t_\mu + t_\delta)^5 - (t_\mu - t_\delta)^5 = 10t_\mu^4 t_\delta + 20t_\mu^2 t_\delta^3 + 2t_\delta^5 = 2t_\delta\left(5t_\mu^4 + 10t_\mu^2 t_\delta^2 + t_\delta^4\right).$$

Substituting into Eq. 23.16 and simplifying yields:

$$\sigma_r^2 = \dot{r}^2\,\frac{3}{20}\cdot\frac{2t_\delta\left(5t_\mu^4 + 10t_\mu^2 t_\delta^2 + t_\delta^4\right)}{2t_\delta\left(3t_\mu^2 + t_\delta^2\right)} = \dot{r}^2\cdot\frac{5t_\mu^4 + 10t_\mu^2 t_\delta^2 + t_\delta^4}{10\left(3t_\mu^2 + t_\delta^2\right)}.$$

Finally, polynomial division gives the paper's stable form:

$$\sigma_r^2 = \dot{r}^2\left(\frac{t_\mu^2}{4} + \frac{5t_\delta^2}{12} - \frac{4t_\delta^4}{15\left(3t_\mu^2 + t_\delta^2\right)}\right). \tag{23.17}$$

Moment-Matched Gaussian in World Space

Given the frustum's axial statistics (μ_t, σ_t^2) and radial variance σ_r^2 from the previous derivation, we can represent its full 3D extent with a Gaussian whose mean and covariance match those of the true uniform distribution inside the frustum. The mean lies along the ray at depth μ_t, while the covariance separates into:

- an *axial* term $\sigma_t^2\,\mathbf{d}\mathbf{d}^\mathsf{T}$, encoding uncertainty along the ray direction $\mathbf{d}$;
- a *radial* term $\sigma_r^2\left(I - \frac{\mathbf{d}\mathbf{d}^\mathsf{T}}{\|\mathbf{d}\|_2^2}\right)$, encoding isotropic spread in the plane orthogonal to $\mathbf{d}$.

This moment-matched Gaussian,

$$\mathcal{N}\left(\mathbf{o} + \mu_t\mathbf{d},\ \sigma_t^2\,\mathbf{d}\mathbf{d}^\mathsf{T} + \sigma_r^2\left(I - \frac{\mathbf{d}\mathbf{d}^\mathsf{T}}{\|\mathbf{d}\|_2^2}\right)\right),$$

compactly captures both the location and shape of the frustum segment in world space. The next steps detail how this form arises from decomposing points into axial and radial components and applying the corresponding projection operators.

Step 1: Decomposition into Axial and Radial Components. Any 3D point $\mathbf{x}$ inside the conical frustum segment can be written as

$$\mathbf{x} \;=\; \mathbf{o} + t\,\mathbf{d} + \mathbf{u},$$

where:

- $\mathbf{o} \in \mathbb{R}^3$ is the ray origin.
- $\mathbf{d} \in \mathbb{R}^3$ is the (possibly unnormalized) ray direction.
- $t \in [t_0, t_1]$ is the *axial* depth coordinate along the ray, with mean $\mathbb{E}[t] = \mu_t$ and variance $\mathrm{Var}(t) = \sigma_t^2$.
- $\mathbf{u} \in \mathbb{R}^3$ is the *radial offset* from the central ray to the actual point, lying in the plane perpendicular to $\mathbf{d}$.

The vector $\mathbf{u}$ appears naturally because the frustum's cross-section at depth t is a filled circle rather than a single point. Sampling uniformly from the frustum means sampling both along the axis (via t) and within the in-plane disk (via $\mathbf{u}$). Rotational symmetry ensures that $\mathbf{u}$ is isotropic within the perpendicular plane and has no component along $\mathbf{d}$.

Step 2: Projectors onto Axial and Radial Subspaces. Any 3D vector can be decomposed into a component *parallel* to the ray direction $\mathbf{d}$ and a component *perpendicular* to it. The orthogonal projection matrix onto the ray direction is

$$P_{\parallel} = \frac{\mathbf{d}\,\mathbf{d}^{\top}}{\|\mathbf{d}\|_2^2},$$

which takes any vector $\mathbf{v}$ and returns its shadow along $\mathbf{d}$. The complementary projection matrix

$$P_{\perp} = I - P_{\parallel}$$

removes the axial component, leaving only the part lying in the plane orthogonal to $\mathbf{d}$. Because the frustum's cross-section is circular, radial offsets are:

$$\mathbb{E}[\mathbf{u}] = \mathbf{0}, \quad \mathrm{Cov}(\mathbf{u}) = \sigma_r^2 P_{\perp}, \quad \mathrm{Cov}(t, \mathbf{u}) = \mathbf{0},$$

meaning they have zero mean, are isotropic in the orthogonal plane, and are independent of depth.

Step 3: Mean in World Space. The expected position inside the frustum is obtained by averaging over t and $\mathbf{u}$. Since $\mathbf{u}$ has zero mean, only the axial displacement contributes:

$$\mu = \mathbb{E}[\mathbf{x}] = \mathbf{o} + \mathbb{E}[t]\,\mathbf{d} = \mathbf{o} + \mu_t\,\mathbf{d}.$$

This places the Gaussian's mean along the ray at depth μ_t.

Step 4: Covariance in World Space. The total covariance Σ comes from two independent sources of variation:

- *Axial variance* from the spread of t along the ray: $\mathrm{Cov}(t\,\mathbf{d}) = \sigma_t^2\,\mathbf{d}\,\mathbf{d}^{\top}$.
- *Radial variance* from the circular footprint: $\mathrm{Cov}(\mathbf{u}) = \sigma_r^2 P_{\perp}$.

Independence means their contributions simply add:

$$\Sigma = \sigma_t^2 (\mathbf{d}\,\mathbf{d}^\top) + \sigma_r^2 P_\perp.$$

Thus, we have isolated the uncertainty along the ray from the uncertainty in the orthogonal plane.

Step 5: Explicit World-Space Formula. Substituting the definition of $P_\perp$ into the covariance expression gives:

$$\boxed{\begin{aligned} &\mu = \mathbf{o} + \mu_t\,\mathbf{d}, \\ &\Sigma = \sigma_t^2 (\mathbf{d}\,\mathbf{d}^\top) + \sigma_r^2 \left(I - \frac{\mathbf{d}\,\mathbf{d}^\top}{\|\mathbf{d}\|_2^2} \right) \end{aligned}} \tag{23.18}$$

This formula is the direct result of Steps 3–4: the mean comes from the depth centroid, and the covariance comes from the sum of axial and radial contributions.

Rewriting positional encoding as Fourier features

Having expressed the frustum segment as a Gaussian $\mathcal{N}(\mu, \Sigma)$ in world coordinates, the next step is to evaluate the *expected positional encoding* of a random point $\mathbf{x}$ drawn from this Gaussian. Recall that in the original NeRF formulation [429], each 3D coordinate $\mathbf{x} \in \mathbb{R}^3$ is mapped to a high-dimensional feature vector via a sinusoidal encoding:

$$\gamma(\mathbf{x}) = \left[\, \sin(2^0 \pi x_1), \cos(2^0 \pi x_1), \ldots, \sin(2^{L-1} \pi x_3), \cos(2^{L-1} \pi x_3) \,\right]^\top,$$

where L denotes the number of frequency bands.

Motivation for the rewrite. Directly taking the expectation $\mathbb{E}_{\mathbf{x}\sim\mathcal{N}(\mu,\Sigma)}[\gamma(\mathbf{x})]$ is cumbersome if we treat each sin and cos term independently. However, note that each channel of $\gamma(\mathbf{x})$ is a sine or cosine of a *linear form* in $\mathbf{x}$, i.e. $\sin(\mathbf{p}^\top \mathbf{x})$ or $\cos(\mathbf{p}^\top \mathbf{x})$ for some frequency vector $\mathbf{p} \in \mathbb{R}^3$. This suggests a more compact *matrix Fourier form* in which all frequencies are collected into a single matrix.

Fourier matrix formulation

We collect all per-axis frequency scales into a single *frequency matrix* $\mathbf{P} \in \mathbb{R}^{3\times 3L}$ whose columns come in triples (for x, y, z) at each band 2^k:

$$\mathbf{P} \;=\; \begin{bmatrix} 2^0 I_3 & 2^1 I_3 & \cdots & 2^{L-1} I_3 \end{bmatrix} \;=\; \begin{bmatrix} 2^0 & 0 & 0 & 2^1 & 0 & 0 & \ldots & 2^{L-1} & 0 & 0 \\ 0 & 2^0 & 0 & 0 & 2^1 & 0 & \ldots & 0 & 2^{L-1} & 0 \\ 0 & 0 & 2^0 & 0 & 0 & 2^1 & \ldots & 0 & 0 & 2^{L-1} \end{bmatrix}.$$

Each block $2^k I_3$ provides the scale 2^k applied independently to x, y, z (no cross-axis mixing). With this notation, NeRF's positional encoding can be written compactly as

$$\gamma(\mathbf{x}) \;=\; \begin{bmatrix} \sin\!\left(\mathbf{P}^\top \mathbf{x}\right) \\ \cos\!\left(\mathbf{P}^\top \mathbf{x}\right) \end{bmatrix},$$

where sin and cos act elementwise on the $3L$-vector $\mathbf{P}^\top \mathbf{x}$.

Why this helps. With the frustum segment modeled as

$$\mathbf{x} \sim \mathcal{N}(\mu, \Sigma),$$

the Fourier form of $\gamma(\mathbf{x})$ applies only a linear projection $\mathbf{P}^\top$ before evaluating sines and cosines. By the affine transformation property of Gaussian random vectors,

$$\mathbf{y} = \mathbf{A}\mathbf{x} + \mathbf{b} \quad \Rightarrow \quad \mathbf{y} \sim \mathcal{N}(\mathbf{A}\mu + \mathbf{b},\, \mathbf{A}\Sigma\mathbf{A}^\top),$$

setting $\mathbf{A} = \mathbf{P}^\top$ and $\mathbf{b} = \mathbf{0}$ yields

$$\mu_\gamma = \mathbf{P}^\top \mu, \qquad \Sigma_\gamma = \mathbf{P}^\top \Sigma \mathbf{P}.$$

Each row $\mathbf{p}^\top$ of $\mathbf{P}^\top$ corresponds to a specific frequency probe; its associated variance in Σ_γ directly measures how much that frequency varies across the frustum.

Closed-form expectations. For one frequency probe $\mathbf{p}^\top$, the encoding channel is $\sin(\mathbf{p}^\top \mathbf{x})$ or $\cos(\mathbf{p}^\top \mathbf{x})$ with

$$z = \mathbf{p}^\top \mathbf{x} \sim \mathcal{N}(\mu_z, \sigma_z^2), \quad \mu_z = \mathbf{p}^\top \mu, \quad \sigma_z^2 = \mathbf{p}^\top \Sigma \mathbf{p}.$$

Here, μ_z is the projected mean of the frustum, and σ_z^2 its variance along $\mathbf{p}$—small values indicate a stable frequency, large values signal rapid oscillations and potential aliasing.

Using the complex exponential trick. The expectations $\mathbb{E}[\sin(z)]$ and $\mathbb{E}[\cos(z)]$ can be computed in closed form using the identity

$$\sin(z) = \Im(e^{iz}), \quad \cos(z) = \Re(e^{iz}),$$

and the known result for the characteristic function of a Gaussian:

$$\mathbb{E}[e^{iz}] = e^{i\mu_z} e^{-\frac{1}{2}\sigma_z^2}.$$

This follows from the moment-generating function of a normal variable, where the factor $e^{-\frac{1}{2}\sigma_z^2}$ comes from integrating the quadratic term in the exponent.

Taking real and imaginary parts yields:

$$\mathbb{E}[\sin(z)] = \sin(\mu_z)\, e^{-\frac{1}{2}\sigma_z^2}, \qquad \mathbb{E}[\cos(z)] = \cos(\mu_z)\, e^{-\frac{1}{2}\sigma_z^2}.$$

Interpretation and anti-aliasing effect. The factor $e^{-\frac{1}{2}\sigma_z^2}$ attenuates each frequency according to its variance over the frustum:

- *High variance:* $\sigma_z^2 \gg 0 \Rightarrow$ strong attenuation of high-frequency oscillations that cannot be reliably represented at the frustum's scale.
- *Low variance:* $\sigma_z^2 \approx 0 \Rightarrow$ little to no attenuation for low-frequency components.

This provides a principled, scale-aware low-pass filtering that suppresses alias-prone frequencies while preserving stable ones—precisely the anti-aliasing behaviour missing from vanilla NeRF.

In vector form, this closed-form computation replaces the costly Monte Carlo integration of the positional encoding over the frustum with a single evaluation per channel, directly yielding the *integrated positional encoding* used in Mip-NeRF's forward pass.

From scalar attenuation to full IPE. For a single channel, we have shown that

$$\mathbb{E}[\sin(z)] = \sin(\mu_z)\, e^{-\frac{1}{2}\sigma_z^2}, \qquad \mathbb{E}[\cos(z)] = \cos(\mu_z)\, e^{-\frac{1}{2}\sigma_z^2}.$$

Stacking all frequency probes (rows of $\mathbf{P}^\top$) into vector form gives the integrated positional encoding:

$$\gamma(\mu, \Sigma) = \begin{bmatrix} \sin(\mu_\gamma) \circ \exp\left(-\frac{1}{2}\operatorname{diag}(\Sigma_\gamma)\right) \\ \cos(\mu_\gamma) \circ \exp\left(-\frac{1}{2}\operatorname{diag}(\Sigma_\gamma)\right) \end{bmatrix},$$

where $\circ$ denotes elementwise multiplication, $\mu_\gamma = \mathbf{P}^\top \mu$, and $\Sigma_\gamma = \mathbf{P}^\top \Sigma \mathbf{P}$. Only the diagonal of Σ_γ is needed because $\gamma(\mathbf{x})$ factorizes over channels: each sine or cosine depends only on its own 1D projection variance.

Efficient diagonal computation. To evaluate the integrated positional encoding, we need the variance of each 1D projected coordinate

$$z = \mathbf{p}^\top \mathbf{x}, \quad \mathbf{x} \sim \mathcal{N}(\mu, \Sigma),$$

for every positional encoding channel. In matrix form, these variances are the diagonal entries of

$$\Sigma_\gamma = \mathbf{P} \Sigma \mathbf{P}^\top,$$

where each row of $\mathbf{P}$ corresponds to a frequency vector in the positional encoding basis.

Forming $\Sigma_\gamma \in \mathbb{R}^{(3L)\times(3L)}$ explicitly is costly when L (the number of frequency bands) is large, because it requires a full matrix product and storage of all frequency–frequency covariances. Fortunately, we never need the full matrix: the expectation of $\sin(z)$ or $\cos(z)$ depends only on the *marginal variance* σ_z^2 for that channel. Since positional encoding applies each frequency independently to each spatial dimension, off-diagonal terms in Σ_γ are irrelevant, and only $\operatorname{diag}(\Sigma_\gamma)$ is required.

Frequency scaling. If the base frequency vector $\mathbf{p}$ has variance $\mathbf{p}^\top \Sigma \mathbf{p}$, then multiplying $\mathbf{p}$ by 2^k scales this variance by $(2^k)^2 = 4^k$. Each positional encoding band is exactly such a scaled copy of the base frequency, so the diagonal entries can be written compactly as

$$\operatorname{diag}(\Sigma_\gamma) = \left[\operatorname{diag}(\Sigma),\, 4\operatorname{diag}(\Sigma),\, \ldots,\, 4^{L-1}\operatorname{diag}(\Sigma)\right]^\top.$$

This reduces the entire problem to computing $\operatorname{diag}(\Sigma) \in \mathbb{R}^3$, the per-axis variance of the 3D Gaussian frustum in world coordinates.

Frustum covariance diagonal. The covariance Σ of the frustum segment encodes both depthwise and cross-sectional spread of points within that volume. It naturally decomposes into:

- an *axial* component σ_t^2 along the ray direction $\mathbf{d}$,
- a *radial* component σ_r^2 orthogonal to $\mathbf{d}$.

Projecting the axial variance into (x, y, z) components requires the squared direction vector $(\mathbf{d} \circ \mathbf{d})$. The radial component must be distributed equally in all directions orthogonal to $\mathbf{d}$, which is achieved by projecting with

$$\mathbf{I} - \frac{\mathbf{d} \circ \mathbf{d}}{\|\mathbf{d}\|_2^2},$$

whose diagonal entries are $1 - (\mathbf{d} \circ \mathbf{d})/\|\mathbf{d}\|_2^2$.

Combining these gives the per-axis variances:

$$\operatorname{diag}(\Sigma) = \sigma_t^2 (\mathbf{d} \circ \mathbf{d}) + \sigma_r^2 \left(\mathbf{1} - \frac{\mathbf{d} \circ \mathbf{d}}{\|\mathbf{d}\|_2^2} \right).$$

Here:

- σ_t^2 is the variance of depth values t along the ray, scaled per coordinate axis.
- σ_r^2 is the variance of points in the circular cross-section at each depth, spread uniformly in the orthogonal plane.
- The projection terms ensure that the decomposition cleanly separates along-ray and cross-ray uncertainty.

This diagonal–only computation is what makes Mip-NeRF's IPE practical: instead of a full covariance in the positional encoding basis, we only evaluate three variances in world space and scale them by known frequency factors. These variances directly control the exponential attenuation $e^{-\frac{1}{2}\sigma_z^2}$ for each channel, suppressing high-frequency features that cannot be resolved within the frustum's extent and thereby providing principled, scale-aware anti-aliasing.

Architecture & Implementation Details

Cone tracing and interval IPE features

Aside from cone tracing and IPE, Mip-NeRF follows the NeRF pipeline. For each pixel, we cast a *cone* from the camera center $\mathbf{o}$ along the view direction $\mathbf{d}$ (rather than a single infinitesimal ray). We then sample a sorted set of $n+1$ depths

$$t_0 < t_1 < \cdots < t_n$$

between near and far planes and form n *conical frustum segments* $[t_k, t_{k+1}]$. For each segment we:

1. moment-match the segment with a world-space Gaussian $\mathcal{N}(\mu_k, \Sigma_k)$ using Eq. (8),
2. compute its *integrated positional encoding* (IPE) by the closed forms in Eqs. (13)–(16).

These IPE features (optionally concatenated with the view-direction encoding as in NeRF) are fed to the network to produce a density τ_k and color $\mathbf{c}_k$ per segment. Volume rendering then proceeds as in NeRF, using the transmittance weights induced by $\{\tau_k\}$ over the segments $\{[t_k, t_{k+1}]\}$.

Single multiscale MLP with hierarchical sampling

NeRF uses two distinct MLPs ("coarse" and "fine") because PE encodes a *single* implicit scale. In contrast, Mip-NeRF's IPE is *scale-aware*: the inputs explicitly carry segment size/shape, allowing a single MLP to model multiple scales. We therefore use *one* MLP with parameters Θ and still perform hierarchical sampling:

- *Coarse pass:* draw n intervals by stratified sampling on $[t_{\text{near}}, t_{\text{far}}]$, compute IPE per interval, render color $\mathbf{C}(\mathbf{r}; \Theta, t^c)$ and weights $\{w_k\}$.
- *Fine pass:* construct a resampling PDF from smoothed weights (see Eq. (18) below), draw another n intervals by inverse transform sampling, compute IPE per interval, and render $\mathbf{C}(\mathbf{r}; \Theta, t^f)$.

Using one network halves the parameter count, simplifies training, and empirically improves accuracy while keeping total MLP evaluations comparable to NeRF.

Training objective

Let $\mathscr{R}$ be the set of rays and $\mathbf{C}^*(\mathbf{r})$ the ground-truth pixel color. With a single MLP, we balance coarse and fine terms by a scalar λ:

$$\min_{\Theta} \sum_{\mathbf{r}\in\mathscr{R}} \Big(\lambda \left\|\mathbf{C}^*(\mathbf{r}) - \mathbf{C}(\mathbf{r};\Theta,t^c)\right\|_2^2 + \left\|\mathbf{C}^*(\mathbf{r}) - \mathbf{C}(\mathbf{r};\Theta,t^f)\right\|_2^2\Big). \tag{23.19}$$

In the paper, the authors set $\lambda = 0.1$ in experiments.

Smoothed importance sampling for the fine pass

In NeRF and Mip-NeRF, the *coarse pass* determines where along the ray the scene is likely to have important structure (surfaces, edges, textures). This information is encoded in the *alpha compositing weights* $\{w_k\}_{k=1}^n$:

$$w_k \;=\; T_k\left(1 - e^{-\tau_k \Delta t_k}\right),$$

where T_k is the transmittance up to segment k (probability that the ray has not terminated before t_k), τ_k is the predicted density, and $\Delta t_k = t_{k+1} - t_k$ is the segment length. Intuitively, w_k is the fraction of the ray's total contribution to the final pixel color coming from segment k. Segments intersecting visible surfaces will have large w_k.

Why these weights are used for sampling. We use $\{w_k\}$ as a discrete *probability density function* (PDF) to guide sampling in the *fine pass*:

- Large $w_k \Rightarrow$ high chance of resampling that region for finer detail.
- Small $w_k \Rightarrow$ low chance, unless we deliberately force exploration.

Given a PDF over the n coarse segments, we can draw new sample depths via *inverse transform sampling*: construct the cumulative distribution function (CDF) from $\{w_k\}$, draw uniform random numbers $u \in [0,1]$, and find the depth bin whose CDF interval contains u.

Why stabilization is needed. Raw $\{w_k\}$ can be:

- *Sparse:* most weights are near zero, concentrating probability on very few bins, which can lead to missing geometry slightly outside those bins.
- *Noisy:* small prediction fluctuations create spiky PDFs, producing unstable fine-pass samples.

This is especially problematic in Mip-NeRF because the coarse and fine passes query *the same MLP* (rather than two separate ones as in NeRF), so bad fine-pass samples can directly harm the shared network's learning.

Smoothing with max and blur filters. To make the PDF more *robust*, Mip-NeRF replaces each w_k with a smoothed envelope w'_k:

1. *2-tap max filter:* For each k, take the maximum weight among (w_{k-1}, w_k) and (w_k, w_{k+1}), then average the two maxima:

   $$m_k = \frac{\max(w_{k-1}, w_k) + \max(w_k, w_{k+1})}{2}.$$

   This widens peaks so that high-probability regions extend to their immediate neighbors (helps catch slightly misaligned samples).
2. *2-tap blur filter:* Apply a local average to m_k, which softens sharp spikes and spreads probability mass across nearby bins.

This sequence—max pooling followed by average pooling—is known in computer vision as a *blurpool* filter [776].

Forcing exploration. After smoothing, a small constant α is added to each bin:

$$w'_k \;=\; m_k + \alpha.$$

This ensures that even "empty" regions of the ray still have a nonzero probability of being resampled, avoiding blind spots. The paper sets $\alpha = 0.01$. Finally, $\{w'_k\}$ is renormalized to sum to 1 before building the fine-pass CDF.

$$w'_k = \frac{1}{2}(\max(w_{k-1}, w_k) + \max(w_k, w_{k+1})) + \alpha, \quad \text{renormalize } \{w'_k\} \text{ to sum to 1.} \tag{23.20}$$

Effect: Compared to NeRF's approach of merging coarse and fine samples into one sorted list, Mip-NeRF's smoothed-PDF resampling:

- Reduces sample collapse into overly narrow regions.
- Guarantees some coverage of empty space.
- Produces more stable fine-pass updates for the shared MLP.

Implementation Details. Mip-NeRF is built on JaxNeRF, a JAX reimplementation of NeRF. Training follows NeRF's schedule: Adam for 1×10^6 iterations with batch size 4096 and a logarithmic learning-rate decay from $5\cdot10^{-4}$ to $5\cdot10^{-6}$. The only substantive architectural changes are:

- Cone tracing with interval IPE.
- A *single* multiscale MLP.
- Smoothed PDF resampling for the fine pass.

Benefits over NeRF

Encoding interval size/shape into the inputs:

- Halves model size (one MLP instead of two).
- Improves multiscale accuracy (coarse+fine are *queries* at different sampling budgets, not different networks).
- Improves runtime a bit (with the same parity, meaning the same total number of per-ray evaluations).
- Eliminates the need to hand-tune the maximum PE frequency: high frequencies beyond a segment's resolvable bandwidth are attenuated automatically by IPE.

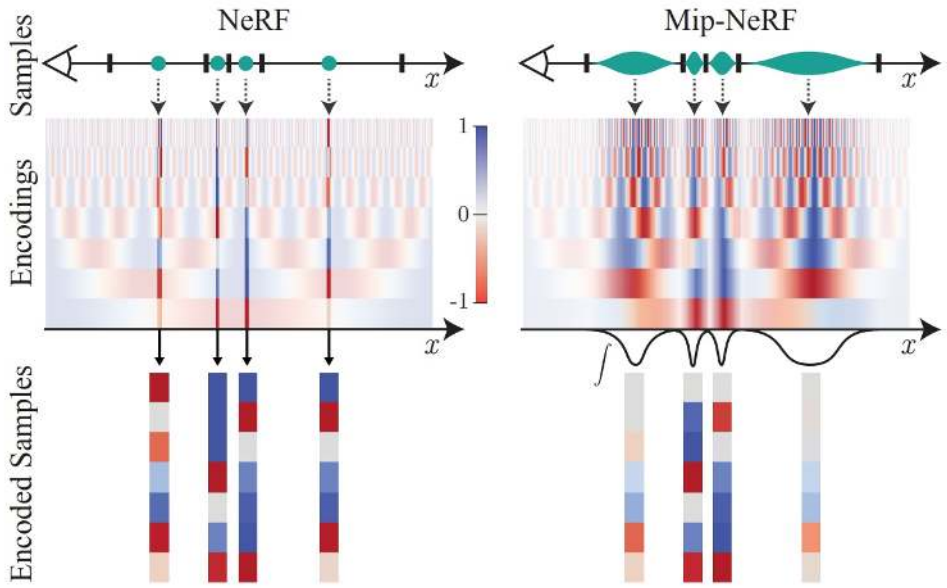

Figure 23.58: Toy 1D visualizations of the positional encoding (PE) used by NeRF (left) and the integrated positional encoding (IPE) used by Mip-NeRF (right), based on the original figure in [30]. **Top row (Samples):** In standard PE, each green dot marks a single infinitesimal sample location along the axis x; in IPE, each green *blob* represents a Gaussian footprint covering a finite ray segment. **Middle row (Encodings):** Each horizontal stripe is a sin or cos channel at a given frequency, with red/blue denoting positive/negative values. In the PE panel, high-frequency channels (upper stripes) oscillate much faster than the spacing between sample points, so the vertical black lines cut through seemingly unrelated phases of the oscillation — a visual sign of aliasing. In IPE, the Gaussian integration (curved $\int$ markers) averages over these oscillations, causing high-frequency stripes to fade toward neutral grey. **Bottom row (Encoded Samples):** In PE, the per-sample feature bars change abruptly from one sample to the next in the high-frequency dimensions, encoding phase noise rather than stable geometry — the hallmark of aliasing. In IPE, the corresponding bars for high-frequency channels are suppressed, while low-frequency channels remain strong, yielding anti-aliased, scale-aware features that also encode the segment's size and, in higher dimensions, its shape.

Results and Ablations

Quantitative performance

The below table reports performance on the multiscale `Blender` dataset (credit: [30]), comparing Mip-NeRF to baseline NeRF and several improved NeRF variants. Mip-NeRF achieves the highest PSNR and SSIM across all scales (Full, 1/2, 1/4, 1/8 resolution), while reducing LPIPS—a perceptual dissimilarity metric—to the lowest values. The performance gap widens as the resolution decreases, demonstrating Mip-NeRF's robustness to scale changes. Notably, removing IPE (*w/o IPE*) drops PSNR by up to 6 dB at the lowest resolution, confirming its central role in anti-aliasing.

	PSNR ↑				SSIM ↑				LPIPS ↓				Avg. ↓	Time (h)	#Params
	FR	1/2	1/4	1/8	FR	1/2	1/4	1/8	FR	1/2	1/4	1/8			
NeRF (Jax Impl.)	31.196	30.647	26.252	22.533	0.9498	0.9560	0.9299	0.8709	0.0546	0.0342	0.0428	0.0750	0.0288	3.05	1,191K
NeRF + Area Loss	27.224	29.578	29.445	25.039	0.9113	0.9394	0.9524	0.9176	0.1041	0.0677	0.0406	0.0469	0.0305	3.03	1,191K
NeRF + Area, Centered Pix.	29.893	32.118	33.399	29.463	0.9376	0.9590	0.9728	0.9620	0.0747	0.0405	0.0245	0.0398	0.0191	3.02	1,191K
NeRF + Area, Center, Misc.	29.900	32.127	33.404	29.470	0.9378	0.9592	0.9730	0.9622	0.0743	0.0402	0.0243	0.0394	0.0190	2.94	1,191K
Mip-NeRF	**32.629**	**34.336**	**35.471**	**35.602**	**0.9579**	**0.9703**	**0.9786**	**0.9833**	**0.0469**	**0.0260**	**0.0168**	**0.0120**	**0.0114**	2.84	612K
Mip-NeRF w/o Misc.	32.610	34.333	35.497	35.638	0.9577	0.9703	0.9787	0.9834	0.0470	0.0259	0.0167	0.0120	0.0114	2.82	612K
Mip-NeRF w/o Single MLP	32.401	34.131	35.462	35.967	0.9566	0.9693	0.9780	0.9834	0.0479	0.0268	0.0169	0.0116	0.0115	3.40	1,191K
Mip-NeRF w/o Area Loss	33.059	34.280	33.866	30.714	0.9605	0.9704	0.9747	0.9679	0.0427	0.0256	0.0213	0.0308	0.0139	2.82	612K
Mip-NeRF w/o IPE	29.876	32.160	33.679	29.647	0.9384	0.9602	0.9742	0.9633	0.0742	0.0393	0.0226	0.0378	0.0186	2.79	612K

Table 23.9: Quantitative comparison of Mip-NeRF and ablations against NeRF and NeRF variants on the multiscale `Blender` dataset. Metrics: PSNR (↑), SSIM (↑), LPIPS (↓). All numbers from [30].

Qualitative performance

The following figure shows visual comparisons on two `Blender` scenes across four scales. We crop a fixed region and display it as an image pyramid; the SSIM for each scale is shown in the lower-right, with the highest values (most successful SSIM results) highlighted in red. Mip-NeRF consistently outperforms NeRF and its improved variants both visually (fewer moiré patterns, crisper low-res textures) and quantitatively. The benefit is most pronounced at extreme downscales (1/8 res), where NeRF exhibits heavy aliasing but Mip-NeRF maintains smooth, faithful structure.

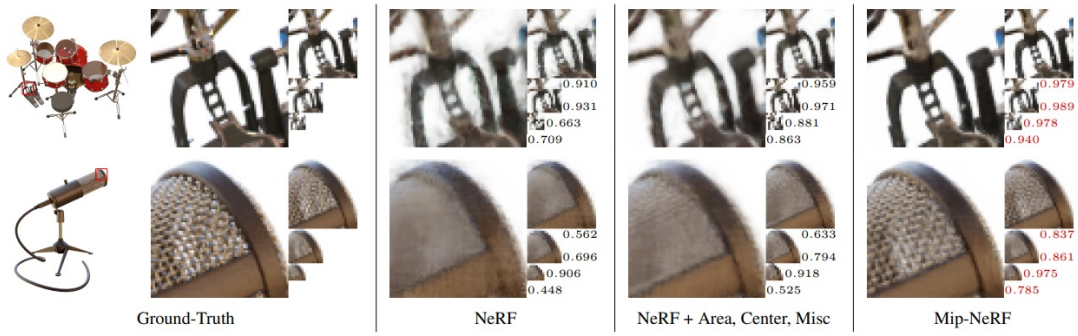

Figure 23.59: Visual comparison of Mip-NeRF, NeRF, and improved NeRF variants on two multiscale `Blender` scenes, cropped and shown at four scales (SSIM at bottom right; highest in red). Mip-NeRF achieves both higher perceptual quality and stronger metrics across scales. Credit: [30].

Ablation insights (following table 23.9)

- **IPE is essential:** Removing IPE reduces PSNR by up to 6 dB at 1/8 resolution and greatly increases LPIPS, confirming it as the core mechanism for anti-aliasing.
- **Moment-matching matters:** Approximations that do not match the frustum's true mean/variance (e.g., naive Gaussian) blur thin structures and lower both SSIM and PSNR.
- **Area loss aids stability:** Removing the area loss degrades performance at extreme scales, suggesting it complements IPE by regularizing footprint integration.
- **Parameter efficiency:** Mip-NeRF achieves superior results with roughly half the parameters of the baseline NeRF (612K vs 1.19M), aided by its single-scale-aware MLP.

Generalization to unseen scales

In experiments with randomized camera zooms at test time, Mip-NeRF preserves detail and avoids aliasing even at scales never seen during training. This supports the mipmap analogy: each sample's feature vector is already pre-filtered to match its footprint, so no extra post-processing is needed.

Limitations and Downsides

While Mip-NeRF mitigates scale aliasing, it inherits several constraints from the original NeRF:

- **Bounded scene assumption:** Optimized for forward-facing or spatially bounded scenes, making it ill-suited for large unbounded environments without further modification.
- **View-dependent aliasing:** IPE attenuates spatial high frequencies but does not pre-filter rapid view-dependent effects (e.g., specular highlights, reflections), which can still alias.
- **Extra per-sample cost:** Computing frustum moments and performing Gaussian integration introduce modest runtime overhead, although the reduced parameter count partly offsets this.
- **Parameter sensitivity:** Inaccurate cone-slope estimates or moment approximations can lead to over-blurring or residual aliasing.

These factors have motivated extensions that adapt IPE to broader settings, improve efficiency, or integrate it into hybrid scene representations.

Notable Works Building on Mip-NeRF

Mip-NeRF's *conical frustum integration* and *integrated positional encoding (IPE)* have proven to be broadly reusable primitives. By explicitly encoding the spatial extent of each ray sample, these techniques offer a general anti-aliasing mechanism that can be slotted into diverse neural scene representations. As a result, subsequent works have adopted Mip-NeRF's ideas to tackle new regimes such as unbounded scenes, high-speed rendering, and multi-modal supervision.

- **Mip-NeRF 360** [29]: Extends Mip-NeRF to large, unbounded 360° scenes via *scene contraction*, a distortion-based sampling loss, and multi-scale proposal networks. Retains the IPE formulation to prevent aliasing under extreme zoom or wide-FOV capture.
- **Zip-NeRF** [31]: Improves generalization to novel scenes by combining Mip-NeRF's IPE with strong geometry priors and data-driven regularization. Achieves higher quality with fewer views and reduced overfitting.
- **Tri-MipRF** [237]: Integrates multi-resolution IPE into a tri-plane radiance field representation, yielding faster rendering while preserving Mip-NeRF's anti-aliasing benefits.
- **Gaussian Splatting with IPE** (e.g., [287], follow-up variants): Adapts Mip-NeRF's scale-aware encoding to initialize or filter point/ellipsoid attributes in real-time splatting pipelines, improving detail retention at varying scales.

Enrichment 23.10.7: NeuS: Neural Implicit Surfaces by Volume Rendering

Motivation

Surface reconstruction from multi-view images is a long-standing problem in computer vision. Classical multi-view stereo (MVS) pipelines such as COLMAP produce dense point clouds and polygon meshes, but often fail to recover fine details or handle challenging lighting and textureless regions. Neural scene representations, notably NeRF [429], have recently demonstrated photorealistic novel view synthesis, but NeRF's *volume rendering* formulation inherently represents scenes as semi-transparent volumes rather than sharp, watertight surfaces. This leads to *fuzzy geometry* and small-scale surface artifacts, particularly when extracting explicit meshes.

An alternative is to represent scenes via a signed distance function (SDF), as in methods like IDR [731], which directly target surface rendering. SDF-based approaches tend to produce cleaner and more accurate surfaces, but prior work couples SDFs with classical *surface rendering* equations that do not model complex light transport along the ray. This makes them susceptible to catastrophic failures under occlusion: for example, IDR can produce visually plausible but *geometrically incorrect* reconstructions that "fill in" occluded spaces with spurious surfaces.

The following figure from the NeuS paper [667] illustrates this trade-off. In the bamboo planter example, IDR produces a clean-looking but topologically incorrect surface by filling the interior; NeRF better preserves the hollow geometry but introduces visible surface noise due to volumetric density smoothness. NeuS aims to combine the strengths of both: the *sharp geometry* of SDF-based surfaces and the *photometric consistency* of volumetric rendering.

To achieve this, NeuS reformulates the volume rendering weights so that they are *derived directly from the SDF*, enabling differentiable, unbiased surface localization while retaining the correct transmittance behavior of volumetric rendering. This addresses a key bias problem in naive SDF-to-density conversions (see the following figure), where the weight distribution shifts away from the true surface, leading to systematic depth errors. By aligning the rendering formulation with the signed distance geometry, NeuS bridges the gap between surface-based and volume-based neural reconstruction.

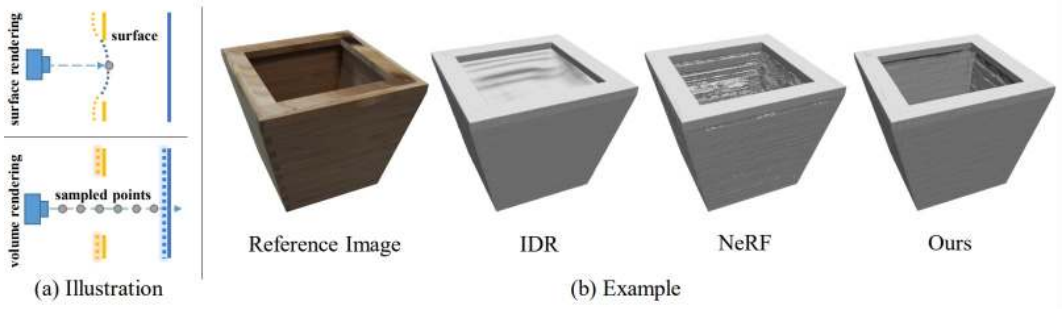

Figure 23.60: **Surface vs. volume rendering in neural scene reconstruction.** (a) Conceptual differences. (b) Bamboo planter example: IDR fills the interior despite a smooth surface, NeRF preserves hollowness but exhibits surface noise, NeuS avoids both issues by combining SDF-based surfaces with volumetric rendering. Image credit: [667].

Method

Scene representation and rendering objective

NeuS [667] directly learns an implicit *Signed Distance Function* (SDF) $f_\theta : \mathbb{R}^3 \to \mathbb{R}$. For any point $\mathbf{x} \in \mathbb{R}^3$, $f_\theta(\mathbf{x})$ is the *signed* Euclidean distance to the **closest** point on the scene's surface, with the zero level set $\{\mathbf{x} \mid f_\theta(\mathbf{x}) = 0\}$ defining the surface itself:

$$f_\theta(\mathbf{x}) = \begin{cases} < 0, & \mathbf{x} \text{ is inside the surface,} \\ = 0, & \mathbf{x} \text{ is on the surface,} \\ > 0, & \mathbf{x} \text{ is outside the surface.} \end{cases}$$

By definition, this covers *any* number of disconnected or self-occluding surfaces — at each spatial location we only care about the distance to the nearest one, so a single continuous function f_θ can represent multi-object scenes and thin structures.

Along a camera ray $\mathbf{r}(t) = \mathbf{o} + t\,\mathbf{d}$, it is possible to have two depths $t_0 < t_1$ such that

$$f_\theta(\mathbf{r}(t_0)) = f_\theta(\mathbf{r}(t_1)),$$

even though these correspond to entirely different physical surfaces (e.g., a nearer front face and a farther back face with the same signed distance magnitude). For physically correct rendering, the nearer point $\mathbf{r}(t_0)$ should contribute more to the pixel color than the farther one $\mathbf{r}(t_1)$, since the latter is occluded by the former. NeuS therefore imposes the *occlusion-aware* requirement: if $t_a < t_b$ and $f_\theta(\mathbf{r}(t_a)) = f_\theta(\mathbf{r}(t_b))$, then $w(t_a) > w(t_b)$, where $w(t)$ is the per-sample weight along the ray.

The pixel color is modeled as a line integral of per-sample radiance contributions:

$$C(\mathbf{r}) \;=\; \int_0^{+\infty} w(t)\; c\big(\mathbf{r}(t), \mathbf{d}\big)\, dt,$$

where $c(\mathbf{r}(t), \mathbf{d})$ is the view-dependent color at position $\mathbf{r}(t)$, and $w(t)$ is a weight we will derive from the SDF following the paper's Eqs. (2)–(13). Intuitively,

- $w(t)$ must (i) *peak* exactly at the zero level set to avoid geometric bias.
- $w(t)$ must *respect occlusion* so that nearer visible surfaces dominate the pixel color.

From SDF to volume rendering

In the previous discussion we treated the signed distance function f_θ as a given geometric primitive. In NeuS [667], this SDF is *not* precomputed — it is represented by a trainable *multi-layer perceptron* (MLP) that maps any 3D coordinate $\mathbf{x} = (x, y, z)$ to its signed distance from the scene surface. The MLP typically uses positional encoding on $\mathbf{x}$ to capture high-frequency detail, residual skip connections for stable optimization, and smooth activations such as Softplus to make the SDF differentiable everywhere. Training this network from multi-view images requires coupling the implicit geometry to a differentiable *volume rendering* model, so that image-space supervision can update the 3D SDF parameters.

The central design question is: *given an SDF field f_θ, how should we convert it into per-ray weights $w(t)$ for rendering, such that surfaces are accurately located and occlusion is respected?* NeuS approaches this by interpreting the SDF along a ray as defining a *probabilistic surface location*.

Specifically, instead of learning a free-form volume density $\sigma(t)$ as in the original NeRF, NeuS derives it directly from the signed distance function f_θ so that the density field is geometrically tied to the zero-level set representing the surface. To do this, NeuS uses the *logistic cumulative distribution function* (CDF) and its derivative:

$$\Phi_s(x) = \frac{1}{1+e^{-sx}}, \qquad \phi_s(x) = \Phi_s'(x) = \frac{s\,e^{-sx}}{\left(1+e^{-sx}\right)^2},$$

where $s > 0$ controls sharpness (spread $1/s$) and is learned jointly with the SDF parameters.

Why the logistic family?

- The derivative $\phi_s(x)$ is a smooth, symmetric, unimodal "bump" centered at $x = 0$, which makes it well-suited for concentrating density exactly at the surface ($f_\theta(\mathbf{x}) = 0$) while avoiding the discontinuities that would make optimization unstable.
- The CDF $\Phi_s(x)$ transitions smoothly from 0 (far inside) to 1 (far outside) across the surface, providing a continuous and differentiable notion of "inside" vs. "outside" that plugs directly into the transmittance computation in volume rendering.
- Learning s allows the method to adapt the *thickness* of the high-density region during training: early on, a lower s produces a wider band of nonzero density around the surface, which increases the number of samples along a ray that contribute gradients and thus stabilizes learning. As training progresses, s increases, narrowing this band to approach the physical reality of an infinitely thin surface — effectively concentrating the density into a subpixel-scale layer for sharper geometry and cleaner renderings.
- In contrast, NeRF learns a free-form volume density $\sigma(\mathbf{x})$ without explicitly enforcing a geometric zero-level surface. This can lead to inconsistencies between the geometry implied by the density field and the appearance in rendered images. NeuS's SDF-driven density formulation ensures that the geometry and appearance are linked through the same underlying surface definition.

When applied along a ray $\mathbf{r}(t)$, $\phi_s(f_\theta(\mathbf{r}(t)))$ acts as a *surface-likelihood profile*: it peaks where the ray intersects the surface and decays smoothly away from it. To produce physically correct renderings, this profile must be combined with an *occlusion-aware* transmittance term so that nearer intersections dominate over farther ones, and it must be constructed to be *unbiased* — i.e., its maximum should occur exactly at $f_\theta(\mathbf{r}(t)) = 0$. The derivation of such an unbiased, occlusion-aware weight $w(t)$ from Φ_s and ϕ_s is the focus of the next section.

Naïve SDF→density conversion and its bias

A straightforward NeRF-style mapping would define

$$w_{\text{naive}}(t) = T(t)\,\sigma(t), \quad T(t) = \exp\Big(-\int_0^t \sigma(u)\,du\Big), \quad \sigma(t) = \phi_s\big(f_\theta(\mathbf{r}(t))\big),$$

where $T(t)$ is the accumulated transmittance and $\sigma(t)$ is the "density" derived from the SDF. This form is naturally occlusion-aware due to $T(t)$, but the product $T(t)\,\sigma(t)$ tends to peak *before* the actual surface intersection $f_\theta(\mathbf{r}(t^*)) = 0$, introducing a geometric bias. Intuitively, as $\sigma(t)$ rises approaching the surface, $T(t)$ is already decaying, shifting the peak forward along the ray (The following figure shows exactly that).

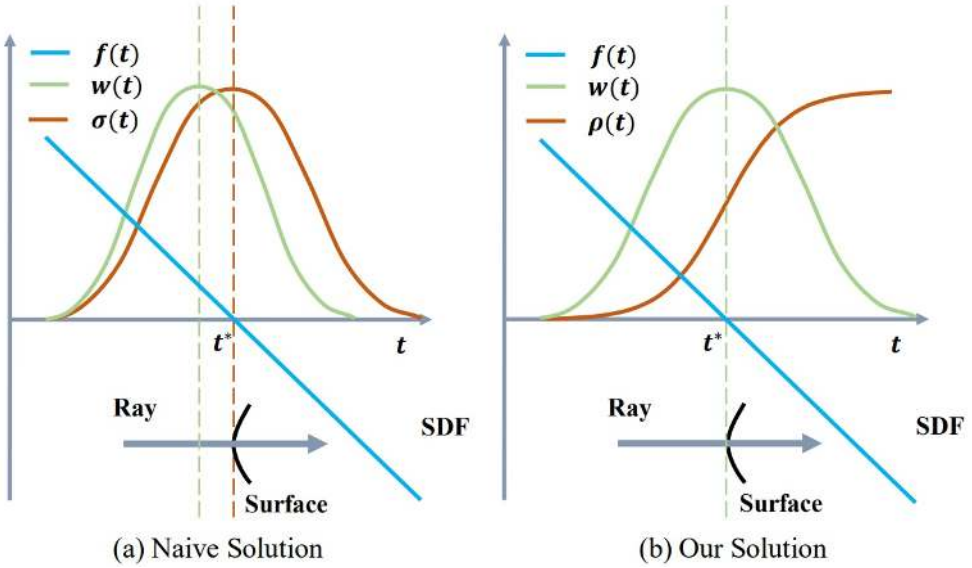

Figure 23.61: **Weight bias vs. unbiased construction.** (a) Naïve approach: The blue curve shows the SDF $f(t)$, whose zero-crossing marks the true surface location. The brown curve is the density $\sigma(t) = \phi_s(f_\theta(\mathbf{r}(t)))$, which is largest when $f(t)$ is near zero. The green curve is the weight $w(t) = T(t)\,\sigma(t)$. Because the transmittance $T(t)$ has already decayed by the time $\sigma(t)$ reaches its peak, the product $w(t)$ achieves its maximum *before* the blue zero-crossing—producing a biased surface estimate. (b) NeuS: By redefining the effective density $\rho(t)$ so that $T(t)$ matches the logistic CDF $\Phi_s(f(t))$ in the first-order SDF approximation, the decay of $T(t)$ and the growth of $\rho(t)$ are balanced. This alignment causes the green weight $w(t) = T(t)\,\rho(t)$ to peak exactly at the blue zero-crossing of $f(t)$, eliminating bias while retaining occlusion handling. Source: [667].

A direct unbiased weighting that fails occlusion

A seemingly natural way to obtain an *unbiased* surface-localization weight from the SDF is to normalize the S-density along the ray:

$$w_{\text{dir}}(t) = \frac{\phi_s\big(f(\mathbf{r}(t))\big)}{\int_0^{+\infty} \phi_s\big(f(\mathbf{r}(u))\big)\,du}.$$

Here, the numerator $\phi_s(f(\mathbf{r}(t)))$ is maximal exactly when $f(\mathbf{r}(t)) = 0$, i.e., at the true surface intersection, because ϕ_s is a smooth, unimodal density centered at zero. This guarantees that $w_{\text{dir}}(t)$ peaks at the correct location—hence "unbiased."

However, this construction *ignores depth ordering* and thus fails to model occlusion. If a ray encounters multiple surfaces, the SDF $f(\mathbf{r}(t))$ will cross zero at each intersection, producing multiple peaks in $\phi_s(f(\mathbf{r}(t)))$. Since $w_{\text{dir}}(t)$ is obtained by global normalization of these peaks, the contributions from all intersections are rescaled to sum to one and are *all* blended into the final color. Crucially, no mechanism here suppresses the influence of farther intersections once a nearer one has been reached—violating the physical visibility constraint that closer surfaces should occlude those behind them.

This limitation motivates the NeuS formulation, which retains the precise, unbiased surface localization of w_{dir} while introducing an occlusion-aware transmittance term so that nearer surfaces dominate the final rendered pixel.

Derivation of the NeuS Weight Function for the Single-Plane Case

We begin with the simplest setting: a single infinite plane intersected by one camera ray.

Step 1: Geometric Setup

Let the ray be parameterized as

$$\mathbf{p}(t) = \mathbf{o} + t\,\mathbf{v}, \quad t \geq 0, \tag{23.21}$$

where $\mathbf{o} \in \mathbb{R}^3$ is the camera origin, $\mathbf{v} \in \mathbb{S}^2$ is a *unit* direction vector, and t denotes depth along the ray. Let t^* be the depth where the signed distance function (SDF) vanishes:

$$f(\mathbf{p}(t^*)) = 0. \tag{23.22}$$

Step 2: Normal and Incidence Angle

Let $\mathbf{n}$ be the unit outward normal of the plane. The *incidence angle* θ is defined by

$$\cos\theta = \mathbf{v} \cdot \mathbf{n}. \tag{23.23}$$

A perpendicular hit yields $|\cos\theta| = 1$, while grazing incidence has $|\cos\theta| \approx 0$.

Step 3: SDF properties (geometry and intuition)

A true signed distance function (SDF) $f : \mathbb{R}^3 \to \mathbb{R}$ satisfies, almost everywhere,

$$\nabla f(\mathbf{x}) = \mathbf{n}(\mathbf{x}), \qquad \|\nabla f(\mathbf{x})\|_2 = 1, \tag{23.24}$$

where $\mathbf{n}(\mathbf{x})$ is the outward unit normal to the surface at the closest point $\pi(\mathbf{x})$.

- **Gradient equals the normal.** Consider moving $\mathbf{x}$ in a tangent direction $\mathbf{t}$ at $\pi(\mathbf{x})$. The closest-point distance does not change to first order:

  $$\frac{\partial f}{\partial t}(\mathbf{x}) = 0 \quad \text{for all tangents } \mathbf{t} \text{ at } \pi(\mathbf{x}).$$

  In contrast, moving along the normal $\mathbf{n}(\pi(\mathbf{x}))$ increases the signed distance at the maximal possible rate:

  $$\frac{\partial f}{\partial n}(\mathbf{x}) = 1.$$

  The gradient $\nabla f(\mathbf{x})$ is the vector collecting all directional derivatives. The fact that tangent derivatives are zero and the normal derivative is exactly 1 implies

  $$\nabla f(\mathbf{x}) = \mathbf{n}(\pi(\mathbf{x})),$$

  i.e., the gradient is not only parallel to the surface normal but *identical* to it.
- **Unit slope.** By the definition of distance, taking a small step δ along the outward normal

  $$\mathbf{x}_\delta = \pi(\mathbf{x}) + \delta\,\mathbf{n}(\pi(\mathbf{x}))$$

  changes the signed distance by exactly δ:

  $$f(\mathbf{x}_\delta) = f(\pi(\mathbf{x})) + \delta = \delta.$$

  Therefore,

  $$\frac{d}{d\delta} f(\mathbf{x}_\delta)\Big|_{\delta=0} = 1$$

  and since this is the derivative in the gradient's direction, we must have $\|\nabla f(\mathbf{x})\|_2 = 1$.

Equivalently, a perfect SDF solves the *Eikonal equation* $\|\nabla f\|_2 = 1$ with $f = 0$ on the surface, except on the medial axis where the nearest point is not unique. In learned SDFs, this property is encouraged by the *Eikonal regularizer* $(\|\nabla f\|_2 - 1)^2$, which ensures correct metric scaling and underpins the angle-based derivations in Step 4.

Step 4: SDF Evolution Along the Ray
By the chain rule,

$$\frac{df}{dt} = \nabla f(\mathbf{p}(t)) \cdot \frac{d\mathbf{p}}{dt} = \mathbf{n} \cdot \mathbf{v} = \cos\theta. \tag{23.25}$$

With the convention $f > 0$ outside the surface, $f < 0$ inside, an *entering* ray satisfies $\cos\theta < 0$:

$$\frac{df}{dt} = -|\cos\theta|. \tag{23.26}$$

Step 5: Local linearization near the surface
Let t^* be the depth at which the ray $\mathbf{p}(t) = \mathbf{o} + t\,\mathbf{v}$ intersects the surface, i.e., $f(\mathbf{p}(t^*)) = 0$. From Step 4 we know that

$$\frac{df}{dt} = \nabla f \cdot \frac{d\mathbf{p}}{dt} = \mathbf{n}(\mathbf{p}(t)) \cdot \mathbf{v}.$$

At $t = t^*$, the gradient equals the outward unit normal, $\mathbf{n}(\mathbf{p}(t^*))$, so

$$\left.\frac{df}{dt}\right|_{t^*} = \mathbf{n}(\mathbf{p}(t^*)) \cdot \mathbf{v} = -|\cos\theta|,$$

where θ is the incidence angle between the ray and the normal; the minus sign follows from the convention $f > 0$ outside the surface.

First-order approximation: Under the tangent-plane assumption near $\mathbf{p}(t^*)$, the unit normal $\mathbf{n}$ is constant in this neighborhood. From Step 4, along the ray $\mathbf{p}(t)$ we have

$$\frac{df}{dt} = \mathbf{n} \cdot \mathbf{v} = -|\cos\theta| \quad \text{(constant)}.$$

This is an ordinary differential equation with constant right-hand side. Integrating both sides with respect to t from t^* to t gives

$$f(\mathbf{p}(t)) - f(\mathbf{p}(t^*)) = -|\cos\theta|\,(t - t^*).$$

Since $f(\mathbf{p}(t^*)) = 0$ (the ray is on the surface at t^*), we obtain

$$f(\mathbf{p}(t)) \;=\; -|\cos\theta|\,\big(t - t^*\big). \tag{23.27}$$

Interpretation:
- $t < t^* \;\Rightarrow\; f > 0$: the sample lies *outside* the surface.
- $t = t^* \;\Rightarrow\; f = 0$: the sample lies *on* the surface.
- $t > t^* \;\Rightarrow\; f < 0$: the sample lies *inside* the surface.

The slope magnitude $|\cos\theta|$ measures how quickly the signed distance changes along the ray: grazing rays (θ near 90°) change f slowly, while near-normal rays (θ near 0°) change it rapidly. This angular factor is exactly what Step 6 will remove to construct a per-depth weight that is *unbiased* with respect to the ray–surface angle.

Step 6: Direct unbiased weight construction

Let Φ_s be the logistic CDF with sharpness s, and $\phi_s = \Phi_s'$ its PDF (the *S-density*). A naive choice,

$$w(t) = \phi_s\big(f(\mathbf{p}(t))\big), \tag{23.28}$$

produces a bell-shaped bump centered at the true hit depth t^*, but its *area in t-space* scales like $1/|\cos\theta|$. *Intuition:* along the ray, $f(\mathbf{p}(t))$ changes at rate $\left|\frac{df}{dt}\right| = |\cos\theta|$ (Step 4). Grazing rays ($|\cos\theta| \ll 1$) sweep through the same range of SDF values more slowly, stretching the bump in depth; hence, *more total weight* accumulates in free space before the hit than for a head-on ray. This angle-dependent "mass inflation" is undesirable: it skews how much a single opaque surface contributes depending on view angle and can over-emphasize pre-surface samples.

Normalization (single-plane model). To remove this geometric inflation, we normalize by the total area along the ray:

$$w_{\text{dir}}(t) \;=\; \frac{\phi_s\big(f(\mathbf{p}(t))\big)}{\displaystyle\int_0^{+\infty} \phi_s\big(f(\mathbf{p}(u))\big)\,du}. \tag{23.29}$$

Under the local planar model of Step 5, $f(\mathbf{p}(u)) = -|\cos\theta|\,(u - t^*)$ and $\frac{df}{du} = -|\cos\theta|$. With the change of variables $x = f(\mathbf{p}(u))$ (so $du = -dx/|\cos\theta|$) we obtain

$$\int_0^{+\infty} \phi_s\big(f(\mathbf{p}(u))\big)\,du \;=\; \frac{1}{|\cos\theta|}\int_{x_{\min}}^{x_{\max}} \phi_s(x)\,dx, \tag{23.30}$$

where $x_{\min} = -|\cos\theta|\,t^*$ and $x_{\max} \to +\infty$. In the idealized infinite-depth limit $t^* \to +\infty$,

$$\lim_{t^*\to+\infty} \int_0^{+\infty} \phi_s\big(f(\mathbf{p}(u))\big)\,du \;=\; \frac{1}{|\cos\theta|}\int_{-\infty}^{+\infty} \phi_s(x)\,dx \;=\; \frac{1}{|\cos\theta|}. \tag{23.31}$$

Hence, in this limit, the *direct* single-plane weight becomes

$$\boxed{w(t) \;=\; |\cos\theta|\,\phi_s\big(f(\mathbf{p}(t))\big).} \tag{23.32}$$

For finite t^*, this expression is an accurate approximation whenever the support of ϕ_s lies well inside the integration domain.

Why normalization removes the bias (formal & intuitive). Let $k := |\cos\theta|$ and $f(\mathbf{p}(t)) = -k\,(t - t^*)$ near t^*.

- **(i) Unit mass, angle-invariant.**

$$\int_0^{+\infty} w(t)\,dt \;=\; k\int_0^{+\infty} \phi_s\big(f(\mathbf{p}(t))\big)\,dt \overset{x=f}{=} k\int_{x=f(\mathbf{p}(+\infty))}^{x=f(\mathbf{p}(0))} \phi_s(x)\,\frac{-dx}{k} \;\approx\; \int_{-\infty}^{+\infty} \phi_s(x)\,dx \;=\; 1, \tag{23.33}$$

  where the approximation becomes exact as $t^* \to +\infty$. *Intuition:* the bump widens by $1/k$ for grazing rays, and the prefactor k exactly scales its height so that the total area remains 1.

- **(ii) No pre-surface overweighting.** Under the same change of variables, $t < t^* \iff x > 0$ and $t > t^* \iff x < 0$. Since ϕ_s is symmetric,

$$\int_{t<t^*} w(t)\,dt \;=\; \int_{x>0} \phi_s(x)\,dx \;=\; \tfrac{1}{2} \;=\; \int_{x<0} \phi_s(x)\,dx \;=\; \int_{t>t^*} w(t)\,dt, \tag{23.34}$$

again exact in the $t^* \to +\infty$ limit (or whenever both tails of ϕ_s are contained in the integration domain). Thus the *fraction* of weight allocated before the hit is fixed at $1/2$—grazing rays do not gain extra early mass. Moreover, the distribution of $(t - t^*)$ under w is symmetric, so $\mathbb{E}_w[t] = t^*$: there is no forward shift of the "center of mass."

- **(iii) Peak at the surface (no forward drift).** Because ϕ_s is unimodal with maximum at $x = 0$, $w(t) \propto \phi_s(f(\mathbf{p}(t)))$ attains its maximum at $f = 0$, i.e., exactly at $t = t^*$. Hence $w(t^*) > w(t)$ for all $t \neq t^*$.

Step 7: Derivative-of-CDF Identity

From Step 4 we know that along the ray

$$\frac{df}{dt} \;=\; \mathbf{n}\cdot\mathbf{v} \;=\; -|\cos\theta|,$$

for an entering ray. Applying the chain rule to the cumulative distribution $\Phi_s(f(\mathbf{p}(t)))$ gives

$$\frac{d}{dt}\Phi_s\big(f(\mathbf{p}(t))\big) \;=\; \phi_s\big(f(\mathbf{p}(t))\big)\,\frac{df}{dt} \;=\; -|\cos\theta|\,\phi_s\big(f(\mathbf{p}(t))\big). \tag{23.35}$$

Thus the NeuS weight may be expressed as

$$\boxed{w(t) \;=\; |\cos\theta|\,\phi_s(f(\mathbf{p}(t))) \;=\; -\tfrac{d}{dt}\Phi_s(f(\mathbf{p}(t)))}. \tag{23.36}$$

Step 8: Interpretation as Soft Visibility

The function $\Phi_s(f(\mathbf{p}(t)))$ acts as a *soft visibility function*:

- Outside the surface ($f > 0$), $\Phi_s \approx 1$, meaning the ray is fully visible.
- Deep inside ($f < 0$), $\Phi_s \approx 0$, meaning the ray has been completely occluded.
- Near the zero-level set, Φ_s smoothly transitions between these values.

The weight $w(t)$ is precisely the *negative slope* of this transition along depth, concentrating probability where the ray crosses the soft band around the surface.

Step 9: Embedding into Volume Rendering

Classical volume rendering defines

$$w(t) \;=\; T(t)\,\rho(t), \qquad T'(t) = -\rho(t)\,T(t).$$

Identifying

$$T(t) \;=\; \Phi_s(f(\mathbf{p}(t))), \tag{23.37}$$

we obtain

$$\rho(t) \;=\; \frac{w(t)}{T(t)} = \frac{-\frac{d}{dt}\Phi_s(f(\mathbf{p}(t)))}{\Phi_s(f(\mathbf{p}(t)))}. \tag{23.38}$$

Hence the NeuS construction ensures

$$w(t) \;=\; T(t)\rho(t),$$

so the derivative-of-CDF weight integrates seamlessly into the unbiased volume rendering framework.

Multi-Surface Generalization

Up to now we have assumed a single, locally planar zero-level set with a consistent orientation (entering side only). In realistic 3D scenes, however, a ray may intersect multiple surfaces (e.g., front and back faces of an object), or may exit a surface region where the signed distance field increases in the viewing direction ($df/dt > 0$). This introduces two problems:

1. The raw expression
$$\rho(t) \;=\; -\frac{d}{dt}\log \Phi_s(f(\mathbf{p}(t)))$$
can become negative when $df/dt > 0$, leading to unphysical "negative density".
2. Without correction, the transmittance $T(t) = \exp\big(-\int_0^t \rho(u)\,du\big)$ could become *increasing*, which contradicts the physical principle that visibility along a ray must monotonically decrease.

Enforcing Physical Validity

NeuS resolves these issues by clipping the density:

$$\rho(t) \;=\; \max\left(-\frac{\frac{d}{dt}\Phi_s(f(\mathbf{p}(t)))}{\Phi_s(f(\mathbf{p}(t)))}, 0\right). \tag{23.39}$$

This guarantees that $\rho(t) \geq 0$, so that transmittance is non-increasing and weights $w(t) = T(t)\rho(t)$ remain physically consistent.

Intuition

One way to view this is to imagine the ray entering and leaving a "soft surface band". On the entering side ($df/dt < 0$), the visibility drops and the derivative contributes positive density. On the exiting side ($df/dt > 0$), visibility recovers; the raw derivative would suggest *negative* density, but NeuS suppresses this contribution to avoid creating "ghost" surfaces with negative opacity. In effect, NeuS only accumulates mass where surfaces occlude the ray, never where they re-open.

Weights Construction Summary

In the single-surface case, the NeuS weight

$$w(t) = |\cos\theta|\,\phi_s(f(\mathbf{p}(t)))$$

is unbiased: it integrates to one, splits symmetrically around the true intersection, and peaks exactly at the surface crossing. The clipping-based generalization ensures that this property extends to arbitrary, multi-surface geometry, embedding the construction into the physically consistent volume rendering framework.

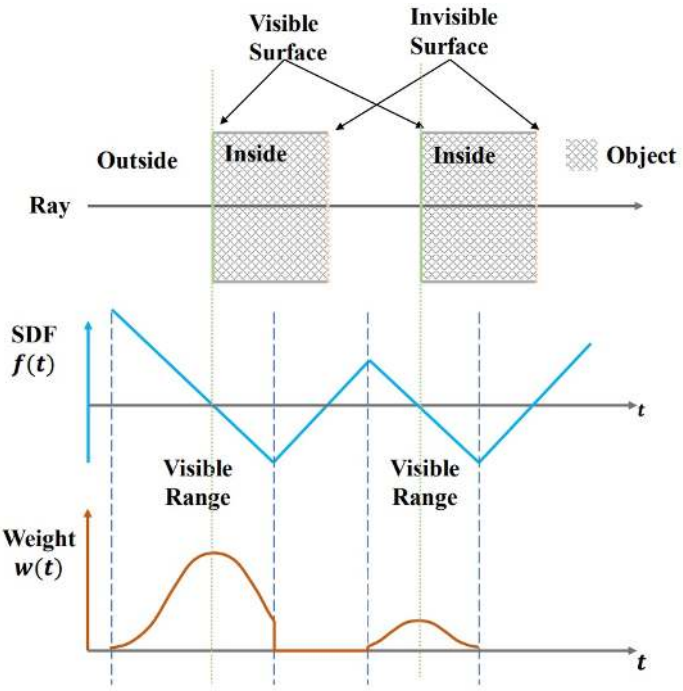

Figure 23.62: **Multiple intersections.** The NeuS weight assigns probability only on *entering* segments ($df/dt < 0$); on *exiting* segments ($df/dt > 0$) the derived opaque density is clipped to zero. This preserves visibility ordering. Image credit: [667].

Discretization

To obtain discrete counterparts of the opacity and weight functions, the authors used the same approximation scheme as used in NeRF [429]. Specifically, they sample n points along a ray,

$$p_i = \mathbf{o} + t_i \mathbf{v}, \quad i = 1, \ldots, n, \quad t_i < t_{i+1},$$

and approximate the pixel color of the ray as

$$\hat{C} = \sum_{i=1}^{n} T_i \, \alpha_i \, c_i, \tag{23.40}$$

where T_i denotes the discrete accumulated transmittance, defined by

$$T_i = \prod_{j=1}^{i-1} (1 - \alpha_j),$$

and α_i represents the discrete opacity given by

$$\alpha_i = 1 - \exp\left(- \int_{t_i}^{t_{i+1}} \rho(t) \, dt \right). \tag{23.41}$$

Using the NeuS definition of the s-density $\rho(t)$, this integral can be shown to yield

$$\alpha_i = \max\left(\frac{\Phi_s(f(p_i)) - \Phi_s(f(p_{i+1}))}{\Phi_s(f(p_i))}, 0 \right), \tag{23.42}$$

where Φ_s is the cumulative distribution induced by the sigmoid with sharpness parameter s. The term c_i is obtained by evaluating the radiance branch of the MLP at the point $\mathbf{x}_i$ and viewing direction $\mathbf{d}$, giving $c_i = c(\mathbf{x}_i, \mathbf{d})$. Importantly, NeuS does not eliminate the MLP; rather, it changes its parameterization. Instead of predicting a free density value $\sigma(\mathbf{x})$ as in NeRF, the network outputs a signed distance value $f_\theta(\mathbf{x})$. This is then converted into densities through the sigmoid-based cumulative distribution $\Phi_s(f_\theta(\mathbf{x}))$, from which the discrete opacities α_i are derived.

The max operator ensures non-negativity by clipping spurious increases of Φ_s across bins. Thus the discretization remains faithful to the continuous NeuS rendering equation.

Compared to NeRF, the forward cost is essentially identical—both require evaluating an MLP for each sample. The key difference lies in representation: NeRF directly predicts densities, while NeuS predicts an SDF and enforces surface-consistency through its transformation. This change does not accelerate rendering, but it yields sharper, geometrically consistent surfaces and avoids the "fuzzy-shell" artifacts common to NeRF.

Training

NeuS is trained without any ground-truth 3D supervision. Instead, it relies on standard 2D image supervision: observed pixel colors and, if available, binary foreground masks. The goal is to optimize the signed distance function f_θ and color head so that the rendered radiance field explains all training views consistently.

Pixel sampling. At each iteration, a batch of m image pixels is sampled. For every pixel we collect its color, optional binary mask, and corresponding camera ray in world space:

$$P = \{C_k, M_k, \mathbf{o}_k, \mathbf{v}_k\}_{k=1}^{m},$$

where $C_k \in \mathbb{R}^3$ is the observed RGB value, $M_k \in \{0,1\}$ is the foreground/background indicator, $\mathbf{o}_k$ is the camera origin, and $\mathbf{v}_k$ the unit ray direction.

Overall objective. For each ray, n points are sampled and rendered through the NeuS volume rendering equation, producing predicted colors $\hat{C}_k$ and occupancies $\hat{O}_k$. The total training loss is

$$\mathscr{L} = \mathscr{L}_{\text{color}} + \lambda\, \mathscr{L}_{\text{reg}} + \beta\, \mathscr{L}_{\text{mask}}, \tag{23.43}$$

where each term enforces a different supervision signal.

Color reconstruction. The primary signal is per-pixel color matching:

$$\mathscr{L}_{\text{color}} = \frac{1}{m} \sum_{k=1}^{m} \mathscr{R}(\hat{C}_k, C_k), \tag{23.44}$$

where $\mathscr{R}$ is an ℓ_1 loss, chosen for robustness to outliers. This term encourages the rendered radiance field to reproduce the ground-truth images.

Eikonal regularization. To ensure that f_θ behaves as a valid signed distance function, NeuS adds an Eikonal loss [189]:

$$\mathscr{L}_{\text{reg}} = \frac{1}{nm} \sum_{k,i} \big(\|\nabla f(\hat{p}_{k,i})\|_2 - 1\big)^2, \tag{23.45}$$

forcing the gradient norm to remain close to 1 almost everywhere.

Mask supervision. When binary foreground masks are available, NeuS includes an additional constraint on ray occupancy:

$$\mathscr{L}_{\text{mask}} = \text{BCE}(M_k, \hat{O}_k), \qquad \hat{O}_k = \sum_{i=1}^{n} T_{k,i}\alpha_{k,i}, \tag{23.46}$$

where $\hat{O}_k \in [0,1]$ is the predicted probability that ray k intersects the object. If $M_k = 0$ (background pixel), the network is penalized for predicting any opacity along that ray. If $M_k = 1$ (foreground), the network must explain the pixel with some nonzero occupancy. This mask loss thus provides strong geometric supervision in cases where silhouettes are known.

Hierarchical sampling. The hierarchical sampling strategy in NeuS is designed to efficiently localize the surface by focusing computation on regions where the signed distance field (SDF) indicates high surface likelihood. Importantly, NeuS achieves this with a *single* MLP, unlike NeRF which maintains separate coarse and fine networks.

- **Stage 1: Uniform sampling with fixed sharpness.** Each ray is first discretized into n_0 uniformly spaced points (e.g., 64). For these coarse samples, NeuS evaluates the S-density function

  $$\phi_s(f(x)) = \Phi_s(-f(x)) \cdot \left|\frac{\partial f}{\partial x}\right|$$

  using a *fixed* sharpness parameter s. This fixed s is not learned but annealed over iterations (e.g., $s = 32 \cdot 2^i$ in iteration i) so that the sampling distribution becomes progressively more peaked near potential surface regions. The goal is to obtain a broad but informative estimate of where surfaces may lie.
- **Stage 2: Importance sampling with learned sharpness.** Based on the coarse distribution, NeuS resamples additional n_1 points (e.g., 4 iterations of 16 points each). For these fine samples, the probability density is computed with the *learned* sharpness parameter s, which is optimized during training. This adaptive s sharpens over time, concentrating samples more tightly around the true surface as the SDF becomes well-defined.

Thus, NeuS does not use two separate networks but instead uses two different regimes of the same S-density function: one with fixed, annealed sharpness for exploration, and one with learned sharpness for exploitation. This hierarchical approach balances efficiency with precision: the fixed s ensures coverage so that surfaces are not missed, while the learned s allows the model to progressively refine and localize surfaces with high fidelity.

Compared to NeRF, where hierarchical sampling requires evaluating two full MLPs (a coarse and a fine model), NeuS is more efficient: only a single MLP is optimized and queried, with different sampling distributions guiding where along the ray the network is evaluated. Moreover, since NeuS is SDF-based, the learned sharpness naturally drives samples toward the zero level set, achieving more accurate and unbiased surface reconstruction than NeRF's density-based formulation.

Training stabilization via geometry initialization

Directly training an SDF-based radiance field from random initialization often leads to vanishing gradients, since no ray finds a valid surface early in optimization. To mitigate this, NeuS biases the final layer of the SDF network such that its zero-level set initially approximates a coarse sphere around the scene. This "geometry initialization" ensures that rays intersect meaningful surfaces at the start of training, stabilizing the optimization process. As learning progresses, the initialized surface quickly deforms to match the actual scene geometry.

Experiments and Ablations

Experimental setup

NeuS is evaluated on the DTU dataset, which provides multi-view images with ground-truth geometry. Reconstructions are reported both *with* and *without* mask supervision. Mask supervision means that a foreground mask of the object is available during training, ensuring that background pixels do not bias the reconstruction. Without mask supervision, the method must disentangle object and background purely from image observations.

Quantitative results

The following table reports Chamfer distance (lower is better) across multiple DTU scans, comparing NeuS to prior implicit reconstruction methods (IDR [731], UNISURF [455]) and to volumetric rendering baselines (NeRF [429]) and COLMAP [553]. NeuS consistently achieves the lowest mean error (0.84), significantly outperforming both NeRF and UNISURF.

ScanID	IDR	NeRF	NeuS	COLMAP	NeRF (w/o mask)	UNISURF	NeuS (w/o mask)
24	1.63	1.83	0.83	0.81	1.90	1.32	1.00
37	1.87	2.39	0.98	2.05	1.60	1.36	1.37
40	0.63	1.79	0.56	0.73	1.85	1.72	0.93
55	0.48	0.66	0.37	1.22	0.58	0.44	0.43
63	1.04	1.79	1.13	1.79	2.28	1.35	1.10
65	0.79	1.44	0.59	1.58	1.27	0.79	0.65
69	0.77	1.50	0.60	1.02	1.47	0.80	0.57
83	1.33	1.20	1.45	3.05	1.67	1.49	1.48
97	1.16	1.96	0.95	1.40	2.05	1.37	1.09
105	0.76	1.27	0.78	2.05	1.07	0.89	0.83
106	0.67	1.44	0.52	1.00	0.88	0.59	0.52
110	0.90	2.61	1.43	1.32	2.53	1.47	1.20
114	0.42	1.04	0.36	0.49	1.06	0.46	0.35
118	0.51	1.13	0.45	0.78	1.15	0.59	0.49
122	0.53	0.99	0.45	1.17	0.96	0.62	0.54
Mean	0.90	1.54	**0.77**	1.36	1.49	1.02	**0.84**

Table 23.10: Quantitative evaluation on the DTU dataset. NeuS achieves the lowest Chamfer distance both with and without mask supervision. COLMAP results use trim=0.

Qualitative comparisons

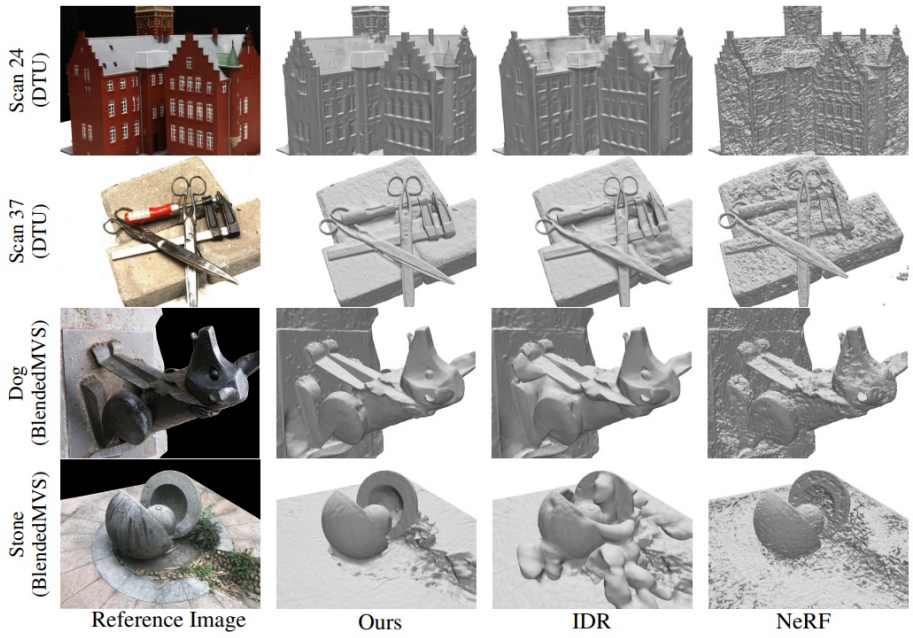

Figure 23.63: Comparison of surface reconstruction with mask supervision. NeuS generates the most accurate surfaces. IDR produces smooth but wrong geometry, while NeRF captures geometry but with many artifacts.

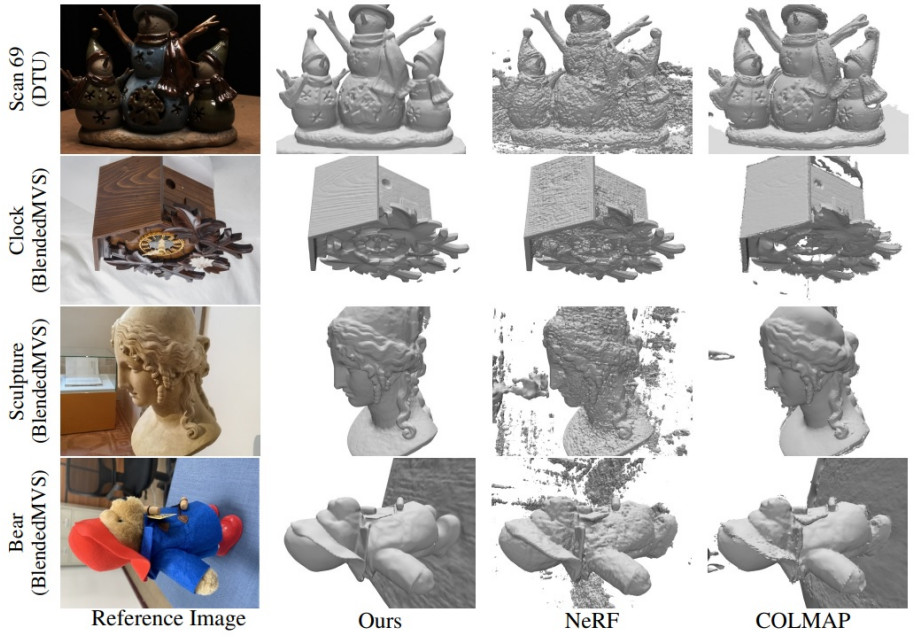

Figure 23.64: Comparison of surface reconstruction without mask supervision. NeuS is robust, while NeRF introduces artifacts and COLMAP removes parts of the object or hallucinates noise.

Ablation studies

The contribution of each component in NeuS is verified via ablation. The following table reports Chamfer distance and mean absolute error (MAE) between ground-truth and predicted SDF values. The results highlight the necessity of all components: naive volume rendering (a) and direct SDF supervision (b) fail catastrophically; removing the Eikonal regularization (c) or geometry initialization (d) significantly degrades performance; only the full model (e) achieves low reconstruction error.

Variant	Chamfer Distance	MAE
(a) Naive Solution	1.49	1.75
(b) Direct Solution	4.45	44.34
(c) w/o Eikonal	0.64	88.94
(d) w/o Geo-Init.	0.62	6.19
(e) Full Model	**0.59**	**0.93**

Table 23.11: Ablation studies on DTU. Removing the Eikonal loss or geometric initialization substantially harms reconstruction accuracy.

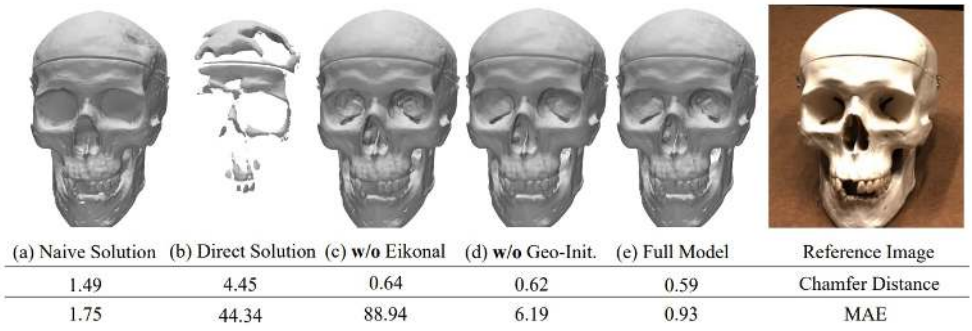

Figure 23.65: Qualitative ablations. NeuS requires all components—S-density, Eikonal regularization, and geometry initialization—for faithful reconstruction.

Limitations and Related Work

While NeuS delivers high-quality surface reconstructions via its signed distance field (SDF)–based volume rendering, it has notable limitations:

- **Computational cost:** The reliance on per-sample MLP evaluations and SDF-to-density conversion makes training and inference slower compared to standard NeRF pipelines.
- **Mask dependency:** Although NeuS works without mask supervision, accurate foreground masks significantly boost reconstruction fidelity; without them, detail in thin or complex structures can suffer.
- **Topology challenges:** Representing highly intricate or open surfaces remains a challenge for closed-surface SDF models.

Previous works.

- **IDR** [731]: Introduced differentiable rendering of implicit surfaces using signed distance functions (SDFs), supervising geometry through surface normals and photometric consistency. While conceptually elegant, IDR struggled with complex or open-topology scenes (e.g., buckets or vases), where normal-based rendering did not provide stable gradients. NeuS builds directly on IDR's use of SDFs but resolves its instability by adopting a volume rendering formulation, yielding more consistent optimization signals and sharper reconstructions.

Concurrent works.

- **VolSDF** [732]: Proposed mapping SDF values to densities via a Laplace cumulative distribution function (CDF), enabling smoother and more stable volume rendering than IDR. However, VolSDF used a *fixed* sharpness parameter, which limited its ability to adapt across varying surface scales. NeuS improved on this by introducing a *learnable* sharpness, allowing adaptive localization of surfaces and producing significantly crisper reconstructions, especially in fine-detail regions.
- **UNISURF** [455]: Presented a unified framework bridging NeRF and implicit surface rendering. Unlike NeuS, UNISURF relied more heavily on external mask supervision, which limited its robustness in unconstrained scenarios. Both works shared the motivation of reconciling surface-based and volumetric representations, but NeuS advanced the field by learning the SDF-to-density mapping directly, reducing reliance on explicit segmentation cues.

Later works.

- **HF-NeuS** [682]: Decomposed the SDF into base and residual frequency components, enabling reconstruction of thin structures and high-frequency detail (e.g., sharp edges or wires). While improving fidelity compared to NeuS, it retained the same runtime bottlenecks since both relied on per-point MLP evaluation.
- **PET-NeuS** [683]: Replaced dense per-point MLP queries with tri-plane encodings, where features were stored in structured 2D planes and interpolated during rendering. This design improved efficiency and detail, addressing NeuS's computational cost while preserving its SDF-based accuracy.
- **NeUDF** [377]: Generalized NeuS-style rendering to unsigned distance functions (UDFs), removing the assumption of closed surfaces inherent to SDFs. This allowed robust reconstructions of open and thin structures (e.g., curtains, leaves, or perforated objects) that NeuS struggled with, thus broadening applicability to more complex real-world geometries.
- **KiloNeuS** [147]: Partitioned the scene into thousands of small MLP "experts," drastically reducing training and inference time. Compared to NeuS, which required hours of optimization, KiloNeuS achieved near real-time performance while maintaining competitive quality, making SDF-based rendering far more practical.
- **NeuS2** [681]: Extended NeuS with hash-grid encodings and optimized CUDA kernels, reducing training from hours to minutes per scene. Crucially, NeuS2 also incorporated support for *dynamic scenes*, handling time-varying geometry and appearance—a limitation in the original NeuS. This positioned NeuS2 as a scalable and general successor.
- **GSDF** [744]: Combined NeuS-style SDF geometry with Gaussian Splatting for appearance modeling. The motivation was that SDFs excel at representing surfaces but are inefficient for view-dependent appearance, while Gaussians offer fast rasterization and smooth view interpolation. By splitting geometry (SDF) and appearance (Gaussians), GSDF improved both quality and rendering efficiency compared to pure NeuS.

Enrichment 23.10.8: Point-NeRF: Point-based Neural Radiance Fields

Point-NeRF [714] introduces a point-based neural radiance field representation that combines the strengths of explicit point clouds and implicit volumetric rendering. Unlike NeRF [429], which fits a global MLP per scene, Point-NeRF leverages neural point clouds that encode local geometry and appearance features, enabling efficient feed-forward initialization and rapid per-scene optimization. This summary details the motivation, method, architecture, experiments, limitations, and follow-up work.

Motivation

Classical NeRF methods achieve impressive view synthesis results but suffer from inefficiency: each scene requires hours or days of optimization, and significant computation is wasted sampling empty space. Point clouds, by contrast, provide explicit geometric priors but often suffer from holes, noise, or sparsity when reconstructed using MVS or SfM pipelines (e.g., COLMAP [553]).

Point-NeRF addresses both challenges by:

- Using neural points distributed near surfaces to avoid sampling empty space.
- Enabling direct feed-forward initialization of neural radiance fields via deep MVS prediction.
- Employing point pruning and growing to repair sparse or noisy point clouds.

This hybrid approach leads to reconstructions that surpass NeRF in quality and efficiency, converging in tens of minutes up to a several hours instead of days.

Figure 23.66: Point-NeRF efficiently reconstructs fine details (e.g., leaf structures) in tens of minutes, unlike NeRF which requires days of optimization. It can also initialize from raw COLMAP point clouds and refine them via pruning and growing. Credit: [714].

Method

Overview

Point-NeRF reconstructs a continuous radiance field by augmenting an *explicit* 3D point set with *neural* attributes and rendering it with a lightweight, local MLP. Crucially, the 3D points and their initial attributes are obtained by **scene-independent, feed-forward** networks that operate directly on posed images—so a new scene can be initialized relatively fast without re-training these networks.

Inputs. We are given a calibrated image set

$$\mathscr{I}_Q = \{(I_q, \Phi_q)\}_{q=1}^{Q}, \quad \Phi_q = (K_q, R_q, t_q),$$

i.e., Q RGB images with known intrinsics/extrinsics.

Scene-independent initialization (learned across many scenes). Point-NeRF trains two modules *across scenes* so they generalize to new inputs and provide a fast, scene-agnostic initialization:

- **Geometry/Confidence module $G_{p,\gamma}$ (MVSNet-style 3D CNN).** For a *reference* view q with a small set of *neighboring* source views $\mathcal{N}(q)$ (typically $|\mathcal{N}(q)|$=2), $G_{p,\gamma}$ proceeds as follows:

  1. *Plane-swept cost volume.* Build a 3D tensor over (u,v,d) by *differentiably warping* source-view feature maps onto *fronto-parallel planes* placed at discrete depths $d \in \mathscr{D}$ in the reference frustum (plane-induced homographies). At each pixel (u,v) and plane d, we compute a *cost* (e.g., channel-wise variance across the warped sources) that measures multi-view *agreement*. *Intuition:* if the hypothesized plane passes through the true surface seen at (u,v), the warped source features align well and the cost is low; otherwise they disagree and the cost is high.
  2. *Regularization and probabilities.* A compact 3D CNN regularizes the noisy cost volume and outputs *depth logits* $L_q(u,v,d)$; applying a softmax along d gives the *depth probability volume*

  $$P_q(u,v,d) = \frac{\exp L_q(u,v,d)}{\sum_{d' \in \mathscr{D}} \exp L_q(u,v,d')} \in [0,1], \quad \sum_{d \in \mathscr{D}} P_q(u,v,d) = 1.$$

  Intuition: the logits are unnormalized scores; after softmax, $P_q(u,v,\cdot)$ becomes a *distribution* along the reference ray stating how likely each depth hypothesis explains pixel (u,v) given all views.
  3. *Depth regression (soft-argmin).* Regress a *single* expected depth per pixel by the probability-weighted average

  $$D_q(u,v) = \sum_{d \in \mathscr{D}} d\, P_q(u,v,d).$$

  Intuition: $D_q(u,v)$ is the (differentiable) expectation of the per-ray depth distribution. If $P_q(u,v,\cdot)$ is sharply peaked at some $d^\star$, then $D_q(u,v) \approx d^\star$ (like an argmax); if it is spread over nearby planes, D_q interpolates them, yielding sub-plane precision.
  4. *Unprojection to 3D points.* Using the reference camera parameters $\Phi_q = (K_q, R_q, t_q)$, back-project each pixel (u,v) with depth $d = D_q(u,v)$ into 3D:

  $$x_{\text{cam}} = d\, K_q^{-1} [u, v, 1]^\top, \qquad p = R_q^\top (x_{\text{cam}} - t_q) \in \mathbb{R}^3,$$

  producing a *per-view* point set $\{p_i^{(q)}\}_{i=1}^{N_q}$. *Intuition:* this lifts the 2D depth map D_q into a cloud of 3D anchors that sit on the most plausible surface along each reference ray.
  5. *Confidence from P_q.* Assign each 3D point a confidence by sampling the *depth probability* at its inferred depth:

  $$\gamma_i^{(q)} \approx P_q\big(u_i, v_i, D_q(u_i, v_i)\big) \in [0,1],$$

  using *tri-linear interpolation* in (u,v,d) to handle non-integer coordinates. *Intuition:* tri-linear sampling blends the eight neighboring grid values to evaluate P_q at the continuous location (u_i, v_i, d_i). If $P_q(u_i, v_i, \cdot)$ is *peaked* near d_i, the pixel's multi-view evidence strongly agrees there, so $\gamma_i^{(q)}$ is large; if it is *flat* or multi-modal, the depth is uncertain and $\gamma_i^{(q)}$ is small.

Generalization. Trained once across diverse scenes, $G_{p,\gamma}$ produces dense geometry and uncertainty-aware confidences for a *new* scene with a single forward pass (no per-scene retraining), yielding a fast and reliable geometric scaffold for Point-NeRF.

- **Feature module G_f (2D CNN).** Independently, G_f extracts multi-scale feature maps from each I_q (shared weights across views). For every 3D point $p_i^{(q)}$, we project it into visible training views and sample the corresponding feature maps; the sampled descriptors are fused (e.g., concatenation/averaging or a small fusion MLP) to obtain a per-point appearance vector $f_i^{(q)}$. G_f is also trained across scenes and reused as-is at inference.

Running $G_{p,\gamma}$ and G_f for several references yields per-view sets $\{(p_i^{(q)}, f_i^{(q)}, \gamma_i^{(q)})\}$. These are *combined* (union with light filtering/deduplication) into a single, scene-level neural point cloud

$$P = \{(p_i, f_i, \gamma_i) \mid i = 1, \ldots, N\},$$

which then drives fast, surface-aware rendering and the subsequent per-scene refinement (with pruning and growing).

Per-scene refinement ($\approx$ tens of minutes). Given the unified neural point cloud $P = \{(p_i, f_i, \gamma_i)\}_{i=1}^{N}$ (points $p_i \in \mathbb{R}^3$ with per-point features f_i from G_f and confidences γ_i), Point-NeRF renders a novel view by *differentiable ray marching* restricted to space *near* the point cloud. This restriction avoids wasting samples in empty regions and is implemented by querying, at each shading location, only the K nearest neural points within a radius R. *All* radiance and density predictions at shading locations are regressed from these local neighbors rather than a global MLP.

Ray setup and sampling (as in NeRF)

For a target camera with intrinsics K and extrinsics (R,t) (world$\to$camera), a pixel (u,v) defines a camera ray with origin at the camera center $o = -R^\top t$ and direction

$$d \;=\; \frac{R^\top K^{-1}[u,\,v,\,1]^\top}{\left\| R^\top K^{-1}[u,\,v,\,1]^\top \right\|}.$$

We sample depths $\{t_j\}_{j=1}^{M}$ along this ray (near$\to$far) and form shading locations $x_j = o + t_j d$ with spacings $\Delta_j = t_{j+1} - t_j$. The pixel color is accumulated via the standard volume-rendering rule

$$c \;=\; \sum_{j=1}^{M} \tau_j \big(1 - e^{-\sigma_j \Delta_j}\big)\, r_j, \qquad \tau_j \;=\; \exp\Big(-\sum_{t=1}^{j-1} \sigma_t \Delta_t\Big).$$

Intuition. At each sample x_j the density σ_j induces an *opacity* $\alpha_j = 1 - e^{-\sigma_j \Delta_j}$ (how much the sample contributes) and a *transmittance* τ_j (how much light survives from the ray origin up to x_j). The emitted/view-dependent color r_j is then weighted by the chance that the ray reaches x_j (τ_j) and "stops" there (α_j). High σ_j increases α_j (more contribution, more occlusion downstream); low σ_j passes energy forward.

Local neighbor query (surface-aware shading)

At each ray sample x_j we gather only the K nearest anchors within a radius R:

$$\mathcal{N}(x_j) \;=\; \Big\{ (p_i, f_i, \gamma_i) \;\Big|\; \|p_i - x_j\| \le R,\; K \text{ nearest} \Big\}.$$

Restricting computation to *nearby* anchors focuses shading near likely surfaces and avoids wasting samples in empty space. In practice, a uniform voxel grid or hash grid over $\{p_i\}$ accelerates neighbor lookup so that only cells intersected by the ray are visited.

Local feature regression (Eq. 3)
Each neighbor $(p_i, f_i, \gamma_i) \in \mathcal{N}(x_j)$ is turned into a *location-specific* descriptor by a small MLP F:

$$f_{i,x_j} = F\big(f_i,\, x_j - p_i\big).$$

Conditioning on the *relative* offset $x_j - p_i$ (with positional encoding in practice) grants translation invariance and lets each neural point act as a local 3D chart around itself.

Radiance aggregation (Eqs. 4–5)
Location-specific features are blended with inverse-distance weights and confidence modulation:

$$f_{x_j} = \frac{\sum_i \gamma_i w_i f_{i,x_j}}{\sum_i w_i}, \qquad w_i = \frac{1}{\|x_j - p_i\|}, \qquad r_j = R\big(f_{x_j}, d\big),$$

where R is a light MLP that also takes the viewing direction d (directional positional encoding). *Intuition:* nearby, high-confidence anchors dominate r_j, while distant or dubious anchors are downweighted.

Density aggregation (Eqs. 6–7)
Densities are produced in two stages:

$$\sigma_i = T\big(f_{i,x_j}\big), \qquad \sigma_j = \frac{\sum_i \sigma_i \gamma_i w_i}{\sum_i w_i}, \quad w_i = \frac{1}{\|x_j - p_i\|}.$$

Why both w_i and γ_i? w_i encodes **geometric proximity** (even a reliable point should not dominate far away), while γ_i encodes **reliability** (even a nearby point should contribute little if its confidence is low). Together they yield robust, surface-aware σ_j.

Putting the pieces together
For each pixel ray: (i) sample $\{x_j\}$, (ii) query $\mathcal{N}(x_j)$, (iii) compute $\{f_{i,x_j}\}$ via F, (iv) aggregate to r_j and σ_j via R and T, and (v) composite with

$$c = \sum_{j=1}^{M} \tau_j \big(1 - e^{-\sigma_j \Delta_j}\big)\, r_j, \qquad \tau_j = \exp\Big(-\sum_{t=1}^{j-1} \sigma_t \Delta_t\Big).$$

End-to-end optimization objective
Rendered colors are supervised by an ℓ_2 photometric loss L_{render} (optionally plus perceptual terms). During *per-scene* refinement, gradients *do* flow into the neural point cloud attributes and the local shading MLPs, while the scene-agnostic generators $G_{p,\gamma}$ and G_f remain *frozen* (they were pretrained across scenes to provide fast initialization). Concretely, we update:

- **Per-point attributes** (f_i, γ_i): f_i specializes to the scene's appearance; γ_i sharpens so anchors truly on-surface receive high confidence while outliers are suppressed.
- **Local MLPs** F, R, T: adapt the mapping from neighbor-conditioned features to (r, σ) for this scene.
- **Topology (discrete edits)**: instead of moving p_i continuously (unstable and unable to close large holes), we use *pruning* and *growing*.

The total loss is

$$L_{\text{total}} \;=\; L_{\text{render}} \;+\; \lambda_{\text{sparse}}\, L_{\text{sparse}}, \qquad L_{\text{sparse}} \;=\; \frac{1}{|\gamma|}\sum_i \big[\log(\gamma_i) + \log(1-\gamma_i)\big],$$

which (per paper Eq. (10)) polarizes confidences toward $\{0,1\}$ and makes pruning decisions unambiguous.

Topology edits during refinement (per paper)

Pruning. Points with persistently low confidence are removed; specifically, every 10K iterations, points with $\gamma_i < 0.1$ are pruned (as in the paper), eliminating outliers and reducing neighborhood clutter.

Growing. To *add* anchors where geometry is missing, use the current field to propose new points along training rays. For a sample at x_j with density σ_j and step Δ_j, define the instantaneous opacity

$$\alpha_j \;=\; 1 - \exp(-\sigma_j \Delta_j).$$

Let $j_g = \arg\max_j \alpha_j$ be the most opaque sample on the ray (paper Eq. (11)). If (i) α_{j_g} exceeds an opacity threshold T_{opacity} (likely surface) and (ii) the distance from x_{j_g} to the nearest existing anchor exceeds T_{dist} (under-anchored region), insert a new point at $p_{\text{new}} = x_{j_g}$. Initialize its attributes as in the paper's pipeline: features f_{new} from G_f by projecting p_{new} into visible views and fusing sampled descriptors; confidence γ_{new} with a moderate prior (e.g., 0.3) that will be driven by $L_{\text{render}}+L_{\text{sparse}}$. Merging near-duplicates and updating the neighbor index keeps queries efficient.

Outcome. Because geometry and initial descriptors come from the *pretrained*, scene-independent generators ($G_{p,\gamma}$ and G_f), per-scene training converges in *tens of minutes* yet achieves quality competitive with or better than NeRF trained for hours. The confidence- and distance-weighted aggregation stabilizes learning, while pruning/growing self-organize the anchor set to close holes and remove outliers, preparing us for the next section on **Architecture & Implementation Details**.

Architecture and Implementation Details

- **Point Generation:** Depth maps predicted via a cost-volume 3D CNN $G_{p,\gamma}$, unprojected into 3D points with confidence γ_i.
- **Feature Extraction:** 2D CNN G_f (VGG-style) produces multi-scale features aligned with points.
- **Radiance/Density MLPs:** Small per-point MLPs regress local features, radiance, and density.
- **Positional Encoding:** Applied to relative positions and view directions.
- **Optimization:** Loss combines rendering error and sparsity penalty:

  $$L_{\text{opt}} = L_{\text{render}} + \alpha L_{\text{sparse}},$$

  with pruning/growing every 10k iterations.

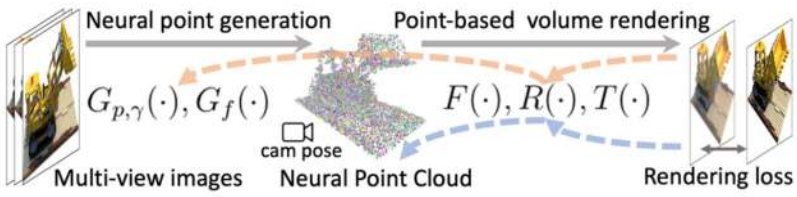

Figure 23.67: Point-NeRF optimization: dashed lines indicate gradient updates during initialization and per-scene finetuning. Credit: [714].

Experiments and Ablations

Point-NeRF is evaluated on DTU [262], NeRF-Synthetic [429], Tanks&Temples [299], and ScanNet [113]. This section reproduces the paper's reported numbers and highlights the main observations.

Table 23.12: DTU [262] (novel-view setting of [79]). Subscripts indicate training iterations.

	No Per-scene Optimization				**Per-scene Optimization**				
	PixelNeRF [739]	MVSNeRF [79]	IBRNet [654]	Point-NeRF	Point-NeRF$_{1K}$	Point-NeRF$_{10K}$	MVSNeRF$_{10K}$	IBRNet$_{10K}$	NeRF$_{200K}$ [429]
PSNR ↑	19.31	26.63	26.04	23.89	28.43	30.12	28.50	**31.35**	27.01
SSIM ↑	0.789	0.931	0.917	0.874	0.929	**0.957**	0.933	0.956	0.902
LPIPS$_{VGG}$ ↓	0.382	0.168	0.190	0.203	0.183	**0.117**	0.179	0.131	0.263
Time ↓	–	–	–	–	**2min**	20min	24min	1h	10h

DTU

With 1K iterations ($\approx$ 2 minutes), Point-NeRF already exceeds a NeRF baseline at 200K iterations ($\approx$ 10 hours) on PSNR/SSIM/LPIPS; at 10K iterations it attains the best SSIM and LPIPS among the listed methods (Table 1).

Table 23.13: NeRF-Synthetic [429]. Point-NeRF matches NeRF at 20K steps and surpasses it at 200K. "col" denotes initialization from COLMAP [553].

	NPBG [9]	NeRF [429]	IBRNet [654]	NSVF [370]	Point-NeRF$^{\text{col}}_{200K}$		
					Point-NeRF$_{20K}$		Point-NeRF$_{200K}$
PSNR ↑	24.56	31.01	28.14	31.75	31.77	30.71	**33.31**
SSIM ↑	0.923	0.947	0.942	0.964	0.973	0.967	**0.978**
LPIPS$_{VGG}$ ↓	0.109	0.081	0.072	–	0.062	0.081	**0.049**
LPIPS$_{Alex}$ ↓	0.095	–	–	0.047	0.040	0.050	**0.027**

NeRF-Synthetic

At 20K iterations ($\approx$ 40 minutes), Point-NeRF reaches NeRF-level quality; at 200K it surpasses NeRF on PSNR/SSIM/LPIPS (Table 2), with qualitative advantages on thin structures.

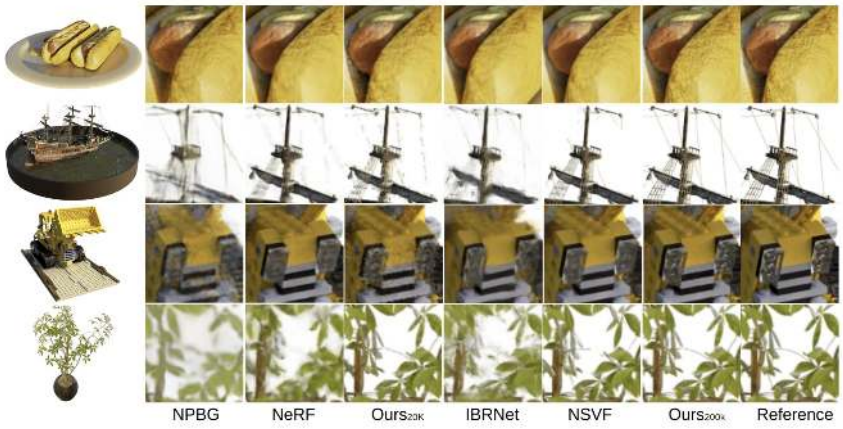

Figure 23.68: Qualitative comparisons on NeRF-Synthetic [429]. Subscripts indicate training iterations. Point-NeRF captures thin structures (e.g., the rope) and converges much faster than NeRF.

Tanks&Temples and ScanNet

On the Tanks&Temples subset of [299] (five scenes: *Ignatius, Truck, Barn, Caterpillar, Family*), Point-NeRF reports a mean 29.61 / 0.954 / 0.080 (PSNR / SSIM / $\text{LPIPS}_{\text{Alex}}$), which improves over NSVF's 28.40 / 0.900 / 0.153 by $+1.21$ dB PSNR, $+0.054$ SSIM, and -0.073 LPIPS (lower is better), indicating higher fidelity and better perceptual quality under larger, real scenes.

For ScanNet [113] (two scenes used by [370]), Point-NeRF achieves 30.32 / 0.909 / 0.220 versus NSVF's 25.48 / 0.688 / 0.301, i.e., $+4.84$ dB PSNR, $+0.221$ SSIM, and -0.081 $\text{LPIPS}_{\text{Alex}}$. These results follow the evaluation protocol of [370] (depth-image–initialized scenes) and show a consistent advantage in both accuracy and perceptual metrics on indoor scans.

Initialization from external COLMAP clouds

When starting from COLMAP points [553], pruning and growing (Sec. 23.10.8) substantially improve geometry and rendering. The following figure shows qualitative effects; The following table (paper's numbers) reports gains on `Ship` and `Hotdog`.

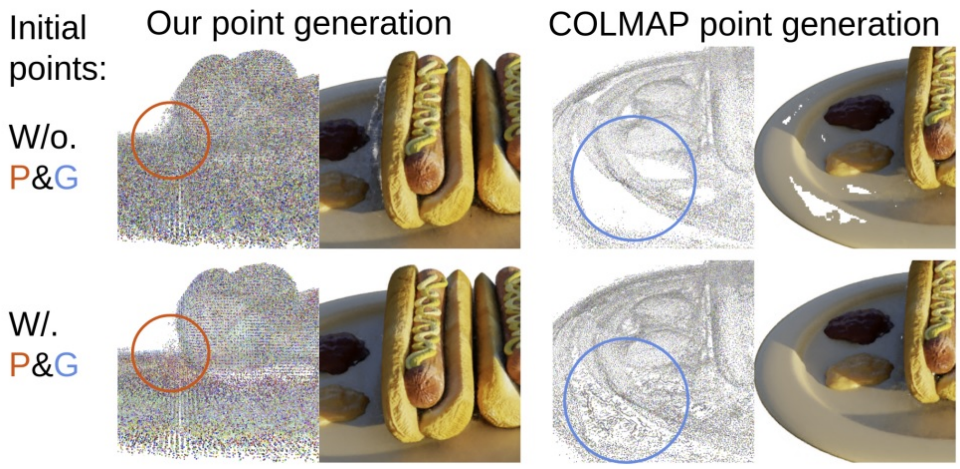

Figure 23.69: Pruning & growing (P&G) ablation. Removing outliers and adding anchors in high-opacity, under-anchored regions improves both geometry and rendering for predicted points and COLMAP-initialized points.

Table 23.14: Effect of pruning & growing (paper's Table 4). COLMAP: initialization from [553].

Method	`Ship` (PSNR / SSIM / $\text{LPIPS}_{\text{VGG}}$)	`Hotdog` (PSNR / SSIM / $\text{LPIPS}_{\text{VGG}}$)
Point-NeRF (No P&G)	25.50 / 0.878 / 0.182	34.91 / 0.983 / 0.067
Point-NeRF (With P&G)	**30.97 / 0.942 / 0.124**	**37.30 / 0.991 / 0.037**
COLMAP init (No P&G)	19.35 / 0.905 / 0.167	29.91 / 0.978 / 0.061
COLMAP init (With P&G)	**30.18 / 0.941 / 0.134**	**35.49 / 0.986** / 0.061

Feature-initialization ablation (paper's Table 5)
Initializing point features with extracted multi-view image features accelerates convergence and improves final metrics versus random initialization: *20K iters* PSNR/SSIM 30.09/0.963 (extracted) vs. 25.44/0.932 (random); *200K iters* 33.00/0.978 (extracted) vs. 32.01/0.972 (random).

Limitations

- **Dependence on seed quality.** The feed-forward initializer greatly accelerates setup, but extremely sparse or noisy initial geometry can still cap fidelity. Pruning/growing helps, yet very large holes or heavy outliers remain challenging to repair quickly.
- **Memory and neighborhood queries.** High point densities increase memory footprint and the cost of building/querying spatial indices. At render time, each shaded sample performs a local KNN aggregation, so throughput is ultimately limited by ray marching *and* repeated neighbor lookups.
- **Mesh extraction.** Even though the representation is anchored by explicit points, producing watertight, topologically consistent meshes from the learned radiance field is non-trivial, as in many radiance-field methods.

Outlook toward 3D Gaussian Splatting.
These bottlenecks motivate alternative *explicit* radiance parameterizations that trade local KNN aggregation and per-sample MLP evaluations for *analytic rasterization* of continuous primitives. A prominent next step is *3D Gaussian Splatting* [287], which represents the scene with anisotropic Gaussians carrying color (e.g., spherical-harmonics coefficients), opacity, and covariance. Rendering then becomes screen-space splatting with differentiable visibility, enabling much higher frame rates. In the following section, a comparison is drawn between Point-NeRF's point-anchored, ray-marched formulation and Gaussian-based splatting, clarifying how the latter alleviates neighbor-query overhead and amortizes rendering—while introducing its own visibility and ordering considerations.

Enrichment 23.10.9: 3D Gaussian Splatting: RT Radiance Field Rendering

Motivation and big picture

Context and objective

Radiance fields deliver high-fidelity novel views, but classic NeRF pipelines are costly at train and render time due to dense ray marching and repeated MLP evaluation. Fast explicit variants (Plenoxels, DVGO, Instant-NGP, TensoRF, etc.) accelerate this by replacing networks with explicit features or compact encodings, while *Point-NeRF* adopts point primitives with differentiable rasterization. *3D Gaussian Splatting (3DGS)* [287] represents the scene with *anisotropic 3D Gaussians* and renders them using a *visibility-aware, differentiable, tile-based* software rasterizer. Each 3D ellipsoid projects to a 2D ellipse whose Gaussian footprint is blended front-to-back, preserving the volumetric accumulation behavior while enabling real-time rendering once optimized.

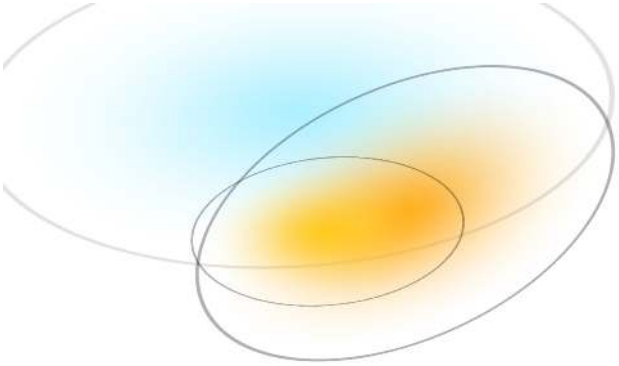

Figure 23.70: **From triangles to Gaussians** Instead of rasterizing mesh triangles, 3DGS renders many anisotropic 3D Gaussians; in screen space these appear as ellipses (borders shown for clarity). Illustration adapted from the Hugging Face overview [139].

Key idea

3D Gaussian Splatting (3DGS) renders scenes by *forward rasterization* instead of backward ray marching [287]. The scene is a collection of learnable *anisotropic 3D Gaussians*. Each Gaussian is projected to a soft 2D ellipse and blended in *front-to-back* depth order using α-compositing; this reproduces volumetric visibility while remaining GPU-friendly.

Core terms

A *3D Gaussian* is defined by a center $\mu \in \mathbb{R}^3$ and covariance $\Sigma \in \mathbb{R}^{3\times 3}$ with (unnormalized) density

$$G(x) \propto \exp\Big(-\tfrac{1}{2}(x-\mu)^\top \Sigma^{-1}(x-\mu)\Big).$$

If $\Sigma = \sigma^2 I$ the spread is the same in all directions (*isotropic*); otherwise it is direction-dependent and the shape is an oriented ellipsoid (*anisotropic*). 3DGS parameterizes the covariance in a sophisticated manner allowing simple optimization with minimal constraints.

How 3DGS uses Gaussians

Each Gaussian stores:

- geometry and opacity: (μ, R, S, a).
- appearance: a set of learned *spherical harmonics* (SH) coefficients for view-dependent color.

All parameters are optimized from posed images via backpropagation (details later).

From 3D to 2D footprints

We use the standard pinhole camera to map a 3D point to pixel *coordinates*. Let a world point be $x \in \mathbb{R}^3$. First apply the *extrinsics* $W = [R_c \,|\, t_c]$ (world→camera):

$$X \;=\; W\tilde{x} \;=\; \begin{bmatrix} X_c \\ Y_c \\ Z_c \end{bmatrix}, \qquad \tilde{x} = \begin{bmatrix} x \\ 1 \end{bmatrix},$$

so (X_c, Y_c, Z_c) are the point's coordinates in the camera frame and $Z_c{>}0$ is its *depth* along the optical axis. Then apply the *intrinsics*

$$K \;=\; \begin{bmatrix} f_x & 0 & c_x \\ 0 & f_y & c_y \\ 0 & 0 & 1 \end{bmatrix},$$

where f_x, f_y are focal lengths measured in *pixels* (scaling image-space units along u and v), and (c_x, c_y) is the principal point (optical center in pixels). The pinhole projection $\pi : \mathbb{R}^3 \to \mathbb{R}^2$ is

$$(u, v) \;=\; \pi(X) \;=\; \Big(f_x \tfrac{X_c}{Z_c} + c_x,\;\; f_y \tfrac{Y_c}{Z_c} + c_y \Big),$$

i.e., we form normalized image coordinates $(X_c/Z_c, Y_c/Z_c)$ and then scale/shift by (f_x, f_y) and (c_x, c_y).

Local linearization and the projection Jacobian To obtain a simple, differentiable footprint for each Gaussian, we linearize the *pixel coordinates* near its center μ. Let $X_0 = W\mu = (X_0, Y_0, Z_0)^\top$ be the center in camera space. The *projection Jacobian* $J \in \mathbb{R}^{2\times 3}$ is the derivative of pixel coordinates with respect to camera coordinates at X_0:

$$J \;=\; \left.\frac{\partial (u, v)}{\partial (X_c, Y_c, Z_c)}\right|_{X_0} \;=\; \begin{bmatrix} \dfrac{f_x}{Z_0} & 0 & -\dfrac{f_x X_0}{Z_0^2} \\[2ex] 0 & \dfrac{f_y}{Z_0} & -\dfrac{f_y Y_0}{Z_0^2} \end{bmatrix}.$$

Thus a small 3D motion δX near X_0 produces a pixel shift $\delta p \approx J\,\delta X$: lateral moves (X_c, Y_c) shift pixels by roughly $f_{x,y}/Z_0$ (more at small depth, less when far), while motion along Z_c changes *scale*, pushing pixels outward as the point approaches the camera.

Induced 2D covariance Gaussian covariances transform under a linear map A as $A\Sigma A^\top$. Since a small world-space displacement δx maps to pixels by $\delta p \approx (JW)\,\delta x$, the *screen-space* covariance is

$$\Sigma' \;=\; JW\Sigma W^\top J^\top.$$

Geometrically, the 3D ellipsoid becomes a 2D ellipse whose orientation and size encode local perspective (rotation, foreshortening, scale). This Σ' defines a soft, rapidly decaying footprint over nearby pixels; farther from the ellipse center, the contribution to the pixel is smaller.

View-dependent color with spherical harmonics

For a fixed view, each projected ellipse contributes *one* RGB color; only its per-pixel weight $\alpha_i(x)$ varies across the footprint. That color is a function on directions $\hat{\mathbf{v}}_i = (o-\mu_i)/\|o-\mu_i\| \in \mathbb{S}^2$ and is expanded in *real spherical harmonics* (an orthonormal basis on the unit sphere, analogous to a Fourier/Taylor basis but for directions):

$$c_i(\hat{\mathbf{v}}_i) = \sum_{l=0}^{L} \sum_{m=-l}^{l} \mathbf{c}_{i,lm}\, Y_{lm}(\hat{\mathbf{v}}_i),$$

where Y_{lm} are basis functions on $\mathbb{S}^2$ and $\mathbf{c}_{i,lm} \in \mathbb{R}^3$ are learned per-Gaussian coefficients. Low degrees L capture smooth, low-frequency view dependence; higher L add directional detail. Training *starts at* L=0 (constant color) to stabilize geometry and opacity, then *ramps L up* (e.g., to a small order) to introduce view dependence without a large decoder [287].

Rasterize and composite

For each view, 3DGS projects all Gaussians, sorts overlapping footprints front-to-back within image tiles, and blends them using α-compositing. If $\alpha_k(x)$ is the per-pixel opacity of the k-th (depth-sorted) Gaussian at pixel x, and c_k is its view-dependent color, the accumulated color uses the *transmittance* $T_{k-1}(x)$ (remaining visibility before k):

$$C(x) \;=\; \sum_k T_{k-1}(x)\,\alpha_k(x)\,c_k, \qquad T_k(x) \;=\; T_{k-1}(x)\,\big(1-\alpha_k(x)\big), \quad T_0(x)=1.$$

This reproduces the effect of volumetric rendering but operates on 2D ellipses (no per-ray samples).

Why this design is effective

- **Quality with compactness** Anisotropic Gaussians align to edges and thin structures, achieving sharp detail with fewer primitives (vs. isotropic point splats or uniformly sampled ray accumulations).
- **Surface alignment and subpixel fidelity** Oriented ellipses capture anisotropic image gradients (edges, ridges), reducing holes and flicker compared with Point-NeRF and classic NeRF.
- **Explicit visibility with dense gradients** Front-to-back α-compositing gives crisp occlusion ordering, and the differentiable rasterizer sends gradients to *many* overlapping splats per pixel, avoiding k-nearest sparsity and per-ray sample sparsity.
- **Efficient view dependence** Per-Gaussian spherical harmonics (SH) produce smooth directional color without a large MLP; degree ramping stabilizes early training. [287].
- **Capacity steering in 3D** The clone/split/prune schedule adapts both the *number* and the *shape/orientation* of primitives, concentrating dof where reprojection errors are high.
- **Real-time rendering** 2D rasterization on projected ellipses replaces expensive ray marching.
- **Tile-wise global ordering** A single radix sort by depth and tile enables coherent front-to-back blending with early termination once transmittance saturates.
- **Stable, fast optimization** The covariance parameterization and closed-form projection to Σ' yield well-behaved gradients; analytic derivatives for the parameters avoid fragile PSD constraints and heavy autodiff through eigendecompositions.

In what follows we derive 3DGS step by step, and then then turn to experiments and ablations, and conclude with limitations and follow-up work.

3D Gaussian Splatting stages

Before we dive into the details, we give a high-level walkthrough of the 3DGS pipeline, linking the core idea—forward rasterization of anisotropic 3D Gaussians—to the concrete steps used for projection, image formation, optimization, and real-time rendering.

1. **Initialization** From calibrated multi-view images, run SfM to recover camera poses and a sparse point cloud. Seed one Gaussian per SfM point with center μ, rotation R (via a unit quaternion), diagonal scale $S = \mathrm{diag}(s_x, s_y, s_z)$, opacity a, and a small set of real spherical-harmonics (SH) coefficients for view-dependent color. For stability, begin with degree L=0 (constant color) and *ramp* L upward as geometry and opacity settle.
2. **Projection** Around each center μ, locally linearize the pinhole camera. With world→camera transform W and the 2×3 projection Jacobian J at $W\mu$, the 3D covariance $\Sigma = (RS)(RS)^\top$ becomes the screen-space covariance

   $$\Sigma' \;=\; JW\Sigma W^\top J^\top.$$

   Thus a 3D ellipsoid projects to a soft 2D ellipse (splat) with image mean $u = \pi(W\mu)$. The camera-space depth Z_c of μ will define *visibility order*.
3. **Image formation** For pixel x, each overlapping splat contributes a *weight* (opacity) that decays with its elliptical distance:

   $$\alpha_i(x) \;\propto\; a_i \exp\Big(-\tfrac{1}{2}(x-u_i)^\top \Sigma_i'^{-1}(x-u_i)\Big).$$

   The splat's *color* is evaluated once per view from its SH expansion at the unit view direction $\hat{\mathbf{v}}_i = (o-\mu_i)/\|o-\mu_i\|$:

   $$c_i(\hat{\mathbf{v}}_i) \;=\; \sum_{l=0}^{L}\sum_{m=-l}^{l} \mathbf{c}_{i,lm}\, Y_{lm}(\hat{\mathbf{v}}_i).$$

   Splat colors are then accumulated using *front-to-back* α-compositing:

   $$C(x) \;=\; \sum_k T_{k-1}(x)\,\alpha_k(x)\,c_k, \qquad T_k(x) \;=\; T_{k-1}(x)\big(1-\alpha_k(x)\big), \quad T_0(x)=1.$$

   Why front-to-back Gaussians are processed from *nearest to farthest* (increasing Z_c). This respects occlusions (near splats naturally hide far ones) and enables *early termination*: once $T_{k-1}(x)$ becomes very small (pixel nearly opaque), remaining far splats can be skipped, saving work without changing the result.
4. **Optimization and adaptive densification** Optimize all parameters $(\mu, R, S, a, \text{SH})$ end-to-end with Adam under a photometric loss (typically L1 + SSIM). Every few iterations, apply *density control* to match detail to error signals: *clone* small Gaussians in high-gradient regions (under-reconstruction), *split* over-large splats into two smaller ones when gradients suggest unresolved structure, and *prune* nearly transparent or excessively large Gaussians. The SH degree L is increased during training so view dependence is learned after geometry stabilizes.
5. **Real-time rendering** A GPU *tile-based* differentiable rasterizer frustum-culls Gaussians, bins them into fixed-size tiles (e.g., 16×16), globally sorts by (tile, depth), and blends per-pixel in *front-to-back* order. The visibility-aware order gives correct occlusion and allows *early-out* when transmittance saturates; a compact backward pass records only touched splats for gradients. Together these yield real-time novel-view synthesis once trained.

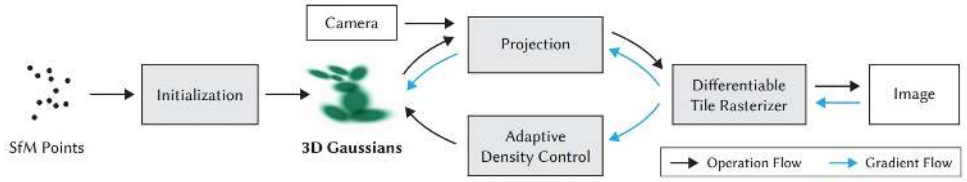

Figure 23.71: **Optimization pipeline** Initialization from a sparse SfM point cloud, followed by interleaved gradient-based optimization and adaptive density control using a fast, tile-based differentiable renderer. Once trained, the representation supports RT novel-view navigation. Adapted from [287].

Representation and parameterization

From mean–covariance to a renderable primitive

A 3D Gaussian is specified by a *mean* $\mu \in \mathbb{R}^3$ and a *covariance* $\Sigma \in \mathbb{R}^{3\times 3}$, with (unnormalized) density

$$G(x) \;\propto\; \exp\Big(-\tfrac{1}{2}(x-\mu)^\top \Sigma^{-1}(x-\mu)\Big).$$

The quadratic form $(x-\mu)^\top \Sigma^{-1}(x-\mu)$ acts like a squared distance (the *Mahalanobis* distance). Let $\Sigma = Q\Lambda Q^\top$ be the eigendecomposition, where $Q = [e_1\ e_2\ e_3]$ has unit, mutually orthogonal columns (the *principal directions*) and $\Lambda = \mathrm{diag}(\lambda_1,\lambda_2,\lambda_3)$ with $\lambda_i \geq 0$ (the *principal variances*). Then:

- **Principal directions** e_i are unit vectors in $\mathbb{R}^3$ that define the ellipsoid's axes. They coincide with the canonical $x/y/z$ axes *only if* Σ is already diagonal in that basis. In general, e_i are rotated versions of $x/y/z$.
- **Level sets** are the sets of points where the density has the same value, equivalently where the Mahalanobis distance is constant:

  $$\{x \in \mathbb{R}^3 : (x-\mu)^\top \Sigma^{-1}(x-\mu) = k\} \quad (k > 0).$$

  In 3D these level sets are ellipsoids centered at μ with semi–axis lengths $\sqrt{k\,\lambda_i}$ along directions e_i. The constant k simply picks "how far out" the surface is (larger $k \Rightarrow$ a larger, similar ellipsoid). Intuitively, you can think of k as selecting a "constant–standard–deviation" contour, generalized to 3D.
- **Isotropy vs. anisotropy** If $\Sigma = \sigma^2 I$, then e_i align with $x/y/z$ and all $\lambda_i = \sigma^2$, producing a sphere (isotropic spread). If the λ_i differ and/or $Q \neq I$, the ellipsoid is stretched and rotated (anisotropic spread).

In practical terms, *increasing a variance* (some λ_i) makes the ellipsoid longer along the corresponding principal direction e_i; introducing *covariance* (nonzero off–diagonals in Σ) rotates the principal directions away from $x/y/z$. After local projection to the image, these adjustments control the width and orientation of the resulting 2D ellipse (the screen–space footprint).

Initialization and the need for valid, optimizable covariances

3DGS initializes one Gaussian per SfM point to cover the coarse geometry, then continuously optimizes the set while *adding, cloning, splitting, and pruning* primitives (densification) as required by the data [287]. During training, every covariance must remain a *valid* covariance (symmetric and positive semidefinite):

$$\Sigma = \Sigma^\top, \qquad x^\top \Sigma x \geq 0 \ \ \forall x.$$

Naively updating the free entries of Σ can violate these constraints (e.g., negative eigenvalues), destabilizing learning and yielding non-physical shapes. A parameterization that preserves validity by construction is therefore essential.

Choosing a geometry parameterization for valid optimization

As directly updating the parameters of the covariance matrix Σ can violate *symmetry* or *positive semidefiniteness* (PSD), which destabilizes learning. 3DGS instead optimizes a *decoupled* set of variables and reconstructs Σ from them:

$$(\mu, R, S) \quad \text{with} \quad \Sigma = RSS^\top R^\top,$$

where

- $\mu \in \mathbb{R}^3$ is the 3D center (learned by gradient descent).
- $R \in \mathbb{R}^{3\times 3}$ is a rotation matrix ($R^\top R = I,\ \det(R) = 1$) obtained from a *unit quaternion* that is re-normalized after each update.
- $S = \mathrm{diag}(s_x, s_y, s_z)$ holds *positive* axis scales (enforced via a positivity reparameterization, e.g., exp or sigmoid activation).

Because $SS^\top$ is PSD and R is orthonormal, $RSS^\top R^\top$ is *always* symmetric PSD, so validity is guaranteed throughout training—no eigen-clamping or PSD projection is needed. Equally important, this form *decouples* orientation (R) from axis lengths (S), yielding interpretable, well-conditioned updates; in contrast, editing Σ directly entangles rotation and scale (off-diagonals simultaneously tilt and shear), making gradients harder to interpret and constrain. The paper also provides closed-form derivatives w.r.t. the scale and quaternion parameters, avoiding fragile eigendecompositions.

Intuition and practical knobs for R and S

Think of S as the *axis lengths* and R as the *steering wheel* that orients those axes in space:

- **Vary s_x or s_y (with R fixed)** stretches or shrinks the ellipsoid along the corresponding rotated axes in world space. After projection the screen-space ellipse widens mainly along the matching image directions, helping one primitive cover elongated features (e.g., edges) with fewer neighbors.
- **Vary s_z (depth thickness)** increases extent roughly along the view-normal direction, adding controllable *thickness*. This improves coverage of slanted, foreshortened surfaces across nearby views and reduces holes.
- **Rotate R (with S fixed)** re-orients the ellipsoid without changing its radii. The projected ellipse rotates accordingly, letting a single primitive align with wires, leaf stems, fence slats, or oblique edges—capturing anisotropic detail compactly and reducing flicker.

These independent knobs let 3DGS *tilt, stretch, and thicken* coverage to match local geometry in 3D while keeping every covariance valid during optimization.

Opacity as a direct parameter

3DGS replaces NeRF's ray–integrated density with a *per–Gaussian* opacity that directly gates the screen–space footprint. For Gaussian i we keep an unconstrained logit $\tilde{a}_i \in \mathbb{R}$ and map it to a bounded opacity

$$a_i = \sigma(\tilde{a}_i) = \frac{1}{1+e^{-\tilde{a}_i}} \in (0,1),$$

optionally clamped to $a_i \in [\varepsilon, 1-\varepsilon]$ (e.g., $\varepsilon = 10^{-3}$) for numerical stability.

After projection, the ellipse has center u_i and screen–space covariance Σ_i'. Its *per–pixel* alpha (used in compositing) is the unnormalized Gaussian falloff scaled by a_i:

$$\alpha_i(x) \;=\; a_i \,\exp\!\Big(-\tfrac{1}{2}\,(x-u_i)^\top \Sigma_i'^{-1}(x-u_i)\Big).$$

Thus $\alpha_i(u_i) = a_i$ and $\alpha_i(x) \le a_i < 1$ elsewhere. Colors are then blended in *front–to–back* order using the transmittance recursion, which both respects occlusion and enables early termination once the remaining visibility is negligible [287].

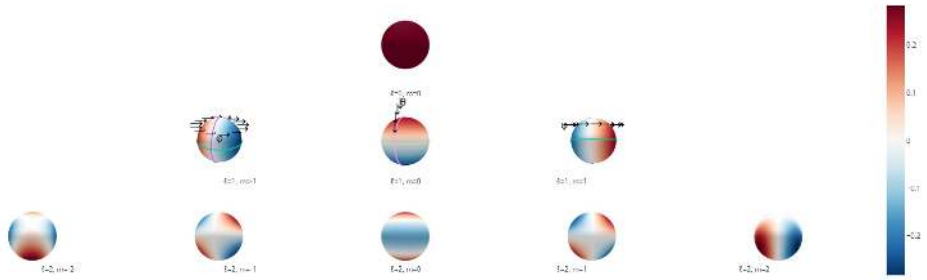

Figure 23.72: **Spherical–harmonics basis intuition.** Each panel shows a real spherical harmonic $Y_{\ell m}(\theta,\phi)$ on the unit sphere. Red/blue indicate positive/negative values and white shows nodal sets (zeros). The degree ℓ controls the number of latitudinal (polar) bands, while $|m|$ controls the number of longitudinal (azimuthal) oscillations. Changing the sign of m rotates the pattern around the vertical axis without altering its node counts. Small glyphs on the $\ell = 1$ row mark whether variation is with ϕ (horizontal, around the equator) or with θ (vertical, pole to equator).

How to read Fig. 23.72 and why SH suit 3DGS. Directions live on the unit sphere $\mathbb{S}^2$, and $\{Y_{\ell m}\}$ form an orthonormal basis, much like Fourier modes on a circle.

- **Degree ℓ:** sets angular resolution. Larger ℓ means more bands in θ (north–south).
- **Order m:** sets azimuthal detail. $|m|$ counts nodal meridians in ϕ (east–west), while $\ell - |m|$ counts nodal circles in θ.

Examples in Fig. 23.72:

- $\ell = 0$ (monopole):
  - $m = 0$: constant everywhere, no variation.
- $\ell = 1$ (dipoles):
  - $m = -1$: varies left–right with ϕ, one vertical nodal plane; vanishes at poles.
  - $m = 0$: varies up–down with θ, node at the equator (north pole red, south pole blue).
  - $m = 1$: same as $m = -1$ but rotated 90° around z.
- $\ell = 2$ (quadrupoles):
  - $m = -2$: four lobes around the equator, separated by two vertical nodal planes (90° apart); zeros at poles.
  - $m = -1$: four lobes alternating across equator and meridian; one vertical plane and one horizontal circle as nodes.
  - $m = 0$: two polar caps of one sign and an equatorial belt of the opposite sign; nodal circles at $\cos^2\theta = \frac{1}{3}$.
  - $m = 1$: same as $m = -1$ but rotated 90° in ϕ.
  - $m = 2$: same as $m = -2$ but rotated 90° in ϕ.

This basis is ideal for 3D Gaussian Splatting: the view direction $\hat{\mathbf{v}}$ lies on $\mathbb{S}^2$, and a low-order SH expansion provides a compact, smooth, differentiable way to represent each Gaussian's view-dependent color.

Appearance as a directional color field

For a fixed camera, each projected ellipse contributes *one* RGB that depends on the unit view direction $\hat{\mathbf{v}} = (o-\mu)/\|o-\mu\| \in \mathbb{S}^2$. 3DGS models this *per channel* with a real spherical–harmonics (SH) expansion

$$c^{(r)}(\hat{\mathbf{v}}) = \sum_{l=0}^{L}\sum_{m=-l}^{l} c_{lm}^{(r)} Y_{lm}(\hat{\mathbf{v}}), \qquad c^{(g)}(\hat{\mathbf{v}}) = \sum_{l=0}^{L}\sum_{m=-l}^{l} c_{lm}^{(g)} Y_{lm}(\hat{\mathbf{v}}),$$
$$c^{(b)}(\hat{\mathbf{v}}) = \sum_{l=0}^{L}\sum_{m=-l}^{l} c_{lm}^{(b)} Y_{lm}(\hat{\mathbf{v}}),$$

so there are $(L+1)^2$ coefficients per channel (e.g., $L=2$ uses 9 per channel, 27 total). Real SH form an orthonormal basis on directions.

Practical intuition.

- $L=0$ (only Y_{00}): view–independent "clay ball" color; good for diffuse walls or matte plastic.
- $L\approx 1$–2: broad, smooth directional changes (fabric sheen, brushed metal, soft grazing–angle brightening).
- $L\approx 2$–3: sharper lobes suitable for glossy paint/ceramic and weak specular highlights.

Very mirror–like effects would require still higher L, but 3DGS typically keeps L small for compactness and stability.

Coarse–to–fine SH ramping for stable training. Rather than enable full view dependence from the start, 3DGS trains with a curriculum [287]:

1. **Begin with $L=0$ (diffuse).** Color is direction–independent, so the optimizer must first fit images via geometry (μ, R, S) and opacity a—reducing "cheating" with spurious view effects and limiting floaters.
2. **Unlock higher L in stages.** After geometry/opacity stabilize, enable $L=1,2,\ldots$ to add higher angular frequencies (specular–like lobes, Fresnel–like changes) without destabilizing the coarse structure. This mirrors frequency annealing used in other neural rendering systems and yields robust geometry first, then progressively richer view dependence with only a handful of extra coefficients.

Image formation and compositing

What each splat provides

For a pixel x and for every Gaussian i whose footprint reaches it, we already have:

- Its screen–space mean u_i and covariance Σ_i' (the ellipse).
- Its per–pixel alpha $\alpha_i(x)$ (peak opacity a_i modulated by the elliptical falloff; Sec. 23.10.9).
- Its view–dependent RGB c_i evaluated once for the current camera using SH.

Depth ordering for visibility

Occlusion is handled by sorting contributors at x from *nearest to farthest* using their camera–space depths $Z_{c,i}$ at the Gaussian centers μ_i. This establishes a visibility–aware sequence $k = 1, 2, \ldots$.

Front–to–back transmittance (premultiplied form)

Let $T_{k-1}(x)$ be the remaining visibility before blending the k-th (already depth–sorted) splat. Using premultiplied colors,

$$C(x) \;=\; \sum_k T_{k-1}(x)\,\alpha_k(x)\,c_k, \qquad T_k(x) \;=\; T_{k-1}(x)\big(1-\alpha_k(x)\big), \quad T_0(x) = 1.$$

- Near splats contribute first; farther ones are attenuated by $T_{k-1}(x)$.
- This mirrors volumetric rendering, but on projected 2D ellipses rather than per–ray samples (NeRF: $T = \exp(-\int \sigma\, ds)$; here α acts as discrete absorption).

Why front–to–back *matters now*

The transmittance recursion is *causal*: T_k depends only on earlier alphas. Consequently,

$$\text{if } T_{k-1}(x) \le \varepsilon_T \;\Rightarrow\; \sum_{j \ge k} T_{j-1}(x)\,\alpha_j(x)\,\|c_j\| \;\le\; \varepsilon_T,$$

since $\alpha_j \in [0,1]$ and $\|c_j\| \le 1$ (normalized colors). Two immediate consequences:

- Occlusion is respected by construction: Near content attenuates or completely hides far content as T decreases.
- The remaining sum is bounded once T is small: A pixel "pre–finishes", so later terms are negligible. We will exploit this property when describing early termination in the rasterizer.

Practical footprint (compact support)

Although a Gaussian has infinite support, its tail is negligible beyond a few standard deviations. Define the elliptical distance

$$d_i^2(x) \;=\; (x-u_i)^\top \Sigma_i'^{-1}(x-u_i),$$

and restrict evaluation to x inside a level set $\{\, d_i^2(x) \le \tau \,\}$ (e.g., $\tau \in [3,5]$). This:

- Focuses computation where the splat meaningfully contributes.
- Avoids numerical noise from summing vanishingly small tails.

Where we are headed. The equations above define the *image formation* the renderer must realize. We next complete the method—adaptive densification and optimization (losses, gradients)—then return to the tile–based rasterizer, which enforces depth order and leverages the transmittance pre–finish for efficiency.

Adaptive densification

Goal and signal

Starting from one Gaussian per SfM point, we *adaptively allocate capacity* so primitives concentrate where reprojection error persists. Every K iterations (e.g., a few hundred), we consult view-space positional gradients $\nabla_\mu \mathscr{L}$ and simple shape statistics to decide whether to *clone*, *split*, or *prune*. This keeps the model compact while resolving missing detail [287].

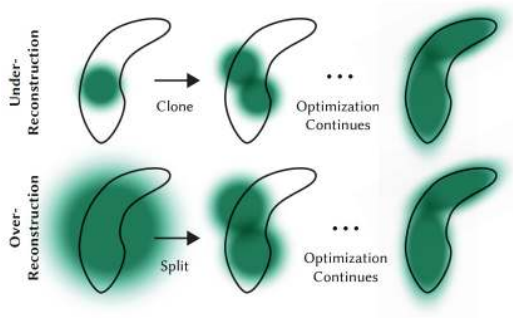

Figure 23.73: **Adaptive Gaussian densification** (illustration following [287]). *Top:* under-reconstruction (black outline not well covered) ⇒ **clone** the Gaussian and nudge along the positional gradient to add coverage. *Bottom:* over-reconstruction by a single large splat ⇒ **split** into two smaller splats to increase spatial resolution.

Clone (add coverage)
If a small splat (e.g., bounded principal axes in S and screen footprint in Σ') exhibits a large view-space positional gradient $\|\nabla_\mu \mathscr{L}\|$ over recent iterations, we **clone** it:

1. Create a copy with the same (R, S, a, SH).
2. Displace the clone's center by a small step along the aggregated gradient direction (optionally normalized and scaled).
3. Optionally damp the parent/clone opacities slightly to avoid transient over-coverage.

Cloning increases local sample density where the renderer still fails to match image evidence (thin structures, high-curvature silhouettes).

Split (resolve detail)
If a splat remains *large* (e.g., one axis of S above a threshold) while residuals stay high, we **split**:

1. Replace the parent by two children whose scales are reduced by a factor ϕ (empirically $\phi \approx 1.6$) along all axes.
2. Sample child centers from the parent's 3D Gaussian (or place them symmetrically along the principal axis with largest spread).
3. Inherit (R, a, SH), optionally perturb R or S minutely to break symmetry.

Splitting preserves coverage but increases spatial frequency capacity, allowing edges and textures to be represented with multiple smaller footprints.

Prune (stay compact)
We **prune** primitives that contribute negligibly or become degenerate:

- Nearly transparent (a below a threshold over a window of iterations).
- Unreasonably large in world space or screen space (guard against splats that try to "cover everything").
- Persistently off-frustum or behind the near plane.

Pruning reduces memory and compute and prevents artifacts such as low-contrast haze.

When and how often

Densification runs periodically and touches only a fraction of splats per pass. Thresholds for gradient magnitude, size (via S or Σ' eigenvalues), and opacity are set conservatively; exact values can be tuned per dataset, but the logic—*clone if small & underfit, split if large & underfit, prune if unused or degenerate*—follows [287]. Because gradients propagate through the differentiable rasterizer to *all* overlapping splats, these decisions are well informed by multi-view evidence.

Effect on optimization

Interleaving gradient steps with densification yields a coarse-to-fine growth of representation: the model first captures broad layout, then allocates more, smaller, and better-oriented Gaussians only where error persists. This shares the spirit of multiresolution strategies in explicit grids, but preserves the flexibility of an unstructured point-based representation.

Training objective and schedules

Photometric objective

We fit rendered images to ground truth using a convex combination of per-pixel ℓ_1 and a differentiable SSIM-based term:

$$\mathscr{L}(C, C^\star) \;=\; (1-\lambda)\,\|C - C^\star\|_1 \;+\; \lambda\,\text{D-SSIM}(C, C^\star), \qquad \lambda \in [0,1],$$

where C is the rendered image and $C^\star$ the target. The SSIM component measures *luminance*, *contrast*, and *structure* agreement in local windows, providing a perceptual anchor that complements the edge-preserving ℓ_1 term.

SSIM, D-SSIM, and the notion of "structure"

For two local patches x, y (e.g., Gaussian-weighted 11×11 windows), SSIM is

$$\text{SSIM}(x,y) = \frac{(2\mu_x\mu_y + C_1)(2\sigma_{xy} + C_2)}{(\mu_x^2 + \mu_y^2 + C_1)(\sigma_x^2 + \sigma_y^2 + C_2)},$$

where:

- **Luminance match** $(2\mu_x\mu_y + C_1)/(\mu_x^2 + \mu_y^2 + C_1)$ compares local means (exposure/brightness).
- **Contrast match** $(2\sigma_x\sigma_y + C_2)/(\sigma_x^2 + \sigma_y^2 + C_2)$ compares local standard deviations (contrast).
- **Structure match** is essentially the normalized correlation $\sigma_{xy}/(\sigma_x\sigma_y)$; it rewards the same *pattern of variation* even when absolute intensity shifts slightly.

We turn similarity into a loss via $\text{D-SSIM}(x,y) = (1 - \text{SSIM}(x,y))/2 \in [0,1]$, averaged over windows and channels. In practice, SSIM's structure term encourages the correct spatial relationships of pixels (textures, edges, fine detail), while the luminance/contrast terms keep exposure and local energy consistent. See [26, 453] for practical guidance.

Why not pure MSE/PSNR

Mean squared error (MSE) underlies PSNR ($\text{PSNR} = -10\log_{10}\text{MSE}$) but correlates poorly with human visual perception: it penalizes small spatial shifts of high-frequency content excessively and often prefers blurry predictions over slightly misaligned sharp ones. In 3DGS, many overlapping splats jointly explain high-frequency detail; a pure MSE/PSNR objective tends to over-smooth such detail. The ℓ_1+D-SSIM blend better matches HVS (Human Vision System) sensitivity: ℓ_1 preserves edges, while SSIM emphasizes local structural fidelity (textures, contrasts) and tolerates mild brightness drifts.

LPIPS vs. SSIM in training

LPIPS [778] compares images in a deep feature space (e.g., VGG/AlexNet), and is strong as an *evaluation* metric for perceptual quality. We do *not* use LPIPS in the 3DGS *training* loss for several reasons:

- **Photometric faithfulness matters.** Supervision comes from posed photos; exact colors and fine correspondences are crucial for stable geometry/opacity learning. LPIPS has feature invariances that can tolerate color/brightness shifts, sometimes encouraging "perceptually OK" but photometrically biased reconstructions.
- **Efficiency and memory.** LPIPS requires a forward/backward pass through a deep CNN per image (or patch), adding nontrivial compute and VRAM on top of the differentiable rasterizer. SSIM is lightweight and fully local.
- **Gradient locality and stability.** SSIM provides short-range, structure-aligned gradients that integrate well with splat-based compositing; LPIPS offers non-local gradients that can destabilize early optimization (especially before geometry has converged).

Empirically, ℓ_1+D-SSIM (with a small λ, e.g., 0.2 as in [287]) yields sharp, photometrically faithful results while keeping training fast and stable. LPIPS remains valuable for *reporting* perceptual quality at test time.

Update schedule and stability

We optimize all parameters $(\mu, R, S, a, \mathrm{SH})$ with Adam over mini-batches of posed images.

- **Learning rates.** Slightly larger for (μ, S) early to quickly settle geometry; smaller for rotation (quaternion) and SH to avoid oscillations.
- **SH degree ramping.** Keep L=0 (view-independent color) until geometry/opacity stabilize, then *unlock* L=$1, 2, \ldots$ in stages. This coarse-to-fine curriculum first fixes layout and coverage, then adds higher angular frequencies (specular-like lobes, Fresnel-like variation) without destabilizing structure [287].
- **Opacity hygiene.** Clamp $a \in [\varepsilon, 1-\varepsilon]$ and optionally apply periodic small resets near the cameras to discourage persistent semi-transparent "floaters" before pruning.

Differentiable tile–based rasterizer

Goal and inputs

The rasterizer must realize the image–formation equations from Sec. 23.10.9 efficiently on GPU, while preserving differentiability. For the current view we assume, per Gaussian i, the following are already available:

- Screen–space mean u_i and covariance Σ_i'.
- Peak opacity a_i and per–pixel alpha definition $\alpha_i(x)$.
- View–dependent color c_i evaluated once from SH for this camera.
- Camera–space depth $Z_{c,i}$ at the center μ_i (for visibility ordering).

Stage A: cull and bound

- Frustum–cull Gaussians whose ellipses lie fully outside the image (use a conservative $d_i^2(x) \le \tau$ mask).
- For each remaining Gaussian, compute the tight axis–aligned bounding box of its ellipse level set $\{x : d_i^2(x) \le \tau\}$ and clip it to the screen.

Stage B: tile binning

Partition the screen into fixed–size tiles (e.g., 16×16). For each Gaussian i:

- Determine the set of tiles overlapped by its clipped ellipse box.
- Emit a record for each overlapped tile t: a pair (i,t) plus the quantities needed downstream (e.g., u_i, $\Sigma_i'^{-1}$, a_i, c_i, $Z_{c,i}$).

Stage C: global sort by (tile, depth)

Construct a 64–bit key per record (i,t) that packs

- The tile id in the most significant bits (groups records by tile).
- A monotone depth key derived from $Z_{c,i}$ in the least significant bits (orders front–to–back).

Globally radix–sort all records by this key; the result is a single array where each tile occupies a contiguous segment with its Gaussians in front–to–back order.

Stage D: per–tile blending (forward)

Launch one CUDA block per tile; within a block, assign one thread per pixel. For the tile's ordered list $(i_1,\dots,i_M)$:

- Initialize $C(x):=\mathbf{0}$ and $T(x):=1$ for every pixel x in the tile.
- For $m=1\dots M$:
  - Compute the elliptical distance $d^2_{i_m}(x)$ and skip if $d^2_{i_m}(x)>\tau$ (compact support).
  - Evaluate $\alpha_{i_m}(x)=a_{i_m}\exp(-\frac{1}{2}d^2_{i_m}(x))$.
  - Accumulate $C(x)\mathrel{+}=T(x)\,\alpha_{i_m}(x)\,c_{i_m}$.
  - Update $T(x)\mathrel{*}=(1-\alpha_{i_m}(x))$.
  - Optionally stop if $T(x)\le\varepsilon_T$ (front–to–back "pre–finish").

Minimal bookkeeping for backprop. While iterating, each pixel thread appends a compact record for every touched splat i_m: store its index, $T_{m-1}(x)$ (the prefix transmittance just before blending), and $\alpha_{i_m}(x)$. This per–pixel visitation list is short due to compact support and pre–finish, and suffices for an efficient backward pass.

Stage E: per–tile gradients (backward)

Given pixel–wise loss gradients $\frac{\partial\mathscr{L}}{\partial C(x)}\in\mathbb{R}^3$, traverse each pixel's visitation list in *reverse* order to accumulate parameter derivatives. Let the k–th visited (depth–sorted) splat at x have $(i_k, T_{k-1}(x), \alpha_{i_k}(x), c_{i_k})$, and define the suffix "background color" seen behind k (normalized) by the recurrence

$$\bar{C}^{(K+1)}_{\text{behind}}(x)=\mathbf{0},\qquad \bar{C}^{(k)}_{\text{behind}}(x)=\alpha_{i_k}(x)\,c_{i_k}\;+\;\big(1-\alpha_{i_k}(x)\big)\,\bar{C}^{(k+1)}_{\text{behind}}(x).$$

Then for each k (from back to front):

- Color coefficients (SH) receive
$$\frac{\partial\mathscr{L}}{\partial c_{i_k}}\mathrel{+}=T_{k-1}(x)\,\alpha_{i_k}(x)\,\frac{\partial\mathscr{L}}{\partial C(x)}.$$
- Opacity (per–pixel) receives
$$\frac{\partial\mathscr{L}}{\partial\alpha_{i_k}(x)}\mathrel{+}=T_{k-1}(x)\,\Big(c_{i_k}\;-\;\bar{C}^{(k+1)}_{\text{behind}}(x)\Big)\cdot\frac{\partial\mathscr{L}}{\partial C(x)}.$$
- Chain to geometric parameters via $\alpha_{i_k}(x)=a_{i_k}\exp(-\frac{1}{2}d^2_{i_k}(x))$:
$$\frac{\partial\mathscr{L}}{\partial a_{i_k}}\mathrel{+}=\exp\!\big(-\tfrac{1}{2}d^2_{i_k}(x)\big)\,\frac{\partial\mathscr{L}}{\partial\alpha_{i_k}(x)},\qquad \frac{\partial\mathscr{L}}{\partial d^2_{i_k}(x)}\mathrel{+}=-\tfrac{1}{2}\,\alpha_{i_k}(x)\,\frac{\partial\mathscr{L}}{\partial\alpha_{i_k}(x)}.$$

- Propagate $\frac{\partial \mathscr{L}}{\partial d^2}$ to u_{i_k} and Σ'_{i_k} using

$$d^2_{i_k}(x) = (x - u_{i_k})^\top {\Sigma'_{i_k}}^{-1}(x - u_{i_k}),$$

and then further to world–space (μ, R, S) through the Jacobian chain $\Sigma' = JW\Sigma W^\top J^\top$.

Because only *touched* pairs (x,i) are revisited, the backward pass scales with the effective overlap, not the total number of Gaussians.

Numerical and implementation notes

- **Tile size.** 16×16 balances occupancy and shared–memory usage; other sizes are possible.
- **Stable alphas.** Keep $a_i \in [\varepsilon, 1-\varepsilon]$ and use $\tau \in [3,5]$ for compact support (Sec. 23.10.9).
- **Recompute vs. store.** To minimize memory, store T_{k-1} and $\alpha_{i_k}(x)$; re–evaluate c_{i_k} from SH on the fly if needed (one evaluation per splat–pixel).
- **Sparse work.** Frustum culling, compact support, and pre–finish together bound both forward work and the size of visitation lists, enabling real–time rendering once trained.

Summary. The rasterizer maps the analytic 2D ellipse footprints to tiles, establishes a per–tile, front–to–back order with a single global sort, and evaluates the premultiplied α–compositing recurrence using only local (tile) data. A compact per–pixel record of touched splats permits an equally local backward pass, with gradients chained to opacity, color (SH), and geometry through closed–form derivatives. This completes the forward/backward machinery of 3DGS.

Experiments and ablations

Datasets and evaluation protocol

Evaluation is conducted on widely used real and synthetic benchmarks:

- **Mip-NeRF360** [29]: real, unbounded 360° captures with large baselines and substantial depth variation (e.g., *Bicycle, Garden, Stump, Counter, Room*). The official train/test splits are used.
- **Tanks&Temples** [299]: real outdoor/vehicle scenes with challenging occlusions and scale changes (commonly *Truck, Train*) and accurate ground-truth poses.
- **Deep Blending** [213]: real indoor environments (*Playroom, DrJohnson*) exhibiting complex view-dependent effects and clutter, with calibrated multi-view imagery.
- **Synthetic NeRF (Blender)** [429]: rendered objects with clean geometry and known ground truth (*Chair, Drums, Ficus, Hotdog, Lego, Materials, Mic, Ship*) for controlled comparisons.

Unless otherwise noted, images are rendered at each dataset's standard resolution. Reported metrics are PSNR (dB; higher is better), SSIM (↑), and LPIPS (↓). Optimization wall-clock time and novel-view FPS are reported on a single high-end GPU, following the protocol of [287].

Figure 23.74: **Real-time quality vs. training budget (Bike).** 3D Gaussian Splatting (3DGS) achieves real-time rendering with image quality competitive with the best prior method (Mip-NeRF360 [29]) while requiring training times comparable to the fastest explicit methods (Plenoxels [160], Instant-NGP [443]). For a training budget similar to Instant-NGP, 3DGS matches its quality; with a longer budget (e.g., ∼51 min), 3DGS reaches state-of-the-art PSNR, even slightly surpassing Mip-NeRF360 on this scene. Higher PSNR is better. Adapted from [287].

Quantitative comparison (held-out views)

We summarize cross-dataset results (reformatted into per-dataset tables for readability).

Table 23.15: **Mip-NeRF360** (test views). Higher SSIM/PSNR, lower LPIPS are better. Training time and inference FPS reported as in [287].

Method	SSIM ↑	PSNR ↑	LPIPS ↓	Train	FPS	Mem
Plenoxels	0.626	23.08	0.463	25m49s	6.79	2.1GB
INGP-Base	0.671	25.30	0.371	5m37s	11.7	13MB
INGP-Big	0.699	25.59	0.331	7m30s	9.43	48MB
Mip-NeRF360	0.792†	**27.69**†	0.237†	48h	0.06	8.6MB
3DGS-7K	0.770	25.60	0.279	6m25s	160	523MB
3DGS-30K	**0.815**	27.21	**0.214**	41m33s	134	734MB

Table 23.16: **Tanks&Temples** (test views). Reported as in [287].

Method	SSIM ↑	PSNR ↑	LPIPS ↓	Train	FPS	Mem
Plenoxels	0.719	21.08	0.379	25m05s	13.0	2.3GB
INGP-Base	0.723	21.72	0.330	5m26s	17.1	13MB
INGP-Big	0.745	21.92	0.305	6m59s	14.4	48MB
Mip-NeRF360	0.759	22.22	0.257	48h	0.14	8.6MB
3DGS-7K	0.767	21.20	0.280	6m55s	197	270MB
3DGS-30K	**0.841**	**23.14**	**0.183**	26m54s	154	411MB

Table 23.17: **Deep Blending** (test views). Reported as in [287].

Method	SSIM ↑	PSNR ↑	LPIPS ↓	Train	FPS	Mem
Plenoxels	0.795	23.06	0.510	27m49s	11.2	2.7GB
INGP-Base	0.797	23.62	0.423	6m31s	3.26	13MB
INGP-Big	0.817	24.96	0.390	8m00s	2.79	48MB
Mip-NeRF360	0.901	29.40	0.245	48h	0.09	8.6MB
3DGS-7K	0.875	27.78	0.317	4m35s	172	386MB
3DGS-30K	**0.903**	**29.41**	**0.243**	36m02s	137	676MB

Qualitative comparisons

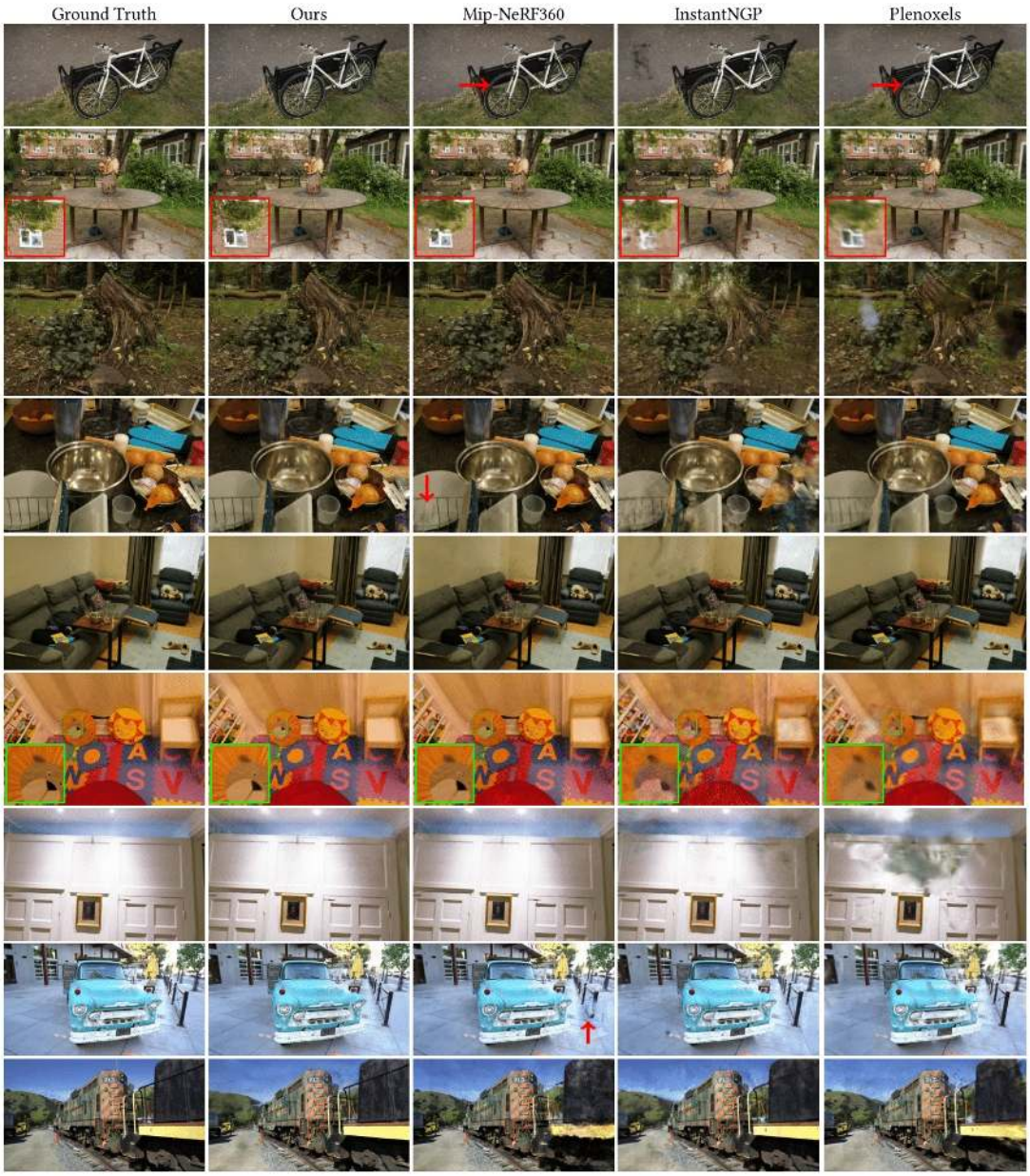

Figure 23.75: **Visual comparisons on held-out views** across Mip-NeRF360 (Bicycle, Garden, Stump, Counter, Room), Deep Blending (Playroom, DrJohnson) and Tanks&Temples (Truck, Train). Insets/arrows highlight non-obvious differences. 3DGS matches or exceeds prior methods detail and stability while rendering in real time. Adapted from [287].

Training-time vs. quality

Figure 23.76: **Quality over training iterations.** Top: at 7K iters (∼5–8 min), the Train scene is already well reconstructed; by 30K iters (∼35 min) background artifacts fade. Bottom: in easier scenes, 7K is nearly indistinguishable from 30K. Adapted from [287].

Synthetic NeRF (Blender) PSNR

Table 23.18: **Synthetic NeRF** (PSNR, ↑). 3DGS uses 100K randomly initialized points. Reported as in [287].

Method	Mic	Chair	Ship	Materials	Lego	Drums	Ficus	Hotdog	Avg.
Plenoxels	33.26	33.98	29.62	29.14	34.10	25.35	31.83	36.81	31.76
INGP-Base	36.22	35.00	**31.10**	29.78	**36.39**	26.02	33.51	37.40	33.18
Mip-NeRF	**36.51**	35.14	30.41	**30.71**	35.70	25.48	33.29	37.48	33.09
Point-NeRF	35.95	35.40	30.97	29.61	35.04	26.06	**36.13**	37.30	33.30
3DGS-30K	35.36	**35.83**	30.80	30.00	35.78	**26.15**	34.87	**37.72**	**33.32**

Ablations

We study design choices via controlled ablations (numbers reproduced from [287]).

Table 23.19: **Ablation PSNR** (downsampled inputs for stability). Average over Truck/Garden/Bicycle at 5K/30K iterations.

Setting	Truck-5K	Garden-5K	Bicycle-5K	Truck-30K	Garden-30K	Bicycle-30K	Avg-5K	Avg-30K
Limited-BW	14.66	22.07	20.77	13.84	22.88	20.87	19.16	19.19
Random Init	16.75	20.90	19.86	18.02	22.19	21.05	19.17	20.42
No-Split	18.31	23.98	22.21	20.59	26.11	25.02	21.50	23.90
No-SH	22.36	25.22	22.88	24.39	26.59	25.08	23.48	25.35
No-Clone	22.29	25.61	22.15	**24.82**	27.47	25.46	23.35	25.91
Isotropic	22.40	25.49	22.81	23.89	27.00	24.81	23.56	25.23
Full	**22.71**	**25.82**	**23.18**	24.81	**27.70**	**25.65**	**23.90**	**26.05**

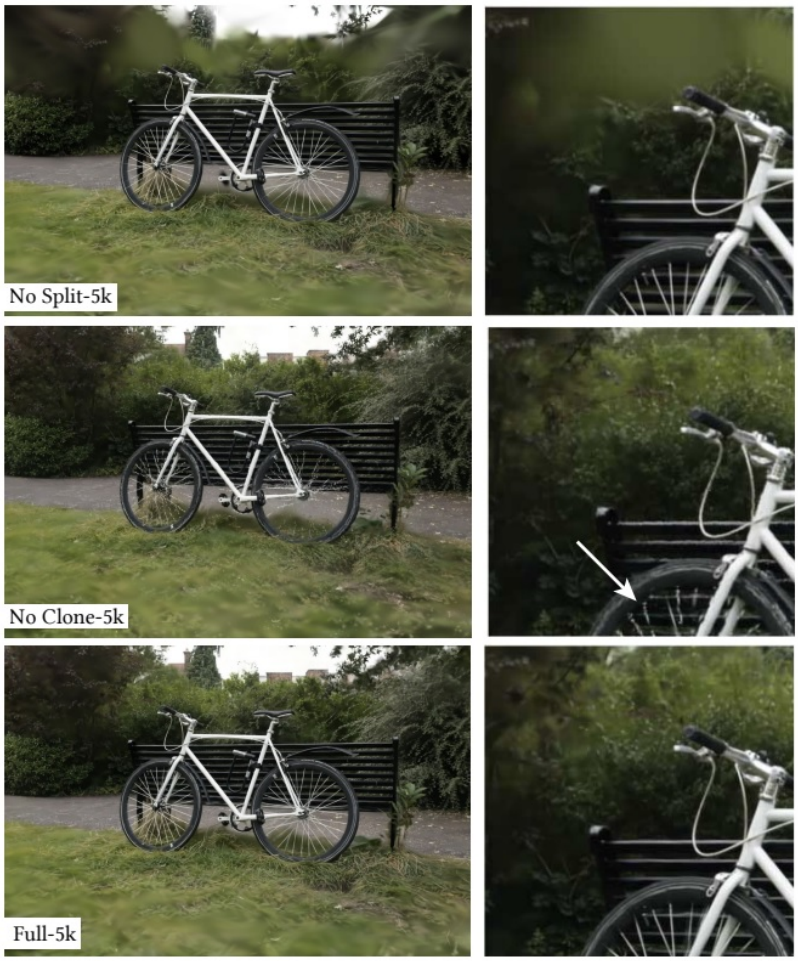

Figure 23.77: **Densification ablation.** Without **split**: background remains blurred. Without **clone**: high-frequency structures (e.g., bike spokes/wheels) artifact. Both operations are needed (cf. Fig. 23.73). Adapted from [287].

Figure 23.78: **Gradient sparsity ablation.** Limiting the number of Gaussians that receive gradients per step severely degrades quality (left); full method (right) benefits from dense, overlapped gradients through the rasterizer. Adapted from [287].

Figure 23.79: **Initialization matters.** Top: random point cloud; bottom: SfM seeding. SfM provides a much better starting geometry, accelerating and stabilizing training. Adapted from [287].

Figure 23.80: **Anisotropy ablation (Ficus, capped at 5k Gaussians).** Enabling *anisotropic* covariances is critical for fine/filamentary structure; isotropic splats require many more primitives and still blur edges. Adapted from [287].

Takeaways

- **Quality vs. speed:** With tens of minutes of training, 3DGS approaches or surpasses Mip-NeRF360 quality while enabling real-time novel-view rendering (≥ 100 FPS) on standard GPUs.
- **Representation matters:** Anisotropy, view-dependent SH, and densification (clone/split) each contribute significantly; removing any one harms PSNR/visual fidelity (Table 23.19).
- **Initialization helps:** SfM seeding outperforms random starts, reducing artifacts and time to quality (Fig. 23.79).

Limitations and future work

Observed failure modes

Figure 23.81: **Failure artifacts (Train).** Compared to Mip-NeRF360 [29] (left), which can exhibit "floaters" and grain in poorly constrained regions, 3DGS [287] (right) may render coarse, anisotropic blobs where multi-view coverage is weak, limiting far-background detail. Adapted from [287].

Figure 23.82: **View extrapolation artifacts (DrJohnson).** When camera poses have little overlap with training views, 3DGS [287] can produce artifacts (right). Mip-NeRF360 [29] also degrades under such extrapolation (left), albeit with different characteristics. Adapted from [287].

Typical limitations include:

- **Sparse coverage or weak overlap.** With limited multi-view support, Gaussians may overgrow (coarse blobs) or under-cover (holes), especially at long range [29, 287].
- **Extreme view dependence.** Very sharp, mirror-like effects exceed low-degree SH; capturing such specularities robustly requires richer reflectance models [287].
- **Memory scaling.** Quality grows with the number of Gaussians; very large scenes can stress memory bandwidth and capacity without compression or streaming [287].
- **Static-scene assumption.** The base formulation targets rigid, static scenes; handling motion or changing illumination requires extensions beyond the original 3DGS pipeline [287].

Future work

Recent, highly cited follow-ups suggest concrete avenues beyond the original formulation:

- **Dynamics and tracking.** Extending splats to time (4D) enables real-time dynamic rendering [703], while dense SLAM systems fuse mapping and tracking directly with Gaussians for online reconstruction [534].
- **Richer appearance / inverse rendering.** Jointly estimating reflectance and lighting with Gaussian splats (inverse rendering) improves specularities and relighting fidelity [680]; surfel-style anisotropic primitives further tighten shading–geometry coupling [286].
- **Initialization and scalability.** Removing reliance on external SfM (e.g., COLMAP-free pipelines) widens applicability and can reduce failure cases tied to sparse/biased points [162]; generative priors with Gaussians help regularize learning and scale content creation [607].
- **Surfaces and hybrids.** Surface-aligned or surface-extractable Gaussian formulations bridge to mesh-like structure for editing and compression [781], complementing the original unstructured point representation.

Enrichment 23.11: NeRF: Real-World Robustness & Sparse Supervision

NeRFs trained "in the wild" must tolerate sparse viewpoints, photometric variation, and even unknown poses. These works inject priors or jointly estimate calibration to make NeRFs usable under realistic capture.

- **BARF** [352]: Jointly optimizes camera poses and NeRF via coarse-to-fine (frequency) scheduling, reducing local minima in self-calibration.
- **NeRF-W** [418]: Handles unconstrained photo collections by separating "transient" appearance (lighting, people) from static scene content.
- **IBRNet** [654]: A generalizable IBR prior that conditions on a few source views to synthesize novel views without per-scene MLP overfitting.
- **PixelNeRF** [739]: Predicts scene radiance directly from one/few images using a CNN encoder, enabling few-shot generalization.

Further influential works (not expanded): **RegNeRF** [452] (regularization for sparse inputs), **Mega-NeRF** [413] (distributed training at landscape scale).

Enrichment 23.11.1: BARF: Bundle-Adjusting Neural Radiance Fields

Motivation and problem setting

Why this problem matters

Neural Radiance Fields (NeRF) achieve high-fidelity novel-view synthesis *only if* all training images come with accurate camera extrinsics. In real captures, however, poses from SfM/SLAM can be noisy, incomplete, or entirely unavailable (e.g., monocular videos, sparse photo collections). This dependency limits NeRF in exactly the regimes we care about for robust, real-world deployment: casual capture, small baselines, texture-poor scenes, or motion that confounds SfM. Removing the reliance on precomputed poses would unlock NeRF for far broader use.

What makes joint optimization hard

If poses are inaccurate or unknown, training becomes a coupled problem over the scene *and* the cameras. Naïvely unfreezing poses in a standard NeRF objective turns the problem highly nonconvex and initialization-sensitive: the network can explain photometric errors either by *moving the cameras* or by *hallucinating geometry/appearance*. In practice this often yields misregistered trajectories, distorted geometry, and rendering artifacts instead of self-correction [352]. The core need is to shape the optimization so that early gradients provide *coherent, consistent* directions for camera updates.

A lesson from classical image alignment

In classical registration, *direct* photometric methods optimize geometric parameters and routinely employ multiscale image pyramids to enlarge the basin of convergence. The strategy is to first align *low-frequency* (blurred or downsampled) images to obtain a robust global displacement, and only then reintroduce *higher-frequency* detail for refinement. Low-pass residuals yield smoother objectives and coherent gradients; exposing high frequencies too early makes the landscape rugged and per-pixel Jacobians oscillatory, impeding convergence. BARF transfers this multiscale idea from images to neural fields by low-passing the *inputs*—via a schedule that gates NeRF's positional-encoding bands during training—so early pose updates are governed by smooth structure and fine detail is deferred until registration stabilizes.

The paper's idea and contribution

BARF reframes NeRF with unknown poses as dense photometric bundle adjustment and makes it tractable by controlling frequency content. Concretely, it:

- *Jointly* optimizes camera poses and the radiance field under the standard rendering loss.
- Applying a smooth coarse-to-fine window over positional-encoding bands that enlarges the basin for pose recovery and only later restores full representational bandwidth. This simple mechanism reliably realigns cameras from noisy or identity initializations and preserves NeRF-level fidelity once all bands are active.

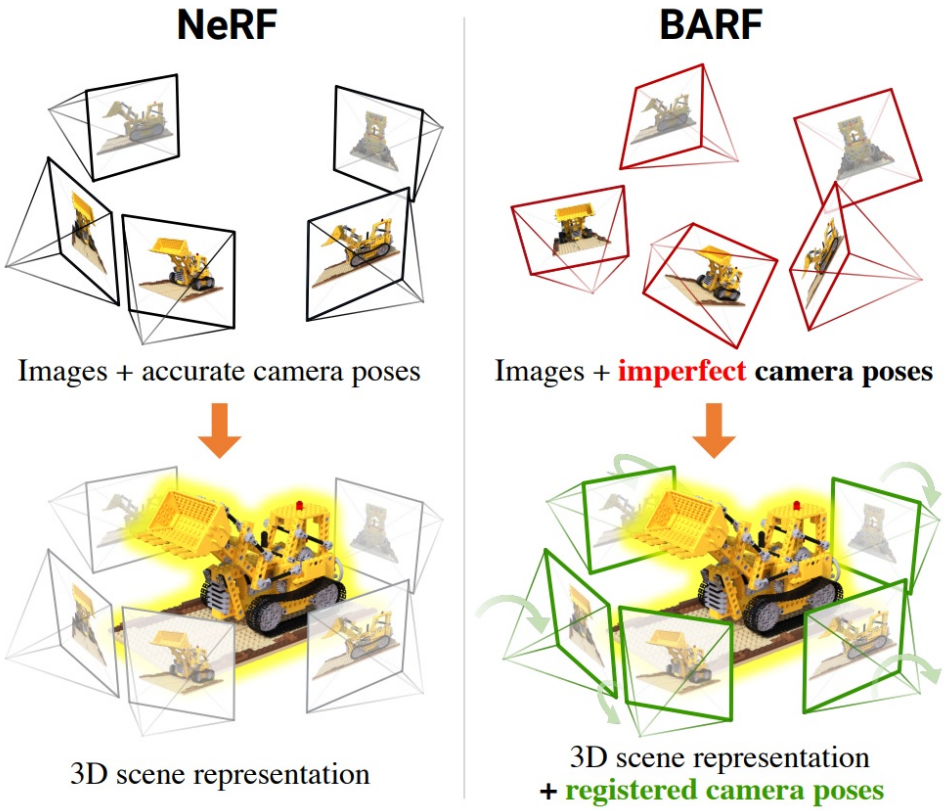

Figure 23.83: **Training NeRF requires accurate camera poses.** BARF jointly optimizes camera registration and neural 3D reconstruction, enabling learning from imperfect or unknown poses. Reproduced from [352].

What we aim to solve and why:

- **Goal** — Learn a high-fidelity neural scene *and* accurate camera poses directly from images, without relying on external SfM/SLAM.
- **Challenge** — Naïve joint optimization is ill-conditioned: high-frequency encodings inject rugged gradients that drive poses to poor local minima.
- **Approach** — Window the frequency bands of positional encoding in a coarse-to-fine schedule so early pose gradients are stable and globally coherent.
- **Impact** — Makes NeRF usable with imperfect/unknown poses, recovering trajectories from scratch and achieving view synthesis competitive with pose-supervised NeRFs [352].

High level overview of BARF

Joint objective

Given images $\{I_i\}_{i=1}^{M}$ and a radiance field f_θ mapping a 3D location and a view direction to density and color,

$$f_\theta : (\mathbf{x}, \mathbf{d}) \mapsto \big(\sigma(\mathbf{x}), \mathbf{c}(\mathbf{x}, \mathbf{d})\big),$$

BARF minimizes a standard photometric synthesis loss while treating *both* the network parameters θ and the camera poses $\{\mathbf{T}_i\}$ as variables. For a pixel $\mathbf{u}$ in image i, let $\widehat{\mathbf{C}}_i(\mathbf{u}; \mathbf{T}_i, \theta)$ denote the differentiably volume–rendered color along the ray defined by $\mathbf{u}$ under pose $\mathbf{T}_i$. The objective is

$$\min_{\theta, \{\mathbf{T}_i\}} \mathscr{L}(\theta, \{\mathbf{T}_i\}) = \sum_{i=1}^{M} \sum_{\mathbf{u} \in \mathscr{R}_i} \Big\| \widehat{\mathbf{C}}_i(\mathbf{u}; \mathbf{T}_i, \theta) - I_i(\mathbf{u}) \Big\|_2^2, \tag{23.47}$$

so image residuals can, in principle, correct both scene and camera. We postpone the exact pose parametrization and update rule to the in–depth derivation, where we show how pose increments are obtained by backpropagating through volume rendering.

Bandwidth scheduling via windowed positional encoding

Why low frequencies matter first Early pose updates must aggregate gradients from many rays that hit *nearby* 3D points while poses are still inaccurate. Low spatial frequencies vary slowly, which yields:

- **Coherent guidance** — Neighboring rays see similar residual structure, so their pose gradients point in similar directions and *add* constructively.
- **Wider linearization radius** — Smooth residuals keep the first–order (local linear) model valid over a larger region, allowing stable steps despite large initial misalignment.
- **Higher SNR for registration** — Slowly varying structure is less sensitive to pixel-level noise/specularities, making the global motion signal easier to extract.

In contrast, for the k-th positional-encoding (PE) band (applied coordinate-wise),

$$\gamma_k(\mathbf{x}) = \big[\cos(2^k \pi \mathbf{x}), \sin(2^k \pi \mathbf{x})\big], \qquad \frac{\partial \gamma_k}{\partial \mathbf{x}} = 2^k \pi \big[-\sin(2^k \pi \mathbf{x}), \cos(2^k \pi \mathbf{x})\big].$$

The spatial period is $\lambda_k = \frac{1}{2^k}$ (direction flips every 2^{-k} offset), and the Jacobian norm scales as $O(2^k)$ (steep, rapidly varying gradients). Together these cause (i) *directional incoherence* across nearby samples—aggregated pose gradients partially cancel—and (ii) a *shrinking trust region* for first–order updates when misalignment is large.

How BARF enforces low→high bandwidth BARF turns PE into a bandwidth knob by *windowing* frequency bands with a single progress variable $\alpha \in [0, L]$. Using the paper's raised–cosine ramp, the modified encoding is

$$\widetilde{\gamma}(\mathbf{x}; \alpha) = \big[\mathbf{x}, w_0(\alpha)\gamma_0(\mathbf{x}), \ldots, w_{L-1}(\alpha)\gamma_{L-1}(\mathbf{x})\big], \quad w_k(\alpha) = \tfrac{1}{2}\big[1 - \cos\big(\pi \,\mathrm{sat}(\alpha - k)\big)\big],$$

where $\mathrm{sat}(t) = \min\{\max\{t, 0\}, 1\}$. A simple linear ramp $\alpha(t)$ increases from 0 to L over a chosen iteration window. This acts as a dynamic low-pass filter on coordinates:

$$\frac{\partial (w_k(\alpha)\gamma_k)}{\partial \mathbf{x}} = w_k(\alpha) \frac{\partial \gamma_k}{\partial \mathbf{x}}.$$

Early on, $w_k(\alpha) \approx 0$ for large k keeps only low-frequency, slowly varying Jacobians (coherent aggregation, wide basin) for robust camera updates; as alignment stabilizes, $w_k(\alpha) \to 1$ progressively restores high-frequency capacity and full NeRF fidelity—without destabilizing registration.

Roadmap

- **Method and derivations** — We write the discretized rendering, pose parameterization in $\mathfrak{se}(3)$, and derive the required Jacobians for joint updates.
- **Coarse-to-fine PE** — We present the exact windowed encoding and schedule, with intuition relating bandwidth control to the optimization basin.
- **Architecture and implementation** — We specify MLP design, sampling, optimizers, and evaluation protocol for faithful reproduction.
- **Experiments and ablations** — We summarize planar alignment, Blender, and LLFF results, highlighting why C2F-PE is critical to registration and fidelity.
- **Limitations and future work** — We discuss schedule sensitivity, efficiency, and assumptions (static scenes, fixed intrinsics), and outline extensions.

Method and derivations

NeRF with differentiable volume rendering

A radiance field f_θ maps a 3D location and a viewing direction to a volume density and an RGB color,

$$f_\theta : (\mathbf{x}, \mathbf{d}) \mapsto \big(\sigma(\mathbf{x}), \mathbf{c}(\mathbf{x}, \mathbf{d})\big).$$

For image I_i and pixel $\mathbf{u} \in \mathscr{R}_i$, the camera-$i$ ray in *camera* coordinates is $\mathbf{r}_i(t) = \mathbf{o}_i + t\,\widehat{\mathbf{d}}_i(\mathbf{u})$, with bounds $t_n < t < t_f$. Under the current extrinsics $\mathbf{T}_i$, each sample at parameter t is evaluated at the corresponding *world* point $\mathbf{x}(t)$, giving the standard emitted-radiance model

$$\widehat{\mathbf{C}}_i(\mathbf{u}; \mathbf{T}_i, \theta) \;=\; \int_{t_n}^{t_f} T(t)\, \sigma\big(\mathbf{x}(t)\big)\, \mathbf{c}\big(\mathbf{x}(t), \widehat{\mathbf{d}}_i(\mathbf{u})\big)\, dt, \qquad T(t) = \exp\Big(-\int_{t_n}^{t} \sigma(\mathbf{x}(s))\, ds\Big).$$

Following NeRF, the integral is approximated with N stratified samples $\{t_j\}_{j=1}^N$:

$$\widehat{\mathbf{C}}_i(\mathbf{u}) = \sum_{j=1}^{N} w_j\, \mathbf{c}_j, \quad w_j = T_j\, \alpha_j, \quad \alpha_j = 1 - \exp(-\sigma_j\, \delta_j), \quad T_j = \prod_{k<j} (1 - \alpha_k),$$

with $\sigma_j = \sigma(\mathbf{x}_j)$, $\mathbf{c}_j = \mathbf{c}(\mathbf{x}_j, \widehat{\mathbf{d}}_i)$, $\mathbf{x}_j = \mathbf{x}(t_j)$, and $\delta_j = t_{j+1} - t_j$. This fully differentiable composition supplies gradients to both f_θ and the camera parameters through the sample locations $\mathbf{x}_j$.

Joint objective (reference)

The global loss is given in (23.47) of the high-level overview (§23.11.1). The remainder of this subsection specifies the pose parametrization and the exact derivatives that backpropagate image residuals to both θ and $\{\mathbf{T}_i\}$.

From rigid motions to minimal pose updates

A camera pose is a rigid motion: a 3D rotation plus a 3D translation. Using homogeneous coordinates,

$$\mathbf{T}_i \;=\; \begin{bmatrix} \mathbf{R}_i & \mathbf{t}_i \\ \mathbf{0}^\top & 1 \end{bmatrix}, \qquad \mathbf{R}_i \in \mathbb{R}^{3\times 3},\ \mathbf{t}_i \in \mathbb{R}^3.$$

A rotation matrix is valid iff $\mathbf{R}_i^\top \mathbf{R}_i = \mathbf{I}_3$ and $\det(\mathbf{R}_i) = 1$. Naïve gradient steps on the nine entries of $\mathbf{R}_i$ generally violate these constraints. BARF therefore applies *minimal* 6D pose increments that are mapped to valid rigid motions via the exponential map and then composed with the current pose. In the paper's functional view, this shows up as a rigid warp $W(\cdot; \mathbf{p}_i)$ applied to 3D points before evaluating the field f_θ and the compositor g; equivalently, the rendered color $\widehat{\mathbf{C}}_i(\mathbf{u}; \mathbf{p}_i, \theta)$ depends differentiably on $\mathbf{p}_i$ through the sample locations along the ray.

Twist updates via the exponential map
A small camera motion is represented by a 6D *twist*

$$\xi_i \;=\; \begin{bmatrix} \omega_i \\ \mathbf{v}_i \end{bmatrix} \in \mathbb{R}^6,$$

where $\omega_i \in \mathbb{R}^3$ is an axis–angle vector and $\mathbf{v}_i \in \mathbb{R}^3$ is a translation increment. *Intuition for ω_i:* let $\theta = \|\omega_i\|$ and $\hat{\mathbf{u}} = \omega_i/\theta$ (if $\theta > 0$). Then $\hat{\mathbf{u}}$ is the *rotation axis* (a unit 3D direction left invariant by the rotation) and θ is the *rotation angle* in radians; points rotate by angle θ in planes orthogonal to $\hat{\mathbf{u}}$.

What $\mathrm{SE}(3)$, $\mathfrak{se}(3)$, and the exponential map mean. $\mathrm{SE}(3)$ (the special Euclidean group) is the set of rigid motions

$$\mathrm{SE}(3) = \left\{ \begin{bmatrix} \mathbf{R} & \mathbf{t} \\ \mathbf{0}^\top & 1 \end{bmatrix} \;\middle|\; \mathbf{R} \in \mathrm{SO}(3),\, \mathbf{t} \in \mathbb{R}^3 \right\}, \qquad \mathrm{SO}(3) = \{\mathbf{R} \in \mathbb{R}^{3\times 3} \mid \mathbf{R}^\top \mathbf{R} = \mathbf{I}_3,\, \det \mathbf{R} = 1\}.$$

$\mathfrak{se}(3)$ (the Lie algebra of $\mathrm{SE}(3)$) is the *tangent space at the identity*:

$$\mathfrak{se}(3) = \left\{ \begin{bmatrix} \widehat{\omega} & \mathbf{v} \\ \mathbf{0}^\top & 0 \end{bmatrix} \;\middle|\; \widehat{\omega}^\top = -\widehat{\omega},\, \mathbf{v} \in \mathbb{R}^3 \right\}.$$

The hat operator $\widehat{(\cdot)} : \mathbb{R}^3 \to \mathbb{R}^{3\times 3}$ encodes the cross product: $\widehat{\mathbf{a}}\,\mathbf{b} = \mathbf{a} \times \mathbf{b}$, i.e.,

$$\widehat{\omega}_i \;=\; \begin{bmatrix} 0 & -\omega_{i,3} & \omega_{i,2} \\ \omega_{i,3} & 0 & -\omega_{i,1} \\ -\omega_{i,2} & \omega_{i,1} & 0 \end{bmatrix}.$$

Embedding the 6D twist into a 4×4 block gives

$$\widehat{\xi}_i \;=\; \begin{bmatrix} \widehat{\omega}_i & \mathbf{v}_i \\ \mathbf{0}^\top & 0 \end{bmatrix} \in \mathfrak{se}(3).$$

The exponential map $\exp : \mathfrak{se}(3) \to \mathrm{SE}(3)$ sends a tangent vector at the identity to a finite rigid motion. Dynamically, it is the time-1 solution of the linear ODE $\dot{\mathbf{T}}(s) = \widehat{\xi}_i \mathbf{T}(s)$ with $\mathbf{T}(0) = \mathbf{I}_4$, namely $\mathbf{T}(1) = \exp(\widehat{\xi}_i)$.

Matrix exponential: why the series converges and what it yields. For any finite matrix $\mathbf{A}$,

$$\exp(\mathbf{A}) \;=\; \sum_{n=0}^{\infty} \frac{\mathbf{A}^n}{n!}$$

converges absolutely because $\left\| \sum_{n=0}^{\infty} \mathbf{A}^n/n! \right\| \le \sum_{n=0}^{\infty} \|\mathbf{A}\|^n/n! = e^{\|\mathbf{A}\|}$ (submultiplicative norm and ratio test). Applying the series to $\widehat{\xi}_i$ and collecting blocks gives the *group* exponential

$$\exp(\widehat{\xi}_i) \;=\; \begin{bmatrix} \mathbf{R}_i & \mathbf{t}_i \\ \mathbf{0}^\top & 1 \end{bmatrix}, \qquad \mathbf{R}_i \;=\; \exp(\widehat{\omega}_i), \quad \mathbf{t}_i \;=\; \mathbf{V}(\omega_i)\,\mathbf{v}_i,$$

with

$$\mathbf{V}(\omega_i) \;=\; \sum_{n=0}^{\infty} \frac{1}{(n+1)!}\, \widehat{\omega}_i^{\,n} \;=\; \mathbf{I}_3 + \frac{1-\cos\theta}{\theta^2}\, \widehat{\omega}_i + \frac{\theta - \sin\theta}{\theta^3}\, \widehat{\omega}_i^{\,2}, \qquad \theta = \|\omega_i\|.$$

Why these closed forms appear: the skew matrix $\widehat{\omega}$ satisfies the polynomial identities $\widehat{\omega}^3 = -\theta^2\widehat{\omega}$ and $\widehat{\omega}^4 = -\theta^2\widehat{\omega}^2$. Grouping even and odd powers in the series produces the sine/cosine Taylor series, yielding Rodrigues' formula for rotation and the companion $\mathbf{V}$ for the translation block.

Why $\exp(\widehat{\omega})$ is a valid rotation. Since $\widehat{\omega}^\top = -\widehat{\omega}$ and $\operatorname{tr}(\widehat{\omega}) = 0$,

$$\mathbf{R}^\top\mathbf{R} = \exp(\widehat{\omega})^\top \exp(\widehat{\omega}) = \exp(-\widehat{\omega})\exp(\widehat{\omega}) = \mathbf{I}_3, \qquad \det(\mathbf{R}) = \exp(\operatorname{tr}(\widehat{\omega})) = 1,$$

so $\mathbf{R} \in \mathrm{SO}(3)$ by construction.

Closed forms and small-angle limits. Rodrigues' formula gives

$$\mathbf{R} = \mathbf{I}_3 + \frac{\sin\theta}{\theta}\,\widehat{\omega} + \frac{1-\cos\theta}{\theta^2}\,\widehat{\omega}^2, \qquad \mathbf{t} = \mathbf{V}(\omega)\,\mathbf{v}.$$

As $\theta \to 0$, $\mathbf{R} \approx \mathbf{I}_3 + \widehat{\omega}$ and $\mathbf{V}(\omega) \approx \mathbf{I}_3 + \frac{1}{2}\widehat{\omega}$, so $\exp(\widehat{\xi}) \approx \mathbf{I}_4 + \widehat{\xi}$. Special cases: $\omega = \mathbf{0}$ gives pure translation ($\mathbf{R} = \mathbf{I}_3,\ \mathbf{t} = \mathbf{v}$); $\mathbf{v} = \mathbf{0}$ gives pure rotation ($\exp(\widehat{\xi}) = \operatorname{diag}(\mathbf{R}, 1)$).

Pose update (left composition) and numerical evaluation. Given the current camera-to-world transform $\mathbf{T}_i$, the update uses a left increment

$$\mathbf{T}_i \;\leftarrow\; \exp\big(\widehat{\xi}_i\big)\,\mathbf{T}_i,$$

which perturbs the camera in world coordinates (consistent with rays being functions of $\mathbf{T}_i$). Closed forms are evaluated as

$$\text{if } \theta > \varepsilon:\ \mathbf{R} = \mathbf{I}_3 + \tfrac{\sin\theta}{\theta}\widehat{\omega} + \tfrac{1-\cos\theta}{\theta^2}\widehat{\omega}^2, \quad \mathbf{t} = \mathbf{V}(\omega)\,\mathbf{v}; \quad \text{else use the Taylor limits above,}$$

which stabilizes computation near $\theta = 0$. Optimizing the unconstrained vector $\xi_i \in \mathbb{R}^6$ is therefore advantageous: each gradient step in $\mathbb{R}^6$ is mapped by exp back to a valid rigid motion, and the small-step behavior matches the familiar axis–angle and translation increments that yield well-scaled Jacobians for backpropagation.

How a pose increment moves 3D samples (and affects colors)

For a pixel $\mathbf{u}$ in view i, the camera–frame ray is

$$\mathbf{r}_i(t) = \mathbf{o}_i + t\,\widehat{\mathbf{d}}_i(\mathbf{u}), \quad t \in [t_n, t_f],$$

and the corresponding world point under $\mathbf{T}_i = [\mathbf{R}_i \mid \mathbf{t}_i]$ is

$$\mathbf{y}(t) = \mathbf{R}_i\big(\mathbf{o}_i + t\,\widehat{\mathbf{d}}_i\big) + \mathbf{t}_i.$$

A small left increment $\xi_i = [\omega_i^\top, \mathbf{v}_i^\top]^\top$ yields the first-order Jacobians

$$\frac{\partial \mathbf{y}}{\partial \omega_i} = -[\mathbf{y}]_\times, \qquad \frac{\partial \mathbf{y}}{\partial \mathbf{v}_i} = \mathbf{I}_3,$$

where $[\mathbf{a}]_\times\mathbf{b} = \mathbf{a} \times \mathbf{b}$. For the j-th world sample $\mathbf{x}_j = \mathbf{y}(t_j)$,

$$\frac{\partial \mathbf{x}_j}{\partial \xi_i} = \big[\, -[\mathbf{x}_j]_\times \;\; \mathbf{I}_3 \,\big] \in \mathbb{R}^{3\times 6}.$$

Backpropagating through the differentiable volume renderer gives the per-pixel pose gradient

$$\frac{\partial \widehat{\mathbf{C}}_i(\mathbf{u})}{\partial \xi_i} = \sum_{j=1}^{N} \frac{\partial \widehat{\mathbf{C}}_i}{\partial \mathbf{x}_j}\big[\, -[\mathbf{x}_j]_\times \;\; \mathbf{I}_3 \,\big],$$

where $\frac{\partial \widehat{\mathbf{C}}_i}{\partial \mathbf{x}_j}$ is provided by autodiff from the field f_θ and the compositing rule.

Ray-compositing gradients (decomposition)
With discrete compositing $\widehat{\mathbf{C}} = \sum_{j=1}^{N} w_j \mathbf{c}_j$ and

$$\alpha_j = 1 - \exp(-\sigma_j \delta_j), \quad T_j = \prod_{k<j} (1 - \alpha_k), \quad w_j = T_j \alpha_j,$$

the pose gradient splits into a *weight path* and a *color path*:

$$\frac{\partial \widehat{\mathbf{C}}}{\partial \xi} = \sum_{j=1}^{N} \Big(\underbrace{\frac{\partial w_j}{\partial \xi} \mathbf{c}_j}_{\text{weight path}} + \underbrace{w_j \frac{\partial \mathbf{c}_j}{\partial \xi}}_{\text{color path}} \Big),$$

with

$$\frac{\partial \mathbf{c}_j}{\partial \xi} = \frac{\partial \mathbf{c}}{\partial \mathbf{x}}\Big|_{\mathbf{x}_j} \frac{\partial \mathbf{x}_j}{\partial \xi}, \qquad \frac{\partial \sigma_j}{\partial \xi} = \frac{\partial \sigma}{\partial \mathbf{x}}\Big|_{\mathbf{x}_j} \frac{\partial \mathbf{x}_j}{\partial \xi}.$$

The weights differentiate as

$$\frac{\partial w_j}{\partial \xi} = \underbrace{\frac{\partial T_j}{\partial \xi} \alpha_j}_{\text{upstream densities}} + \underbrace{T_j \frac{\partial \alpha_j}{\partial \xi}}_{\text{local density}}, \qquad \frac{\partial \alpha_j}{\partial \xi} = e^{-\sigma_j \delta_j} \delta_j \frac{\partial \sigma_j}{\partial \xi},$$

and, using $1 - \alpha_k = \exp(-\sigma_k \delta_k)$,

$$\frac{\partial T_j}{\partial \xi} = T_j \sum_{k<j} \frac{-1}{1 - \alpha_k} \frac{\partial \alpha_k}{\partial \xi} = -T_j \sum_{k<j} \delta_k \frac{\partial \sigma_k}{\partial \xi}.$$

Every term factors through the geometric Jacobian $\frac{\partial \mathbf{x}_j}{\partial \xi}$, enabling joint updates of θ and $\{\mathbf{T}_i\}$.

Why smooth inputs help pose gradients
For a pixel $\mathbf{u}$ in view i, the pose gradient aggregates sample-wise contributions

$$\frac{\partial \widehat{\mathbf{C}}_i(\mathbf{u})}{\partial \xi_i} = \sum_{j=1}^{N} \underbrace{\frac{\partial \widehat{\mathbf{C}}_i}{\partial \mathbf{x}_j}}_{\text{appearance/density}} \underbrace{\frac{\partial \mathbf{x}_j}{\partial \xi_i}}_{\text{geometry}}, \qquad \frac{\partial \widehat{\mathbf{C}}_i}{\partial \mathbf{x}_j} = \frac{\partial \widehat{\mathbf{C}}_i}{\partial \sigma_j} \frac{\partial \sigma}{\partial \mathbf{x}}\Big|_{\mathbf{x}_j} + \frac{\partial \widehat{\mathbf{C}}_i}{\partial \mathbf{c}_j} \frac{\partial \mathbf{c}}{\partial \mathbf{x}}\Big|_{\mathbf{x}_j}.$$

The geometry term $\frac{\partial \mathbf{x}_j}{\partial \xi_i}$ is smooth (Sec. 23.11.1); the stability of the sum is therefore governed by how smoothly $\frac{\partial \sigma}{\partial \mathbf{x}}$ and $\frac{\partial \mathbf{c}}{\partial \mathbf{x}}$ vary across neighboring samples.

With positional encoding (PE), the field is composed as $f_\theta = f'_\theta \circ \gamma$ with input $\phi = \gamma(\mathbf{x})$. By the chain rule,

$$\frac{\partial \sigma}{\partial \mathbf{x}} = \frac{\partial \sigma}{\partial \phi} \frac{\partial \gamma(\mathbf{x})}{\partial \mathbf{x}}, \qquad \frac{\partial \mathbf{c}}{\partial \mathbf{x}} = \frac{\partial \mathbf{c}}{\partial \phi} \frac{\partial \gamma(\mathbf{x})}{\partial \mathbf{x}}.$$

Hence the spatial variation and magnitude of the PE Jacobian $\frac{\partial \gamma}{\partial \mathbf{x}}$ directly set the smoothness of the appearance/density factor $\frac{\partial \widehat{\mathbf{C}}_i}{\partial \mathbf{x}_j}$.

Effect of high-frequency PE. BARF defines the L-band PE (coordinate-wise) as

$$\gamma(\mathbf{x}) = \big[\mathbf{x},\, \gamma_0(\mathbf{x}), \ldots, \gamma_{L-1}(\mathbf{x})\big] \in \mathbb{R}^{3+6L}, \quad \gamma_k(\mathbf{x}) = \big[\cos(2^k\pi\mathbf{x}), \sin(2^k\pi\mathbf{x})\big] \in \mathbb{R}^6,$$

whose Jacobian is

$$\frac{\partial \gamma_k(\mathbf{x})}{\partial \mathbf{x}} = 2^k\pi\,\big[-\sin(2^k\pi\mathbf{x}),\, \cos(2^k\pi\mathbf{x})\big]. \tag{23.48}$$

Equation (23.48) shows two issues for registration at large k: (i) the Jacobian norm scales as $O(2^k)$ (very steep), and (ii) its direction flips with spatial period $\lambda_k \approx 2^{-k}$ (very rapid sign changes). When high-k bands dominate early, adjacent samples $\mathbf{x}_j$ and $\mathbf{x}_{j+1}$ frequently lie on opposite sides of a sine/cosine lobe, so their $\frac{\partial \widehat{\mathbf{C}}_i}{\partial \mathbf{x}_j}$ directions disagree and partially cancel in the sum over j. The net pose gradient becomes weak/noisy and the first-order update has a small trust region.

Coarse-to-fine positional encoding

Windowed positional encoding

To restore directional coherence early and full fidelity later, BARF modulates each band by a smooth window $w_k(\alpha) \in [0,1]$ driven by progress $\alpha \in [0, L]$:

$$\gamma_k(\mathbf{x};\alpha) = w_k(\alpha)\,\big[\cos(2^k\pi\mathbf{x}),\, \sin(2^k\pi\mathbf{x})\big], \tag{23.49}$$

with the raised-cosine schedule

$$w_k(\alpha) = \begin{cases} 0 & \text{if } \alpha < k, \\ \dfrac{1-\cos\big((\alpha-k)\pi\big)}{2} & \text{if } 0 \le \alpha - k < 1, \\ 1 & \text{if } \alpha - k \ge 1. \end{cases} \tag{23.50}$$

Differentiating (23.49) yields

$$\frac{\partial \gamma_k(\mathbf{x};\alpha)}{\partial \mathbf{x}} = w_k(\alpha)\,2^k\pi\,\big[-\sin(2^k\pi\mathbf{x}),\, \cos(2^k\pi\mathbf{x})\big], \tag{23.51}$$

i.e., the PE Jacobian's magnitude and oscillation are attenuated by $w_k(\alpha)$.

Curriculum. A simple linear ramp $\alpha(t)$ from 0 to L over a chosen iteration window implements coarse→fine training: early iterations keep $w_k(\alpha) \approx 0$ for large k, suppressing the high-frequency, rapidly flipping factors in (23.51); neighboring $\frac{\partial \widehat{\mathbf{C}}_i}{\partial \mathbf{x}_j}$ then vary slowly and add constructively, enlarging the trust region for pose updates. As alignment stabilizes, $w_k(\alpha) \to 1$ for all k, restoring full bandwidth so the radiance field recovers fine detail without destabilizing registration.

Architecture and implementation details

We follow BARF's NeRF setup with minor simplifications [352]. Training uses a single MLP (128 hidden units per layer) without hierarchical sampling. Images are resized to 400×400, and 1024 pixel rays are sampled per step. Each ray is discretized into N=128 points; density σ is stabilized with `softplus`. Optimization uses Adam for 200K iterations with learning rates decayed from $5\times10^{-4} \to 10^{-4}$ for the network f and $10^{-3} \to 10^{-5}$ for the poses. The coarse→fine positional encoding (PE) schedule linearly ramps α from iterations 20K → 100K, after which all bands up to L=10 are active.

Network and sampling

The network f_θ follows NeRF's design with separate density and color heads, stratified sampling of N points per ray, and standard α-compositing. Hierarchical sampling is omitted to isolate registration effects.

Optimization

Parameters θ and $\{\mathbf{p}_i\}$ are optimized jointly with Adam. The PE progress α is ramped linearly over a preset iteration range; once $\alpha = L$, all bands remain active. Camera intrinsics are assumed known; poses are updated via the Lie-algebra increments above. Unless otherwise noted, evaluation follows the paper: Procrustes alignment for pose errors and PSNR/SSIM/LPIPS for synthesis quality.

Experiments and ablations

Datasets and evaluation protocol

Evaluation is conducted on widely used real and synthetic benchmarks. For pose accuracy, optimized trajectories are first aligned to ground truth via Procrustes on camera centers, after which mean rotation and translation errors are reported. For view-synthesis quality (PSNR, SSIM, LPIPS), BARF follows NeRF's rendering pipeline but includes a brief *test-time photometric refinement* step to reduce residual pose errors before reporting metrics. This ensures that differences in image quality reflect scene modeling rather than leftover misregistration.

Planar image alignment

BARF jointly learns a coordinate-based image and patch warps. Compared to naïve (full) positional encoding (PE) and no-PE baselines, BARF recovers accurate alignment and a sharper image representation [352].

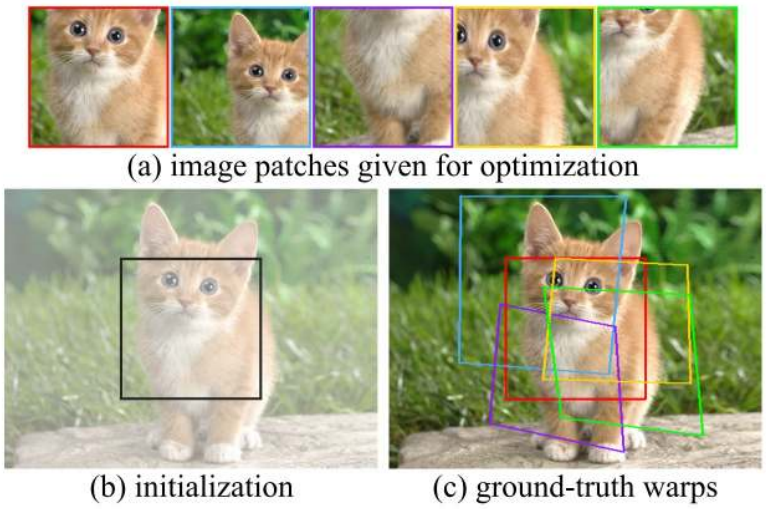

Figure 23.84: Planar alignment setup and ground-truth warps. Reproduced from [352].

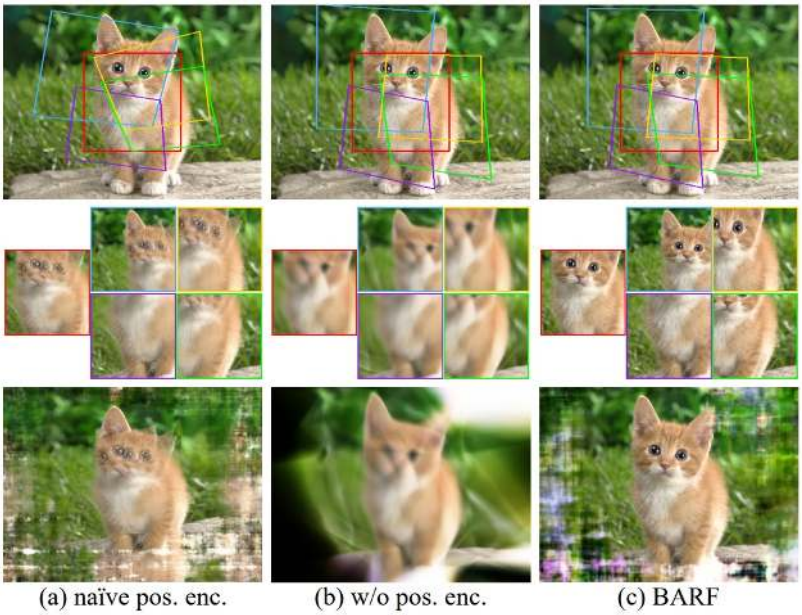

Figure 23.85: Qualitative planar alignment: optimized warps (top), patch reconstructions (middle), and recovered image representation (bottom). BARF attains accurate warps and high-fidelity reconstruction; full PE misregisters and no-PE blurs. Reproduced from [352].

Positional encoding	$\mathrm{SL}(3)$ registration error $\downarrow$	Patch PSNR (dB) $\uparrow$
naïve (full)	0.2949	23.41
without	0.0641	24.72
BARF (coarse-to-fine)	**0.0096**	**35.30**

Table 23.20: Planar alignment ablation on positional encoding (values from [352]). Homographies are estimated by minimizing photometric error and compared to ground truth via the geodesic/log metric on $\mathrm{SL}(3)$, $d_{\mathrm{SL}(3)}(H_{\mathrm{est}}, H_{\mathrm{gt}}) = \|\log(H_{\mathrm{est}} H_{\mathrm{gt}}^{-1})\|_F$ (lower is better). Reconstruction quality is measured by PSNR on a target patch after warping with H_{est} (higher is better). Coarse-to-fine PE yields both the most accurate registration and the best reconstruction.

Synthetic NeRF scenes

With synthetic pose noise, BARF realigns cameras and matches the view quality of a pose-supervised NeRF [352].

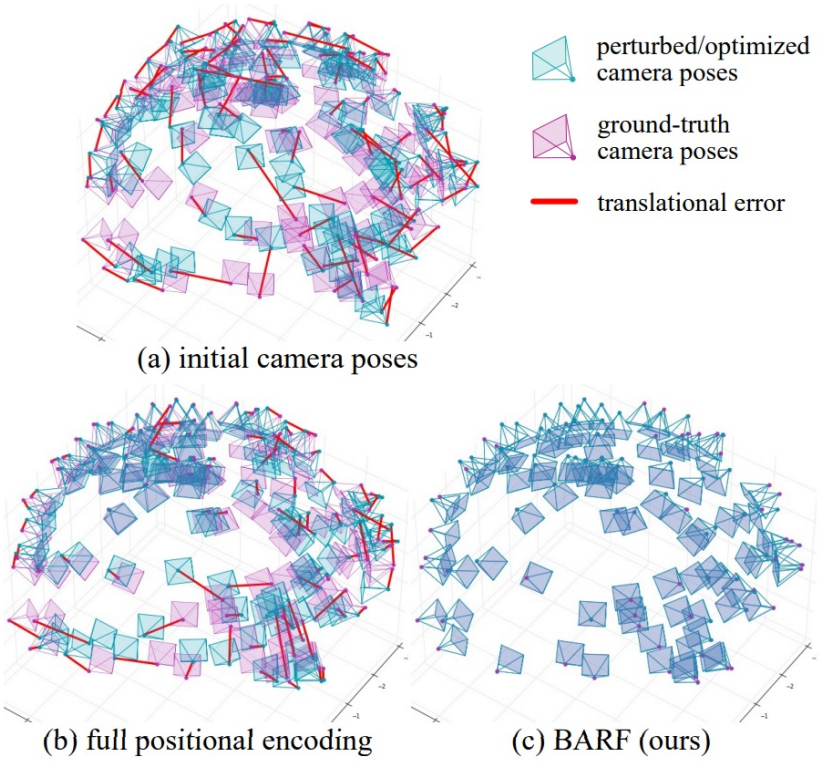

Figure 23.86: Initial versus optimized poses on `chair` (Procrustes aligned). BARF realigns the trajectory; full PE gets stuck. Reproduced from [352].

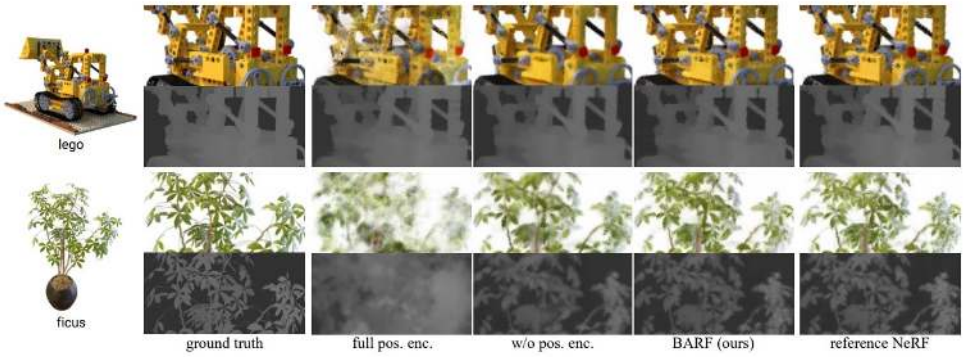

Figure 23.87: Synthetic scenes: image synthesis (top row for each image) and expected depth (bottom row for each image). BARF achieves quality comparable to NeRF trained with perfect poses. Reproduced from [352].

Table 23.21: NeRF on synthetic scenes with perturbed poses. BARF optimizes registration while maintaining synthesis quality near the pose-supervised reference. Numbers from [352].

Scene	Rotation (°)↓			Translation↓			PSNR↑			PSNR (ref.)	SSIM↑			SSIM (ref.)	LPIPS↓			LPIPS (ref.)
	full	w/o	BARF	full	w/o	BARF	full	w/o	BARF		full	w/o	BARF		full	w/o	BARF	
Chair	7.186	0.110	**0.096**	16.638	0.555	**0.428**	19.02	30.22	**31.16**	31.91	0.804	0.942	**0.954**	0.961	0.223	0.065	**0.044**	0.036
Drums	3.208	0.057	**0.043**	3.222	0.255	**0.225**	20.83	23.56	**23.91**	23.96	0.840	0.893	**0.900**	0.902	0.166	0.116	**0.099**	0.095
Ficus	9.368	0.095	**0.085**	10.135	0.430	**0.474**	19.75	25.58	**26.26**	26.68	0.836	0.922	**0.934**	0.941	0.182	0.070	**0.058**	0.051
Hotdog	3.290	**0.225**	0.248	6.344	**1.122**	1.308	28.15	34.00	**34.54**	34.91	0.923	0.967	**0.970**	0.973	0.083	0.040	**0.032**	0.032
Lego	3.252	0.108	**0.082**	4.841	0.391	**0.291**	24.23	26.37	**28.33**	29.28	0.876	0.898	**0.927**	0.942	0.102	0.112	**0.050**	0.037
Materials	6.971	**0.845**	1.188	2.287	0.678	**0.422**	22.45	26.86	**27.84**	28.92	0.891	0.905	**0.940**	0.944	0.249	0.068	**0.045**	0.041
Mic	10.554	0.081	**0.071**	22.724	0.356	**0.301**	15.10	19.93	**21.18**	31.98	0.788	0.968	**0.971**	0.971	0.334	0.050	**0.048**	0.044
Ship	5.506	0.095	**0.075**	7.232	0.354	**0.326**	22.12	26.78	**27.50**	28.00	0.755	0.833	**0.849**	0.858	0.255	0.175	**0.132**	0.118
Mean	6.167	0.202	**0.193**	11.303	0.768	**0.756**	22.12	26.78	**27.50**	29.40	0.821	0.917	**0.930**	0.936	0.205	0.087	**0.065**	0.057

Real LLFF scenes with unknown poses

BARF localizes from identity initialization and achieves synthesis quality comparable to a reference NeRF trained with SfM poses [352].

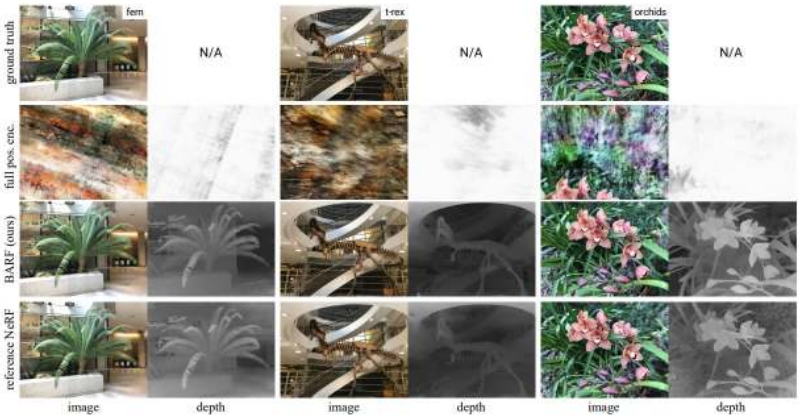

Figure 23.88: Real scenes from unknown poses. BARF jointly recovers poses and scene; full PE diverges. Reproduced from [352].

Table 23.22: LLFF forward-facing scenes from unknown poses. BARF localizes from scratch and attains high-fidelity synthesis. Numbers from [352].

Scene	Rotation (°)↓		Translation↓		PSNR↑		PSNR (ref.)	SSIM↑		SSIM (ref.)	LPIPS↓		LPIPS (ref.)
	full	BARF	full	BARF	full	BARF		full	BARF		full	BARF	
Fern	74.452	**0.191**	30.167	**0.192**	9.81	**23.79**	23.72	0.187	**0.710**	0.733	0.853	**0.311**	0.262
Flower	2.525	**0.251**	2.635	**0.224**	17.08	**23.37**	23.24	0.344	**0.698**	0.668	0.490	**0.211**	0.244
Fortress	75.094	**0.479**	33.231	**0.364**	12.15	**29.08**	25.97	0.270	**0.823**	0.786	0.807	**0.132**	0.185
Horns	58.764	**0.304**	32.664	**0.222**	8.89	**22.78**	20.35	0.158	**0.727**	0.624	0.805	**0.298**	0.421
Leaves	88.091	**1.272**	13.540	**0.249**	9.64	**18.78**	15.33	0.067	**0.537**	0.306	0.782	**0.353**	0.526
Orchids	37.104	**0.627**	20.312	**0.404**	9.42	**19.45**	17.34	0.085	**0.574**	0.518	0.806	**0.291**	0.307
Room	173.811	**0.320**	66.922	**0.270**	10.78	**31.95**	32.48	0.278	**0.940**	0.948	0.871	**0.099**	0.083
T-rex	166.231	**1.138**	53.309	**0.720**	10.48	**22.55**	22.12	0.158	**0.767**	0.739	0.885	**0.206**	0.244
Mean	84.509	**0.573**	31.598	**0.331**	11.03	**23.97**	22.56	0.193	**0.722**	0.665	0.787	**0.238**	0.283

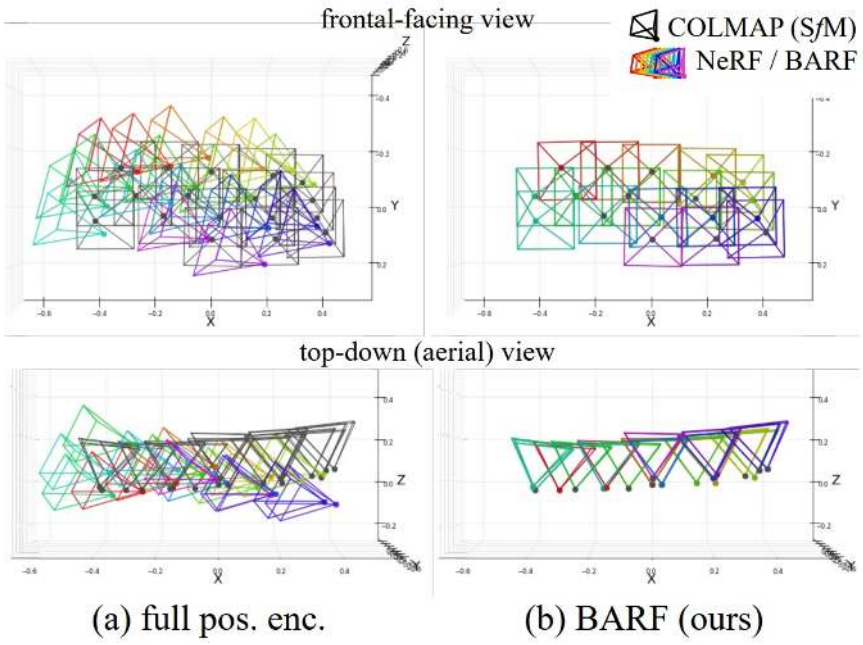

Figure 23.89: Optimized poses on `fern` (Procrustes aligned). BARF closely agrees with SfM. Reproduced from [352].

Limitations and future work

Limitations

- **Schedule sensitivity** The coarse→fine bandwidth schedule ($\alpha(t)$, window w_k) is hand-set; poor schedules can under/over-regularize early registration and shrink the convergence basin.
- **Compute and sampling** Jointly optimizing poses and a volumetric field requires dense per-ray sampling and long training, so runtime scales with samples per ray and number of images.
- **Scene/model assumptions** The formulation assumes static scenes, photometric consistency, and known intrinsics; motion blur, rolling shutter, illumination/exposure shifts, and unknown intrinsics are out of scope.

Follow-ups addressing BARF's limitations

- **Pose robustness with sparse/noisy inputs** *SPARF* augments BARF's photometric objective with multi-view feature correspondences to jointly refine NeRF and poses from very few, noisy views, improving pose stability when geometric signal is weak [633].
- **Pose-free initialization** *NoPe-NeRF* removes the need for pose priors by jointly recovering camera poses and the field from raw images, expanding BARF's setting to completely unknown extrinsics [44].
- **Photometric violations: motion blur** *BAD-NeRF* handles significant motion blur while bundle-adjusting, coupling a deblurring model with pose refinement so that residuals remain informative for registration under real camera shake [666].
- **Generalization and efficiency** *DBARF* marries BARF-style bundle adjustment with a generalizable NeRF backbone, improving data-efficiency and robustness across scenes while still refining poses end-to-end [97].

Enrichment 23.11.2: NeRF-W: NeRF for Unconstrained Photo Collections

Motivation

Vanilla NeRF [429] assumes a *static*, photometrically consistent scene in which geometry, reflectance, and illumination are constant across views. In-the-wild photo collections such as Phototourism [577] break these assumptions due to:

- Substantial photometric shifts (time of day, weather, exposure/white balance, post-processing).
- *Transient* occluders (people, vehicles, scaffolding).

which, when trained naively, lead NeRF to produce colored fog, ghosting, and biased geometry.

(a) Photos (b) Renderings

Figure 23.90: **Variable illumination control with NeRF-W.** (a) Given only an internet photo collection NeRF-W renders novel views with variable illumination (b) Slices from renderings driven by appearance embeddings associated with four training images (Phototourism). Photos by Flickr users dbowie78, vasnic64, punch / CC BY. *Credit:* [418].

NeRF-W at a glance

NeRF-W [418] extends NeRF to Internet photo collections by keeping a *single, shared* static geometry and routing nuisances into two learned, image-specific factors. Before diving into equations, it helps to fix the data flow and what each part sees and produces:

- **Inputs and data flow.** Each pixel in image I_i defines a calibrated ray with world-space samples $\mathbf{x}$ and a viewing direction $\mathbf{d}$. The model consumes: position encodings of $\mathbf{x}$ for geometry, a directional encoding of $\mathbf{d}$ for view dependence, and two small per-image codes $\ell_i^{(a)}$ (appearance) and $\ell_i^{(\tau)}$ (transient). Geometry is predicted without any image-specific code; color may depend on both $\mathbf{d}$ and $\ell_i^{(a)}$.
- **Trunk and static field.** A NeRF-style trunk maps the position-encoded 3D sample $\mathbf{x}$ to a *static* volume density $\sigma(\mathbf{x})$ and a learned feature vector $\mathbf{z}(\mathbf{x})$. These features summarize local scene properties beyond coordinates (e.g., geometry/material cues) and are passed to lightweight heads, while $\sigma(\mathbf{x})$ is computed *without* any image-specific latent so that one shared geometry is enforced across all images.

- **Appearance embedding $\ell_i^{(a)}$ and static color head.** Each training image I_i carries a low-dimensional appearance code $\ell_i^{(a)}$ that enters *only* the color branch. The static color head takes the geometric features extracted from the basic geometry network, $\mathbf{z}(\mathbf{x})$, a directional encoding of $\mathbf{d}$, and $\ell_i^{(a)}$ to produce RGB radiance $\mathbf{c}_i(\mathbf{x}, \mathbf{d})$. Intuition: exposure, white balance, tone mapping, and illumination differences are absorbed by $\ell_i^{(a)}$, allowing color to adapt while geometry stays fixed.
- **Transient embedding $\ell_i^{(\tau)}$ and transient head.** A second per-image code $\ell_i^{(\tau)}$ drives a transient head that, from $\mathbf{z}(\mathbf{x})$, predicts an image-dependent density $\sigma_i^{(\tau)}(\mathbf{x})$, a transient color $\mathbf{c}_i^{(\tau)}(\mathbf{x})$, and a per-sample uncertainty signal used during training. Intuition: content that appears only in some photos (people, cars, flags, scaffolding) is explained by this *per-image* layer instead of corrupting the shared static scene.
- **Compositing and learning signal.** Along each ray, static and transient opacities jointly control transmittance, and their colors are alpha-composited into a single prediction that is compared to the observed RGB under a Gaussian negative log-likelihood. The rendered per-ray uncertainty down-weights unreliable pixels, and an ℓ_1 sparsity prior discourages overuse of the transient density. Intuition: persistent structure must be explained by the static field; ephemeral phenomena are explained *sparingly* by the transient field; photometric shifts are handled by $\ell_i^{(a)}$.
- **Inference-time behavior.** For novel-view synthesis without a reference image, the transient path is disabled and only the static field is rendered to produce clean, temporally stable views, while the appearance can be controlled by fixing, averaging, or interpolating $\ell^{(a)}$ of the scene training images. For a held-out photo, a small $\ell^{(a)}$ can be optimized on a subset of its pixels to match its look, with geometry remaining shared because the static $\sigma(\cdot)$ never depends on $\ell^{(a)}$.

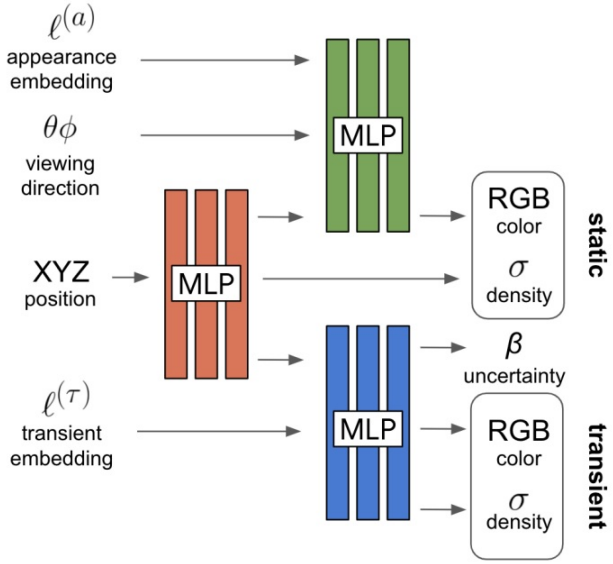

Figure 23.91: **NeRF-W model architecture.** Given a 3D position $\mathbf{x}$, viewing direction $\mathbf{d}$, and learned per-image embeddings $\ell_i^{(a)}$ (appearance) and $\ell_i^{(\tau)}$ (transient), the network outputs static and transient colors and densities, along with a training-time uncertainty. Static opacity is produced before conditioning on appearance, enforcing a single shared geometry across images. *Credit:* [418].

Method: Formulation and Derivation

Rendering operator

Let a calibrated ray be $\mathbf{r}(t) = \mathbf{o} + t\,\mathbf{d}$, $t \in [t_n, t_f]$, with samples $t_1, \ldots, t_K$ and steps $\delta_k = t_{k+1} - t_k$. The discrete volume–rendering operator is

$$R(\mathbf{r},\, f,\, \sigma) \;=\; \sum_{k=1}^{K} T(t_k)\; \alpha\big(\sigma(t_k)\,\delta_k\big)\; f(t_k), \qquad \alpha(x) = 1 - e^{-x}. \tag{23.52}$$

Here $T(t_k) = \prod_{k'=1}^{k-1} \exp(-\sigma(t_{k'})\,\delta_{k'}) = \exp(-\sum_{k'=1}^{k-1} \sigma(t_{k'})\,\delta_{k'})$ is the cumulative *transmittance* to the start of slab k, and $\alpha(\sigma(t_k)\delta_k) = 1 - \exp(-\sigma(t_k)\delta_k)$ is the *per-interval opacity*, i.e., the probability the first interaction happens inside slab k given survival to its entrance.

What f is in practice and how NeRF-W instantiates R

The operator R is a generic "first-hit expectation" that composites a per-sample quantity $f(t)$ under the same probabilistic survival/termination process. NeRF-W uses this operator in two concrete ways: to mix *colors* from a shared static field and an image-dependent transient field, and to render a *per-ray uncertainty* that only affects the training loss.

- **Single-field baseline (orientation).** With one density $\sigma(\mathbf{x})$ and one per-sample RGB $\mathbf{c}(\mathbf{x}, \mathbf{d})$, taking $f = \mathbf{c}$ yields the expected color $R(\mathbf{r}, \mathbf{c}, \sigma)$, as in vanilla NeRF's emission–absorption model.
- **Two-field color in NeRF-W.** NeRF-W adds an image-dependent transient field with density $\sigma_i^{(\tau)}$ and color $\mathbf{c}_i^{(\tau)}$ alongside the shared static field $(\sigma, \mathbf{c}_i)$. During training, both densities attenuate the ray, so survival uses the *joint* density,

  $$T_i(t_k) \;=\; \exp\Big(-\sum_{k'<k} \big[\sigma(t_{k'}) + \sigma_i^{(\tau)}(t_{k'})\big]\,\delta_{k'}\Big).$$

  The expected color is then the sum of two contributions—one from each field—weighted by their own opacities:

  $$\hat{\mathbf{C}}_i(\mathbf{r}) \;=\; \sum_{k=1}^{K} T_i(t_k)\Big(\alpha(\sigma(t_k)\delta_k)\,\mathbf{c}_i(t_k) \;+\; \alpha(\sigma_i^{(\tau)}(t_k)\delta_k)\,\mathbf{c}_i^{(\tau)}(t_k)\Big). \tag{23.53}$$

  Intuition: Persistent structure is explained by the appearance-conditioned *static* color, while image-specific occluders are explained by the *transient* color; because both densities enter survival, they *compete* to explain where the first interaction lies.
- **Rendered per-ray uncertainty (definition and why transient-only).** The transient head, conditioned on the image-specific code $\ell_i^{(\tau)}$, outputs an unconstrained value $\tilde{\beta}_i(t)$ per sample, which we map to a nonnegative scale with a shifted softplus

  $$\beta_i(t) \;=\; \beta_{\min} \;+\; \log\big(1 + \exp(\tilde{\beta}_i(t))\big),$$

  where $\beta_{\min} > 0$ avoids zero-variance and prevents the optimizer from entirely ignoring any ray. We then *render* a ray-wise uncertainty (standard deviation) by alpha-compositing $\beta_i(t)$ *through the transient opacity*:

  $$\hat{\beta}_i(\mathbf{r}) \;=\; \sum_{k=1}^{K} T_i(t_k)\,\alpha\big(\sigma_i^{(\tau)}(t_k)\,\delta_k\big)\,\beta_i(t_k), \tag{23.54}$$

with survival T_i computed from the joint density $\sigma + \sigma_i^{(\tau)}$. Routing via $\sigma_i^{(\tau)}$ is intentional: the same transient mechanism that boosts opacity for ephemeral content also gates how much $\beta_i(t)$ contributes to $\hat{\beta}_i(\mathbf{r})$. This ties uncertainty *exactly* to occluders and photometric outliers explained by the transient pathway, rather than diluting it over persistent static structure.

- **How picture-specific content shows up in the transient/uncertainty path.**
  - *What the transient head drives.* The transient branch produces a density $\sigma^{(\tau)}(t)$, a color $\mathbf{c}^{(\tau)}(t)$, and an uncertainty carrier $\beta(t)$. In the color compositor (Eq. (23.53)), $\sigma^{(\tau)}$ enters via its opacity $\alpha(\sigma^{(\tau)}\delta)$. In the uncertainty compositor (Eq. (23.54)), the same opacity gates how $\beta(t)$ accumulates into the ray-wise $\hat{\beta}(\mathbf{r})$.
  - *When a ray hits ephemeral content.* If a ray passes through an occluder or a photometric outlier, training can increase $\sigma^{(\tau)}$ on those samples. Two coupled effects follow: (i) $\alpha(\sigma^{(\tau)}\delta)$ grows, so $\mathbf{c}^{(\tau)}$ gets more weight in Eq. (23.53); (ii) the same $\alpha(\sigma^{(\tau)}\delta)$ also increases the contribution of $\beta(t)$ to $\hat{\beta}(\mathbf{r})$ in Eq. (23.54), making that ray's supervision softer in the loss.
  - *When the content is absent.* Where no ephemeral content is present, $\sigma^{(\tau)} \approx 0 \Rightarrow \alpha(\sigma^{(\tau)}\delta) \approx 0$; both the transient color and the rendered uncertainty vanish, and the ray is supervised normally by the static pathway.
- **Gaussian NLL (training-time reweighting).** ***Notation:*** **dropping image indices.** For clarity, when we write $\mathbf{C}(\mathbf{r})$, $\hat{\mathbf{C}}(\mathbf{r})$, and $\hat{\beta}(\mathbf{r})$ *without* image index, we mean "for the image that $\mathbf{r}$ comes from". Concretely, if $\mathbf{r}$ is sampled from image i,

$$\mathbf{C}(\mathbf{r}) \equiv \mathbf{C}_i(\mathbf{r}), \quad \hat{\mathbf{C}}(\mathbf{r}) \equiv \hat{\mathbf{C}}_i(\mathbf{r}) \text{ (Eq. (23.53) using } \ell_i^{(a)}, \ell_i^{(\tau)}), \quad \hat{\beta}(\mathbf{r}) \equiv \hat{\beta}_i(\mathbf{r}) \text{ (Eq. (23.54))},$$

and in the sparsity term $\sigma^{(\tau)}(t_k) \equiv \sigma_i^{(\tau)}(t_k)$. With this shorthand, we assume isotropic, ray-specific noise, $\mathbf{C}(\mathbf{r}) \sim \mathcal{N}\big(\hat{\mathbf{C}}(\mathbf{r}), \hat{\beta}(\mathbf{r})^2\mathbf{I}\big)$, giving the per-ray NLL (up to a constant)

$$\mathscr{L}(\mathbf{r}) = \underbrace{\frac{\big\|\mathbf{C}(\mathbf{r}) - \hat{\mathbf{C}}(\mathbf{r})\big\|_2^2}{2\hat{\beta}(\mathbf{r})^2}}_{\text{(a) data fit: down-weight uncertain rays}} + \underbrace{\tfrac{1}{2}\log\big(\hat{\beta}(\mathbf{r})^2\big)}_{\text{(b) variance regularizer}} + \underbrace{\lambda_u \frac{1}{K}\sum_{k=1}^{K} \sigma^{(\tau)}(t_k)}_{\text{(c) transient sparsity}}. \tag{23.55}$$

  - **(a) Data fit.** With $\mathbf{e} = \mathbf{C} - \hat{\mathbf{C}}$, the residual is scaled by $1/\hat{\beta}^2$: larger predicted uncertainty $\Rightarrow$ the ray *pays less* in the loss and contributes weaker gradients. Because $\hat{\beta}$ is composited through transient opacity (Eq. (23.54)), this down-weighting targets rays affected by transient phenomena.
  - **(b) Variance regularizer.** The $\frac{1}{2}\log\hat{\beta}^2$ term is the Gaussian normalizer; it prevents the trivial escape $\hat{\beta} \to \infty$ and calibrates the learned scale. Minimizing (a)+(b) w.r.t. $\hat{\beta}^2$ gives $\hat{\beta}^2 = \|\mathbf{e}\|^2$: *intuitively*, the model is nudged to predict a per-ray variance commensurate with that ray's squared error—big errors (noisy/hard rays) push $\hat{\beta}$ up; small errors pull it down. This keeps $\hat{\beta}$ neither exploding (penalized by log) nor collapsing to zero (penalized by the data term).
  - **(c) Transient sparsity.** The ℓ_1-style penalty on nonnegative $\sigma^{(\tau)}$ discourages using the transient density to explain persistent structure, preserving a clean static reconstruction.

  Training vs. inference. This NLL is used only during training to make supervision robust (via $\hat{\beta}$) and to keep transients sparse. At inference, the transient/uncertainty branches are disabled and we render only with $f = \mathbf{c}$ from the static field, yielding clean, temporally stable views. The dataset-level objective simply sums $\mathscr{L}(\mathbf{r})$ over all sampled training rays (equivalently $\sum_i \sum_{\mathbf{r}\in\mathscr{R}_i} \mathscr{L}_i(\mathbf{r})$).

Figure 23.92: **Training-time composition and uncertainty.** NeRF-W separately renders the static (a) and transient (b) elements of the scene, composites them (c), and compares to the image (d) with a loss weighted by a rendered uncertainty map (e) that discounts anomalous regions. Photo by Flickr user vasnic64 / CC BY. *Credit:* [418].

Architecture & Implementation Details

Cameras. Poses and intrinsics (with radial/tangential distortion) are estimated using COLMAP. **Training.** Hierarchical sampling (coarse→fine) as in NeRF; Adam with $(\beta_1{=}0.9, \beta_2{=}0.999, \varepsilon{=}10^{-7})$, batch size 2048, 300,000 steps on 8 GPUs. Hyperparameters ($\beta_{\min}$, λ_u, $n^{(a)}$, $n^{(\tau)}$) are selected on Brandenburg Gate and reused across scenes [418]. **Evaluation protocol.** NeRF–W learns appearance embeddings only for *training* images. For a held-out test image, the appearance code is unknown, so at test time we introduce a new variable $\ell^{(a)}_{\text{test}}$ and *optimize it while freezing all network weights and all other latents*. Concretely, we minimize the same per-ray color objective used in training, but **only** over rays from the **left half** of the test image:

$$\ell^{(a)}_{\text{test}} \leftarrow \arg\min_{\ell} \sum_{\mathbf{r}\in\text{left-half}} \mathscr{L}\big(\mathbf{r}; \ell^{(a)}{=}\ell\big),$$

where $\mathscr{L}$ is the Gaussian NLL (or ℓ_2 in the coarse pass) evaluated with the *frozen* fields. After this brief adaptation, we render with the *static* field (transient/uncertainty branches disabled) using $\ell^{(a)}_{\text{test}}$ and compute PSNR/SSIM/LPIPS **only on the right half** (Fig. 23.93).

This split-half protocol prevents information leakage: the pixels used to tune $\ell^{(a)}_{\text{test}}$ are disjoint from the pixels used to score. It also leverages a key design property of NeRF–W—$\sigma(\cdot)$ is appearance-free—so test-time appearance tuning cannot change geometry, only photometric factors (exposure/white balance/lighting), yielding fair and stable evaluation of novel-view synthesis under the test image's appearance.

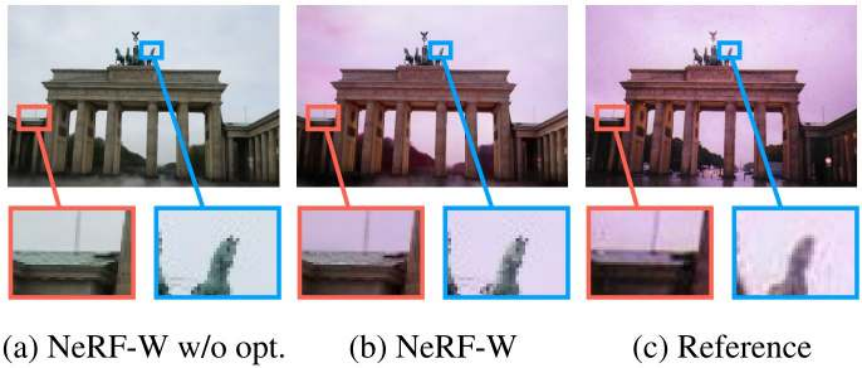

Figure 23.93: **Half-image optimization for test-time appearance.** During evaluation, $\ell^{(a)}$ is optimized on the left half of the test image; metrics use the right half. Photo by Flickr user eadaoinflynn / CC BY. *Credit:* [418].

Experiments and Ablations

NeRF-W is evaluated on six Phototourism landmarks and compared against NRW [426], NeRF [429], and two ablations: **NeRF-A** (appearance only; no transient) and **NeRF-U** (uncertainty only; no appearance). NeRF-W attains the best PSNR and MS-SSIM across all scenes and competitive LPIPS.

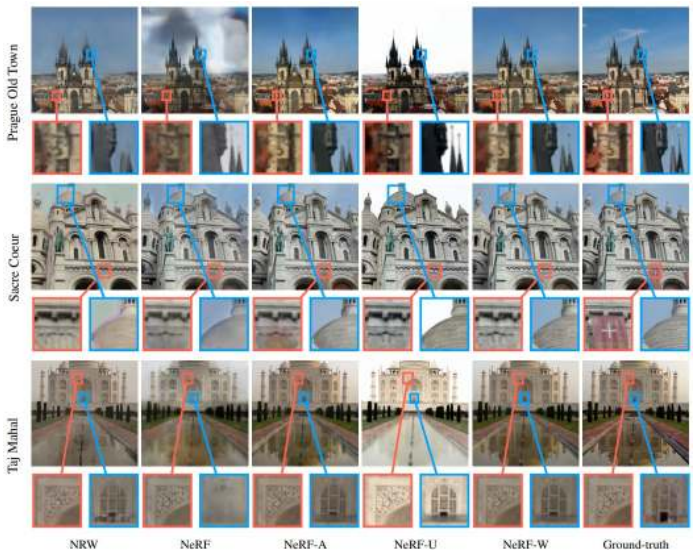

Figure 23.94: **Qualitative results on the Phototourism dataset.** Columns show methods (NRW, NeRF, NeRF-A, NeRF-U, NeRF-W) and the held-out ground-truth view; rows show scenes: *Prague Old Town* (appearance variation), *Sacre Coeur* (transient occluder: flag), and *Taj Mahal* (fine geometric/detail reconstruction). Red/blue insets zoom into regions that highlight the differences. NeRF-W simultaneously adapts to appearance changes (top), removes image-specific occluders (middle), and preserves fine details (bottom). More scenes are provided in Fig. 14 (supplementary). Photos by Flickr users *firewave*, *clintonjeff*, *leoglenn_g* / CC BY. *Credit:* [418].

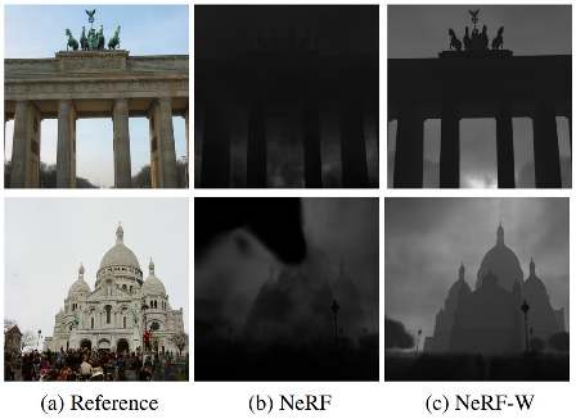

Figure 23.95: **Depth maps (expected termination).** NeRF's geometry is corrupted by appearance variation and occluders; NeRF-W is robust and produces accurate reconstructions. Photos by Flickr users burkeandhare, photogreuhphies / CC BY. *Credit:* [418].

Figure 23.96: **Appearance-space interpolation.** Interpolating between two $\ell^{(a)}$ produces renderings where color/illumination vary smoothly while geometry remains fixed. Photos by Flickr users mightyohm, blatez / CC BY. *Credit:* [418].

Figure 23.97: **Temporal consistency via EPIs.** Epipolar plane images (EPI) synthesized from rendered videos on Brandenburg Gate. NRW exhibits flicker; NeRF shows ghosting; NeRF-W yields clean, smooth EPIs (high temporal consistency). *Credit:* [418].

Limitations and Future Work

Failure modes. Despite its robustness to in-the-wild photos, NeRF-W still fails in predictable ways:

- *Sparse or weak supervision.* Regions that are rarely seen, far from cameras, or only observed at oblique angles (e.g., large ground/sky areas) are poorly constrained and often reconstruct with **localized blur**. The model has too little multi-view evidence to pin down both geometry and appearance (examples in Fig. 23.98).
- *Pose/camera errors from SfM.* NeRF-W assumes accurate COLMAP poses/intrinsics. Bad estimates introduce inconsistent rays, which the model cannot reconcile, leading to **blur/ghosting** or wrong structure in affected regions; see discussion in [418].
- *Appearance outside the training manifold.* The per-image appearance code captures global photometric effects, but extreme illumination/exposure shifts or strong non-Lambertian effects may not be representable, yielding **color mismatches** even when geometry is correct.
- *Imperfect transient separation.* Without labels, the transient branch can under/over-explain clutter: some truly static details may be treated as transient (causing **holes/softening**), or transient residue can remain as **faint "fog"**.

Future directions.

(i) *Joint camera / radiance-field optimization with photometric calibration.* Optimizing poses, intrinsics, exposure, and the field together (a neural analogue of bundle adjustment) could correct SfM drift and harmonize brightness/white balance across views, reducing blur and ghosting.

(ii) *Stronger disentanglement of illumination vs. exposure/white balance.* Factorizing the appearance code into physically meaningful components would enable finer control (e.g., change lighting without altering exposure) and reduce leakage of photometric variation into geometry.

(iii) *Learned priors for transient segmentation and temporal consistency.* Incorporating priors (e.g., semantic or motion cues) could make the static/transient split more reliable and stabilize renderings across viewpoints, further limiting colored-fog artifacts.

(iv) *Scaling to very sparse, long-tail photo collections with better uncertainty calibration.* Improving the calibration of per-ray uncertainty (so predicted variances match actual errors) would help the model down-weight unreliable rays more appropriately, making reconstructions more accurate when data are scarce or noisy.

Figure 23.98: **Limitations on Phototourism.** Rarely-seen parts of the scene (ground, left) and incorrect camera poses (lamp post, right) can result in blur. *Credit:* [418].

Enrichment 23.11.3: IBRNet: Learning Multi-View Image-Based Rendering

Motivation

Problem. Given a sparse set of posed *source* images, synthesize photorealistic *novel* views of *unseen* scenes *without any per-scene fine-tuning*. A single model should generalize zero-shot to new scenes. (An *optional* short per-scene fine-tune can further improve fidelity; see IBRNet$_{\text{ft}}$).

Background: What is Image-Based Rendering (IBR)? IBR produces new views by *reusing captured rays* from nearby images rather than fitting a global scene-specific field. A representative classical pipeline (e.g., LLFF [428], which *predates and is not based on* NeRF) typically contains:

(1) **Source selection:** choose a small working set of nearby views for the target camera.
(2) **Geometric proxy:** estimate coarse geometry (e.g., SfM/colmap depths, plane-sweep volumes, or multi-plane images) to relate target pixels to source pixels/features.
(3) **Reprojection/warping:** use camera intrinsics/extrinsics to warp source evidence (pixels or learned features) toward the target viewpoint.
(4) **Blending & visibility:** combine warped evidence with view-dependent weights (heuristic or learned). Errors in proxy geometry or weighting often cause ghosting near occlusions and thin structures.

IBR preserves high-frequency appearance because it copies *real* image content, but its success hinges on good proxies and robust visibility reasoning under sparse views.

How NeRF differs (and how IBR can build on it). NeRF [429] represents a *single scene* as a continuous radiance+density field parameterized by an MLP, trained *per scene* by minimizing a photometric loss under differentiable *volume rendering*. This yields accurate geometry/appearance but requires scene-specific optimization. Modern IBR-style methods can *reuse* NeRF's rendering formulation (sampling, transmittance, composition) while replacing the *scene-specific field* with mechanisms that *aggregate multi-view image evidence on the fly*. Thus, IBR can be viewed as *image-conditioned* rendering, whereas NeRF is *scene-parameterized* rendering.

Key idea. *IBRNet* [654] is trained *once*, across many diverse scenes, to *interpret* a small, pose–proximal set of source images from the *current* scene and convert them into per-ray volumetric properties that a standard NeRF-style volume renderer [429] can compose. The learned modules—a shared per-image CNN, lightweight MLP heads for visibility-aware blending and pooling, and a single-layer *ray transformer* that reasons *along a ray*—do not memorize a particular scene; instead, they encode *transferable priors* for fusing multi-view evidence. At test time, these same modules run in a purely feed-forward manner on the new scene's images, so no per-scene optimization is required (a short optional fine-tune, IBRNet$_{\text{ft}}$, can further refine thin structures and specular detail when capture is very sparse) [654].

Method: image-conditioned RGB–σ prediction and NeRF-style rendering

Setup and notation.

Given a target camera ray $\mathbf{r}(t) = \mathbf{o} + t\mathbf{d}$ and a small working set of N nearby *source* images with known intrinsics/extrinsics, IBRNet predicts, for each sampled 5D query $(\mathbf{x}, \mathbf{d})$ on $\mathbf{r}$, a color $\mathbf{c} \in [0,1]^3$ and a density $\sigma \geq 0$ by aggregating multi-view evidence from the source views and composing them with the standard differentiable volume renderer [429, 654]. Throughout, $\mathbf{C}_i$ and $\mathbf{f}_i$ denote the RGB and CNN feature sampled from source view i at the projection of $\mathbf{x}$; $\mathbf{d}_i$ is the source viewing direction; and $\Delta\mathbf{d}_i = \mathbf{d} - \mathbf{d}_i$ encodes the relative direction.

Pipeline overview (stages).

- **Stage 1 — View selection & feature extraction (per selected source view, once).** Select *N neighboring* source images whose cameras are close to the target pose, whose headings are similar to $\mathbf{d}$, and whose frusta overlap the target frustum. Each selected image is passed *once* through a shared encoder–decoder CNN to produce a dense 2D *feature map* (at reduced resolution). *Every pixel* of this map encodes a local descriptor mixing appearance and coarse geometric cues (e.g., texture, edges, occlusion hints from context). These learned features are later sampled (via projection) at arbitrary 3D queries to provide per-view evidence about what the scene looks like from that camera. We cache, for each view i, its RGB image, its feature map, and its viewing direction $\mathbf{d}_i$ so they can be reused for all target pixels/rays.
- **Stage 2 — Per-ray volumetric prediction (uses all N views at each sampled 3D point).** For each target pixel, cast a ray and sample M points $\{\mathbf{x}_k\}_{k=1}^{M}$ (near→far). At each sample $\mathbf{x}_k$ we use *all* selected views:
  - *Multi-view gathering.* Project $\mathbf{x}_k$ into each source view i with the known cameras; bilinearly read the view's RGB $\mathbf{C}_i$ and feature vector $\mathbf{f}_i$ at the projected coordinates (invalid/out-of-frustum projections are skipped or downweighted). Form the *relative* viewing direction $\Delta\mathbf{d}_i = \mathbf{d} - \mathbf{d}_i$ (or an angular encoding).
  - *Color via learned blending.* A small shared MLP takes $[\mathbf{f}_i,\ \Delta\mathbf{d}_i]$ and outputs a blending logit α_i. Convert logits to weights via a softmax

    $$w_i^c = \frac{\exp(\alpha_i)}{\sum_{j=1}^{N}\exp(\alpha_j)}, \qquad \sum_i w_i^c = 1,$$

    and compute the sample color as a convex combination

    $$\mathbf{c}_k = \sum_{i=1}^{N} w_i^c\,\mathbf{C}_i.$$

    Why view dependence is preserved: $\mathbf{c}_k$ is a *weighted copy* of *actual* source pixels, so specularities and other view-dependent effects present in appropriately aligned views are naturally carried into the synthesized color; $\Delta\mathbf{d}_i$ steers weights toward sources with similar viewing directions [654].
  - *Density via ray-wise reasoning.*
    - **(i) Density feature by multi-view pooling (per sample; permutation-invariant).** Using the gathered per-view features $\{\mathbf{f}_i\}_{i=1}^{N}$ at $\mathbf{x}_k$, compute global statistics to expose agreement/disagreement across views:

      $$\mu = \tfrac{1}{N}\sum_{i=1}^{N}\mathbf{f}_i, \qquad \mathbf{v} = \tfrac{1}{N}\sum_{i=1}^{N}(\mathbf{f}_i - \mu)^{\odot 2}.$$

      For each view i, concatenate local and global cues and pass through a *shared* PointNet-like MLP:

      $$\big[\mathbf{f}_i,\ \mu,\ \mathbf{v}\big] \xrightarrow{\text{MLP}_\phi} \big(\mathbf{f}_i',\ s_i\big),$$

      yielding a multi-view–aware feature $\mathbf{f}_i'$ and a reliability score s_i. Normalize scores into *visibility-aware* weights

      $$w_i = \frac{\exp(s_i)}{\sum_{j=1}^{N}\exp(s_j)},$$

then form weighted first- and second-order statistics and map them to a compact density feature:

$$\mu_w = \sum_{i=1}^{N} w_i \mathbf{f}'_i, \qquad \mathbf{v}_w = \sum_{i=1}^{N} w_i (\mathbf{f}'_i - \mu_w)^{\odot 2}, \qquad \mathbf{f}_\sigma(\mathbf{x}_k) = \mathrm{MLP}_\psi\big([\mu_w, \mathbf{v}_w]\big) \in \mathbb{R}^{d_\sigma}.$$

This pooling handles a variable number of views, downweights inconsistent/occluded views, and summarizes multi-view agreement at $\mathbf{x}_k$ into a fixed-length descriptor predictive of occupancy [654].

* **(ii) Ray transformer for coherent densities (per ray).** Collect the near-to-far sequence $\{\mathbf{f}_\sigma(\mathbf{x}_k)\}_{k=1}^{M}$ for *one* ray and add depth-wise positional encodings p_k (e.g., sinusoidal in ray parameter t_k):

$$\mathbf{z}_k = \mathbf{f}_\sigma(\mathbf{x}_k) + p_k, \quad k = 1, \ldots, M.$$

A lightweight *ray transformer* (single multi-head self-attention layer) processes $\{\mathbf{z}_k\}$ so each sample attends to the others along the same ray. Intuitively, strong near-field evidence can suppress spurious far-field candidates, and clusters of consistent samples reinforce surfaces. The attended features $\{\hat{\mathbf{z}}_k\}$ are passed through a tiny head to obtain nonnegative densities:

$$\sigma_k = \mathrm{MLP}_\rho\big(\hat{\mathbf{z}}_k\big), \qquad k = 1, \ldots, M.$$

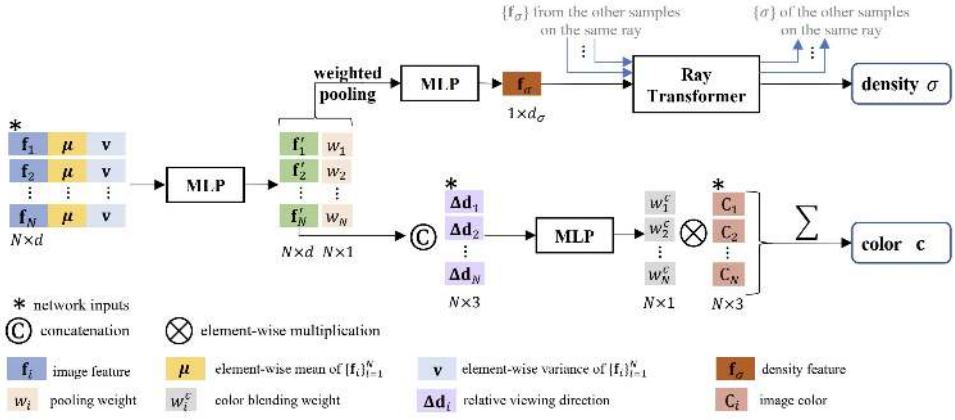

Figure 23.99: **Density and color prediction at a 5D location** $(\mathbf{x}, \mathbf{d})$ in IBRNet [654]. Per-view features $\{\mathbf{f}_i\}$ are combined with global statistics (mean/variance) by a PointNet-like MLP to produce multi-view–aware features and *visibility-aware* weights; weighted pooling yields a compact density feature $\mathbf{f}_\sigma$. A *ray transformer* consumes the sequence $\{\mathbf{f}_\sigma(\mathbf{x}_k)\}$ on a ray (with positional encodings) and outputs coherent densities $\{\sigma_k\}$. For color, a blending head uses $[\mathbf{f}_i, \Delta\mathbf{d}_i]$ to predict weights that form $\mathbf{c}_k$ as a weighted average of source colors, preserving view-dependent effects.

- **Stage 3 — NeRF-style volume rendering & training (per pixel).** With $(\mathbf{c}_k, \sigma_k)$ at sorted depths along the ray, let δ_k denote the spacing between consecutive samples (e.g., $\delta_k = t_{k+1} - t_k$ in ray-parameter units). The *transmittance* to sample k is

$$T_k = \exp\Big(- \sum_{j=1}^{k-1} \sigma_j \, \delta_j \Big),$$

and the rendered pixel color is

$$\tilde{\mathbf{C}}(\mathbf{r}) = \sum_{k=1}^{M} T_k \Big(1 - e^{-\sigma_k \delta_k} \Big) \mathbf{c}_k.$$

Training follows the familiar coarse/fine hierarchical sampling and an ℓ_2 photometric loss on both passes. The *renderer* is unchanged from NeRF [429]; what differs is how $(\mathbf{c}, \sigma)$ are *predicted*: here they are inferred on-the-fly from the target scene's *images and features*, using weights learned across many training scenes [654].

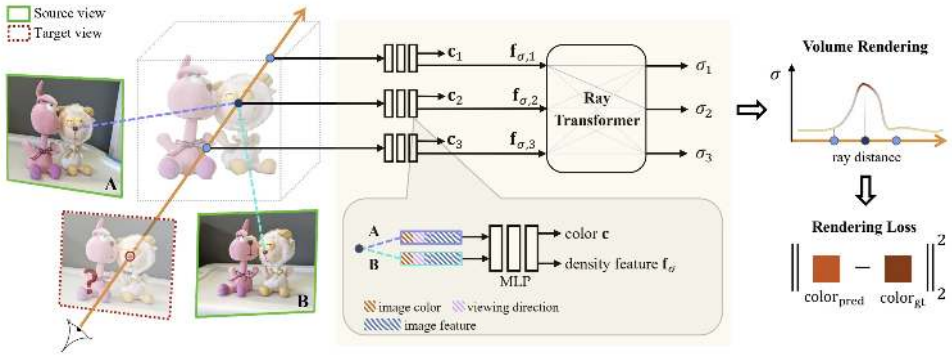

Figure 23.100: **IBRNet system overview for novel view synthesis** [654]. To render a target view (red dashed frustum), the pipeline: (1) selects N neighboring source images (by pose proximity, viewing-direction similarity, and frustum overlap) and computes a dense CNN feature map for each (cached and reused); (2) for each target ray sample $(\mathbf{x}_k, \mathbf{d})$, projects into all sources to read colors $\{\mathbf{C}_i\}$ and features $\{\mathbf{f}_i\}$, forms relative directions $\{\Delta\mathbf{d}_i\}$, predicts a view-dependent color $\mathbf{c}_k$ by learned blending of $\{\mathbf{C}_i\}$, and aggregates $\{\mathbf{f}_i\}$ with visibility-aware weights into a compact density feature $\mathbf{f}_\sigma(\mathbf{x}_k)$; (3) feeds the sequence $\{\mathbf{f}_\sigma(\mathbf{x}_k)\}_{k=1}^{M}$ to a lightweight ray transformer to obtain coherent per-sample densities $\{\sigma_k\}$, and composes $(\mathbf{c}_k, \sigma_k)$ using the standard NeRF volume renderer with coarse/fine hierarchical sampling and an ℓ_2 reconstruction loss.

Why fast and zero-shot.

Per-source-view features are computed once and reused; per-sample heads are tiny MLPs; the only attention is a single, lightweight transformer along each ray. Because the scene content resides in the *images* and the network merely *aggregates* them using learned, transferable priors, a new scene needs no optimization loop—yet the same pipeline admits a brief fine-tune ($\text{IBRNet}_{\text{ft}}$) when desired to adapt to extreme sparsity or challenging reflectance, without altering the rendering formulation [654].

Architecture & Implementation Details

High-level architecture.

IBRNet comprises three lightweight components trained jointly across many scenes [654]:

- **Per-image encoder–decoder CNN (shared).** A U-Net/ResNet34-style encoder–decoder (Instance Normalization as replacement of BatchNorm) processes each selected source image once to produce a dense 2D feature map at reduced resolution (output: $160\times120\times64$).[1] These features are cached and later sampled by projection at arbitrary 3D queries.
- **Per-sample MLP heads (shared across views and rays).**
  - *Color head (blending).* Given a projected feature $\mathbf{f}_i$ from view i and the relative viewing direction $\Delta\mathbf{d}_i$, a small MLP outputs a scalar blending logit whose softmax across views yields weights $\{w_i^c\}$. The sample color is $\mathbf{c}_k = \sum_i w_i^c \mathbf{C}_i$ (a convex blend of *actual* source colors), preserving view dependence.
  - *Density pooling head.* For density, a PointNet-like shared MLP maps $[\mathbf{f}_i, \mu, \mathbf{v}]$ (local feature with global across-view mean/variance) to a multi-view–aware feature $\mathbf{f}_i'$ and a reliability score s_i. Softmax-normalized scores provide visibility-aware weights $w_i \propto \exp(s_i)$. Weighted mean/variance over $\{\mathbf{f}_i'\}$ are then mapped by a tiny MLP to a compact density feature $\mathbf{f}_\sigma(\mathbf{x}_k) \in \mathbb{R}^{d_\sigma}$ (e.g., d_σ=16).
- **Ray transformer (single layer, along-ray self-attention).** For one ray, the sequence $\{\mathbf{f}_\sigma(\mathbf{x}_k)\}_{k=1}^M$ (with depth-wise positional encodings) is processed by a single multi-head self-attention layer (4 heads). The attended features feed a tiny head to produce nonnegative densities $\{\sigma_k\}$ jointly for all samples, improving depth ordering and occlusion handling.

Feature extraction network.

Input (id: dimension)	Layer	Output (id: dimension)
0: $640\times480\times3$	7×7 Conv, 64, stride 2	**1:** $320\times240\times64$
1: $320\times240\times64$	Residual Block 1	**2:** $160\times120\times64$
2: $160\times120\times64$	Residual Block 2	**3:** $80\times60\times128$
3: $80\times60\times128$	Residual Block 3	**4:** $40\times30\times256$
5: $40\times30\times256$	3×3 Upconv, 128, factor 2	**6:** $80\times60\times128$
[3, 6]: $80\times60\times256$	3×3 Conv, 128	**7:** $80\times60\times128$
7: $80\times60\times128$	3×3 Upconv, 64, factor 2	**8:** $160\times120\times64$
[2, 8]: $160\times120\times128$	3×3 Conv, 64	**9:** $160\times120\times64$
9: $160\times120\times64$	1×1 Conv, 64	**Out:** $160\times120\times64$

Table 23.24: **Feature extraction network architecture** [654]. "Conv" denotes conv + ReLU + InstanceNorm; "Upconv" is bilinear upsampling then a stride-1 conv. The 64-D output map is split into two 32-D maps for the coarse and fine branches, respectively.

[1] See Table 23.24 for exact layers and shapes. The 64-D map is split into two 32-D maps for the coarse/fine branches.

Network size and compute.

Method	#Params	#Src.Views	#FLOPs	PSNR↑	SSIM↑	LPIPS↓
SRN	0.55M	–	5M	22.84	0.668	0.378
NeRF [429]	1.19M	–	304M	26.50	0.811	0.250
$\text{IBRNet}_{\text{ft}}$	0.04M	5	29M	25.80	0.828	0.190
$\text{IBRNet}_{\text{ft}}$	0.04M	8	45M	26.56	0.847	0.176
$\text{IBRNet}_{\text{ft}}$	0.04M	10	55M	**26.73**	**0.851**	**0.175**

Table 23.25: **Complexity vs. quality (Real Forward-Facing)** [654]. IBRNet's per-sample heads are tiny; FLOPs scale roughly linearly with the number of source views used at inference.

Experiments & Ablations

Datasets and evaluation protocol.

IBRNet is evaluated on three standard benchmarks: *Diffuse Synthetic 360°* (DeepVoxels subset), *Realistic Synthetic 360°* (NeRF synthetic), and *Real Forward-Facing* (LLFF forward-facing scenes). Following the original evaluation, each test view is rendered using $N{=}10$ selected source views. Image quality is reported with PSNR/SSIM (higher is better) and LPIPS (lower is better) [654].

Baselines.

The scene-agnostic (no per-scene tuning) setting is compared to LLFF [428]. The per-scene optimization setting is compared to SRN [573], NV (Neural Volumes) [389], and NeRF [429]. An optional short per-scene fine-tuning variant ($\text{IBRNet}_{\text{ft}}$) is also reported.

Quantitative comparison (synthetic datasets).

Method	**Setting**	**Diffuse Synthetic 360°**			**Realistic Synthetic 360°**		
		PSNR↑	SSIM↑	LPIPS↓	PSNR↑	SSIM↑	LPIPS↓
LLFF [428]	No per-scene opt.	34.38	0.985	0.048	24.88	0.911	0.114
IBRNet [654]	No per-scene opt.	**37.17**	**0.990**	**0.017**	**25.49**	**0.916**	**0.100**
SRN [573]	Per-scene opt.	33.20	0.963	0.073	22.26	0.846	0.170
NV [389]	Per-scene opt.	29.62	0.929	0.099	26.05	0.893	0.160
NeRF [429]	Per-scene opt.	40.15	0.991	0.023	**31.01**	**0.947**	0.081
$\text{IBRNet}_{\text{ft}}$ [654]	Per-scene opt.	**42.93**	**0.997**	**0.009**	28.14	0.942	**0.072**

Table 23.26: **Synthetic datasets** [654]. In the *no per-scene* regime, IBRNet outperforms LLFF on both synthetic benchmarks, indicating effective zero-shot generalization from learned multi-view priors. With *per-scene* tuning, $\text{IBRNet}_{\text{ft}}$ becomes competitive with state-of-the-art per-scene methods on the Diffuse set and reduces the gap on the Realistic set.

Quantitative comparison (Real Forward-Facing).

Method	**Setting**	PSNR↑	SSIM↑	LPIPS↓
LLFF [428]	No per-scene opt.	24.13	0.798	0.212
IBRNet [654]	No per-scene opt.	**25.13**	**0.817**	**0.205**
SRN [573]	Per-scene opt.	22.84	0.668	0.378
NeRF [429]	Per-scene opt.	26.50	0.811	0.250
$\text{IBRNet}_{\text{ft}}$ [654]	Per-scene opt.	**26.73**	**0.851**	**0.175**

Table 23.27: **Real Forward-Facing** [654]. IBRNet improves over LLFF without per-scene optimization, supporting that image-conditioned blending and along-ray attention transfer across scenes. Optional fine-tuning ($\text{IBRNet}_{\text{ft}}$) further sharpens thin structures and reflections, surpassing NeRF on SSIM/LPIPS and slightly on PSNR.

Ablation studies.

	PSNR↑	SSIM↑	LPIPS↓
No ray transformer	21.31	0.675	0.355
No view directions	24.20	0.796	0.243
Direct color regression	24.73	0.810	0.220
Full model (IBRNet)	**25.13**	**0.817**	**0.205**

Table 23.28: **Ablations on Real Forward-Facing (pretrained, no per-scene tuning)** [654]. Along-ray self-attention (ray transformer) is critical for resolving occlusions/depth; relative view directions improve view-dependent appearance; blending *observed* colors outperforms direct RGB regression.

Sensitivity to source-view density.

Input view sparsity denotes limiting both the number and angular spread of available source images for rendering. In the IBRNet evaluation protocol [654]:

- Cameras on the upper hemisphere are *subsampled* by factors $\{2,4,6,8,10\}$ to simulate progressively sparser capture.
- Hence, for a given target view, the number of selectable neighbors N and baselines decrease, reducing parallax and multi-view agreement.
- The rendering pipeline and loss remain unchanged; only the available inputs differ.

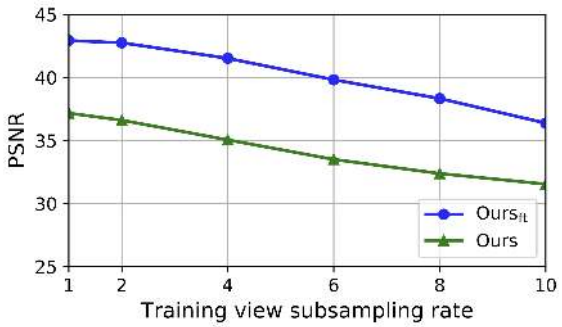

Figure 23.101: **Sensitivity to input view sparsity** [654]. Source views are uniformly subsampled on the upper hemisphere by factors $\{2,4,6,8,10\}$ to create varying densities. Results are shown for the pretrained model (no per-scene tuning) and for a per-scene fine-tuned variant ($\text{IBRNet}_{\text{ft}}$).

What the figure shows and why it matters.

- *Observed effect of sparsity (Figure 23.101).* As source views become sparser, errors grow near thin structures, specular regions, and occlusion boundaries. This is consistent with weaker multi-view consistency and fewer reliable visibility cues.
- *Zero-shot robustness.* The pretrained (scene-agnostic) model degrades gracefully: despite reduced inputs, the learned fusion recovers large-scale structure and many details, indicating effective cross-scene priors.

Per-scene fine-tuning (IBRNet$_{\text{ft}}$): how it is done and why it helps.

- *Procedure.*
  - Initialize all network parameters from the scene-agnostic pretrained model (shared encoder–decoder CNN, per-sample MLP heads for color and density pooling, and the ray transformer).
  - Optimize on the *posed images of the target scene* using the *same* NeRF-style objective: coarse/fine hierarchical sampling of ray points and an ℓ_2 photometric loss between rendered and ground-truth pixel colors [654].
  - Keep the rendering pipeline, view selection (N neighbors), sampling strategy, and losses unchanged; only the weights are updated. In practice, rays are randomly sampled across training images each iteration, and both coarse and fine branches are trained jointly as in the pretrained model.
- *What is adapted.* Fine-tuning specializes the generic, cross-scene priors to the geometry/appearance and camera layout of the specific scene by calibrating:
  - **Visibility-aware pooling.** The PointNet-like density-pooling head refines the reliability scores $\{s_i\}$ and resulting weights $\{w_i\}$ so that views inconsistent or occluded at a sample location receive lower influence when forming the compact density feature $\mathbf{f}_\sigma(\mathbf{x}_k)$.
  - **Color blending.** The color head adjusts how relative viewing directions $\Delta\mathbf{d}_i$ and per-view features $\mathbf{f}_i$ are mapped to blending weights $\{w_i^c\}$, improving reproduction of scene-specific view-dependent effects (e.g., specularities) under the available baselines.
  - **Along-ray reasoning.** The ray transformer adapts its self-attention to the scene's depth statistics, helping resolve near–far ordering and occlusions more decisively when aggregating $\{\mathbf{f}_\sigma(\mathbf{x}_k)\}_{k=1}^M$.
  - **Low-level features.** The shared encoder–decoder CNN updates its filters so that the 2D feature maps align with the target scene's photometric characteristics (exposure, material cues, texture scale), which strengthens the multi-view consistency signal used downstream.
- *Why it helps under sparsity.*
  - With few and narrowly spaced source views, the generic priors learned across many scenes may be insufficient to disambiguate thin structures and complex occlusions. Fine-tuning reduces this domain gap by aligning the priors to the target scene's actual pose/appearance distribution.
  - Calibrated visibility weights decrease uncertainty in $\mathbf{f}_\sigma$, steering density toward physically plausible surfaces and away from "black-hole" artifacts.
  - Refined color blending emphasizes the most reliable source rays for each 3D sample, improving view-dependent appearance without introducing high-frequency regression artifacts.
  - The adapted ray transformer strengthens along-ray suppression of spurious far samples once a nearer surface is explained, yielding cleaner boundaries and fewer floaters.

- *Empirical takeaway (Figure 23.101).*
  - As input views are made sparser, $\text{IBRNet}_{\text{ft}}$ consistently degrades more gracefully than the zero-shot model: edges remain sharper, thin structures persist longer, and occlusion boundaries are cleaner, while the rendering objective and architecture remain unchanged [654].

Qualitative comparisons.

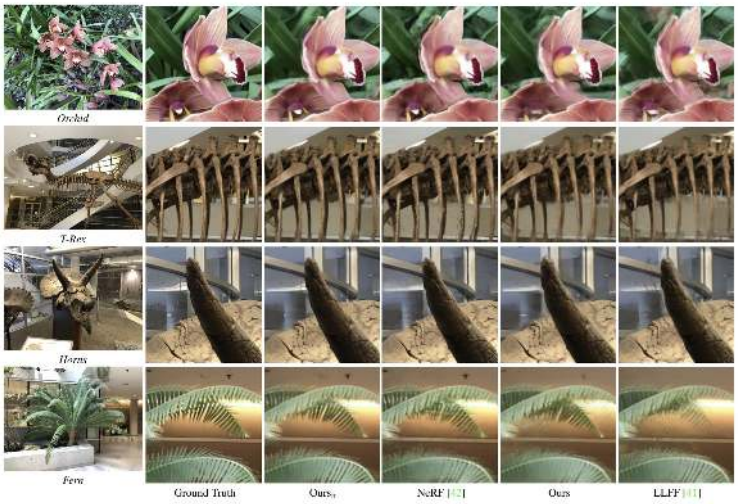

Figure 23.102: **Qualitative comparison on Real Forward-Facing** [654]. IBRNet reconstructs fine geometric and appearance details while avoiding ghosting near boundaries and thin structures where LLFF struggles; compared to NeRF, it reduces high-frequency artifacts and better preserves reflections in several scenes.

With/without ray transformer.

Figure 23.103: **With vs. without the ray transformer** [654]. Each triplet shows (left) the pretrained model *without* the ray transformer, (middle) the model *with* the ray transformer, and (right) the ground truth. Without along-ray self-attention, densities are predicted from per-sample cues only, frequently yielding "black-hole" voids and boundary ghosting near occlusions. Adding a single along-ray self-attention layer (with depth-wise positional encodings) aggregates density features across all samples on the ray, enforcing coherent near–far ordering and markedly cleaner edges.

Geometry and additional results.

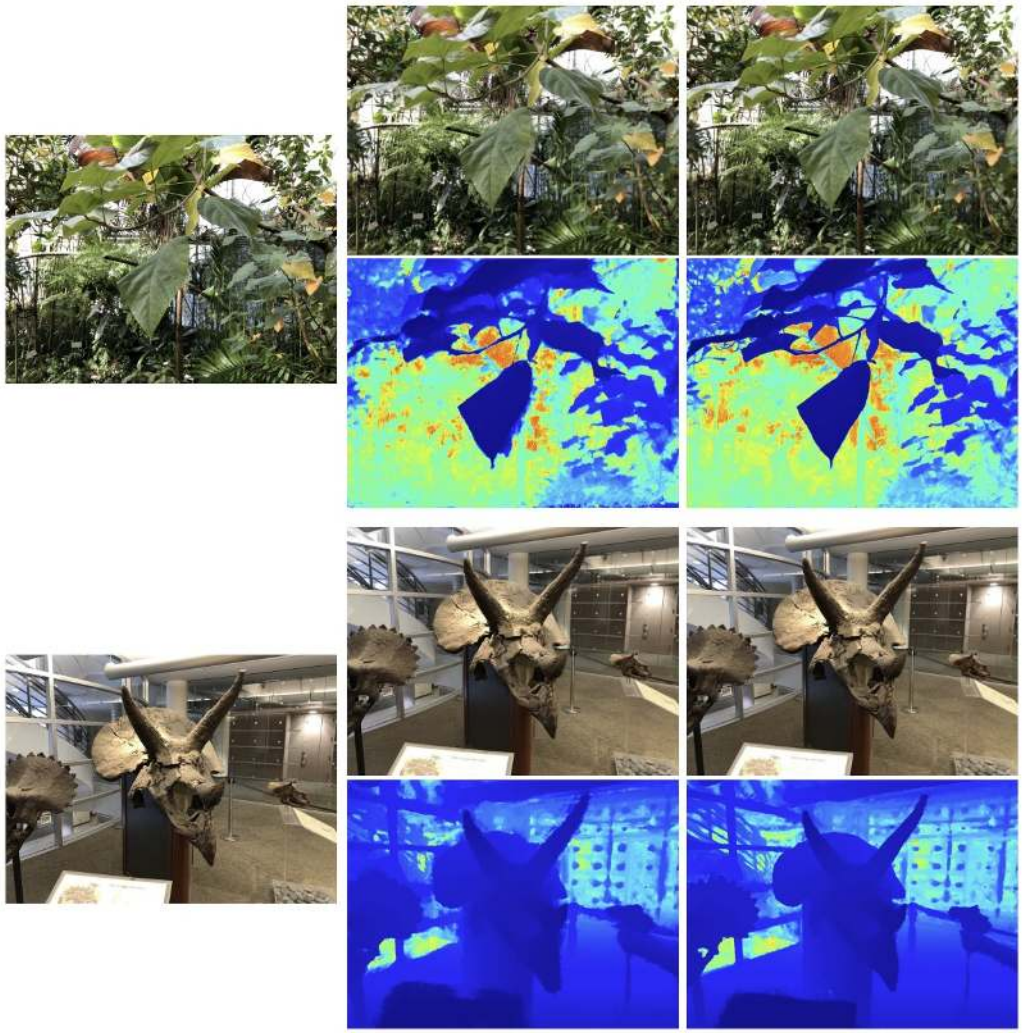

Figure 23.104: **Proxy geometry and rendering on two scenes (Leaves, Horns)** [654]. For each scene, columns show: *left*—ground-truth image; *middle*—pretrained IBRNet (no per-scene tuning), with synthesized RGB (top) and estimated depth (bottom); *right*—IBRNet fine-tuned on the scene ($\text{IBRNet}_{\text{ft}}$), again with synthesized RGB (top) and depth (bottom). Fine-tuning sharpens geometry and improves view-dependent appearance, yielding cleaner boundaries and more stable thin structures.

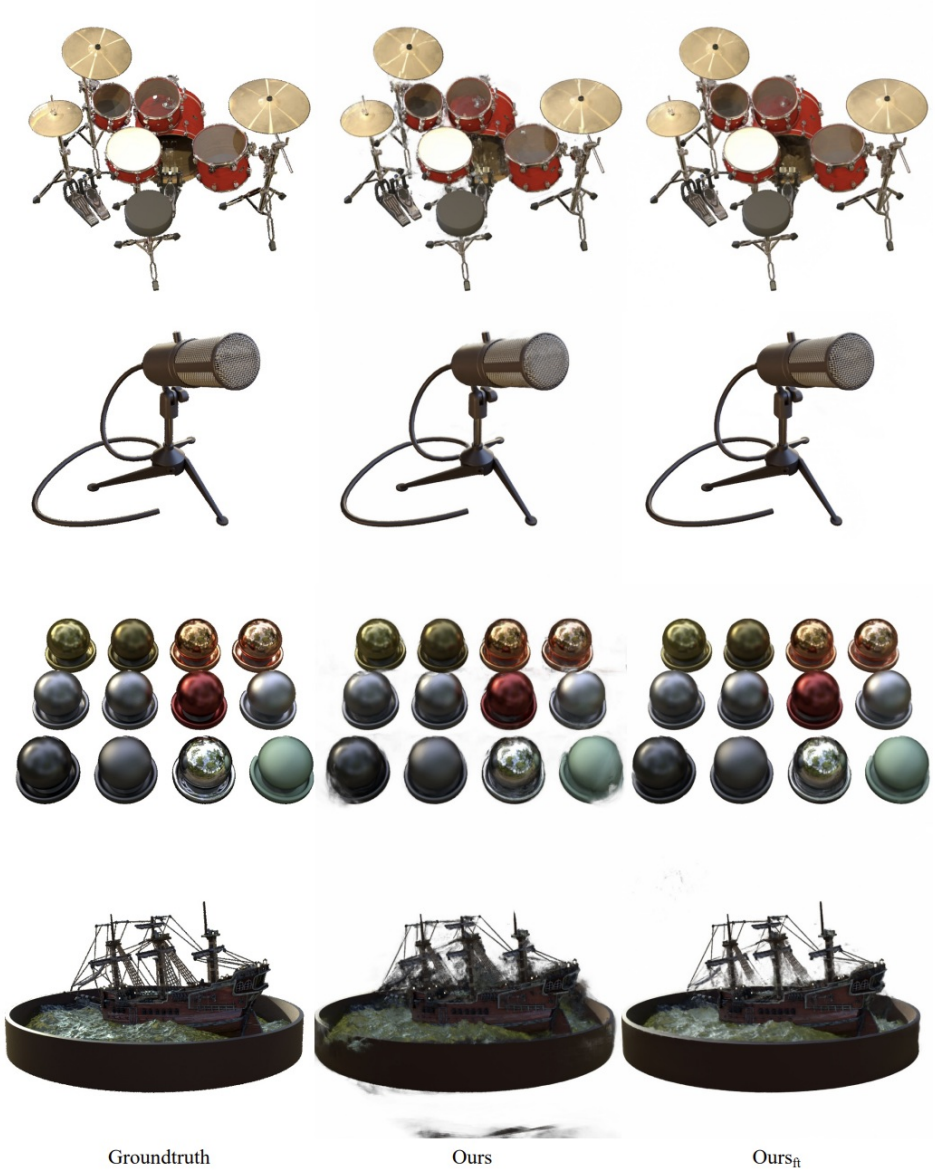

Figure 23.105: **Realistic Synthetic 360° results** [654]. High-fidelity renderings are achieved without per-scene optimization; remaining failures appear under very sparse views and complex geometry, where additional per-scene adaptation can help.

Limitations and Future Directions

Limitations.

IBRNet can degrade under extremely sparse inputs and complex occlusions; although the ray transformer mitigates "black holes", challenging specular/transparent regions may still benefit from scene-specific adaptation. Quality depends on source-view selection, pose accuracy, and coverage; thin structures and reflections improve with brief per-scene fine-tuning (IBRNet$_{ft}$) [654].

Concurrent and prior generalizable radiance-field methods.
Several highly cited works contemporaneous with (or preceding) IBRNet pursue *generalizable* novel view synthesis with related but distinct designs:

- **pixelNeRF** [739] (CVPR 2021): conditions a NeRF directly on *image-aligned features* from one/few inputs and *regresses* color/density. Unlike IBRNet's explicit color blending and along-ray transformer, pixelNeRF relies on a fully convolutional conditioning pipeline for feed-forward generalization.
- **GRF** [632] (ICCV 2021; arXiv 2020): learns a *general radiance field* by projecting pixel features to 3D and aggregating across views (with attention). Compared to IBRNet, GRF eschews pixel copying/blending and focuses on implicit field regression conditioned on inputs.
- **MVSNeRF** [79] (ICCV 2021): imports *plane-sweep cost volumes* and 3D CNNs from MVS for geometry-aware aggregation. In contrast to IBRNet's PointNet-style pooling plus a ray transformer, MVSNeRF leverages explicit multi-plane geometry priors to guide density/color regression and supports fast feed-forward reconstruction with optional per-scene fine-tune.

Subsequent follow-ups building on IBRNet's goals.
A line of work pursues the same objective—high-quality novel views from sparse inputs with little or no per-scene optimization—by relocating where priors and visibility reasoning live in the pipeline:

- **NeuRay** [382] (CVPR 2022): augments feature aggregation with an explicit, learned *per-view visibility field*. For each 3D query, the method predicts how visible it is from every source camera and downweights occluded/inconsistent evidence *before* color/density prediction. Compared to IBRNet's implicit, score-based pooling, NeuRay disentangles visibility estimation from appearance blending.
- **GeoNeRF** [267] (CVPR 2022): injects stronger geometry by constructing multi-scale *cost volumes* (plane-sweep style) and fusing them with a Transformer. This emphasizes epipolar consistency and depth reasoning more explicitly than IBRNet's PointNet-like pooling, improving few-view robustness and occlusion handling.
- **Point-NeRF** [714] (CVPR 2022): anchors features on a *neural point cloud* and renders through point-based volume rendering. In contrast to IBRNet's pixel-aligned (per-view) feature sampling, Point-NeRF shifts to a scene-adaptive, point-anchored representation that can be efficient and accurate when reliable points are available.
- **RegNeRF** [452] (CVPR 2022): remains *per-scene* but targets the same sparse-input failure modes via strong regularization (e.g., unseen-view patch losses, sampling annealing). While not cross-scene like IBRNet, it offers complementary loss/regularization ideas that can inspire priors for generalizable renderers.

Key design axes highlighted by these follow-ups.

- *Conditioning mechanism:* pixel-aligned sampling (IBRNet) vs. cost-volume aggregation (GeoNeRF) vs. point-anchored features (Point-NeRF).
- *Visibility modeling:* implicit reliability pooling + along-ray attention (IBRNet) vs. explicit per-view visibility fields (NeuRay) vs. geometry-constrained matching in volumes (GeoNeRF).
- *Training regime:* cross-scene, feed-forward generalization (IBRNet, NeuRay, often GeoNeRF variants) vs. per-scene but robustly regularized optimization (RegNeRF).
- *Trade-offs:* stronger geometry priors tend to improve occlusions and thin structures under extreme sparsity, while pixel/feature-conditioned designs often yield higher throughput and simpler deployment across scenes.

Enrichment 23.11.4: pixelNeRF: Neural Radiance Fields from One or Few Images

Motivation

Neural Radiance Fields (NeRF) [429] achieve impressive photorealism in novel view synthesis but require dense multi-view supervision and time-intensive per-scene optimization. This limitation makes them unsuitable for scenarios with only one or few input views. PixelNeRF [739] addresses this shortcoming by learning a *scene prior* across multiple objects and categories, enabling feed-forward prediction of radiance fields conditioned on sparse input images. The key insight is to incorporate pixel-aligned image features into NeRF's volumetric formulation, thereby leveraging visual evidence for generalization across scenes.

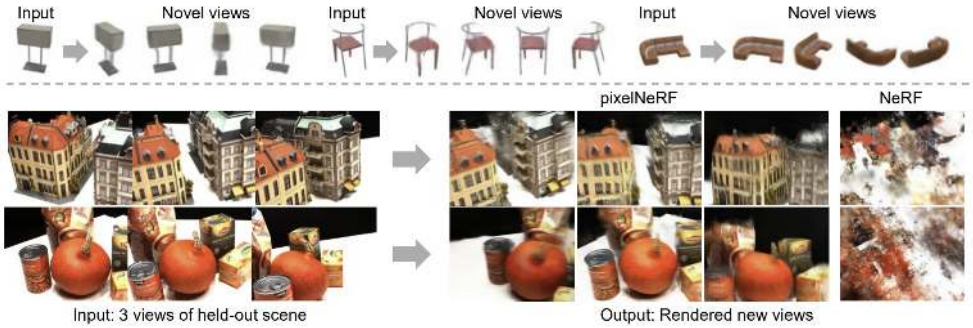

Figure 23.106: **NeRF from one or few images.** PixelNeRF predicts neural radiance fields from a single (top) or few posed images (bottom). Unlike NeRF, which requires dense views to work, PixelNeRF generalizes across scenes and performs robustly even with sparse views [739].

Method

PixelNeRF modifies the classical NeRF formulation by conditioning the radiance field on features extracted from input images. This conditioning transforms NeRF from a per-scene optimization problem into a feed-forward prediction pipeline that can generalize to unseen objects and scenes.

Radiance field prediction

As in NeRF, the radiance field is a continuous function

$$f(\mathbf{x}, \mathbf{d}) = (\sigma, \mathbf{c}),$$

that maps a 3D point $\mathbf{x} \in \mathbb{R}^3$ and viewing direction $\mathbf{d} \in \mathbb{R}^3$ to a density σ and color $\mathbf{c}$. In NeRF, this mapping is optimized independently for each scene. PixelNeRF instead conditions f on features aligned with the input pixels.

Feature encoding and alignment

An encoder E (a ResNet-34 backbone pretrained on ImageNet) processes each input image I into a pixel-aligned feature grid $W = E(I)$. Given a query point $\mathbf{x}$ in the camera space of an input image, PixelNeRF projects $\mathbf{x}$ onto the image plane:

$$\pi(\mathbf{x}) = K[R \mid t]\mathbf{x},$$

where K are the camera intrinsics and $[R|t]$ are extrinsics. The local image feature is then sampled via bilinear interpolation:

$$\mathbf{w} = W(\pi(\mathbf{x})).$$

This feature encodes appearance cues and geometric context at the projection of $\mathbf{x}$.

Feature-conditioned NeRF

The NeRF network f receives the positional encoding $\gamma(\mathbf{x})$, the viewing direction $\mathbf{d}$, and the interpolated feature $\mathbf{w}$:

$$f(\gamma(\mathbf{x}), \mathbf{d}; \mathbf{w}) = (\sigma, \mathbf{c}).$$

Instead of concatenating $\mathbf{w}$ to the input, PixelNeRF injects it as a residual modulation at each layer of the MLP, inspired by style transfer methods such as AdaIN and SPADE. This design improves stability and ensures features influence the radiance field consistently across depths.

Volume rendering loss

Rendered colors are computed as in NeRF:

$$\hat{C}(r) = \int_{t_n}^{t_f} T(t)\,\sigma(t)\,\mathbf{c}(t)\,dt, \quad T(t) = \exp\Big(-\int_{t_n}^{t} \sigma(s)\,ds\Big).$$

Training minimizes pixel-wise squared error:

$$\mathscr{L} = \sum_{r \in \mathscr{R}(P)} \|\hat{C}(r) - C(r)\|_2^2.$$

Why view-space conditioning

Most reconstruction frameworks define radiance fields in a canonical object-centered frame, requiring all instances to share alignment. PixelNeRF instead operates in *view space*, i.e., the coordinate frame of each input camera. This removes the need for a canonical alignment, improving generalization to unseen categories, multiple-object scenes, and real-world captures where canonical orientation does not exist.

Multi-view extension

For multiple input images $\{I^{(i)}\}_{i=1}^{n}$ with poses $P^{(i)} = [R^{(i)}|t^{(i)}]$, query points are transformed into each view:

$$\mathbf{x}^{(i)} = P^{(i)}\mathbf{x}, \qquad \mathbf{d}^{(i)} = R^{(i)}\mathbf{d}.$$

Each view provides intermediate features:

$$V^{(i)} = f_1(\gamma(\mathbf{x}^{(i)}), \mathbf{d}^{(i)}; W^{(i)}(\pi(\mathbf{x}^{(i)}))).$$

These are pooled using an order-independent operator ψ (average pooling) and passed to a final network f_2:

$$(\sigma, \mathbf{c}) = f_2(\psi(V^{(1)}, \ldots, V^{(n)})).$$

This architecture allows variable numbers of input images at test time without retraining.

Intuition and significance

PixelNeRF can be understood as embedding a strong inductive bias into NeRF: each query point consults features sampled from projected 2D observations. This design provides two critical benefits: (1) *appearance grounding*, since colors derive from aligned image evidence; and (2) *geometric priors*, since features across views encode spatial structure. Consequently, PixelNeRF learns to hallucinate plausible completions when input views are sparse, a task impossible for vanilla NeRF.

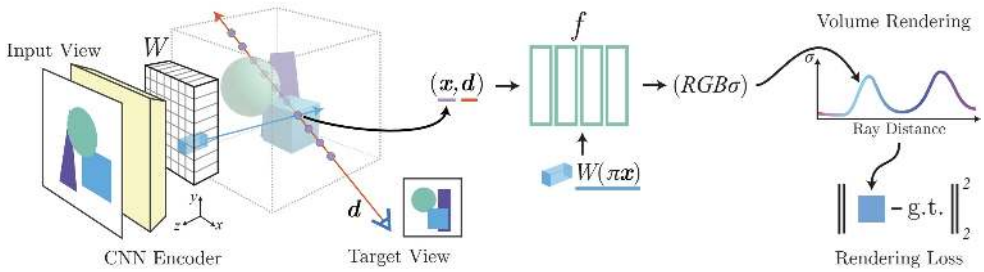

Figure 23.107: **PixelNeRF pipeline in the single-view case.** Query features are sampled from image-encoded feature volumes and combined with spatial coordinates before passing through the NeRF network [739].

Architecture and Implementation

PixelNeRF uses a ResNet-34 encoder with a feature pyramid to capture local and global cues. Features from multiple scales are upsampled and concatenated, resulting in 512-dimensional descriptors aligned with image pixels. The NeRF network f is implemented as a residual MLP. Instead of concatenating features directly, linear layers map each feature vector into per-block residuals added within ResNet blocks. This design stabilizes training and enables feature modulation across layers.

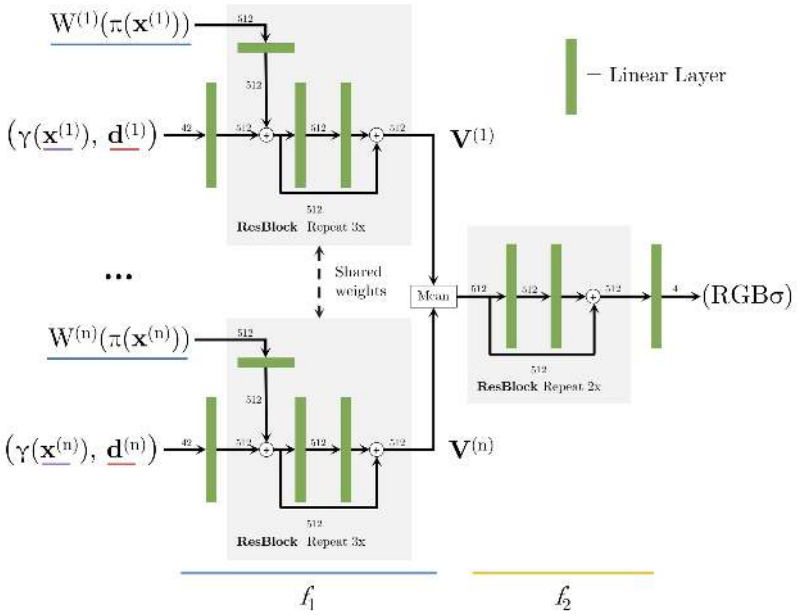

Figure 23.108: **Multi-view PixelNeRF architecture.** Separate encoders produce feature grids per view, which are transformed, pooled, and aggregated through f_1 and f_2 [739].

Experiments and Ablations

PixelNeRF is evaluated across *category-specific* (chairs, cars), *category-agnostic* (13 ShapeNet classes), *unseen categories*, *multi-object* scenes, and *real-world* datasets (Stanford Cars; DTU MVS), demonstrating consistent gains over SRN [573] and DVR [451]. Ablations confirm the necessity of pixel-aligned local features and view-direction inputs.

Category-specific single-view reconstruction

A separate PixelNeRF is trained per category using multi-view 2D supervision; qualitative examples include a chair, sofa, van, and police car.

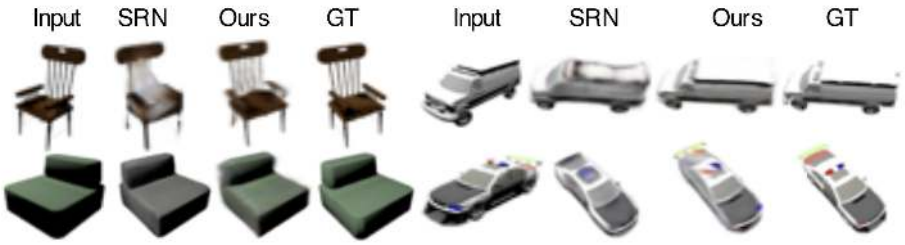

Figure 23.109: **Category-specific single-view reconstruction benchmark.** Separate models for cars and chairs; qualitative comparison with SRN [573]. *Credit:* [739].

Category-specific two-view reconstruction

Two input images are encoded; two novel renderings are shown per example for chairs and cars.

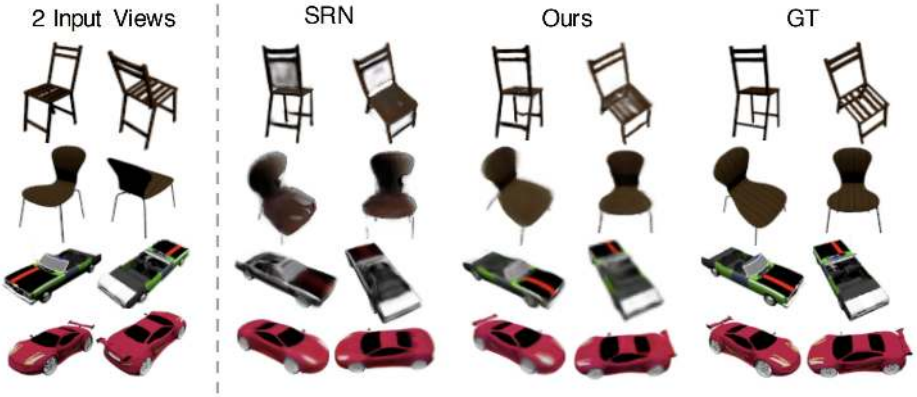

Figure 23.110: **Category-specific 2-view reconstruction benchmark.** *Credit:* [739].

Method	1-view		2-view	
	PSNR↑	SSIM↑	PSNR↑	SSIM↑
Chairs				
GRF [632]	21.25	0.86	22.65	0.88
TCO* [610]	21.27	0.88	21.33	0.88
dGQN [146]	21.59	0.87	22.36	0.89
ENR* [137]	22.83	–	–	–
SRN [573]	22.89	0.89	24.48	0.92
PixelNeRF* [739]	**23.72**	**0.91**	**26.20**	**0.94**
Cars				
SRN [573]	22.25	0.89	24.84	0.92
ENR* [137]	22.26	–	–	–
PixelNeRF* [739]	**23.17**	**0.90**	**25.66**	**0.94**

Table 23.29: **Category-specific 1- and 2-view reconstruction.** Methods marked * do not require canonical poses at test time. One model per category is evaluated in both settings. Values match the original paper's Table 2.

Ablation on local features and view directions

Goal This ablation on `ShapeNet chairs` isolates the contributions of two architectural choices in PixelNeRF [739]: *pixel-aligned local features* and *explicit view directions*. The objective is to determine how each component affects few-shot reconstruction quality in single-view and two-view settings within PixelNeRF's viewer-centric, feed-forward formulation.

Design of the variants

- **Full** The complete PixelNeRF model conditions the radiance field on fine-grained, pixel-aligned image features and includes the NeRF-style viewing direction input $\mathbf{d}$ to capture view-dependent appearance.
- `- Local` Replaces pixel-aligned features with a single global image code. This removes spatially precise conditioning at projected locations $\pi(\mathbf{x})$, testing whether per-pixel alignment is essential for shape/detail recovery.
- `- Dirs` Removes the explicit direction input $\mathbf{d}$ to test the importance of view-dependent effects (e.g., specularities) under sparse supervision.

Mechanism and expected effects PixelNeRF uses a ResNet-34 encoder to produce a multi-scale feature pyramid that is upsampled and concatenated into ∼512-D descriptors aligned to input pixels. For a 3D query point $\mathbf{x}$, the point is projected to each input image, and a bilinearly interpolated feature $\mathbf{w} = W(\pi(\mathbf{x}))$ modulates the NeRF MLP through residual injections at block entrances. This pixel-level conditioning supplies localized appearance and geometry cues tied to $\mathbf{x}$'s projections. Removing local features (`- Local`) collapses this spatially precise conditioning to a global code, reducing fidelity in thin structures and high-frequency textures. Removing directions (`- Dirs`) suppresses view-dependent modeling, impairing consistency under large baselines or glossy surfaces.

Findings The following table shows that both components are important. Relative to **Full**, `- Local` exhibits noticeable drops in PSNR/SSIM and worse LPIPS, indicating that pixel-aligned evidence is helpful for accurate shape and texture reconstruction from few views. `- Dirs` also degrades all metrics, confirming the choice of using explicit viewing direction inputs for high-fidelity, view-dependent rendering. The **Full** model achieves the best performance in both 1-view and 2-view settings.

Variant	1-view			2-view		
	PSNR↑	SSIM↑	LPIPS↓	PSNR↑	SSIM↑	LPIPS↓
– Local	20.39	0.848	0.196	21.17	0.865	0.175
– Dirs	21.93	0.885	0.139	23.50	0.909	0.121
Full	**23.43**	**0.911**	**0.104**	**25.95**	**0.939**	**0.071**

Table 23.30: **Ablation on `ShapeNet` chairs.** Pixel-aligned local features and explicit view directions are both essential for few-shot quality; the **Full** PixelNeRF model attains the best PSNR/SSIM and lowest LPIPS in 1-view and 2-view regimes (matches Table 3 in [739]).

Category-agnostic single-view reconstruction

A single PixelNeRF trained jointly on the 13 largest ShapeNet categories preserves thin structures and small textures, while outperforming baselines quantitatively (exactly as reported).

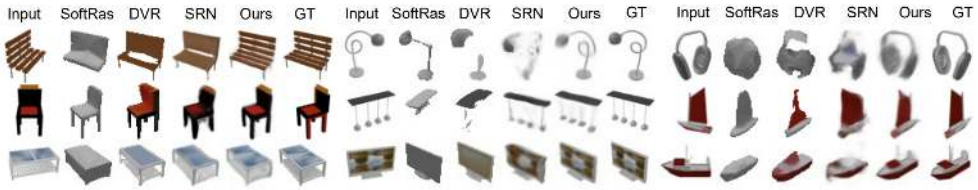

Figure 23.111: **Category-agnostic single-view reconstruction.** PixelNeRF is trained as a single model across 13 ShapeNet categories, without category-specific specialization. The results show superior recovery of fine structures such as chair legs, monitors, and tabletop textures compared to methods that compress the scene into a single latent vector. Competing baselines such as SRN struggle in this setting, with degraded reconstructions and unreliable test-time latent inversion.

Unseen categories and multi-object scenes

Training only on `plane`, `car`, `chair`, PixelNeRF generalizes to 10 unseen categories and handles composed scenes of multiple chairs by predicting in view space.

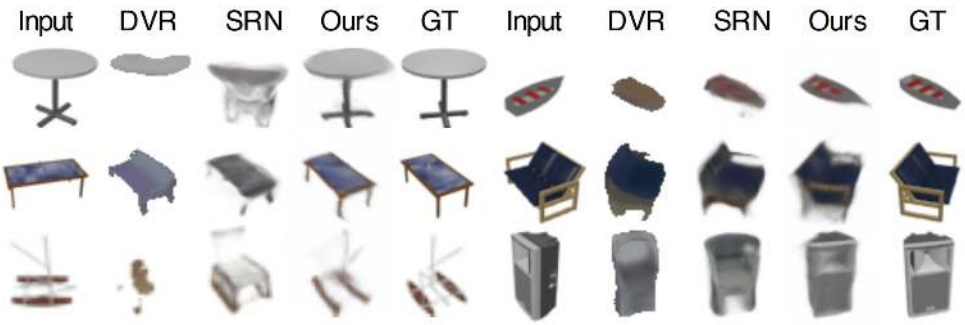

Figure 23.112: **Generalization to unseen categories.** A model trained only on `plane`, `car`, and `chair` generalizes to 10 unseen ShapeNet categories. Despite not being exposed to these categories during training, PixelNeRF produces structurally reasonable and visually coherent reconstructions, demonstrating strong cross-category priors. *Credit:* [739].

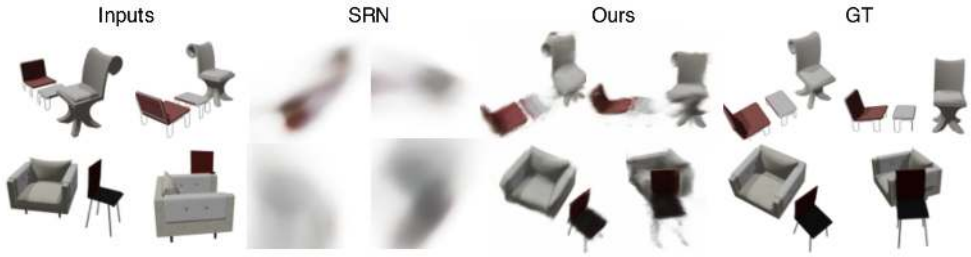

Figure 23.113: **360° view prediction with multiple objects.** PixelNeRF naturally handles multi-object scenes, such as multiple ShapeNet chairs, because its prediction is conditioned in view space. In contrast, canonical-space models like SRN struggle with alignment when multiple objects are present. *Credit:* [739].

	Unseen category			Multiple chairs		
Method	PSNR↑	SSIM↑	LPIPS↓	PSNR↑	SSIM↑	LPIPS↓
DVR [451]	17.72	0.716	0.240	–	–	–
SRN [573]	18.71	0.684	0.280	14.67	0.664	0.431
PixelNeRF [739]	**22.71**	**0.825**	**0.182**	**23.40**	**0.832**	**0.207**

Table 23.32: **Challenging ShapeNet tasks.** Left: zero-shot generalization to 10 unseen categories using a model trained on only three classes (`plane`, `car`, `chair`). Right: two-view reconstruction of scenes with multiple chairs. PixelNeRF clearly surpasses baselines in both settings, showcasing robustness to unseen object types and multi-object compositions. Matches Table 5 in [739].

Real images: Stanford Cars and DTU MVS

A car model transfers to Stanford Cars after background removal with PointRend; on DTU, feed-forward wide-baseline synthesis is demonstrated from three posed inputs; PSNR quantiles versus per-scene NeRF are reported in the paper.

Figure 23.114: **Results on real car photos.** PixelNeRF trained on ShapeNet cars is directly applied to the Stanford Cars dataset [303]. Backgrounds are removed using PointRend [295]. The model generates plausible view rotations about the vertical axis without any fine-tuning, demonstrating cross-dataset transfer. *Credit:* [739].

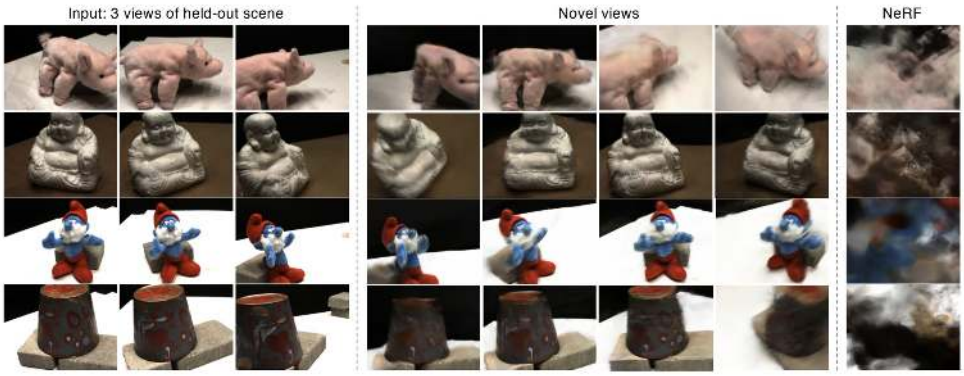

Figure 23.115: **Wide-baseline novel view synthesis on DTU.** On the DTU MVS dataset [262], PixelNeRF synthesizes novel views from as few as three posed input images. Notably, the training and test sets share no scenes, yet reconstructions remain consistent, highlighting the generalization ability of learned priors under wide-baseline, real-scene conditions. *Credit:* [739].

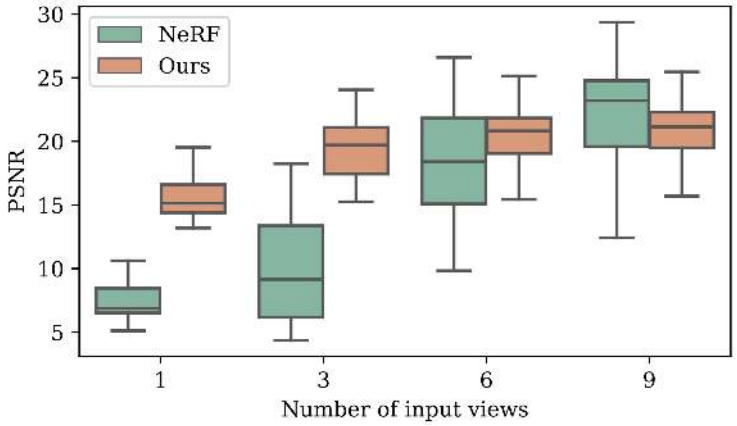

Figure 23.116: **Few-shot reconstruction performance on DTU.** PSNR quantiles across scenes with 1, 3, 6, or 9 input views. PixelNeRF uses a single trained model with 3-view conditioning, while NeRF is retrained per scene and per view count. PixelNeRF maintains competitive or superior performance without test-time optimization. Matches Figure 9 in [739].

Limitations and Future Work

Limitations

- **Rendering speed.** PixelNeRF inherits NeRF's slow volumetric rendering, with runtime scaling linearly with the number of input views. This makes interactive applications infeasible.
- **Positional encoding scale.** The choice of frequency bands in $\gamma(\cdot)$ and manually tuned ray sampling bounds limit scale invariance. PixelNeRF struggles when scenes deviate strongly in scale or depth range.
- **Dataset constraints.** Training and evaluation rely on ShapeNet and DTU, which are synthetic or controlled. Generalization to in-the-wild 360° captures is still limited.

Future work and influence

PixelNeRF inspired numerous follow-ups addressing its limitations:

- **IBRNet** [654] improved multi-view aggregation with attention-based pooling, enhancing generalization across unseen scenes.
- **MVSNeRF** [79] introduced cost-volume features to better exploit geometric consistency under sparse views.
- **PixelNeRF++** and other variants investigated scaling the approach to more complex outdoor or dynamic settings.
- **Vision transformers for NeRF priors** (e.g., [267, 382]) replaced CNN encoders with transformers for improved visibility reasoning and global context.

These directions show how PixelNeRF provided the first bridge between feed-forward image-conditioned priors and NeRF-based volumetric rendering, catalyzing a wave of methods tackling sparse-view reconstruction and real-world generalization.

Enrichment 23.12: NeRF: Unbounded, Dynamic, Large-Scale Scenes

Scaling beyond tabletop scenes requires anti-aliasing across scales, compositional scene structure, and deformation fields for motion.

- **Block-NeRF** [602]: Composes geographic "blocks" to model city-scale environments with streaming and modular training.
- **Mip-NeRF 360** [29]: Tackles unbounded 360° scenes with integrated positional encoding and anti-aliased cones.
- **Nerfies** [469]: Learns continuous deformation fields from casual handheld videos for non-rigid, dynamic scenes.
- **D-NeRF** [488]: Extends NeRF with time as an input for explicit scene dynamics.

Further influential works (not expanded): **HyperNeRF** [468] (handles topological changes in dynamic scenes), **Mega-NeRF** [413] (city-to-landscape scale).

Enrichment 23.12.1: Block-NeRF: Scalable Large Scene Neural View Synthesis

Motivation

Neural Radiance Fields (NeRF) and its multiscale extension mip-NeRF (see 23.10.6) have demonstrated remarkable performance on small-scale, object-centric, or single-building scenes. However, scaling such methods to city-sized environments introduces severe bottlenecks: limited model capacity, memory constraints, and inconsistent appearance due to data collected across different days, times, and weather conditions. For practical applications in mapping and autonomous driving, the ability to reconstruct neighborhoods with temporal consistency and update regions without retraining the full model is crucial. Block-NeRF [602] introduces a decomposition strategy that splits the environment into compact, geographically bounded NeRFs (*blocks*). Each block is trained independently and later merged at inference to produce seamless renderings, decoupling rendering cost from the overall environment size.

Figure 23.117: **City-scale reconstruction with Block-NeRF.** The Alamo Square neighborhood in San Francisco reconstructed using multiple Block-NeRFs trained on data from three months. Updates can be applied locally (e.g., construction area on the right) without retraining the entire model. *Credit:* [29].

Method

High-level overview

Block-NeRF [602] scales neural view synthesis to neighborhoods by *structuring the scene geographically* and *decoupling capacity and rendering from global extent*. The pipeline proceeds in four stages:

- **Geographic tiling** of the street network into overlapping blocks using priors such as intersection coordinates and segment lengths (from maps or HD-road graphs).
- **Per-block training** of compact mip-NeRFs (see 23.10.6) on geographically filtered images, with appearance embeddings, exposure conditioning, and pose refinement to absorb long-term capture variability.
- **Visibility-driven selection** of only the few blocks that actually see the current view, using a small visibility network to cull irrelevant blocks.
- **Cross-block compositing and appearance alignment** to merge rendered images smoothly and reconcile style differences across time, weather, and cameras.

Block partitioning and structure

The partitioning strategy employed by Block-NeRF is designed to make large-scale reconstruction, such as multi-block urban scenes, tractable by dividing the environment into smaller, manageable sub-regions. Instead of training one monolithic NeRF for an entire city—which would exceed memory and compute limits—Block-NeRF constructs a structured grid of compact NeRFs that can be trained and updated independently.

Why overlapping sub-regions? Each Block-NeRF is defined to overlap about 50% with its neighbors. This deliberate redundancy serves two roles:

- *Geometric continuity*: Overlap ensures that street geometry and building façades crossing block boundaries are represented consistently by at least two models, reducing visible seams during rendering.
- *Appearance alignment*: Because training images are captured under different conditions (day/night, clear/cloudy, varied camera exposure), overlap provides shared pixels where neighboring blocks can align their appearance embeddings. Without overlap, blocks could converge to inconsistent colors or lighting, producing sharp discontinuities.

During inference, this overlap also supports seamless compositing when multiple blocks contribute to a target view, avoiding visual jumps at block boundaries.

Why place origins at intersections? Block origins are typically anchored at road intersections. Intersections serve as natural hubs in city topology: they connect multiple streets, maximize shared visibility across trajectories, and ensure that blocks cover semantically meaningful spatial units. Placing block centers at intersections also yields a regular, interpretable tiling of the urban grid. In practice, a block covers its local intersection and extends along adjacent streets.

How are partitions built? From these origins, each block's coverage extends roughly 75% of the way to neighboring intersections. This produces the desired $\sim 50\%$ overlap across adjacent blocks. Building the partitions proceeds as follows:

1. *Geographic initialization*: Block origins are selected at intersections or uniformly along long street segments, using map priors such as OpenStreetMap or HD-road graphs.
2. *Coverage definition*: Each block is defined as a sphere or radius around the origin, extending most of the way toward neighbors to enforce overlap.

3. *Geographic filtering of training data*: Each training image is assigned to blocks based on whether its camera frustum intersects the block's coverage region. This ensures that each Block-NeRF only sees the data relevant to its intended sub-region.
4. *Independent training*: Blocks are trained independently in parallel, producing a modular set of models. This modularity allows retraining only the affected blocks when local changes occur (e.g., construction on one street), rather than reoptimizing the entire city.

This decomposition yields a scalable representation: a city becomes a grid of compact NeRFs with intentional redundancy at boundaries. The overlap is key not only for geometric continuity but also for appearance alignment, enabling Block-NeRF to harmonize heterogeneous data collected across days, weather conditions, and camera settings.

Architectural design choices

Each Block-NeRF extends mip-NeRF with three critical augmentations:

- **Appearance embeddings** (per-image latent codes) absorb day-to-day or seasonal shifts in illumination and weather, ensuring that lighting changes are captured photometrically rather than as spurious geometry.
- **Exposure conditioning** encodes camera exposure values (e.g., shutter speed $\times$ gain) with a sinusoidal positional encoding, stabilizing training under brightness fluctuations and enabling interpretable exposure control at inference.
- **Pose refinement** introduces small, regularized SE(3) offsets per driving segment to correct residual odometry drift, mitigating ghosting and duplication artifacts at block boundaries.

In addition, a lightweight **visibility network** f_v is trained to predict whether a spatial sample *would be visible* from a given camera viewpoint. Unlike computing transmittance T directly from each block's density field (which requires full ray marching), f_v is a cheap learned proxy supervised by training-time transmittance. This decoupled approximation plays two roles in the Block-NeRF pipeline: (i) *block selection* at inference, where it prevents unnecessary evaluation of irrelevant or occluded blocks, and (ii) *appearance matching*, where it identifies reliable overlap regions between neighboring blocks for cross-block alignment.

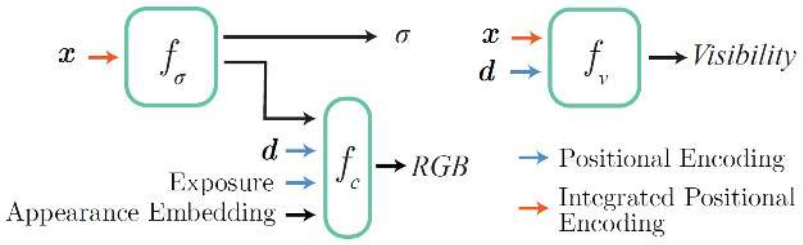

Figure 23.118: **Block-NeRF architecture.** Built on mip-NeRF (see 23.10.6). The density MLP f_σ outputs σ and features; the color MLP f_c consumes features, view direction, exposure encoding, and appearance embedding to predict RGB; the visibility MLP f_v regresses training-time transmittance, supporting block selection and overlap-based appearance alignment. *Credit:* [29].

How f_v integrates into the pipeline

During training. For every training ray, Block-NeRF already computes sample weights

$$T_i = \exp\Big(-\sum_{j<i} \sigma_j \delta_j\Big),$$

the transmittance at depth t_i. These values supervise $f_v(\mathbf{x}_i, \mathbf{d})$ at sampled points, teaching the auxiliary network to approximate visibility directly from $(\mathbf{x}, \mathbf{d})$ without performing volume accumulation. Thus f_v becomes a fast surrogate of NeRF's own visibility reasoning.

During inference. Given a novel camera:

1. *Candidate selection:* Gather blocks within radius R_{select} of the camera center c.
2. *Visibility pruning:* For each candidate, probe f_v at a sparse set of sample points/rays from c and average predictions. Blocks with low mean visibility are culled. Typically only 1–3 remain, preventing compute waste on blocks that are occluded or irrelevant.
3. *Rendering:* Surviving blocks are fully rendered with mip-NeRF ray marching.
4. *Compositing:* Per-block images $\mathbf{I}_i$ are combined with inverse-distance weights, producing a seamless output. Distance-based blending is temporally stable, avoiding flicker in flythroughs.
5. *Appearance alignment:* To harmonize across different lighting conditions, f_v also identifies high-visibility overlap between neighboring blocks. In these regions, adjacent blocks adjust their latent appearance codes so that colors match the reference block, yielding globally consistent appearance (time-of-day, weather, white balance).

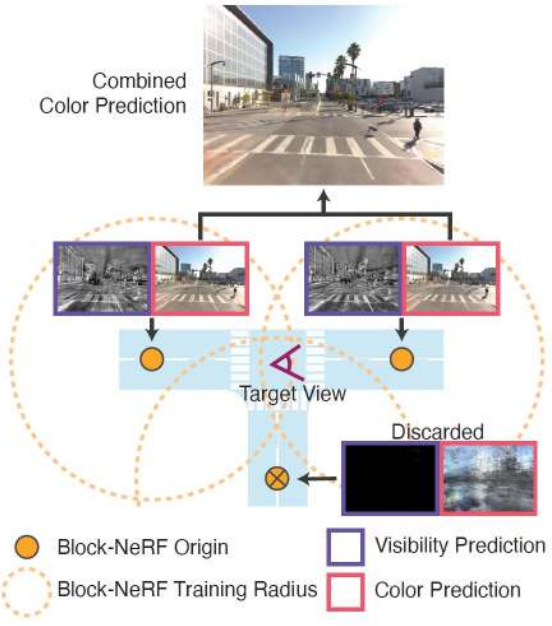

Figure 23.119: **Visibility-guided compositing.** Candidate blocks near the camera are scored by f_v. Blocks with low predicted visibility (bottom) are culled. The remaining per-block renderings are blended in image space with distance-based weights, producing seamless transitions across block boundaries while avoiding seams from irrelevant blocks. *Credit:* [29].

Why f_v is essential

Without f_v, Block-NeRF would need to partially render *all* nearby blocks to check visibility. This is computationally intractable for hundreds of blocks. f_v serves as a fast scout: trained once during supervision, then deployed at inference to prune irrelevant blocks and guide alignment. This makes city-scale rendering practical while preserving seamless transitions across block boundaries.

Compositing across blocks

After visibility pruning, the surviving blocks are rendered with mip-NeRF's volumetric ray marching (Sec. 23.10.6). Their outputs $\mathbf{I}_i$ are then blended in raster space using inverse-distance weights relative to the camera:

$$w_i \propto \|c - x_i\|^{-p}, \qquad \sum_i w_i = 1,$$

with p controlling the sharpness of transitions. This global weighting strategy is simple to compute, avoids per-pixel overhead, and—most importantly—yields temporally stable results for long fly-throughs. In practice, distance-based blending reliably hides seams in overlap regions; more complex schemes (e.g., depth- or visibility-based blending) can sharpen stills but often introduce flicker over time.

Appearance control and cross-block alignment

A remaining challenge is that independently trained blocks do not share a common appearance embedding space: the same latent index can correspond to different global looks (e.g., sunny in one block, cloudy in another). When blended directly, such inconsistencies manifest as visible seams. To harmonize the output, Block-NeRF performs *appearance matching* across overlaps:

1. Fix a reference block with a chosen appearance code ℓ^{ref}.
2. For each neighboring block j, use f_v to identify overlap regions that are simultaneously visible.
3. Optimize only ℓ_j, keeping network weights frozen, to minimize color differences over the shared patch:

$$\min_{\ell_j} \sum_{p \in \mathscr{P}} \left\| \mathbf{I}_{\text{ref}}(p; \ell^{\text{ref}}) - \mathbf{I}_j(p; \ell_j) \right\|^2.$$

4. Propagate alignment outward across the block graph.

This process aligns low-frequency appearance factors such as illumination, weather, and time-of-day, producing a globally coherent style while preserving local geometry. Once aligned, the entire city-scale environment can be rendered consistently under any desired appearance (e.g., dusk everywhere).

Figure 23.120: **Appearance embeddings** Per-image latents represent weather/illumination diversity (day/night, clear/cloudy), preventing geometry corruption and enabling controllable appearance during inference. *Credit:* [29].

Figure 23.121: **Exposure conditioning** Conditioning on exposure stabilizes training across brightness variation and provides an interpretable control knob at render time (e.g., brighten/darken without altering geometry). *Credit:* [29].

Figure 23.122: **Cross-block appearance matching** A fixed target appearance (left) is propagated to neighbors by optimizing only their appearance codes on overlapping, high-visibility regions, yielding a consistent global style (e.g., coherent night appearance) across blocks. *Credit:* [29].

Why this design works

Geographic tiling concentrates capacity where needed and enables local updates. *Visibility-driven selection* avoids wasting compute and prevents seam artifacts from blocks that cannot explain the view. *Distance-based blending* is temporally stable and simple. *Appearance embeddings + exposure conditioning* disentangle nuisance factors (time, weather, camera settings) from scene structure, while *appearance matching* reconciles independently trained blocks into a coherent city-scale radiance field.

Experiments and Ablations

Ablations on Alamo Square

Appearance embeddings, exposure conditioning, and pose refinement all contribute significantly to fidelity. Removing appearance embeddings forces the model to encode weather variations as geometry, introducing artifacts. Disabling pose refinement produces blur and duplication from misalignment. Removing exposure slightly lowers accuracy but eliminates exposure control.

Model	PSNR↑	SSIM↑	LPIPS↓
mip-NeRF [30]	17.86	0.563	0.509
-Block-NeRF (no appearance)	20.13	0.611	0.458
-Block-NeRF (no exposure)	23.55	**0.649**	0.418
-Block-NeRF (no pose opt.)	23.05	0.625	0.442
Full Block-NeRF	**23.60**	**0.649**	**0.417**

Table 23.33: **Ablation study on Alamo Square.** Each architectural component contributes: appearance embeddings mitigate geometry hallucinations; pose refinement sharpens alignment; exposure conditioning improves stability and control.

Figure 23.123: **Qualitative ablations.** Without appearance embeddings, cloudy geometry is introduced. Without pose optimization, ghosting occurs (e.g., duplicated telephone pole in the first row). Exposure conditioning provides modest improvements in fidelity and crucial control at inference. *Credit:* [29].

Block granularity on Mission Bay

Splitting into finer blocks improves accuracy even when the total parameter count is fixed. With smaller block sizes, each block specializes to local geometry and appearance, and only a few blocks are active per frame, keeping inference efficient.

# Blocks	Weights / Total	Block size	Compute	PSNR↑	SSIM↑	LPIPS↓
1	0.25M / 0.25M	544 m	1×	23.83	0.825	0.381
4	0.25M / 1.00M	271 m	2×	25.55	0.868	0.318
8	0.25M / 2.00M	116 m	2×	26.59	0.890	0.278
16	0.25M / 4.00M	54 m	2×	**27.40**	**0.907**	**0.242**
1	1.00M / 1.00M	544 m	1×	24.90	0.852	0.340
4	0.25M / 1.00M	271 m	0.5×	25.55	0.868	0.318
8	0.13M / 1.00M	116 m	0.25×	25.92	0.875	0.306
16	0.07M / 1.00M	54 m	0.125×	**25.98**	**0.877**	**0.305**

Table 23.34: **Effect of block granularity on Mission Bay.** More blocks yield higher reconstruction fidelity. Even with fixed total parameters (bottom), splitting capacity into multiple small blocks improves accuracy and reduces per-frame compute since only a subset of blocks is active. *Credit:* [29].

Limitations and Future Work

Block-NeRF inherits Mip-NeRF's high rendering cost and struggles with unmasked dynamic content. Transient objects leave artifacts such as shadows; vegetation and seasonal changes lead to blurred trees; construction requires retraining of affected blocks. Distant structures are under-sampled, producing lower fidelity. Future directions to combat these and improve results include:

- **Dynamic radiance fields** for explicitly modeling moving objects.
- **Unbounded representations** (e.g., NeRF++ [772], mip-NeRF 360 [29]) for sharper distant reconstructions.
- **Acceleration techniques** such as voxel caching [370, 740] or hash encodings [443] for real-time rendering and faster training.

Enrichment 23.12.2: Mip-NeRF 360: Unbounded Anti-Aliased NeRF

Motivation

Real-world *unbounded* scenes (full 360° rotations, sky and horizons, distant buildings) reveal persistent weaknesses in NeRF-style pipelines: distant regions render blurry, scaling capacity becomes costly, and ambiguity induces artifacts such as semi-transparent *floaters* and background collapse. Readers are referred to the prior subsection on mip-NeRF for anti-aliasing via integrated positional encoding (IPE) over conical-frustum Gaussians (§23.10.6) [30]. MipNeRF360 [29] builds on that foundation to make 360° unbounded scenes numerically well-posed, sample-efficient, and less ambiguous.

Challenges in unbounded 360° scenes

- **Global parameterization.** Fitting an unbounded world into a fixed near/far box squeezes very distant geometry into a tiny coordinate range, so equal steps in model space correspond to huge steps in world space at the far field, leaving too few effective intervals for the entire background and causing blur despite intra-interval anti-aliasing [29, 30].
- **Sampling geometry.** Uniform steps in metric depth t devote many samples to nearby content (large pixel footprint) but too few to distant content (tiny footprint), which yields aliasing and loss of detail in horizons and skies for fully 360° captures [29].
- **Capacity vs. efficiency.** Large, real scenes mix extremely near and far structure; making a single mip-NeRF MLP sufficiently large and supervising it at multiple scales is expensive, so capacity is constrained by training cost [30].
- **Ambiguity and artifacts.** The inverse problem is underconstrained at scale; optimization can explain pixels via semi-transparent blobs (*floaters*) or by dragging distant matter toward the camera (*background collapse*). Noise injection and multi-scale supervision help but neither controls how mass is arranged along a ray nor fixes the global parameterization mismatch [30, 429].

MipNeRF360 solutions to unbounded scenes challenges

1. **Nonlinear scene reparameterization.** A smooth *contraction* maps $\mathbb{R}^3$ into an isotropic ball of radius 2 while leaving the unit ball around the camera unchanged. Preserving the unit ball keeps *local* metric geometry faithful where pixels are most sensitive (foreground parallax and high-frequency detail). Compressing the exterior into the shell $1 \to 2$ makes "infinity" finite and numerically well-behaved, and the extra radius beyond 1 provides dynamic range so far depths do not collapse onto a single boundary. The spherical target avoids axis/corner biases of a cube, treating all directions symmetrically. Paired with *disparity-linear* spacing along rays, equal steps in the contracted coordinate correspond more closely to equal changes in image footprint at long range, restoring a well-conditioned sampling geometry for unbounded scenes.
2. **Proposal-driven hierarchical sampling.** Each camera ray is divided into contiguous segments (intervals) in a normalized coordinate $s \in [0, 1]$, yielding a 1D histogram with a nonnegative weight per interval that reflects its contribution to the pixel after volumetric compositing. *What changes versus mip-NeRF* is the division of labor: rather than repeatedly querying and supervising the *same* MLP at multiple scales, MipNeRF360 [29] *decouples where to sample* from *what to predict*. A small *proposal MLP* is evaluated on a coarse, roughly uniform partition (in the contracted, disparity-linear coordinate) to produce a coarse weight profile that *guides* where the ray should be refined; the ray is then re-partitioned so intervals concentrate around the predicted peaks (optionally repeating this proposal step once more). Only after this final, content-focused partition has been built is the high-capacity *NeRF MLP* run—*once per ray at a single stage*, namely on the *final* set of intervals—by querying it at each final interval to predict densities and colors for the actual rendering. To make the proposal reliable without adding another image loss, a lightweight *histogram-consistency* objective trains the proposal to *cover* the support that the NeRF MLP ultimately uses (gradients flow only into the proposal in this term), ensuring the sampler does not overlook mass that the renderer needs. In short, mip-NeRF's multi-scale rendering is replaced by a cheap *sampler* (proposal MLP) plus a single high-fidelity *renderer* (NeRF MLP), concentrating expensive computation exactly where it matters most [29].
   Why this improves things:
   - The proposal amortizes search, so the final intervals rapidly cluster near actual surfaces instead of being wasted in empty space.
   - The NeRF MLP avoids redundant coarse-and-fine rendering passes, enabling higher capacity without prohibitive training cost.
   - The consistency term keeps proposals conservative (they must cover what NeRF uses), reducing missed surfaces and aliasing in unbounded scenes.
3. **Distortion regularization.** Like mip-NeRF, each interval is a conical frustum approximated by a 3D Gaussian and is anti-aliased *within* the interval via integrated positional encoding; what those methods *do not* control is *how the total weight is distributed* across *intervals* along the ray. In unbounded scenes this longitudinal ambiguity is a major failure mode: the optimization can explain a pixel by spreading small weights over many separated intervals (yielding semi-transparent *floaters*), or by shifting mass into near intervals to shorten optical paths (*background collapse*). MipNeRF360 [29] adds a *distortion* loss that penalizes *spread* of the per-ray weight histogram in the normalized coordinate s (via pairwise distances between interval midpoints plus a width term).

High level: the loss softly prefers compact, near-unimodal allocations *across* intervals when consistent with the images, steering the solution toward "a surface here" rather than many faint lobes along the line of sight. This complements the within-interval anti-aliasing (unchanged) and, together with the proposal-guided sampling and contraction, reduces floaters, discourages background collapse, and yields sharper, more plausible geometry in 360° environments [29].

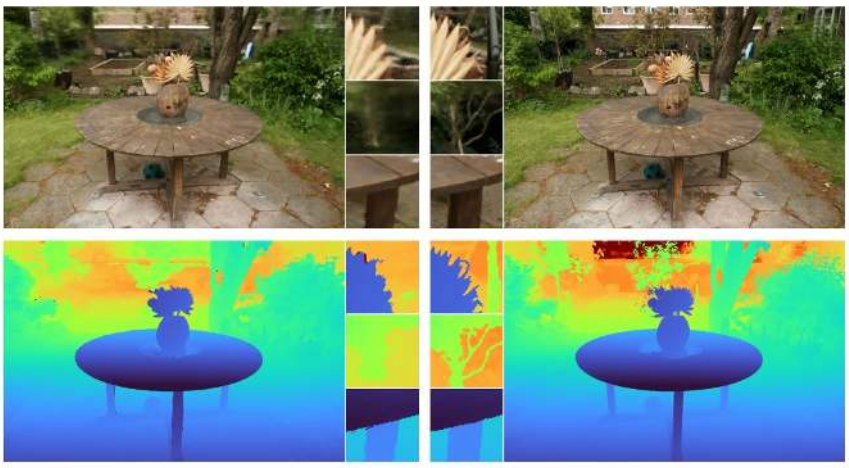

(a) mip-NeRF [3], SSIM=0.526 (b) Our Model, SSIM=0.804

Figure 23.124: **Comparison to mip-NeRF.** (a) Though mip-NeRF is able to produce accurate renderings of objects, for unbounded scenes it often generates blurry backgrounds and low-detail foregrounds. (b) MipNeRF360 produces detailed realistic renderings of these unbounded scenes, as evidenced by the renderings (top) and depth maps (bottom) from both models. See the supplemental video for additional results. *Credit:* [29].

Method

MipNeRF360 extends mip-NeRF (§23.10.6) to unbounded 360° scenes with three coupled components: a smooth **nonlinear scene reparameterization** that makes "infinity" finite while preserving near-camera geometry; a **proposal-driven hierarchical sampling** scheme that decouples *where to sample* from *what to predict* via online histogram consistency; and a **distortion** regularizer that shapes per-ray weight distributions to suppress floaters and discourage background collapse [29].

Preliminaries: mip-NeRF

For a ray $\mathbf{r}(t) = \mathbf{o} + t\mathbf{d}$ with distances $t = \{t_i\}_{i=0}^{N}$ partitioning intervals $T_i = [t_i, t_{i+1})$, mip-NeRF approximates each conical frustum by a 3D Gaussian with mean μ and covariance Σ and featurizes it with integrated positional encoding (IPE):

$$\gamma(\mu,\Sigma) = \left\{ \begin{bmatrix} \sin(2^\ell \mu)\exp\big(-2^{2\ell-1}\operatorname{diag}(\Sigma)\big) \\ \cos(2^\ell \mu)\exp\big(-2^{2\ell-1}\operatorname{diag}(\Sigma)\big) \end{bmatrix} \right\}_{\ell=0}^{L-1} \tag{23.56}$$

These features drive an MLP (NeRF MLP) to produce density τ_i and color $\mathbf{c}_i$:

$$(\tau_i, \mathbf{c}_i) = \mathrm{MLP}\big(\gamma(\mathbf{r}(T_i)); \Theta_{\mathrm{NeRF}}\big) \tag{23.57}$$

Pixel color is rendered by volumetric compositing:

$$\mathbf{C}(\mathbf{r},t) = \sum_i w_i \mathbf{c}_i, \tag{23.58}$$

$$w_i = \big(1 - e^{-\tau_i (t_{i+1}-t_i)}\big) \exp\Big(- \sum_{i'<i} \tau_{i'} (t_{i'+1} - t_{i'}) \Big) \tag{23.59}$$

Coarse intervals are sampled uniformly in $[t_n, t_f]$:

$$t^{\mathrm{c}} \sim \mathscr{U}[t_n, t_f], \qquad t^{\mathrm{c}} = \mathrm{sort}(\{t^{\mathrm{c}}\}) \tag{23.60}$$

then refined via inverse-transform sampling from the coarse histogram:

$$t^{\mathrm{f}} \sim \mathrm{hist}\big(t^{\mathrm{c}}, w^{\mathrm{c}}\big), \qquad t^{\mathrm{f}} = \mathrm{sort}(\{t^{\mathrm{f}}\}) \tag{23.61}$$

Training minimizes a weighted sum of coarse/fine reconstruction losses:

$$\sum_{\mathbf{r}\in\mathscr{R}} \frac{1}{10} \mathscr{L}_{\mathrm{recon}}\big(\mathbf{C}(\mathbf{r},t^{\mathrm{c}}), \mathbf{C}^*(\mathbf{r})\big) \; + \; \mathscr{L}_{\mathrm{recon}}\big(\mathbf{C}(\mathbf{r},t^{\mathrm{f}}), \mathbf{C}^*(\mathbf{r})\big) \tag{23.62}$$

See §23.10.6 for details [30].

Scene and ray parameterization

Context and goal. In mip-NeRF, each ray interval (a conical frustum) is approximated by a 3D Gaussian with mean μ and covariance Σ, and features are computed directly in *Euclidean* coordinates via integrated positional encoding (IPE). For truly unbounded 360° scenes, this Euclidean parameterization becomes ill-conditioned at long range. MipNeRF360 changes *where* those features are computed: it first *reparameterizes the scene* by a smooth warp $f : \mathbb{R}^3 \to \mathbb{R}^3$ that makes infinity finite, and only then encodes the frustum-Gaussians. This has two consequences. First, the Gaussian must be *pushed through* the nonlinear f so that both its center and its spatial extent are correctly warped. Second, ray distances must be reparameterized to align sample placement with the new geometry. Together, these steps define MipNeRF360's scene and ray parameterization [29].

Pushing Gaussians through a smooth warp (Eq. 9). Because f is nonlinear, the image of a Gaussian is not Gaussian in closed form. MipNeRF360 therefore adopts the standard first–order (Extended Kalman Filter–style) approximation: linearize f at the mean and propagate mean and covariance through that local linear map,

$$f(\mathbf{x}) \approx f(\mu) + J_f(\mu)\,(\mathbf{x} - \mu), \qquad f(\mu,\Sigma) \;=\; \Big(f(\mu),\; J_f(\mu)\,\Sigma\, J_f(\mu)^{\top} \Big). \tag{23.63}$$

Here $J_f(\mu)$ is the 3×3 Jacobian of f at μ, capturing the local stretch/rotation induced by f. This "Kalman-like" pushforward is essential: it preserves not only the warped *position* $f(\mu)$ but also the warped *extent and orientation* $J_f \Sigma J_f^{\top}$ of the frustum. Without updating the covariance, far-field frustums—often highly anisotropic—would be misrepresented after warping, undermining mip-NeRF's anti-aliasing.

Choosing the warp: contraction (Eq. 10). In MipNeRF360 the scene warp f is a smooth *contraction* that maps all of $\mathbb{R}^3$ into a closed ball of radius 2 while leaving the unit ball unchanged:

$$f(\mathbf{x}) \;=\; \mathrm{contract}(\mathbf{x}) \;=\; \begin{cases} \mathbf{x}, & \|\mathbf{x}\| \le 1, \\ \Big(2 - \dfrac{1}{\|\mathbf{x}\|}\Big) \dfrac{\mathbf{x}}{\|\mathbf{x}\|}, & \|\mathbf{x}\| > 1. \end{cases} \tag{23.64}$$

Why keep $\|\mathbf{x}\| \le 1$ *unchanged, and why a shell* $[1,2]$ *for the far field?* The unit ball fixes a normalized near-field scale around the camera where small metric errors drive perceived sharpness (parallax, fine texture). Keeping $f(\mathbf{x}) = \mathbf{x}$ there preserves *exact* Euclidean geometry and the anti-aliasing behavior inherited from mip-NeRF. Mapping everything beyond the unit sphere into the finite shell $1 \to 2$ preserves *dynamic range* for large depths: depths just beyond 1 map near 1, while depths $\|\mathbf{x}\| \to \infty$ map smoothly toward 2—so "far" and "very far" remain separable after warping, instead of collapsing onto a single boundary. Because the target is spherical, all directions are treated symmetrically.

Why this reduces common failure modes (mechanism, not just outcome):

- **Background blur.** In Euclidean t, a fixed number of intervals must span an enormous depth range, so each far interval covers a huge swath of world space; its Gaussian/IPE averages many distinct background colors, appearing blurry. After contraction *paired with* disparity-linear spacing (explained below), the far field occupies a finite, uniformly coverable band in the warped coordinate. Intervals become *approximately equal-sized in the contracted radius*, so the background is represented by *many* small, distinct bins rather than a few massive ones. Less averaging $\Rightarrow$ sharper backgrounds.
- **Background collapse.** With poor far-field resolution, optimization can "cheat" by pulling density toward the camera: shorter paths can reproduce colors with fewer samples, so mass drifts forward. In the contracted domain, moving density from the far shell toward the near region causes *large displacements* in the warped coordinate (and hence stronger reconstruction penalties), while the far band itself now has sufficient resolution to place density where images demand it. The optimization no longer gains an easy advantage by collapsing the background forward.

After pushing the frustum-Gaussian (μ, Σ) through f via the linearization in Eq. (23.63), features are computed from the *contracted* Gaussian

$$\gamma\big(\text{contract}(\mu, \Sigma)\big),$$

so within-interval anti-aliasing is preserved but now in a bounded, well-conditioned coordinate system [29].

Off-axis IPE—where it fits and why it matters After the scene is *contracted* and each frustum-Gaussian (μ, Σ) is pushed through the warp using the EKF-style update in Eq. (23.63), MipNeRF360 computes features *in the contracted space* with Integrated Positional Encoding (IPE). IPE is mip-NeRF's anti-aliasing mechanism: instead of encoding a single point, it encodes the *expected* sine/cosine responses under the Gaussian, so pixel footprint and frustum extent are baked into the features. In the original, *axis-aligned* version, these sinusoids are taken along the coordinate axes, which means only the *diagonal* of Σ (per-axis variance) can modulate the features.

The contraction plus the Kalman-like pushforward typically yields *full, rotated* covariances in the warped space—far-field frustums are elongated and oriented off-axis—so restricting IPE to axis directions discards the very orientation cues that distinguish different Gaussians. MipNeRF360 therefore adopts *off-axis* IPE (Appendix of [29]): it projects the Gaussian onto a fixed bank of non-axis-aligned unit directions (the vertices of a twice-tessellated icosahedron), allowing *off-diagonal* covariance to influence the features. Intuitively, two Gaussians can share the same per-axis spreads yet differ in orientation; axis-aligned IPE conflates them, while off-axis IPE keeps them separate. The result is a richer, orientation-sensitive encoding of elongated, distant frustums, which improves discrimination and stability in the far field [29].

Reparameterizing the ray: disparity-linear coordinate (Eq. 11). The contraction makes the *space* finite; the ray parameter determines *how samples populate* that space. MipNeRF360 maps Euclidean distance $t \in [t_n, t_f]$ to a normalized coordinate $s \in [0,1]$ via an invertible g:

$$s = \frac{g(t) - g(t_n)}{g(t_f) - g(t_n)}, \qquad t = g^{-1}\big(s\, g(t_f) + (1-s)\, g(t_n)\big), \tag{23.65}$$

and sets $g(x) = 1/x$ so bins are *uniform in inverse depth* (disparity). *Why s (disparity) behaves better than t (metric depth):*

- **Matches image sensitivity.** In a pinhole camera, a fronto-parallel patch at depth z projects with scale $\propto 1/z$; small image changes are roughly proportional to changes in *disparity* $d = 1/z$ (since $\partial\,\text{image}/\partial d$ stays more nearly depth-invariant than $\partial\,\text{image}/\partial z$). Uniform steps in s therefore allocate samples in proportion to *perceptual/photometric change* along the ray, especially at long range, improving coverage of sky and distant objects.
- **Pairs with contraction.** For a camera at the origin, the contraction radius along a ray is $r'(t) = 2 - \frac{1}{t}$. Uniform steps in s with $g(t) = 1/t$ (i.e., uniform disparity) produce *approximately uniform steps in* r' across the outer shell. Thus, a fixed sample budget yields near-uniform spatial coverage in the warped domain, which is the domain where features are computed.
- **Numerical stability and consistency.** Normalizing every ray to $s \in [0,1]$ makes histograms, losses (proposal consistency, distortion), and resampling *ray-agnostic*: bin sizes, gradients, and learning rates do not depend on unknown scene scales or ad-hoc near/far ranges. The mapping in Eq. (23.65) recovers t only where metric distances are required (e.g., transmittance factors), avoiding depth-scale–dependent conditioning in the rest of the pipeline.

Together, Eq. (10) makes "infinity" finite with preserved depth *resolution*, and Eq. (11) distributes a fixed number of samples where the image is most sensitive—yielding sharper backgrounds, fewer collapse incentives, and more stable optimization in unbounded 360° scenes [29].

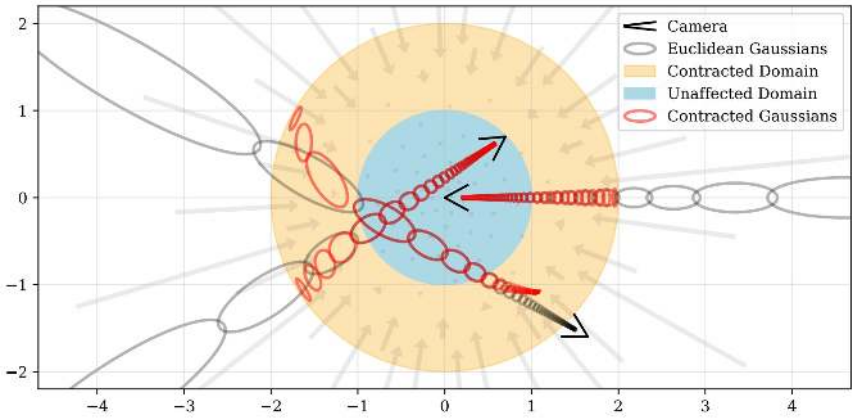

Figure 23.125: **Scene reparameterization visualization.** A 2D visualization of the scene parameterization. The operator contract$(\cdot)$ (Eq. (10), arrows) maps coordinates onto a ball of radius 2 (orange), leaving points within radius 1 (blue) unchanged. This contraction is applied to mip-NeRF Gaussians in Euclidean 3D (gray ellipses) similarly to a Kalman filter to produce contracted Gaussians (red ellipses), whose centers lie within radius 2. The design of contract$(\cdot)$, combined with linear-in-disparity ray spacing, yields equidistant intervals in the orange region for rays cast from the origin. *Credit:* [29].

Coarse-to-fine online distillation

Where this fits in the pipeline. Having reparameterized the scene with the contraction f and the ray with the disparity-linear coordinate s (Sec. 23.12.2), MipNeRF360 must still decide *where along* $s \in [0,1]$ *to place computation*. Rather than supervising a single MLP at multiple scales (mip-NeRF), MipNeRF360 *separates where to sample* from *what to predict*: a lightweight network proposes *sampling distributions* along the ray, and a high-capacity network predicts *densities and colors* [29].

Two-MLP cascade. The model uses (i) a small *proposal MLP* that outputs only densities (hence interval *weights*, no colors), and (ii) a large *NeRF MLP* that outputs both density and color. Work proceeds along the normalized coordinate s:

- *Coarse partition and proposal histogram.* Start by partitioning $s \in [0,1]$ into contiguous bins with endpoints $\hat{t} = \{\hat{t}_0, \ldots, \hat{t}_M\}$ (paper notation uses t for bin edges; here $\hat{t}$ indicates the *proposal* partition; $t/\hat{t}$ can be read as any monotone ray coordinate, e.g., s). Evaluate the proposal MLP at these bins and convert predicted densities to a *proposal weight histogram* $(\hat{t}, \hat{w})$ using the standard volumetric compositing weights (cf. NeRF/mip-NeRF; see Eq. (23.59) in the previous subsection).
- *Importance resampling.* Treat $\hat{w}$ as a distribution over the ray and resample to form a *finer* partition that concentrates bins where $\hat{w}$ is large (near likely surfaces). The paper uses one or two proposal stages, each producing its own $(\hat{t}, \hat{w})$ and a refined partition.
- *Final rendering pass.* Only after the final, content-focused partition is constructed, evaluate the high-capacity *NeRF MLP once per ray at a single stage*: query it at each *final* interval to predict density and color, and composite to the pixel. This avoids redundant coarse-and-fine renderings of the same ray while still guiding samples to informative regions.

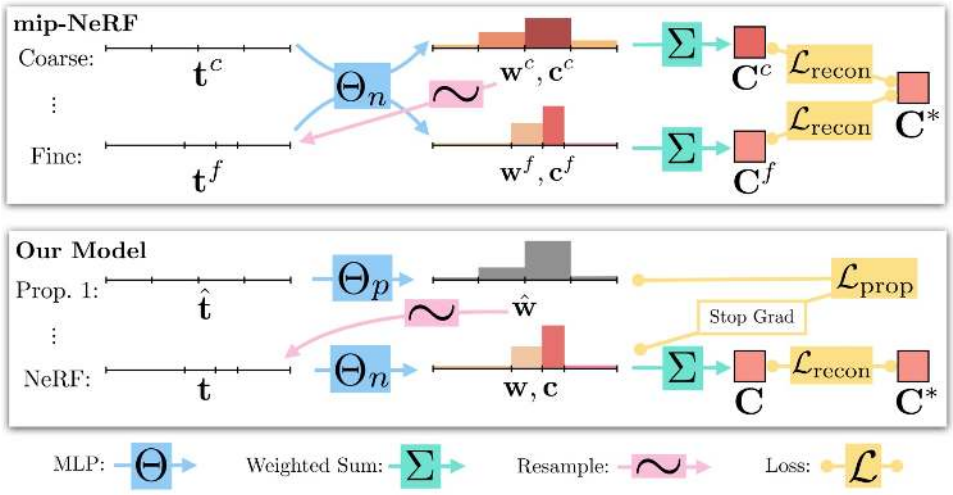

Figure 23.126: **Architecture vs. mip-NeRF.** mip-NeRF reuses one MLP across scales and supervises all scales. MipNeRF360 replaces early image-supervised passes with a *proposal MLP* that emits weights (no color) to guide resampling, and a single final *NeRF MLP* that outputs weights and colors for supervision. The proposal MLP is trained so its weights $\hat{w}$ are consistent with the NeRF MLP's final weights w. A small proposal MLP plus a large NeRF MLP yields high capacity while remaining tractable. *Credit:* [29].

From proposal to final histogram. Building on the two–MLP cascade, each ray is processed in two stages: (i) one or two *proposal* passes produce a coarse, then refined sampling partition together with a coarse weight histogram; (ii) a single *final* pass evaluates the high-capacity NeRF MLP on the last, content-focused partition to obtain the weights and colors used for rendering. The proposal is trained to *safely guide* the final pass via a one-sided consistency loss; the NeRF MLP is trained by the usual image reconstruction (and later, distortion) losses. Crucially, the consistency loss uses *stop-gradient* on the NeRF outputs so that NeRF "leads" and the proposal "follows", preventing the two networks from colluding by making NeRF artificially easier to cover [29].

Notation and partitions (one ray). Along a ray we keep a 1D histogram: a strictly increasing list of bin edges and one nonnegative weight per bin that sums to 1. During the *proposal* stage the small network is evaluated on a *coarse* partition, yielding a proposal histogram with edges $\hat{t} = \{\hat{t}_j\}_{j=0}^{\hat{M}}$ and weights $\hat{w} = \{\hat{w}_j\}_{j=1}^{\hat{M}}$ (weights computed from proposal densities via standard NeRF compositing). After importance resampling around peaks of $\hat{w}$, we obtain a *refined* partition on which the NeRF MLP is run once to produce the *final* histogram (t, w) with edges $t = \{t_i\}_{i=0}^{M}$ and weights $w = \{w_i\}_{i=1}^{M}$. Typically $\hat{M} < M$ and proposal bins are wider. This is an intended difference in bin counts/widths that we denote as different "step size". Because the refined edges are created *from* the coarse proposal via resampling, the two partitions need not align; they are allowed to be misaligned by design.

About coordinates. The paper actually samples and resamples in the disparity-linear coordinate $s \in [0,1]$. For notational continuity we write edges as t, but you can read t as "whatever *monotone* ray coordinate is used to lay out edges" (in practice, $t \equiv s$ here). This choice does not affect the consistency machinery: the check asks whether a final interval $T_i = [t_i, t_{i+1})$ is *covered* by the coarse proposal, which we test by summing proposal weights over all proposal bins that *overlap* T_i. Summing over overlaps depends only on which portions of the ray are covered, not on how those portions are parametrized, so it remains valid even when the two histograms have different edge locations, widths, or numbers of bins.

Histogram-consistency bound (Eqs. 12–13). The proposal is trained with a one-sided *don't-miss-mass* constraint so that importance resampling can always find regions the final pass relies on. Let the final bins be $T_i = [t_i, t_{i+1})$ and the proposal bins be $\hat{T}_j = [\hat{t}_j, \hat{t}_{j+1})$. Define the overlap-based bound for any interval T:

$$\text{bound}(\hat{t}, \hat{w}, T) \;=\; \sum_{j : T \cap \hat{T}_j \neq \emptyset} \hat{w}_j. \tag{23.66}$$

Consistency requires $w_i \le \text{bound}(\hat{t}, \hat{w}, T_i)$ for all i. Any *excess* final mass above this bound is penalized:

$$\mathscr{L}_{\text{prop}}(t, w, \hat{t}, \hat{w}) \;=\; \sum_i \frac{1}{w_i} \max\Big(0,\, w_i - \text{bound}(\hat{t}, \hat{w}, T_i)\Big)^2, \tag{23.67}$$

with stop-gradient on (t, w) so that only the proposal MLP is updated.

Intuition.

- **Coarse may over-cover, must not under-cover.** A coarse proposal can safely spread mass broadly—resampling will zoom into its peaks—but it must not *omit* mass where the final pass concentrates; otherwise, that region could never be discovered. The bound in Eq. (23.66) encodes exactly this asymmetry by demanding that every final-bin weight be "explainable" by overlapping proposal mass.

- **Independent of bin layout and size.** Because the bound sums proposal mass over overlaps, it tolerates different bin counts and widths and does not assume aligned edges. Merging or splitting proposal bins while conserving mass does not change whether a region is covered.
- **Loss roles at a glance.** The NeRF MLP optimizes image reconstruction (and, later, distortion) on the *final* partition, while the proposal MLP optimizes $\mathscr{L}_{\text{prop}}$ to learn a conservative cover around NeRF's weight distribution. This division of labor lets the small network amortize "where to look" and the large network focus capacity on "what to predict", improving both speed and accuracy in unbounded scenes.

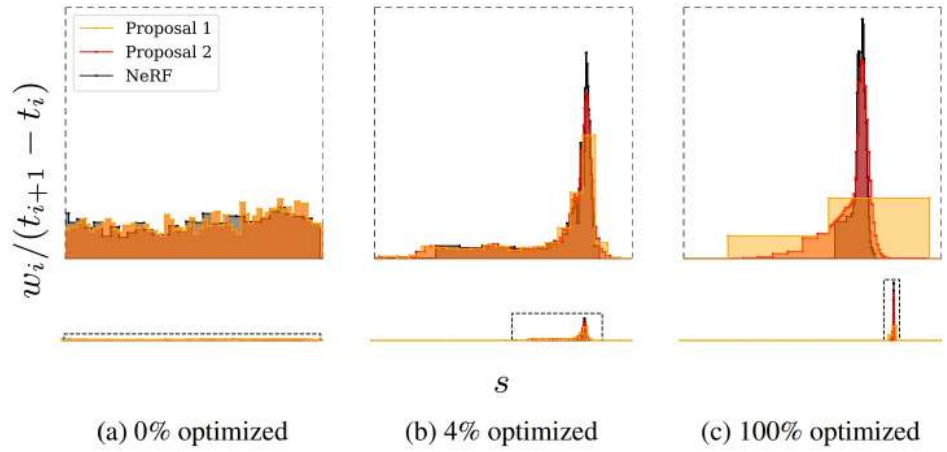

(a) 0% optimized (b) 4% optimized (c) 100% optimized

Figure 23.127: **Histogram evolution over training.** For a single ray in *bicycle*, the NeRF histogram (t,w) (black) and two proposal histograms $(\hat{t},\hat{w})$ (yellow, orange) across training. Early weights are near-uniform; later, NeRF concentrates at a surface while proposals adapt to cover it, enabling robust resampling. *Credit:* [29].

Sampling refinements: what they do and why they help.

- *Annealing.* Before drawing fine samples from $\hat{w}$, raise weights with a Schlick-biased schedule over step $n \in [0,N]$,

$$\hat{w}_n \propto \hat{w}^{\frac{bn/N}{(b-1)n/N+1}}, \quad b = 10.$$

  Early in training, this flattens the distribution (exploration across the ray); as training proceeds, it sharpens back to $\hat{w}$ (exploitation near predicted surfaces). This avoids premature lock-in to spurious peaks.
- *Dilation.* Convert the histogram to a density $\hat{p}_i = \hat{w}_i/(\hat{t}_{i+1}-\hat{t}_i)$, replace $\hat{p}$ by a local maximum over $s \pm \varepsilon_k$ with

$$\varepsilon_k = \frac{a}{\prod_{k'=1}^{k-1} n_{k'}} + b, \quad a = 0.5,\ b = 0.0025,$$

  where n_k is the number of fine samples drawn at proposal level k, then integrate back and renormalize. This creates a small, scale-aware safety margin around peaks so that minor pose/view changes do not cause the proposal to *miss* a thin surface (reduces rotational aliasing).

- *Midpoint resampling.* Draw $n+1$ sorted samples from the coarse histogram and use *midpoints* of adjacent samples (including reflected endpoints) as the new bin edges. Using raw samples as edges erodes peaks and creates irregular gaps; midpoints preserve modes and yield more even, low-alias partitions.

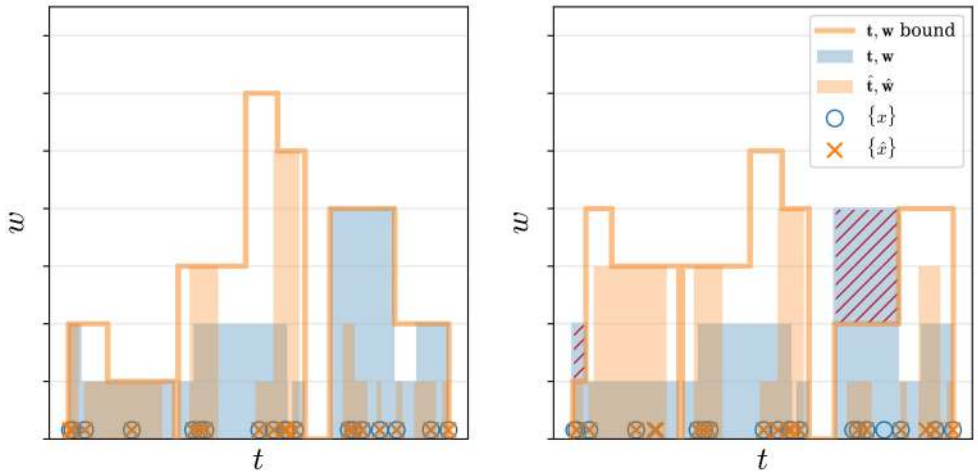

Figure 23.128: **Motivation behind $\mathscr{L}_{\text{prop}}$.** If two histograms could arise from the same underlying distribution, the bound induced by $(\hat{t}, \hat{w})$ upper-bounds (t, w) and the loss is zero; otherwise, any surplus final mass (red) is penalized, teaching the proposal to cover regions NeRF actually uses. *Credit:* [29].

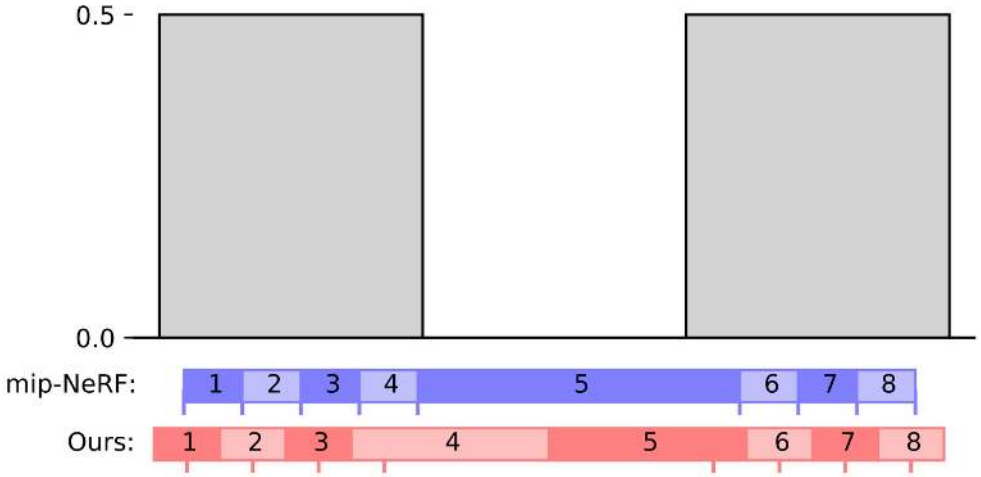

Figure 23.129: **Midpoint resampling.** Using sampled points as endpoints (blue) erodes coarse modes and spans gaps asymmetrically; midpoints between sorted samples (red) yield more regular refinements and reduce aliasing. *Credit:* [29].

Regularization for interval-based models

Even with contraction and proposal guidance, the inverse problem remains ambiguous along the ray: colors can be matched by distributing small weights across many separated intervals (floaters) or by shifting mass toward the camera (background collapse). MipNeRF360 therefore adds a **distortion** loss on the per-ray step function $w_s(\cdot) = \sum_i w_i \mathbf{1}_{[s_i, s_{i+1})}(\cdot)$ over $s \in [0,1]$:

$$\mathscr{L}_{\text{dist}}(s,w) = \int\int w_s(u)\, w_s(v)\, |u-v|\, \mathrm{d}u\, \mathrm{d}v. \tag{23.68}$$

Evaluated on piecewise-constant histograms, this yields the efficient discrete form

$$\mathscr{L}_{\text{dist}}(s,w) = \sum_{i,j} w_i w_j \left| \frac{s_i + s_{i+1}}{2} - \frac{s_j + s_{j+1}}{2} \right| + \frac{1}{3} \sum_i w_i^2 \,(s_{i+1} - s_i). \tag{23.69}$$

The pairwise-midpoint term penalizes spreading weight across distant intervals, while the width term penalizes placing large mass in wide bins. Minimizing $\mathscr{L}_{\text{dist}}$ thus favors compact, minimally fragmented weight layouts consistent with the image evidence, which suppresses floaters and reduces the incentive for background collapse. Gradients of this loss naturally pull nearby weighted intervals together, shrink overly wide bins, and drive weights to zero when a ray is empty [29].

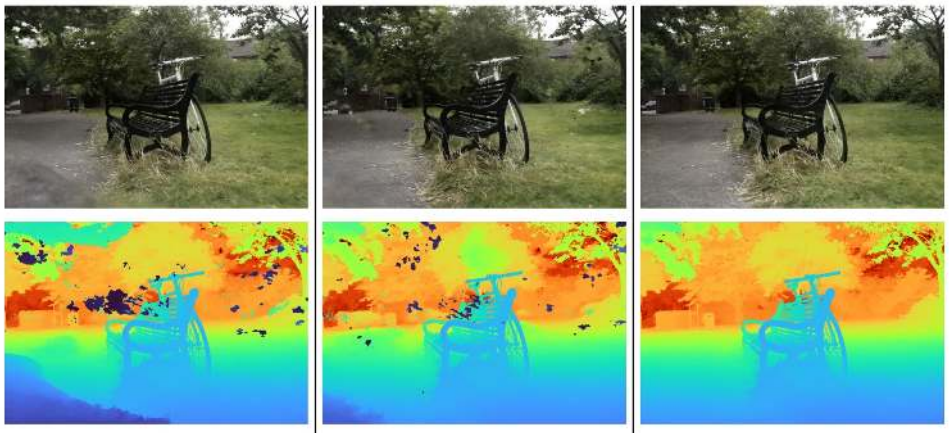

Figure 23.130: **Effect of $\mathscr{L}_{\text{dist}}$.** The regularizer suppresses floaters and prevents background collapse more effectively than density-noise injection [429], which can also reduce reconstruction detail. *Credit:* [29].

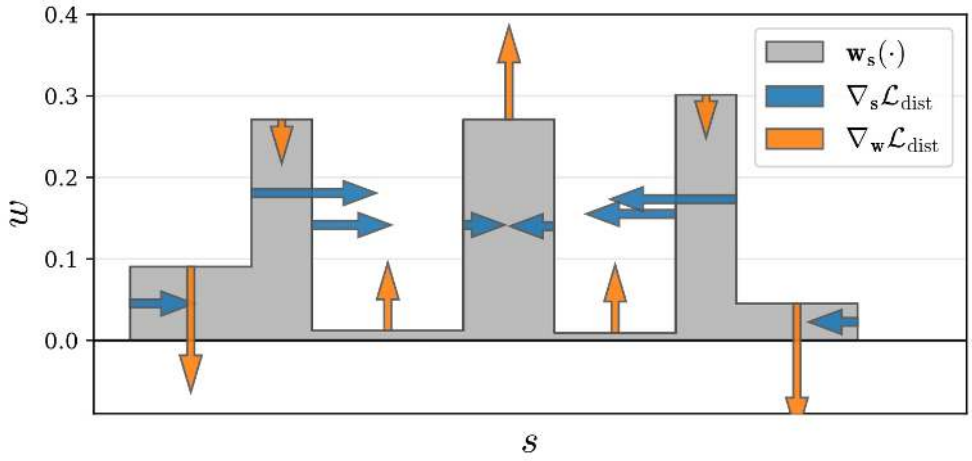

Figure 23.131: **Gradients of $\mathscr{L}_{\text{dist}}$.** Visualization of $\nabla\mathscr{L}_{\text{dist}}$ on a toy step function: it shrinks interval widths, pulls distant intervals together, consolidates mass into a small number of nearby intervals, and drives all weights to zero when the ray is empty. *Credit:* [29].

Optimization and training recipe

Network sizes and sampling. The proposal MLP uses 4 layers with 256 hidden units; the NeRF MLP uses 8 layers with 1024 units; ReLU internals and softplus density. Two proposal stages are evaluated (each with 64 samples) to produce $(\hat{s}^{(0)},\hat{w}^{(0)})$ and $(\hat{s}^{(1)},\hat{w}^{(1)})$, followed by one NeRF stage with 32 samples to produce (s,w) [29].

Loss. The overall objective is

$$\mathscr{L} = \mathscr{L}_{\text{recon}}(\mathbf{C}(t),\mathbf{C}^*) + \lambda\,\mathscr{L}_{\text{dist}}(s,w) + \sum_{k=0}^{1}\mathscr{L}_{\text{prop}}\big(s,w,\hat{s}^{(k)},\hat{w}^{(k)}\big), \qquad \lambda = 0.01 \tag{23.70}$$

with stop-grad on (s,w) inside $\mathscr{L}_{\text{prop}}$. $\mathscr{L}_{\text{recon}}$ uses the Charbonnier loss $\sqrt{(x-x^*)^2+\varepsilon^2}$ with $\varepsilon = 10^{-3}$.

Schedule and stabilization. Train for 250k iterations, batch size 2^{14} rays, Adam with $(\beta_1,\beta_2,\varepsilon) = (0.9, 0.999, 10^{-6})$, log-linear LR from 2×10^{-3} to 2×10^{-5} with 512-step warm-up, gradient clipping to norm 10^{-3}. Random RGB backgrounds during training encourage opaque backgrounds; at test time use $(0.5,0.5,0.5)$ [29].

Implementation notes. Apply the Jacobian efficiently via autodiff *linearize*/JVP primitives without explicitly forming J_f. When a full covariance is computed, off-axis IPE (Appendix; fixed non-axis-aligned basis P from a twice-tessellated icosahedron) leverages anisotropy information that axis-aligned IPE discards.

Results and Ablations

Quantitative evaluation

MipNeRF360 is evaluated on the new 360° unbounded dataset introduced in the paper, as well as on prior benchmarks. On the synthetic *Tanks and Temples* and *LLFF* datasets, it achieves state-of-the-art results, substantially improving PSNR, SSIM, and LPIPS compared to NeRF and Mip-NeRF. The distortion loss is particularly important in suppressing floaters and stabilizing reconstructions in unbounded scenes [29].

Qualitative comparison

Figures in the paper show that MipNeRF360 produces sharper details, cleaner geometry, and more consistent background rendering compared to both NeRF and Mip-NeRF. Floaters that plague earlier methods are effectively eliminated, and distant backgrounds are reconstructed without collapse.

Ablations

The authors conduct extensive ablation studies:

- **Proposal guidance.** Removing the proposal MLP stages and sampling only from the final network leads to degraded quality and visible floaters, confirming the necessity of the histogram-consistency training.
- **Distortion loss.** Disabling $\mathscr{L}_{\text{dist}}$ produces fragmented weight distributions along rays, resulting in floaters and background collapse. Compared to density-noise injection, $\mathscr{L}_{\text{dist}}$ yields superior suppression of artifacts without sacrificing fine detail.
- **IPE vs. standard PE.** Replacing integrated positional encoding with ordinary positional encoding reduces performance in unbounded scenes, especially where anti-aliasing is critical. Off-axis IPE further improves handling of anisotropic footprints.
- **Single vs. multi-proposal.** Using two proposal stages instead of one refines the sampling distribution more reliably, especially in challenging rays with both near and far content.

Generalization across datasets

Ablations also demonstrate that the combination of contraction, histogram consistency, and distortion regularization is robust across different scene scales.

Limitations

Despite its advances, MipNeRF360 has limitations:

- **Training cost.** The multi-stage proposal guidance and large NeRF MLP make training computationally demanding compared to lightweight or grid-based alternatives.
- **Rendering speed.** At test time, inference is slower than real-time systems such as PlenOctrees or Instant-NGP, since MipNeRF360 still relies on MLP queries along rays.
- **Over-regularization.** In some cases, the distortion loss can oversimplify weight distributions, slightly reducing fine detail in favor of compactness.
- **Scene priors.** While contraction handles unbounded domains, scenes with extreme depth ranges or severe occlusion patterns may still exhibit artifacts or require many proposal samples to converge.

Outlook

These limitations motivate subsequent work on accelerating unbounded NeRF training and inference (e.g., via hash encodings or tensor decompositions) and on refining regularizers to balance artifact suppression with fine detail preservation.

Enrichment 23.12.3: D-NeRF: Neural Radiance Fields for Dynamic Scenes

Motivation

Rendering novel views of a scene from a sparse set of images is a fundamental challenge in computer vision and graphics, with applications in augmented reality, virtual reality, and film production. Neural Radiance Fields (NeRF) [429] demonstrated that a static 3D scene can be encoded as a continuous volumetric radiance field, enabling photo-realistic novel view synthesis. However, the core assumption of NeRF is *staticity*: every spatial location corresponds to a fixed geometry and appearance across all observations. This assumption breaks down in the presence of dynamic, non-rigid motion, such as humans moving, articulated objects deforming, or shadows shifting with time. Directly extending NeRF by adding a time parameter fails, as temporal redundancy and correspondences across frames are not effectively exploited.

D-NeRF, introduced by Pumarola et al. [488], addresses this limitation by explicitly modeling temporal dynamics. The key idea is to represent dynamic scenes via a **canonical configuration** and learn a **deformation field** that maps any observed state of the scene back to this canonical space. This canonical anchor allows the model to share information across different time instants and learn consistent geometry and appearance, despite each temporal state being seen from only a single viewpoint.

Figure 23.132: **Dynamic scene synthesis with D-NeRF.** The authors propose a method to render novel views at arbitrary time instants for dynamic scenes with complex non-rigid geometry. Results include a dinosaur skeleton moving over time (top) and a construction worker changing poses (bottom). Each frame is synthesized from sparse monocular input without requiring ground-truth geometry or multi-view capture [488].

Problem Setup

The problem considered by D-NeRF is illustrated in the below figure. Given a sparse set of images of a non-rigid dynamic scene captured by a moving monocular camera, the objective is to implicitly encode the scene such that novel views at arbitrary times can be synthesized. Formally, the model must learn a mapping

$$M : (\mathbf{x}, \mathbf{d}, t) \mapsto (\mathbf{c}, \sigma),$$

where $\mathbf{x} \in \mathbb{R}^3$ is a 3D point, $\mathbf{d}$ is the viewing direction, t is a time parameter, $\mathbf{c} \in \mathbb{R}^3$ is the emitted color, and $\sigma \in \mathbb{R}_{\geq 0}$ is the volume density.

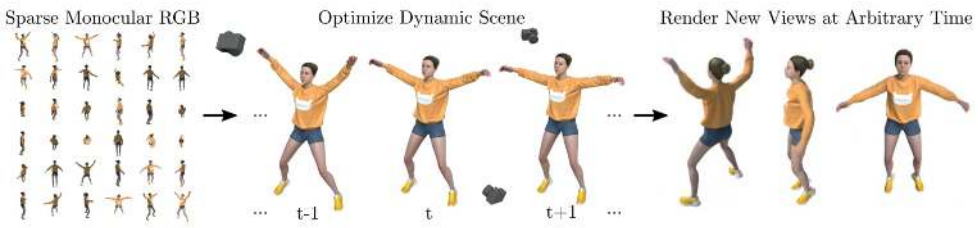

Figure 23.133: **Problem setup of D-NeRF.** From a sparse set of monocular frames of a non-rigid dynamic scene, paired with camera parameters, D-NeRF learns an implicit scene representation. The model synthesizes novel views at arbitrary time instants, as shown on the right [488].

Challenges of direct spatio-temporal regression.
A straightforward idea might be to extend NeRF by regressing color and density directly from both space and time,

$$M : (\mathbf{x}, \mathbf{d}, t) \mapsto (\mathbf{c}, \sigma).$$

Yet this formulation quickly breaks down: a surface point that moves or deforms across frames is assigned different coordinates at each time t, and the model has no way of knowing that these correspond to the same physical entity. As a result, temporal redundancy is ignored, leading to blurred reconstructions and unstable geometry.

To address this, D-NeRF introduces an intermediate **canonical configuration** that serves as a shared reference for all time instants. Instead of relearning radiance for every frame, the model learns a *deformation field* that warps observed points back to the canonical space. Radiance and density are then predicted only once in this space, ensuring that appearance remains consistent over time.

This decomposition has clear benefits:

- **Temporal consistency.** Consider the tip of a moving finger: without alignment, the network must memorize its material properties at every position along its trajectory. With the canonical anchor, the finger tip maps to a single coordinate, preserving sharp detail.
- **Separation of dynamics from statics.** Static background points (e.g., walls) map trivially to themselves, while dynamic objects (e.g., a bouncing ball) are displaced by the learned deformation. The canonical network can thus specialize in view-dependent appearance, while motion complexity is isolated in the deformation field.

This design reflects how humans perceive motion: despite deformations, objects are recognized as consistent entities by mentally aligning them to an internal reference. Analogously, D-NeRF aligns all observations to its canonical configuration, laying the foundation for the method described next.

Method

The D-NeRF method generalizes NeRF to handle dynamic, non-rigid scenes by decomposing the mapping

$$M : (\mathbf{x}, \mathbf{d}, t) \mapsto (\mathbf{c}, \sigma)$$

into two learnable modules:

- a **deformation network** Ψ_t, which aligns points observed at time t with a canonical space,
- a **canonical network** Ψ_x, which predicts density and radiance in the canonical configuration.

The resulting architecture, as can be seen in the following figure, learns how geometry changes over time via Ψ_t while maintaining appearance consistency through Ψ_x.

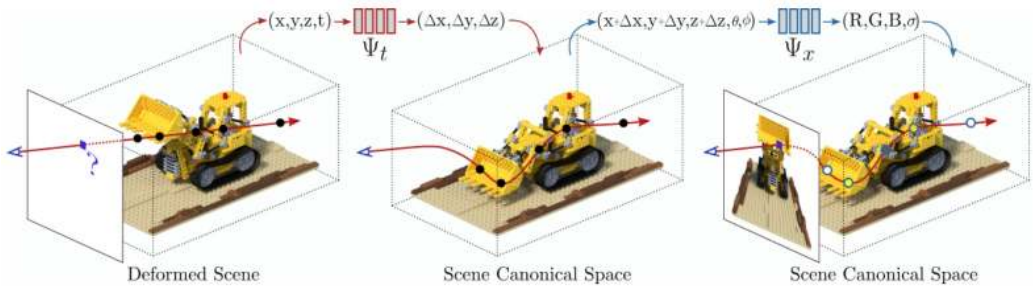

Figure 23.134: **Model architecture of D-NeRF.** The deformation network Ψ_t maps points observed at time t to a canonical space. The canonical network Ψ_x assigns volume density and view-dependent radiance in this canonical configuration [488].

Canonical network

The canonical network Ψ_x learns to represent the scene at a fixed reference state, chosen as $t = 0$. It predicts color $\mathbf{c}$ and density σ for each canonical point and viewing direction:

$$\Psi_x : (\mathbf{x} + \Delta\mathbf{x}, \mathbf{d}) \mapsto (\mathbf{c}, \sigma).$$

This canonical anchor integrates information from all time instants, so that missing or occluded details in one frame can be inferred from others. Intuitively, Ψ_x functions as a static NeRF defined in canonical space, ensuring that geometry and appearance remain temporally consistent.

Deformation network

The deformation network Ψ_t estimates a displacement field that maps points observed at time t into the canonical configuration:

$$\Psi_t : (\mathbf{x}, t) \mapsto \Delta\mathbf{x},$$

so that the canonical coordinate is given by $\mathbf{x} + \Delta\mathbf{x}$. Formally, the network is constrained as

$$\Psi_t(\mathbf{x}, 0) = 0,$$

ensuring that the canonical state coincides with the scene at $t = 0$. Dynamic regions (such as moving limbs or bouncing balls) receive non-zero displacements, while static background points map (hopefully) to themselves. This separation of deformation from radiance allows the canonical network to remain agnostic to motion.

Volume rendering with deformations

To render an image, D-NeRF adapts the NeRF volume rendering equation to account for canonical warping. Given a ray defined by origin $\mathbf{o}$ and direction $\mathbf{d}$, a 3D point along the ray is $\mathbf{x}(h) = \mathbf{o} + h\mathbf{d}$. The color of a pixel p at time t is computed as

$$C(p,t) = \int_{h_n}^{h_f} T(h,t)\, \sigma(\mathbf{p}(h,t))\, \mathbf{c}(\mathbf{p}(h,t), \mathbf{d})\, \mathrm{d}h, \tag{23.71}$$

where

$$\mathbf{p}(h,t) = \mathbf{x}(h) + \Psi_t(\mathbf{x}(h),t), \tag{23.72}$$

$$[\mathbf{c}(\mathbf{p}(h,t),\mathbf{d}),\, \sigma(\mathbf{p}(h,t))] = \Psi_x(\mathbf{p}(h,t),\mathbf{d}), \tag{23.73}$$

$$T(h,t) = \exp\left(- \int_{h_n}^{h} \sigma(\mathbf{p}(s,t))\, \mathrm{d}s \right). \tag{23.74}$$

Here $\mathbf{p}(h,t)$ is the warped canonical point corresponding to $\mathbf{x}(h)$, and $T(h,t)$ is the accumulated transmittance probability along the ray. Equations 23.71–23.74 mirror NeRF's rendering formulation, but crucially, density and radiance are queried in canonical space.

For practical training, the integrals are approximated using stratified quadrature with N samples along each ray. The discrete approximation is

$$C'(p,t) = \sum_{n=1}^{N} T'(h_n,t)\, \alpha(h_n,t,\delta_n)\, \mathbf{c}(\mathbf{p}(h_n,t),\mathbf{d}), \tag{23.75}$$

with

$$\alpha(h,t,\delta) = 1 - \exp(-\sigma(\mathbf{p}(h,t))\, \delta)\,, \tag{23.76}$$

$$T'(h_n,t) = \exp\left(- \sum_{m=1}^{n-1} \sigma(\mathbf{p}(h_m,t))\, \delta_m \right), \tag{23.77}$$

where $\delta_n = h_{n+1} - h_n$ is the distance between samples.

Learning objective

The networks Ψ_x and Ψ_t are trained jointly by minimizing the mean squared error between rendered pixels and ground-truth images:

$$\mathscr{L} = \frac{1}{N_s} \sum_{i=1}^{N_s} \left\| \hat{\mathbf{C}}(p_i,t) - C'(p_i,t) \right\|_2^2, \tag{23.78}$$

where N_s rays are sampled per batch, $\hat{\mathbf{C}}$ denotes the ground-truth pixel colors, and C' is the predicted color from Eq. 23.75. This supervision requires only monocular images with known camera poses, without multi-view consistency or 3D ground truth.

Architecture and Implementation Details

Network design

Both the canonical network Ψ_x and the deformation network Ψ_t are implemented as multilayer perceptrons (MLPs) with eight fully connected layers of 256 units each and ReLU activations. The canonical network outputs color $\mathbf{c}$ and density σ with a final sigmoid activation to constrain values to valid ranges, while the deformation network outputs displacement vectors $\Delta\mathbf{x}$ with no final non-linearity. This separation ensures that the canonical branch specializes in appearance and geometry, while the deformation branch is free to model continuous spatial displacements.

Positional encoding

As in NeRF [429], D-NeRF does not feed raw coordinates and viewing directions directly into the networks. Instead, each scalar input p is mapped to a higher-dimensional Fourier feature space:

$$\gamma(p) = \left(\sin(2^0\pi p), \cos(2^0\pi p), \ldots, \sin(2^L\pi p), \cos(2^L\pi p)\right).$$

This positional encoding enables the MLPs to represent highly oscillatory functions, which is crucial for capturing fine geometric detail and sharp appearance boundaries.

D-NeRF applies the encoding separately to spatial coordinates $\mathbf{x}$, viewing directions $\mathbf{d}$, and time t, but with different frequency depths L. Spatial coordinates require high-frequency capacity to model detailed surfaces and textures, so $L = 10$ is used. By contrast, time and viewing direction are more smoothly varying quantities—motions are continuous and shading changes gradually—so a smaller frequency budget ($L = 4$) suffices. This allocation balances expressivity and stability, ensuring the model can capture fine spatial details without overfitting to noise in temporal or directional variation.

Canonical reference frame

The canonical configuration serves as a temporal anchor for the entire dynamic scene. Without loss of generality, D-NeRF defines the frame at $t = 0$ as canonical, imposing the constraint

$$\Psi_t(\mathbf{x}, 0) = 0.$$

This choice is practical: one reference frame must be selected, and picking the first observed frame avoids ambiguity while ensuring that the deformation network only learns displacements for $t \neq 0$. Anchoring to $t = 0$ guarantees that all temporal states are consistently mapped to a single geometry, so that the canonical network Ψ_x always operates in a stable coordinate system.

Curriculum strategy

Training D-NeRF directly on the full temporal range is challenging, since large deformations between distant time instants make optimization unstable. To mitigate this, the authors introduce a curriculum learning strategy: input frames are ordered chronologically and introduced gradually, starting from those close to the canonical frame and progressively extending to more distant time instants. This approach allows the networks to first master small deformations, then progressively handle larger ones. The effect is similar to learning a language by starting with simple phrases before moving to complex sentences—by staging the difficulty, convergence is improved and the learned deformation fields remain smoother and more coherent.

Optimization details

Training is conducted on 400×400 images for 800k iterations. Each batch samples $N_s = 4096$ rays, with 64 samples per ray. The Adam optimizer [293] is used with initial learning rate 5×10^{-4}, exponential decay to 5×10^{-5}, and momentum parameters $\beta_1 = 0.9$, $\beta_2 = 0.999$. On a single Nvidia GTX 1080 GPU, training takes approximately two days.

Experiments and Ablations

D-NeRF is evaluated on a dataset of eight synthetic dynamic scenes rendered with complex motions and non-Lambertian materials. Each sequence contains between 100 and 200 frames at 800×800 resolution, with ground-truth train/validation/test splits. The experiments aim to dissect the contributions of the canonical and deformation networks, and to compare D-NeRF against two alternatives:

- **NeRF** [429], which assumes static scenes and therefore cannot handle motion.
- **T-NeRF**, a temporal baseline that directly regresses

$$(\mathbf{x}, \mathbf{d}, t) \mapsto (\mathbf{c}, \sigma),$$

  without using a canonical space or deformation field. T-NeRF highlights the shortcomings of naive temporal modeling: while it can capture coarse changes over time, it treats the same physical point at different instants as unrelated, leading to blurred details and inconsistent geometry. Importantly, T-NeRF is not D-NeRF without curriculum learning, but rather the simplest 6D extension of NeRF used as a baseline.

Learned canonical scene and displacement fields

D-NeRF successfully learns a displacement field $\Delta\mathbf{x}$ that aligns all observations to a sharp canonical space. The following figure illustrates this mapping: dynamic inputs at different time instants are warped into the canonical configuration, where geometry and appearance remain stable. The figure shows radiance rendering, density mesh, depth map, and color-coded correspondences. Matching colors across canonical and deformed meshes demonstrate that temporal correspondences are preserved, even though each deformation state is only seen from a single viewpoint.

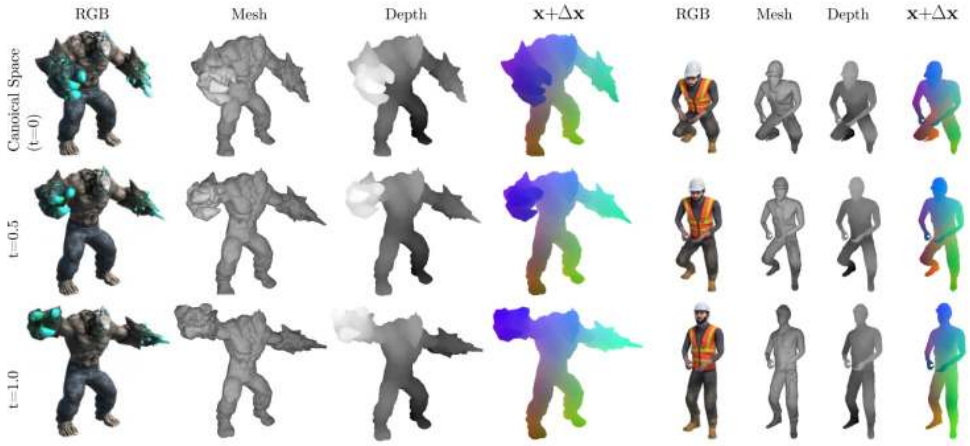

Figure 23.135: **Visualization of the learned canonical scene.** A dynamic scene at time t is mapped into a canonical configuration via the learned displacement field $\Delta\mathbf{x}$. From left to right: rendered radiance, density mesh, depth map, and color-coded correspondences between canonical and deformed meshes. Consistent colors indicate correct alignment across time [488].

Shading and appearance consistency

A key challenge is handling shading effects and appearance changes over time. The following figure shows a scene with three balls made of plastic (green), translucent glass (blue), and metal (red). Although shadows and highlights move across the floor as objects deform, D-NeRF encodes these changes by warping the canonical configuration. For instance, shadows cast by the red ball at $t = 0.5$ and $t = 1$ are aligned to different canonical regions, yet the network synthesizes them consistently. This demonstrates that D-NeRF can separate geometry from shading variation, producing coherent results without explicitly modeling illumination.

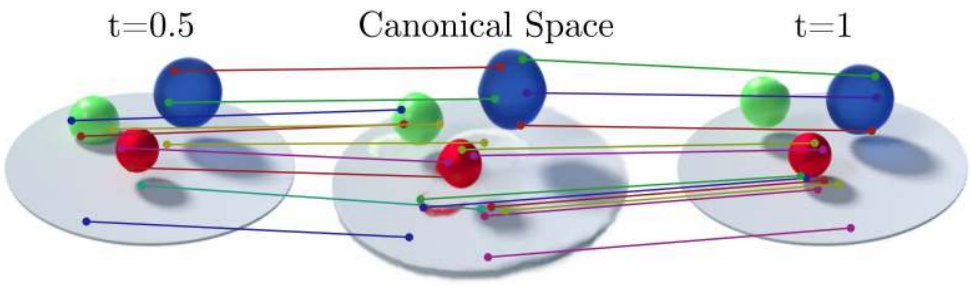

Figure 23.136: **Analyzing shading effects.** Correspondences between canonical space and observed scenes at $t = 0.5$ and $t = 1$ for three balls of different materials. Shading changes, such as floor shadows, are synthesized by warping the canonical configuration, preserving temporal coherence [488].

Quantitative and qualitative comparisons

D-NeRF is compared against two baselines:

- **NeRF** [429], which assumes static scenes.
- **T-NeRF**, a 6D extension that directly regresses $(\mathbf{x}, \mathbf{d}, t) \mapsto (\mathbf{c}, \sigma)$ without canonical warping.

As shown in the following table, D-NeRF consistently outperforms both baselines across metrics including MSE, PSNR, SSIM, and LPIPS. Qualitatively, NeRF collapses to blurry averages of motion, while T-NeRF captures coarse dynamics but fails on high-frequency details such as textures and fine structures. D-NeRF preserves sharpness and reproduces fine detail, despite each time instant being observed from only a single camera.

	Hell Warrior				**Mutant**				**Hook**				**Bouncing Balls**			
Method	MSE↓	PSNR↑	SSIM↑	LPIPS↓	MSE↓	PSNR↑	SSIM↑	LPIPS↓	MSE↓	PSNR↑	SSIM↑	LPIPS↓	MSE↓	PSNR↑	SSIM↑	LPIPS↓
NeRF [429]	44e-3	13.52	0.81	0.25	9e-4	20.31	0.91	0.09	21e-3	16.65	0.84	0.19	1e-2	18.28	0.88	0.23
T-NeRF (temporal baseline)	47e-4	23.19	0.93	0.08	8e-4	30.56	0.96	0.04	18e-4	27.21	0.94	**0.06**	6e-4	32.01	0.97	0.04
D-NeRF [488]	**31e-4**	**25.02**	**0.95**	**0.06**	**7e-4**	**31.29**	**0.97**	**0.02**	**11e-4**	**29.25**	**0.96**	0.11	**5e-4**	**32.80**	**0.98**	**0.03**
	Lego				**T-Rex**				**Stand Up**				**Jumping Jacks**			
Method	MSE↓	PSNR↑	SSIM↑	LPIPS↓	MSE↓	PSNR↑	SSIM↑	LPIPS↓	MSE↓	PSNR↑	SSIM↑	LPIPS↓	MSE↓	PSNR↑	SSIM↑	LPIPS↓
NeRF [429]	9e-4	20.30	0.79	0.23	3e-3	24.49	0.93	0.13	1e-2	18.19	0.89	0.14	1e-2	18.28	0.88	0.23
T-NeRF (temporal baseline)	**3e-4**	**23.82**	**0.90**	**0.15**	9e-4	30.19	0.96	0.13	7e-4	31.24	0.97	**0.02**	6e-4	32.01	0.97	0.03
D-NeRF [488]	6e-4	21.64	0.83	0.16	**6e-4**	**31.75**	**0.97**	**0.03**	**5e-4**	**32.79**	**0.98**	**0.02**	**5e-4**	**32.80**	**0.98**	**0.03**

Table 23.35: **Quantitative comparison** MSE/LPIPS (lower is better) and PSNR/SSIM (higher is better) across eight dynamic scenes.

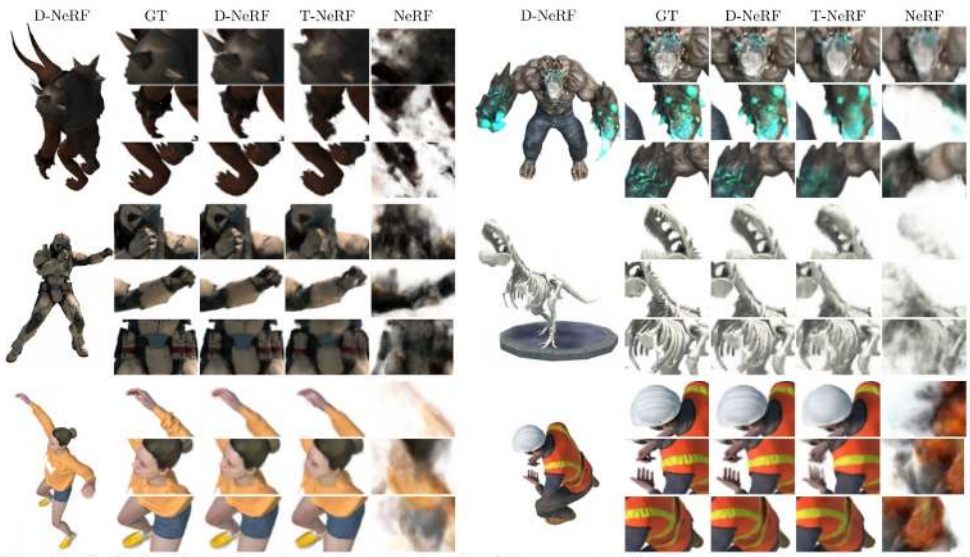

Figure 6: **Qualitative Comparison.** Novel view synthesis results of dynamic scenes. For every scene we show an image synthesised from a novel view at an arbitrary time by our method, and three close-ups for: ground-truth, NeRF, T-NeRF, and D-NeRF (ours).

Figure 23.137: **Qualitative comparisons.** Novel view synthesis at arbitrary time instants for dynamic scenes. Close-ups show ground truth, NeRF, T-NeRF, and D-NeRF. NeRF fails to represent motion, T-NeRF captures dynamics but loses high-frequency detail, while D-NeRF produces sharp reconstructions [488].

Time and view conditioning

Finally, D-NeRF demonstrates robust novel-view synthesis across both space and time. The following figure shows renderings of diverse dynamic scenes from novel viewpoints at multiple time instants. The first column displays the canonical configuration, while subsequent columns show warped renderings across time. The model generalizes to articulated human motion, asynchronous object motion, and complex deformations. Interestingly, even when the canonical space appears slightly blurry (as in the Jumping Jacks scene), the warped renderings remain sharp, indicating that the deformation field compensates to maximize rendering quality.

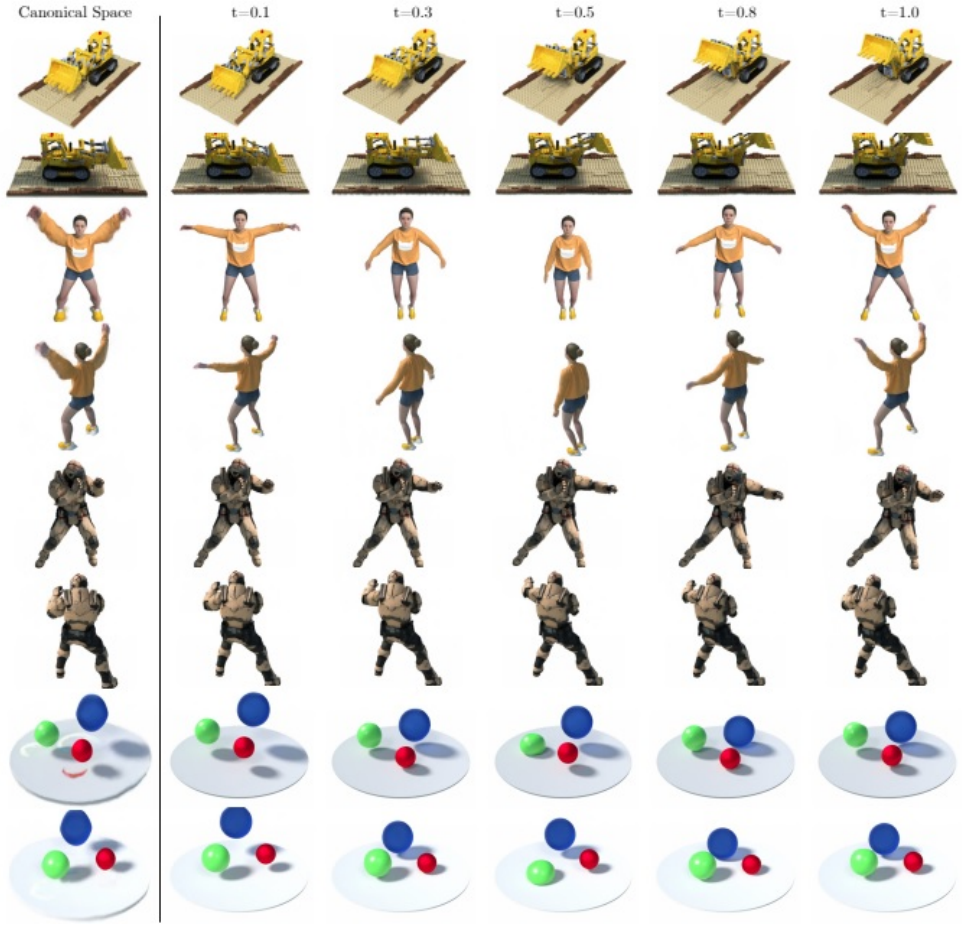

Figure 23.138: **Time and view conditioning.** Novel renderings from two unseen viewpoints across time. Scenes include articulated motion (Tractor), human motion (Jumping Jacks, Warrior), and asynchronous dynamics (Bouncing Balls). Canonical spaces (first column) serve as anchors for consistent geometry [488].

Limitations

Although D-NeRF represents an important step beyond static NeRF by explicitly modeling dynamics through a canonical scene representation and a time-conditioned deformation network, it still exhibits several notable limitations:

- **Training cost.** Like NeRF, D-NeRF relies on volumetric rendering that requires querying MLPs hundreds of times per ray. The addition of a deformation network compounds this cost, making training slow and memory-intensive (on the order of days on a single GPU).
- **Synthetic focus.** D-NeRF's evaluation is confined to clean, synthetic sequences with known camera parameters and dense coverage. Its performance on real-world captures—with noise, sparse viewpoints, and imperfect calibration—remains unexplored.
- **Deformation capacity.** The deformation field is assumed to be smooth and bijective, mapping each observation into the canonical space. While effective for simple motions, this assumption struggles with complex dynamics such as large occlusions, self-contact, or true topological changes (e.g., an object splitting or a mouth opening/closing).
- **Canonical anchoring.** D-NeRF typically fixes the canonical frame at $t = 0$, which is arbitrary. If the first frame is occluded or atypical, this choice can bias correspondences across time and destabilize optimization.

Future directions

These limitations motivated a wave of follow-up research that sought to make dynamic NeRFs more practical and robust:

- **From synthetic to real-world capture.** Extending canonical–deformation frameworks to unconstrained mobile videos requires handling photometric inconsistency, calibration errors, and drifting backgrounds.
- **From weak to stronger priors.** Beyond smoothness assumptions, deformation fields benefit from geometric regularizers that bias them toward locally rigid or cycle-consistent warps, preventing collapse into degenerate solutions.
- **From arbitrary to flexible canonicalization.** Conditioning deformations purely on time anchors the canonical space too rigidly; more adaptive conditioning strategies are needed to capture variations across diverse observations.
- **From expensive to efficient training.** Reducing the heavy computational footprint of dynamic NeRFs—without sacrificing fidelity—remains a central challenge, inspiring later work on acceleration and hybrid representations.

In summary, D-NeRF established the usefulness of canonicalization for dynamic scene reconstruction but remained limited by its computational demands, reliance on synthetic settings, and difficulty with complex deformations. The next method we examine, *Nerfies*, was developed precisely to address these shortcomings, adapting the canonical–deformation formulation to casually captured real-world videos.

Enrichment 23.12.4: Nerfies: Deformable Neural Radiance Fields

Motivation

Dynamic NeRFs such as D-NeRF [488] demonstrated that a canonical radiance field plus a deformation mechanism can reconstruct non-rigid scenes; however, D-NeRF was validated primarily on synthetic data with known calibration and dense coverage. *Nerfies* [469] adapts this canonical–deformation paradigm to *casual, real-world* captures (handheld mobile selfies), introducing design choices to handle photometric inconsistency, large yet locally rigid motion, and under-constrained optimization. The goal of the work is photorealistic, free-viewpoint renderings of people and everyday scenes captured outside controlled rigs.

Figure 23.139: **Results from Nerfies.** Photo-realistic reconstructions from handheld mobile captures: casual waving sequences (a) and selfie photos/videos (b) are turned into free-viewpoint renderings (c) with accurate geometry (d). Source: [469].

Method

Nerfies retains a canonical radiance field but replaces time-conditioned displacements with *per-image latent*–conditioned $\mathrm{SE}(3)$ deformation fields, stabilized by elastic regularization and a coarse-to-fine (c2f) schedule on positional encodings. Compared to D-NeRF's $(\mathbf{x},t) \mapsto \Delta\mathbf{x}$, this design introduces the following key shifts:

- **Decoupling from absolute time:** Conditioning deformations on a per-image latent code ω_i instead of the scalar time index t removes an arbitrary temporal anchor (e.g., $t{=}0$) and improves flexibility for casually captured sequences with irregular motion
- **Locally rigid motion modeling:** Using dense $\mathrm{SE}(3)$ transforms allows compact, coherent representation of rotations and translations across space, addressing ambiguity that displacement fields face when mimicking rotation via spatially varying translations
- **Bias toward plausible deformations:** Elastic regularization on the deformation Jacobian and a c2f frequency-annealing schedule guide optimization away from degenerate warps in under-constrained settings

Motivation relative to D-NeRF

While D-NeRF established the value of canonicalization for dynamic scenes, its reliance on synthetic data and time-conditioned displacements limited applicability to real-world captures. Nerfies adapts the same blueprint to unconstrained videos, focusing on robustness to casual data collection, realistic motion modeling, and training stability. In doing so, it addresses D-NeRF's key weaknesses—pose anchoring, rotational ambiguity, and fragile optimization—while preserving the benefits of a canonical template

Canonical radiance field
A canonical NeRF

$$F : (\mathbf{x}', \mathbf{d}, \psi_i) \mapsto (\mathbf{c}, \sigma)$$

maps canonical 3D position $\mathbf{x}'$, view direction $\mathbf{d}$, and an *appearance* latent ψ_i to color and density. The use of per-image appearance latents follows the idea introduced in NeRF-W (see Enrichment 23.11.2), where such codes compensate for photometric variations across casually captured images (e.g., exposure, white balance, or tone mapping). This differs from D-NeRF, where the canonical template is tied to the frame at t=0, effectively anchoring the scene to an arbitrary temporal reference. In Nerfies, the canonical radiance field instead represents a learned, temporally invariant template of the subject, disentangled from both time and observation-specific appearance. The canonical configuration is not selected from a single frame but is optimized jointly during training so that all deformed observations can be consistently mapped into it.

Observation-to-canonical deformation
Each input image i is associated with two learned latents: an *appearance* code ψ_i (as in NeRF-W; see Enrichment 23.11.2) that absorbs photometric variations, and a *deformation* code ω_i that indexes a per-image deformation field. For a sample $\mathbf{x}$ on a camera ray in the observation frame,

$$T : (\mathbf{x}, \omega_i) \mapsto \mathbf{x}', \qquad G(\mathbf{x}, \mathbf{d}, \psi_i, \omega_i) = F\big(T(\mathbf{x}, \omega_i), \mathbf{d}, \psi_i\big).$$

Rendering proceeds by sampling along the ray in the observation frame, mapping samples to the canonical frame via T, querying the canonical field F, and volumetrically integrating as in NeRF.

Relation to D-NeRF. D-NeRF ties deformation to an explicit time index t, which implicitly anchors the canonical to a particular frame and encourages frame-tracking warps. Nerfies instead replaces t with per-image deformation indices ω_i and learns the canonical jointly with F and T. This shift has several practical consequences:

- **Removal of arbitrary anchoring:** Deformations are no longer tied to t=0, avoiding bias toward whichever frame was chosen as the reference.
- **Observation-based indexing:** States are referenced by observation identity rather than clock time, allowing out-of-order or irregular captures to be modeled consistently.
- **Interpolatable state space:** The latent deformation codes live in a continuous space, so smooth synthesis of intermediate states is possible by interpolating between codes.

Inference for new views (same scene). During training, each input image is assigned two codes: a deformation code ω_i (capturing the *pose or state of the scene* in that frame) and an appearance code ψ_i (capturing its photometric style, e.g., exposure). Once training is complete, we can render the scene from *any new camera* without retraining:

- **Novel view of a training frame.** Suppose we want to see frame i (same body pose, same facial expression, etc.) but from a new camera angle. We simply reuse its learned codes (ω_i, ψ_i). Rays are cast from the new camera, warped into canonical space by $T(\mathbf{x}, \omega_i)$, and rendered through the canonical NeRF F. No new optimization is required.
- **Novel view of an in-between frame.** If we want to synthesize a pose that was not captured exactly, we can interpolate between nearby deformation codes. For instance,

  $$\omega(\alpha) = (1-\alpha)\,\omega_i + \alpha\,\omega_j, \quad \alpha \in [0,1],$$

  smoothly blends the deformations of frames i and j. This produces a plausible intermediate motion that can then be rendered from any viewpoint.

- **Appearance.** The appearance code ψ_i can be reused from a particular frame (to match its look), or set to a certain training image value or an interpolation between such codes, as shown with the deformation code.

In short, Nerfies inference works by treating each frame's latent codes as a handle on the scene's configuration. By reusing or interpolating these codes, the model can render captured or novel states from arbitrary viewpoints, and with arbitrary appearance settings, something that time-anchored methods like D-NeRF cannot easily achieve.

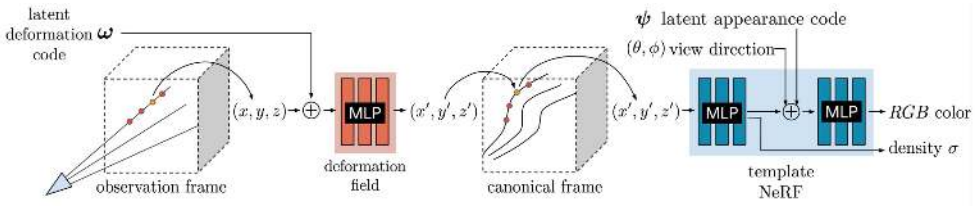

Figure 23.140: **Architecture overview.** Each image has a deformation code ω and an appearance code ψ. Samples are traced in the observation frame, mapped to the canonical frame by a deformation field (an MLP conditioned on ω), then the canonical NeRF is queried and integrated. Source: [469].

Why dense SE(3) *fields*

A naive displacement field writes $\mathbf{x}' = \mathbf{x} + V(\mathbf{x}, \omega_i)$. While universal in principle, it is cumbersome for coherent rotations: a single rigid rotation must be approximated by spatially varying translations whose magnitudes grow with distance from the axis. This entangles motion type and spatial location, making the mapping hard to learn consistently and prone to shear-like artifacts.

Nerfies instead predicts a *dense* SE(3) transform at each location, using a screw-axis parameterization $S = (\mathbf{r}; \mathbf{v}) \in \mathbb{R}^6$ (the Lie algebra $\mathfrak{se}(3)$). Intuitively, $\mathbf{r}$ encodes the local *rotation axis and angle*, and $\mathbf{v}$ encodes the accompanying *translation* consistent with that rotation (a "twist"). Let $\theta = \|\mathbf{r}\|$ be the rotation angle, and let $[\mathbf{r}]_\times$ denote the 3×3 skew-symmetric matrix for cross products. The exponential map yields the rigid transform

$$e^{\mathbf{r}} = I + \frac{\sin\theta}{\theta}[\mathbf{r}]_\times + \frac{1-\cos\theta}{\theta^2}[\mathbf{r}]_\times^2, \qquad G = I + \frac{1-\cos\theta}{\theta^2}[\mathbf{r}]_\times + \frac{\theta-\sin\theta}{\theta^3}[\mathbf{r}]_\times^2,$$

$$\mathbf{x}' = e^S\mathbf{x} = e^{\mathbf{r}}\mathbf{x} + G\mathbf{v}.$$

Intuition. The term $e^{\mathbf{r}}$ rotates $\mathbf{x}$ by angle θ around axis $\mathbf{r}/\theta$. The matrix G converts the "velocity" $\mathbf{v}$ in the Lie algebra into a translation that is *compatible* with the rotation (so that rotation and translation form a single rigid motion). When $\theta \to 0$, the series reduce to $e^{\mathbf{r}} \approx I + [\mathbf{r}]_\times$ and $G \approx I + \frac{1}{2}[\mathbf{r}]_\times$, smoothly recovering pure translations and infinitesimal rotations. This parameterization lets the MLP express rotations *coherently* (one angle shared over a region) rather than reconstructing them as inconsistent, location-dependent shifts.

The deformation network $W : (\mathbf{x}, \omega_i) \mapsto (\mathbf{r}, \mathbf{v})$ is initialized near identity (small outputs for $\mathbf{r}, \mathbf{v}$), so that $e^S \approx I$ at the start of training. This stabilizes optimization: the model learns residual motion away from no-warp, while additional priors (elastic/background regularization and the coarse-to-fine schedule) bias solutions toward plausible, near-rigid deformations where supervision is weak.

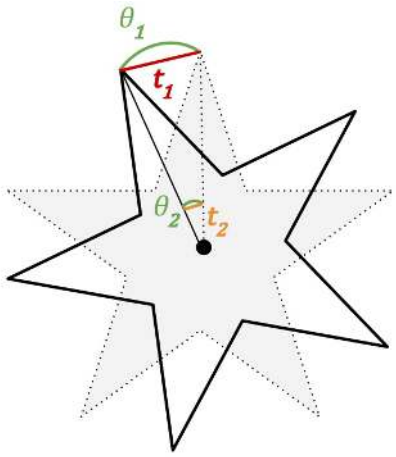

Figure 23.141: **SE(3) vs. translation fields.** To represent a simple rigid rotation of the star, a translation field must assign *different* displacement vectors depending on location: a faraway point requires a long translation t_1, while a point closer to the center requires a shorter one t_2. This spatially varying pattern complicates learning, since the network must coordinate many different magnitudes and directions just to encode one global rotation. In contrast, an $\mathrm{SE}(3)$ field expresses the same motion with a single rotation angle θ applied consistently across space. The network only needs to learn one compact parameterization of the rigid transform, making optimization easier and the resulting deformations more coherent. Source: [469].

Observation vs. canonical frames

The central idea of Nerfies is to disentangle *appearance* from *motion* by mapping every observed image into a common reference. Each input frame is an *observation frame*—the subject in its actual pose, expression, or transient configuration at capture time. The network jointly learns a static *canonical frame*—a pose-agnostic 3D template—along with a deformation field that warps each observation back to this shared canonical space. The displacement vectors encode how geometry must be shifted (e.g., sideways or front–back) so that all observations reconcile into a single, consistent template.

Figure 23.142: **Observation vs. canonical frames.** The *observation frame* (left) shows the raw geometry as captured in a specific image, here with the head turned and displaced. The *canonical frame* (right) shows the learned static template in a standardized pose. Insets highlight displacements (sideways or front–back shifts) that the learned deformation field applies to map observed points into the canonical configuration. Source: [469].

Elastic regularization (why, what, how)

Why. Jointly fitting the canonical radiance field F and the deformation T from only photometric supervision is under–constrained: many different (F,T) pairs can reproduce the same pixels. In practice, the optimizer may "explain" motion by letting T *shrink*, *stretch*, or *shear* space (degenerate but photometrically cheap), rather than by learning the intended near–rigid motion. Plain smoothness penalties (as in D-NeRF) do not directly discourage such volume changes.

What. Nerfies therefore adds an *as-rigid-as-possible* prior: locally, a small neighborhood should behave like a rigid body (rotation + translation), i.e., preserve lengths/areas/volumes. This explicitly targets "shrink/grow" modes.

How. Let $J_T(\mathbf{x}) = \partial T(\mathbf{x},\omega_i)/\partial \mathbf{x}$ be the Jacobian of the deformation at a sample $\mathbf{x}$. With the SVD $J_T = U\Sigma V^\top$ and singular values $\{\sigma_k\}$, rigidity corresponds to $\Sigma = I$ (no local scaling). We penalize deviation from this condition using the log-scale error

$$\mathscr{L}_{\text{elastic}}(\mathbf{x}) \;=\; \big\|\log\Sigma\big\|_F^2,$$

where $\log\Sigma = \operatorname{diag}(\log\sigma_1, \log\sigma_2, \log\sigma_3)$. Using log makes expansion and contraction symmetric (e.g., σ=2 and σ=0.5 incur equal cost in magnitude). For robustness to truly non-rigid regions and occasional outliers, Nerfies applies a Geman–McClure penalty to the log-scale magnitude,

$$\mathscr{L}_{\text{elastic-r}}(\mathbf{x}) \;=\; \rho\big(\big\|\log\Sigma\big\|_F,\, c\big)\,,$$

and weights the term by ray transmittance so that empty space (which should be free to warp to account for foreground motion against a static background) is not over-regularized.

Intuition in one sentence. The loss tells the network: "prefer deformations that look locally rigid (rotate/translate) and only scale when necessary," which steers optimization away from photometrically convenient but geometrically implausible solutions that simple smoothness cannot prevent.

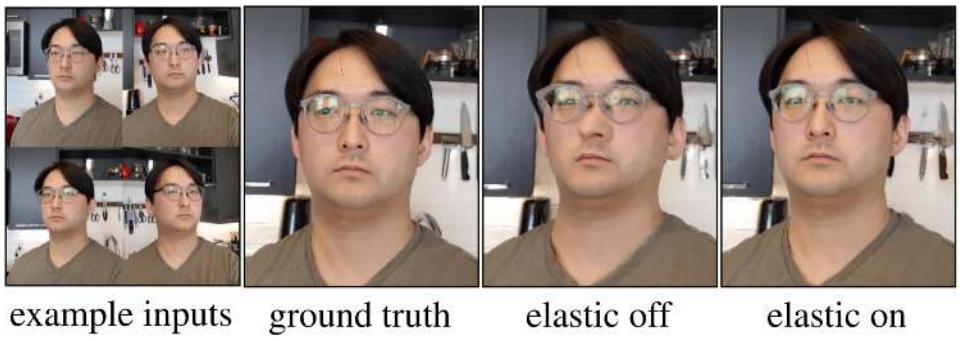

Figure 23.143: **Elastic regularization effect.** Under-constrained captures (few, biased views) are prone to distortion; the elastic prior substantially reduces such artifacts. Source: [469].

Background regularization

Static points (e.g., from SfM) are softly encouraged to remain fixed in canonical space to prevent background drift:

$$\mathscr{L}_{\text{bg}} \;=\; \frac{1}{K}\sum_{k=1}^{K}\big\|T(\mathbf{x}_k,\omega_i) - \mathbf{x}_k\big\|_2^2.$$

Coarse-to-fine optimization (why, what, how)

Why. If the deformation network can express high spatial frequencies from the start, it may overfit tiny appearance cues and settle in poor local minima before the large, global motion is discovered.

What. We therefore *curriculum* the capacity of the deformation MLP: begin with only low-frequency (smooth) warps, then gradually admit higher frequencies so the model first aligns the big motion and only later refines fine detail.

How. Let $\gamma(\mathbf{x})$ denote the positional encoding of coordinates used by the deformation network T. Its j-th frequency band is multiplied by a Hann window weight

$$w_j(\alpha) = \frac{1-\cos\big(\pi\,\mathrm{clamp}(\alpha-j,0,1)\big)}{2}, \qquad \alpha(t) = \frac{mt}{N},$$

where m is the maximum number of bands and $t \in [0,N]$ indexes training. Early on $\alpha \approx 0$, so $w_j(\alpha) \approx 0$ for all high j and only the lowest bands are active (smooth warps). As t increases, the window slides to the right, smoothly turning on higher bands until, at $\alpha = m$, all are fully active.

Effect. The network first solves the easy, low-frequency alignment (rigid/large motions), then safely adds high-frequency corrections (facial wrinkles, cloth folds, small non-rigid motion). This schedule consistently avoids bad minima while preserving the ability to model fine motion by the end of training.

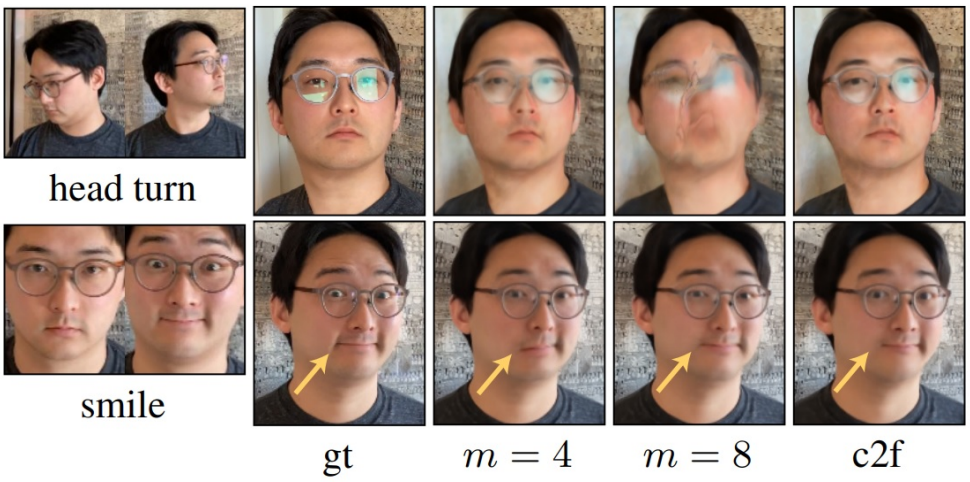

Figure 23.144: **Effect of coarse-to-fine optimization.** Comparison of three training strategies for dynamic scenes (*head turn*, *smile*). *gt:* Ground-truth reference frame. *m*=4*:* Training with only a few low-frequency positional-encoding bands produces overly smooth results—large motions are captured but fine details (e.g., cheek deformation in a smile) are blurred. *m*=8*:* Allowing all frequency bands from the start destabilizes training: the network overfits local details before learning the global motion, leading to severe artifacts (e.g., head turn collapse). *c2f:* The proposed coarse-to-fine schedule gradually introduces higher frequencies. This curriculum lets the model first align global motion and later refine fine-scale details, yielding sharp and accurate reconstructions closely matching the ground truth. Source: [469].

Latent-code interpolation

Per-image conditioning means each training frame i carries two learned embeddings: an *appearance* code ψ_i and a *deformation* code ω_i. Because ω_i indexes the scene *state* (pose/deformation) independently of camera, we can synthesize intermediate states by interpolating in the deformation-latent space while rendering from any camera:

$$\omega(\alpha) = (1-\alpha)\,\omega_{\text{start}} + \alpha\,\omega_{\text{end}}, \qquad \alpha \in [0,1].$$

Holding ψ fixed (or blending it similarly) produces smooth motion with consistent geometry and appearance in novel views.

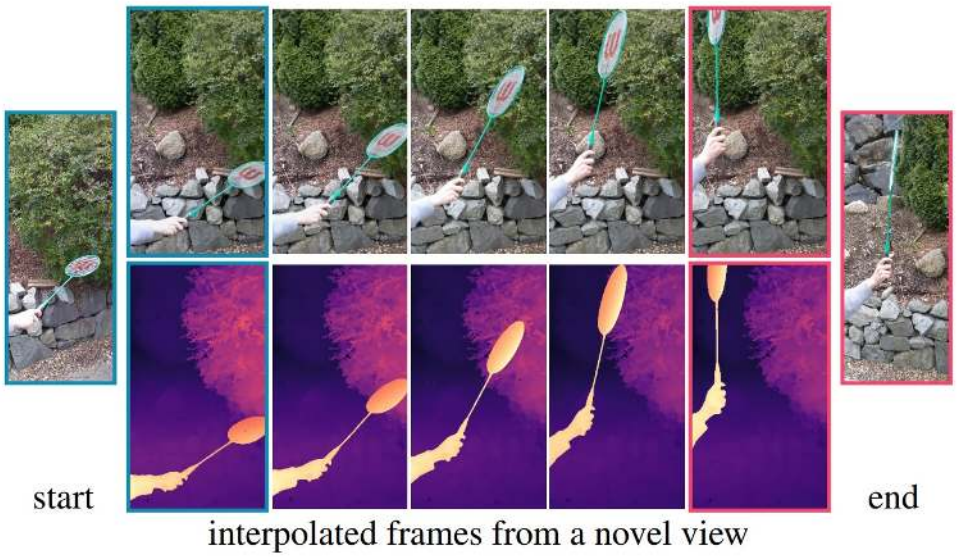

Figure 23.145: **Latent-code interpolation from a novel viewpoint.** Start/end frames (cyan/pink borders) from *BADMINTON* define two observed states. The middle columns are *synthetic* frames rendered from a *novel camera* by linearly interpolating the corresponding deformation codes ω and evaluating $F(T(\cdot,\omega(\alpha)),\cdot,\psi)$. Top row: RGB; bottom row: depth. The racquet sweeps smoothly and depth varies coherently, illustrating that per-image deformation latents form a state space that supports continuous interpolation. Source: [469].

Architecture and implementation details

Canonical field. A NeRF-style MLP $F : (\mathbf{x}', \mathbf{d}, \psi_i) \mapsto (\mathbf{c}, \sigma)$ with sinusoidal positional encodings predicts color and density in a *canonical* space; density uses a Softplus activation to ensure valid densities.

Deformation network. An MLP W predicts a dense SE(3) field via screw parameters $(\mathbf{r}, \mathbf{v})$ from encoded observation-space points and a per-image deformation code:

$$W : (\mathbf{x}, \omega_i) \mapsto (\mathbf{r}, \mathbf{v}), \qquad T(\mathbf{x}, \omega_i) = e^{(\mathbf{r};\mathbf{v})}\mathbf{x}.$$

Per-image latents. Appearance latents $\{\psi_i\}$ absorb photometric variation (exposure/white balance). Deformation latents $\{\omega_i\}$ index the non-rigid state for each observation and enable state interpolation.

Experiments and Ablations

Evaluation uses synchronized dual-phone captures to obtain validation views of the same dynamic state. Baselines include NeRF, NeRF+latent, Neural Volumes, NSFF†, and a D-NeRF–style $\gamma(t)$+Translation†. Qualitative results show recovery of fine structures (e.g., hair strands) and full-body details; quantitative comparisons (PSNR/LPIPS) and ablations validate the contributions of $\mathrm{SE}(3)$ deformations, elastic regularization, background constraints, and c2f.

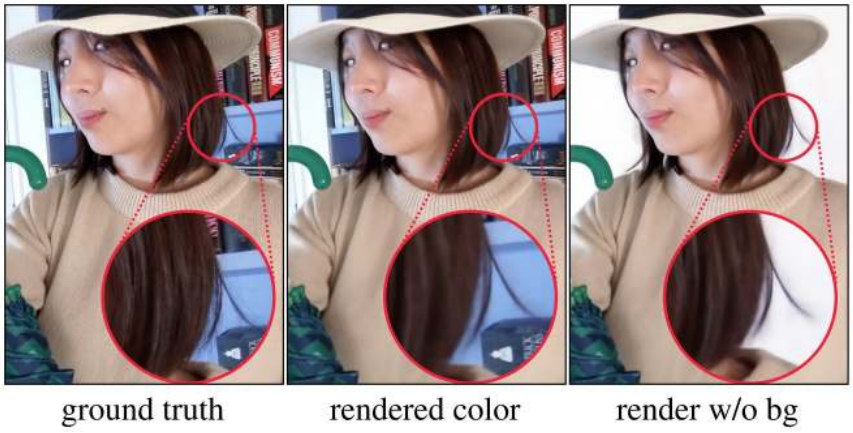

Figure 23.146: **Thin hair strands.** Adjusting the far plane allows rendering against a flat background, highlighting fine geometry. Source: [469].

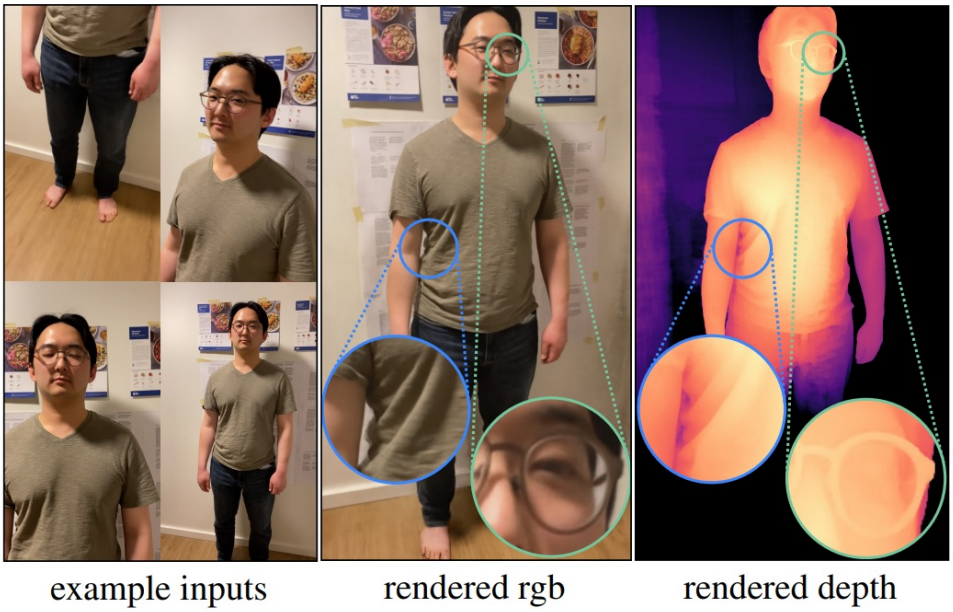

Figure 23.147: **Full-body reconstructions.** High-quality details such as fabric wrinkles and eyeglasses are captured from casual recordings. Source: [469].

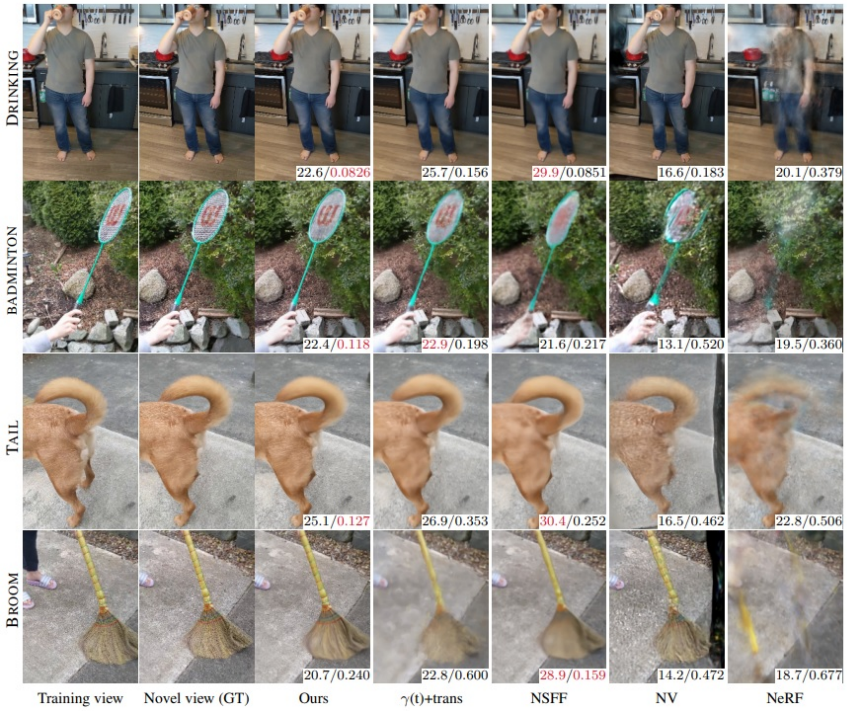

Figure 23.148: **Dynamic scenes comparison.** Side-by-side baselines with PSNR/LPIPS (best highlighted in red) illustrate that numerical gains do not always reflect perceptual quality. Source: [469].

Figure 23.149: **Quasi-static scenes comparison.** Similar trends appear on mostly static captures; perceptual quality correlates imperfectly with PSNR. Source: [469].

Table 23.36: **Quasi-static captures** from [469]. Each entry is *PSNR/LPIPS* (dB/unitless). **Bold** marks the best value per column for each metric (higher PSNR, lower LPIPS).

Method	Glasses PSNR/LPIPS	Beanie PSNR/LPIPS	Curls PSNR/LPIPS	Kitchen PSNR/LPIPS	Lamp PSNR/LPIPS	Toby Sit PSNR/LPIPS	Mean PSNR/LPIPS
NeRF [429]	18.10/0.474	16.80/0.583	14.40/0.616	19.10/0.434	17.40/0.444	22.80/0.463	18.10/0.502
NeRF + latent	19.50/0.463	19.50/0.535	17.30/0.539	20.10/0.403	18.90/0.386	19.40/0.385	19.10/0.452
Neural Volumes [389]	15.40/0.616	15.70/0.595	15.20/0.588	16.20/0.569	13.80/0.533	13.70/0.473	15.10/0.562
NSFF† [349]	19.60/0.407	21.50/0.402	18.00/0.432	21.40/0.317	20.50/0.239	**26.90**/0.208	21.30/0.334
$\gamma(t)$ + Trans† [488]	22.20/0.354	20.80/0.471	20.07/0.426	22.50/0.344	21.90/0.283	25.30/0.420	22.20/0.383
Nerfies (λ=0.01)	23.40/**0.305**	22.20/0.391	24.60/0.319	23.90/0.280	23.60/0.232	22.90/0.159	23.40/**0.281**
Nerfies (λ=0.001)	**24.20**/0.307	23.20/0.391	**24.90/0.312**	23.50/0.279	**23.70/0.230**	22.80/0.174	**23.70**/0.282
No elastic	23.10/0.317	**24.20/0.382**	24.10/0.322	22.90/0.290	23.70/0.230	23.00/0.257	23.50/0.300
No coarse-to-fine	23.80/0.312	21.90/0.408	24.50/0.321	**24.00/0.277**	22.80/0.242	22.70/0.244	23.30/0.301
No SE3	23.50/0.314	21.90/0.401	24.50/0.317	23.70/0.282	22.70/0.235	22.90/0.206	23.20/0.293
Nerfies (base)	24.00/0.319	20.90/0.466	23.50/0.345	22.40/0.323	22.10/0.254	22.70/0.184	22.60/0.314
No BG Loss	22.30/0.317	21.50/0.395	20.10/0.371	22.50/0.290	20.03/0.260	22.30/**0.145**	21.50/0.296

Table 23.37: **Dynamic captures** from [469]. Each entry is *PSNR/LPIPS* (dB/unitless). **Bold** marks the best value per column for each metric (higher PSNR, lower LPIPS).

Method	Drinking PSNR/LPIPS	Tail PSNR/LPIPS	Badminton PSNR/LPIPS	Broom PSNR/LPIPS	Mean PSNR/LPIPS
NeRF [429]	18.60/0.397	23.00/0.571	18.80/0.392	21.00/0.667	20.30/0.506
NeRF + latent	21.90/0.233	24.90/0.404	20.00/0.308	21.90/0.576	22.20/0.380
Neural Volumes [389]	16.20/0.198	18.50/0.559	13.10/0.516	16.10/0.544	16.00/0.454
NSFF† [349]	**27.70/0.080**	**30.60**/0.245	21.70/0.205	**28.20/0.202**	**27.10**/0.183
$\gamma(t)$ + Trans† [488]	23.70/0.151	27.20/0.391	**22.90**/0.221	23.40/0.627	24.30/0.347
Nerfies (λ=0.01)	22.40/0.087	23.90/**0.161**	22.40/**0.130**	21.50/0.245	22.50/**0.156**
Nerfies (λ=0.001)	21.80/0.096	23.60/0.175	22.10/0.132	21.00/0.270	22.10/0.168
No elastic	22.20/0.086	23.70/0.174	22.00/0.132	20.90/0.287	22.20/0.170
No coarse-to-fine	22.30/0.096	24.30/0.257	21.80/0.151	21.90/0.406	22.60/0.228
No SE3	22.40/0.086	23.50/0.191	21.20/0.156	20.90/0.276	22.60/0.228
Nerfies (base)	22.60/0.127	24.30/0.298	21.10/0.173	22.10/0.503	22.50/0.275
No BG Loss	22.30/0.085	23.50/0.210	20.40/0.161	20.90/0.330	21.80/0.196

Limitations and Future Work

Like other diffeomorphic-warp dynamic NeRFs, Nerfies faces difficulty with genuine topology changes (e.g., mouth opening/closing) and very rapid motion, where geometry can become inconsistent despite plausible colors. This is a great limitation and a focus for future works to improve.

Figure 23.150: **Topological limitations.** Color renderings may remain plausible while geometry degrades under topology changes or rapid motion. Source: [469].

Enrichment 23.13: NeRF: Editing, Controllability & Semantic Manipulation

Decoupling geometry, appearance, and semantics enables targeted edits, retrieval, and instruction following.

- **LERF** [288]: Language-embedded radiance fields support text queries and localized edits grounded in semantics.
- **Instruct-NeRF2NeRF** [202]: Uses instruction-following priors to edit existing NeRFs while preserving scene identity and structure.

Further influential works (not expanded): **NeRF-Editing** [165] (factorized edits via differentiable decompositions). We note broader text-guided approaches, but keep focus on language-driven interfaces directly usable for scene editing.

Enrichment 23.13.1: Language Embedded Radiance Fields (LERF)

Motivation

Neural Radiance Fields (NeRFs) [429] reconstruct scenes as continuous volumetric functions, producing photorealistic novel views. Yet despite this visual fidelity, the representation itself is *semantically opaque*: the field encodes only colors and densities, without grounding in human-interpretable concepts. This opacity restricts interaction and control—for example, one cannot simply ask where the "utensils" are in a kitchen or identify objects based on abstract properties and affordances.

In contrast, 2D open-vocabulary methods such as LSeg [326] and OWL-ViT [433] enable language-driven reasoning about images. However, they often depend on region proposals or supervision from curated segmentation datasets, which biases generalization toward in-distribution categories and weakens expressivity for rare or long-tail queries.

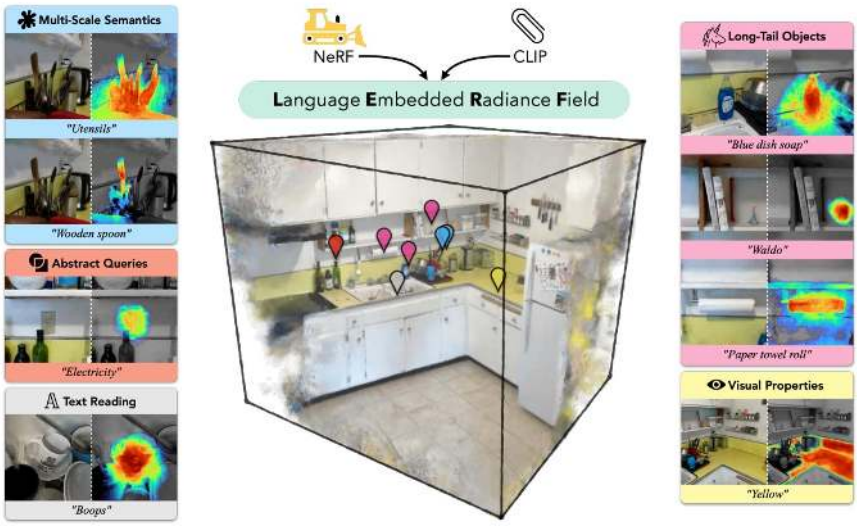

Figure 23.151: **Language Embedded Radiance Fields (LERF).** CLIP representations are distilled into a dense, multi-scale 3D field that can be reconstructed from a hand-held phone capture in under 45 minutes. Once trained, LERF supports real-time natural-language queries, producing relevancy maps for prompts ranging from abstract concepts to fine-grained attributes and even scene text. Source: [288].

High-level overview

Language Embedded Radiance Fields (LERF) [288] close the semantics gap by grounding raw CLIP [498] embeddings in a dense, multi-scale 3D field that is optimized alongside a NeRF backbone. Unlike proposal- or dataset-driven 2D pipelines, LERF *does not* fine-tune CLIP and *does not* rely on segmentation masks. The key idea is to make language supervision *volumetric and scale-aware*: instead of supervising infinitesimal points (ill-posed for patch-based CLIP), LERF learns a view-independent language field:

$$F_{\text{lang}}(\mathbf{x}, s) \in \mathbb{R}^d$$

that outputs a CLIP vector for a 3D cube centered at $\mathbf{x}$ with physical side length s. Supervision comes from a precomputed multi-scale pyramid of CLIP embeddings derived from image crops of training views. During rendering, NeRF's density weights integrate these features along rays to produce pixel-aligned, view-consistent *relevancy maps* for arbitrary text prompts.

How it works at a glance

- **1) Capture and NeRF:** Optimize a NeRF backbone for geometry and appearance from a casual hand-held sequence.
- **2) CLIP supervision pyramid:** Precompute a multi-scale feature pyramid of CLIP embeddings from image crops between s_{min} and s_{max}.
- **3) Language field over volumes:** Train $F_{\text{lang}}(\mathbf{x}, s)$ to match the (interpolated) CLIP embedding of the crop corresponding to the projected physical volume, keeping it view-independent.
- **4) Volumetric language rendering:** Along a ray $\mathbf{r}(t)$, evaluate $F_{\text{lang}}(\mathbf{x}(t), s(t))$ and integrate with NeRF's density-based weights to obtain a per-pixel language embedding.
- **5) Relevancy maps for text prompts:** Embed the query text with CLIP and score cosine similarity against rendered language embeddings to obtain a 3D-consistent heatmap.

Why this suits open-vocabulary 3D queries

LERF transforms a static NeRF reconstruction into a semantic 3D interface that can be queried directly with natural text. Its design provides three key advantages:

- **3D consistency:** NeRF's volumetric rendering fuses information across views; LERF ties language to geometry at each 3D location and scale, eliminating per-view inconsistencies common in 2D detectors. This ensures that queries like "yellow" highlight the same regions from all viewpoints.
- **Open-vocabulary generality in 3D** Both LERF and OWL-ViT inherit CLIP's open vocabulary, but LERF avoids 2D detection biases (per-view boxes/masks) by learning a *volumetric* semantic field. This improves long-tail and abstract queries in practice—for instance "electricity" activates outlets and cords jointly, and rare entities like "Waldo" localize coherently within the 3D scene.
- **Hierarchical semantics via scale:** The explicit physical scale s allows the same 3D location to carry different meanings depending on context (e.g., "utensils" at a coarse scale versus "wooden spoon" at a fine scale). This also extends naturally to scene text, such as localizing the printed word "Boops" on a mug.

In practice, these capabilities can be realized from a casual hand-held capture: a scene is reconstructed in under one hour, after which relevancy maps for arbitrary text prompts can be generated interactively in real time.

Method

The central contribution of LERF [288] is to extend the NeRF framework with a language field that grounds natural language in 3D space. Below, we detail the method from the field definition and supervision to volumetric rendering and regularization.

Language field definition

Standard NeRF parameterizes a continuous volumetric function

$$F(\mathbf{x}, \mathbf{d}) \mapsto (\sigma, c),$$

where each 3D sample $\mathbf{x}$ and viewing direction $\mathbf{d}$ yield a density σ and view-dependent color c. This encodes only geometry and appearance, with no semantics. LERF augments this with a view-independent *language field* computed from a shared semantic backbone E_{feat}:

$$\mathbf{h}(\mathbf{x}) \;=\; E_{\text{feat}}(\mathbf{x}), \qquad F_{\text{lang}}\big(\mathbf{h}(\mathbf{x}), s\big) \in \mathbb{R}^{512}.$$

Unlike NeRF's infinitesimal point queries, F_{lang} is defined over *volumes*: for a cube centered at $\mathbf{x}$ with side length s, the output is a CLIP feature vector describing that region's semantics. The explicit physical scale s is essential: large s aggregates broad context (e.g., "utensils" across a drawer), while small s isolates fine parts (e.g., a "wooden spoon"). F_{lang} is view-independent, so multiple views of the same 3D region reinforce a single semantic embedding.

Supervision via CLIP pyramid

CLIP produces semantics for *image patches with context*, while NeRF samples 3D points. LERF supervises a world-space volume $(\mathbf{x}, s)$ using the CLIP embedding of the image patch onto which it projects. The pipeline: (i) precompute, for each training image, a multi-scale "textbook" of CLIP features in image coordinates; (ii) during training, project $(\mathbf{x}, s)$ into a view and read the matching embedding via interpolation.

Part 1 — Precomputation: building the image-space textbook

1. **Choose image scales:** Define discrete square crop sizes $\{s_{\text{img}}^{(k)}\}$ in pixels between $s_{\min}$ and $s_{\max}$ (often log-spaced).
2. **Slide and embed:** For each training image and each $s_{\text{img}}^{(k)}$, slide a square window on a regular grid with overlap ($\sim 50\%$), resize to CLIP's input, and encode with the frozen CLIP image encoder to obtain

   $$\varphi^{\text{CLIP}}(u, v, s_{\text{img}}^{(k)}) \in \mathbb{R}^{512},$$

   stored at crop center (u, v) for that scale.
3. **Form the multi-scale feature pyramid:** Stack the per-scale grids to obtain, per image, a pyramid indexed by (u, v) and $s_{\text{img}}^{(k)}$ (large crops $\rightarrow$ scene/objects; small crops $\rightarrow$ parts/text).

Part 2 — Training: supervising a world-space volume with an image-space patch

1. **Pick a pixel and a CLIP scale:** Choose a training pixel (u, v) and a pyramid scale s_{img} (crop size, in pixels). Cast the camera ray $\mathbf{r}(t)$ through (u, v) and sample depths $\{t_i\}$ with camera-frame depths z_i.
2. **Backbone features and scale in world space:** For each sample $\mathbf{x}_i = \mathbf{r}(t_i)$, compute backbone features

   $$\mathbf{h}(\mathbf{x}_i) = E_{\text{feat}}(\mathbf{x}_i),$$

   and set a *world-space* receptive field that projects to the chosen image crop:

   $$s(t_i) \;=\; \frac{z_i}{f}\, s_{\text{img}},$$

   where f is the focal length in pixels. This makes farther samples use a larger physical support so that all samples along the ray correspond to the *same* image receptive field s_{img}.
3. **Query the language head and volume-render:** Evaluate the language head per sample and aggregate with the standard NeRF weights $w_i = T_i \alpha_i$:

   $$\hat{\varphi}_{\text{lang}}(u, v; s_{\text{img}}) \;=\; \sum_i w_i\, F_{\text{lang}}\big(\mathbf{h}(\mathbf{x}_i), s(t_i)\big), \qquad \widehat{\hat{\varphi}}_{\text{lang}} \;=\; \frac{\hat{\varphi}_{\text{lang}}}{\big\|\hat{\varphi}_{\text{lang}}\big\|_2}.$$

   This yields a *rendered* per-pixel language embedding aligned with scene geometry.
4. **Retrieve the CLIP target (image space):** Trilinearly interpolate the precomputed CLIP pyramid at (u, v, s_{img}) (bilinear over (u, v) and linear over adjacent scales) to get

   $$\varphi^{\text{CLIP}}_{\text{target}}(u, v, s_{\text{img}}) \in \mathbb{R}^{512}, \qquad \widehat{\varphi}^{\text{CLIP}}_{\text{target}} \;=\; \frac{\varphi^{\text{CLIP}}_{\text{target}}}{\big\|\varphi^{\text{CLIP}}_{\text{target}}\big\|_2}.$$

5. **Align rendered prediction to CLIP target:** Use cosine similarity on unit-normalized vectors:

   $$\mathscr{L}_{\text{lang}} \;=\; 1 - \cos\Big(\widehat{\hat{\varphi}}_{\text{lang}}(u, v; s_{\text{img}}),\; \widehat{\varphi}^{\text{CLIP}}_{\text{target}}(u, v, s_{\text{img}})\Big).$$

Notes on correctness and design

- *What is* $\mathbf{h}(\mathbf{x})$*?* It is the shared, multi-resolution hashgrid feature produced by E_{feat} at 3D position $\mathbf{x}$; both semantic heads read these same features.
- *Where is the "cube"?* The cube is implicit in the scale argument $s(t_i)$ of F_{lang}: it specifies the physical support in 3D over which the language head aggregates semantics at each sample. No explicit 3D voxelization or 2D rasterization of a cube is required.
- *Why render before supervising?* CLIP targets live at *image patches*. By volume-rendering F_{lang} along the ray with NeRF's transmittance weights, the predicted embedding becomes a geometry-aware, per-pixel descriptor that is commensurate with the image-space CLIP patch, making the supervision well-posed.
- *Faithful scale coupling:* The mapping $s(t_i) = (z_i/f)\, s_{\text{img}}$ preserves a fixed *image* receptive field while adapting the *world* receptive field by depth, ensuring consistent coarse-to-fine behavior across views.

Volumetric language rendering

The NeRF scene is trained photometrically to predict (σ, c); this backbone is unchanged. LERF adds a parallel, view-independent semantic layer rendered with the same sampler and transmittance. Along $\mathbf{r}(t) = \mathbf{o} + t\mathbf{d}$ with step size δ_i, opacity $\alpha_i = 1 - \exp(-\sigma_i \delta_i)$, and transmittance $T_i = \prod_{j<i}(1-\alpha_j)$,

$$\hat{\varphi}_{\text{lang}}(u, v; s) \;=\; \sum_i w_i \, F_{\text{lang}}\big(\mathbf{h}(\mathbf{r}(t_i)), s(t_i)\big), \qquad w_i \;=\; T_i \, \alpha_i,$$

followed by ℓ_2 normalization. The depth-dependent $s(t)$ mirrors the projective coupling used in supervision. Given a text query, the CLIP text encoder yields φ_{text}; cosine similarity with $\hat{\varphi}_{\text{lang}}$ produces a view-consistent *relevancy map*. During training,

$$\mathscr{L}_{\text{lang}} \;=\; 1 - \cos\Big(\,\hat{\varphi}_{\text{lang}},\; \varphi^{\text{CLIP}}_{\text{target}}\Big),$$

where $\varphi^{\text{CLIP}}_{\text{target}}$ is retrieved from the pyramid at the projected location and scale.

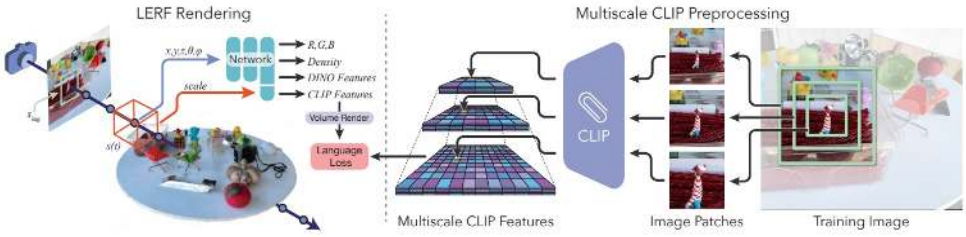

Figure 23.152: **LERF optimization** Left: a language field over 3D volumes $(\mathbf{x}, s)$ is sampled along rays and aggregated with NeRF transmittance weights. Right: supervision comes from a precomputed multi-scale CLIP pyramid; features are interpolated at the projected location and scale. Source: [288].

Regularization with DINO

LERF augments the CLIP-driven language supervision with a second, *structural* head that reads the same latent features but *not* the scale:

$$F_{\text{dino}}\big(\mathbf{h}(\mathbf{x})\big) \in \mathbb{R}^{d_{\text{dino}}}.$$

Precomputation (DINO). Each training image is passed once through a frozen DINO ViT, producing *dense, pixel-aligned* descriptors

$$\varphi^{\text{DINO}}(u, v) \in \mathbb{R}^{d_{\text{dino}}}.$$

Unlike CLIP, which supplies a *multi-scale pyramid of patch embeddings* to supervise scale-aware semantics, DINO descriptors are already dense at the native image resolution and require *no pyramid or scale interpolation*. They provide local, category-agnostic cues (smooth within objects, sharp at boundaries).

Volumetric rendering and loss. Using the same transmittance weights w_i as RGB and the CLIP head,

$$\hat{\varphi}_{\text{dino}}(u,v) \;=\; \sum_i w_i \, F_{\text{dino}}\big(\mathbf{h}(\mathbf{r}(t_i))\big), \qquad \mathscr{L}_{\text{dino}} \;=\; \big\|\hat{\varphi}_{\text{dino}}(u,v) - \varphi^{\text{DINO}}(u,v)\big\|_2^2.$$

Both $\mathscr{L}_{\text{lang}}$ (patch-based, multi-scale CLIP) and $\mathscr{L}_{\text{dino}}$ (dense, pixel-aligned DINO) backpropagate through their heads *and* into the shared backbone E_{feat}, shaping $\mathbf{h}(\mathbf{x})$ to be smooth on object interiors and to change sharply at boundaries. This regularizes the latent space that the CLIP head consumes, yielding crisper, less patchy semantics at inference—despite the DINO head never being matched to text at test time.

Inference: scale selection and heatmap rendering

At inference time, LERF produces a *text-driven heatmap* indicating where a natural-language query is likely to be grounded in the 3D scene. Importantly, only the *CLIP head* and the NeRF rendering pipeline are used; the DINO head serves only as a training-time regularizer and is not involved at test time.

Scale selection (global per query). The CLIP head is conditioned on a physical scale parameter s, which ties a 3D neighborhood in world coordinates to the patch sizes that CLIP was trained on. Because the optimal scale depends on the query ("kitchen" spans meters, while "wooden spoon" spans centimeters), LERF sweeps over a discrete set of candidate scales:

1. Render the CLIP feature field $\hat{\varphi}_{\text{lang}}(u,v;s)$ for each candidate s (e.g., ~ 30 uniformly spaced values in $[0,2]$ m).
2. For each s, compute a relevancy map by comparing rendered features to the text embedding (see below).
3. Reduce each map to a scalar activation (e.g., the mean similarity of the top-k pixels).
4. Select the scale s with the highest activation and keep its relevancy map for visualization.

This procedure balances global and local queries: scene-level concepts favor larger s, while fine-grained part queries favor smaller s. Fixing a single global s per query stabilizes the visualization, though it assumes objects of interest are roughly consistent in size.

Text embeddings. For a user-specified query (e.g., "wooden spoon"), a frozen CLIP text encoder produces a unit-normalized embedding vector

$$\varphi_{\text{text}} \;\in\; \mathbb{R}^{512}.$$

This serves as the reference against which all rendered CLIP features are compared.

Relevancy computation (CLIP + NeRF aggregation). Given a viewpoint and the chosen scale s, each pixel (u,v) accumulates semantic features along its camera ray:

$$\hat{\varphi}_{\text{lang}}(u,v;s) \;=\; \sum_i w_i \, F_{\text{lang}}\big(\mathbf{h}(\mathbf{r}(t_i)),\, s(t_i)\big),$$

where $\mathbf{r}(t)$ is the ray, $\mathbf{h}(\cdot)$ the shared latent features, and

$$w_i = T_i \alpha_i, \qquad \alpha_i = 1 - \exp(-\sigma_i \delta_i), \qquad T_i = \prod_{j<i} (1-\alpha_j).$$

These weights are identical to those used in NeRF's RGB rendering, ensuring that semantic aggregation is geometry- and opacity-aware. The per-pixel relevancy score is then the cosine similarity:

$$\text{score}(u,v) \;=\; \cos\big(\hat{\varphi}_{\text{lang}}(u,v;s),\, \varphi_{\text{text}}\big).$$

Refinements. Two additional steps sharpen the resulting heatmap:

- *Null phrase calibration:* The mean similarity to generic prompts ("object", "things", "stuff", "texture") is subtracted to suppress spurious activations that are semantically uninformative.
- *Visibility and opacity filtering:* Pixels with low accumulated opacity are discarded, and only rays with sufficient multi-view support (e.g., visible in ≥ 5 training images) are retained, suppressing background clutter and artifacts.

Intuition. This inference process ensures that:

- CLIP supervision remains faithful to its training context (patch-level embeddings), thanks to explicit scale coupling.
- NeRF's volumetric rendering guarantees view-consistency and geometry alignment in the heatmaps.
- Post-processing steps mitigate noise, producing sharp, interpretable visualizations that localize natural-language queries in 3D scenes.

Architecture and factorization (overview, sharing, and why DINO helps). LERF is trained end-to-end with three cooperating modules: (1) a NeRF backbone (σ, c) for appearance/geometry that receives only $\mathscr{L}_{\text{rgb}}$; (2) a *shared* feature backbone E_{feat} (multi-resolution hashgrid) that outputs $\mathbf{h}(\mathbf{x})$; and (3) two disjoint semantic heads that *both* read $\mathbf{h}(\mathbf{x})$:

$$\underbrace{F_{\text{lang}}\big(\mathbf{h}(\mathbf{x}), s\big)}_{\text{CLIP head}} \in \mathbb{R}^{512}, \qquad \underbrace{F_{\text{dino}}\big(\mathbf{h}(\mathbf{x})\big)}_{\text{DINO head}} \in \mathbb{R}^{d_{\text{dino}}}.$$

Because $\mathscr{L}_{\text{lang}}$ and $\mathscr{L}_{\text{dino}}$ both update E_{feat}, DINO's dense, pixel-aligned supervision *sculpts the shared latent space* into geometry-aware features that directly benefit the CLIP head at inference.

Why DINO (and not SAM or detector/segmenter baselines).

- *Dense, label-free, pixel-aligned targets:* DINO preserves open-vocabulary zero-shot behavior without prompts or class lists.
- *Continuous supervision matches volumetric training:* DINO's smooth-within / sharp-at-boundary behavior fits differentiable volumetric ℓ_2 regression; hard masks (e.g., SAM) introduce discrete topology, prompt dependence, and dataset biases ill-suited to continuous multi-view rendering.
- *Regularizing the shared latent space:* Since both heads read $\mathbf{h}(\mathbf{x})$, DINO improves the very features the CLIP head uses; mask pipelines would require non-differentiable steps (masking/reprojection) and would not densify the latent space end-to-end.
- *Practicality:* A single frozen DINO pass per image yields cheap regression targets; mask generators add runtime/brittleness and risk constraining open-vocabulary behavior.

Thus, DINO acts as an effective *training-time structural regularizer* on the shared backbone, while CLIP remains the sole driver of text matching at inference.

Training objective. LERF trains all of its components end-to-end from scratch on the target scene. The CLIP and DINO encoders that provide semantic supervision are *frozen*, but both the NeRF branch (σ, c) and the semantic backbone E_{feat} are actively optimized. The total loss is

$$\mathscr{L} \;=\; \mathscr{L}_{\text{rgb}} \;+\; \lambda_{\text{lang}}\,\mathscr{L}_{\text{lang}} \;+\; \lambda_{\text{dino}}\,\mathscr{L}_{\text{dino}}\,.$$

- $\mathscr{L}_{\textbf{rgb}}$ **(photometric).** The NeRF branch is trained in the standard way: for each ray r, the rendered color $\hat{C}(r)$ is matched to the ground-truth pixel $C^*(r)$ using MSE,

  $$\mathscr{L}_{\text{rgb}} \;=\; \tfrac{1}{|\mathscr{R}|} \sum_{r\in\mathscr{R}} \|\hat{C}(r) - C^*(r)\|_2^2.$$

  This is necessary because NeRFs are not "once-for-all" pretrained models; they must be optimized *per scene*. A NeRF trained on Scene A carries no useful weights for Scene B. Without this photometric loss, the geometry and appearance of the new scene would never be recovered.
- $\mathscr{L}_{\textbf{lang}}$ **(language).** Cosine similarity between the rendered, unit-normalized CLIP embedding $\hat{\varphi}_{\text{lang}}$ and the interpolated CLIP target from the multi-scale crop pyramid. This updates the shared semantic backbone and the CLIP head.
- $\mathscr{L}_{\textbf{dino}}$ **(structure).** ℓ_2 regression between the rendered DINO embedding $\hat{\varphi}_{\text{dino}}$ and frozen per-pixel descriptors $\varphi^{\text{DINO}}(u,v)$. This updates the shared backbone and the DINO head.

Why train jointly? If we were to freeze a separately trained NeRF and only add semantics afterwards, the semantic heads would be forced to sit on top of whatever ambiguities or artifacts the NeRF geometry contains (e.g., smoky volumes in textureless regions). By co-optimizing $\mathscr{L}_{\text{rgb}}$, $\mathscr{L}_{\text{lang}}$, and $\mathscr{L}_{\text{dino}}$ together, the geometry and semantics *co-adapt*: RGB loss guarantees photometric fidelity, while the semantic losses push the backbone to place sharper boundaries and consistent features at object borders. The result is a decoupled but synergistic training process: geometry is accurate, semantics are consistent, and the final heatmaps are crisp and view-consistent.

Results and Ablations

Qualitative results

LERF enables open-vocabulary, language-driven exploration of reconstructed 3D scenes. Given a text query (e.g., “coffee mug”), the model renders a relevancy heatmap that highlights the corresponding 3D region across novel views, acting as a soft segmentation without predefined categories or manual masks. Representative results show robust localization across: objects (“eggs”, “shoes”), parts (“hand”, “fingers”), attributes/materials (“wooden”, “glass”), abstract categories (“cartoon”, “bath toy”), long-tail named entities (“waldo”, “jake from adventure time”), and even text strings on book spines (“the cookie bible”). These maps remain view-consistent due to volumetric aggregation and the shared 3D geometry. (Adapted from [288].)

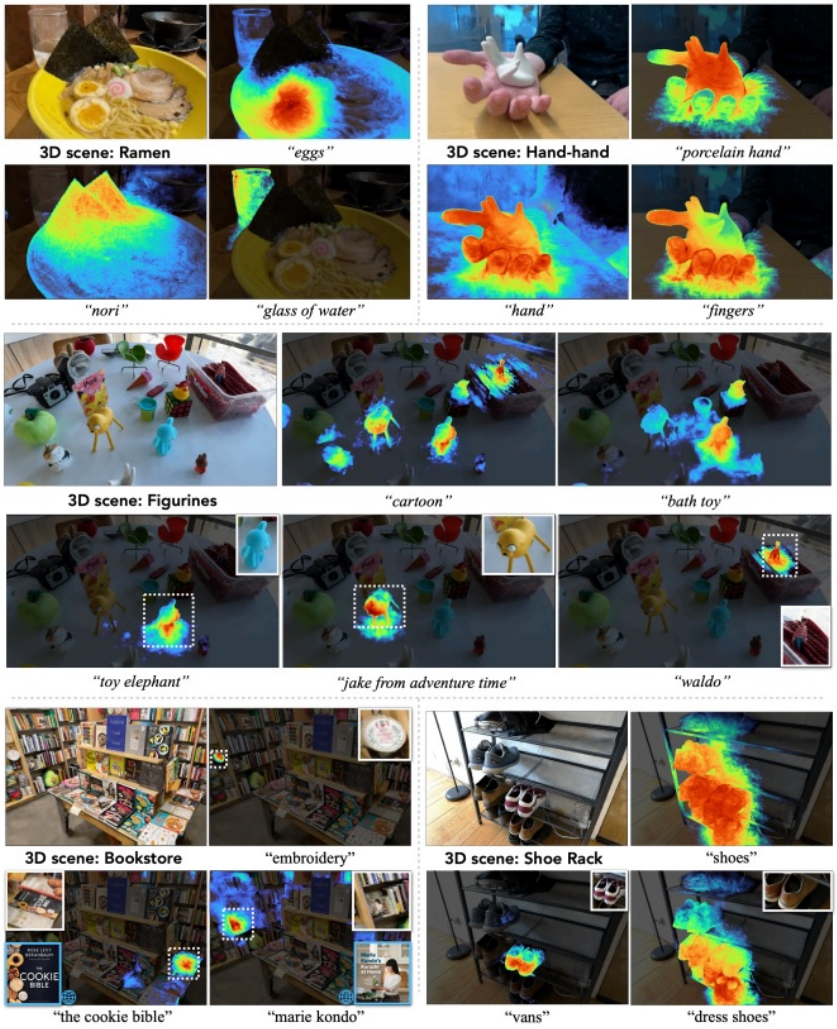

Figure 23.153: **Qualitative results across diverse scenes.** LERF grounds free-form queries in 3D for in-the-wild captures (ramen, hand object, figurines, bookstore, shoe rack). Queries span categories (“cartoon”), attributes (“glass of water”), parts (“fingers”), long-tail entities (“waldo”, “jake from adventure time”), brands (“vans”), and book titles (“the cookie bible”). Heatmaps are view-consistent and multi-scale. Source: [288].

2D CLIP vs. volumetric LERF

A direct 2D baseline interpolates similarity over patchwise CLIP embeddings in image space, which ignores multi-view geometry. In contrast, LERF renders language features volumetrically using NeRF transmittance, improving alignment with 3D structure.

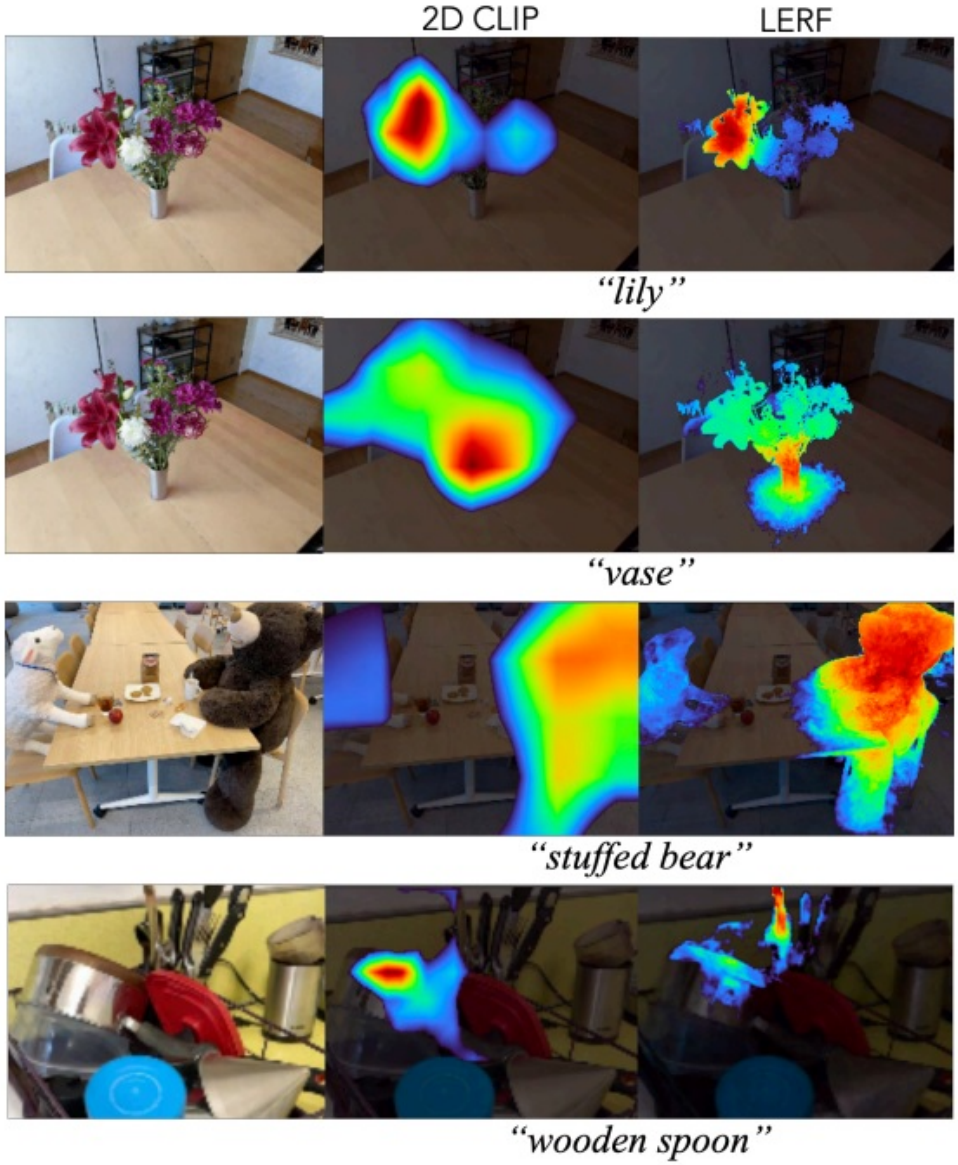

Figure 23.154: **2D CLIP interpolation vs. LERF.** Per-image 2D CLIP heatmaps (middle) are blob-like and inconsistent, while LERF (right) produces crisp, geometry-aligned activations for prompts such as "lily", "vase", and "wooden spoon". Source: [288].

Localization against LSeg (3D) and OWL-ViT

LERF is further compared to baselines that rely on 2D vision-language models projected into 3D. Results show stronger localization for long-tail concepts from novel views.

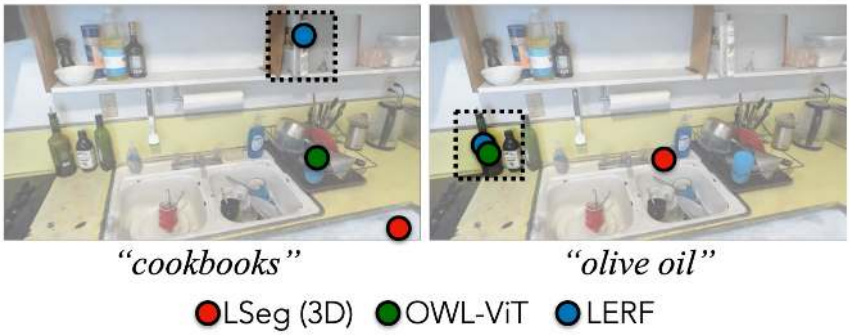

Figure 23.155: **Localization comparison in novel views.** LERF correctly localizes long-tail targets such as "cookbooks" and "olive oil" where LSeg(3D) and OWL-ViT often fail. Source: [288].

Figure 23.156: **Comparison to LSeg(3D).** LSeg succeeds on in-distribution labels (e.g., "glass of water") but struggles with out-of-distribution queries (e.g., "egg"); LERF handles both via open-vocabulary volumetric grounding. Source: [288].

Test Scene	LSeg (3D)	OWL-ViT	LERF
waldo kitchen	13.0%	42.6%	**81.5%**
bouquet	50.0%	66.7%	**91.7%**
ramen	15.0%	**92.5%**	62.5%
teatime	28.1%	75.0%	**93.8%**
figurines	8.9%	38.5%	**79.5%**
Overall	18.0%	54.8%	**80.3%**

Table 23.38: **Localization accuracy.** Comparison between LSeg(3D), OWL-ViT, and LERF across scenes. LERF substantially improves performance on long-tail queries. Source: [288].

3D existence: precision–recall

The task evaluates whether a queried concept *exists anywhere* in a scene, independently of precise localization. For each {scene, query} pair:

- **Rendering and calibration**
  - Render the volumetric language map by integrating the language field along camera rays with NeRF transmittance weights:

$$\hat{\varphi}_{\text{lang}}(u,v;s) = \sum_i w_i F_{\text{lang}}\big(\mathbf{h}(\mathbf{r}(t_i)), s(t_i)\big), \quad w_i = T_i \alpha_i,\ \alpha_i = 1 - e^{-\sigma_i \delta_i}.$$

  - Compute per-pixel relevancy scores via cosine similarity to the text query embedding from the frozen CLIP text encoder, φ_{text}, and apply *null-phrase calibration* by subtracting the mean similarity to generic phrases (“object”, “things”, “stuff”, “texture”).
  - Apply *visibility/opacity masking*: discard pixels with low accumulated opacity and suppress samples observed by fewer than ~ 5 training views to reduce noise in poorly constrained regions.
- **Score aggregation to a scene-level value**
  - Aggregate per-pixel scores within each view using top-k pooling (over high-confidence pixels).
  - Aggregate across views (e.g., max or mean) to produce a single scene-level score indicating the strongest evidence of the concept anywhere in the scene.
- **Precision–recall computation**
  - Sweep a threshold over the scene-level score to trace out the PR curve; positives/negatives derive from human annotations.
  - Report results on two query sets:
    - **COCO-like**: frequent, closed-vocabulary-style labels where baselines are comparatively strong.
    - **Long-tail**: in-the-wild labels (brands, book titles, parts, attributes) that stress open-vocabulary generalization.

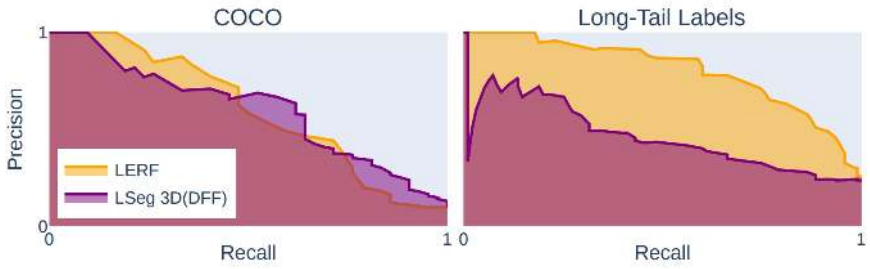

Figure 23.157: **Precision–recall on 3D existence queries.** LERF (orange) dominates 3D LSeg (purple) across operating points. On *COCO-like* labels (left), both methods reach high precision at low recall, but LERF sustains better recall as thresholds relax. On the *long-tail* set (right), LSeg collapses while LERF maintains a wide, high-precision regime, reflecting the advantages of volumetric rendering, multi-scale supervision, and open-vocabulary text alignment. Source: [288].

Ablation studies

The contribution of DINO regularization and multi-scale CLIP supervision can be isolated through ablations. Removing DINO weakens object-level grouping and boundary sharpness, producing patchy features that bleed into the background, particularly in sparsely observed areas. Training without the CLIP pyramid (single-scale) harms both coarse context and fine parts: large objects lose global coherence and small items lose discriminative detail. Together these components regularize the shared semantic backbone and stabilize the language field across scales.

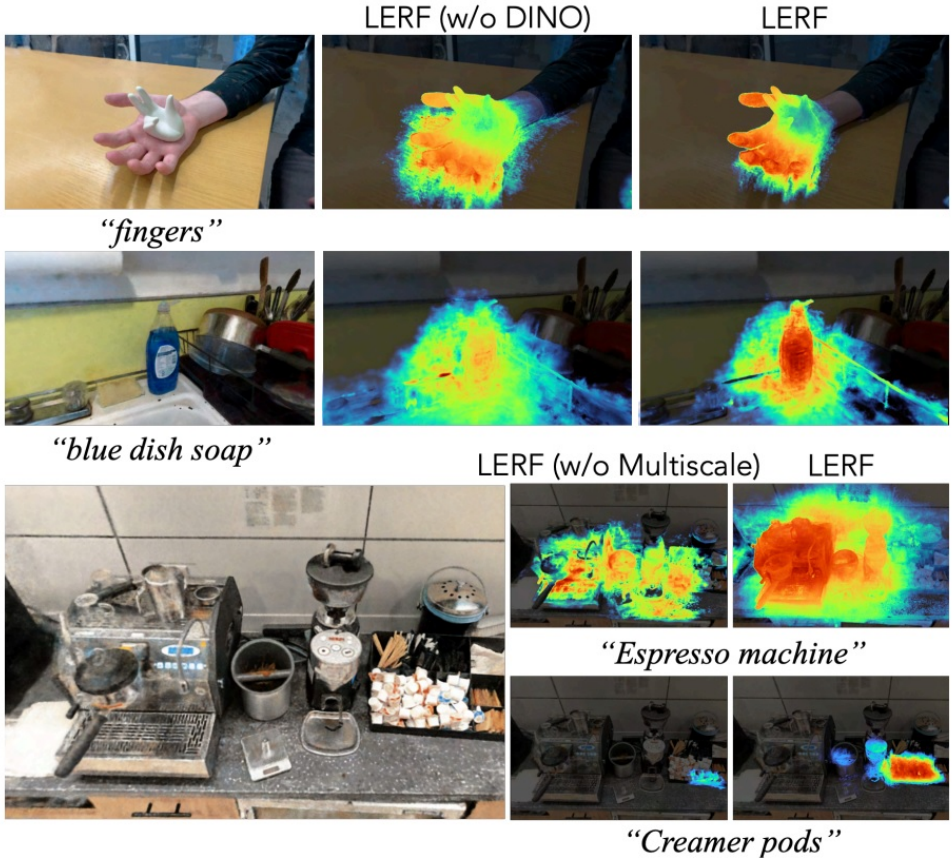

Figure 23.158: **Ablations.** *Top:* Without DINO, activations become diffuse and off-surface, bleeding across object boundaries; with DINO, crisp object-aligned maps are recovered (e.g., hand/fingers, blue dish soap). *Bottom:* Without multi-scale supervision, both large concepts ("espresso machine") and tiny details ("creamer pods") are missed; full multi-scale training restores correct localization at the appropriate scale. DINO acts only as a training-time regularizer; inference uses the CLIP head. Source: [288].

Failure cases and ambiguities

Typical errors stem from (i) fine-grained category proximity in CLIP space (e.g., “zucchini” vs. other long green vegetables), (ii) visual look-alikes or texture priors (“leaf” firing on green plastic), and (iii) global context gaps where volumetric aggregation over thin structures favors edges (“table”). These issues reflect both biases in the teacher model and geometric ambiguities in under-constrained regions.

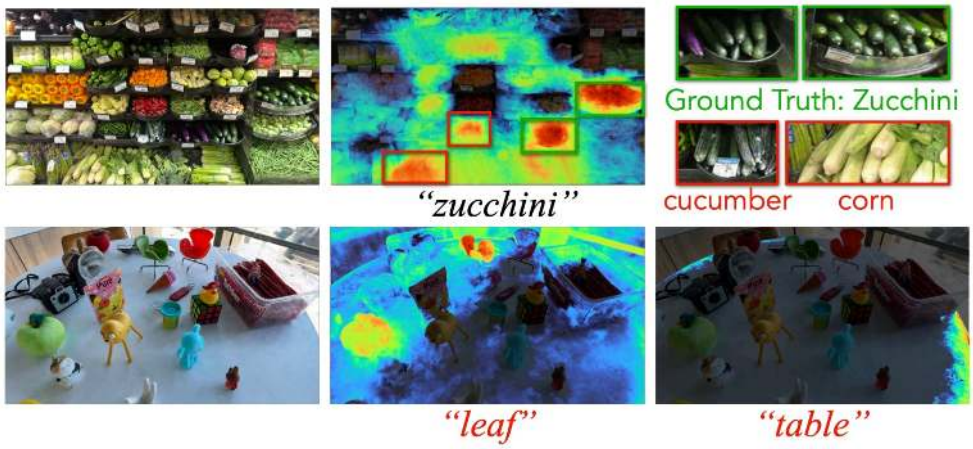

Figure 23.159: **Common failure modes.** (Top) Long-tail mix-ups under similar appearance (“zucchini” activating on cucumbers/corn). (Bottom) Texture and shape confusions (“leaf” on green plastics) and weak global reasoning (“table” edges dominate). Source: [288].

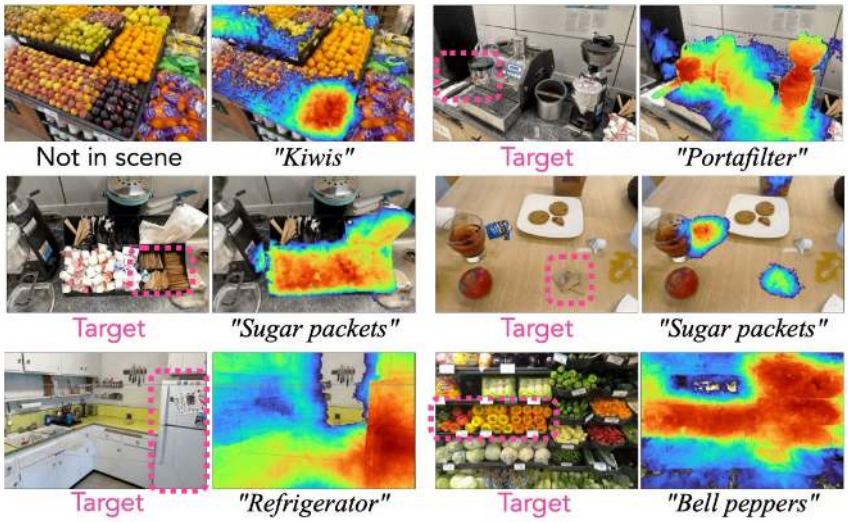

Figure 23.160: **CLIP-driven ambiguities.** Errors often trace to the frozen teacher: (left) grocery queries where visually similar produce cluster in feature space (“bell peppers” vs. jalapeños); (right) metallic context around “portafilter”; and absent queries (“kiwis”) that nevertheless elicit responses. Source: [288].

Prompt sensitivity (prompt tuning)

Because CLIP embeddings are highly sensitive to text phrasing, LERF inherits this prompt sensitivity. Adding discriminative modifiers (color, material, container type) reduces ambiguity and improves accuracy, particularly when geometry is ambiguous or coverage is sparse.

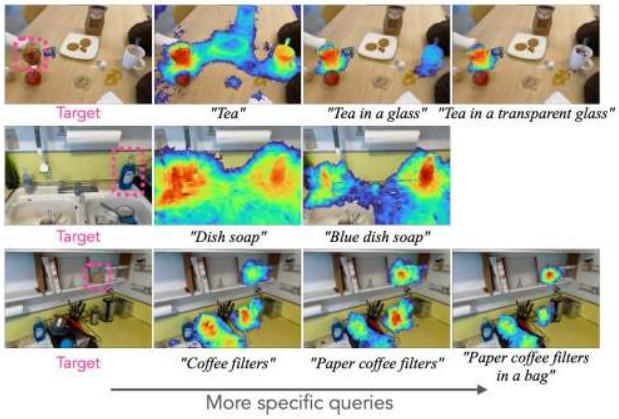

Figure 23.161: **Prompt specificity matters.** Refined queries ("blue dish soap" vs. "dish soap"; "tea in a transparent glass" vs. "tea") suppress distractors and sharpen activations, highlighting the sensitivity of the system to linguistic detail. Source: [288].

CLIP bag-of-words behavior

Supervision from frozen CLIP also introduces token-level quirks: compositional structure may be underweighted and nouns can dominate parts or attributes unless explicitly disambiguated. Typos that remain close in token space may also mislead supervision.

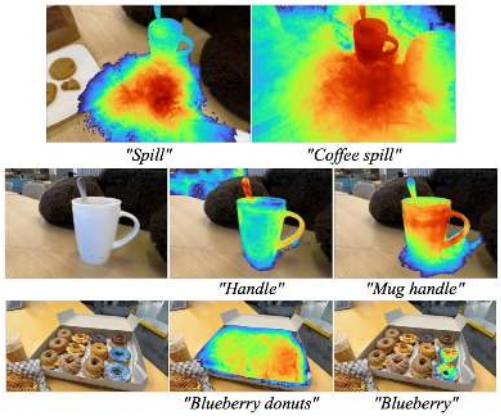

Figure 23.162: **Bag-of-words effects in CLIP.** Query phrasing reveals CLIP's tendency toward bag-of-words behavior. A single-word query like "blueberry" correctly isolates the blueberry donuts, but the seemingly more specific phrase "blueberry donuts" instead highlights *all* donuts, dominated by the noun. Similarly, part-level queries such as "handle" produce diffuse activations, while "mug handle" strengthens the focus near the handle yet still covers most of the mug. These effects illustrate the limits of CLIP's compositional reasoning. Source: [288].

Efficiency analysis

Training overhead relative to a vanilla NeRF is modest: CLIP crop pyramids and dense DINO descriptors are precomputed once per image, and training reduces to fast lookups and ℓ_2 regression to frozen targets. At inference, rendering language maps reuses the same rays and transmittance weights as RGB; the DINO head is inactive. Overall runtime and scaling remain comparable to standard NeRF pipelines while providing richer, open-vocabulary semantics.

Summary of findings

Experimental analyses identify three design choices as critical:

1. **Volumetric, scale-aware supervision** that couples world-space volumes to multi-scale CLIP patch embeddings.
2. **Auxiliary DINO regularization** that imposes within-object smoothness and sharp inter-object boundaries on the shared semantic backbone.
3. **Factorized architecture** that decouples geometry (trained only by $\mathscr{L}_{\text{rgb}}$) from semantics (trained by $\mathscr{L}_{\text{lang}}/\mathscr{L}_{\text{dino}}$), preventing geometric drift.

Together these elements yield view-consistent, open-vocabulary 3D semantic maps that answer existence queries robustly and localize fine-grained concepts across novel viewpoints.

Enrichment 23.13.2: InstructNeRF2NeRF: Editing 3D Scenes with Instructions

Motivation

Editing implicit 3D representations is nontrivial: traditional 3D tools presuppose explicit geometry and expert workflows, whereas neural radiance fields provide no direct handles for intuitive manipulation. CLIP-guided or physics-based approaches have enabled stylization or property tweaks but often struggle with localized, instruction-driven edits that remain consistent across viewpoints. InstructNeRF2NeRF [202] proposes a language-based interface for NeRF editing by harnessing an instruction-following 2D diffusion prior and consolidating those edits into a coherent 3D scene via iterative retraining.

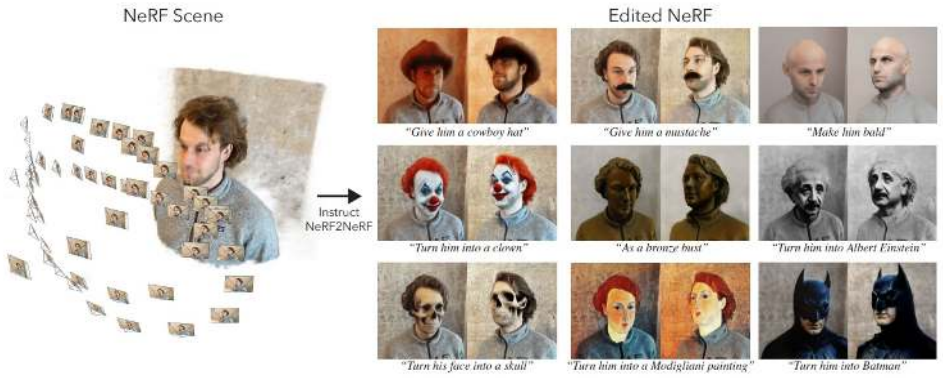

Figure 23.163: **Editing 3D scenes with instructions.** InstructNeRF2NeRF performs diverse global and local edits on a reconstructed NeRF using only natural language. Shown prompts include: "Give him a cowboy hat", "Give him a mustache", "Make him bald", "Turn him into a clown", "As a bronze bust", etc., demonstrating the abilities of this work. Source: [202].

Background on InstructPix2Pix

The InstructNeRF2NeRF (I2N2) framework enables intuitive, language-based 3D scene editing by leveraging **InstructPix2Pix (IP2P)** [57], a diffusion model trained specifically for instruction-following *image editing*. I2N2 employs IP2P to iteratively modify the multi-view images that supervise a NeRF, thereby nudging the underlying 3D scene toward the desired text instruction. For diffusion fundamentals and classifier-free guidance, see Ch. 20, §20.9.1 and §20.9.4.

Core idea of InstructPix2Pix

IP2P differs from text-to-image models by conditioning on *both* an input image c_I (to ground the edit) and a natural-language instruction c_T (to specify the change). Editing is performed in the latent domain by progressively denoising a noisy latent z_t toward an edited latent z_0. The denoising network ε_θ predicts the injected noise,

$$\hat{\varepsilon} = \varepsilon_\theta(z_t; t, c_I, c_T),$$

from which the edited latent is obtained and decoded to pixels. This single-pass, dual-conditioned formulation avoids per-example inversion or fine-tuning while enabling localized, instruction-aligned edits.

Crucial controls: dual guidance scales

IP2P extends classifier-free guidance with two independent scales that balance fidelity and edit strength:

- **Image guidance** s_I controls similarity to the conditioning image c_I (content preservation)
- **Instruction guidance** s_T controls adherence to the instruction c_T (edit strength)

Tuning (s_I, s_T) is essential for multi-view consistency when IP2P is used to edit the many camera views that supervise a 3D scene.

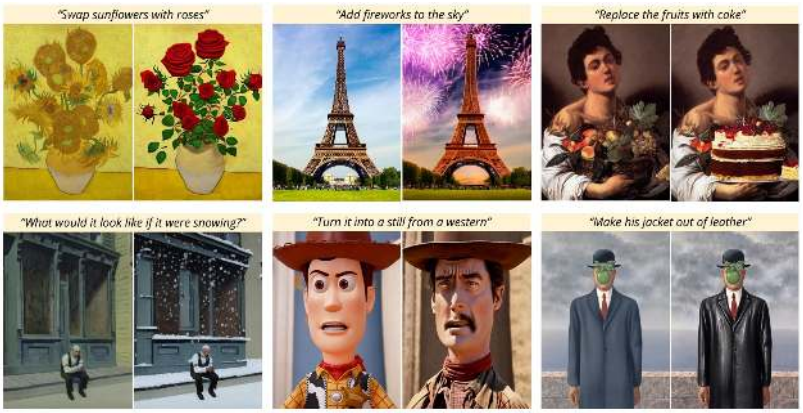

Figure 23.164: **InstructPix2Pix examples.** Given an image and a text instruction, IP2P applies the appropriate edit in a single forward pass without per-example inversion or fine-tuning. For instance: "Swap sunflowers with roses" (top left), "Add fireworks to the sky" (top row, middle), and "Make his jacket out of leather" (bottom right). Source: [57].

How InstructPix2Pix is trained and why Prompt-to-Prompt alone is insufficient

IP2P is trained on a large-scale *instruction–edit* dataset constructed synthetically [57]. Instead of hand-drawn masks, structural consistency between "original" and "edited" images is enforced at *data-generation time* using **Prompt-to-Prompt** 20.11.5.1 with Stable Diffusion 20.11.4: the same random seed and cross-attention structure are reused so pose, layout, and background align, and only the instructed change varies. The pipeline is:

- **Instruction and caption generation** A finetuned GPT–3 proposes an initial caption, an instruction, and a corresponding edited caption.
- **Consistent image pair synthesis** Stable Diffusion with Prompt-to-Prompt generates the *original* and *edited* images with shared seeds and attention maps to preserve structure.
- **Triplet assembly at scale** Over $\sim$450,000 triplets are collected: (original image, instruction, edited image).
- **Diffusion training** A diffusion model is trained on these triplets to perform instruction-following edits on arbitrary input images.

At inference, IP2P edits *real* images by directly conditioning on (c_I, c_T) and controlling (s_I, s_T). This capability is precisely what Prompt-to-Prompt (P2P) lacks: P2P is an *inference-time technique* for editing images *as they are generated from text*, requiring the source and target prompts and access to the generation trajectory. It cannot edit arbitrary photographs because those internal states are absent. IP2P, trained on P2P-aligned pairs, *learns* the general skill of editing any given image from an instruction.

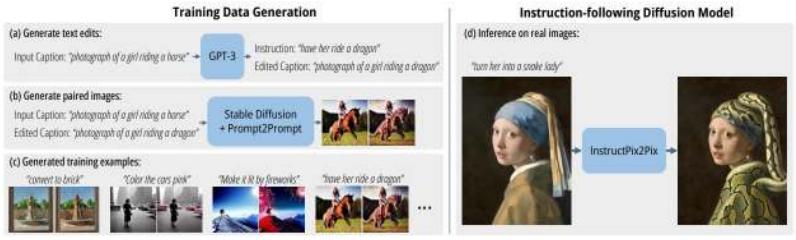

Figure 23.165: **Training pipeline of InstructPix2Pix.** (a) Finetuned GPT-3 generates instructions and edited captions; (b) Stable Diffusion with Prompt-to-Prompt produces aligned original/edited image pairs; (c) over 450k training triplets are assembled; (d) a diffusion model is trained to follow instructions for image editing. At inference, the model edits real images using natural instructions. Source: [57].

What IP2P brings beyond text-to-image diffusion and Prompt-to-Prompt

- **Real-image editing from instructions** Unlike text-to-image models, IP2P accepts an existing image c_I and modifies it according to c_T, rather than synthesizing a new scene from scratch.
- **Grounded edits with controllable fidelity** Image conditioning and the s_I scale preserve. identity, layout, and fine details; s_T controls edit strength, enabling cross-view consistency when editing NeRF training images.
- **Generalization to arbitrary inputs** Training on many aligned before–after pairs teaches the model to apply edits to photographs without access to diffusion internals, which P2P requires.

Connection to InstructNeRF2NeRF

Text-only diffusion priors struggle on reconstructed scenes because each view would need a perfectly faithful textual description, often causing blur or divergence. InstructNeRF2NeRF (I2N2) resolves this by embedding InstructPix2Pix (IP2P) inside an **Iterative Dataset Update** loop that edits supervision images *in the Stable-Diffusion–style latent space* and then retrains the NeRF. At a high level, each cycle consists of:

- **Original capture anchoring:** Use the unedited capture I_v^0 as conditioning to preserve scene identity, viewpoint geometry, and fine detail.
- **Latent-space editing:** Edit the current NeRF render I_v^i in the latent domain using the instruction c_T and guidance scales (s_I, s_T).
- **Dataset refinement:** Replace the edited images in the training set and fine-tune the NeRF on this partially updated dataset.

Repetition consolidates potentially inconsistent per-view edits into a *single, 3D-consistent* solution.

Method

The core mechanism is an **Iterative Dataset Update (Iterative DU)** that alternates between latent-space editing of training views with InstructPix2Pix (IP2P) and NeRF optimization on the evolving dataset. Rather than modifying the NeRF loss directly with diffusion gradients, as in Score Distillation Sampling (SDS), edits are injected *indirectly* by refreshing the supervision images. This design retains the stability of conventional NeRF optimization while leveraging the semantic power of diffusion models.

Editing a single dataset image

Given a calibrated view v with original capture I_v^0, current render I_v^i from the evolving NeRF, and a global instruction c_T, IP2P outputs an updated image

$$I_v^{i+1} \leftarrow U_\theta\big(I_v^i, t; I_v^0, c_T\big),$$

where U_θ denotes the *latent-domain* editing pipeline:

$$\begin{aligned}
z_{I,0} &= \mathscr{E}(I_v^0) && \text{(encode original capture for image conditioning } c_I\text{)},\\
z_0 &= \mathscr{E}(I_v^i) && \text{(encode current NeRF render)},\\
z_t &= \text{ForwardDiffuse}(z_0, t) && \text{(add noise in latent space)},\\
\hat{\varepsilon} &= \varepsilon_\theta(z_t; t, c_I{=}z_{I,0}, c_T) && \text{(IP2P U-Net noise prediction with dual conditioning)},\\
\tilde{z}_0 &= \text{Denoise}(z_t, \hat{\varepsilon}, s_I, s_T) && \text{(classifier-free guidance with } s_I, s_T\text{)},\\
I_v^{i+1} &= \mathscr{D}(\tilde{z}_0) && \text{(decode edited latent to RGB)}.
\end{aligned}$$

The noise level $t \in [t_{\min}, t_{\max}]$ trades off structure preservation (lower t) versus stronger edits (higher t).

Iterative Dataset Update

At each outer iteration, the following sequence is performed:

- **Render** One or more views are rendered from the current NeRF
- **Edit in latent space** Each rendering is edited by IP2P using the original-capture latent $c_I = \mathscr{E}(I_v^0)$ and instruction c_T
- **Decode and replace** Edited latents are decoded to RGB and replace the corresponding training images
- **Retrain NeRF** Standard NeRF optimization is run on rays sampled from the full, partially edited dataset

Anchoring edits with I_v^0 prevents drift across iterations, while guidance scales (s_I, s_T) balance fidelity and edit strength. Repeated alternation reconciles per-view edits into a consistent 3D radiance field.

Training objective and relation to SDS

The NeRF is trained with a conventional photometric reconstruction loss:

$$\mathscr{L}_{\text{NeRF}} = \sum_{r \in \mathscr{R}} \big\| C_\theta(r) - \hat{C}(r) \big\|_2^2,$$

where $C_\theta(r)$ is the color predicted by the NeRF for ray r, and $\hat{C}(r)$ is the RGB from the current dataset image after any IP2P updates.

This contrasts with methods that use **Score Distillation Sampling (SDS)**, where the diffusion model provides a gradient directly on NeRF-rendered images to guide optimization toward the text prompt. While SDS can align NeRF to a description without paired data, it often yields blurry density or divergence when applied to real captures, because each camera view would require a perfectly accurate textual description.

InstructNeRF2NeRF avoids this instability by letting IP2P generate updated images that already satisfy the textual instruction. The NeRF is then trained *only* on image-level supervision, preserving the stability and geometric grounding of the reconstruction while still inheriting the semantic flexibility of diffusion editing.

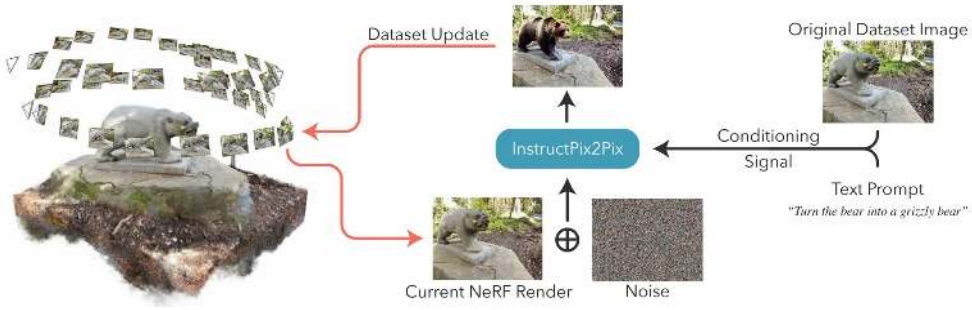

Figure 23.166: **Overview.** InstructNeRF2NeRF alternates between rendering, instruction-based 2D editing (InstructPix2Pix), dataset replacement, and continued NeRF training to gradually realize the edit in 3D. Source: [202].

Figure 23.167: **Dataset evolution.** Early edited views can be inconsistent; alternating IP2P updates with NeRF optimization consolidates them into a 3D-consistent scene. Source: [202].

Architecture and Implementation Details

Implementation follows `nerfacto` in Nerfstudio. Latent noise levels are sampled from $[t_{\min}, t_{\max}] = [0.02, 0.98]$; IP2P runs for 20 denoising steps per update. Classifier-free guidance typically uses $s_I = 1.5$ and $s_T = 7.5$. Each outer cycle updates one image ($d = 1$) and performs $n = 10$ NeRF optimization steps. Training proceeds up to 30k iterations on a single Titan RTX GPU. Hyperparameters such as edit scheduling and ray sampling strategies follow the InstructNeRF2NeRF paper [202].

Figure 23.168: **Guidance scale.** Varying the image guidance controls resemblance to the original scene; text guidance controls adherence to the instruction. Renderings are from the edited 3D scenes. Source: [202].

Experiments and Ablation

Qualitative edits span global scene changes (time of day, weather, material and style) and localized object or identity modifications while maintaining cross-view consistency across novel viewpoints.

Figure 23.169: **Qualitative results.** Diverse contextual and localized edits on real scenes, including environmental changes (e.g., time of day, weather) and object-specific modifications. These are renderings from the edited 3D scenes produced by InstructNeRF2NeRF. Source: [202].

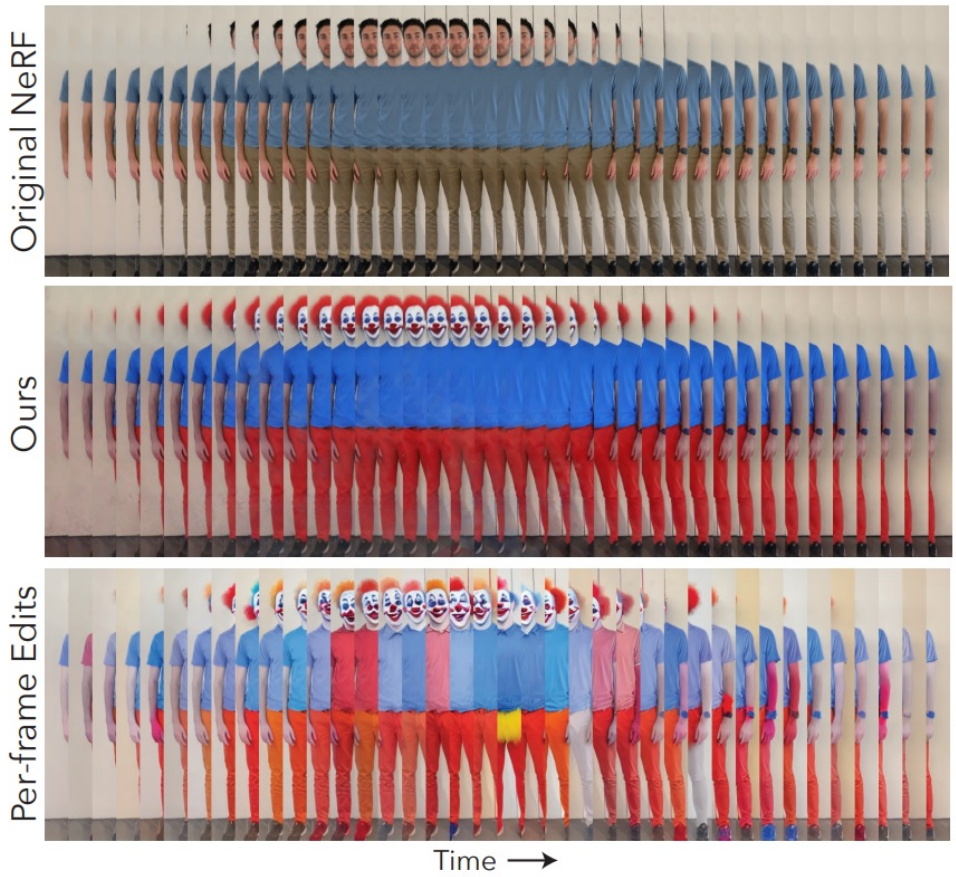

Figure 23.170: **Viewpoint consistency.** Vertical slice montage along a camera path. Top: original NeRF. Middle: InstructNeRF2NeRF with the instruction "turn him into a clown" produces consistent appearance across viewpoints. Bottom: per-frame InstructPix2Pix edits on renderings lead to inconsistencies such as changing hair and shirt colors. Source: [202].

Baselines and iterative update importance

The ablation suite isolates the impact of image conditioning and the iterative dataset update:

- **Per-frame IP2P on novel-path renderings:** Applying InstructPix2Pix independently to each rendered frame yields strong single-frame edits but significant view-to-view variance, breaking 3D consistency.
- **One-time dataset update:** Editing every training image once and training to convergence depends heavily on initial 2D consistency; typical outcomes are blurry, artifact-prone 3D scenes.
- **DreamFusion-style SDS with text-only diffusion:** Using SDS with a text-only Stable Diffusion prior on a real scene tends to diverge because each view would require an exact textual description of the entire scene.
- **SDS with InstructPix2Pix:** Image conditioning prevents divergence, yet optimization that samples only from a few full images yields unreliable supervision and more artifacts.
- **IN2N + Stable Diffusion:** Replacing IP2P with text-only Stable Diffusion inside the iterative loop produces blurry, incoherent density due to the lack of image conditioning.

Figure 23.171: **Baselines and ablations.** Left to right in each block: Original NeRF, IN2N + Stable Diffusion (no image conditioning), SDS + IP2P, One-time dataset update, and InstructNeRF2NeRF (full method with Iterative DU and IP2P). The full method best preserves geometry while producing coherent semantic edits across views. Source: [202].

Quantitative evaluation

Following the paper, two CLIP-space metrics are reported across 10 edits on two scenes: *Text–image direction similarity* (edit alignment) and *Consistency* across frames along a novel path. Results show that InstructNeRF2NeRF matches the edit strength of per-frame IP2P while achieving the best multi-view consistency.

Method	**CLIP Direction Similarity ↑**	**Consistency ↑**
Per-frame IP2P [57]	**0.1603**	0.8185
One-time DU	0.1157	0.8823
SDS + IP2P [57]	0.0266	0.9160
InstructNeRF2NeRF	0.1600	**0.9191**

Table 23.39: **Quantitative metrics.** Alignment with the textual edit and inter-frame consistency in CLIP space. InstructNeRF2NeRF preserves edit strength comparable to per-frame IP2P while achieving the best consistency. Source: [202].

Limitations and Future Work

Performance inherits the strengths and weaknesses of the 2D editor. When InstructPix2Pix fails to carry out the desired instruction or yields inconsistent 2D updates, consolidation into a clean 3D edit can fail. Challenging cases include large structural rearrangements, difficult removals, or subtle material edits that are under-specified.

Figure 23.172: **Limitations.** Top: instruction "Delete the bear statue" results in weak or inconsistent inpainting from the 2D editor, limiting 3D removal. Bottom: instruction "Give him a checkered jacket" is applied weakly and inconsistently in 2D, and the effect washes out after NeRF training. Source: [202].

Observed failure modes

- **Editor failure or ambiguity:** Certain instructions are not faithfully executed by InstructPix2Pix, leading to missing or incorrect edits in the supervision images.
- **Inconsistent 2D updates:** View-dependent differences in edited details can be irreconcilable during volumetric optimization, producing blur or artifacts.
- **Large geometric changes:** Edits that imply topological change or wide-scale geometry rearrangement remain challenging under image-conditioned editing.

Future directions

- **Stronger 3D priors during editing:** Incorporate multi-view or depth-aware constraints into the editing stage to reduce cross-view variance.
- **Structure-aware regularization:** Encourage locality and geometric plausibility (e.g., semantic masks or learned attention priors without manual annotation).
- **Interactive guidance:** Human-in-the-loop strategies to refine ambiguous instructions or correct inconsistent edits during Iterative DU.

Enrichment 23.14: NeRF: Generative & Cross-Modal Foundations

Linking NeRFs with large pretrained priors (diffusion, language) enables text-to-3D and cross-modal supervision, a step toward 3D foundation models.

- **DreamFusion** [487]: Distills a 2D text-to-image diffusion model into a NeRF for text-to-3D synthesis via score distillation.
- **Latent-NeRF / DreamFields** [427, 606]: Trains radiance fields in latent spaces or with strong 2D guidance to boost fidelity and efficiency.

Further influential works (not expanded): **Magic3D** [353], **Fantasia3D** [85] (two-stage, high-res pipelines). Mentioned for context; emphasis remains on NeRF-centric generation and cross-modal supervision.

Enrichment 23.14.1: DreamFusion: Text-to-3D with Score Distillation Sampling

DreamFusion [487] tackles the ambitious goal of generating a valid 3D NeRF model *directly from text*, without relying on paired 3D supervision. The method's central innovation is **Score Distillation Sampling (SDS)**, which couples a frozen 2D diffusion model to a differentiable renderer: the diffusion prior acts as a semantic critic that supplies image-space gradients, and these are backpropagated into a NeRF to sculpt a 3D scene consistent with the text prompt.

Motivation

The aim is to produce a valid, view-consistent 3D NeRF *from a single text caption*, i.e., without any paired multi-view images. This problem is deeply *underconstrained*: many different 3D scenes can render to images that look plausible to an image-level critic at a single viewpoint. Naively optimizing photometric appearance is therefore not enough to guarantee correct geometry.

Why "many valid 2D views" need not imply valid 3D

Even if each individual view looks correct, the training signal in text-to-3D is typically *per-step, single-view* and *unpaired across time*. This creates several loopholes:

- **No cross-view correspondence.** In supervised NeRF, *the same real scene* must simultaneously satisfy dozens of fixed cameras; pixels across views are tied by projective geometry, leaving little room for degenerate solutions. In DreamFusion-like setups, each step samples a new random camera and a fresh critic; there is no explicit constraint that a pixel explaining the "nose" in one view must correspond to the *same 3D locus* explaining the nose in later views.
- **View-dependent radiance enables per-view "explanations".** A classical NeRF uses $\mathbf{c}(\mathbf{x}, \mathbf{d})$: color may change with viewing direction $\mathbf{d}$. With only a single camera per step, a network can satisfy the critic by repainting appearance per view while keeping density nearly flat, yielding *billboards/multi-faced* artifacts.
- **Ill-posedness and missing parts.** A single projection collapses depth; occluded/back-facing regions are unobserved. Even with multiple *independently sampled* views over training, nothing forces the model to make those views arise from one coherent shape rather than a union of per-view "sheets."
- **Scale and transmittance trade-offs.** Volume rendering allows different combinations of density and color to produce similar pixel intensities; without geometric signals, optimization may settle on thin, view-specific, semi-opaque structures that look right but encode poor shape.

Intuition (the "fog sheets" thought experiment): Think of the NeRF as controlling a cube of fog. At the start there is no object at all—the model must somehow conjure a *cat* from a caption. At training step t, the diffusion critic looks from the front and asks for a cat. The simplest trick is to condense a thin fog sheet and paint on a flat image of a cat's face. From the front this looks fine. At step $t+1$, the critic moves to the side and again asks for a cat. Nothing forces the network to keep the same cat consistent across views: it can just create a new perpendicular fog sheet with a different painted cat profile. Each request is satisfied—the critic always sees "a cat" from its current angle—but the fog volume now contains multiple inconsistent 2D cats stitched together, not a single coherent 3D cat.

How DreamFusion closes the loophole

The root problem is that many distinct 3D explanations can project to equally valid 2D images. To avoid this "per-view repainting", DreamFusion changes the rules of rendering. Instead of allowing arbitrary view-dependent color, it splits appearance into *albedo* (intrinsic, view-independent surface color) and *shading* (appearance derived from surface normals and lighting). With this setup, the only way to make the same cat look correct from different angles is to actually form a stable 3D shape whose shading and albedo explain the critic's feedback. Randomized camera viewpoints and lightweight view prompts bind these perspectives together, while the diffusion prior supplies semantics and realism. The result is that 2D guidance becomes not just image supervision, but a force that sculpts consistent geometry across views—even though no ground-truth 3D scene is available as in classical NeRF training.

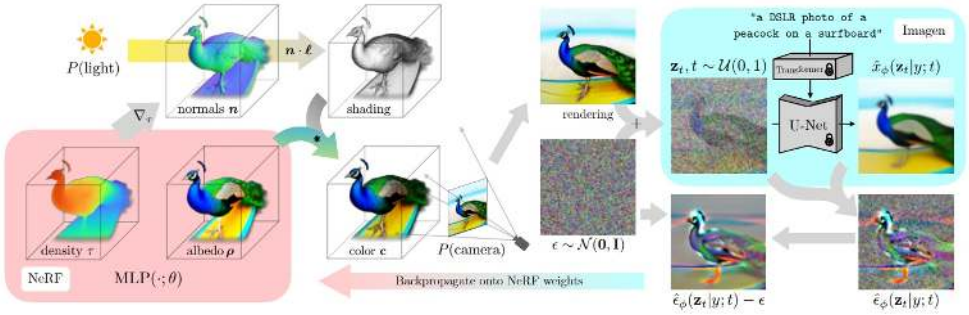

Figure 23.173: **DreamFusion training loop overview.** A NeRF parameterized by weights θ predicts two intrinsic fields: *density* $\tau(\mathbf{x})$, which encodes geometry, and *albedo* $\rho(\mathbf{x})$, the view-independent base color. Surface normals from $-\nabla_\mu \tau$ combined with randomized point lighting yield shaded renders, while volume rendering integrates along rays from randomly sampled cameras to produce 2D images. These images are noised to form $\mathbf{z}_t$, then passed with the text prompt y into a frozen text-to-image diffusion prior (Imagen). The diffusion model predicts the added noise $\hat{\varepsilon}_\phi(\mathbf{z}_t|y,t)$; comparing against the true noise ε defines the Score Distillation Sampling (SDS) loss. The residual $w(t)(\hat{\varepsilon}_\phi - \varepsilon)$ provides a low-variance update direction that is backpropagated through the differentiable renderer, adjusting NeRF parameters θ. Iterating this loop with randomized cameras and lighting gradually sculpts the fog-like NeRF volume into a coherent, view-consistent 3D object faithful to the caption. Credit: DreamFusion [487].

Method

High-level optimization loop

At each training step DreamFusion renders an image from the current 3D field, queries a frozen diffusion prior for an *image-space correction*, and backpropagates that correction into the field's parameters. The loop is:

1. **Sample view and light:** a random camera and a nearby point light are chosen; the caption is augmented with lightweight *view tokens* (front/side/overhead) to match the sampled viewpoint.
2. **Select a render mode:** one of *albedo*, *shaded*, or *textureless shaded* is chosen (described below).
3. **Render:** a differentiable volume renderer integrates density τ and albedo ρ, with shading tied to surface normals from $-\nabla\tau$.
4. **SDS guidance:** the rendered image is noised to z_t, the frozen diffusion prior predicts $\hat{\varepsilon}_\phi(z_t|y,t)$, and the residual with the injected noise ε is formed.
5. **Update:** the residual is backpropagated through the renderer and used to update NeRF parameters θ.

Foreground–background separation

A single NeRF that tries to explain both the object and the environment tends to take an easy shortcut: it smears low density across space or "repaints" colors per view, satisfying a 2D critic without sculpting a compact 3D shape. DreamFusion avoids this by giving the object and the environment *different jobs*:

- **Foreground object field.** Inside a bounded sphere, an MLP $f_\theta : \mathbf{x} \mapsto (\tau(\mathbf{x}), \rho(\mathbf{x}))$ predicts volumetric density τ (shape) and *view-independent* albedo ρ (base color). Because ρ does not depend on view direction, variability across viewpoints must come from *geometry and lighting*, not from re-painting appearance.
- **Directional background.** A lightweight function $\mathbf{b}(\hat{\mathbf{r}})$ of ray direction supplies the distant backdrop (a "skybox"). It cannot produce density or geometry—only colors—so it cannot be used to explain images by adding fog in 3D.

The renderer combines the two with standard alpha compositing:

$$C_{\text{img}} \;=\; C_{\text{fg}} + (1-A)\,\mathbf{b}(\hat{\mathbf{r}}), \qquad C_{\text{fg}} = \sum_i w_i\,\mathbf{c}_i,\;\; A = \sum_i w_i.$$

If the object along the ray is opaque ($A \approx 1$), the background is hidden; if the ray is empty ($A \approx 0$), the background shows through. Trained end-to-end with SDS, the object field learns compact shape and albedo, while the background head explains the environment without inviting density "spill". For purely scenic prompts (e.g., "a sunset"), the object field can remain nearly transparent and the background carries the content; for object-centric prompts, they cooperate naturally.

From density to orientation: making shape visible

Once foreground and background are disentangled, the next step is to make the object's *geometry* perceptible from a single rendered view. In images, 3D shape is revealed primarily through *shading*, which depends on how surfaces are oriented relative to light. To compute shading, DreamFusion derives surface orientation directly from the NeRF's density field.

The volumetric density $\tau(\mathbf{x})$ is a scalar field: low in empty space, high inside the object. Its gradient $\nabla_{\mathbf{x}}\tau$ points toward the direction of steepest increase, i.e., into the solid. Flipping the sign yields an outward-pointing vector aligned with the local surface normal:

$$\mathbf{n}(\mathbf{x}) \propto -\nabla_{\mathbf{x}}\tau(\mathbf{x}), \qquad \hat{\mathbf{n}} = \frac{\sum_i w_i \mathbf{n}_i}{\sum_i w_i},$$

where the ray-normal $\hat{\mathbf{n}}$ is an opacity-weighted average of sample-level normals. This construction provides the critic with orientation cues even though the NeRF never predicts normals explicitly.

With normals available, DreamFusion can introduce randomized lighting. A point light direction $\hat{\mathbf{l}}$, ambient term ℓ_a, and diffuse color ℓ_ρ define a Lambertian shading factor:

$$s_i = \ell_a + \ell_\rho \cdot \max\{0, \langle \mathbf{n}_i, \hat{\mathbf{l}} \rangle\}.$$

This factor modulates albedo ρ_i at each sample to yield intensity variations that depend on surface curvature.

By alternating whether albedo is included, modulated, or removed, DreamFusion creates complementary renderings that expose different signals about appearance and shape. These become the three render modes described next, each designed to steer the critic's gradients toward the right part of the scene representation.

Render modes: complementary recipes for supervision

The object head always outputs the same raw ingredients at each 3D point: volumetric density $\tau(\mathbf{x})$ (which sculpts shape) and albedo $\rho(\mathbf{x})$ (the base, unlit color). From τ we also derive a surface normal via $-\nabla\tau$, and with a randomized light we compute a shading factor s. The three render modes are not extra networks, but three different *recipes* for combining these ingredients into a 2D image. By showing the critic different combinations, DreamFusion exposes both texture and geometry.

- **Albedo (color only).**

  $$\mathbf{c}_i^{\text{alb}} = \rho_i.$$

  This mode shows the critic just the raw pigment without any lighting. It ensures that caption semantics (e.g. "a red apple") anchor to the right places in the 3D volume. Gradients flow mainly into albedo ρ, with weaker updates to density τ through transmittance. On its own, however, this admits the "billboard" shortcut: painting a flat plane with the right texture.

- **Shaded (color + light).**

  $$\mathbf{c}_i^{\text{shaded}} = \rho_i \odot s_i, \qquad s_i = \ell_a + \ell_\rho \max\{0, \langle \mathbf{n}_i, \hat{\mathbf{l}} \rangle\}, \;\; \mathbf{n}_i \propto -\nabla_{\mathbf{x}}\tau(\mathbf{x}_i).$$

  Here the albedo is modulated by diffuse shading. Because s_i depends on surface normals, and normals depend on $\nabla\tau$, feedback now flows through the density field as well as the albedo. This couples appearance to geometry: the critic's judgment of brightness directly sharpens the shape.

- **Textureless shaded (shape only).**

  $$\mathbf{c}_i^{\text{texless}} = s_i \quad (\rho \equiv \mathbf{1}).$$

  By setting albedo to white, the only variations in the rendered image come from light and surface orientation. The critic can no longer be satisfied by painting details onto flat surfaces: the only way to improve is to refine geometry so that shading patterns look realistic. Gradients thus flow almost exclusively into τ.

Why alternate between all three? Each mode alone is insufficient. Albedo anchors colors but ignores shape; textureless shading enforces shape but discards semantics; shaded rendering mixes both but can be ambiguous about whether an error is due to color or geometry. By cycling among them, DreamFusion forces the critic's gradients to supervise *both* appearance and geometry, closing off shortcuts and gradually sculpting a coherent 3D object.

This sets up the final ingredient: a way to turn the critic's judgment into gradients. The critic is a frozen text-to-image diffusion model, and the mechanism is *Score Distillation Sampling (SDS)*, described next.

Score Distillation Sampling: turning a 2D prior into 3D updates

Goal. Use a frozen 2D diffusion model as a critic to guide a 3D NeRF. The critic never trains; only the NeRF parameters θ are updated.

Rendering and forward noising. For a sampled camera, light, and render mode $m \in \{\text{alb}, \text{shaded}, \text{texless}\}$, render

$$x^{(m)}(\theta) \in \mathbb{R}^{H\times W\times 3}.$$

Draw timestep t and add VP noise:

$$z_t = \alpha_t\, x^{(m)}(\theta) + \sigma_t\, \varepsilon, \qquad \varepsilon \sim \mathcal{N}(0, I), \quad \alpha_t^2 + \sigma_t^2 = 1.$$

Frozen critic (diffusion prior). The diffusion network predicts the injected noise

$$\hat{\varepsilon}_\phi = \hat{\varepsilon}_\phi(z_t \,|\, y, t)$$

(with CFG inside the call). If the render already lies on the prompt manifold, $\hat{\varepsilon}_\phi \approx \varepsilon$; otherwise the difference $(\hat{\varepsilon}_\phi - \varepsilon)$ is a pixel-space correction.

SDS gradient (definition and derivation). DreamFusion *defines* the update via the critic's score, chained through the renderer:

$$\nabla_\theta \mathscr{L}_{\text{SDS}}(\theta) = \mathbb{E}_{t,\varepsilon}\left[w(t)\left(\hat{\varepsilon}_\phi(z_t \,|\, y, t) - \varepsilon\right) \frac{\partial x^{(m)}}{\partial \theta} \right].$$

Diffusion theory gives $\nabla_{z_t} \log p_\phi(z_t \,|\, y) \propto -(\hat{\varepsilon}_\phi - \varepsilon)/\sigma_t$, so the term $\left(\hat{\varepsilon}_\phi - \varepsilon\right)$ is an *image-space residual direction*. No gradient flows through $\hat{\varepsilon}_\phi$; all learning happens by multiplying this residual with the renderer Jacobian $\partial x^{(m)}/\partial\theta$.

How the image residual becomes NeRF updates. Let $G \doteq w(t)\,(\hat{\varepsilon}_\phi - \varepsilon) \in \mathbb{R}^{H\times W\times 3}$. Then

$$\nabla_\theta \mathscr{L}_{\text{SDS}} = \left\langle G,\, \frac{\partial x^{(m)}}{\partial \theta} \right\rangle = \sum_{\text{pixels } p} G_p^\top \frac{\partial x_p^{(m)}}{\partial \theta}.$$

For a pixel p with ray samples $\{\mathbf{x}_i\}_{i=1}^N$,

$$C = \sum_{i=1}^N w_i\, \mathbf{c}_i, \quad A = \sum_{i=1}^N w_i, \quad w_i = T_i\, \alpha_i, \quad T_i = \prod_{j<i}(1-\alpha_j), \quad \alpha_i = 1 - e^{-\tau_i \delta_i}.$$

Useful partials:

$$\frac{\partial \alpha_i}{\partial \tau_i} = \delta_i e^{-\tau_i \delta_i} = \delta_i (1-\alpha_i), \qquad \frac{\partial C}{\partial \rho_i} = w_i \mathbf{I}_3.$$

We keep the standard NeRF transmittance pathway symbolic via $\frac{\partial C}{\partial \alpha_i}$, which accounts for how changing opacity at any sample modulates all farther contributions through T_k ($k \geq i$).

Mode-specific decompositions. The render mode m sets $\mathbf{c}_i$ and therefore which parameters receive strong gradients.

Albedo (unlit): appearance-centric updates

$\mathbf{c}_i^{\text{alb}} = \rho_i$.

Chain rule:

$$\frac{\partial x^{\text{alb}}}{\partial \theta} = \sum_i \underbrace{\frac{\partial C}{\partial \rho_i}}_{w_i} \frac{\partial \rho_i}{\partial \theta} + \sum_i \underbrace{\frac{\partial C}{\partial \alpha_i}}_{\text{via } T,\, w} \underbrace{\frac{\partial \alpha_i}{\partial \tau_i}}_{\delta_i(1-\alpha_i)} \frac{\partial \tau_i}{\partial \theta}.$$

Effect. The first sum (strong) refines ρ (textures/colors). The second (weaker) adjusts τ only through transmittance—insufficient to robustly sculpt geometry on its own.

Shaded color (lit): coupled appearance→geometry updates

$\mathbf{c}_i^{\text{shaded}} = \rho_i \odot s_i, \qquad s_i = \ell_a + \ell_\rho \cdot \max\{0, \langle \mathbf{n}_i, \hat{\mathbf{l}} \rangle\}, \quad \mathbf{n}_i \propto -\nabla_{\mathbf{x}} \tau(\mathbf{x}_i)$.

Chain rule (grouping terms):

$$\frac{\partial x^{\text{shaded}}}{\partial \theta} = \underbrace{\sum_i \frac{\partial C}{\partial \rho_i} \frac{\partial (\rho_i \odot s_i)}{\partial \rho_i} \frac{\partial \rho_i}{\partial \theta}}_{\text{appearance (as in albedo)}} + \underbrace{\sum_i \frac{\partial C}{\partial \mathbf{c}_i} \frac{\partial (\rho_i \odot s_i)}{\partial \mathbf{n}_i} \frac{\partial \mathbf{n}_i}{\partial \tau_i} \frac{\partial \tau_i}{\partial \theta}}_{\text{geometry via normals}} + \underbrace{\sum_i \frac{\partial C}{\partial \alpha_i} \frac{\partial \alpha_i}{\partial \tau_i} \frac{\partial \tau_i}{\partial \theta}}_{\text{geometry via transmittance}}.$$

Effect. Two geometry channels appear: (i) via normals ($\mathbf{n}_i \propto -\nabla\tau$, which introduces derivatives of $\nabla\tau$ w.r.t. θ; autodiff handles these), and (ii) via α. Shaded mode therefore sculpts τ while still refining ρ.

Textureless shaded (lit, no texture): pure geometry updates

$\mathbf{c}_i^{\text{texless}} = s_i \quad (\rho \equiv \mathbf{1})$.

Chain rule:

$$\frac{\partial x^{\text{texless}}}{\partial \theta} = \underbrace{\sum_i \frac{\partial C}{\partial \mathbf{c}_i} \frac{\partial s_i}{\partial \mathbf{n}_i} \frac{\partial \mathbf{n}_i}{\partial \tau_i} \frac{\partial \tau_i}{\partial \theta}}_{\text{geometry via normals}} + \underbrace{\sum_i \frac{\partial C}{\partial \alpha_i} \frac{\partial \alpha_i}{\partial \tau_i} \frac{\partial \tau_i}{\partial \theta}}_{\text{geometry via transmittance}}.$$

Effect. With ρ removed, *all* signal flows into τ. The only way to please the critic is to improve geometry (normals/curvature and occupancy).

Intuition. SDS provides a pixel-space "correction image". The renderer's Jacobian routes that correction into ρ in albedo mode, and into τ (via normals and opacity) in shaded/textureless modes. Cycling the three modes resolves the classic ambiguity: albedo learns caption-faithful appearance; shaded couples appearance to curvature; textureless removes the paintbrush entirely, hardening geometry. High CFG increases realism of the supervising direction but may reduce diversity; $w(t)$ balances contribution across noise levels.

View sampling and view-aware prompting

Each iteration samples a random camera (azimuth, elevation, distance, focal multiplier) and a point light near the camera. Captions are augmented with lightweight *view tokens* (front/side/overhead) to align the diffusion prior's expectations with the current viewpoint. Because albedo ρ is view-independent, variation across views must be accounted for by *geometry and lighting*, encouraging one coherent 3D asset rather than per-view repainting.

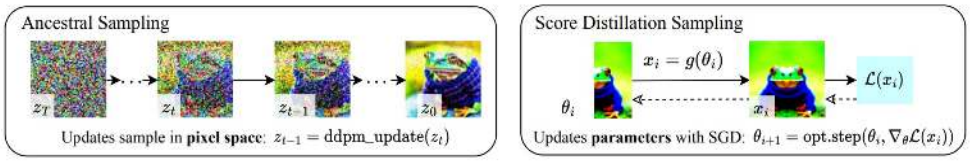

Figure 23.174: **Sampling an image vs. sculpting a 3D field.** *Left (ancestral diffusion):* a standard diffusion model synthesizes a 2D image by denoising $z_T \to z_0$ directly in pixel space. *Right (SDS in DreamFusion):* the diffusion model is used as a *critic*. A NeRF render $x = g(\theta)$ is noised to $z_t = \alpha_t x + \sigma_t \varepsilon$; the model predicts $\hat{\varepsilon}_\phi$, and the residual $(\hat{\varepsilon}_\phi - \varepsilon)$ becomes an image-space update that is backpropagated through the differentiable renderer to adjust the NeRF parameters θ. Thus, SDS does not generate pixels; it provides gradients that *sculpt* the 3D field. Credit: DreamFusion [487].

Putting the loop together

Each iteration interleaves appearance- and geometry-focused signals so that SDS sculpts both ρ and τ:

1. **Sample view and light.** Draw a random camera and a point light; add *view tokens* (front, side, overhead, etc.) to the caption.
2. **Pick a render mode.** Alternate among *albedo* (anchors color semantics), *shaded* (injects curvature/normal cues), and *textureless shaded* (removes texture shortcuts to force geometry).
3. **Render and diffuse.** Render $x^{(m)}(\theta)$ at low resolution; sample t and form $z_t = \alpha_t x^{(m)} + \sigma_t \varepsilon$.
4. **Apply SDS.** Evaluate $\hat{\varepsilon}_\phi(z_t|y,t)$; form $g_t = w(t)(\hat{\varepsilon}_\phi - \varepsilon)$; backpropagate g_t through the renderer to update θ.

Albedo steps maintain caption-faithful appearance; shaded steps sharpen geometry via normal-dependent shading; textureless steps consolidate shape by eliminating albedo as a degree of freedom. View-aware prompting stabilizes semantics across viewpoints, randomized lighting diversifies geometric cues, and background factorization prevents degenerate density fills—together converting 2D diffusion feedback into reliable, 3D-consistent supervision.

Implementation Details

Frozen diffusion prior

DreamFusion employs the *base* Imagen model at 64×64 with classifier-free guidance and a strong language encoder (e.g., T5-XXL). Larger guidance typically improves realism at the cost of diversity.

Foreground–background composition

The object field is confined to a bounded sphere to discourage diffuse density spread. The background head provides direction-conditioned colors and is alpha-composited via transmittance, yielding object-centric assets without fog.

Experiments and Ablation

Qualitative gallery and comparisons

DreamFusion produces diverse, compositionally rich assets with multi-view consistency and clean geometry.

Figure 23.175: **DreamFusion gallery of text-to-3D assets.** Each cell shows results for one text prompt (examples include *"a raccoon astronaut holding his helmet"*, *"a baby bunny sitting on top of a stack of pancakes"*, *"a sliced loaf of fresh bread"*, and *"Sydney Opera House, aerial view"*). For every prompt, two novel viewpoints demonstrate *multi-view consistency* of the learned 3D NeRF. Insets provide disentangled visualizations: *textureless shading* reveals the learned geometry independent of albedo, while *normal maps* expose smooth surfaces and curvature. The collection highlights DreamFusion's ability to (i) synthesize creative and compositional scenes (e.g., *a robot and dinosaur playing chess*), (ii) generate faithful geometry and detailed textures across diverse categories (animals, food, vehicles, architecture), and (iii) disentangle shape from appearance by supervising both albedo and geometry. Prompt modifiers ($*$, †, ‡) correspond to stylistic cues improving realism. Videos and interactive results available at `dreamfusion3d.github.io`. *Credit:* DreamFusion [487].

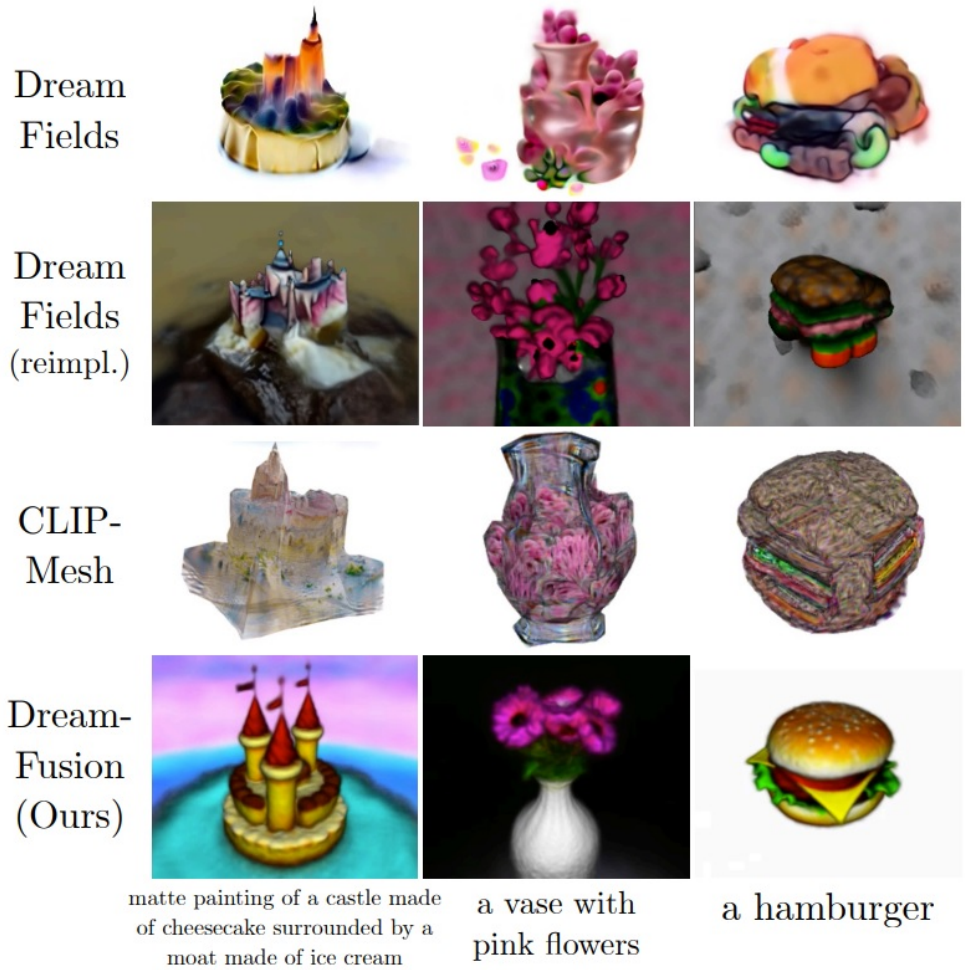

Figure 23.176: **Qualitative comparison of text-to-3D methods.** Each column corresponds to the same text prompt (e.g., *"a matte painting of a castle made of cheesecake surrounded by a moat made of ice cream"*, *"a vase with pink flowers"*, *"a hamburger"*); The figure compares between Dream Fields (original), Dream Fields (reimplementation) [258], CLIP-Mesh [548], and DreamFusion. *Dream Fields* often produces amorphous, low-detail shapes with color patterns loosely matching the text. *CLIP-Mesh* improves geometric definition (e.g., a recognizable vase or castle) but introduces noisy, unrealistic textures typical of CLIP-guided optimization. *DreamFusion*, guided by a diffusion prior via SDS, produces coherent 3D structures with clean silhouettes, semantically faithful details, and plausible textures across views. *Credit:* DreamFusion [487].

Caption–image coherence via CLIP retrieval

Goal. To test whether generated 3D assets truly match their captions, DreamFusion evaluates *caption–image coherence* using CLIP retrieval, following the protocol in [487]. CLIP serves as a frozen "judge" that compares rendered images against text captions.

Metric (R-Precision). The evaluation is framed as a retrieval task:

- Render an image from the 3D model (two views per asset).
- Present CLIP with this image and its correct caption, alongside 40 random distractor captions.
- Count success if CLIP assigns the highest similarity to the correct caption.

R-Precision is the fraction of correct matches. Higher values indicate stronger text–image alignment.

Encoders. Results are reported across three CLIP backbones: B/32, B/16, and L/14. This ensures robustness across different embedding granularities.

Two evaluation modes. To disentangle appearance from geometry, renders are produced under two conditions:

- **Color renders:** full shaded images that test *joint shape and texture* alignment.
- **Textureless renders ("Geo"):** albedo removed, leaving only shading from geometry. This isolates whether the 3D *shape alone* matches the caption, eliminating texture-only shortcuts.

Caveat. Baselines like Dream Fields and CLIP-Mesh are trained directly with CLIP supervision. Their scores may be optimistic when evaluated with the *same* CLIP family, while DreamFusion relies on a diffusion prior (Imagen) and therefore does not benefit from this alignment.

Table 23.40: **CLIP R-Precision (%) on object-centric COCO.** "Geo" uses *textureless* shaded renders (albedo removed) to test geometry–text alignment. † evaluated with one seed. Baseline numbers in parentheses may be inflated when training and evaluation share the same CLIP model.

Method	CLIP B/32		CLIP B/16		CLIP L/14	
	Color	Geo	Color	Geo	Color	Geo
GT Images	77.1	–	79.1	–	–	–
Dream Fields (reimpl.) [258]	68.3	–	74.2	–	–	–
CLIP-Mesh [548]	67.8	–	75.8	–	74.5†	–
DreamFusion	**75.1**	**42.5**	**77.5**	**46.6**	**79.7**	**58.5**

Findings.

- **Color renders.** DreamFusion matches or surpasses prior work across all CLIP backbones, confirming strong *caption–appearance* coherence. Generated models are not only textured plausibly but also semantically faithful to prompts.
- **Textureless renders.** DreamFusion achieves much higher R-Precision than baselines. This shows that even without texture, the geometry itself is aligned with the caption. By contrast, CLIP-supervised methods often rely on painting textures onto weak shapes.
- **Mechanism.** These gains come from DreamFusion's design: *view-independent albedo*, shading-based supervision, and Score Distillation Sampling. Together, they prevent degenerate "billboard" solutions and force the model to sculpt volumetric geometry that remains recognizable even when stripped of texture.

In summary, CLIP retrieval confirms that DreamFusion succeeds not just at painting caption-faithful textures but also at learning consistent 3D geometry that aligns with the text prompt.

Ablations: what unlocks geometry?

What we test. Starting from a minimal setup, components are added one at a time to see which choices turn 2D supervision into reliable 3D shape:

- **View-aware prompting.** Append tokens that match the sampled camera (e.g., *front*, *side*, *back*, *overhead*) so the text prior "expects" the current viewpoint.
- **View-independent reflectance (with normals).** Replace a view-dependent RGB head with an object field that outputs density τ and *view-independent* albedo ρ; compute surface normals from the density gradient ($\mathbf{n} \propto -\nabla\tau$) and use them for shading.
- **Randomized diffuse lighting.** Sample a point light (typically near the camera) every step so different parts of the surface are illuminated over training.
- **Textureless shaded passes.** Interleave renders where albedo is removed ($\rho \equiv \mathbf{1}$) so the image depends only on geometry through shading.

Why they matter.

- **View tokens $\Rightarrow$ single identity across views.** Without them, the critic judges each view in isolation; the model can learn *Janus* artifacts (multi-faced subjects) and flat, view-specific fixes. Aligning the caption to the camera ties all views to the *same* object.
- **View-independent ρ + normals $\Rightarrow$ "paint" no longer helps.** When color cannot vary with view, appearance changes must come from *lighting on geometry*. Normals derived from $-\nabla\tau$ route supervision into τ, improving curvature and smoothness rather than re-painting per view.
- **Random lighting $\Rightarrow$ all bumps get seen.** A fixed light can hide geometry on the dark side. Varying light direction exposes different surface patches across steps, yielding denser, less biased geometric gradients.
- **Textureless passes $\Rightarrow$ unambiguous shape signal.** Removing albedo eliminates the "texture shortcut". The only way to satisfy the critic is to sculpt τ so shading alone explains the image. *Trade-off:* overuse can encourage carving high-contrast texture edges into geometry, so these passes are interleaved rather than used exclusively.

Empirical takeaway. In the ablation (see the below figure), improvements are smallest on *albedo* evaluations and largest on *shaded/textureless* evaluations—precisely where geometry matters. The progression

1. base (no view tokens),
2. + view-aware prompting,
3. + lighting/shaded renders,
4. + textureless shaded passes

monotonically increases geometry-sensitive R-Precision and visually turns multi-faced, flat subjects into smooth, volumetric shapes with cleaner silhouettes.

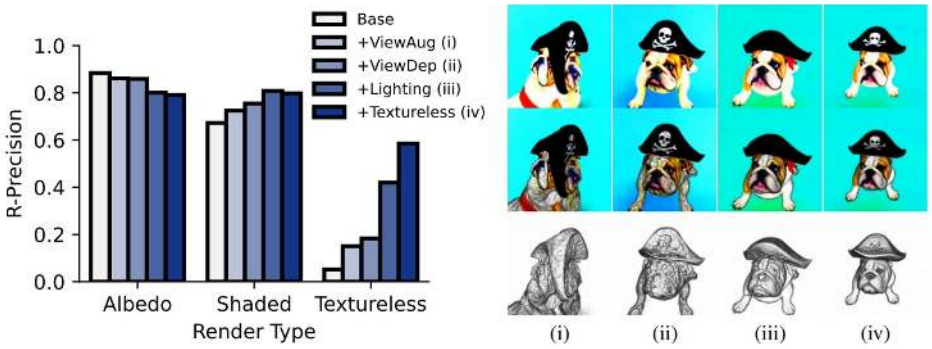

Figure 23.177: **Ablation: components that improve geometry.** *Left:* CLIP L/14 R-Precision measured on three evaluation renders (Albedo, Shaded, Textureless) as components are added. Gains are largest for geometry-sensitive evaluations (Shaded/Textureless). *Right:* Prompt "A bulldog is wearing a black pirate hat". Progression shows: base → +view tokens → +lighting → +textureless shading. Tokens stabilize semantics; lighting exposes curvature; textureless passes remove the billboard shortcut and yield more volumetric geometry. *Credit:* DreamFusion [487].

Iterative refinement and compositional editing

Editing protocol. DreamFusion allows continued optimization from intermediate checkpoints. A single NeRF is retained while the caption is modified, and SDS fine-tuning resumes on the updated text. This means new content is *composed onto* the existing asset rather than starting over.

What this enables.

- Start from a base object (e.g., *"a squirrel"*).
- Add attributes sequentially: *"wearing a leather jacket"*, then *"riding a motorcycle"*. Each edit accumulates without breaking identity or view consistency.
- Branch into creative variants: the same squirrel can be edited to be *"carved out of wood"*, or placed in new environments like *"on a road made of ice"* vs. *"through a field of lava"*.

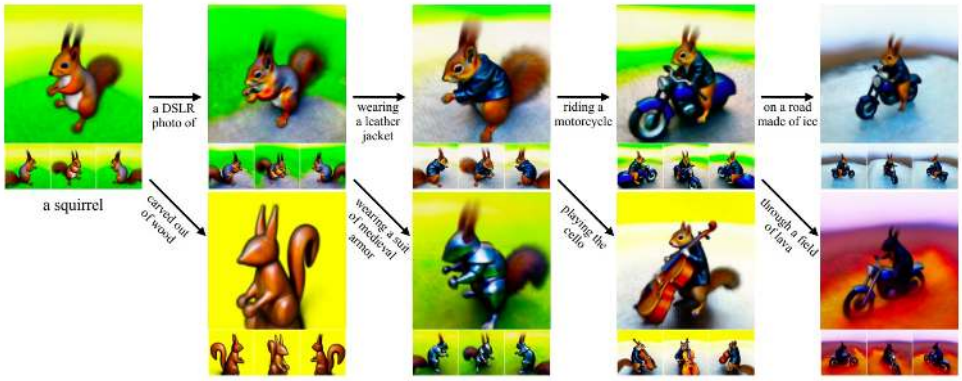

Figure 23.178: **Iterative refinement with compositional editing.** From a base model, optimization continues as the text is edited (attributes, style, background). Top rows show two novel views per edit; strips give additional viewpoints. Because a *single* NeRF is optimized throughout, new attributes are layered onto the same geometry rather than regenerated from scratch, maintaining view consistency and identity while enabling interactive scene building. *Credit:* DreamFusion [487].

Limitations and Future Work

While DreamFusion establishes a powerful pipeline for text-to-3D generation, several limitations remain:

- **Diversity vs. guidance.** Extremely strong classifier-free guidance (CFG) is required to achieve high-fidelity supervision. This often induces *mode seeking*, reducing sample diversity across random seeds and causing repeated "canonical" solutions for a given prompt.
- **Material and lighting realism.** The use of diffuse Lambertian shading simplifies training but underrepresents specular highlights, translucency, and complex BRDF effects. As a result, generated assets often appear matte or plasticky rather than photorealistic.
- **Scene complexity.** DreamFusion is fundamentally *object-centric*: it assumes a single foreground object within a bounded volume and a separate background. This restricts its ability to model multi-object interactions, cluttered layouts, or spatially structured environments.
- **Compute bottleneck.** The most significant drawback is efficiency. SDS guidance requires repeatedly rendering full-resolution images from the NeRF and passing them through the frozen diffusion prior. This is slow and memory-intensive, limiting scalability and making interactive use challenging.

These limitations motivated subsequent methods that trade DreamFusion's *image-space guidance* for more efficient *latent-space guidance*. Approaches such as **LatentNeRF** [427], **Fantasia3D** [85], and **Magic3D** [353] directly distill supervision from latent diffusion models (e.g., Stable Diffusion) rather than pixel-space denoisers. This substantially reduces computational cost while preserving geometric consistency. In addition, Fantasia3D explores disentangled control over *geometry* and *appearance*, addressing the shading/material realism issue, while Magic3D introduces a coarse-to-fine optimization pipeline that improves both detail and efficiency.

Looking forward, promising directions include:

- **Diversity-aware guidance**, balancing CFG fidelity with variability.
- **Richer reflectance models**, capturing specularities and complex light transport.
- **Scene-level modeling**, extending beyond single objects to structured, multi-object environments.
- **Hybrid pipelines**, combining DreamFusion's explicit geometry supervision with latent diffusion efficiency, as seen in later works.

In the next part, we examine **LatentNeRF**, a direct response to DreamFusion's computational bottlenecks, which achieves faster optimization by shifting SDS guidance from image-space to latent-space, while also keeping/improving the resultant image quality.

Enrichment 23.14.2: Latent-NeRF for Shape-Guided 3D Generation

Motivation

From DreamFusion to Latent-NeRF

DreamFusion 23.14.1 established that a powerful *2D* text-to-image diffusion model can supervise a *3D* NeRF via Score Distillation Sampling (SDS), but it operates in RGB space and originally relied on a heavy, proprietary backbone (Imagen). Latent-NeRF adopts the same SDS principle yet relocates supervision and rendering into *Stable Diffusion's VAE latent space Z*, thereby reducing computational load while maintaining multi-view consistency through NeRF's volumetric rendering. Beyond efficiency, the central goal is *controllability*: text-only guidance is underconstrained in 3D, so the paper introduces **Sketch-Shape** geometry guidance and **Latent-Paint** for texturing explicit meshes.

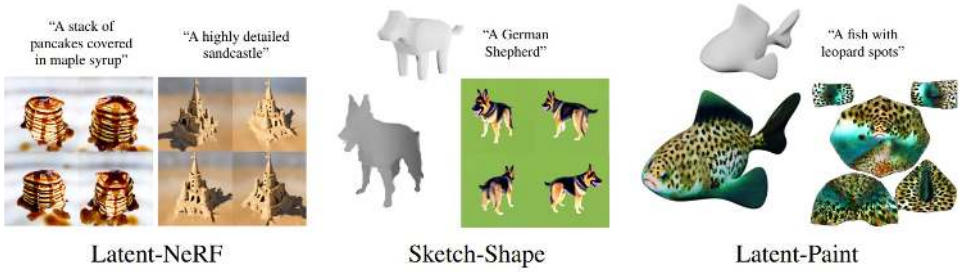

Figure 23.179: **Latent-NeRF's three text-guided modes.** Left: *Latent-NeRF* (text-only text-to-3D). Middle: *Sketch-Shape* for coarse shape control. Right: *Latent-Paint* for text-guided texture on explicit shapes. The top row shows inputs. Examples include: "A stack of pancakes covered in maple syrup", "A highly detailed sandcastle", "A German Shepherd", and "A fish with leopard spots". Source: [427].

Why latent supervision

Volumetric rendering is fundamentally a linear operation that blends feature vectors along rays. The convolutional encoder used in the VAE ensures that each latent vector at coordinate (u, v) encodes a localized patch of pixels, often called a *super-pixel*. These super-pixels preserve **spatial coherence**, so interpolating them along a ray produces meaningful blends in latent space. Empirically, decoding linear combinations of latents results in plausible local textures and structures, just as decoding linearly blended RGB colors yields plausible photometric mixtures. This property justifies treating $\mathbf{Z}$ (typically $64\times64\times4$) as a continuous radiance field suitable for NeRF-style volume rendering, even though its channels are abstract features rather than raw RGB.

In effect, the latent radiance field serves as a dense 3D representation in which NeRF's differentiable rendering can be applied directly, producing latent images that are natively compatible with Stable Diffusion's denoiser. This eliminates the bottleneck of pixel-to-latent encoding at each iteration and allows gradients from the diffusion model to flow efficiently into the NeRF.

Method

Overview and connection to DreamFusion

Latent-NeRF builds directly on the **Score Distillation Sampling (SDS)** framework introduced in DreamFusion, but shifts the entire process into the latent space. Whereas DreamFusion renders RGB images from NeRF and then re-encodes them into latents for diffusion guidance, Latent-NeRF trains a NeRF whose outputs are *already latents*. This simple yet powerful modification removes redundant encoding steps and ensures consistency between the NeRF's output domain and the Stable Diffusion denoiser.

Concretely, the NeRF MLP maps a 5D input—3D position plus 2D viewing direction—to a volume density σ and a 4-dimensional latent feature vector $\mathbf{c} \in \mathbb{R}^4$. Standard volumetric rendering integrates these outputs along each ray, yielding a latent image

$$\mathbf{z} \in \mathbb{R}^{64\times64\times4}.$$

At each training step, Latent-NeRF applies SDS in latent space:

1. A random diffusion time t is sampled.
2. Gaussian noise ε is added to the rendered latent $\mathbf{z}$, producing $x_t = \sqrt{\alpha_t}\mathbf{z} + \sqrt{1-\alpha_t}\varepsilon$.
3. The frozen Stable Diffusion denoiser $\varepsilon_\phi(x_t, T, t)$ predicts the noise, conditioned on the text prompt T.
4. The SDS gradient is computed from the residual $(\varepsilon_\phi - \varepsilon)$, which backpropagates through the rendering process to update the NeRF parameters θ.

This procedure is structurally analogous to DreamFusion, but by performing all operations in the latent domain, Latent-NeRF achieves both **efficiency** and **training stability**. Subsequent refinement stages can optionally decode the latent radiance field back into RGB using the VAE decoder, enabling high-fidelity visualization while retaining the computational benefits of latent-space supervision.

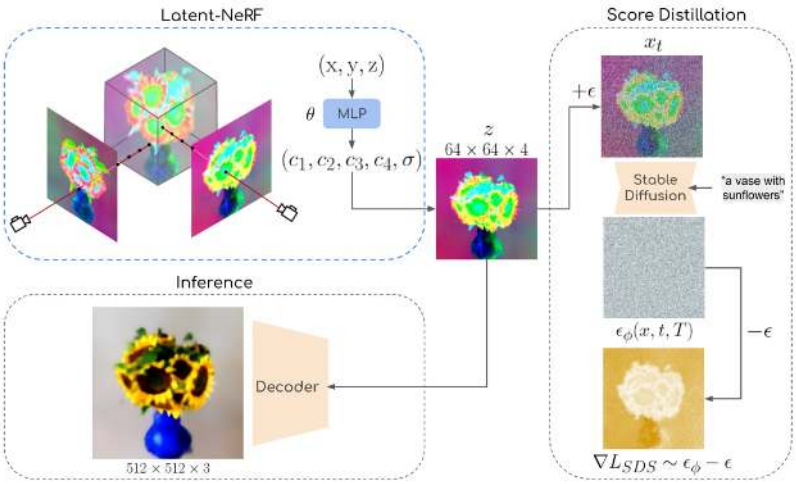

Figure 23.180: **Overview of latent-space SDS for Latent-NeRF.** A rendered latent map $\mathbf{z}$ is noised at time t and denoised by Stable Diffusion; the difference between predicted and injected noise yields gradients that update the NeRF in latent space. Inference decodes $\mathbf{z}$ to RGB via the VAE decoder. Source: [427].

NeRF in Stable Diffusion latent space

Given a point $\mathbf{x}$ and view direction, the MLP outputs (c_1, c_2, c_3, c_4) and density σ. Standard volumetric rendering aggregates these along the ray to yield $\mathbf{z}$. This retains the multi-view coupling of NeRF while aligning supervision to the latent domain where the teacher denoiser operates.

SDS in latent space

At each step, with $\varepsilon \sim \mathcal{N}(0, I)$ and schedule constant $\bar{\alpha}_t$,

$$x_t \;=\; \sqrt{\bar{\alpha}_t}\, x \;+\; \sqrt{1-\bar{\alpha}_t}\, \varepsilon, \tag{23.79}$$

and the per-pixel SDS gradient is

$$\nabla_x \mathscr{L}_{\text{SDS}} \;=\; w(t)\,\big(\varepsilon_\phi(x_t, t, T) \;-\; \varepsilon\big), \tag{23.80}$$

where ε_ϕ denotes the denoiser, T is the prompt, and $w(t)$ depends on the noise schedule. Latent-NeRF minimizes

$$\mathscr{L} \;=\; \lambda_{\text{SDS}}\, \mathscr{L}_{\text{SDS}} \;+\; \lambda_{\text{sparse}}\, \mathscr{L}_{\text{sparse}}, \tag{23.81}$$

with $\mathscr{L}_{\text{sparse}} = \text{BE}(w_{\text{blend}})$ to suppress floaters/background fog.

Step-by-step training loop

```
# Pretrained Stable Diffusion: encoder E, decoder D, UNet eps_phi
# Radiance field f_theta: (x, y, z, d) -> (c1..c4, sigma)

for step in range(num_steps):
    # 1) Random camera pose; render latent z via volumetric rendering
    z = render_latent(f_theta, sample_camera())

    # 2) Pick diffusion time t and add noise
    t   = sample_t()
    eps = torch.randn_like(z)
    x_t = sqrt(alpha_bar[t]) * z + sqrt(1 - alpha_bar[t]) * eps

    # 3) Denoise with text T and form SDS gradient wrt z
    eps_pred = eps_phi(x_t, t, T)                # Stable Diffusion UNet
    g_sds    = w(t) * (eps_pred - eps)

    # 4) Backprop through rendering to update theta
    loss_main   = (g_sds.detach() * z).sum()     # autograd handles chain rule
    loss_sparse = binary_entropy(w_blend(z))
    loss        = lambda_sds*loss_main + lambda_sparse*loss_sparse
    loss.backward(); optimizer.step(); optimizer.zero_grad()
```

Rendering and latent image formation

Let $\{\mathbf{x}_i\}_{i=1}^{N}$ be the stratified samples along a camera ray with spacings Δ_i. The field outputs $(\mathbf{c}_i, \sigma_i) = f_\theta(\mathbf{x}_i, \mathbf{d})$ where $\mathbf{c}_i \in \mathbb{R}^4$ are Stable-Diffusion VAE latents and $\sigma_i \geq 0$ are densities. Using standard alpha compositing:

$$\alpha_i = 1 - \exp(-\sigma_i \Delta_i), \qquad T_i \;=\; \prod_{j<i} (1-\alpha_j), \tag{23.82}$$

$$w_i = T_i\, \alpha_i, \qquad \mathbf{z}(u,v) \;=\; \sum_{i=1}^{N} w_i\, \mathbf{c}_i \;\in\; \mathbb{R}^4, \tag{23.83}$$

so the rendered latent image $\mathbf{z} \in \mathbb{R}^{64\times 64\times 4}$ is obtained by evaluating (23.83) per pixel (u,v).

Diffusion guidance in latent space (SDS)

For a randomly drawn diffusion step t and Gaussian noise $\varepsilon \sim \mathcal{N}(0, I)$, the forward noising is

$$x_t \;=\; \sqrt{\bar{\alpha}_t}\, \mathbf{z} \;+\; \sqrt{1-\bar{\alpha}_t}\, \varepsilon, \tag{23.84}$$

and the per-pixel SDS gradient applied to $\mathbf{z}$ is

$$\nabla_{\mathbf{z}} \mathscr{L}_{\text{SDS}} \;=\; w(t)\, \big(\, \varepsilon_\phi(x_t, t, T) \;-\; \varepsilon \,\big), \tag{23.85}$$

where ε_ϕ is the frozen Stable Diffusion denoiser and $w(t)$ follows the noise schedule (scaling can absorb the $\sqrt{1-\bar{\alpha}_t}$ factor used in some SDS variants). Gradients backpropagate through (23.83) and (23.82) into θ.

Classifier-free guidance (CFG) in latent SDS

When using CFG, the denoiser is queried twice (with/without the text):

$$\hat{\varepsilon}_{\text{cfg}} \;=\; (1+s)\, \varepsilon_\phi(x_t, t, T) \;-\; s\, \varepsilon_\phi(x_t, t, \varnothing), \quad s \geq 0, \tag{23.86}$$

and ε_ϕ in (23.85) is replaced by $\hat{\varepsilon}_{\text{cfg}}$. This preserves the SDS form while strengthening text adherence.

Sparsity / anti-fog regularization

A well-known failure mode in NeRF optimization is the tendency to produce "floaters" (detached blobs of density) or a diffuse "fog" spread throughout the volume. Both artifacts can satisfy the supervision signal (e.g., SDS) from certain views, but they yield incoherent or implausible 3D structure. To combat this, Latent-NeRF introduces a sparsity prior on the *ray termination probability*.

Let w_i denote the volumetric weight at sample i along a ray, and define the ray's termination probability as

$$w_{\text{term}} \;=\; \sum_i w_i \;=\; 1 - T_{N+1},$$

where T_{N+1} is the residual transmittance at the end of the ray. Intuitively, w_{term} measures whether the ray "hit something" (value close to 1) or passed entirely through empty space (value close to 0).

The sparsity penalty applies the *binary entropy* function:

$$\mathscr{L}_{\text{sparse}} \;=\; -\, w_{\text{term}} \log w_{\text{term}} - \,(1-w_{\text{term}}) \log(1-w_{\text{term}}). \tag{23.87}$$

Why this works.

- The binary entropy function is minimized at $w_{\text{term}} = 0$ or 1, meaning the ray makes a *confident, binary decision*: either no surface was encountered, or a solid surface terminated the ray.
- The function peaks at $w_{\text{term}} = 0.5$, corresponding to maximum ambiguity. This case occurs when the model spreads low opacity across many samples, effectively creating fog. The loss strongly penalizes this outcome.

Effect on geometry. Minimizing $\mathscr{L}_{\text{sparse}}$ discourages semi-transparent mass and pushes density into compact, surface-like structures. This leads to:

1. *Suppression of floaters*: small blobs of density that contribute minor opacity become disfavored, since they push w_{term} away from 0 or 1.
2. *Crisp object boundaries*: instead of a gradual haze, rays either fully terminate on an object (opacity near 1) or pass cleanly through empty space (opacity near 0).

Relation to other regularizers. This objective serves the same purpose as the "opacity penalty" in DreamFusion and resembles distortion-based losses in Mip-NeRF 360, which also discourage opacity from being spread diffusely along rays. The key distinction here is its simplicity: the binary entropy prior directly penalizes uncertainty in ray termination, providing a lightweight yet effective "anti-fog" constraint that integrates seamlessly with SDS.

Total objective (normal/text-only mode)
Combining latent SDS with sparsity yields:

$$\mathscr{L}_{\text{total}} \;=\; \lambda_{\text{SDS}}\,\mathscr{L}_{\text{SDS}} \;+\; \lambda_{\text{sparse}}\,\mathscr{L}_{\text{sparse}}, \tag{23.88}$$

with $\mathscr{L}_{\text{SDS}}$ applied by integrating (23.85) over all pixels of $\mathbf{z}$ for the current camera. Typical implementation details include:

- *Camera sampling.* Uniform azimuth/elevation around the object with radius jitter; FoV drawn from a range to expose multiple scales.
- *t-sampling.* Uniform or cosine-weighted over diffusion steps; $w(t)$ chosen to balance early/late noise levels.
- *Gradient stabilization.* Stop-gradient on $\hat{\varepsilon}_{\text{cfg}}$ (teacher) and optional gradient clipping on $\nabla_{\mathbf{z}}\mathscr{L}_{\text{SDS}}$ before backpropagating through volume rendering.

Sketch-Shape guidance: Rationale and Mechanism

Why it is needed. Text-to-3D generation guided only by natural language is often *underspecified*: prompts such as "a wooden chair" or "a German Shepherd" describe appearance but rarely pin down a unique geometry. This lack of geometric priors can produce ambiguous or unstable reconstructions (e.g., Janus-like multiple faces, inconsistent body proportions). To mitigate this, Latent-NeRF introduces *Sketch-Shape guidance*, which supplies a coarse 3D proxy (e.g., composed of primitive shapes or a rough mesh) that defines global structure and pose. The text prompt then refines this scaffold by providing details, texture, and style. This decoupling of *geometry* (from the Sketch-Shape) and *appearance* (from text guidance) yields controllable, stable synthesis.

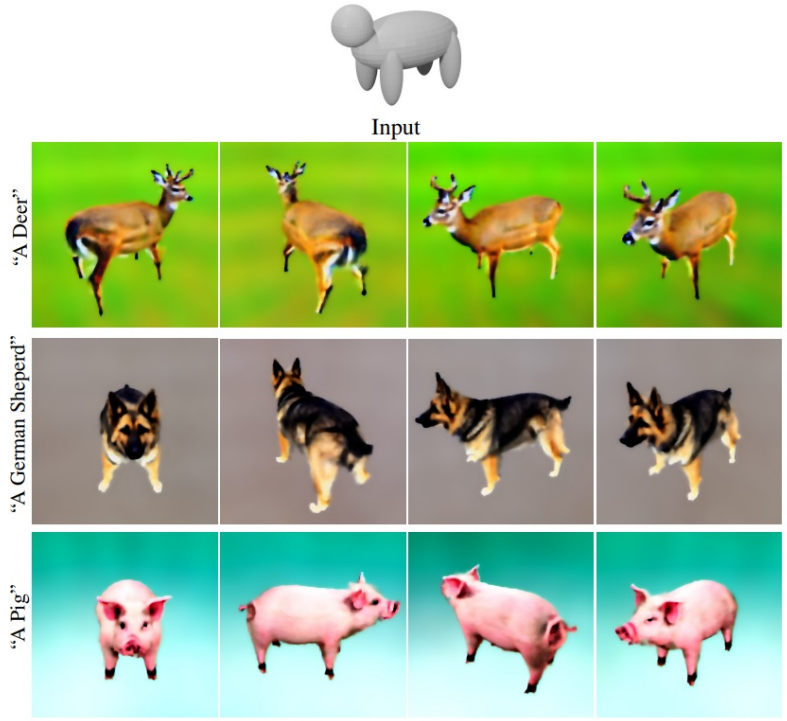

Figure 23.181: **Sketch-Shape results under different prompts.** One simple animal-like mesh guides distinct objects (*deer*, *German Shepherd*, *pig*); four views per result demonstrate 3D consistency. Source: [427].

How it works. The coarse shape is converted into a binary occupancy function, $\alpha_{\text{GT}}(p) \in \{0,1\}$, which marks whether a sampled point p along a camera ray lies inside or outside the proxy. The NeRF MLP is *not replaced* by a separate network; rather, the same radiance field MLP outputs its usual density σ and opacity $\alpha_{\text{NeRF}}(p)$. A distance-weighted cross-entropy loss then encourages α_{NeRF} to match α_{GT}:

$$\mathscr{L}_{\text{Sketch-Shape}} = \text{CE}\big(\alpha_{\text{NeRF}}(p), \alpha_{\text{GT}}(p)\big) \cdot \Big(1 - e^{-\frac{d^2}{2\sigma_S^2}}\Big), \tag{23.89}$$

where d is the distance from p to the Sketch-Shape surface, and σ_S controls the softness of the constraint.

Interpretation of the weighting. The exponential term modulates how strictly the constraint is enforced:

- Far from the surface (large d), the weight $\to 1$, so the NeRF is strongly penalized if its occupancy diverges from the proxy. This preserves the global volume.
- Near the surface ($d \approx 0$), the weight $\to 0$, relaxing the constraint. Here, the NeRF is free to deviate from the coarse proxy and follow gradients from the text-conditioned SDS loss. This enables addition of fine details (fur, ornaments, textures) without being locked into the proxy's crude geometry.

The parameter σ_S tunes this tradeoff: small values enforce tight adherence to the proxy, while larger values allow more stylistic freedom.

Integration. The Sketch-Shape loss is evaluated on the *same set of ray samples* already used for volumetric rendering, so no additional forward passes are needed. The NeRF MLP remains the sole predictor of densities and latents; the proxy only contributes distance and occupancy values for loss computation. This design makes Sketch-Shape guidance a lightweight addition that integrates seamlessly with the main SDS optimization, combining coarse geometric supervision with text-driven refinement.

Effect of the leniency parameter σ_S

Increasing σ_S relaxes the constraint, enabling the NeRF geometry to deviate more from the input shape under textual pressure.

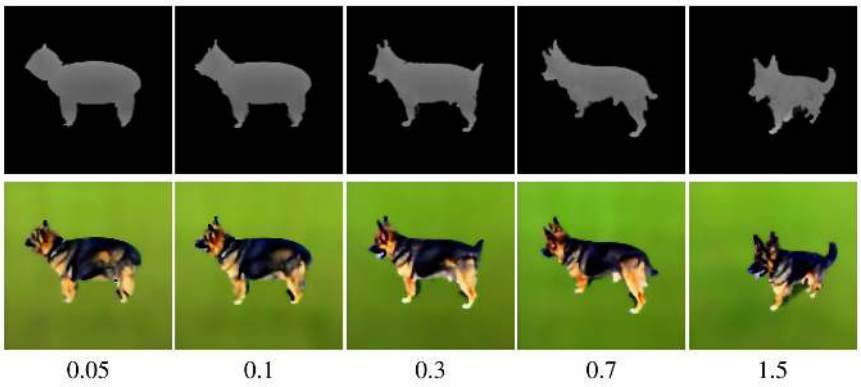

Figure 23.182: **Ablation over σ_S in Eq. 23.89.** Larger σ_S yields more lenient alignment and greater geometric evolution. Source: [427].

Latent-Paint for explicit meshes

When an explicit mesh with known UV coordinates is available, Latent-Paint enables texture optimization directly in the Stable Diffusion latent space.

UV coordinates. UVs are a standard graphics convention for mapping points on a 3D surface to positions in a 2D texture image. Each vertex on the mesh is assigned a (u, v) coordinate in $[0, 1]^2$, so that a 2D image can be "wrapped" around the 3D surface. If a mesh does not come with UVs, they can be automatically computed with algorithms such as *XAtlas*, which unfold the surface into a set of non-overlapping charts.

Mechanism. Latent-Paint defines a *latent texture image* $\Theta \in \mathbb{R}^{H\times W\times 4}$ in the same 4-channel space as Stable Diffusion's VAE. Differentiable rasterization maps each triangle of the mesh to the corresponding latent pixels of Θ, producing a rendered latent image from a given camera viewpoint. This image is then supervised by the same latent SDS rule used in Latent-NeRF: it is noised, denoised by the Stable Diffusion UNet, and the residual between predicted and injected noise provides gradients. These gradients backpropagate through the differentiable renderer to update the pixels of Θ.

After convergence, a *single decode* of Θ with the VAE decoder produces a high-resolution RGB texture image. The benefit of this approach is that it avoids per-pixel optimization in RGB space and instead leverages Stable Diffusion's compact latent representation to guide texture generation efficiently.

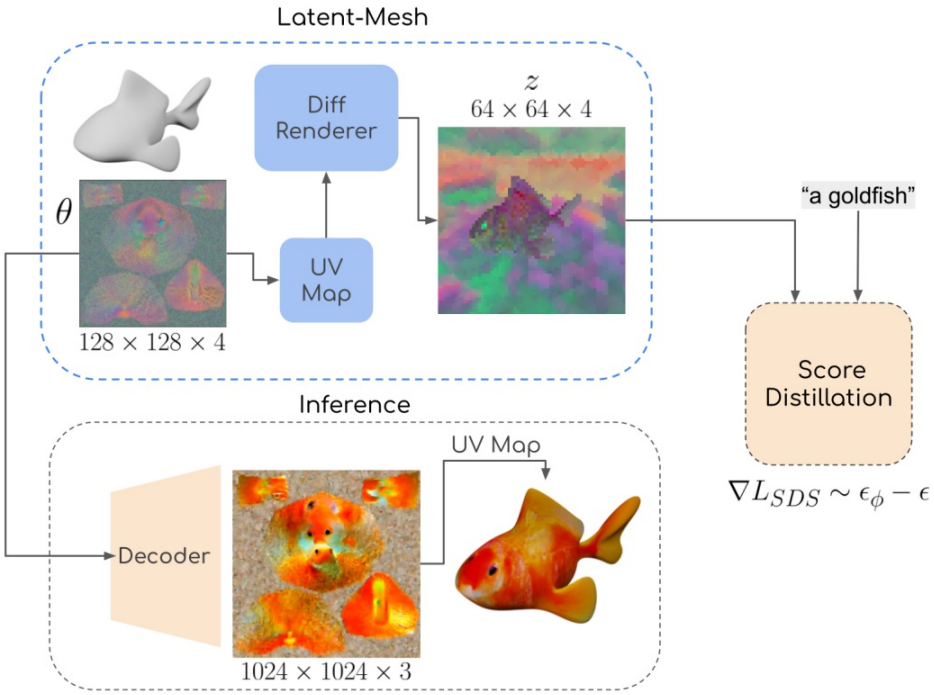

Figure 23.183: **Latent-Paint pipeline.** A $128\times128\times4$ latent texture is optimized by latent SDS through a differentiable renderer; a single VAE decode yields the final RGB texture. Source: [427].

RGB refinement with a learnable linear adapter

Although latent-space training is efficient, many applications (visualization, export, rendering) require a NeRF that emits RGB directly. To bridge this gap, Latent-NeRF adds a small *linear adapter* on top of the NeRF's four latent output channels $(c_1, \ldots, c_4)$. This adapter maps the latent channels to approximate RGB $(\hat{r}, \hat{g}, \hat{b})$ using a 3×4 matrix, initialized to a hand-fit linearization of the Stable Diffusion VAE decoder:

$$\begin{pmatrix} \hat{r} \\ \hat{g} \\ \hat{b} \end{pmatrix} = \begin{pmatrix} 0.298 & 0.187 & -0.158 & -0.184 \\ 0.207 & 0.286 & 0.189 & -0.271 \\ 0.208 & 0.173 & 0.264 & -0.473 \end{pmatrix} \begin{pmatrix} c_1 \\ c_2 \\ c_3 \\ c_4 \end{pmatrix}. \tag{23.90}$$

This initialization is only a starting point; the matrix is made *trainable* and updated during refinement.

What parameters are trained.

- *NeRF MLP weights* (geometry and latent features): the network that outputs densities σ and latent channels $(c_1, \ldots, c_4)$ continues to be optimized.
- *Adapter weights* (the 3×4 matrix): this layer learns a better mapping from the four latent channels to RGB.

Both components co-adapt: the NeRF learns to emit latent features that decode to better colors, and the adapter learns how to colorize those features effectively.

How RGB participates in the loss.

- The NeRF with the adapter renders an RGB image $\hat{I}_{\text{RGB}}$ (via volumetric compositing of $(\hat{r}, \hat{g}, \hat{b})$ and σ).
- $\hat{I}_{\text{RGB}}$ is passed through the (frozen) VAE encoder to obtain a latent code z'.
- Score Distillation Sampling (SDS) is applied *in latent space* on z' using the text-conditioned denoiser; this yields gradients.
- Gradients backpropagate through the encoder (no updates), then through the RGB image, adapter, volume renderer, and into the NeRF MLP.

Thus, even though the supervision remains in Z, the RGB pathway *matters*: the only way to make z' align with the text-conditioned score is to render RGB that, when re-encoded, produces better latents. This couples pixel-space fidelity to the latent-space objective.

Why this matrix and how it improves.

- *Initialization:* the matrix in Eq. 23.90 approximates the VAE decoder's local colorization, providing coherent initial RGB previews rather than arbitrary colors.
- *Learning signal:* there is no ground-truth RGB. Improvement is measured by how well the *re-encoded* latents z' satisfy SDS. Lower SDS loss implies better alignment; gradients adjust both the adapter matrix and NeRF MLP accordingly.
- *Why not decode with the full VAE decoder* $\mathbf{D}$ *each step?* Inserting a deep CNN into every volumetric rendering iteration would be prohibitively slow, and SDS still requires returning to Z. The adapter achieves a fast, differentiable RGB bridge without dragging $\mathbf{D}$ through the ray-marching loop.

Why refinement helps.

- Latent-only training captures semantics but can under-express pixel-space sharpness due to decoder limitations.
- The refinement loop biases the field toward RGB detail: the NeRF learns to place and modulate high-frequency color directly, while SDS—applied after re-encoding—keeps the result text-faithful and multi-view consistent.

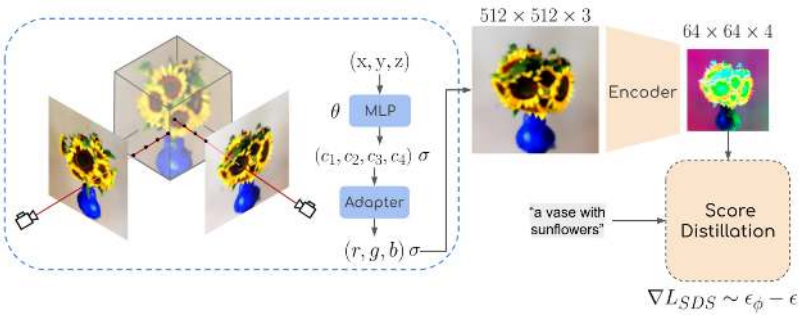

Figure 23.184: **RGB fine-tuning strategy.** Starting from a Latent-NeRF trained in *latent space*, a trainable matrix adapter maps the four latent channels to RGB to obtain an RGB preview. The system then continues optimization with *supervision in RGB*: render an RGB view, *re-encode* it with the VAE encoder to Z, and apply the same SDS guidance. Gradients update both the NeRF MLP and the adapter, improving high-frequency color/detail while retaining the robustness of latent-space supervision. Source: [427].

Architecture and Implementation Details

Backbones

Stable Diffusion v1-4 (HuggingFace Diffusers) provides the VAE (E, D) and UNet denoiser ε_ϕ; Instant-NGP serves as the NeRF backbone for efficiency. Latent rendering uses $64\times64\times4$ maps; Latent-Paint uses $H = W = 128$ latent textures by default.

Schedules and regularizers

SDS uses Eq. 23.84–23.85 with $w(t)$ tied to the diffusion schedule. A binary-entropy sparsity term $\mathrm{BE}(w_{\text{blend}})$ suppresses floaters and encourages strict object/background blending. Sketch-Shape uses Eq. 23.89 over the point set already sampled for volumetric rendering.

Experiments and Ablations

Text-only generation and multi-view consistency

Latent-NeRF produces coherent 3D assets under text-only guidance; view sweeps confirm stable geometry and appearance.

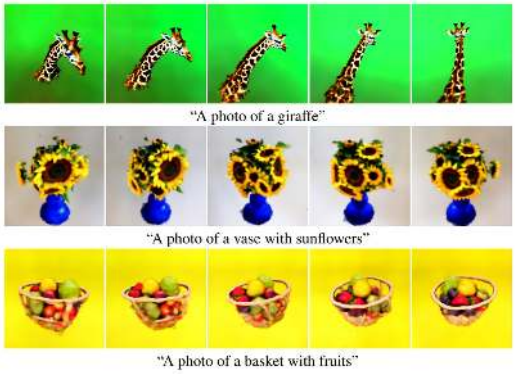

Figure 23.185: **Results from different viewpoints.** Examples include "A photo of a giraffe", "A photo of a vase with sunflowers", and "A photo of a basket with fruits", rendered from multiple views to demonstrate 3D consistency. Source: [427].

Qualitative comparison

Against DreamFields, CLIPMesh, and DreamFusion, Latent-NeRF typically shows sharper textures and more plausible geometry for identical prompts.

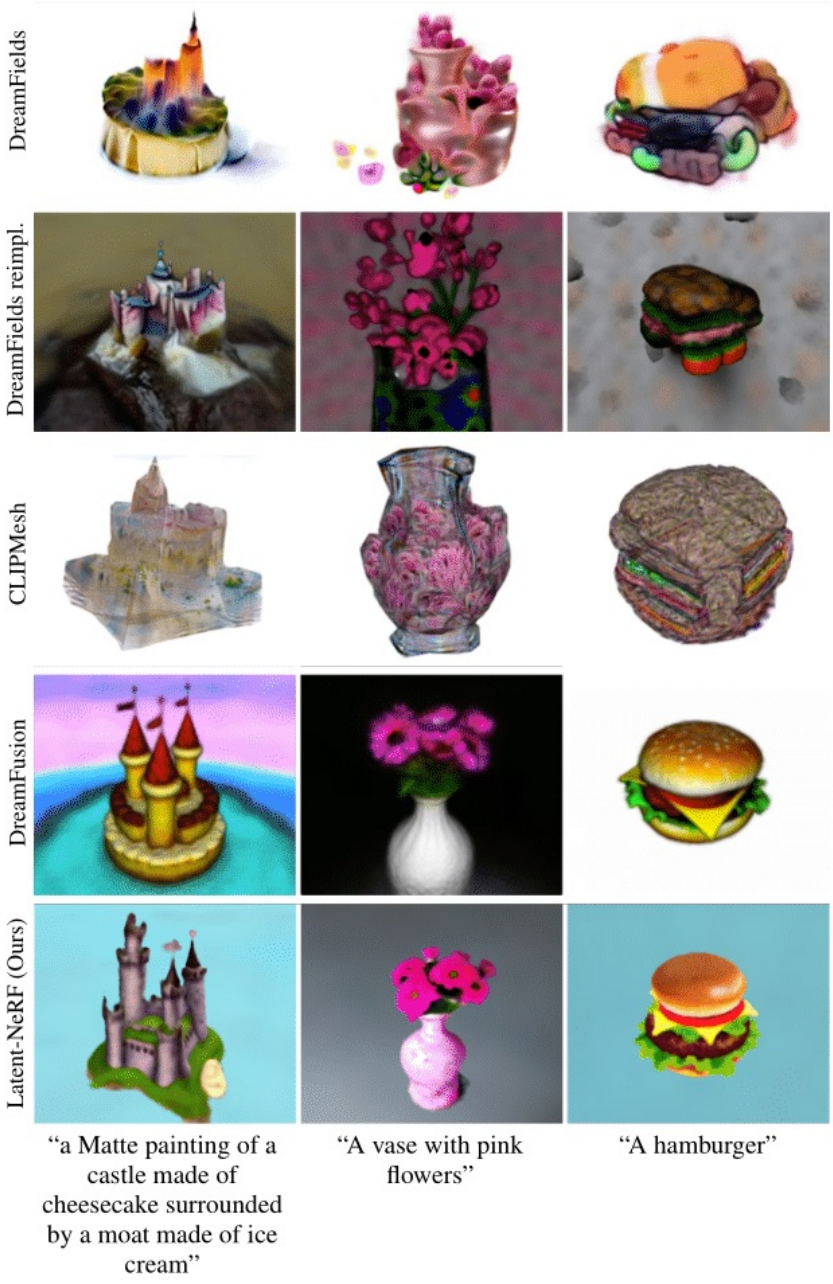

Figure 23.186: **Qualitative comparison.** Rows: DreamFields/reimpl., CLIPMesh, DreamFusion, Latent-NeRF. Columns: prompts such as *castle*, *vase*, *hamburger*. Latent-NeRF yields detailed and prompt-faithful geometry and materials. Source: [427].

RGB refinement improvements

Refinement enhances high-frequency detail (textures, material cues) beyond what the VAE decoder alone produces.

Figure 23.187: **RGB refinement results.** Improvements are shown for latent text-to-3D (ice cream, temple) and Sketch-Shape (lego, car); per-pixel normals visualize geometry. Source: [427].

Controllability via Sketch-Shape

Using identical prompts with and without shape guidance reveals strong benefits for geometric coherence.

Figure 23.188: **Ablation on shape guidance.** With vs. without Sketch-Shape under identical prompts (*robot hand*, *lego man*) shows the role of geometric priors in eliminating wispy, incoherent structures. Source: [427].

More Sketch-Shape results

A simple house prior can be styled in multiple ways; further examples span hands, toys, and vehicles.

Figure 23.189: **House prior under multiple styles.** *Lego*, *gingerbread*, *gothic*, and *candy*; RGB refinement is applied for detail. Source: [427].

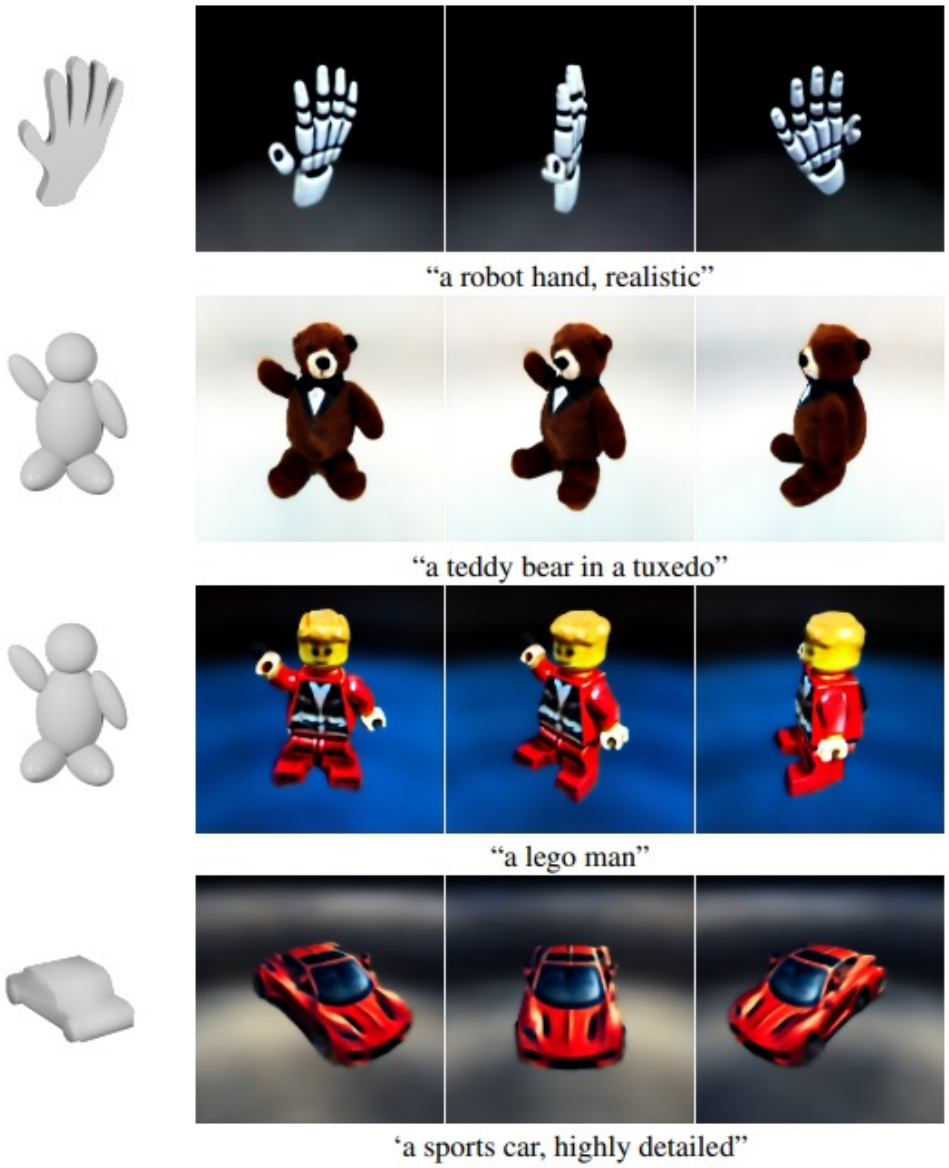

Figure 23.190: **Additional Sketch-Shape examples.** *Robot hand*, *teddy bear in a tuxedo*, *lego man* demonstrate cross-category controllability. Source: [427].

Latent-Paint on generic meshes

Text-driven textures can be applied to shapes without UVs (computed on-the-fly) or with precomputed UVs.

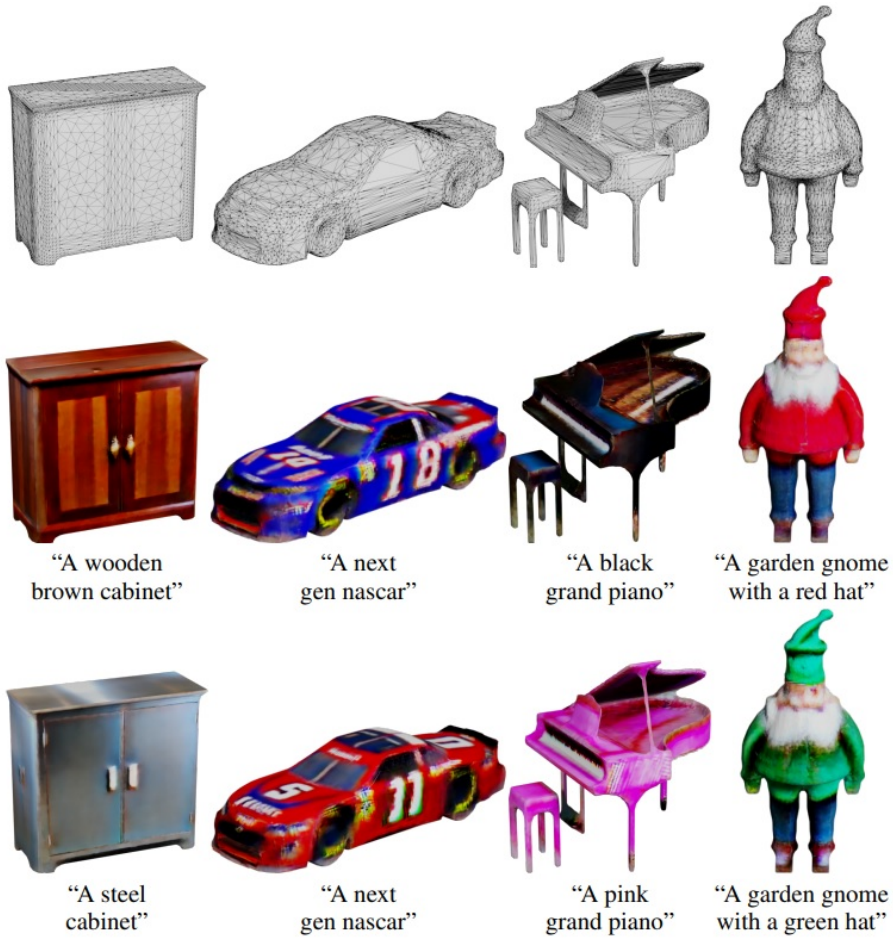

Figure 23.191: **Latent-Paint on ModelNet40 meshes.** UVs absent in inputs; XAtlas is used. Variation across seeds is shown on NASCAR; material/style shifts illustrated on cabinet, piano, and gnome. Source: [427].

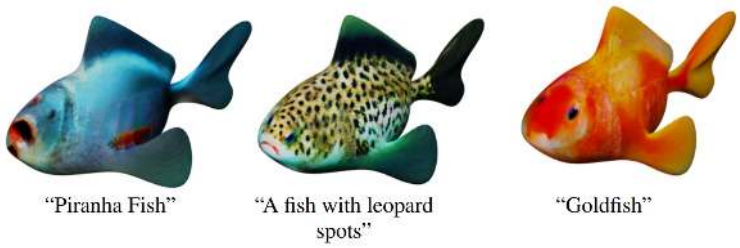

Figure 23.192: **Latent-Paint with precomputed UVs.** A single fish mesh textured as *piranha*, *leopard-spotted fish*, and *goldfish*. Source: [427].

Texturing comparison on a common mesh

Latent-Paint produces textures that are more realistic and prompt-faithful than CLIP-guided baselines.

Figure 23.193: **Boot texturing comparison.** Rows: Tango, CLIPMesh, Latent-Paint. Columns: *black boot*, *blue Converse All-Star*, *UGG boot*. Latent-Paint captures correct materials and iconic details. Source: [427].

Personalization via Textual Inversion

Latent-NeRF inherits the ability to use learned tokens for novel objects/styles, enabling faithful reconstruction and creative composition.

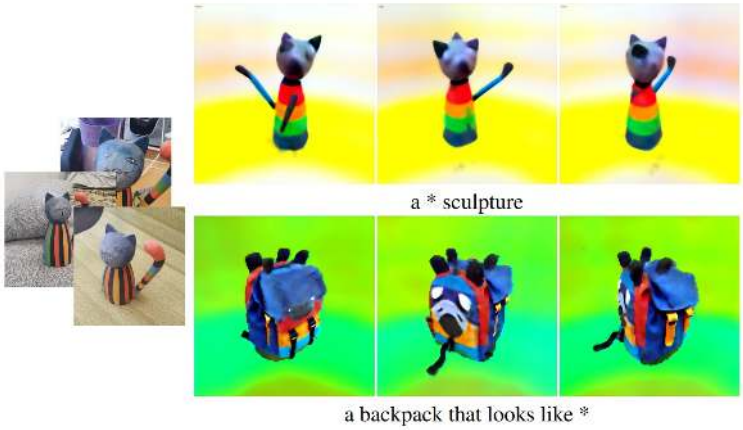

Figure 23.194: **Textual Inversion.** A token learned from few images enables generating "a * sculpture" and composing "a backpack that looks like *". Source: [427].

Limitations and Future Work

View ambiguity and Janus artifacts

Because Latent-NeRF relies on a 2D prior, supervision for unseen views is weak. This often causes *Janus artifacts*, such as multi-faced geometry (e.g., a squirrel with two faces), where the denoiser defaults to canonical front views rather than plausible backs.

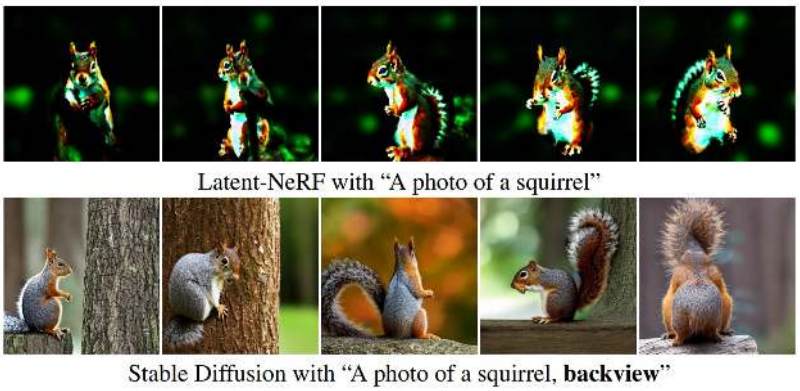

Figure 23.195: **Janus artifact.** A "squirrel" generated with Latent-NeRF shows two faces from different views, caused by the 2D diffusion prior failing on unseen backs. Source: [427].

Controllability and future directions

Controllability remains limited: results vary with seed, and prompts can be ambiguous. The paper mitigates this with shape priors (Sketch-Shape), explicit texturing (Latent-Paint), and opacity regularization, but these do not fully solve view inconsistency. Future directions include integrating other, possibly stronger, 3D priors (depth or normal cues), exploring 3D-native diffusion backbones, and extending beyond UV textures to richer material models such as BRDFs.